



TECHNICAL REPORT 0-7039-1
TxDOT PROJECT NUMBER 0-7039

The Development of Knowledge in the Application of Strut-and-Tie Methods

Hwa-Ching Wang
Anas Daou
Ayah Alomari
Jongkwon Choi
Thinh Dinh
Yibin Shao
Yousun Yi
Zach Webb
Oguzhan Bayrak

May 2023

<http://library.ctr.utexas.edu/ctr-publications/0-7039-1.pdf>



Technical Report Documentation Page

1. Report No. FHWA/TX-23/0-7039-1		2. Government Accession No.		3. Recipient's Catalog No.	
4. Title and Subtitle The Development of Knowledge in the Application of Strut-and-Tie Method				5. Report Date Submitted: May 2023	
				6. Performing Organization Code	
7. Author(s) Hwa-Ching Wang, Anas Daou, Ayah Alomari, Jongkwon Choi, Thinh Dinh, Yibin Shao, Yousun Yi, Zach Webb, Oguzhan Bayrak				8. Performing Organization Report No. 0-7039	
9. Performing Organization Name and Address Center for Transportation Research The University of Texas at Austin 3925 W. Braker Lane, 4 th Floor Austin, TX 78759				10. Work Unit No. (TRAIS)	
				11. Contract or Grant No. 0-7039	
12. Sponsoring Agency Name and Address Texas Department of Transportation Research and Technology Implementation Division P.O. Box 5080 Austin, TX 78763-5080				13. Type of Report and Period Covered Technical Report September 2020 – May 2023	
				14. Sponsoring Agency Code	
15. Supplementary Notes Project performed in cooperation with the Texas Department of Transportation.					
16. Abstract The strut-and-tie method (STM) is a reliable and widely used approach for designing reinforced concrete members, but there are still gaps in knowledge that need to be addressed to optimize its use in common design scenarios. Addressing these gaps would lead to more efficient and cost-effective design solutions. This requires additional experimental data to inform design codes and practices related to key areas, such as tri-axial tension anchorage, curved-bar nodes, confining reinforcement in nodal zones, and crack control reinforcement spacing. Chapters 3-6 of the research report describe the experimental investigations conducted to address some of these knowledge gaps. Chapter 3 presents insights into the behavior of drilled shaft reinforcement under tri-axial tension and the validity of the design recommendation. Chapter 4 investigates the effect of the bend radius on the behavior of closing knee joints and recommends an equation for designing curved-bar nodes. Chapter 5 examines the effect of nodal zone confinement on nodal strength, concluding that effective confining reinforcement can increase nodal strength. Lastly, Chapter 6 investigates the possibility of relaxing crack control reinforcement spacing and recommends a new maximum spacing. Overall, the research findings provide valuable insights into the behavior of reinforced concrete members and suggest improvements for STM design practices.					
17. Key Words Strut and tie method, reinforced concrete design, footing, deep beam, frame corner, curved-bar node, crack control reinforcement, nodal confinement				18. Distribution Statement No restrictions. This document is available to the public through the National Technical Information Service, Springfield, Virginia 22161; www.ntis.gov .	
19. Security Classif. (of report) Unclassified	20. Security Classif. (of this page) Unclassified		21. No. of pages 309		22. Price



**THE UNIVERSITY OF TEXAS AT AUSTIN
CENTER FOR TRANSPORTATION RESEARCH**

The Development of Knowledge in the Application of Strut-and-Tie Method

Hwa-Ching Wang
Anas Daou
Ayah Alomari
Jongkwon Choi
Thinh Dinh
Yibin Shao
Yousun Yi
Zachary D. Webb
Oguzhan Bayrak

CTR Technical Report:	0-7039-1
Report Date:	Submitted: May 2023
Project:	0-7039
Project Title:	Development of Knowledge in the Application of Strut-and-Tie Modeling
Sponsoring Agency:	Texas Department of Transportation
Performing Agency:	Center for Transportation Research at The University of Texas at Austin

Project performed in cooperation with the Texas Department of Transportation and the Federal Highway Administration.

Center for Transportation Research
The University of Texas at Austin
3925 W. Braker Lane, 4th floor
Austin, TX 78759

<http://ctr.utexas.edu/>

Disclaimers

Author's Disclaimer: The contents of this report reflect the views of the authors, who are responsible for the facts and the accuracy of the data presented herein. The contents do not necessarily reflect the official view or policies of the Federal Highway Administration or the Texas Department of Transportation (TxDOT). This report does not constitute a standard, specification, or regulation.

Patent Disclaimer: There was no invention or discovery conceived or first actually reduced to practice in the course of or under this contract, including any art, method, process, machine manufacture, design or composition of matter, or any new useful improvement thereof, or any variety of plant, which is or may be patentable under the patent laws of the United States of America or any foreign country.

Engineering Disclaimer

NOT INTENDED FOR CONSTRUCTION, BIDDING, OR PERMIT PURPOSES.

Project Engineer: Oguzhan Bayrak

Professional Engineer License State and Number: Texas No. 106598

P.E. Designation: Research Supervisor

Acknowledgments

The authors express deep appreciation to the Texas Department of Transportation (TxDOT) for providing the funds and supports to conduct this research study. The contributions of the project manager Martin Dassi (RTI Division) and other members of the Project Monitoring Committee – Anthony Felderhoff, Hunter Walton, Sara Watts, Seth Cole, and Victoria McCammon – facilitated great improvements to the outcome of this project.

Table of Contents

Chapter 1. Introduction	1
1.1. Overview	1
1.2. Project Scope and Objective	3
1.3. Organization.....	3
Chapter 2. Literature Review	5
2.1. Introduction.....	5
2.2. Rebar Development at Nodes under Three Orthogonal Ties.....	5
2.2.1. Experimental and Analytical Studies on Drilled Shaft Footings	6
2.2.2. Findings and Research Needs	8
2.3. Curved-Bar Nodes	8
2.3.1. STM Provisions in Code Specifications	9
2.3.2. Experimental and Analytical Studies.....	11
2.3.3. Findings and Research Needs	17
2.4. Confined Nodal Regions.....	18
2.4.1. STM Provisions in Code Specifications	18
2.4.2. Experimental and Analytical Studies.....	20
2.4.3. Findings and Research Needs	29
2.5. Spacing Limits for Crack Control Reinforcement	30
2.5.1. STM Provisions in Code Specifications	30
2.5.2. Experimental & Analytical Research Studies.....	32
2.5.3. Findings and Research Needs	40
2.6. Summary	41
Chapter 3. Nodes under Tri-Axial Tension.....	43
3.1. Introduction.....	43
3.2. Experimental Program	45
3.2.1. Specimen Design	45
3.2.2. Instrumentation	56
3.2.3. Fabrication of Specimen	60
3.2.4. Test Frame	62
3.2.5. Test Procedure	64
3.3. Experimental Results and Discussion.....	64
3.3.1. Summary of Strength Results	64
3.3.2. Visual Observation.....	65

3.3.3. Load-deflection Response.....	67
3.3.4. Strain Distribution in Bottom Mat Reinforcement	68
3.3.5. Strain Distribution in Skin Reinforcement	69
3.3.6. Stress Profiles and Bond Stress Profiles of Drilled Shaft Reinforcement.....	70
3.4. Assessment of Design Recommendation of Project 0-6953.....	74
3.5. Summary	76
Chapter 4. Curved-bar Nodes	78
4.1. Introduction.....	78
4.2. Experimental Program	79
4.2.1. Specimen Design	79
4.2.2. Fabrication of Specimens.....	85
4.2.3. Test Frame	87
4.2.4. Instrumentation	89
4.2.5. Test Procedure	91
4.3. Experimental Results and Discussion.....	91
4.3.1. Summary of Strength Results	91
4.3.2. Load-Displacement Behavior and Damage Pattern.....	93
4.3.3. Bar Development and Digital Image Correlation (DIC).....	104
4.4. Evaluation of Strength and Failure Modes	111
4.4.1. Effect of Bend Radius and Diagonal Strut Angle.....	111
4.4.2. Effect of Diagonal Strut Angle	112
4.4.3. Effect of Arrangement of Reinforcement	113
4.4.4. General Discussion on Strength and Failure Modes.....	113
4.5. Evaluation of Design Expression for Curved-bar Nodes.....	115
4.5.1. Bend Radius Considering Radial Stresses	115
4.5.2. Bend Radius Considering Circumferential Bond Stresses.....	117
4.6. Assessment of Serviceability	118
4.7. Structural Capacity using the STM.....	120
4.7.1. Dimensions of Specimen of Interest	120
4.7.2. Selection of Strut-and-tie Models	121
4.7.3. Determination of Forces	122
4.7.4. Sizing Nodal Zones.....	122
4.7.5. Determination of Analytical Ultimate Capacity	124
4.7.6. Selection of Efficiency Factors	126

4.7.7. Results and Discussion	127
4.8. Finite Element Analysis	132
4.8.1. Model Preparation	132
4.8.2. Results and Discussion	137
4.9. Design Recommendations	142
4.9.1. Design Expressions for Curved-bar Node	142
4.9.2. Design Example using the STM with a Curved-bar Node	143
4.10. Summary	151
Chapter 5. Nodal Confinement	153
5.1. Introduction	153
5.2. Experimental Program	154
5.2.1. Specimen Design	154
5.2.2. Fabrication of Specimens	160
5.2.3. Test Setup and Instrumentation	164
5.2.4. Test Procedure	168
5.3. Test Results	169
5.3.1. Summary of Strength Results	169
5.3.2. Failure Patterns	171
5.3.3. Visual Observations	174
5.3.4. Strains and Damage Patterns	176
5.3.5. Digital Image Correlation Results	186
5.4. Analysis of Test Results	192
5.4.1. Evaluation of Strength with Sectional Shear Strength	192
5.4.2. Evaluation of AASHTO LRFD's STM Provisions	195
5.5. Design Recommendations	202
5.6. Summary	203
Chapter 6. Spacing of Web Reinforcement	205
6.1. Introduction	205
6.2. Experimental Program	206
6.2.1. Specimen Design	206
6.2.2. Specimen Fabrication and Strain Gauging	213
6.2.3. Test Setup	217
6.2.4. Testing Procedure	221
6.3. Test Results and Discussion	222

6.3.1. Summary of Strength Results and Material Testing Data	222
6.3.2. Ultimate Strength Results and Comparison to STM Estimations.....	226
6.3.3. Comparison to Project 0-5253 Companion Specimens	228
6.3.4. Serviceability Results and Analysis.....	240
6.3.5. Crack Control Reinforcement Engagement	251
6.3.6. Longitudinal Strains.....	257
6.3.7. Digital Image Correlation Measurements.....	263
6.4. Finite Element and Parametric Study	265
6.4.1. FE Model Preparation	265
6.4.2. FE Model Validation.....	269
6.4.3. FE Parametric Analysis.....	271
6.5. Summary	283
6.5.1. Summary of Experimental Program and FEA	283
6.5.2. Suggested modification to AASHTO LRFD design provisions and Future Studies	284
Chapter 7. Conclusions	285
References	288
Appendix A. Intermediate Results of Strut-and-Tie Models of Test Portal Specimens	296
A-1 General Sizing Method	296
A-2 Simplified Sizing Method.....	297
Appendix B. Analysis Example using the STM	299
B-1. Geometries of Strut-and-Tie Model.....	299
B-2. Estimated Capacities per AASHTO LRFD 2020	301
B-3. V_{test} and V_{STM_Calc} Sample Calculation.....	303
Appendix C. Proposed Changes to AASHTO LRFD (2008) Bridge Design Specification	304

List of Tables

Table 3-1 Test Matrix	47
Table 3-2 Concrete mixture proportions for footing specimens	62
Table 3-3 Summary of experimental results	65
Table 3-4 Anchorage Checks performed with the recommendation of Project 0-6953.....	76
Table 4-1 Test matrix.....	81
Table 4-2 Summary of key specimen geometry	81
Table 4-3 Concrete mixture proportions for all specimens	87
Table 4-4 Summary of test results	92
Table 4-5 Summary of analytical results for curved-bar nodes per Eq. (2-1)	116
Table 4-6 Summary of analytical results for curved-bar nodes per Eq. (2-3)	117
Table 4-7 Member forces of the strut-and-tie model	122
Table 4-8 Efficiency factors used for the STM analysis.....	127
Table 4-9 Summary of analytical results using the general sizing method	127
Table 4-10 Summary of analytical results using the simplified sizing method..	130
Table 4-11 Concrete material parameters used in the FEA	133
Table 4-12 Reinforcement material parameters.....	133
Table 4-13 Elastic material parameters.....	134
Table 4-14 Efficiency factors for the design example	149
Table 4-15 Evaluation of Node H.....	149
Table 5-1 Test Matrix	156
Table 5-2 Resulting Confinement Ratio	157
Table 5-3 Concrete mixture design.....	161
Table 5-4 Summary of Strength Results.....	170
Table 5-5 Sizing results of CCC node and CCT node	197
Table 5-6 Efficiency factor of CCC node	198
Table 5-7 Efficiency factor of CCT node	201
Table 6-1 Specimen testing details	207
Table 6-2 Concrete mixture proportions for all specimens	216
Table 6-3 Summary of material testing results from all specimens.....	217
Table 6-4 Summary of Experimental Results	224

Table 6-5 Tolerable widths of flexural cracks per design provisions at the time of Project 0-5253	240
Table 6-6 Tolerable widths of flexural cracks	241
Table 6-7 Concrete material “3D Nonlinear Cementitious” parameters	266
Table 6-8 Reinforcement material parameters.....	267
Table 6-9 Elastic material parameters.....	267
Table 6-10 Summary of number of numerical specimens	272
Table 6-11 Web reinforcement spacings for deep beams of 21 in. by 42 in. with $a/d=1.85$	272
Table 6-12 Web reinforcement spacings for deep beams of 21 in. by 42 in. with $a/d=1.2$	273
Table 6-13 Web reinforcement spacings for deep beams of 21 in. by 75 in. with $a/d=1.85$	273
Table 6-14 Web reinforcement spacings for deep beams of 21 in. by 75 in. with $a/d=1.2$	273
Table 6-15 Concrete material parameters for numerical deep beam of 21 in. by 42 in.	276
Table 6-16 Concrete material parameters for numerical deep beam of 21 in. by 75 in.	277
Table 6-17 Summary of analytical results	278

List of Figures

Figure 2-1 The STM on drilled shaft footing with column having tension side (Williams et al. 2012)	6
Figure 2-2 Strut-and-tie model for drilled shaft footing of which two drilled shafts are in tension (Yousun et al. 2021)	7
Figure 2-3 Compression field and critical section for drilled shaft reinforcement (Yousun et al. 2021).....	7
Figure 2-4 Curved-bar node at outside of frame corner under closing moments (ACI 318-19, 2019).....	9
Figure 2-5 Free body diagram of curved-bar nodes (ACI 318-19).....	10
Figure 2-6 Strut-and-tie model with curved-bar node of frame corner under closing moments	11
Figure 2-7 Design example of cantilever bent cap (from Williams et al. 2012) ..	13
Figure 2-8 Deep beam to be designed in Martinez et al. (2017) (from Martinez et al. 2017)	13

Figure 2-9 Truss models used in Martinez et al. (2017) (from Martinez et al. 2017)	14
Figure 2-10 Design results for Truss model S1 (from Martinez et al. 2017).....	14
Figure 2-11 Strut-and-tie model and curved-bar node in Wang et al. (2020, 2020, and 2022)	15
Figure 2-12 Specimen and test setup used in Wang et al. (2020, 2020, and 2022)	15
Figure 2-13 Stress transmission along the bar (Ingham 1995, Wang et al. 2020)	16
Figure 2-14 Bearing stress distribution (from AASHTO LRFD 2020)	19
Figure 2-15 Distribution for partially loaded area (from CEB-FIP Model Code 2010 and Eurocode 2)	20
Figure 2-16 Examples of typical failure modes (from Hawkins 1968)	21
Figure 2-17 Schematic of test setup (from Adebar and Zhou 1993)	22
Figure 2-18 Typical slab specimens (Furuuchi et al. 1998).....	24
Figure 2-19 Details of CCT nodal zone (Thompson et al. 2002)	25
Figure 2-20 Triaxially confined node tests (from Tuchsherer et al. 2010)	27
Figure 2-21 Details of specimens (from Geevar and Menon 2019)	28
Figure 2-22 Confined strength from lateral confining stresses (from Mander et al. 1988)	29
Figure 2-23 Stress concentration of diagonal strut mechanism (from Anderson and Ramirez 1989).....	32
Figure 2-24 Details of beam specimens (from Yoon et al. 1996).....	33
Figure 2-25 Investigated types of web reinforcement (from Tan et al. 1997)	34
Figure 2-26 Specimens and test setup (from Angelakos et al. 2001)	35
Figure 2-27 Example deep beam specimen design from Febres et al (2006).....	36
Figure 2-28 Deep beam specimen layouts and test frame (from Tuchschrer et al. 2011)	37
Figure 2-29 Specimen design parameters (from Zhang et al. 2020).....	39
Figure 2-30 Nodal efficiency factors selected for evaluation database analysis (from Zaborac et al.)	40
Figure 3-1 Generalized 3D strut-and-tie model for drilled shaft footings under pure axial load (from Project 0-6953).....	43
Figure 3-2 3D strut-and-tie model for drilled shaft footing of which shafts are in tension (from Project 0-6953)	44
Figure 3-3 Compression field and critical section for drilled shaft reinforcement	44
Figure 3-4 Strut-and-tie model for drilled-shaft footing with reduced height	46

Figure 3-5 Specimen Design.....	47
Figure 3-6 Altered load path in footing specimen	48
Figure 3-7 Specimen design and detail	49
Figure 3-8 Nomenclature for specimens.....	53
Figure 3-9 Finite element model of test specimens	54
Figure 3-10 Total load on drill shaft versus vertical displacement.....	55
Figure 3-11 Stress variation along drill shaft bars	56
Figure 3-12 Instrumentation – top view.....	57
Figure 3-13 Strain gauge layout on surface reinforcement (Specimen I).....	58
Figure 3-14 Strain gauge layout on surface reinforcement (Specimen II).....	58
Figure 3-15 Strain gauge positions installed at drilled shaft reinforcement	59
Figure 3-16 Procedure of footing specimen fabrication	60
Figure 3-17 Lenton Terminators for headed bars	61
Figure 3-18 Test setup for planned equivalent loading	63
Figure 3-19 Detail of connection between drilled shaft reinforcement and adopter plate.....	64
Figure 3-20 Crack maps of test specimens	66
Figure 3-21 Visual inspection at loading plate after testing	67
Figure 3-22 Overall structural behavior of tests	68
Figure 3-23 Strain distribution in bottom mat reinforcement at 400 kip.....	69
Figure 3-24 Bar stress profiles of drilled shaft reinforcement.....	71
Figure 3-25 Bond stress profiles of drilled shaft reinforcement	73
Figure 3-26 Available length estimation based on the design recommendation of Project 0-6953	74
Figure 4-1 Strut-and-tie model for closing moment at a frame corner	78
Figure 4-2 Specimen geometry and definition of parameters.....	80
Figure 4-3 General reinforcement layout.....	82
Figure 4-4 Reinforcement detail of specimens in Series A	83
Figure 4-5 Reinforcement detail of specimens in Series B.....	83
Figure 4-6 Reinforcement detail of specimens in Series C.....	84
Figure 4-7 Reinforcement detail of specimens in Series D	84
Figure 4-8 Nomenclature	85
Figure 4-9 Fabrication of specimen	86

Figure 4-10 Measuring bend radius	87
Figure 4-11 Test frame.....	88
Figure 4-12 Sensors	89
Figure 4-13 Layout of sensors	90
Figure 4-14 DIC system.....	91
Figure 4-15 Normalization of joint shear.....	93
Figure 4-16 Load-displacement relationship of Series A	93
Figure 4-17 Damage pattern after failure of Series A.....	94
Figure 4-18 Comparison of crack width in Series A	95
Figure 4-19 Effect of heavy reinforcement on crack growing of Series A.....	96
Figure 4-20 Load-displacement relationship of Series D	97
Figure 4-21 Damage pattern after failure of Series D.....	97
Figure 4-22 Comparison of crack width in Series D	98
Figure 4-23 Effect of heavy reinforcement on crack growing of Series D.....	98
Figure 4-24 Load-displacement relationship of Series B	99
Figure 4-25 Damage pattern after end of test of Series B.....	100
Figure 4-26 Comparison of crack width in Series B.....	100
Figure 4-27 Effect of heavy reinforcement on crack growing of Series B.....	101
Figure 4-28 Load-displacement relationship of Series C	102
Figure 4-29 Damage pattern after failure of Series C.....	102
Figure 4-30 Comparison of crack width in Series C.....	103
Figure 4-31 Effect of heavy reinforcement on crack growing of Series C.....	103
Figure 4-32 Bar stress distribution and concrete strain in the joint of Specimen A-R6-45.....	105
Figure 4-33 Bar stress distribution and concrete strain in the joint of Specimen A-R11-45.....	106
Figure 4-34 Bar stress distribution and concrete strain in the joint of Specimen A-R9-45.....	106
Figure 4-35 Bar stress distribution and concrete strain in the joint of Specimen D-R11-45(T)	107
Figure 4-36 Bar stress distribution and concrete strain in the joint of Specimen D-R11-45(B)	107
Figure 4-37 Bar stress distribution and concrete strain in the joint of Specimen B-R6-30.....	108

Figure 4-38 Bar stress distribution and concrete strain in the joint of Specimen B-R11-30.....	109
Figure 4-39 Bar stress distribution and concrete strain in the joint of Specimen C-R6-60.....	110
Figure 4-40 Bar stress distribution and concrete strain in the joint of Specimen C-R11-60.....	110
Figure 4-41 Effect of bend radius on normalized joint shear capacity	111
Figure 4-42 Effect of diagonal strut angle on normalized joint shear capacity ..	112
Figure 4-43 Effect of arrangement of reinforcement on joint shear capacity	113
Figure 4-44 General evaluation of bend radius.....	114
Figure 4-45 Correlation between strength ratio and bend radius ratio per Eq. (2-1)	116
Figure 4-46 Correlation between strength ratio and bend radius ratio per Eq. (2-3)	118
Figure 4-47 Assessment of serviceability of test specimens	119
Figure 4-48 Configuration and terminology of portal specimens.....	120
Figure 4-49 General strut-and-tie model for portal frames.....	121
Figure 4-50 Sizing Node C near the re-entrant corner.....	123
Figure 4-51 Procedures of determining of ultimate analytical capacity	126
Figure 4-52 Evaluation of the STM with general sizing method regarding bend radius ratio	129
Figure 4-53 Evaluation of the STM with simplified sizing method regarding bend radius ratio	131
Figure 4-54 Macroelement of numerical specimens.....	134
Figure 4-55 1-D reinforcement model	135
Figure 4-56 Boundary conditions for FE analysis	135
Figure 4-57 Meshing result.....	136
Figure 4-58 Comparison among FEM results, STM results and experimental results for Series A.....	137
Figure 4-59 Analytical damage pattern and stress distribution of Series A near failure	138
Figure 4-60 Comparison among FEM results, STM results and experimental results for Series D.....	139
Figure 4-61 Analytical damage pattern and stress distribution of Series D near failure	139

Figure 4-62 Comparison among FEM results, STM results and experimental results for Series B	140
Figure 4-63 Analytical damage pattern and stress distribution of Series B near failure	140
Figure 4-64 Comparison among FEM results, STM results and experimental results for Series C	141
Figure 4-65 Analytical damage pattern and stress distribution of Series C near failure	141
Figure 4-66 Design example of cantilever bent cap	144
Figure 4-67 Stress distribution at B-D region interface.....	145
Figure 4-68 Permissible strut-and-tie model for the example structure	146
Figure 4-69 Dimensions of the strut-and-tie model and internal forces in the elements	147
Figure 4-70 Force system at Node F.....	148
Figure 4-71 Non-hydraulic nodal shape of Node F	148
Figure 4-72 Summary of design result.....	151
Figure 5-1 Control specimen from Project 0-5253 (figure from Report No. 0-5253-1).....	154
Figure 5-2 Stress concentration determined by preliminary finite element analysis results	155
Figure 5-3 Region near CCC node to be confined.....	155
Figure 5-4 Nomenclature	157
Figure 5-5 Design of beam I	158
Figure 5-6 Design of beam II.....	159
Figure 5-7 Design of beam III	160
Figure 5-8 Fabrication of rebar cage.....	162
Figure 5-9 Cast of deep beam specimen	163
Figure 5-10 Cause of honeycombing and repair.....	164
Figure 5-11 Improved design of confinement	164
Figure 5-12 Testing setup (from TxDOT 0-5253-R1).....	165
Figure 5-13 Locations of linear potentiometers (from Project No. 0-5253-1) ...	166
Figure 5-14 Strain gauge layout on crack control reinforcement	166
Figure 5-15 Example strain gauge layout on confining reinforcement	167
Figure 5-16 Test setup	167
Figure 5-17 Concrete crack marking and measuring.....	168

Figure 5-18 Post-tension clamping as external protection.....	169
Figure 5-19 Force diagram of a typical specimen test (adopted from Project 0-5253)	170
Figure 5-20 Crack pattern at failure of Series I specimens.....	171
Figure 5-21 Crack pattern at the failure of Series II specimens	172
Figure 5-22 Crack pattern at the failure of Series II specimens	173
Figure 5-23 Crack pattern at failure.....	174
Figure 5-24 Growth of crack width versus normalized load	175
Figure 5-25 Strain readings and damage patterns of Series I	177
Figure 5-26 Strain readings and damage patterns of Series II	178
Figure 5-27 Strain readings and damage patterns of Series III.....	179
Figure 5-28 Strain profile along shear span at 400 kip	181
Figure 5-29 Strain profile along shear span at 95% of peak load	181
Figure 5-30 Engagement of confining reinforcement in Series I specimens.....	183
Figure 5-31 Engagement of confining reinforcement in Series II specimens	185
Figure 5-32 Engagement of confining reinforcement in Specimen III-CCC/CCT-L	186
Figure 5-33 Strain map at peak load and before crushing	187
Figure 5-34 Example categorization of strain map within monitored region	188
Figure 5-35 Comparison between STM nodal zone and DIC strain map	190
Figure 5-36 DIC virtual extensometer and average compressive stress on nodal face	191
Figure 5-37 Efficiency factor versus compressive/transverse strain readings....	191
Figure 5-38 Comparison of sectional shear strength of specimens with confined CCC node.....	193
Figure 5-39 Comparison of sectional shear strength of specimens with confinement of both or neither nodes	194
Figure 5-40 Geometry of test region and diagonal strut.....	196
Figure 5-41 Size of CCC node and CCT node	197
Figure 5-42 Efficiency factor of the CCC strut-to-node interface	199
Figure 5-43 CCC nodal efficiency factor from evaluation database from Project 0-5253.....	200
Figure 5-44 Efficiency factor of the CCT strut-to-node interface	201
Figure 5-45 CCT nodal factor from evaluation database from Project 0-5253 ..	202

Figure 6-1 Definition of vertical and horizontal web reinforcement (Tuchscherer et al. 2008)	208
Figure 6-2 Description of nomenclature for specimen I.D.	209
Figure 6-3 Beams B1 and B2 details	209
Figure 6-4 Beam B3 details	210
Figure 6-5 Reinforcement cage design of Beam B1	211
Figure 6-6 Reinforcement cage design of Beam B2	212
Figure 6-7 Reinforcement cage design of Beam B3	212
Figure 6-8 Fabrication setup for cage assembly	213
Figure 6-9 Strain gauge placement for this experimental program (Adopted from Project 0-5253).....	214
Figure 6-10 Gauges along the strut with wiring and packaging for B1	214
Figure 6-11 Cage lift onto steel soffit and placement in formwork.....	215
Figure 6-12 Specimen casting and vibration techniques	215
Figure 6-13 Cylinder samples and slump procedure on cast days.....	216
Figure 6-14 Test frame for all structural tests.....	218
Figure 6-15 Test setup	219
Figure 6-16 Linear potentiometer locations among the test setup (Adopted from Project 0-5253).....	220
Figure 6-17 Speckling for DIC applied to area of interest.....	221
Figure 6-18 Post-tensioned clamp added to specimen after Test 1 in preparations for Test 2	222
Figure 6-19 Force and shear diagram for all structural beam tests (adopted from Project 0-5253).....	226
Figure 6-20 Summary of normalized ultimate capacities of structural tests with their normalized STM estimation and their Project 0-5253 counterpart	227
Figure 6-21 Normalized shear capacity ratio to compressive concrete strength for B1, B2, B3, and Project 0-5253 companion specimens.....	229
Figure 6-22 Normalized shear capacity ratio to spacing and effective depth ratio for B1, B2, B3, and Project 0-5253 companion specimens	230
Figure 6-23 III-1.2-03a-v(ii)'s and its Project 0-5253's normalized ultimate capacities with STM estimations	231
Figure 6-24 Beam 1 Test 2's and its Project 0-5253's normalized ultimate capacities with STM estimations	232
Figure 6-25: Normalized Capacities of Beam 1 Test 2 and additional Project 0-5253 specimens	233

Figure 6-26 Beam 2 Test 1's and its Project 0-5253's normalized ultimate capacities with STM estimations	234
Figure 6-27 Beam 2 Test 2's and its Project 0-5253's normalized ultimate capacities with STM estimations	236
Figure 6-28 Normalized capacities of Beam 2 Test 2 and additional TX Project 0-5253 specimens	237
Figure 6-29 Beam 3 Test 1's and its Project 0-5253's normalized ultimate capacities with STM estimations	238
Figure 6-30 Beam 3 Test 2's and its Project 0-5253's normalized ultimate capacities with STM estimations	238
Figure 6-31 Estimate of service load as a function of experimental capacity	242
Figure 6-32 Crack width data for all 6 structural tests.....	243
Figure 6-33 Crack width data for B1 and B2 along with their TX Project 0-5253 companion specimen.....	245
Figure 6-34 Diagonal crack widths for III-1.2-03a-v(ii), 21" X 42" $a/d = 1.20$.	246
Figure 6-35 Diagonal crack widths for III-1.85-03b-v(ii), 21" X 42" $a/d = 1.85$	247
Figure 6-36 Diagonal crack widths for III-1.2-03a-h(ii), 21" X 42" $a/d = 1.20$.	248
Figure 6-37 Diagonal crack widths for III-1.85-03a-h(ii), 21" X 42" $a/d = 1.85$	249
Figure 6-38 Diagonal crack widths for IV-2123-1.85-03a-v(ii), 21" X 23" $a/d = 1.85$	250
Figure 6-39 Diagonal crack widths for IV-2123-1.85-03b-v(ii), 21" X 23" $a/d = 1.85$	250
Figure 6-40 Strain engagement along the strut for III-1.2-03a-v(ii), $a/d = 1.20$.	252
Figure 6-41 Strain engagement along the strut for III-1.85-03b-v(ii), $a/d = 1.85$	253
Figure 6-42 Strain engagement along the strut for III-1.2-03a-h(ii), $a/d = 1.20$.	254
Figure 6-43 Strain engagement along the strut for III-1.85-03a-h(ii), $a/d = 1.85$	255
Figure 6-44 Strain engagement along the strut for IV-2123-1.85-03a-v(ii), $a/d = 1.85$	256
Figure 6-45 Strain engagement along the strut for IV-2123-1.85-03b-v(ii), $a/d = 1.85$	257
Figure 6-46 Engagement of longitudinal reinforcement of Specimen III-1.2-03a-v(ii).....	258
Figure 6-47 Engagement of longitudinal reinforcement of Specimen III-1.85-03b-v(ii).....	259
Figure 6-48 Engagement of longitudinal reinforcement of Specimen III-1.2-03a-h(ii).....	260

Figure 6-49 Engagement of longitudinal reinforcement of Specimen III-1.85-03a-h(ii).....	261
Figure 6-50 Engagement of longitudinal reinforcement of Specimen IV-2123-1.85-03a-v(ii)	262
Figure 6-51 Engagement of longitudinal reinforcement of Specimen IV-2123-1.85-03b-v(ii)	263
Figure 6-52 DIC compressive principal strain map at the end of test	264
Figure 6-53 Macroelements of deep beam and steel plates	268
Figure 6-54 Layout of 1-D Reinforcement elements	268
Figure 6-55 Meshing result.....	269
Figure 6-56 Comparison of load-displacement relationship between experiment and FEA	270
Figure 6-57 Comparison between experimental and FE analytical crack patterns	271
Figure 6-58 Nomenclature of numerical test specimens.....	274
Figure 6-59 General configuration of numerical specimens.....	275
Figure 6-60 Example arrangement of 1-D elements for reinforcement.....	275
Figure 6-61 Strength ratio comparing to control specimen for 21 in. by 42 in. .	279
Figure 6-62 Strength ratio comparing to control specimen for 21 in. by 75 in. .	280
Figure 6-63 Strength compared to STM results.....	281
Figure 6-64 Evaluation of strength generated from FEM and STM vs. spacing requirements.....	282
Figure B-7-1 Truss model and variables (Tuchscherer et al. 2008)	299
Figure B-7-2 CCC and CCT nodes and variables (Tuchscherer et al. 2008)	299

Chapter 1. Introduction

This chapter introduces the current research background, including the objectives and the scope of the research project. The organization of this report is also included.

1.1. Overview

Generally reinforced concrete (RC) members can be categorized as B-regions and D-regions. In B-regions, the member cross-section follows the assumption “plane sections remaining plane” when loaded. That is, strain profile remains linear over the height of the cross-section. Flexural stresses and bending moments can be then derived on the basis. B-regions appear at locations away from concentrated point loads and locations without geometric discontinuities. However, RC members always have regions that are located near point loads or geometric discontinuities. In this case, plane sections do not remain plane, and strain profiles are no longer linear. Complex stress states are anticipated and can be difficult to determine. Such regions are named D-regions because the stresses are “disturbed” or the regions are “discontinuous.”

Designing D-regions is never a simple job, as there is no simple way to determine the distribution and magnitude of the stresses. Although applicable, sophisticated models such as solid mechanics and the finite element method can take a long time, great effort, and specialized expertise, which is discouraging for structural designers. Thus, simple methods have been studied and proposed for designing D-regions. In this background, the strut-and-tie method (STM) was born. The development of the STM can be dated back to 1899 and 1912 in studies by Ritter and Morsch in which it was suggested to use a truss analogy for RC members. After over 120 years of refinement, the STM has evolved to be a simple, rational, and conservative method for D-regions. The basis of the STM was summarized in the legendary study by Schlaich and Schafer (1987). Based on the lower bound theorem of plasticity, the STM visualizes the principal stress state in RC D-regions as struts representing compression and ties representing tension. In addition, nodes are used to represent where principal stresses change directions. Reinforcement is proportioned, and nodal capacity checks are performed to ensure a successful design.

In the more recent past, over a span of 12 years, the Texas Department of Transportation (TxDOT) funded four consecutive research projects to optimize conservatism in their structural designs resulting from STM. Their commitment to financing practical research for over a decade on this topic resulted in significant improvements in the state of practice of STM. The key steps that the researchers took in the derivation of the new provisions include 1) the development of an evaluation database consisting of more than 800 deep beam tests, 2) the selection of a strut-and-tie model, 3) the use of non-hydrostatic nodes, 4) the calibration of efficiency factors, 5) the elimination of stress checks at the back face of CCT nodes, and 6) the triaxial confinement. The refinements were adopted in the eighth edition of AASHTO LRFD Bridge Design Specifications

(2017). The new provisions significantly improve accuracy without compromising conservatism. The applicability of these provisions has recently been tested on beams with bent-up bars (i.e., truss bars) and subjected to contra-flexure¹⁶ and on double corbel specimens. New test results obtained in different types of specimens further confirmed the accuracy and conservativeness of the new AASHTO LRFD's STM provisions.

Nevertheless, the application of current AASHTO LRFD's STM provisions to common design scenarios has revealed the need to develop additional guidance for bridge engineers. TxDOT designs can significantly benefit if these knowledge gaps can be filled. The identified areas of improvement include the following:

- No tests have been performed where there are three orthogonal directions of tension ties, such as would occur above a drilled shaft in tension where a column is supported on a four-drilled shaft footing. It is believed that the effective compressive strength of concrete is reduced in nodes where more tension ties are framed into. In addition, the anchorage behavior for drilled shaft reinforcement is also expected to be compromised. Until structural testing is done, the current practice may be regarding the behavior of these nodes incorrectly.
- ACI 318 building code has recently incorporated the requirements for curved-bar nodes in the STM. It is required to size the bar bends at the outside of frame corners subjected to closing moments. The *fib* model code also regards the bend radius as a critical element when using the STM. It is believed that the average stress within the bar bend of hooked bars can be significant. Providing a larger bar bend than a standard bend to prevent overstressing the area can be essential. However, AASHTO LRFD Bridge Design Manual does not specifically require checking the stresses in this type of node, while TxDOT views it as a good engineering practice. It is imperative that the behavior of curved-bar nodes be experimentally addressed.
- Currently, AASHTO LRFD does not provide any benefit to the confinement provided by the presence of passive confinement reinforcement for the nodal capacities. Triaxial concrete confinement increases the capacity of concrete, so it is logical to assume passive confinements could increase the capacity of the nodes.
- AASHTO LRFD Bridge Design Specifications limit the spacing of crack control reinforcing to the lesser of $d/4$ and 12 in. This limit is based on the existing state of knowledge developed on the basis of experiments. In other words, the limits of bar spacing seen in past tests drove the implementation of "the $d/4$ limit". However, the " $d/4$ limit" usually causes congestion and reduced constructability in the field. Additional experimental research could show that the maximum web rebar spacing can be increased for crack control reinforcement, resulting in substantial savings with respect to the reinforcing bars specified to meet the " $d/4$ limit".

1.2. Project Scope and Objective

The current research project, funded by TxDOT, aims to fill the knowledge gaps mentioned above through an extensive literature review, experimental programs that tackle the topics separately, and supplemental numerical analysis. In the literature review, each topic being addressed includes a review of code specifications and representative experimental and analytical work. The experimental programs include footing specimens designed to address nodal regions subjected to three orthogonal tensions, portal frame specimens intended to investigate curved-bar nodes, and deep beam specimens for examining nodal confinement and relaxing the spacing requirements. The finite element method was employed to conduct “numerical tests” and provide preliminary and supplementary numerical data to enhance confidence in applying the specimen design and design considerations.

Through the research project, the following topics were addressed:

- Examine the anchorage behavior of drilled shaft reinforcement using straight rebars or headed bars at nodal zones subjected to three orthogonal tensions under the framework of the 3D strut-and-tie method.
- Experimentally investigate the behavior of curved-bar nodes in frame corners. The effects of the size of the bar bend, the diagonal strut angle, and the arrangement of the longitudinal reinforcement on the frame corner of portal frames were investigated.
- Attempt to correlate the amount of confinement provided to a nodal zone with the nodal effective compressive strength of concrete.
- Verify the feasibility of relaxing the spacing requirement for web crack control reinforcement from the lesser of $d/4$ and 12 in. to the lesser of $d/2$ and 24 in.
- Apply the finite element method when needed to provide supplementary numerical data supporting the findings of the test programs.
- Make recommendations for constructing straightforward strut-and-tie models for RC members investigated in the current research project.
- Deliver recommendations for improvements of the STM provisions of the AASHTO LRFD Bridge Design Specifications and TxDOT design guidelines.

1.3. Organization

This research project was organized into a series of tasks, including bibliographical, experimental, and analytical work. Each chapter of this report presents the results and main findings obtained from each of these tasks. Chapter 2 presents the main findings of a literature review on international code provisions of the STM. Chapter 3 includes a comprehensive investigation of

footing specimens, including experimental and analytical work. Chapter 4 presents the experimental program on portal frames in order to investigate the behavior of curved-bar nodes. Chapters 5 and 6 present experimental programs on deep beams in order to determine the benefit of nodal confinement and relaxing the requirements on the spacing of web crack control reinforcement. Lastly, Chapter 7 concludes the research project by summarizing the findings.

Chapter 2. Literature Review

2.1. Introduction

In this chapter, precedent studies and design code specifications pertaining to the STM, especially relevant to applying the STM on RC members investigated in the current research project. The scope includes using 3D-STM on footings, frame corners under closing moments, bridge bend caps, and deep beams. In addition, the behavior of confined concrete and anchorage design under the framework of the STM are included. The literature review summarized in this chapter is organized as follows:

- Section 2.2 summarizes studies on applying 3D STM on footings with nodes under three orthogonal tensions and the development of reinforcing bars in a three-dimensional tensile stress field.
- Section 2.3 presents a review of published literature on curved-bar nodes. This review also includes design methods and code specifications for curved-bar nodes.
- Section 2.4 presents a review of the effect of confinement on concrete strength and nodal efficiency of the STM code provisions. Application of confinement on deep beam design is also included.
- Section 2.5 includes a review of code specifications and requirements for spacing crack control reinforcement and a summary of relevant literature.

2.2. Rebar Development at Nodes under Three Orthogonal Ties

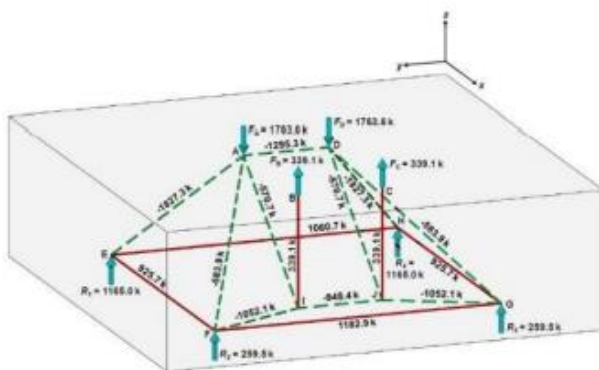
Drilled shaft footings commonly support complex force paths that develop in bridge piers. In the absence of a bending moment, the strut-and-tie model can be straightforward. The compression flows into four drilled shafts supporting the footing. However, with increasing levels of bending moment at the column-to-footing interface, the back face of the column goes into tension. With further increases in bending moment, two of the four drilled shafts go into tension, in addition to the back face of the column being in tension. In such cases, a non-contact splice problem in a three-dimension space exists. To develop a test program, the research team investigated potential 3D strut-and-tie models proposed in literature and the advancement of anchoring drilled shaft reinforcement approaches, as summarized in this section.

2.2.1. Experimental and Analytical Studies on Drilled Shaft Footings

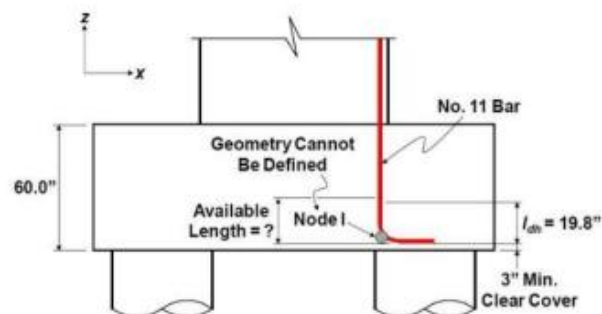
Williams, Deschenes, and Bayrak (2012)

Williams et al. (2012) authored a series of five design examples and design guidelines using the STM on the basis of TxDOT Project 0-5253 (Birrcher et al., 2009). One of the design examples details three-dimensional strut-and-tie models representing the transmission of stresses in a deep drilled shaft footing. One of the developed strut-and-tie models is modeling a drilled shaft footing under an axial load and a uniaxial bending moment. That is, the pier of the drilled shaft footing is under an eccentric axial load.

In the strut-and-tie model, the authors suggest that flexural stresses on the pier section be used to determine the positions of the centroid of the resultant compression and tension, where struts and ties are to be originated. The depth of the top nodes is placed at 0.1 times the total height lower than the top surface, and a ring of ties is located in alignment with the bottom mat reinforcement. The two ties from the pier are extended to the bottom mat reinforcement. Lastly, nodes are connected with struts and ties to maintain equilibrium. The finished strut-and-tie model is shown in Figure 2-1(a).



(a) Suggested strut-and-tie model



(b) Anchorage detail of column rebar

Figure 2-1 The STM on drilled shaft footing with column having tension side (Williams et al. 2012)

The authors pointed out that the end of the vertical ties proportioned with column reinforcement is considered a smear node with no particular nodal faces. The available length for the development of the column reinforcement remains undetermined. Therefore, it is suggested in the report that 90-degree hooks be utilized for anchoring the column reinforcement.

Yousun et al. (2021)

Yousun et al. (2021) conducted an extensive experimental program and finite element analysis on drilled shaft footings under various load conditions. The research project was TxDOT Project 0-6953. One series of the test specimens was designed to address the available length for the development of drilled shaft reinforcement when the footing is under a high eccentric axial load in the pier. Regarding this type of drilled shaft footings, the authors suggested a strut-and-tie model

that represents the complex force transmission caused by the load condition, as shown in Figure 2-2. The suggested strut-and-tie model has a ring of ties in alignment with both the top mat reinforcement and the bottom mat reinforcement. Struts and ties between the top and the bottom ring and underneath the column are provided to maintain equilibrium.

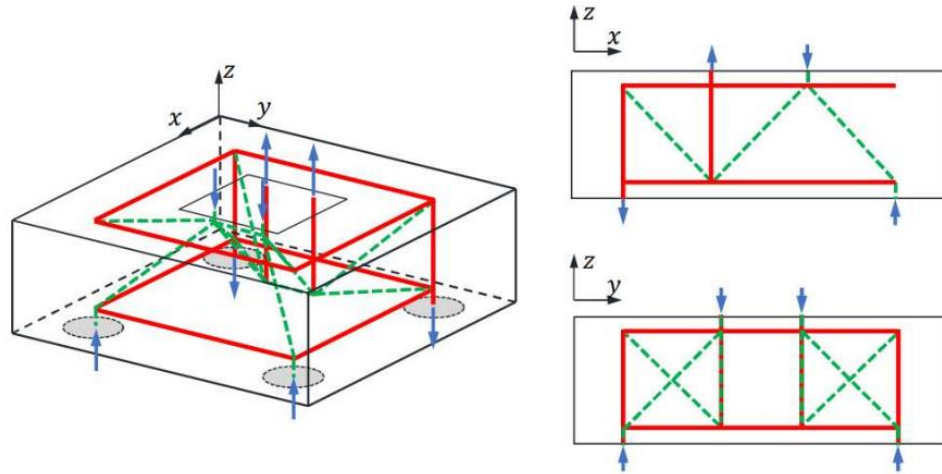


Figure 2-2 Strut-and-tie model for drilled shaft footing of which two drilled shafts are in tension (Yousun et al. 2021)

The strut-and-tie model includes nodes under three orthogonal tensions, which is of interest to the current study. Yousun et al. (2021) designed a test frame that created tension in drilled shaft reinforcement to investigate the anchorage behavior of the drilled shaft reinforcement and verify the load transmission. The research project included four tests on the anchorage behavior of straight bars and headed bars in the drilled shafts. As a result, the project suggested that the non-contact splice can be addressed by defining a fan-shaped strut between the two ties. In particular, the available length for developing the drilled shaft reinforcement can be delineated by the boundary of the fan-shaped strut, as indicated by the shaded area shown in Figure 2-3. In addition, the minimum requirement for the surface reinforcement was suggested to be 0.3% to maintain the development of the fan-shaped strut. This approach largely improves the viability of the available length.

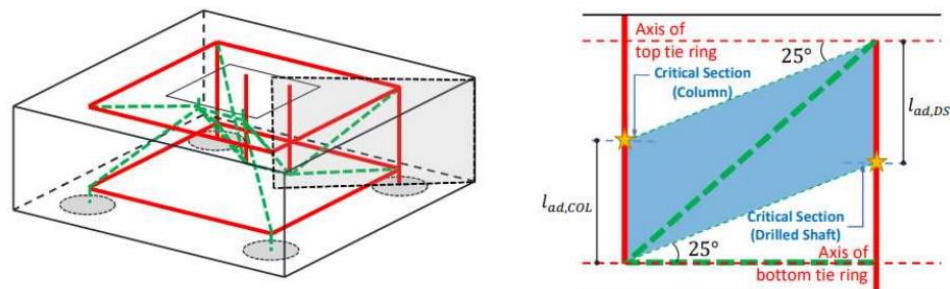


Figure 2-3 Compression field and critical section for drilled shaft reinforcement (Yousun et al. 2021)

2.2.2. Findings and Research Needs

Research on nodes under three orthogonal tensions in 3D strut-and-tie models is limited. The two studies reviewed above were the only known existing analytical and experimental work on this topic.

Williams et al. (2012) pointed out the difficulties of evaluating the available length of the smear node at the bottom of the vertical tie. Without supporting test data, hooked bars were conservatively suggested following practice in Texas. Following TxDOT Project 0-5253 (Bircher et al., 2009) and Williams et al. (2012), Yousun et al. (2021) experimentally investigated drilled shaft footings with nodes under three orthogonal tensions. It was suggested that the available length be within a fan-shaped compression field caused by the mechanism of the non-contact splice. The approach is rational and straightforward, giving structural designers large flexibility when detailing drilled shaft reinforcement.

Nevertheless, the approach was developed based on only four footings tests by Yousun et al. (2021). It remained unclear if more factors should be taken into account when using the fan-shaped compression field. Firstly, the tested footing specimens all had the same height of 40 in. Lacking specimens with different heights, it was impossible to correlate the formation of the compression field to the footing geometry. Secondly, 0.3% of crack control reinforcement was required per the STM provisions, which differed from the requirement for footing surface reinforcement (0.18%). More test data and further research were imperative.

2.3. Curved-Bar Nodes

In a strut-and-tie model, a curved-bar node can be used to model the bend region of continuous bars where two ties are equilibrated by a strut. Such nodes occur at the frame corners commonly encountered in cantilever caps (i.e., C-caps) and straddle bents that are designed to transfer moments from the cap beam to supporting columns (i.e., frame corners.). When a frame corner is subjected to closing moments, the internal force transmission into the bar bend of the reinforcement at the outside of the frame corner embodies a curved-bar node, as depicted in Figure 2-4.

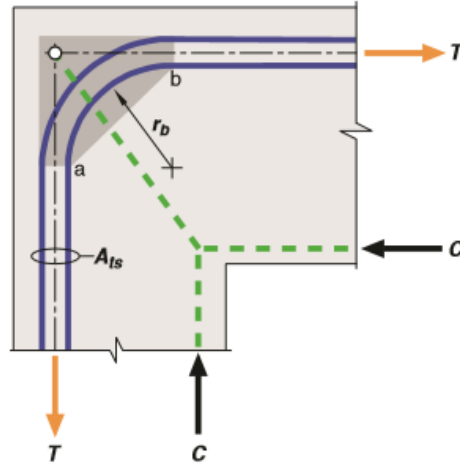


Figure 2-4 Curved-bar node at outside of frame corner under closing moments (ACI 318-19, 2019)

Example problems developed under TxDOT implementation project 5-5253 also highlighted cases in which stress checks at curved-bar nodes can be essential. Past studies [Luo et al. (1994), Stroband and Kolpa (1983), and Ostund (1963)] indicated the importance of the size of the bend radius and experimentally investigated the behavior of curved-bar nodes. Design expressions for curved-bar nodes were also formulated and incorporated in design codes such as ACI 318-19 and European codes. However, Curved-bar nodes were acknowledged in AASHTO LRFD Bridge Design Specifications (2020) only in the commentary without detailed recommendations. Bridge designs based on the current state of practice may lead to overstressing curved-bar nodes.

2.3.1. STM Provisions in Code Specifications

The following codes of practice set forth specifications regarding curved-bar nodes.

AASHTO LRFD Bridge Design Specifications (2020)

AASHTO LRFD (2020) does not incorporate curved-bar nodes in the specification. Instead, curved-bar nodes are only mentioned in the commentary, as experimental data do not sufficiently support the effects of curved-bar nodes on the behavior of RC members.

ACI 318-19 Building Code Requirements for Structural Concrete (2019)

ACI 318-19 (2019) specifies requirements for designing curved-bar nodes in Section 23.10. The design expressions are meant to avoid overstressing concrete within the bar bend by ensuring the bend radius is sufficiently large, as follows:

- (a) Curved bar nodes with bends less than 180 degrees:

$$r_b \geq \frac{2A_{ts}f_y}{b_s f'_c} \quad (2-1)$$

(b) Ties anchored by 180-degree bends:

$$r_b \geq \frac{1.5A_{ts}f_y}{w_t f'_c} \quad (2-2)$$

where r_b is the bend radius; A_{ts} is the area of proportioned reinforcement for the ties; f_y is the yield strength of the reinforcement; f'_c is compressive strength of concrete; w_t is the width of the diagonal strut; b_s is the width of the diagonal strut; w_t is the effective tie width.

When the tie forces are unequal, and thus the strut (or the resultant of two or more struts) does not bisect the angle formed by the ties at each end of the bend, the difference in tie force should be developed along the bar bend. In this case, circumferential bond stress develops along the bar, as shown in Figure 2-5.

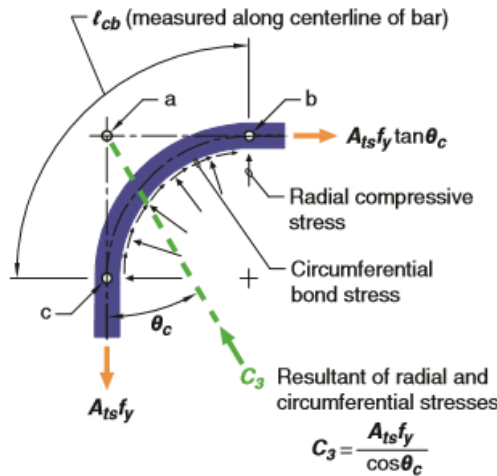


Figure 2-5 Free body diagram of curved-bar nodes (ACI 318-19)

The length of the bar bend ℓ_{cb} has to be sufficient long to develop the stress, given by

$$\ell_{cb} > \ell_d (1 - \tan \theta_c) \quad (2-3)$$

where θ_c is the smaller of the two angles between the axis of the strut and the ties extending from a curved-bar node, and ℓ_d is the development length calculated in accordance with Section 25.4.2 of ACI 318-19 (2019).

In addition, if the specified clear side cover of the bar bend is smaller than twice the bar diameter, the design bend radius should be further enlarged according to Section 23.10.3 of ACI 318-19 (2019).

FIP Commission 3 – Practical Design of Structural Concrete (1996)

The recommendation of FIP on designing curved-bar nodes suggests that the average compressive stress f_c at a curved-bar node be generally written as

$$f_c = \frac{A_{ts}f_y}{2r_b b_s \sin \theta_c \cos \theta_c} \quad (2-4)$$

The required bend radius in Equation (2-4) can be back-calculated by specifying the upper limit of the average compressive stress in concrete.

2.3.2. Experimental and Analytical Studies

Klein (2008)

Klein (2008) first introduced the concept of curved-bar nodes in a study that provided a detailing tool for establishing strut-and-tie models for the beam-column connections and dapped-end beams. The formulation was then adopted by ACI 318-19 after being experimentally verified. In this study, the author suggested that CTT nodes can be modeled as curved-bar nodes if the proportioned reinforcing bars pass through the node continuously with a bar bend. Concrete within the curved region should take compressive stress in equilibrium with the two ties, as shown in Figure 2-6.

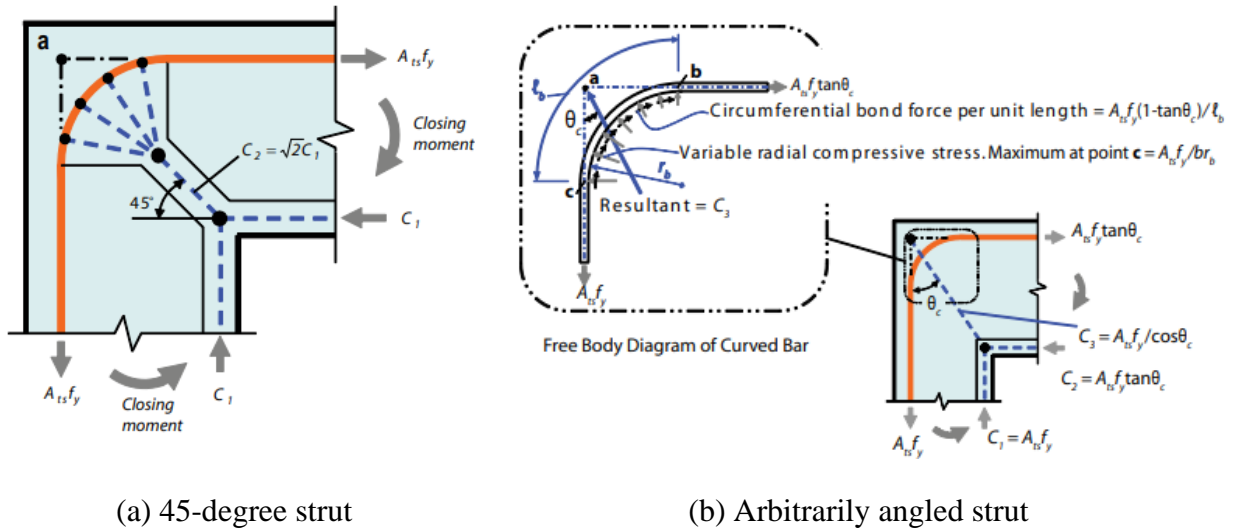


Figure 2-6 Strut-and-tie model with curved-bar node of frame corner under closing moments

In particular, when the diagonal strut has an angle of 45 degrees, the interface of the curved-bar node is subjected to a resultant force of $\sqrt{2}A_{ts}f_y$, which causes stresses over the interface given by

$$f_c = \frac{A_{ts}f_t}{b_s r_b} \quad (2-5)$$

To avoid overstressing the curved-bar node, the author suggested limiting the compressive stress according to the effective concrete strength of CTT nodes. In other words, substituting f_c in Equation (2-5) with $(0.85)(0.6)f'_c$ derives the minimum required bend radius, given by

$$r_{b,min} = \frac{A_{ts}f_t}{0.51b_s f'_c} \quad (2-6)$$

The author also addressed the case in which the two ties have different forces, causing circumferential bond stresses along the bar bend. As shown in Figure 2-6(b), the difference in the forces has a magnitude of $A_{ts}f_y(1-\tan\theta_c)$. In other words, a development length of $l_d(1-\tan\theta_c)$ is needed to ensure the circumferential bond stresses. By geometry, the minimum required inner bend radius is therefore given by

$$r_{b,min} = \frac{2l_d}{\pi}(1 - \tan \theta_c) - \frac{d_b}{2} \quad (2-7)$$

In addition, if multiple layers of reinforcement are provided, the innermost layer has to be considered. Clear side cover normal to the bar bend region of a curved-bar node should be at least twice the bar diameter to prevent splitting of the concrete; otherwise, further enlargement should be enforced.

It is worth noting that designing curved-bar nodes usually provides a required minimum bend radius smaller than the standard bend radius. There are, however, exceptions, such as corners with large member dimensions; a typical example is a tunnel junction. In these types of structures, using the standard bend radius would result in high stresses in the concrete strut, plausibly causing the crushing of the concrete. Therefore, further investigation may be required to evaluate the design expression of curved-bar nodes for structures with large member dimensions.

Williams et al. (2012)

A design example using the STM with a curved-bar node first appeared in the TxDOT implementation Project 5-5253. The example structure was a cantilever bent cap, as illustrated in Figure 2-7. Node A in the figure was considered a CTT node to be modeled as a curved-bar node. Following the design expression by Klein (2008), the authors performed nodal stress check and determined that the bend radius was larger than standard mandrels for No. 11 bars. The design result echoes the fact that large reinforcement at the outside of a frame corner requires a bend radius than a radius of the standard bar bend, as Klein (2008) implied.

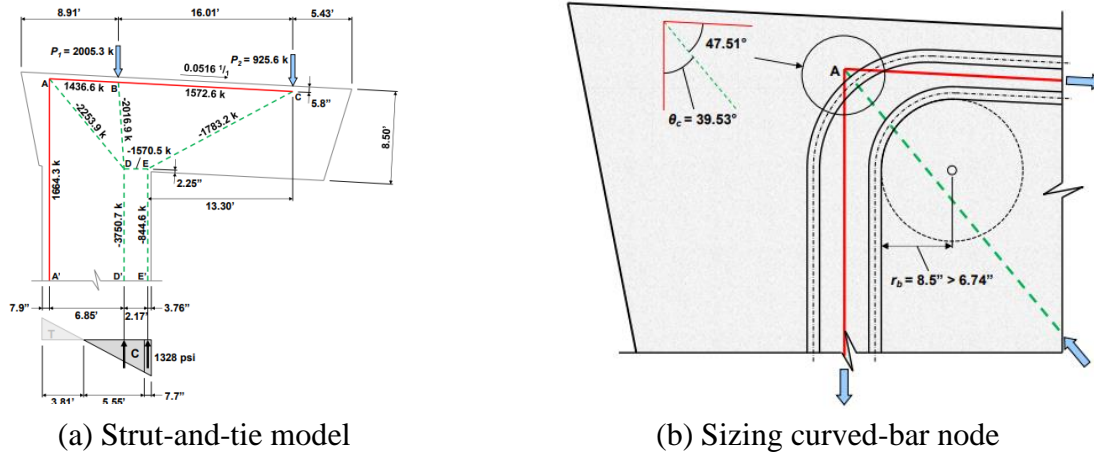


Figure 2-7 Design example of cantilever bent cap (from Williams et al. 2012)

Martinez et al. 2017

In order to study the validity and accuracy of the revised provisions of AASHTO LRFD (2017) Martinez et al. (2017), as part of a coursework at the University of Texas at Austin, guided graduate students through laboratory investigation of RC deep beam designed with the STM and the FEM. Students were required to design a deep beam having an inflection point, as illustrated in Figure 2-8.

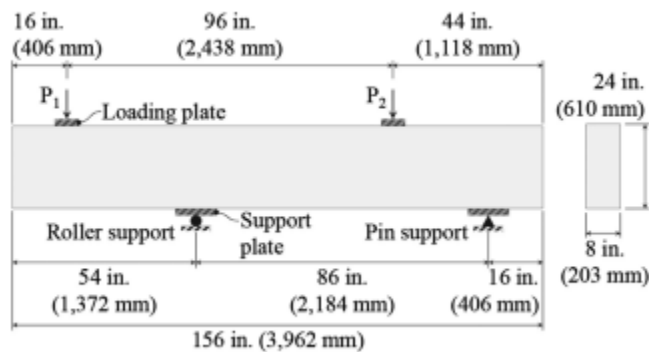
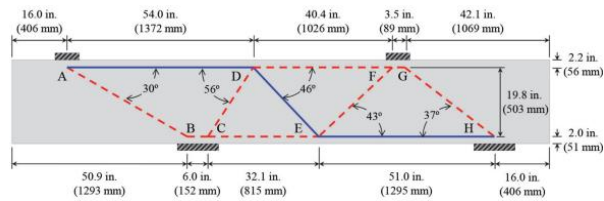
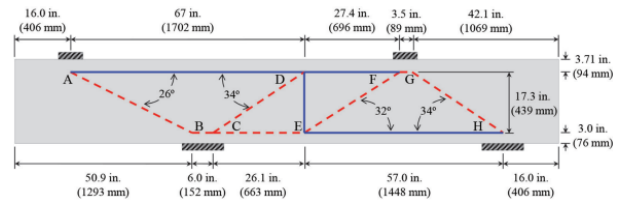


Figure 2-8 Deep beam to be designed in Martinez et al. (2017) (from Martinez et al. 2017)

Two different truss models (S1 and S2) were developed per principles based on Schlaich and Schafer (1987) and provisions in AASHTO LRFD (2017), as shown in Figure 2-9. The first truss model S1 [see Figure 2-9(a)] had Nodes D and E as CTT nodes to be modeled as curved-bar nodes. As AASHTO LRFD had not introduced the design of curved-bar nodes in the provisions, the authors examined the nodes using the formulation proposed in Klein (2008). It was then determined that the bar bend passing through Nodes D and E should be larger than 4.6 in. Here, a standard bend radius 4.5 in. typically for No. 9 bars was specified for No. 8 Z-bars proportioned in this deep beam, as shown in Figure 2-10. In this case, crushing of concrete at the curved-bar nodes was likely to occur because the concrete strength controlled the failure mode.



(a) Truss model S1



(a) Truss model S2

Figure 2-9 Truss models used in Martinez et al. (2017) (from Martinez et al. 2017)

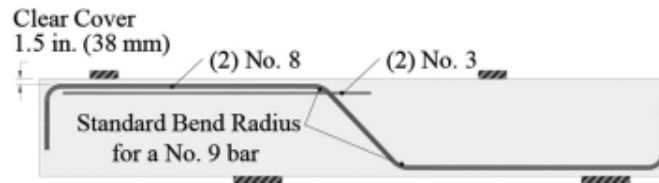


Figure 2-10 Design results for Truss model S1 (from Martinez et al. 2017)

Test results, as expected, showed that the deep beams designed on the basis of Truss model S1 were more likely to fail at the top bend of the Z-shaped bars. The measured capacity also scattered at a higher level, which was attributed to the use of curved reinforcement. Nevertheless, predictions of the STM were conservative as a lower-bound method.

The study revealed the importance of using well-sized curved-bar nodes and how curved-bar nodes become critical in the design of deep beams. It was imperative that the design expressions of curved-bar nodes be addressed.

Wang et al. (2020), Wang et al. (2022), and Wang et al. (2022)

It was acknowledged that the bend radius, or the curved-bar node, plays an important role in the behavior of frame corners under closing moments. Design expressions and the use of curved-bar nodes could also be seen in studies. However, there was no experimental investigation particularly for factors affecting curved-bar nodes' behavior. In order to systematically address and verify the design expressions that appear in Klein (2008) and ACI 318-19, Wang et al. (2020, 2022, and 2022) conducted a comprehensive experimental program in which 24 knee joint specimens were tested under closing moments, forming a strut-and-tie model and a curved-bar node as shown in Figure 2-11. The test variables included the size of the bend radius, multiple layers of reinforcement, the clear side cove, the angle of the diagonal strut, and the existence of crack control reinforcement in the joint.

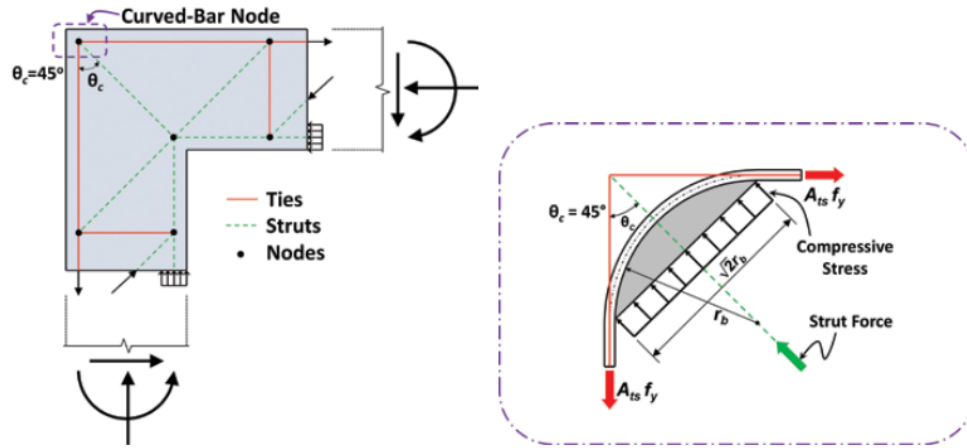


Figure 2-11 Strut-and-tie model and curved-bar node in Wang et al. (2020, 2020, and 2022)

As shown in Figure 2-12, the knee joint specimens consisted of a joint and two adjacent members (legs). The end of each leg was designed to have a vertical surface and a horizontal surface to facilitate supporting and loading using a self-reacting test frame, also as shown in Figure 2-12.



Figure 2-12 Specimen and test setup used in Wang et al. (2020, 2020, and 2022)

After testing the specimens, the authors concluded that the bend radius of curved bar nodes plays an important role in altering the strength, ductility, and failure modes of knee joints under closing moments. In particular, if the bend radius was designed per design expressions for radial stresses in ACI 318-19, specimens not only reached their full capacity with entering load plateau but also had superior ductility than specimens with smaller bend radius, whether having a single layer or multiple layers of tie reinforcement. The failure mode tended to be a flexural failure at the joint faces. For specimens with a small bend radius, the ductility or even the strength was compromised; the failure mode became joint shear failure or splitting along the bar bend. In addition, further enlargement of the bend radius for thin clear side covers was found appropriate. It was also found that the assumed strut-and-tie model could be achieved if sufficiently large bend radii were used. However, the minimum bend radius that addresses circumferential bond stresses was found to be

too conservative and not necessary. No failure related to circumferential bond stresses was identified, even though smaller bend radii were proportioned.

Moreover, the existence of a minimum amount of crack control reinforcement was found not to compensate for compromised strength or ductility. If the bar bend did not satisfy the requirements for curved-bar nodes, even though crack control reinforcement was provided, the strength was still compromised, but the load drop after the peak load was milder. The research project pointed out that the joint shear analysis is insufficient because the bend radius is not accounted for. Instead, the strut-and-tie model with a curved-bar node better represents the behavior of knee joints under closing moments.

In addition, stress transmission within the joint, the interaction among stresses, and cracking were discussed in the studies. Echoing the study by Ingham (1995), Wang et al. (2020) explained the mechanism of bond stresses, tensile stresses in the bar and diagonal compressive stresses, as shown in Figure 2-13. Along the straight portion of the bars, total bond force is equilibrated by the resultant tension and compression in the orientation toward the re-entrant corner, as shown in Figure 2-13(a), causing cracks and fanned-shaped compression zones. A similar equilibrium can be established near the bar bend portion, as shown in Figure 2-13(b). The stress transmission mechanism explains the forming of the diagonal strut and fan-shaped struts.

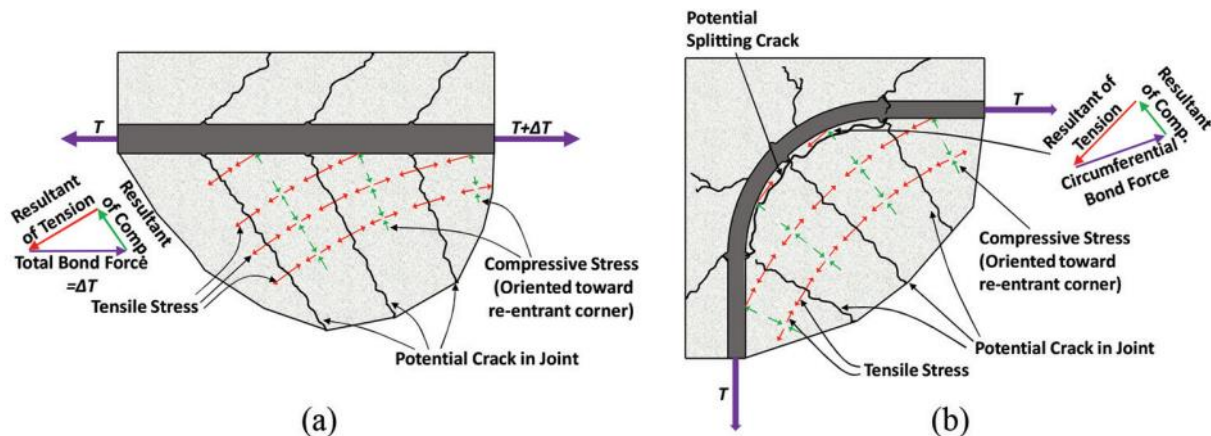


Figure 2-13 Stress transmission along the bar (Ingham 1995, Wang et al. 2020)

Wang (2020)

In the same research project, Wang (2020) conducted a database analysis in order to evaluate the conservatism of using the STM and the sectional analysis on knee joints under closing moments. The database collected by Wang (2020) included 154 past closing knee joint tests. After being filtered, 116 tests remained in the evaluation database for analysis. The author then used both the sectional analysis and the STM to calculate a predicted strength for each specimen in the evaluation

database. The author also developed an algorithm to optimize the selection of strut-and-tie models for closing knee joints under different load patterns.

The analytical results revealed that the sectional analysis yielded unconservative results when the bend radius was smaller than the ACI-required bend radius for curved-bar nodes, even if the joint shear capacity was accounted for. On the other hand, effectively taking the bend radius into consideration, the STM with a curved-bar node for closing knee joints delivered conservative results. However, overly conservative predictions appeared largely for closing knee joints with a very small bend radius. It was believed that the overconservativeness was due to the fact that the STM does not account for bond stresses and bar development in the ties. The other possibility was that the nodal efficiency factors suggested in ACI 318-19 could be too low.

The author also modeled test specimens using the nonlinear 3D finite element (FE) software ATENA 3D in order to provide supplementary numerical data. The FE analysis successfully captured the impact of different bend radii on the behavior of knee joints subjected to closing moments based on the benchmark specimens of the experimental program. A parametric FE analysis on the basis of the calibrated FE models also supported the conclusion drawn from the experimental program. The importance of designing for curved-bar nodes in the STM was well established.

2.3.3. Findings and Research Needs

- AASHTO LRFD (2020) provisions for the design of curved-bar nodes are limited due to the availability of test data. ACI 318-19 (2019) and *fib* (1992) required that the bend radius be sufficiently large to reduce stress on the interface.
- The current state of knowledge related to curved bar nodes is summarized as follows: In order to resist stress concentration at the bend region (curved-bar node), the longitudinal reinforcement at the bend region must satisfy two criteria: (1) the inside radius of the bar bend must be large enough to limit the radial compressive stresses acting at the node to an allowable value, and (2) the length of the bend must be sufficient to allow any differences in the tie forces to be developed along the bend region of the bar.
- The design examples and equations presented in the literature for curved-bar nodes provide conservative designs that are consistent with the nodal stress limits in strut-and-tie models.
- The performance of frame-corner connections designed with curved-bar nodes was found to be appropriate, provided that the ACI 318 code limits are respected. Tests have shown that failure may be caused by bearing failure of concrete in the diagonal compression strut, splitting of the strut, or splitting of the bar bend, depending on the size of the bend radius. Limiting the concrete compressive strength and design expressions given in ACI 318-19 appear appropriate.

- The equation that addresses circumferential bond stresses appears not necessary. However, the conclusion is based on very limited test data. More research is needed.
- The joint shear analysis appears insufficient because the method does not account for the bend radius. On the other hand, the STM yields conservative predictions if curved-bar nodes are well considered. However, the STM tends to be overly conservative, which can be attributed to the ignorance of bond stresses and low nodal efficiency factors.

2.4. Confined Nodal Regions

Nodes in the STM are used at locations where struts and ties intersect, representing the change of orientation of principal stresses. Types of nodes include CCC, CCT, CTT, and TTT, according to the number of tensile ties framed into the node. The nodal strength check is one of the most important STM procedures. It is acknowledged that different node types lead to different nodal efficiencies. That is, the more ties are connected to a node, the lower strength the node has. Nevertheless, if a node is confined by concrete, the nodal strength can be enhanced. The effect of concrete confinement on nodal regions can usually be seen when the bearing plate has a width smaller than the member's width. The confinement effect has long been studied, and therefore almost all major design codes incorporate factors to account for the confinement effect on nodal strength. This section presents a summary of the design provisions of the STM in various design specifications and briefly discusses potential improvements of the STM provisions. Research studies contributing to developing and understanding nodal confinement provisions are summarized.

2.4.1. STM Provisions in Code Specifications

AASHTO LRFD Bridge Design Specifications (2020)

Per Section 5.8.2.5 of AASHTO LRFD (2020), the load-carrying capacities of nodal regions can be generally expressed as

$$P_n = mvf'_c A_{cn} \quad (2-8)$$

where P_n is the nominal resistance of a node face (kip); v is the concrete efficiency factor; f'_c is the compressive strength of concrete for use in design (ksi); A_{cn} is effective cross-sectional area of the node face as specified in Article 5.8.2.5.2 (in.²); m is confinement modification factor.

Among the parameters in Equation (2-8), the m -factor is of interest to the current study. The m -factor describes a coefficient that increases the compressive strength of concrete in a nodal zone, taken as $\sqrt{A_2/A_1}$ but not greater than 2.0. Defined as shown in Figure 2-14, A_1 is the loaded area taken as the area of the bearing surface; A_2 reflects an area after bearing stress disperses within the member.

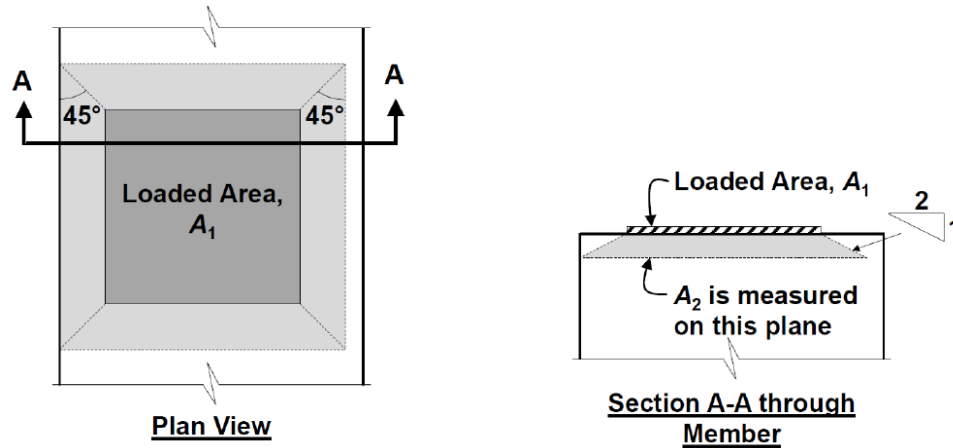


Figure 2-14 Bearing stress distribution (from AASHTO LRFD 2020)

CSA A23.3-14 (2014)

Similar to AASHTO LRFD (2020), the Canadian design code CSA A23.3-14 (2014) also modifies concrete compressive strength due to confinement. The modification factor has the same expression as AASHTO LRFD (2020).

ACI 318-19 (2019)

Unlike the above-mentioned code specifications, ACI 318-19 (2019) does not apply a similar modification factor to nodal strength in the STM provisions. Instead, the code allows an increased strength of concrete in nodal zones if confining reinforcement is provided within the nodal zone, and its effect is documented by tests and analyses.

CEB-FIP Model Code (1990 and 2010)

CEB-FIP Model Code incorporates the modification factor with a similar expression to AASHTO LRFD (2020), taken as $\sqrt{A_{c1}/A_{c0}}$, as shown in Figure 2-15. However, increasing strength only applies to CCC nodes subjected to triaxial confinement. In addition, the upper limit of increase in strength is higher, 4.0 in the 1990 version and 3.0 in the 2010 version. For nodal regions subjected to biaxial compression stresses, the design value of the concrete compressive strength may be increased by 10%.

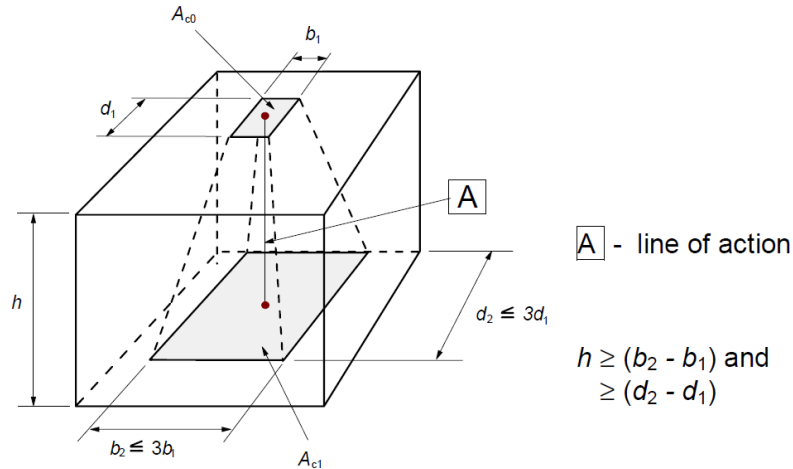


Figure 2-15 Distribution for partially loaded area (from CEB-FIP Model Code 2010 and Eurocode 2)

Eurocode 2 (1992)

Eurocode 2 (1992) also allowed an increase in strength for partially loaded areas, as shown in Figure 2-15, with the same expression as CEB-FIP Model Code. The upper limit of the modification factor for confinement is 3.0. In addition, Eurocode 2 (1992) allows a possible increase in strength due to passive confinement provided by reinforcement. In particular, nodal strength may be increased by up to 10% if at least one of the following conditions applies:

1. Triaxial compression is assured,
2. all angles between struts and ties are greater than 55 degrees,
3. the stresses applied at supports or at point loads are uniform, and the node is confined by stirrups,
4. the reinforcement is arranged in multiple layers, and
5. the node is reliably confined by means of bearing arrangement or friction.

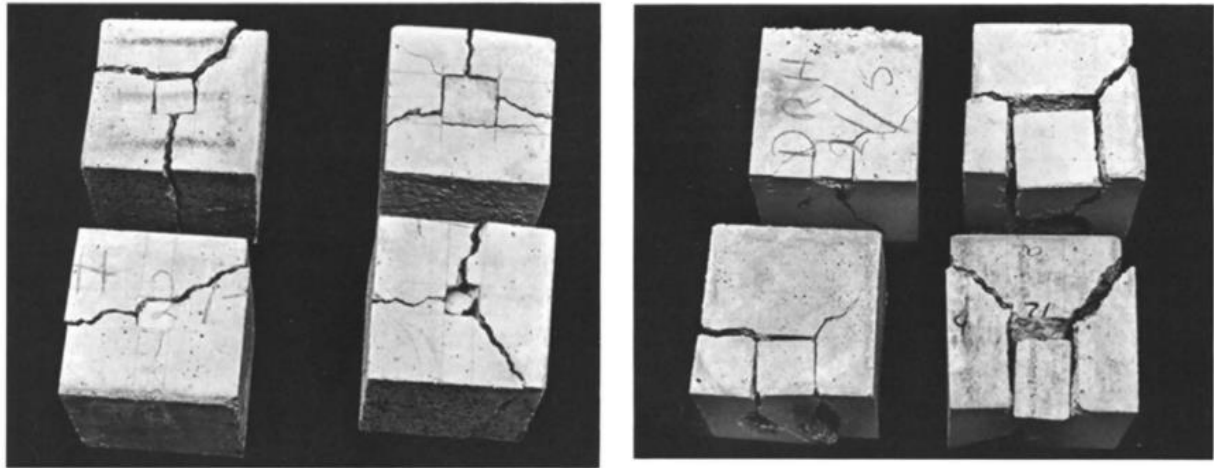
2.4.2. Experimental and Analytical Studies

This section presents a review of past experimental and analytical studies on the effect of confinement on the behavior of reinforced concrete members. These studies denote how confinement is essential in affecting strength and altering failure modes. These studies are also fundamental to major design codes regarding the increase in concrete strength due to confinement.

Hawkins 1968

In the 1950s to 1960s, when the allowable stress design method was popular, it was acknowledged that the allowable bearing stress for concrete dictated the member dimensions. Questioning the belief, Hawkins (1968) experimentally investigated the bearing strength of concrete on 230 small-scale specimens divided into 18 series. The specimens included 6-in. cubes, 9-in. cubes, 4-in. by 8-in. cylinders, and 6-in. by 12-in. cylinders. The study aimed to evaluate the effects of concentric

and eccentric loadings, the geometry of the specimens and loading plates, and concrete strength. Tests were conducted by applying load through a rigid bearing plate on top of the specimen until failure. The average bearing stress and the failure mode were recorded. It was observed that the ratio of the bearing area to the unloaded area and the eccentricity impact the bearing strength and the failure load. Unlike eccentrically loaded cubes, concentrically loaded specimens failed due to punching out of an inverted cone inside the concrete under the loaded area, as shown in Figure 2-16. Concentrically loaded specimens also appeared to have higher bearing strength.



(a) Concentrically loaded cubes

(b) Eccentrically loaded cubes

Figure 2-16 Examples of typical failure modes (from Hawkins 1968)

The author attributed the failure patterns of concentrically loaded cubes to the fact that the radial pressures exerted by this cone led to the splitting of the specimen. The mechanism was resisted if triaxial confinement was present, which increased the bearing strength. On the other hand, the specimen's depth was found to have no effect on the bearing strength.

In general, the bearing strength was found to be affected by the bearing plate relative to the plane dimensions of the specimens, shape, and position of the bearing plates (at centers, corners, or outside faces of the specimens), tensile strength of concrete, internal friction along the failure plane, and the size of aggregates. The author formulated a conservative estimate of the bearing strength for concentric loading, given by

$$\frac{q}{f'_c} = 1 + \frac{K}{\sqrt{f'_c}} (\sqrt{R} - 1) \quad (2-9)$$

Where q is the bearing strength; K is a constant reflecting characteristic of concrete, taken as 50 for practical purposes; R is the ratio of unloaded area to loaded area. The author also formulated a simplified expression for edge loading, given by

$$\frac{q}{f'_c} = \left(1 + \frac{a}{2b}\right) \quad (2-10)$$

where a is half the length of the shorter side of a rectangular plate, and b is half the length of the longer side of a rectangular plate. Equation (2-10) applies when the specimen's side length is at least twice the length of the longer side of the bearing plate.

Adebar and Zhou 1993

Adebar and Zhou (1993) investigated the effect of plain concrete confinement on the bearing strength of compressive concrete struts. A total of 59 concrete cylinders of varying diameters and varying heights were loaded over a constant bearing area. In particular, the diameter of the cylinders ranged from 6 in. to 24 in., while the diameter of the loaded circular plates was kept 6 in. The height of the cylinders varied between 9 in. to 36 in. In addition, the compressive strength of concrete included 3 ksi and 4 ksi. The effect of the confinement parameter, defined by the ratio of the cylinder diameter to the loaded circular diameter D/d , was evaluated. Also, the geometric factor, defined by the ratio of the height of the cylinder to the loaded circular diameter and the ratio of the height of the cylinder to the loaded circular diameter, H/d , was evaluated. Figure 2-17 provides a schematic test setup of this study.

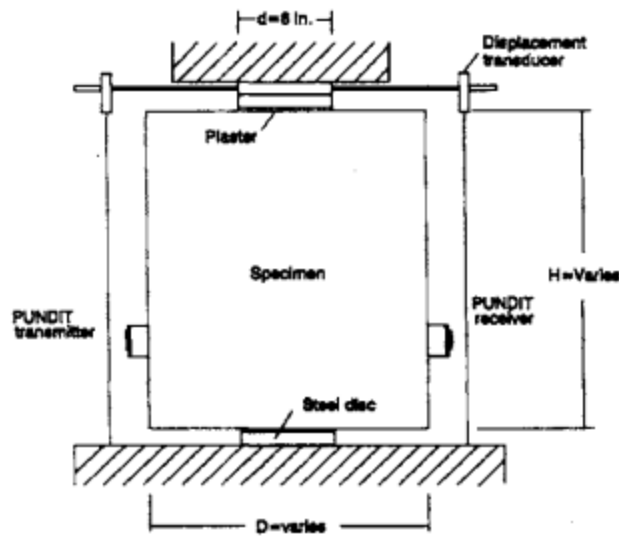


Figure 2-17 Schematic of test setup (from Adebar and Zhou 1993)

Comparisons between the test results and ACI code revealed that the ACI predictions of the bearing strength were unconservative for a large number of tests in a range of $1.5 \leq D/d \leq 3.5$. It was indicated that in order to prevent failure of the concrete struts, the bearing stress in the nodal zones must be restricted, which strongly depends on the amount of confinement ratio D/d , otherwise $\sqrt{A_2/A_1}$ and the geometric ratio H/d of the strut. Based on the test results, the authors

proposed a simple equation for the maximum bearing stress of a plain concrete without sufficient web reinforcement given by

$$f_b \leq 0.6f'_c(1 + 2\alpha\beta) \quad (2-11)$$

in which

$$\alpha = 0.33 \left(\sqrt{\frac{A_2}{A_1}} - 1 \right) \leq 1.0 \quad (2-12)$$

$$\beta = 0.33 \left(\frac{H}{d} - 1 \right) \leq 1.0 \quad (2-13)$$

The equations were based on concrete compressive strength up to 4 ksi. If the concrete compressive strength is greater than 5 ksi, the authors proposed a modification to the above equation, given by

$$f_b \leq 0.6f'_c + 72\sqrt{f'_c}(\alpha\beta) \quad (2-14)$$

Further investigations may be required to study the bearing capacity for specimens with high-strength concrete.

Adebar and Zhou 1996

Adebar and Zhou (1996) evaluated design methods that had appeared in different code specifications for deep pile caps. Investigated design methods included ACI 318 sectional analysis, CRSI Handbook empirical method, and the STM. When applying the STM, the authors utilized the design expression for an increase in strength of confined nodes proposed in Adebar and Zhou (1993). In total, 48 deep pile caps from Deutsch and Walker (1963), Blevot and Fremy (1967), Clarke (1973), and Adebar et al. (1990) were collected and analyzed.

The analytical results revealed that considering the confinement effect, the STM generated more accurate and conservative predictions. That is, evaluating maximum bearing stress for pile caps according to Equation (2-11) better estimated the capacity against the test results. Traditional design procedures provided by ACI 318-89 and CRSI Handbook were frequently found unconservative for deep pile caps.

Furuuchi et al. 1998

Furuuchi et al. (1998) experimentally investigated the shear behavior of reinforced concrete deep slabs. The main investigated variables included the effective width, the shear span ratio, and the dimensions of loading/supporting plates. Thirteen reinforced concrete deep slabs were constructed and tested. The slab depth and reinforcement ratio were kept constant for all test specimens: a depth of 8 in., and 2.2% and 0.3% longitudinal tension and compression reinforcement, respectively. The shear span-depth ratio varied between 1.25 and 2.25, while the length of the loading and supporting plates ranged from 4 in. to 20 in., and from 4 in. to 12 in., at the positions

of the load and support, respectively, with constant width of 2 in. Two slab widths of 4 in. to 25.5 in. were considered, with concrete compressive strength varied between 3 ksi and 5 ksi, as shown in Figure 2-18.

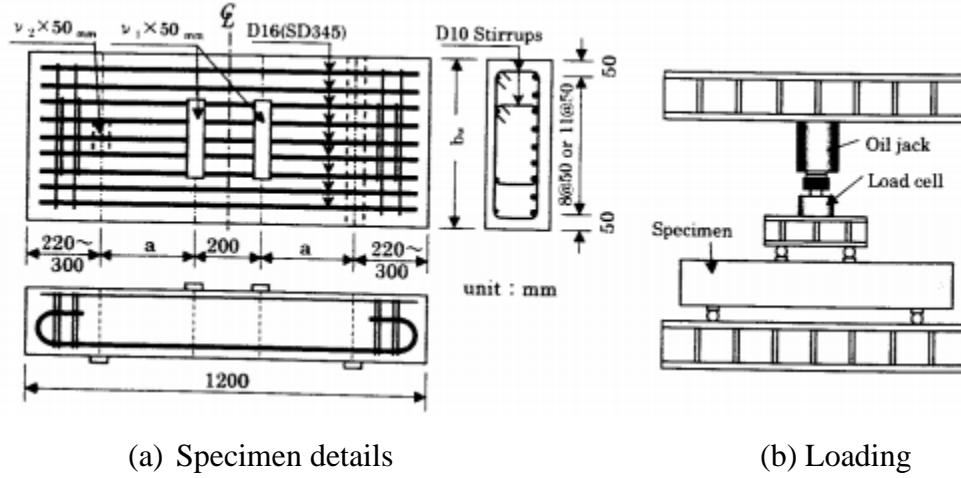


Figure 2-18 Typical slab specimens (Furuuchi et al. 1998)

It was observed that all specimens failed suddenly due to the formation of diagonal shear cracks with varying crack patterns dependent on the shear span-depth ratios and size of the bearing/loading plates. A three-dimensional crack pattern was formed when the lengths of the loading and bearing plates were shorter than the width of the slab, showing the effects of triaxial confinement. It was concluded that the effective width is related to a three-dimensional strut formed between the loading and the support plate and is delineated by the sizes of the loading/supporting plates. An equation for deep beams in the JSCE Standard Specification was used for the analysis of deep slabs because of shared characteristics.

$$V_{wd} = \frac{0.24 f_c'^{2/3} (1 + \sqrt{p_w}) (1 + 3.33 r/d)}{1 + \left(\frac{a}{d}\right)^2} b_w d \quad (2-15)$$

where V_{wd} is the shear capacity; p_w is 100 times the reinforcement ratio, r is the width of the supporting plate; a is the shear span; b_w is the width; d is the effective depth.

Foster and Malik 2002

The design of reinforced concrete members using the STM is on the bases of the lower bound theory of plasticity. In other words, materials, including concrete, are assumed to be perfectly plastic. However, the assumption is far from reality when concrete struts fail in compression. To address the discrepancy, an efficiency factor is introduced to modify the uniaxial compressive strength of concrete. In this study, Foster and Malik (2002) reviewed past expressions for the efficiency factor and proposed a new model evaluated against available test data, which included 135 specimens that failed due to compression in struts of non-flexural members. The authors

generally categorized the equations of the efficiency factor into three main types: 1) Compressive strength of concrete based, 2) multi-parameter, and 3) the MCFT-based models.

The authors concluded that the results do not show a significant correlation between the concrete strength and the efficiency factor. Further, multi-parameter models can give a poor correlation. The strut angle shall be included in the equation to obtain agreeing correlation against the test data. It was also pointed out that boundary conditions considerably affect the determination of failure modes and scattered data, implying the importance of triaxial confinement at the nodes (size of the loading/supporting bearing plates).

Thompson et al. 2005

The anchorage behavior of headed reinforcement in CCT nodes was studied experimentally by Thompson et al. (2005). The capacity of unconfined CCT nodes and confined CCT nodes anchored with headed bars were evaluated, and a model for the anchorage capacity of headed bars at CCT nodes was developed. This study tested and analyzed 64 deep beam specimens with a CCT node anchored by headed bars. The main variables are the strut inclination θ , bar diameter d_b , and the ratio of net head area to bar area A_{nh}/A_b . During the tests, the maximum reaction at the node P_{max} , bar stress at $1d_b$ and at $7d_b$ away from the face of the head were monitored. The typical detail of the CCT nodal zone is shown in Figure 2-19. The experimental tests identified Four types of failure: (1) pullout failure (due to pull-out of the tie bar from the node, which occurred in specimens with no heads), (2) splitting failure (due to lateral splitting of the concrete at the node), (3) crushing failure (due to crushing of the concrete at the node), and (4) yielding of the tie bar near the node.

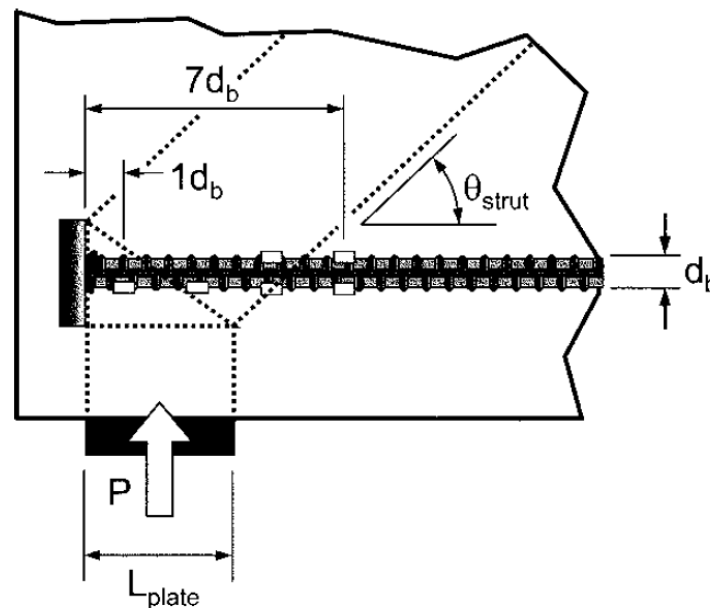


Figure 2-19 Details of CCT nodal zone (Thompson et al. 2002)

Excluding the failure modes of yielding and pullout, the test results were analyzed per ACI 318-02. It was found the method suggested in ACI 318-02 was overly conservative and largely scattered. The author suggested that the side cover ratio and confinement to the nodal zone be included in design expressions and proposed a model for head-bearing capacity as follows:

$$\frac{N}{A_{nh}} = 0.9\phi f'_c \left(\frac{2C}{\sqrt{A_{nh}}} \right) \varphi \quad (2-16)$$

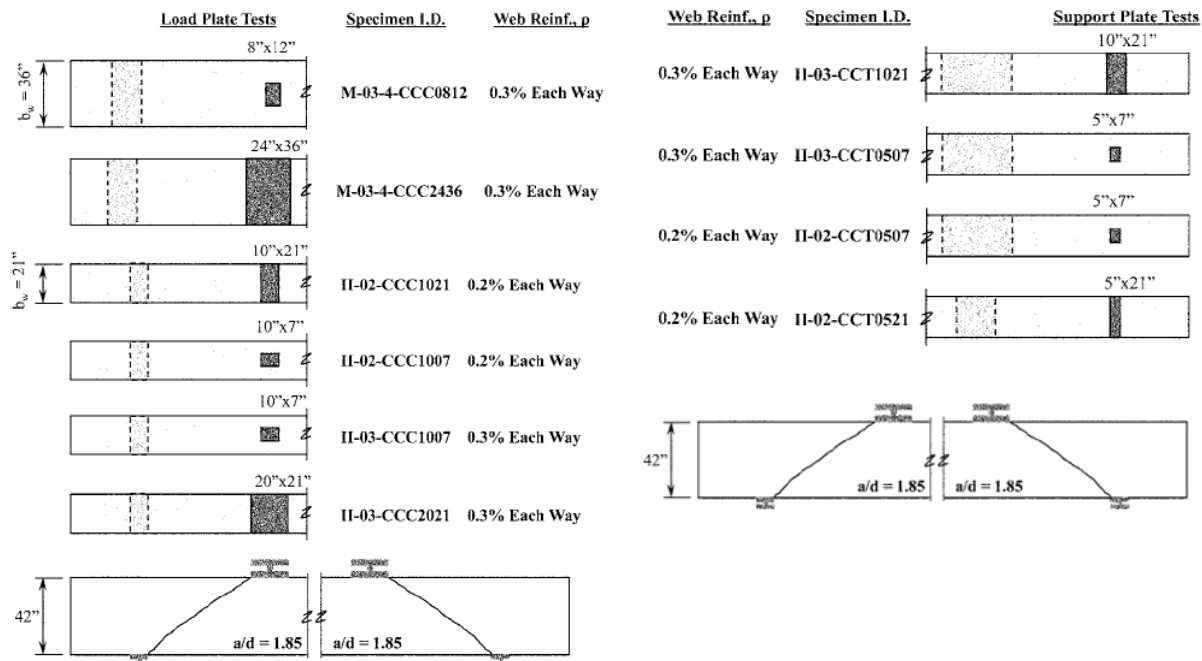
$$\varphi = 0.6 + 0.4 \left(\frac{C_2}{C} \right) \leq 2 \quad (2-17)$$

where C and C_2 are the minimum cover dimensions; ϕ is the material reduction factor, taken as 0.7.

Tuchsherer et al. 2010

Tuchsherer et al. (2010), as part of TxDOT Project 0-5253, investigated the advantages of triaxial confinement given the loaded/supported area of a strut-and-tie model. Triaxially confined concrete was known to have higher compressive strength; however, ACI 318 did not incorporate the effect for nodal zones in the STM, leading to an overly conservative design. This study aimed to bridge the gap by experimenting with deep specimens.

Five full-scale beams consisting of ten tests were constructed and tested. Four beams had cross-sections of 21 in. by 42 in., and one beam had a cross-section of 36 in. by 48 in. The shear span-depth ratio was selected to be 1.84. The main variables were the size of the loading and supporting plates and the amount of web reinforcement. The loading plate (representing the CCC node) had a size ranging from 7 in. by 10 in. to 24 in. to 36 in.; the supporting plate (representing the CCT node) had a size ranging from 5 in. by 7 in. to 10 in. by 21 in. The web reinforcement ratios included 0.3% and 0.2% in both directions. Details of the test beams are shown in Figure 2-20.



(a) Evaluating load bearing area

(b) Evaluating support bearing area

Figure 2-20 Triaxially confined node tests (from Tuchsherer et al. 2010)

Test results revealed that triaxial confinement produced higher bearing strength in the nodal region, exceeding the concrete compressive strength. The failing bearing stress at unconfined support nodes and unconfined load nodes ranged from $0.69f'_c$ to $1.1f'_c$ and $0.45f'_c$ to $0.5f'_c$, respectively. However, for confined support nodes and confined load nodes, the failing bearing stress ranged from $3.7f'_c$ to $4.1f'_c$ and $2.1f'_c$ to $4.6f'_c$. Within the test results obtained in this study, the bearing stresses at failure with confined load plates were significantly higher than those allowed by the design codes.

Comparing the shear capacity of the test results with that calculated per the STM provisions in ACI 318-08 disclosed that the code specifications were overly conservative for deep beams with bearing areas confined by a larger area of concrete. It was suggested that nodal strength be modified by a factor of the lesser of $\sqrt{A_2/A_1}$ and 2.0 to reflect the increase in strength due to triaxial confinement. With the triaxial confinement factor, predictions became more accurate but still conservative against the test results.

Geevar and Menon 2019

Reinforced concrete bridge piers are commonly used to support wide bridge decks and subjected to high shear and flexural stresses with a very small shear span-depth ratio, which is considered D-regions and can be designed using the STM. Geevar and Menon (2019), in this study, experimentally verify the validity of the STM on RC pier caps. Eight pier cap scaled-down specimens were constructed and tested. The dimensions of seven specimens had a scale factor of

1/3.5 in linear dimension, compared to prototypes used in bridge construction, and one specimen with a smaller scale factor of 1/5.6. Each pier cap was subjected to four concentrated loads. The main variables included the amount of main tensile reinforcement, the amount of distributed reinforcement (vertical and horizontal reinforcement), the size of the bearing plates, and eccentricity in loading. Specimen details are shown in Figure 2-21. It should be noted that the unit in the figure is in SI.

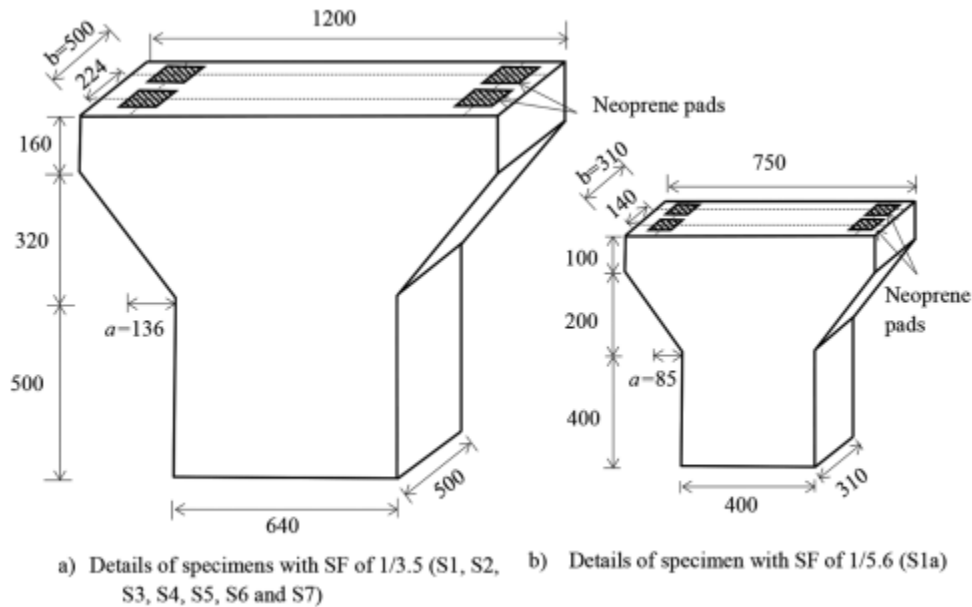


Figure 2-21 Details of specimens (from Geevar and Menon 2019)

It was shown that including the triaxial confinement factor significantly improved the load capacity predictions. The mean ratio of the experimental strength to the predicted strength was 1.32 and 1.96, using the STM per ACI 318 with and without the triaxial confinement factor. Ignoring the bearing node check at the CCT node delivered even better predictions with a mean ratio of 1.26. Using the STM per AASHTO LRFD, on the other hand, led to very conservative predictions with a mean ratio of 1.61. The high conservatism was attributed to the efficiency factor in AASHTO LRFD being lower than ACI 318 for web reinforcement ratios lower than 0.3%. Further research may be required to study the effects of distributed reinforcement and the size of the bearing plates on the ultimate loads of reinforced concrete pier caps.

Mander et al. (1988)

Mander et al. (1988) developed a stress-strain model for uniaxially loaded concrete with transverse reinforcement as confinement. Provided with transverse confinement, the confined compressive strength f'_{cc} by circular hoops or spirals can be given by

$$f'_{cc} = f'_{co} \left(-1.254 + 2.254 \sqrt{1 + \frac{7.94 f'_l}{f'_{co}}} - 2 \frac{f'_l}{f'_{co}} \right) \quad (2-18)$$

where f'_{co} is unconfined compressive strength; f'_l is effective lateral confining stress, which can be calculated as follows:

$$f'_l = \frac{1}{2} k_e \rho_s f_{yh} \quad (2-19)$$

$$k_e = \frac{A_e}{A_{cc}} \quad (2-20)$$

where ρ_s is the confinement ratio; A_e is the effective confined area; A_{cc} is the perimeter of the spiral or the hoop.

If rectangular sections are considered, a chart that correlates the confined strength ratio to confining stress ratio in each direction can be used, as shown in Figure 2-22.

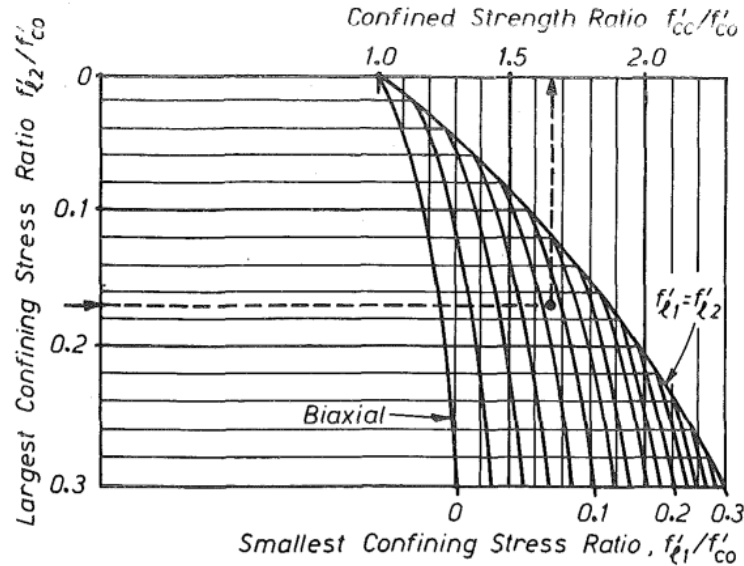


Figure 2-22 Confined strength from lateral confining stresses (from Mander et al. 1988)

2.4.3. Findings and Research Needs

This literature review was conducted on a broad range of research relevant to the confinement of nodal regions, focusing in particular on experimental research, investigation of specifications, and analytical research. This review yielded the following key points:

- Tests on concrete members with various load/support plate sizes smaller than the member dimensions revealed three-dimensional crack patterns and failure modes. The phenomenon indicated the existence of triaxial confinement by surrounding concrete.

- When compression struts are confined by plain concrete, the maximum bearing stress that causes transverse splitting depends on the amount of concrete confinement. The confined compressive strength of concrete can be much higher than the unconfined compressive strength of concrete.
- The strength of triaxially confined CCC and CCT nodes (CCC or CCT) can be calculated by introducing a triaxial confinement factor ($\sqrt{A_2/A_1} \leq 2$). The use of the triaxial confinement factor was validated to be more accurate without losing conservatism than the original code provisions. The effect of triaxial confinement also applies to the behavior of head anchorages.
- Strength increase resulting from confinement owing to transverse reinforcement, otherwise lateral confining stresses, was described in the literature. European codes also acknowledge the application of passive confinement by providing confining reinforcement in the STM. However, further research is needed to quantify the effect and develop applicable details for nodal zones in the STM.

2.5. Spacing Limits for Crack Control Reinforcement

It is widely accepted that the minimum amount of web crack control reinforcement should be provided to prevent premature failures of struts. Further, the web crack control reinforcement spacing should be smaller than the upper limit. However, the amount and the spacing requirement vary among major design code specifications. This section summarizes the spacing and amount of crack control reinforcement specified in STM provisions of various code specifications, as well as the previous research studies relevant to crack control reinforcement.

2.5.1. STM Provisions in Code Specifications

AASHTO LRFD (2020), ACI 318-19 (2019), CSA A23.3-14 (2014), CEB-FIP Model Code (1990), CEB-FIP Model Code (2010), and Eurocode 2 (1992) were selected and the STM provisions in those code specifications are summarized in this section.

AASHTO LRFD Bridge Design Specifications (2020)

The minimum crack control reinforcement ratio required by AASHTO LRFD (2020) is 0.3% in two perpendicular directions spaced at less than the minimum of one-quarter the effective depth of the section ($d/4$) and 12 in. This reinforcement should be distributed evenly near the sides of the strut in each direction. If provided amount of crack control reinforcement is less than required, the value of the efficiency factor for the strut should be 0.45.

CSA A23.3-14 (2014)

The Canadian Standards Association (CSA) A23, 43-14 specifies a minimum ratio of crack control reinforcement not less than 0.2% in each direction with a spacing not greater than 12 in. The efficiency factor is not directly related to the minimum amount of web reinforcement ratio but instead depends on the tensile strain of the tie reinforcement and the inclination of the strut.

ACI 318-19 (2019)

ACI 318-19 (2019) provides two approaches to calculate the requirement for minimum distributed reinforcement across struts. Firstly, it is required that at least 0.25% of orthogonal reinforcement be provided in each direction. Alternatively, if only reinforcement is provided in only one direction, the minimum amount is given by

$$\frac{0.0025}{\sin^2 \alpha} \quad (2-21)$$

where α is the smaller angle between the orientation of the reinforcement and the strut; the value of α should be less than 40 degrees. Other than the requirement for the amount of the minimum distributed reinforcement, the spacing is limited to not greater than 12 in.

CEB-FIP Model Code (1990 and 2010) and Eurocode 2 (1992)

Neither the CEB-FIB Model code (1990 and 2010) nor Eurocode 2 (1992) provide guidance within the STM section. Instead, the codes require a minimum reinforcement area ($A_{s,min}$) for crack control in deep elements (with a depth larger than 31.5 in) given by

$$A_{s,min} = k_c k f_{ct,eff} \frac{A_{ct}}{\sigma_s} \quad (2-22)$$

where A_{ct} is the area of concrete within the tensile zone; $f_{ct,eff}$ is the effective tensile strength of concrete when first cracking occurs; k is the coefficient which takes account of member depth; k_c is coefficient which takes account of scheme of tensile stress distribution; σ_s is maximum reinforcement stress after cracking (assumed to be specified yield strength in general).

CEB-FIB Model code (2010) provides a similar relationship for the minimum reinforcement area for crack control in fiber-reinforced concrete deep elements as

$$A_{s,min} = k_c k (f_{ctm} - f_{Ftsm}) \frac{A_{ct}}{\sigma_s} \quad (2-23)$$

where f_{ctm} is the average tensile strength of concrete when first cracking occurs; f_{Ftsm} is the average residual strength of fiber-reinforced concrete.

2.5.2. Experimental & Analytical Research Studies

This section summarizes research studies contributing to the development and understanding of the crack control reinforcement provisions.

Frantz and Breen 1980

Frantz and Breen (1980) constructed and tested 44 inverted T-beams designed per AASHTO LRFD in order to investigate the effect of side surface crack control reinforcement on serviceability in terms of web crack widths. Investigated factors included the location, quantity, and arrangement of skin reinforcement. In addition, the type of web reinforcement and cross-sectional dimensions were investigated. It was found that the skin reinforcement ratio affects crack width on the side surface. The depth of the tension zone was found important; the required skin reinforcement ratio increases as the depth increases. Based on the test results, the study suggested that distributing many small bars instead of a few large bars within the tension zone is the most effective.

Anderson and Ramirez 1989

Anderson and Ramirez (1989) experimentally investigated the effect of the detailing of stirrups on the shear behavior of RC beams. Per truss analogy, it was believed that compressive stresses flow diagonally and concentrate on the outside longitudinal bars where a two-legged stirrup intersects, causing premature failures due to the crushing of concrete (see Figure 2-23). To address the phenomenon, this study investigated the characteristics of stirrups, including the type of stirrups, the number of legs, and the spacing. The beam specimens had two different cross-sectional dimensions, referencing narrow beams (8 in. by 20 in.) and wide beams (16 in. by 16 in.). The shear span, the amount of longitudinal reinforcement ratio and web reinforcement ratio were kept constant.

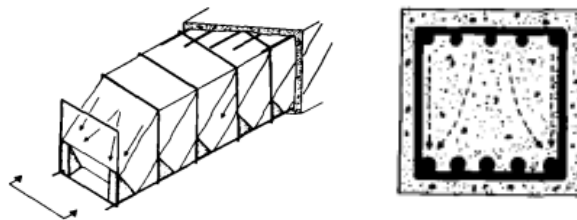


Figure 2-23 Stress concentration of diagonal strut mechanism (from Anderson and Ramirez 1989)

Test results revealed that in beams with two stirrup legs only, the diagonal compression strut concentrated on the outside joints between the stirrup legs and longitudinal reinforcement, which resulted in a large crack width. In contrast, beams with three and four legs allowed the formation of additional truss joints inside the concrete core, leading to better crack distribution, uniform development of the concrete compression strut across the section in the shear zone, and improved ultimate load behavior.

Based on the test results, it was concluded that stirrup legs should be transversely distributed across the web width for wide beams. If U-stirrups are used, the ends should be anchored by a standard hook bent into the confined concrete core.

Yoon et al. 1996

The adequacy of the minimum shear reinforcement requirements in reinforced concrete beams with normal, medium, and high-strength concrete was investigated by Yoon et al. (1996). The study was intended to investigate the idea that higher compressive strength requires a higher amount of minimum shear reinforcement. A total of twelve shear tests were conducted on full-scale simply-supported reinforced beams with varying amounts of shear reinforcement and compression strength: 5.22 ksi, 9.72 ksi, and 12.63 ksi. The beams had the minimum amount of shear reinforcement according to the 1983 ACI Code, the 1984 CSA Standard, the revised 1989 ACI Code, and the 1994 CSA Standard. The mode of failure, the ductility, and crack control at service levels were also investigated. Details of beam specimens and instrumentation are shown in Figure 2-24.

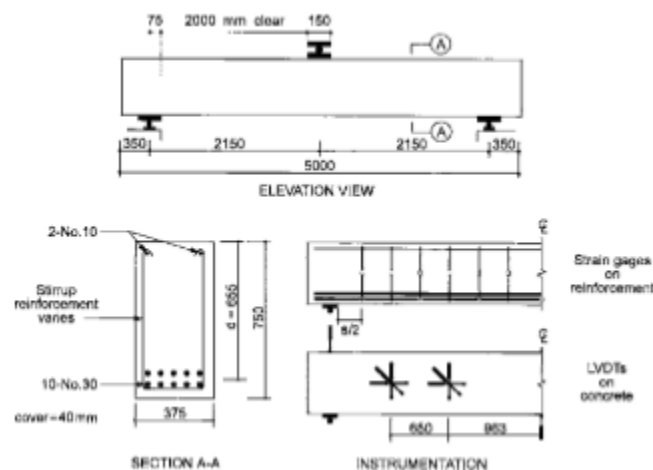


Figure 2-24 Details of beam specimens (from Yoon et al. 1996)

It was concluded that design expressions that do not account for the compressive strength of concrete (1983 ACI Code and 1984 CSA Standards) might cause specimens with high-strength concrete to have lower shear strength compared to those with regular concrete. However, 1989 ACI Codes, although containing compressive strength of concrete, permits the minimum amount of shear reinforcement for beams with concrete strength up to 10 ksi. In this case, enough reserve strength cannot be expected without strain hardening. 1994 CSA Standards, on the other hand, the design expression for the minimum shear reinforcement includes the compressive strength of concrete, leading to adequate reserve strength after cracking.

Tan et al. 1997

Tan et al. (1997) aimed to investigate the effects of web reinforcement patterns on RC deep beams with higher-strength concrete. Eighteen high-strength full-scale reinforced concrete deep beams were constructed and tested. The cross-sectional dimensions were 4.4 in. by 20 in., and the shear span ratio ranged from 0.85 to 1.69. Six types of web reinforcement (vertically, horizontally, or orthogonally distributed rebar) and two different yield strengths of rebar were used in the test program. Failure modes, the ultimate shear capacity and serviceability were evaluated. Investigated web reinforcement patterns are shown in Figure 2-25.

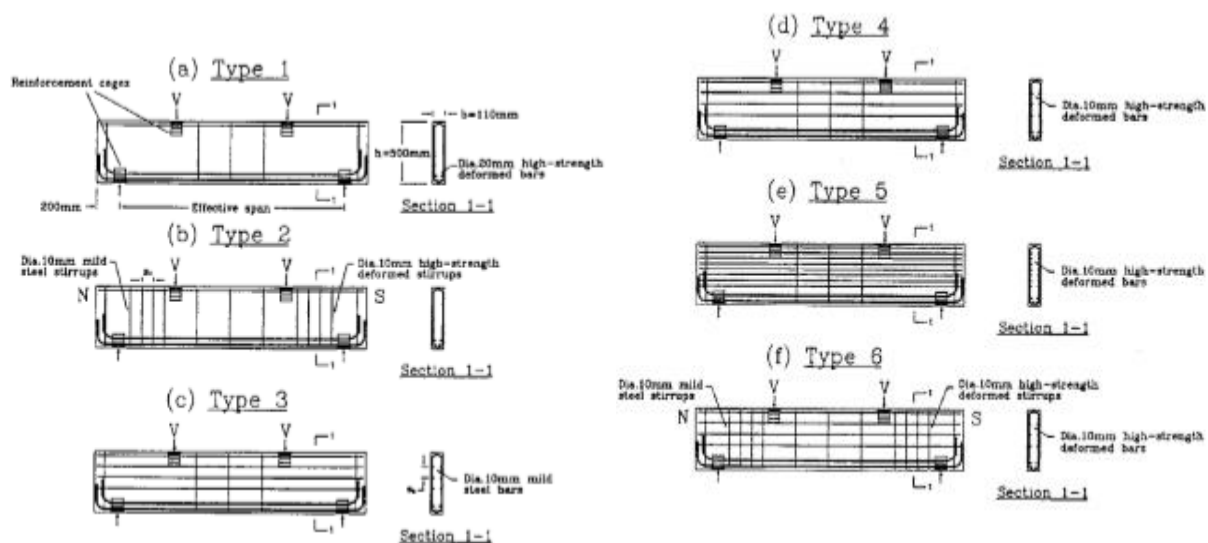


Figure 2-25 Investigated types of web reinforcement (from Tan et al. 1997)

It was observed that the stiffness of the beams depends on the shear span-depth ratio and the web reinforcement. That is, beams with high-strength web reinforcement (Types 4 and 5) with the shear span ratio 0.85 (series I) are stiffer than beams with lower-strength horizontal bars (Type 3) or with only vertical web reinforcement (Type 2). However, this effect was not observed as the shear span ratio increased (series II and III). It was concluded that providing vertical web reinforcement is more effective than horizontal web reinforcement when the shear span ratio is less than 1.0 in controlling diagonal crack widths. Orthogonally distributed web reinforcement (Type 6) had the best serviceability, ultimate strength, and performance. Design codes were also evaluated against the test results, and it was found that the Canadian Code delivers conservative results while the ACI Code tends to overestimate the contribution of horizontal web reinforcement, which required revision to the upper limit on the efficacy of the horizontal reinforcement ratio.

Angelakos et al. 2001

Angelakos et al. (2001), in this study, addressed a concern that the old version of ACI provisions tends to be unconservative for large beams containing only a minimum area of stirrups. Twelve simply supported deep beams were constructed and tested. For the sake of completeness, nine deep

beams similar to those previously tested by Collins and Kuchma (1999) were included in this study. The primary variables were concrete compression strength, longitudinal reinforcement, and transverse reinforcement ratios. Figure 2-26 shows details of the test beams and the test frame.

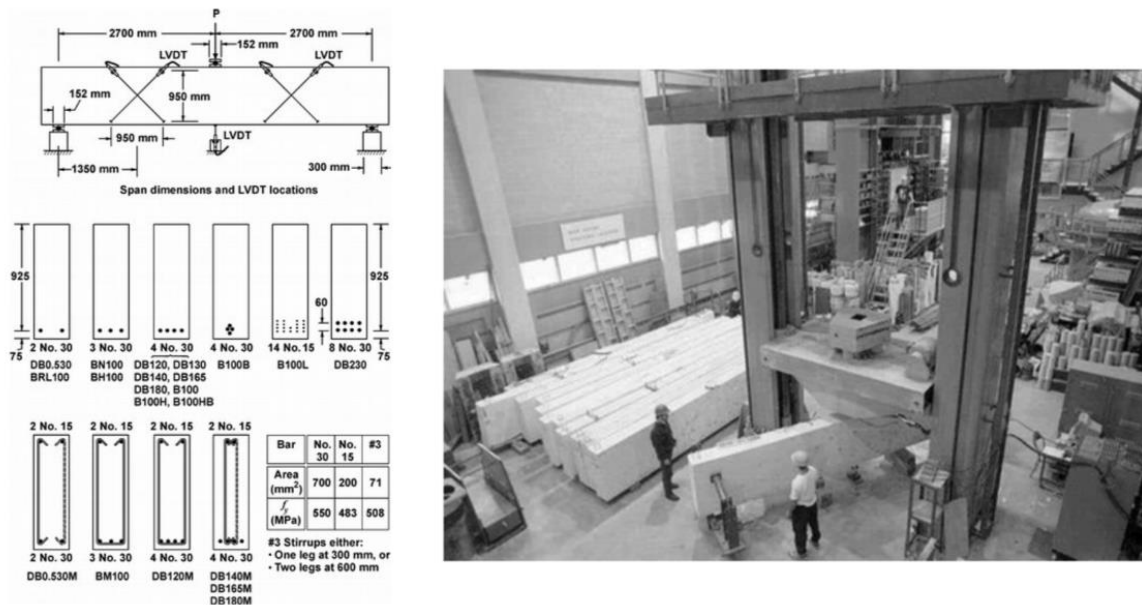


Figure 2-26 Specimens and test setup (from Angelakos et al. 2001)

The test results revealed that increases in concrete cylinder strengths do not necessarily result in increased failing shear stress. The member size and longitudinal reinforcement ratio can significantly affect the shear strength of deep beams. Comparing the test results with the ACI code indicated that the ACI code provisions for shear are very unconservative for large members. Therefore, it appears that the ACI shear equation may require modifications in order to consider large concrete members. Using AASHTO LRFD equations to predict the shear capacity of the tested beams led to better correlations. It was suggested that AASHTO LRFD provisions are better when designing deep beam members before the ACI Codes are modified.

Febres et al. 2006

Febres et al. (2006) experimentally evaluated the adequacy of the strength efficiency factors (β_s) given in the STM provisions of ACI 318 at the time. This study primarily focused on the required minimum web reinforcement ratio across regular and high-strength concrete struts. Twelve reinforced concrete deep beam specimens were constructed and tested. Eight beams were cast using normal-weight concrete, and the other four were made using high-strength concrete.

In addition to the compressive strength of concrete, the strut angle with respect to the longitudinal reinforcement axis and the web reinforcement ratio were included as variables. The longitudinal reinforcement ratio was provided sufficiently to force a diagonal strut failure first. Based on the design variables, three series of specimens were created. Series A consisted of beams with normal

strength concrete with concrete strength of 22 MPa (3.19 ksi) and a strut angle of 28 degrees; Series B had beams with concrete strength of 32.4 MPa (4.70 ksi) and strut angles ranging between 41 and 44 degrees; Series H included beams with high strength concrete of 50.3 MPa (7.30 ksi) and strut angles between 25 degrees to 38 degrees. The vertical web reinforcement ratio in the shear zone of interest ranged from zero to 0.42% for Series A and B. In series H, the vertical reinforcement ratio ranged from zero to 0.85%. A constant horizontal reinforcement ratio of 0.115% was provided for beams with vertical web reinforcement. Example specimen design of Series A is shown in Figure 2-27.

Figure 2-27 Example deep beam specimen design from Febres et al. (2006) (unit: mm)

Tuchschrer et al. 2011

directions. The stirrups were either two-legged or four-legged across the area of interest shear zone. Details of the test specimens and web reinforcement are shown in Figure 2-28.

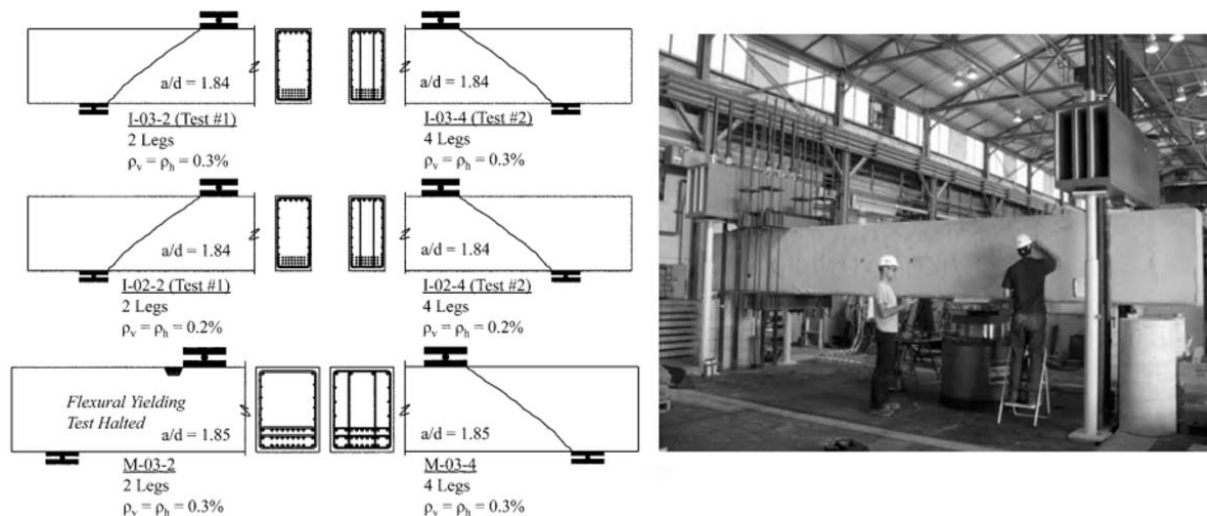


Figure 2-28 Deep beam specimen layouts and test frame (from Tuchscherer et al. 2011)

It was found that the distribution of closely spaced stirrups did not significantly enhance the shear strength of deep beams in terms of strength and serviceability. Examination of the strain in the longitudinal reinforcement indicated that the distribution of stirrups across the web section did not influence the distribution of longitudinal strain. This was in contrast to the findings obtained by Anderson and Ramirez (1989), which showed that beams with closed stirrups exhibited well-distributed strains in longitudinal reinforcement. This difference may have arisen because the test beams in the study had an a/d ratio of 2.65, which corresponds to the sectional shear region, not in the direct strut shear zone in deep beams.

There were currently no limitations for or suggested transverse distribution of stirrups across the web in any code provisions. However, Tuchscherer et al. (2011) concluded that no matter the quantity of stirrup legs, the exterior stirrup legs need to be transverse and should not be spaced greater than the effective depth of the deep beam.

Tuchscherer et al. 2014

Tuchscherer et al. (2014), as part of TxDOT Project 0-5253, established an evaluation database consisting of 868 deep beam shear tests in the literature and 37 deep beam tests from the study to evaluate the STM provisions and provide refinements for AASHTO LRFD. One of the major recommendations to AASHTO LRFD was changing the strength efficiency factor for strut-to-node interface to be related to the concrete strength, given by

$$v = 0.45 \leq 0.85 - \frac{f'_c}{20} \leq 0.65 \quad (2-24)$$

Equation (2-24) holds if the minimum web reinforcement ratio 0.3% is provided and if the spacing requirements for web reinforcement are satisfied in both directions. Other changes included:

1. The allowable stress of all faces of a node may be increased when triaxial confinement is present—that is, a triaxial confinement factor at the position of the nodes.
2. When the longitudinal reinforcement is properly anchored, crushing of the concrete at the back node face does not occur.
3. The effective concrete stress at the back face and bearing face of a CCC node = $0.85f'_c$
4. The effective concrete stress at the bearing face of a CCT node should be taken $0.7f'_c$
5. The effective concrete stress at the CCC strut-to-node interface should be the same as the effective concrete stress at the CCT strut-to-node interface.

The revisions were then incorporated into AASHTO LRFD (2020), becoming the STM provisions for structural designers' use.

Ismail et al. 2017

The STM is based on the lower bound theory of plasticity, in which both concrete and steel are assumed to be perfectly plastic materials. In an attempt to account for the imperfect behavior of concrete struts, Ismail et al. (2017) developed a unified procedure of reinforced concrete deep beams based on modified effective factors for the materials. In conclusion, the authors proposed a relationship between the efficiency factor for reinforced concrete deep beams based on the theory of fracture mechanics developed by Bazant et al. (1997), given by

$$v = \alpha \sqrt{\frac{2EG_f}{W_s \epsilon_1}} \frac{1}{f'_c} \quad (2-25)$$

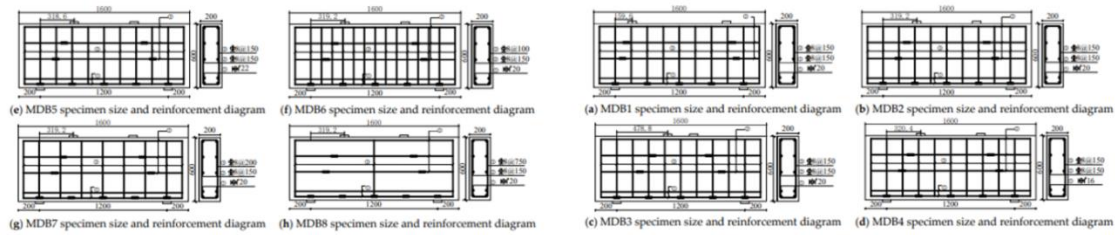
where E and G_f are the moduli of elasticity and fracture energy of concrete, respectively; W_s is the width of the strut; ϵ_1 is the lateral tensile strain in the shear zone that depends on the shear span-depth ratio and the section depth d , given by

$$\epsilon_1 = 0.02 \frac{\left(\frac{a}{d}\right)^{0.5}}{\left(\frac{d}{150}\right)^{0.35}} \quad (2-26)$$

where α is a calibration factor related to web reinforcement ratio, which was obtained from experimental results. α is equal to 400 for reinforced concrete deep beams without shear reinforcement ratio or with a ratio less than 0.1%, and equal to 450 for reinforced concrete deep beams with a shear reinforcement ratio greater than or equal 0.1%.

Zhang et al. 2020

Zhang et al. (2020) conducted an extensive study to investigate the shear capacity performance high strength concrete deep beams. Eight simply-supported reinforced concrete deep beams with dimensions 200 mm by 600 mm by 1600 mm (7.9 in. by 23.6 in. by 63.0 in.) were tested. The variables included shear span-depth ratios of 0.3, 0.6, and 0.9; the longitudinal reinforcement ratio of 0.67%, 1.05%, and 1.27%; the vertical stirrups ratio of 0%, 0.25%, and 0.5%. High-strength grade steel bars with yield strengths of 670 MPa (97.2 ksi) and 420 MPa (60.9 ksi) were used for tension longitudinal reinforcing bars and web reinforcing bars, respectively. The study aimed to investigate the effects of the above variables on the shear capacity, mode of failure, load-deformation behavior, strain distribution across the section, and crack width. The specimen geometry is shown in Figure 2-29.



Component Number	$l \times b \times l$ /mm	Shear Span-Depth Ratio λ	Span Height Ratio l_0/h	Longitudinal Reinforcement Ratio ρ_s (%)	Horizontal Reinforcement Ratio ρ_{sh} (%)	Vertical Stirrup Ratio ρ_{sv} (%)
MDB1	$1600 \times 200 \times 600$	0.3	2	1.05	0.33	0.33
MDB2	$1600 \times 200 \times 600$	0.6	2	1.05	0.33	0.33
MDB3	$1600 \times 200 \times 600$	0.9	2	1.05	0.33	0.33
MDB4	$1600 \times 200 \times 600$	0.6	2	0.67	0.33	0.33
MDB5	$1600 \times 200 \times 600$	0.6	2	1.27	0.33	0.33
MDB6	$1600 \times 200 \times 600$	0.6	2	1.05	0.33	0.50
MDB7	$1600 \times 200 \times 600$	0.6	2	1.05	0.33	0.25
MDB8	$1600 \times 200 \times 600$	0.6	2	1.05	0.33	0

Figure 2-29 Specimen design parameters (from Zhang et al. 2020)

After evaluating the effect of each factor on the behavior of deep beams, the author concluded that the shear span-depth ratio significantly influences the performance. That is, smaller a/d ratios increase the overall ultimate strength of deep beams. However, with such small shear span-depth ratios, the amount of vertical reinforcement seems to have little changes to the cracking load and the ultimate strength, which the authors attributed to the fact that the strut-and-tie mechanism dominates the load transmission of very deep beams.

Zaborac et al. (2020)

Zaborac et al. (2020) investigated the efficiency factor of structures with non-code-compliant web reinforcement ratio using the evaluation database developed by Tuchscherer et al. (2014). In the

AASHTO LRFD, the efficiency factor in the STM provides a binary method. That is, when the web reinforcement is not provided per the code provision (0.3% each direction and a spacing smaller than $d/2$ or 12 in.), the lowest efficiency factor (0.45) is required. However, the test program in Project 0-5253 revealed that using a web reinforcement ratio of 0.2% does not lead to significant reduction in strength as implied by the code. The study aimed to evaluate the discrepancy. In the analysis, 905 deep beam tests were filtered down to 253 tests to fit the purpose of the study.

Six different methods of determining the efficiency factor were used to calculate the strength of deep beams in the database. The methods were categorized into three major categories, and each had two expressions, as summarized in Figure 2-30. Eq. (1) in the figure is expressed as

$$\rho_{\perp} = \rho_v \cos \theta + \rho_h \sin \theta \geq \rho_{\perp min} = \frac{v f'_c \sin \theta}{f_y b d k} \quad (2-27)$$

where ρ_{\perp} is the perpendicular reinforcement ratio; ρ_v and ρ_h are the vertical and horizontal reinforcement, respectively; θ is the inclination of the strut; v is the concrete efficiency factor; b is the beam width; d is the beam effective depth; k is the slope of the dispersion of the compression strut.

Method	Reinforcement condition	Efficiency factor, v^*	Comment
1a	$\rho_{\perp} < \rho_{\perp min} = 0.003 \cdot (\cos \theta + \sin \theta)$	0.45	Cutoff based on meeting reinforcement volume required by AASHTO [4] indirectly.
1b	$\rho_{\perp} \geq \rho_{\perp min} = 0.003 \cdot (\cos \theta + \sin \theta)$	v_{max}	
2a	$\rho_{\perp} < \text{Eq. (1)}$	0.45	Cutoff based on equilibrium of a bottle-shaped strut [69].
2b	$\rho_{\perp} \geq \text{Eq. (1)}$	v_{max}	
3a	$\rho_{\perp} < \rho_{\perp min} = 0.0015 \cdot (\cos \theta + \sin \theta)$	0.45	Cutoff based on meeting half of reinforcement volume required by AASHTO [4] indirectly.
3b	$\rho_{\perp} \geq \rho_{\perp min} = 0.0015 \cdot (\cos \theta + \sin \theta)$	v_{max}	

*Maximum efficiency factor, v_{max} , is selected based on AASHTO LRFD Table 5.8.2.5.3a-1, as if adequate crack control reinforcement has been provided.

Figure 2-30 Nodal efficiency factors selected for evaluation database analysis (from Zaborac et al. 2020)

It was found that the maximum efficiency factors were safe to use for non-code-compliant crack control reinforcement detailing, provided that the minimum perpendicular reinforcement ratio was satisfied. In the case of structures with less than the minimum required ratio, the minimum efficiency factor may be used. For simplicity, an average minimum value corresponding to 0.15% in the vertical and horizontal directions ($\rho_{\perp min} = 0.2\%$) may be considered.

2.5.3. Findings and Research Needs

This literature review was conducted on a broad range of research relevant to web crack control reinforcement and the effect of web reinforcement ratio on the efficiency factor. This review

yielded the following key points with respect to relaxing the current spacing limits for crack control reinforcement as follows:

- The spacing of web reinforcement and the number of legs affect the behavior of reinforced concrete beams in terms of truss mechanism. However, the effect becomes not as significant when applied on deep beams.
- The effect of the web reinforcement ratio and the angle of the diagonal strut on the efficiency factor has been well-studied. However, the “ $d/4$ limit” (i.e., the lesser of $d/4$ or 12 in.) of AASHTO LRFD (2020) in the STM provisions for the spacing of crack control reinforcement is not well-based on experimental data.
- Analytical evaluation of a test database conducted by Zaborac et al. (2020) revealed promising results for structures with non-code-compliant details of web reinforcement. It is required that experimental data be provided to support the feasibility of relaxing the “ $d/4$ limit.”

2.6. Summary

Past studies and design codes pertinent to the application and development of the STM were extensively reviewed. The scope of the literature review encompassed nodes under three orthogonal tensions, curved bar nodes, passive confinement, and spacing requirements for crack control reinforcement. Based on the literature review, primary findings and research needs are summarized as follows:

1. The anchorage of drilled shaft reinforcement in a drilled shaft footing has not been subjected to sufficient research. Using hooked reinforcing bars or mechanical terminators was suggested to develop bar stresses in drilled shaft reinforcement. It was also suggested that a fan-shaped compressive stress field and non-contact splice mechanism be taken to determine the available length for anchorage. Nonetheless, either approach lacks experimental data, which limits the viability. Further, the fan-shaped compressive stress field is formed when sufficient crack control reinforcement is provided. However, the amount of required crack control reinforcement in the STM provisions differs from the requirement for footing surface reinforcement.
2. The curved-bar node appears when longitudinal reinforcement continuously passes through a reinforced concrete member with a bar bend region. The bend radius of such nodes needs to be carefully sized in order to avoid overstressing the concrete within the bar bend region. The clear side cover to the bar bend and circumferential bond stresses are also key to successfully proportioning curved-bar nodes. Design codes ACI 318-19 and *fib* have incorporated the design expressions of curved-bar nodes, while AASHTO LRFD has not due to the lack of experimental data.

3. Strength enhancement in nodal zones derived from triaxial confinement has been well-studied and incorporated into major design codes. However, the effect of passive confinement provided by reinforcement on nodal zones has few available studies, although confining reinforcement increasing the compressive strength of concrete is widely used in practice. Regarding the effect of confining reinforcement, only *fib* has a few comments among major design codes. No specific design guidelines or recommendations for confining reinforcement in nodal zones exist.
4. Enough crack control reinforcement (0.3%) should be provided across struts to prevent premature failure. The spacing of crack control reinforcement should also be under the lesser of $d/4$ or 12 in. for both orthogonal directions. However, the “ $d/4$ limit” of AASHTO LRFD in the STM provisions for the spacing of crack control reinforcement is not well based on experimental data. In fact, the engagement of horizontal web reinforcement and that of vertical web reinforcement are different. There should be more research on such requirements.

Chapter 3. Nodes under Tri-Axial Tension

This chapter presents an experimental program intended to investigate the anchorage behavior of the reinforcement anchored at nodes subjected to a tri-axial tension in drilled shaft footings under a largely eccentric axial load.

3.1. Introduction

Drilled shaft footings commonly support complex sets of forces that are transmitted from bridge piers. Being considered a D-region, where nonlinear stress distribution is disturbed, drilled shaft footings can be modeled and designed using the strut-and-tie method (STM). When drilled shaft footings support a single column subjected to pure axial load, using the STM for the drilled shaft footing is straightforward and has been proven effective in past studies and in Project 0-6953. As shown in Figure 3-1, a typical strut-and-tie model for such drilled shaft footings consists of four ties forming a ring above the bottom in alignment with the height of the bottom mat reinforcement. In addition to the bottom tie ring, four struts forming a strut ring are placed beneath the top surface. The top strut and bottom tie rings are then connected with four more struts representing compressions that flow into the four drilled shafts. With the established strut-and-tie model, one is able to perform nodal strength checks and proportion reinforcement.

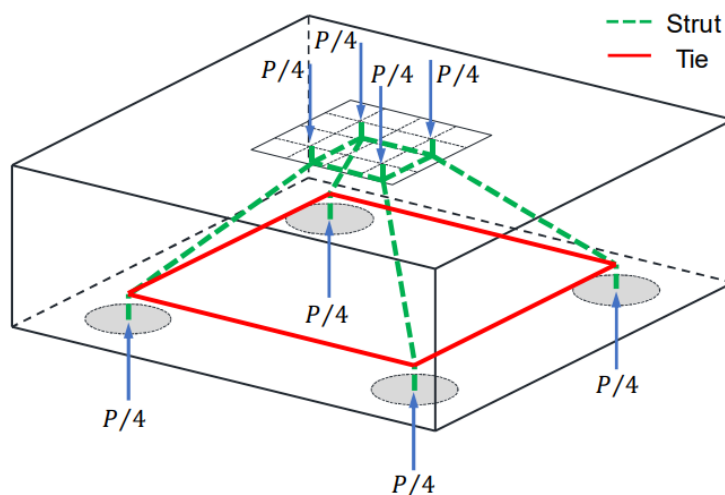


Figure 3-1 Generalized 3D strut-and-tie model for drilled shaft footings under pure axial load (from Project 0-6953)

Challenges, however, arise when the axial load has an eccentricity. In other words, a bending moment acts in the column and transmits into the drilled shaft footing through the column-to-footing interface. As the magnitude of the bending moment increases, one side of the column potentially becomes in tension, eventually resulting in the two drilled shafts on the same side being in tension. In order to model the force transmission, the strut-and-tie model can be perplexing, as shown in Figure 3-2. Unlike the case of a pure axial load, the considered case scenario requires

addressing a non-contact splice problem between the two vertical ties for the column and drilled shaft. Also, each of the nodes above the drilled shafts in tension connects three orthogonal tensions and one diagonal strut. Such a complex nodal zone has not been systematically studied, and AASHTO LRFD 2020 remains silent in this regard.

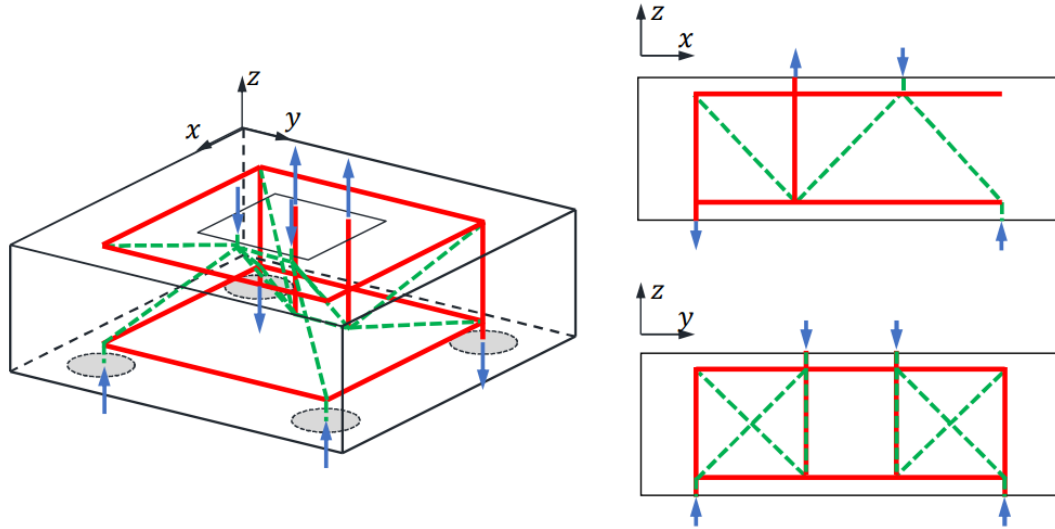


Figure 3-2 3-D strut-and-tie model for drilled shaft footing of which shafts are in tension (from Project 0-6953)

Regarding the knowledge gap, Project 0-6953 delivers guidelines based on the experimental investigation into large-scale drilled shaft footings. The project conducted four tests on various anchorage of drilled shaft reinforcement proportioned for the vertical ties framed into the node in question. The footings were conservatively designed with a skin reinforcement ratio of 0.30%, and the anchorage methods included straight bars, headed bars, and hooked bars. As a result, the project suggested that the non-contact splice can be addressed by defining a fan-shaped strut between the two ties. In particular, the available length (l_{ad}) for developing the drilled shaft reinforcement can be delineated by the boundary of the fan-shaped strut, as indicated by the shaded area shown in Figure 3-3.

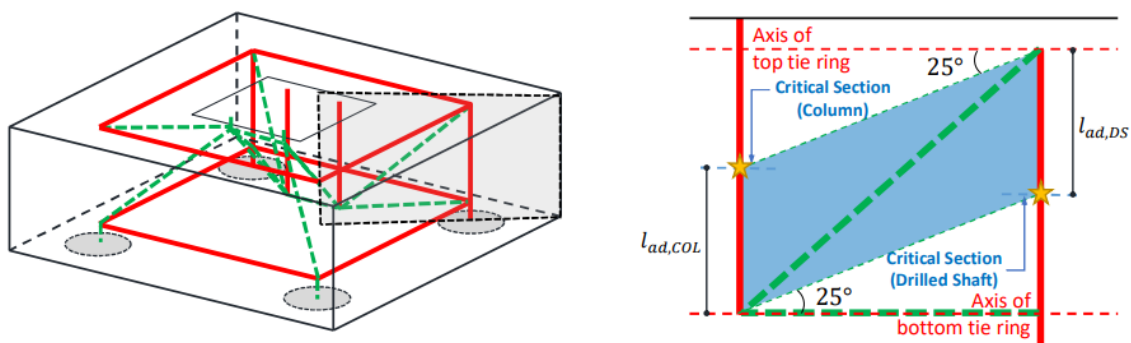


Figure 3-3 Compression field and critical section for drilled shaft reinforcement

However, the approach provided in Project 0-6953 left unsolved questions because of the limited number of tests. First off, the suggestions were deduced from a single span-to-depth ratio. It is unclear if the span-to-depth ratio of footings affects the formation of the fan-shaped strut. Secondly, Project 0-6953 proposed to provide a minimum of 0.18% skin reinforcement ratio for the use of the current nodal efficiency factors specified in AASHTO LRFD 2020. However, the validity of the proposed compression field formed between the vertical ties was not examined for the suggested minimum skin reinforcement ratio (0.18%). Lacking experimental data weakens the applicability of the approach.

Thus, this study aimed to experimentally investigate drilled shaft footings under a largely eccentric axial load for the purpose of bridging the knowledge gaps. In this task, two footing specimens were fabricated and tested. Each of the footing specimens included two tests. One of the investigated variables was the anchorage of drilled shaft reinforcement: straight bars versus headed bars. The other variable was the amount of surface reinforcement: 0.30% versus 0.15%.

3.2. Experimental Program

This section presents the development of the experimental program, including specimen design, fabrication of specimens, test frame, instrumentation, and test procedures.

3.2.1. Specimen Design

3.2.1.1. Design Consideration

The primary purpose of the current study was to evaluate the viability of the suggested available development length by Project 0-6953. The method addresses the non-contact splice between the column reinforcement and the drilled shaft reinforcement using a fanned-shaped compression field under the STM framework, as illustrated in Figure 3-3. According to the method, a fanned-shaped compression field is delineated by two straight boundaries with an angle of 25 degrees, as the shaded area shown in the figure. The 25 degrees was employed from the minimum strut angle specified in AASHTO LRFD 2020. The point where the lower boundary of the fanned strut across the tie proportioned with drilled shaft reinforcement can be taken as the critical section. That is, the portion of the drilled shaft reinforcement from the point to the tip of the bar is taken as the available development length, which is required to be longer than the minimum development length of the drilled shaft reinforcement.

The method, however, was developed on the basis of test results from specimens with a height of 40 in. only. In other words, the availability of the method is limited to a single shear span-to-depth ratio (a/d). It remained questionable if the method was still applicable if the a/d ratio changes. In particular, when the overall height of a drilled shaft footing is smaller, the critical section of the drilled shaft reinforcement determined by the method becomes shifted lower. Therefore, the lowered critical section (marked with a purple start) causes a shorter available development length

for the drilled shaft reinforcement, as shown in Figure 3-4. It should be noted that the figure presents an upside-down drilled shaft footing to be in alignment with the experimental program. However, it is unclear if the assumption that a straight boundary with an angle of 25 degrees still holds. More tests on drilled shaft footings with reduced height are needed.

In order to examine the validity of the method by Project 0-6953 on drilled shaft footings with a reduced height, it was decided to start the task with specimens with a height of 32 in. The designed height was 8 in. shallower than that of specimens in Project 0-6953, resulting in a shorter available length.

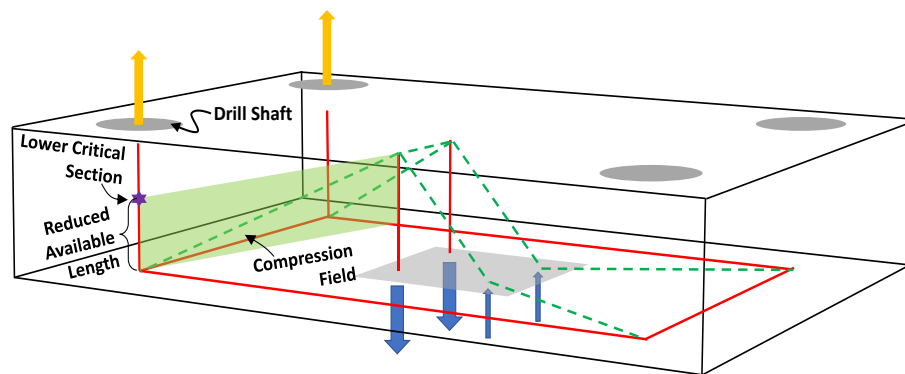


Figure 3-4 Strut-and-tie model for drilled-shaft footing with reduced height

Moreover, the effect of the skin reinforcement ratio on the formation of the compression field between the column and drilled shaft ties has not been studied. According to AASHTO LRFD 2020, a minimum reinforcement ratio of 0.30% for crack control should be provided in the plane of a strut. However, this requirement is challenging in drilled shaft footings where the 3D strut-and-tie model is typically developed. Instead, all faces of a footing should have a minimum amount of 0.18% skin reinforcement to control shrinkage and temperature cracks in accordance with AASHTO LRFD 2020. The experimental and numerical research on drilled shaft footing subjected to uniaxial compression conducted by Project 0-6953 concluded that 0.18% skin reinforcement could ensure the use of the nodal efficiency factors currently employed in AASHTO LRFD 2020. The effect of the skin reinforcement ratio, however, was not examined in drilled shaft footing subjected to axial compression combined with flexural loading scenarios. To supplement the conclusion, this research aimed to investigate the effect of the skin reinforcement ratio on the development of the assumed compression field forming between the column and drilled shaft ties. Therefore, two footing specimens were designed with different skin reinforcement ratios (0.30% and 0.15%).

Except for the two parameters: the height and the skin reinforcement ratio, other dimensions were determined to be the same as what was used in Project 0-6953. The reinforcing details were not changed either in order to eliminate undesired effects. The amount of reinforcement was designed to prevent undesired flexural failure.

3.2.1.2. Test Matrix and Specimen Details

Following the design considerations, the research team planned two footing specimens which had two sides to be tested, as summarized in Table 3-1. Each of the specimens was sized as 96 in. by 132 in. by 32 in., as shown in Figure 3-5.

Table 3-1 Test Matrix

Series No.	Test No.	Test I.D.	Footing Dimension (in.)	Shaft Diameter (in.)	Reinforcement per Shaft	Anchorage	Skin Reinforcement Ratio
I	1	I-32-S-0.3	96x132x32	16	5-#6 (1.09%)	Straight	0.30%
	2	I-32-H-0.3	96x132x32	16	5-#6 (1.09%)	Head	0.30%
II	1	II-32-S-0.15	96x132x32	16	5-#6 (1.09%)	Straight	0.15%
	2	II-32-H-0.15	96x132x32	16	5-#6 (1.09%)	Head	0.15%

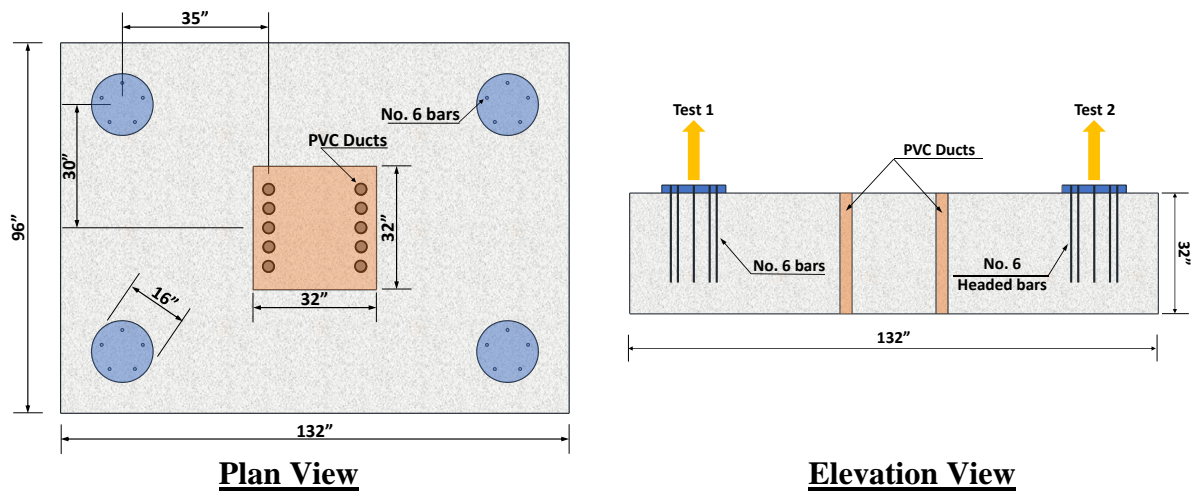


Figure 3-5 Specimen Design

Each of the specimens has four 16-in. square loading plates simulating drilled shafts with a diameter of 16 in. on each corner. The steel plates were located 30-in. transversely and 48-in. longitudinally away from the center of the footing specimen. The steel plates were designed to transfer the loading applied from an actuator.

Based on the parameter study conducted for drilled shaft footings constructed in the State of Texas in Project 0-6953, five No.6 bars were provided to represent the standard drilled shaft reinforcement ratio employed in drilled shaft footings. The provided reinforcement amount is equivalent to a shaft reinforcement ratio of 1.09%. Two different anchorage types – headed and straight – are employed for the drilled shaft reinforcement anchorages in each specimen. In addition to the anchorage method, two different skin reinforcement ratios were provided to the test specimens to investigate their effect on the anchorage response of the drilled shaft reinforcement. The first specimen had a skin reinforcement ratio of approximately 0.30%, almost identical to that

provided to the specimens of Project 0-6953. The second specimen, on the other hand, had a surface reinforcement ratio of approximately 0.15%.

It was extremely challenging to create a largely eccentric axial load inducing tension in the drilled shaft bars for the concern of safety. Hence, the equivalent loading condition proposed in Project 0-6953 was also used for the experimental program. By employing the equivalent loading condition, the drilled shaft reinforcement is subjected to direct tension, and it generates a large bending moment at the column region. A large amount of column reinforcement is required to resist the bending moment; therefore, the column tie elements in the model were replaced with post-tensioning forces (a total of 750 kips) to preclude the failure induced by the column tie elements. To facilitate the application of the equivalent loading condition, the specimens were fabricated upside down. As illustrated in Figure 3-6, the 3D strut-and-tie model resulting from the equivalent loading condition exhibits the same load path induced by a large eccentric axial loading (Figure 3-2). Tri-axial orthogonal ties and a diagonal strut (i.e., compression field) intersect at the end node of the drilled shaft tie element.

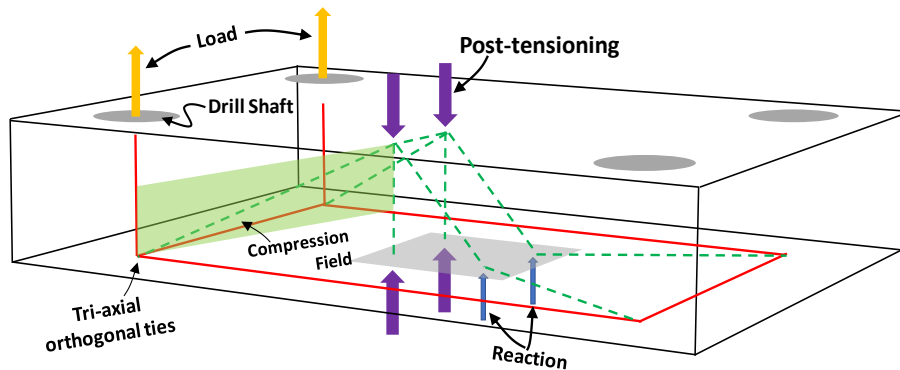
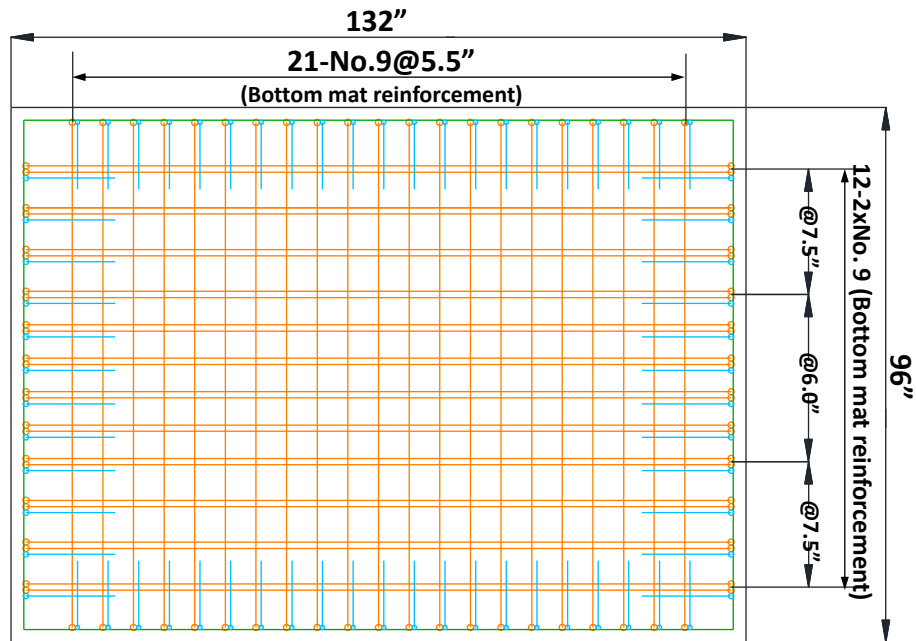


Figure 3-6 Altered load path in footing specimen

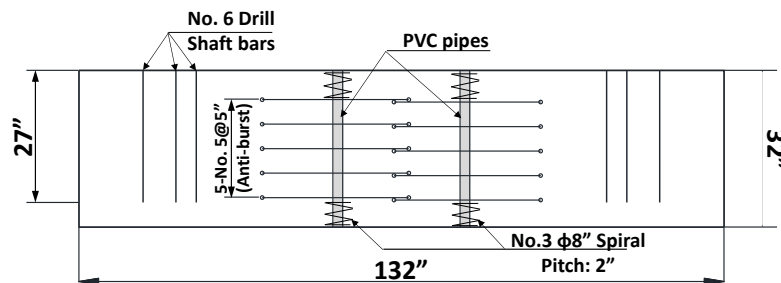
To apply the post-tensioning force, a steel plate of 32 in. by 14 in. is placed on the top surface of the specimen at the post-tensioning region. Five pre-embedded PVC ducts were set up on each side of the steel plate to install post-tensioning rods. The row of post-tensioning rods was 35-in. away from the center of the steel plate representing the drilled shaft.

3.2.1.3. Specimen Detail

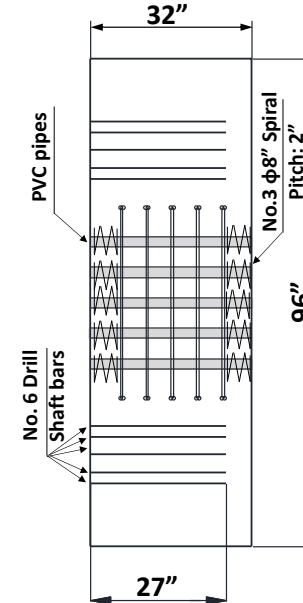
Based on the design considerations introduced in the previous section, the research team detailed the reinforcement and necessary accessories. The complete design is presented in Figure 3-7. Both specimens are provided with the same patterns of top mat reinforcement and bottom mat reinforcement as did in Project 0-6953 to avoid undesired effects on the test results. The top mat consisted of twenty-one No. 5 bars spaced at 5.5 in. in the E-W direction, while twelve No.7 bars spaced at varying spacings of 7.5 in. and 6 in. in the N-S direction. For the bottom mat, both directions were provided with No. 9 bars at positions matching the top mat. The amount of reinforcement in the bottom mat was designed to carry potential tensile stresses.



Plan view (Top mat)



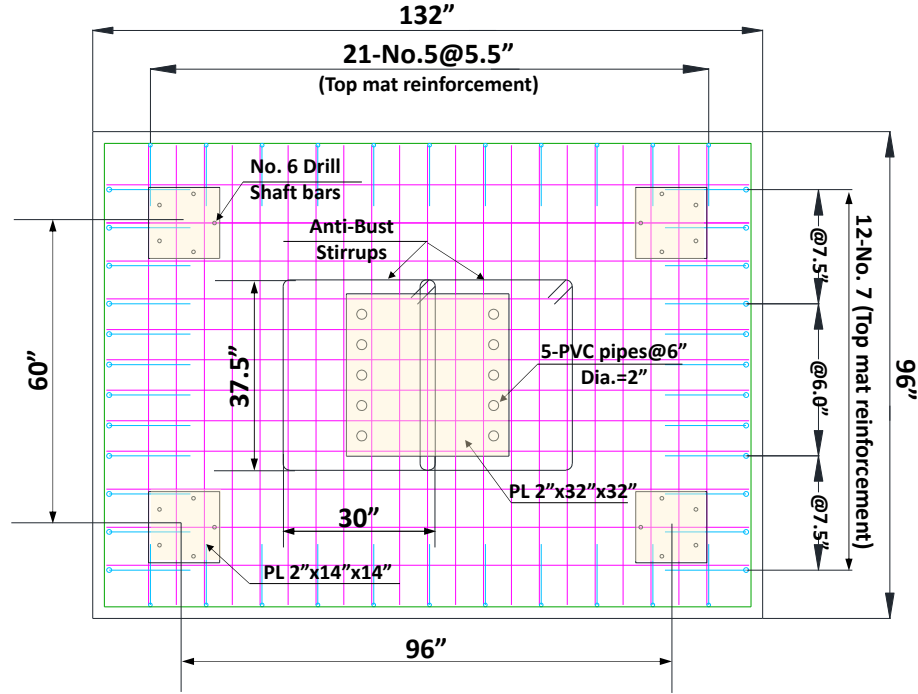
Side view (E-W)



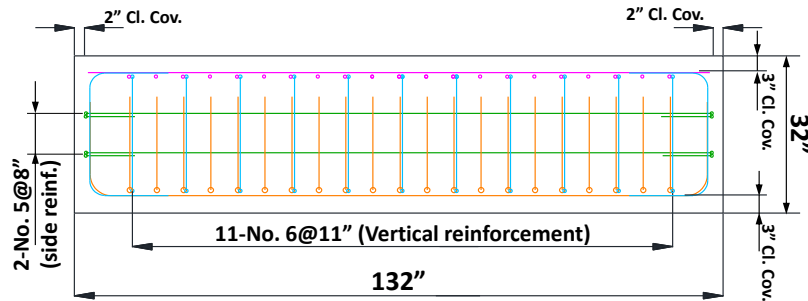
Side view (N-S)

Series I

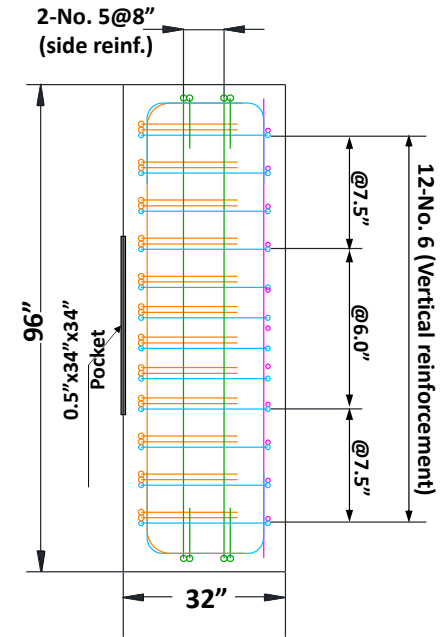
Figure 3-7 (continued) Specimen design and detail



Plan view (Top mat)



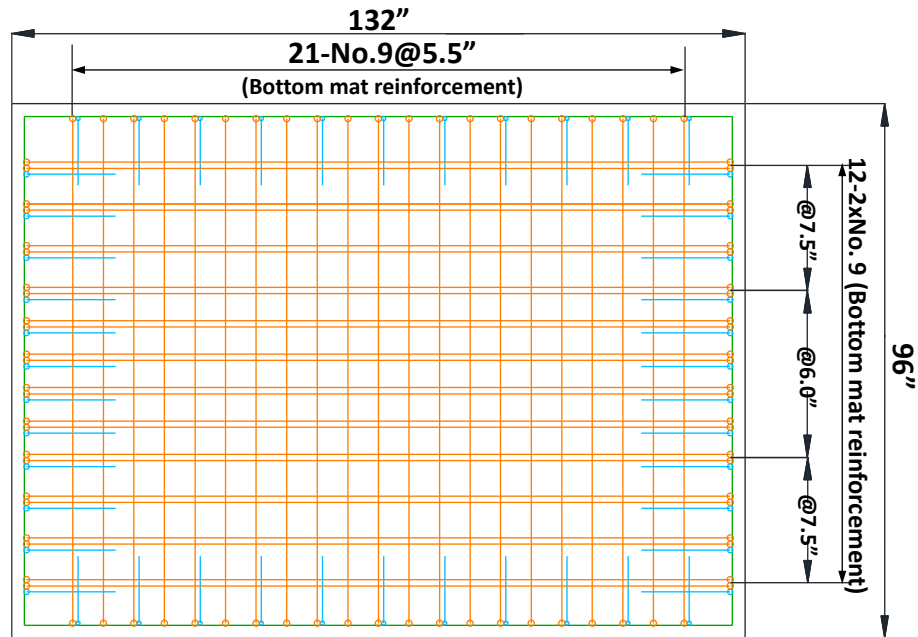
Side view (E-W)



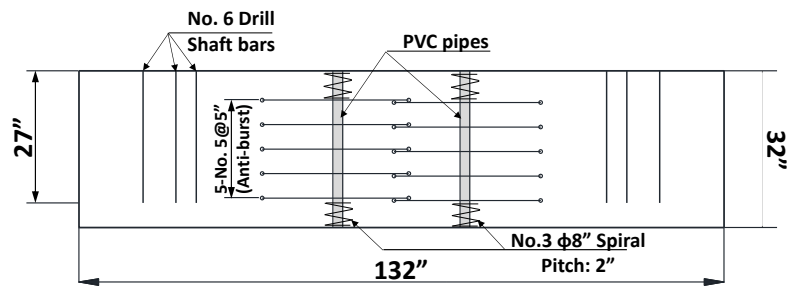
Side view (N-S)

Series II

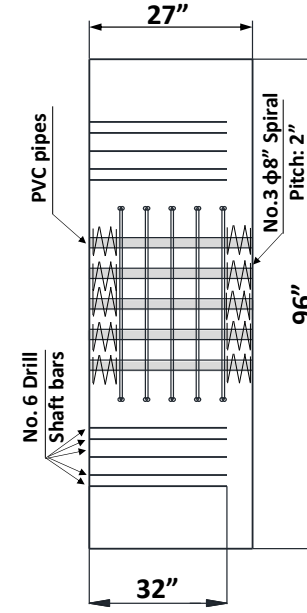
Figure 3-7 (continued) Specimen design and detail



Plan view (Top mat)



Side view (E-W)



Side view (N-S)

Series II

Figure 3-7 (continued) Specimen design and detail

As one of the primary variables, the skin reinforcement ratio was different between the two specimens. For Series I, the target amount of skin reinforcement was 0.30%, remaining the same as the project 0-6953. In particular, on the E-W surface, four horizontal No. 5 bars at a spacing of 6 in. were provided, and twenty-one vertical No. 6 bars at a spacing of 5.5 in. were provided. The vertical rebars were positioned to match the top and bottom mats. On the N-S surface, four horizontal No. 5 bars were provided too at the same height as the E-W surface, while the vertical reinforcement consists of 12 No. 8 bars spaced at 6 in. and 7.5 in, matching the top and bottom mats.

Series II was designed to have approximately half the amount of the skin reinforcement ratio of Specimen I, which was 0.15%. Specifically, on the E-W side, two No. 5 bars spaced at 8 in. were provided horizontally, while eleven No. 6 vertical bars were provided and spaced at 11 in. On the N-S surface, two No. 5 bars, again, were provided at a spacing of 8 in., and twelve No. 6 bars were vertically provided at spacings of 6 in. and 7.5 in.

Ten 2-in.-diameter PVC pipes arranged in two rows were pre-embedded 13-in. away from the center line for the post-tensioning application. Additional confining reinforcement was provided to prevent cracking induced by post-tensioning. The confinement includes anti-burst stirrups and spirals. The anti-burst stirrups comprised two groups of No. 5 stirrups enclosing pre-embedded PVC pipes. A No. 3 spiral with a pitch of 2 in. on the top and bottom of each PVC pipes was provided to prevent localized crushing. A pocket with dimensions of 34 in. by 34 in. by 0.5 in. was provided on the bottom of the specimen, resulting from a steel plate for anchoring the PVC pipes at their desired positions during concrete casting.

3.2.1.4. Nomenclature

A nomenclature was developed, as shown in Figure 3-8. Specimen IDs included four parts: 1) Series No., 2) the specimen height, 3) the anchorage method of drilled shaft reinforcement, S for straight bars, and H for headed bars, and 4) the skin reinforcement ratio.

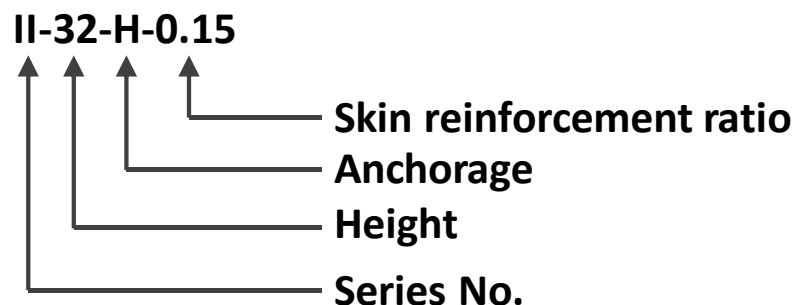


Figure 3-8 Nomenclature for specimens

3.2.1.5. Preliminary Analysis using the Finite Element Method

3.2.1.5.1. Model Preparation

The non-linear finite element analysis software ATENA 3D was used to construct finite element models of the planned test specimens. The structural responses were examined before large-scale structural testing. As shown in Figure 3-9, the finite element model consisted of a concrete footing, steel plates simulating drill shafts, and an anchoring plate for post-tension. All the components were modeled based off of the planned specimen.

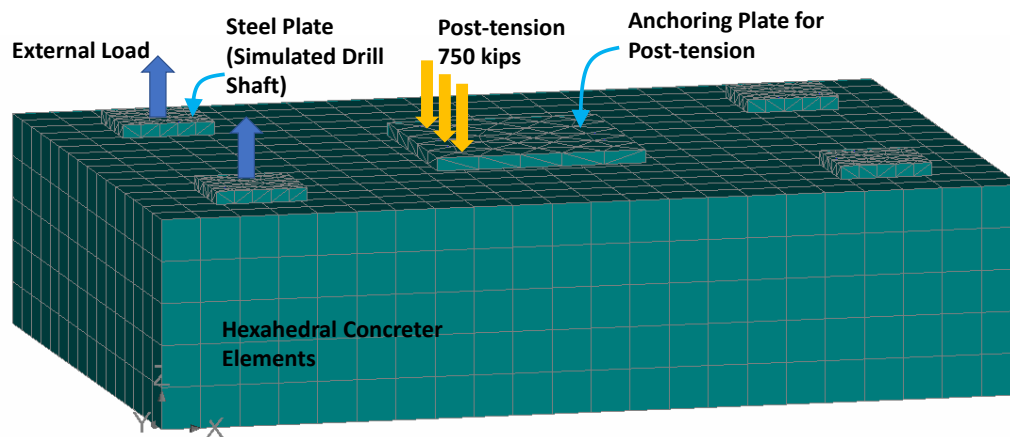


Figure 3-9 Finite element model of test specimens

Five post-tensioning rods were modeled using 1-D elements and were embedded in the concrete footing. An external load directed upward was incrementally applied at the center of each steel plate. Each rod was assigned 150 kips for post-tension; therefore, a total of 750 kips of post-tension was applied onto the concrete footing.

No actual material properties were available before the structural testing, so common concrete and reinforcement properties were assigned to the corresponding elements. The compressive strength of concrete was assumed to be 4 ksi, and the tensile and ultimate strengths of reinforcing bars were specified as 67 ksi and 100 ksi. Other related mechanical properties were automatically generated by the program.

The concrete footing was meshed using 8-point hexahedral elements with a size of 6 in. by 6 in. by 6 in. The steel plates, on the other hand, were meshed using 4-point tetrahedral elements with an overall size of 4 in. All the contacts were assumed perfect because no detailed contact information was available. Nevertheless, default bond properties in the program were assigned to the drill shaft bars to investigate the bond behavior numerically.

3.2.1.5.2. Preliminary FE Analytical Results

A plot that shows the total load applied on the two drill shafts versus the vertical displacement at the load point for each of the two numerical tests is presented in Figure 3-10. Both tests demonstrated almost identical load-displacement behavior prior to a displacement of 0.125 in. The numerical specimen with a skin reinforcement ratio of 0.15% had a sudden load drop and gained the load-carrying capacity back. The other numerical specimen, which had a skin reinforcement ratio of 0.3%, had a similar load drop and a gaining back of the load-carrying capacity at a displacement of approximately 0.15 in. In addition, the ultimate load-carrying capacity was slightly higher.

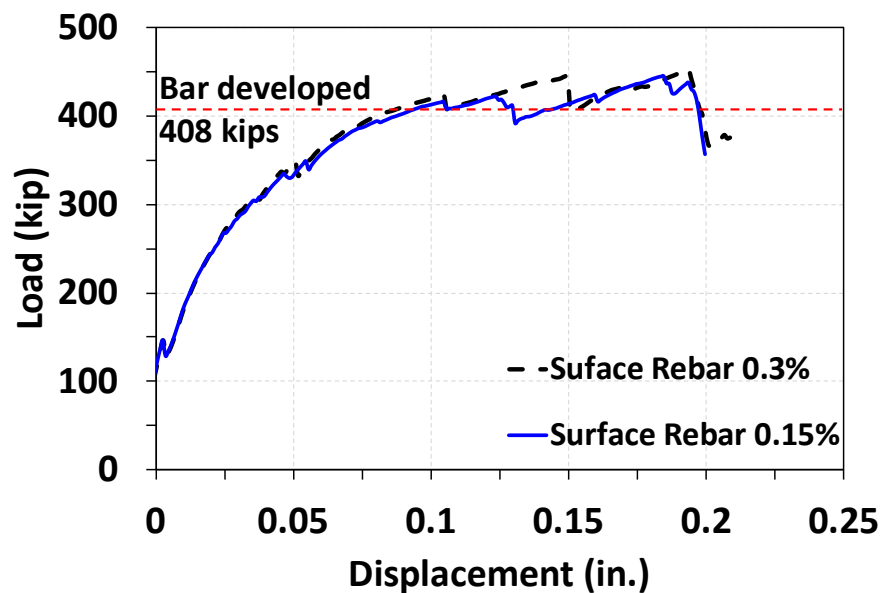
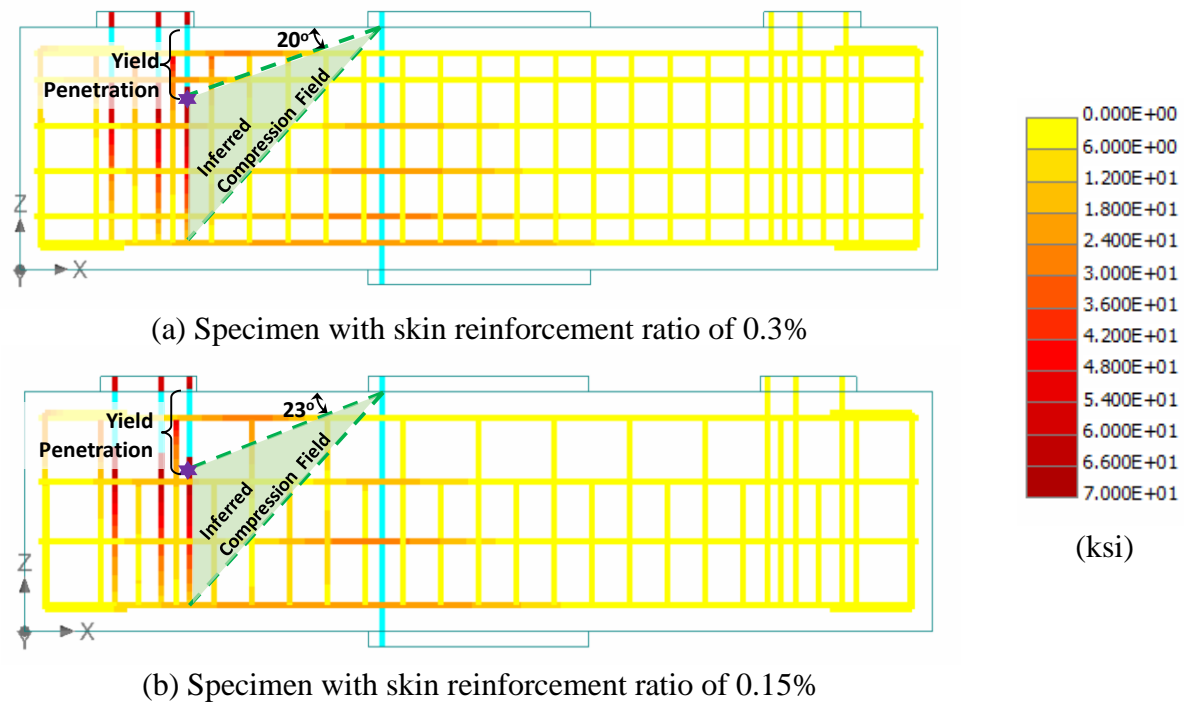


Figure 3-10 Total load on drill shaft versus vertical displacement

Stress variations along drill shaft bars of both numerical specimens at the end of the analyses are presented in Figure 3-11. Both numerical specimens showed yield penetration into the footing; however, the depth of the yield penetration was slightly different. For the specimen with a higher skin reinforcement ratio [see Figure 3-11(a)], the yielding of the bar that was closest to the post-tension extended between the first and the second horizontal skin reinforcing bars. From the point, a straight line was connected to the intersection of the line of action of the post-tension and the concrete surface. The straight line was then defined as the upper boundary of the inferred compression field, as suggested in Project 0-6953. Another straight line, as the lower boundary of the inferred compression field, was connected from the bottom tip to the post-tension. It can be seen in Figure 3-11(a) that the inferred fan-shaped strut began at an angle of approximately 20 degrees. The same procedure was applied to the specimen with a skin reinforcement ratio of 0.15%, as shown in Figure 3-11(b). It was found that the inferred fan-shaped strut began at an angle of approximately 23 degrees.



The preliminary FEA results disclose that the ratio of skin reinforcement might have affected the behavior of footings subjected to idealized high-eccentricity unit axial loads that caused tension in the drill shafts. For one thing, the ultimate strength was higher if the code-required amount of crack control reinforcement was provided. Nevertheless, the difference was not prominent, and all bars yielded at the concrete surface. For the other, skin reinforcement ratios lower than the code requirement resulted in a slightly deeper yield penetration, leading to a narrower fan-shaped strut between the drill shaft bars and the post-tensioning rods. Even though a skin reinforcement ratio lower than required might lead to a lower critical section, an angle of 25 degrees to delineate the boundary of a fan-shaped strut is still conservatively held. The preliminary FEA boosted confidence in the use of the suggested approach for the non-contact splice between ties.

3.2.2. Instrumentation

Three types of sensors were installed onto the specimen to collect data during the testing, including strain gauges, linear potentiometers, and load cells. Strain gauges were used to monitor strains in bottom mat reinforcing bars, skin reinforcement, and drilled shaft reinforcement. Strain data was anticipated to be converted to the stresses in the bars to verify the strut-and-tie model shown in Figure 3-4. The bond stresses along the drilled shaft reinforcement could also be examined. The findings from the data could be used to verify the conservativeness of the compressive field. Linear potentiometers were utilized to monitor the slip of drilled shaft bars and measure the elongation of the drilled shaft reinforcement at the loading side during the tests. Load cells were installed along

with the test frame to monitor the reaction forces, and the applied loading was also monitored by the load cells embedded in the MTS actuators, which is introduced in detail in Section 3.2.4.

Twenty-eight strain gauges were layout out as shown in Figure 3-12 along with selected reinforcing bars on the bottom mat in both the N-S and E-W directions. Sixteen strain gauges were distributed in four rows for the N-S direction while twelve strain gauges were also distributed in four rows for the E-W direction. Four linear potentiometers were placed surrounding each load plate to measure the load plate's relative displacement to the top surface of the footing specimen during testing.

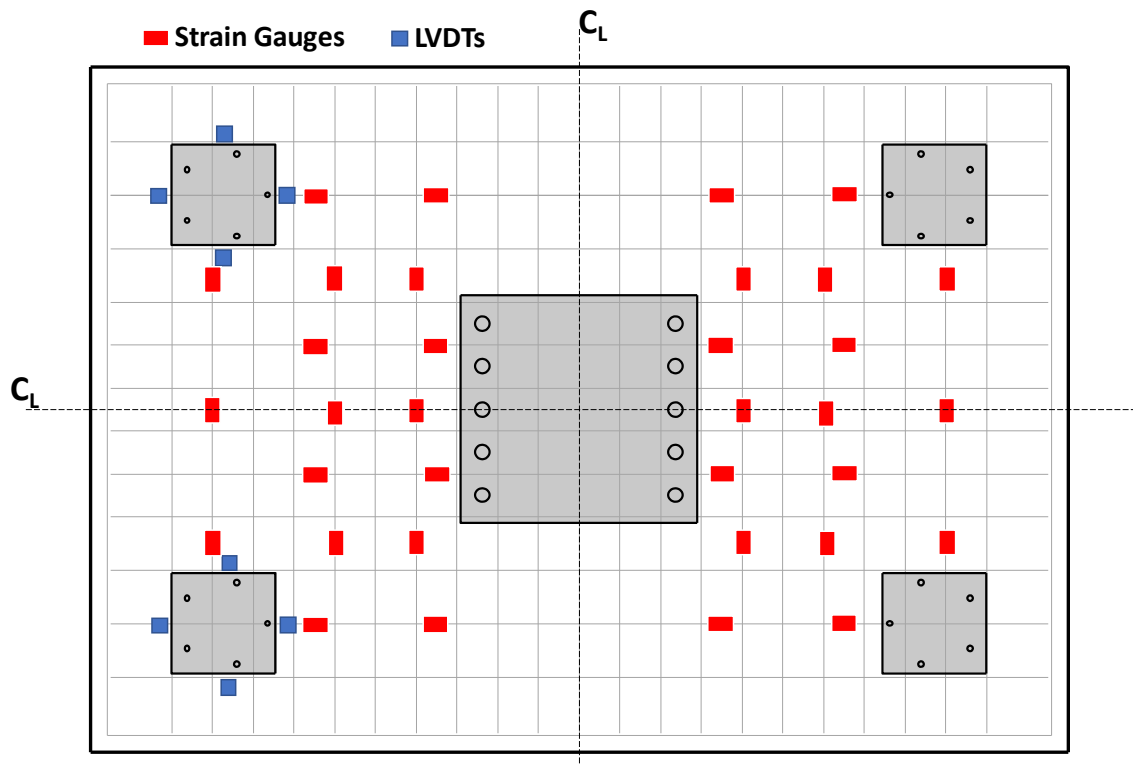
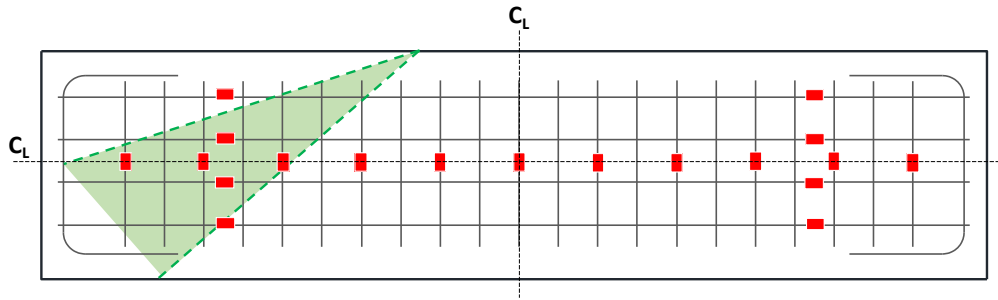
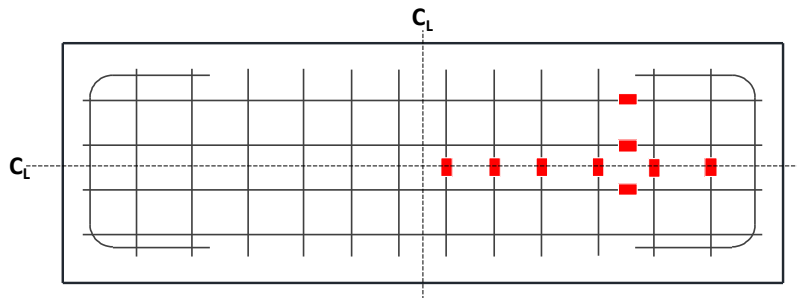


Figure 3-12 Instrumentation – top view

Besides the bottom mat reinforcement, strain gauges were attached to skin reinforcement on both N-S and E-W sides at positions indicated in Figure 3-13 and Figure 3-14 for Specimens I and II, respectively. In the figures, a green shade is drawn to delineate the anticipated compressive stress field. The layout of the strain gauge distribution was expected to capture the stress flow.



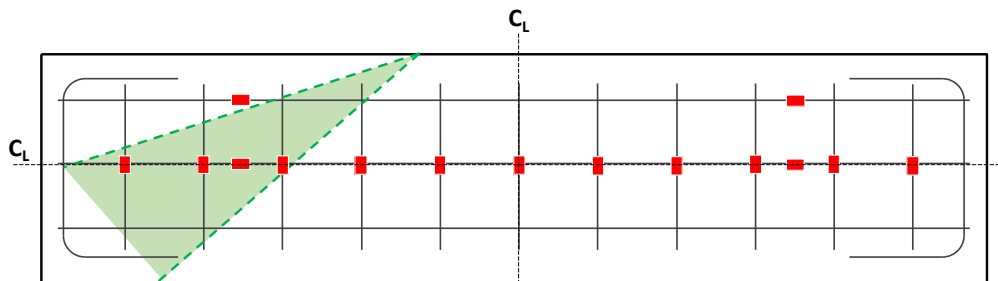
(a) N-S side



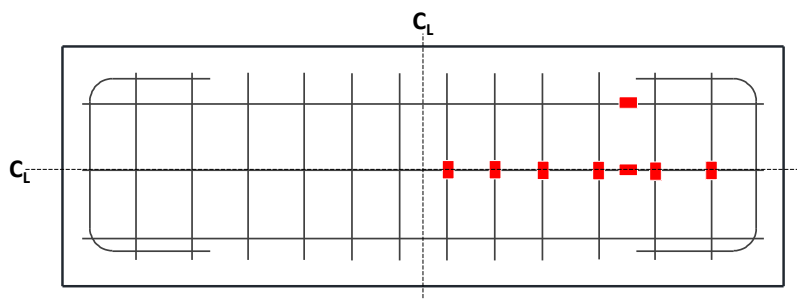
■ Strain Gauges

(b) E-W side

Figure 3-13 Strain gauge layout on surface reinforcement (Specimen I)



(a) N-S side



■ Strain Gauges

(b) E-W side

Figure 3-14 Strain gauge layout on surface reinforcement (Specimen II)

Strain gauges were also distributed along three of five drilled shaft bars attached to each load plate to monitor strain variations. As illustrated in Figure 3-15, along the drilled shaft bar to be gauged, four strain gauges spaced at 7-in. were installed; the first strain gauge was placed 2 in. below the top surface. In addition, a linear potentiometer was placed underneath two of five drilled shaft reinforcing bars at each loading plate to measure the slip of the drilled shaft reinforcing bar through a slot.

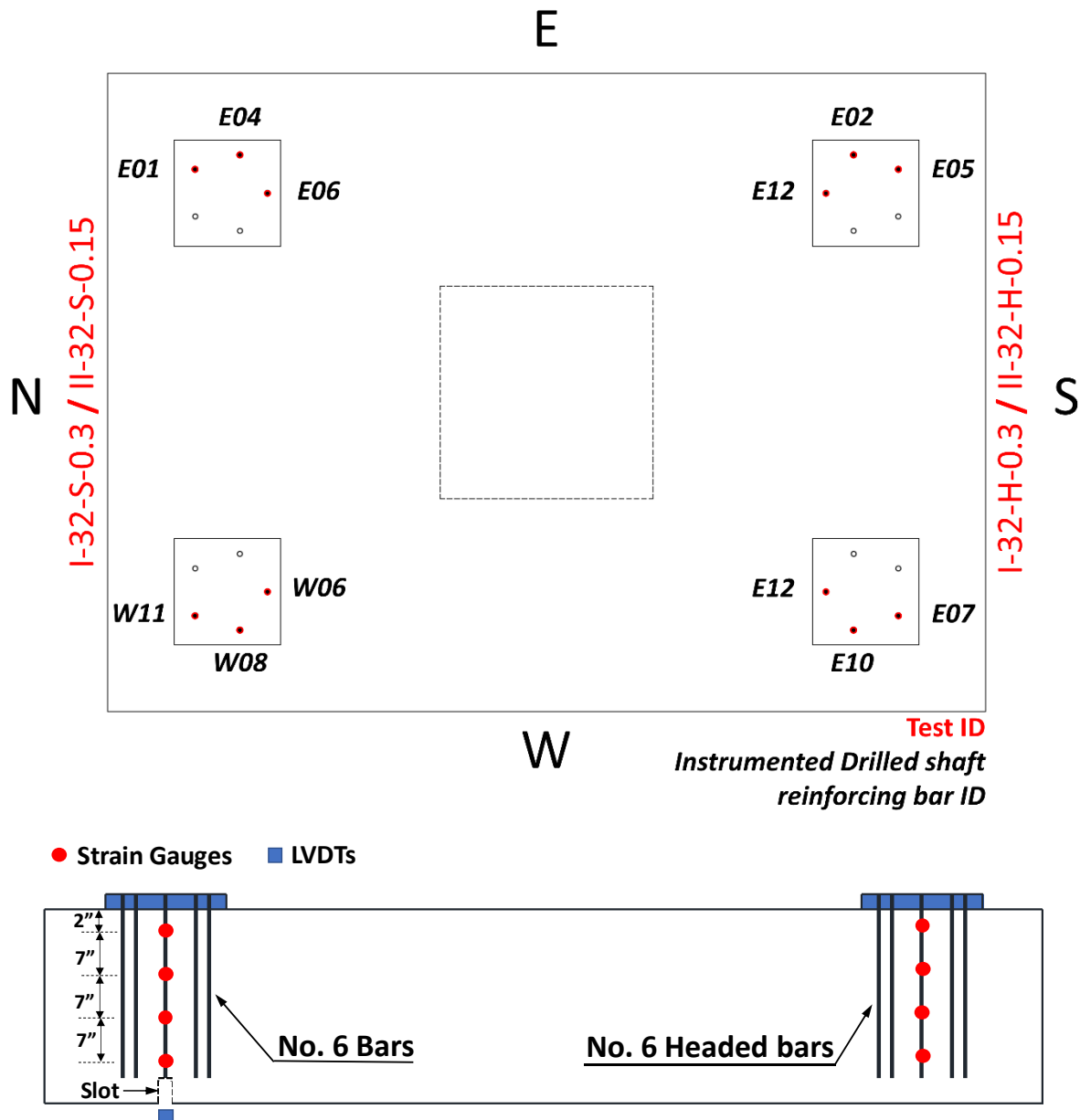


Figure 3-15 Strain gauge positions installed at drilled shaft reinforcement

3.2.3. Fabrication of Specimen

Fabrication procedures for the footing specimens are summarized in Figure 3-16. The steel formwork allows two footing specimens to be fabricated simultaneously.



(a) Steel formwork



(b) Modified steel formwork



(c) Installed strain gauges



(d) Reinforcement cage



(e) Concrete placement



(f) Fabrication of cylinders

Figure 3-16 Procedure of footing specimen fabrication

Firstly, strain gauges were attached to reinforcement at the planned measuring positions. The desired strain gauging locations on the reinforcement were ground to a flat surface and polished before installing strain gauges. The strain gauges were attached with an adhesive and covered with waterproof material and epoxy for protection from potential damage during cast concrete. The

instrumented reinforcing bars were assembled with plain bars in accordance with the designed reinforcement details. The lower layer of bottom mat reinforcement in the north-south direction (e.g., top mat reinforcement of actual footings) was placed on 3-in. height bolsters. The upper layer of bottom mat reinforcement, comprising bundled No. 9 reinforcing bars, was placed above the lower layer in the east-west direction. Both layers of the bottom mat reinforcement were tied with tie wires to secure the designed reinforcement layout. The transverse and longitudinal side face reinforcement and top mat reinforcement (e.g., bottom mat reinforcement of actual footings) were also tied subsequently. Further, 2-in. plastic wheel spacers were inserted into the longitudinal face reinforcement to maintain clear spacing between the cage and the side forms.

Voids were created in the specimen by embedding PVC pipes in the reinforcing bar cage so that the high-strength rods connecting the specimen and the support frame could be inserted when assembling the test setup. Additionally, anti-burst reinforcement and spiral reinforcement were provided at the center of the specimen to preclude any damages caused by the post-tensioning force applied through the high-strength threaded rods. Lastly, the drilled shaft reinforcing bars, which are also exploited as a component of the loading frame, were carefully installed in the cage to ensure their desired position. The drilled shaft reinforcement was extended above the footing and will be adopted as a connection to the loading frame for applying the direct tensile force to the drilled shaft reinforcement, which is described in detail in Section 3.2.4. Based on the planned anchorage types to be tested in the experimental program, two different anchorage types—straight and headed—of drilled shaft reinforcement were installed in the cage. This project employed tapered thread-type headed reinforcement for the headed anchorage detail; therefore, Lenton Terminators produced by nVent LENTON were installed to the reinforcing bars with a tapered thread by applying the required torque (Figure 3-17). The net bearing area of the head was equal to four times the cross-sectional area of the reinforcing bar.



(a) Lenton Terminator



(b) Lenton Terminator installed

Figure 3-17 Lenton Terminators for headed bars

After the reinforcing bar cages were ready, strain gauge cables were arranged outside the cage to avoid being buried inside the concrete. The formwork was closed afterward, and the dimension of the specimen was secured by installing the top and bottom ties of the formwork.

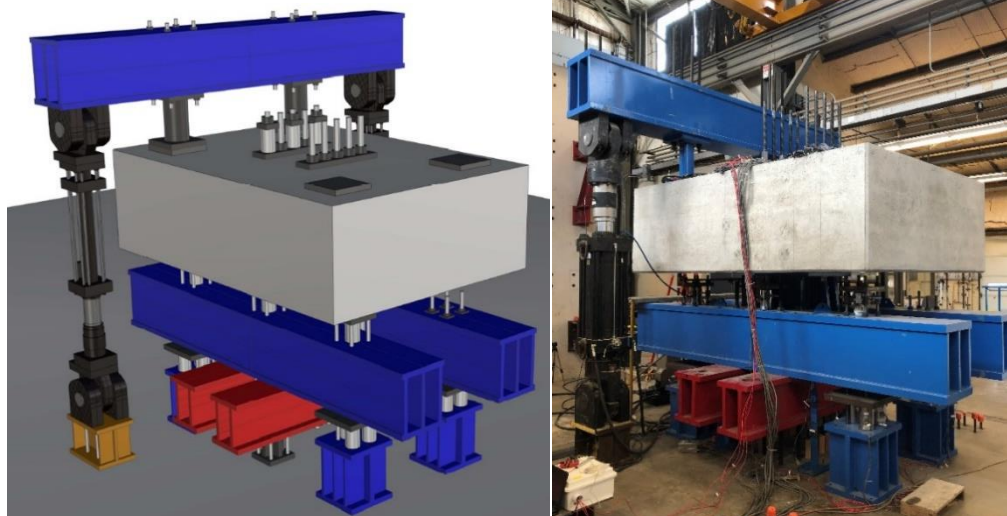
The design concrete strength was specified as 3.6 ksi for all the footing specimens. Its mixture design is the same as in Project 0-6953 and summarized in Table 3-2. The concrete placement on two specimens was conducted on a single day. Due to the maximum volume of the truck, three batches of concrete were delivered via ready-mix trucks to place the concrete for two specimens; therefore, one batch was shared with two specimens. Concrete cylinders per batch were also fabricated to measure the material properties on the test day.

Table 3-2 Concrete mixture proportions for footing specimens

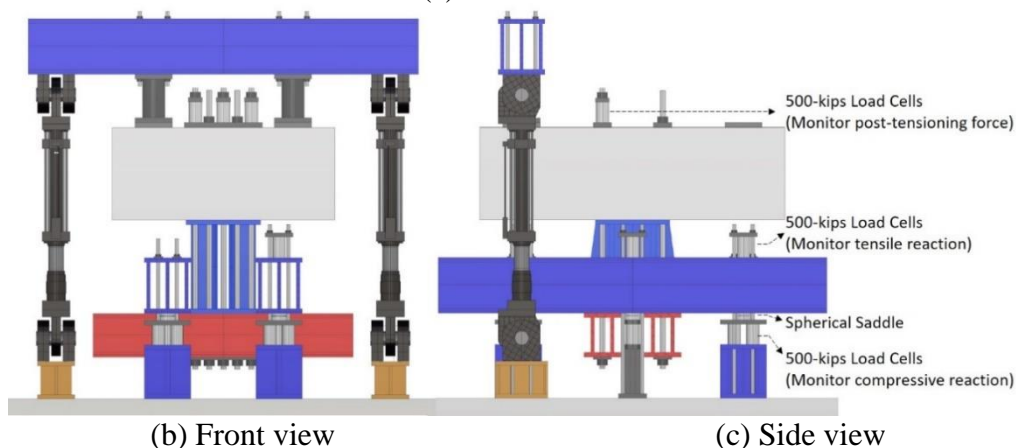
Material Type	Description	Weight
Cement	ASTM C-150 Type I/II	338 lb/cy
Fly Ash	Class F	112 lb/cy
Coarse Aggregate	Maximum aggregate size: 1.0"	1915 lb/cy
Fine Aggregate	Concrete Sand	1479 lb/cy
Water	Water	30 gal/cy

3.2.4. Test Frame

The equivalent loading scenario for large-scale drilled shaft footing tests under the loading condition of axial compression combined with large uniaxial flexure proposed by Project 0-6953 was also employed in the experimental program of this chapter. Therefore, the same test setup as that of Project 0-6953 was used for testing the footing specimens. The test setup configuration is presented in Figure 3-18.



(a) Isometric view



(b) Front view

(c) Side view

Figure 3-18 Test setup for planned equivalent loading

The test setup was designed to apply direct tensile force to the drilled shaft reinforcement. The drilled shaft reinforcing bars extended above the specimen were welded to an adapter plate inside a 0.75-inch-deep and 2.5-inch diameter pocket. As illustrated in Figure 3-19, the adapter plate is connected to a crosshead box beam through a squat steel pedestal. In this way, two 330-kip capacity actuators connected underneath both ends of the crosshead box beam can apply the tensile force to the drilled shaft reinforcement. The connection detail can preclude the failure at the connection before the ultimate state of the drilled shaft reinforcement and verified from Project 0-6953.

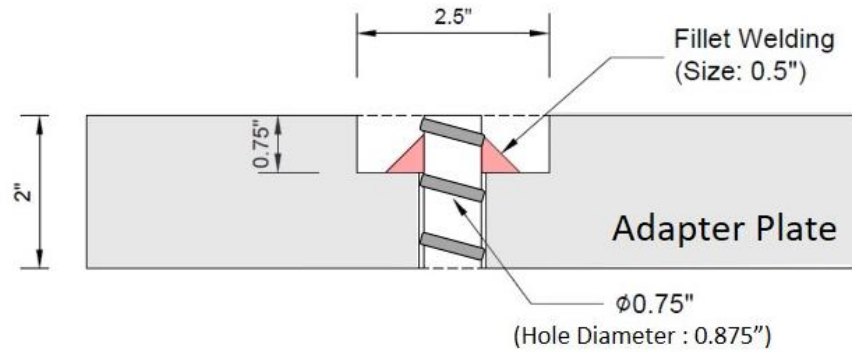


Figure 3-19 Detail of connection between drilled shaft reinforcement and adapter plate

A significant overturning moment resulting from the eccentric upward loading occurred at the center region on the bottom side of the specimen. Therefore, a staggered box beam support frame underneath the specimen was designed and placed on the six support pedestals for redistributing the moment to the strong floor with tensile and compressive reactions. Each support pedestal comprised 500-kip load cell and spherical saddle layer and was connected to the box beam with four grade B7 rods, post-tensioned with 50 kips, respectively. The post-tensioning force of 150 kips per rod was considered to be able to compensate for the tensile reactions and prevent a slack between the pedestal and the box beam. The test specimen was installed on the support frame using two rows of five large-diameter high-strength threaded rods through the embedded PVC pipes.

3.2.5. Test Procedure

The same test protocol as that employed in Project 0-6953 was used for the testing. Test specimens were loaded with displacement-controlled load from the MTS actuators with a 0.025-in. per minute loading rate. During the test, the test was stopped at every 50-kip load increment up to the load when at least one drilled shaft reinforcement at each loading plate yields, and the specimen was visually inspected for crack mapping. Beyond the last inspection step, the specimens were continuously loaded and stopped at 400 kips, about 95% of the expected ultimate load, to prevent any damages caused by the fracture of the drilled shaft reinforcement.

3.3. Experimental Results and Discussion

3.3.1. Summary of Strength Results

The test results are summarized in Table 3-3. The first yielding load of the drilled shaft reinforcement was captured from the strain gauges attached to six of the ten drilled shaft reinforcing bars. The first yielding load of the drilled shaft reinforcement ($P_{fy,s}$) measured in I-32-S-0.3 was relatively higher than the other tests. It should be noted that only six of the ten drilled shaft reinforcing bars were monitored through strain gauges; therefore, the first yielding could have occurred at different drilled shaft reinforcement without installed strain gauges. Due to the same reason, the load when all monitored drilled shaft bars yielded was considered the load at

yielding all drilled shaft reinforcement ($P_{y,s}$). The yielding loads of all specimens were comparable regardless of the anchorage types and skin reinforcement ratios. The load discrepancy between $P_{fy,s}$ and $P_{y,s}$ resulted from the applied loading not being evenly distributed to all drilled shaft reinforcing bars due to the deflection of the footing component during the testing. Thus, some reinforcing bars experienced relatively higher stresses than the other bars and yielded under a lower loading level than the expected yielding load (295 kips), assuming that the applied force is uniformly distributed over all drilled shaft bars. The maximum stresses of all drilled shaft bars were measured at the strain gauges installed at 2-in. below the top surface of the specimen.

Table 3-3 Summary of experimental results

Test ID	I-32-S-0.3	I-32-H-0.3	II-32-S-0.15	II-32-H-0.15
Anchorage Detail of Drilled Shaft Reinforcement	Straight	Headed	Straight	Headed
Skin Reinforcement Ratio [%]	0.30	0.30	0.15	0.15
Compressive Strength of Concrete on Test Day [ksi]	4.86	4.96	4.00	4.00
Yield Strength of Drilled Shaft Reinforcement [ksi]	67.0			
Tensile Strength of Drilled Shaft Reinforcement [ksi]	94.5			
$P_{fy,s}$ [kip] (Reinforcing bar position*)	224 (W06)	149 (W10)	165 (E12)	166 (E04)
$P_{y,s}$ [kip]	324	338	332	320

*Refer to Figure 3-15

3.3.2. Visual Observation

The specimens were visually inspected between every 50-kip load increment. The last inspection loading step was at 250-kip since the yielding of at least one drill shaft bar on each of the two loading plates was confirmed at the loading step. Beyond the last inspection loading step, the specimens were continuously loaded up to 400 kips and unloaded. Therefore, the crack maps presented in this section were compared for those observed until the last inspection loading step: 250 kips. The crack maps of all tests are presented in Figure 3-20.

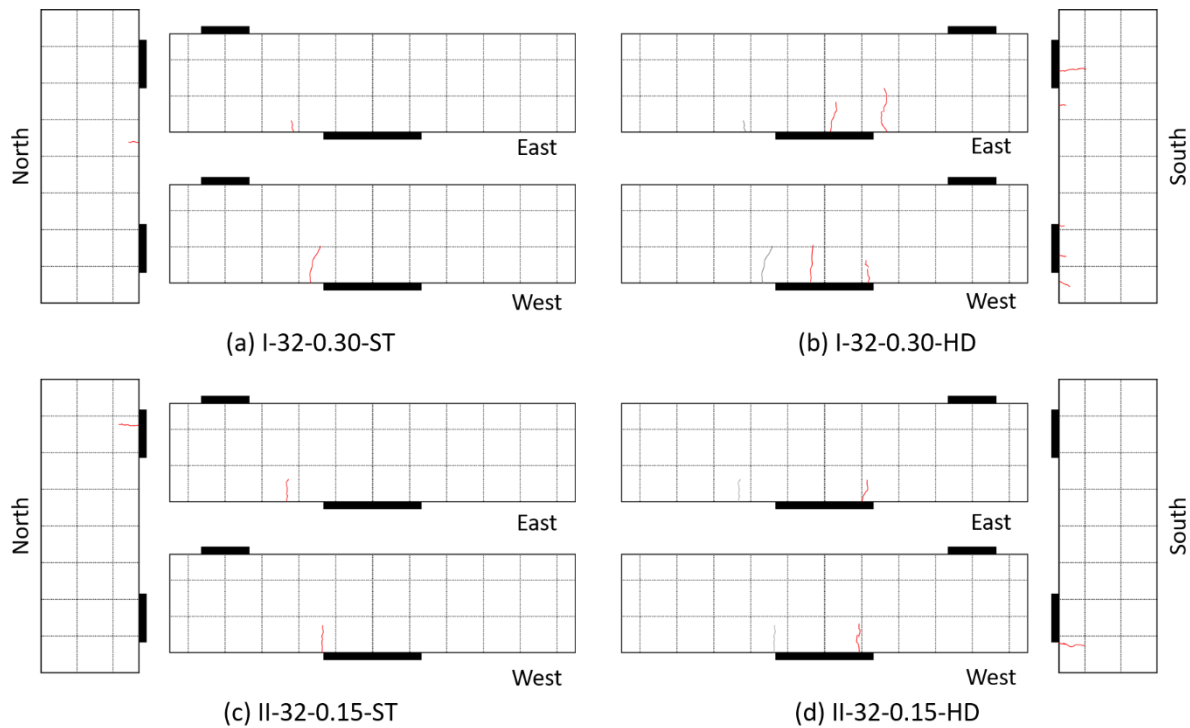


Figure 3-20 Crack maps of test specimens

During the tests, some vertical hairline cracks were found on the side surfaces of the test span at the loading steps of 100 kips and 150 kips; however, the cracks did not propagate as the load increased. Therefore, the cracks were considered micro-cracks, which might have already formed in the specimens during the curing period. In addition, a flexural crack was identified at the loading step of 250 kips near the support in all tests.

After the tests, the welding connections were inspected, but no damage was detected at all drilled shaft reinforcing bar positions. Instead, spalling of the concrete near the loading plate was found in all tests due to the conical cracks that occurred at the drilled shaft reinforcement near the top surface of the specimen, as presented in Figure 3-21. Overall, there were no noticeable visual differences between the tests, regardless of the anchorage types and skin reinforcement ratios. Compared to specimens from Project 0-6953, those from this project exhibited more developed flexural cracks due to their shallow depth.



(a) Undamaged connection after testing



(b) Concrete spalling formed around loading plate

Figure 3-21 Visual inspection at loading plate after testing

3.3.3. Load-deflection Response

Project 0-6953 extracted the data measured from linear potentiometers installed surrounding the loading plates to compare the structural behavior monitored from the tests. The research team also employed the same approach to compare the structural responses between the tests, as shown in Figure 3-22. The relative displacements measured from four side faces of a loading plate were averaged to represent the average elongation of the drilled shaft reinforcement at the top surface of the specimen. Due to the concrete spalling identified after the tests around the loading plates, the data measured from the linear potentiometers installed at the spalling region could not be used. Therefore, the relative displacements measured at the load plate with only linear potentiometers unaffected by the concrete spalling were averaged for comparison. By dividing the total applied load by the overall area of the drilled shaft reinforcement, the average bar stress level assumed to be uniformly distributed to all reinforcing bars under the applied loading could also be presented in the same plot.

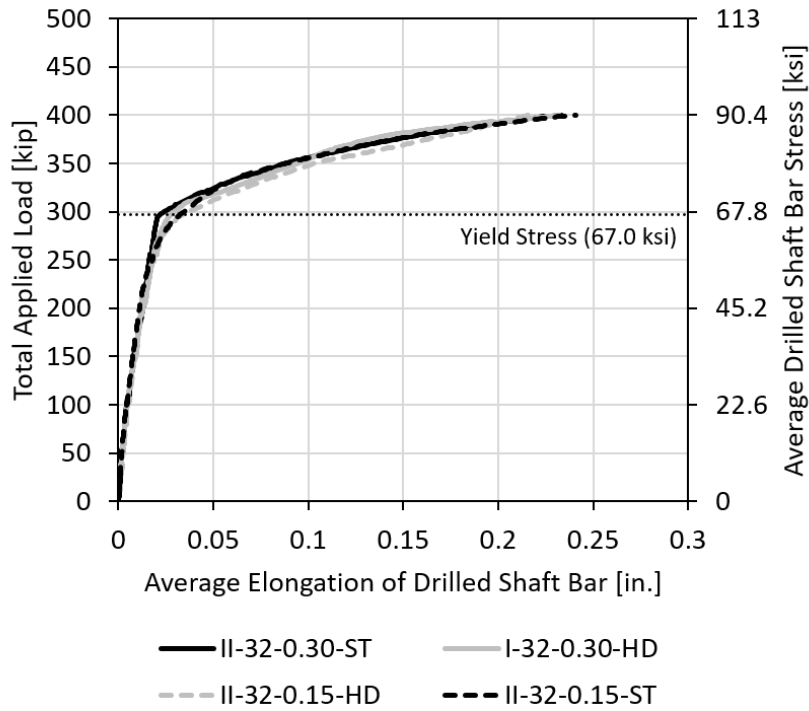


Figure 3-22 Overall structural behavior of tests

As shown in Figure 3-22, the plots obtained from all tests were comparable. Until the average bar stress reached the yield stress of the drilled shaft reinforcement, the drilled shaft reinforcement was almost linearly elongated, and the elongation rate was rapidly increased beyond the yield stress. It indicates that the anchorage behavior of the drilled shaft reinforcement was almost identical regardless of the anchorage types and skin reinforcement since the strain development at the top surface of the footing is also correlated to the strain development at the anchorage region. This fact could be confirmed through the data measured from the strain gauges attached to the drilled shaft reinforcing bars, and the results will be covered in Section 3.3.6.

The research team also monitored the reinforcement slips at the bottom tip of four of ten drilled shaft reinforcing bars; however, the measured slips until the end of all tests were insignificant (less than 1.0×10^{-4} in.). Thus, the provided embedment length and anchorage details of the drilled shaft reinforcement were sufficient to develop its yield stress.

3.3.4. Strain Distribution in Bottom Mat Reinforcement

The strains of the bottom mat reinforcement were measured through the strain gauges. Some strain gauges were damaged and lost signals during the concrete cast. The strain distributions in the bottom mat reinforcement at the test limit load (400 kips) of all tests are provided in Figure 3-23. The numbers in the circles indicate the ratios of strains to the yield strain of the bottom mat reinforcement. The strain distributions were also comparable regardless of the test variables. All bottom mat reinforcing bars did not yield until a 400-kip loading, and the bottom mat reinforcing bars placed in the north-south direction experienced a relatively higher strain than those in the east-



During the tests, almost no strains (less than equivalent to the strain

observations showing almost no cracks on the side surfaces of the specimens. Therefore, it can conclude that the change in the skin reinforcement ratio did not significantly influence the structural response of the specimen.

3.3.6. Stress Profiles and Bond Stress Profiles of Drilled Shaft Reinforcement

Per each test, the strains in six of the ten drilled shaft reinforcing bars were monitored through a series of strain gauges installed on the reinforcement. The measured strains were converted to stresses using the stress-strain relationships obtained from the material test. The converted stresses at a specific loading stage were used to develop a stress profile of a drilled shaft reinforcing bar at the corresponding load. The research team developed bar stress profiles of all monitored drilled shaft reinforcing bars at the loading from 100 kips to 400 kips with 100-kip intervals. The stress profiles obtained in the same test were comparable to each other regardless of the bar position. The bar stress profile of the drilled shaft reinforcement first yielded during each test is presented in Figure 3-24 to compare the anchorage response of the drilled shaft reinforcement between the tests.

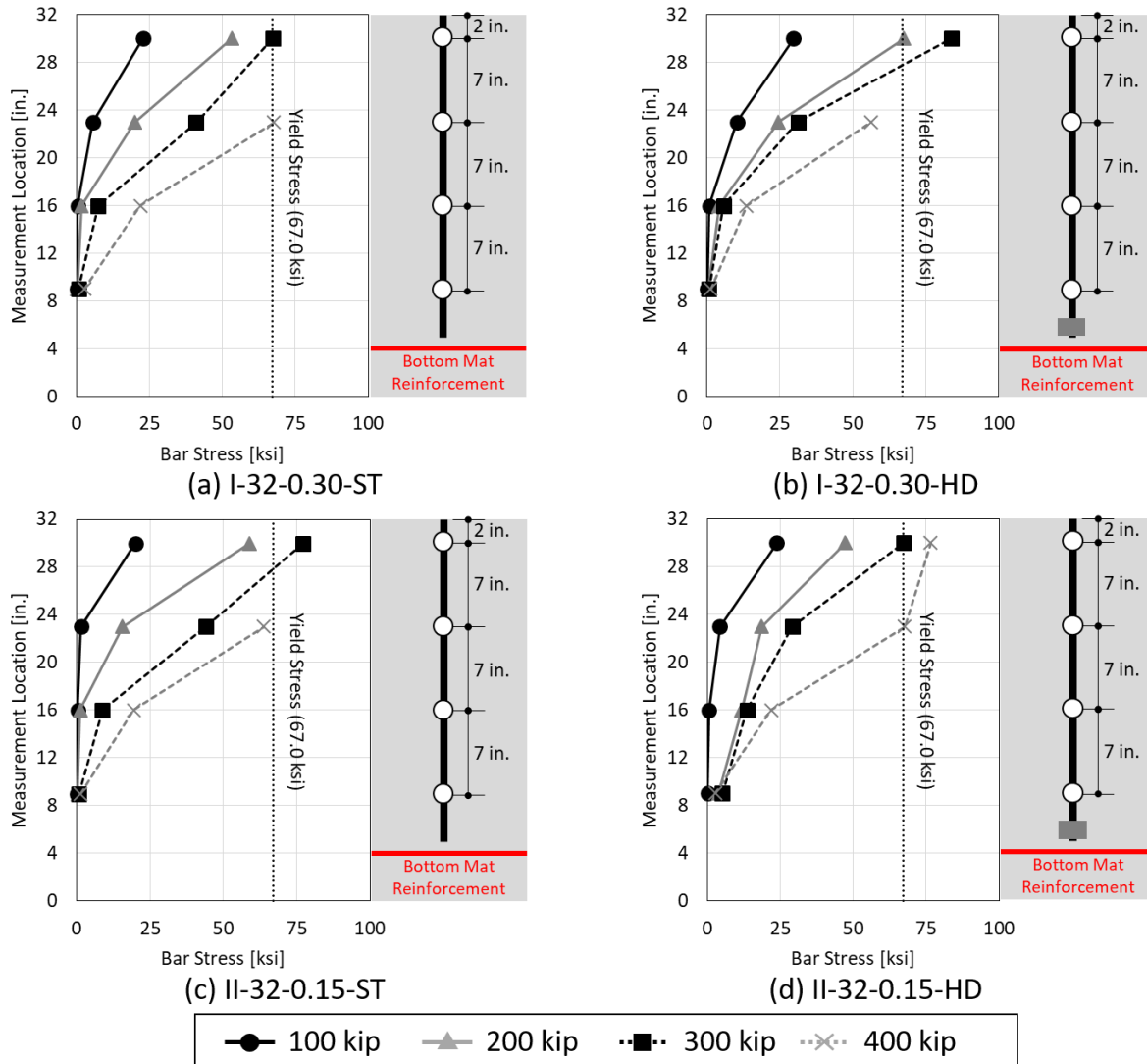


Figure 3-24 Bar stress profiles of drilled shaft reinforcement

Overall, the bar stress profiles developed from each test exhibited almost identical trends. Like the preliminary analysis results (Section 3.2.1.5), it can be seen that the strain gages installed closer to the top surface of the specimen experienced higher stresses. Therefore, all drilled shaft reinforcing bars first yielded near the top surface of the footing, and yield penetration into the specimen was concentrated near the top surface of the specimen, which represents the interface between the drilled shaft footing and the drilled shaft. The stresses measured at the anchorage region were negligible regardless of the anchorage types and skin reinforcement ratios. Therefore, the bearing action of the headed bar could not be activated, and the tension applied to straight and headed bars was solely resisted by the bond resistance of bar surfaces near the top surface of the specimen. Furthermore, this mechanism maintained the same regardless of changes in the skin reinforcement ratio.

The bar stress profiles were converted to bond stress profiles by assuming a uniform bond stress distribution between two adjacent strain measuring positions. The bond stress profiles obtained from the bar stress profiles of all tests are presented in Figure 3-25. Since the concrete spalling caused by splitting cracks was found around the loading plates after all tests, the computed bond stresses were compared with the local splitting bond strength, $\tau_{bu,split}$ specified in fib Model Code 2010 [Eq (3-1)].

$$\tau_{bu,split} = \eta_2 6.5 \left(\frac{f_{cm}}{25} \right)^{0.25} \left(\frac{25}{\phi} \right)^{0.2} \left[\left(\frac{c_{min}}{\phi} \right)^{0.33} \left(\frac{c_{max}}{c_{min}} \right)^{0.1} + k_m K_{Tr} \right] \quad (3-1)$$

where:

$\tau_{bu,split}$ = local splitting bond strength [MPa]

η = 1.0 (good bond condition: 90-degree to the horizontal during concreting)

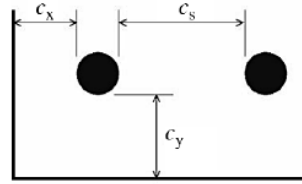
f_{cm} = mean cylinder concrete compressive strength [MPa]

ϕ = diameter of the anchored bar considered [mm]

c_{min} = $\min \{c_s/2, c_x, c_y\}$ [mm]
 $\left(0.5 \leq \left(\frac{c_{min}}{\phi} \right) \leq 3.5 \right)$

c_{max} = $\max \{c_s/2, c_x\}$ [mm]
 $\left(1.0 \leq \left(\frac{c_{max}}{c_{min}} \right) \leq 5.0 \right)$

$k_m K_{Tr}$ = passive confinement factor from transverse reinforcement
 (=0; not considered in this section since no transverse reinforcement was provided to the column reinforcement)



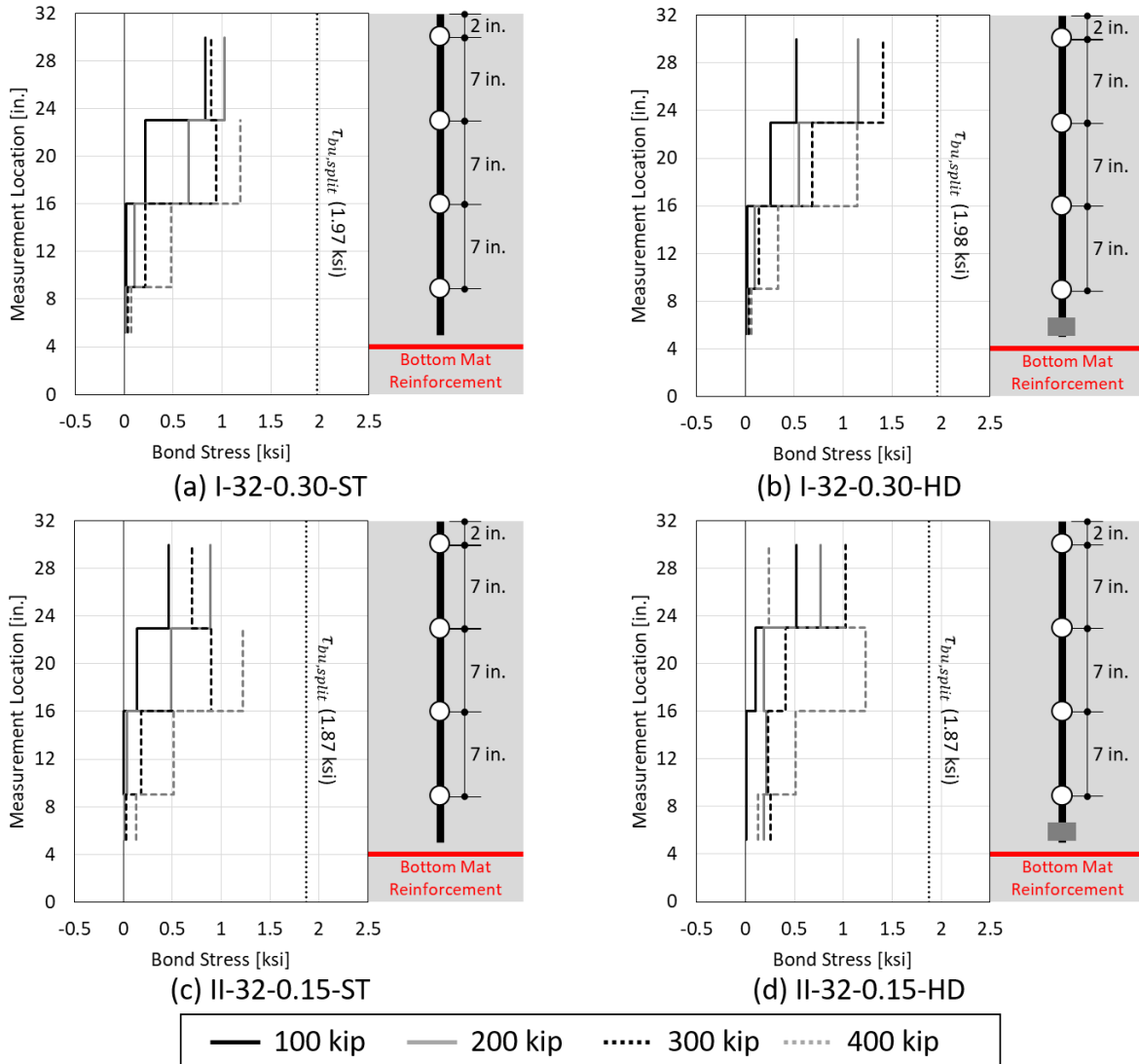


Figure 3-25 Bond stress profiles of drilled shaft reinforcement

The bond stress profiles can solidify the findings from the visual observations and bar stress profiles. Almost no bond stresses were developed at the anchorage regions regardless of the anchorage types and skin reinforcement ratios. Therefore, the bar stresses developed in the drilled shaft reinforcement could be achieved only by surficial bond stresses near the top surface of the specimens. The maximum bond stress computed from the bar stresses was comparable to but slightly smaller than the local splitting bond strength. This is because the assumed uniform bond stress distribution cannot capture the maximum bond stress that can occur between two adjacent strain measuring positions.

3.4. Assessment of Design Recommendation of Project 0-6953

In accordance with the design recommendation proposed by Project 0-6953, the anchorage check based on the compressive stress field, representing a non-contact lap splice between the column and drilled shaft ties, was performed for the drilled shaft reinforcing bars of this project. Since changing the skin reinforcement ratio did not affect the overall anchorage response of the drilled shaft reinforcement, the available development length of the drilled shaft reinforcement is estimated to be 13.0 in., as illustrated in Figure 3-26.

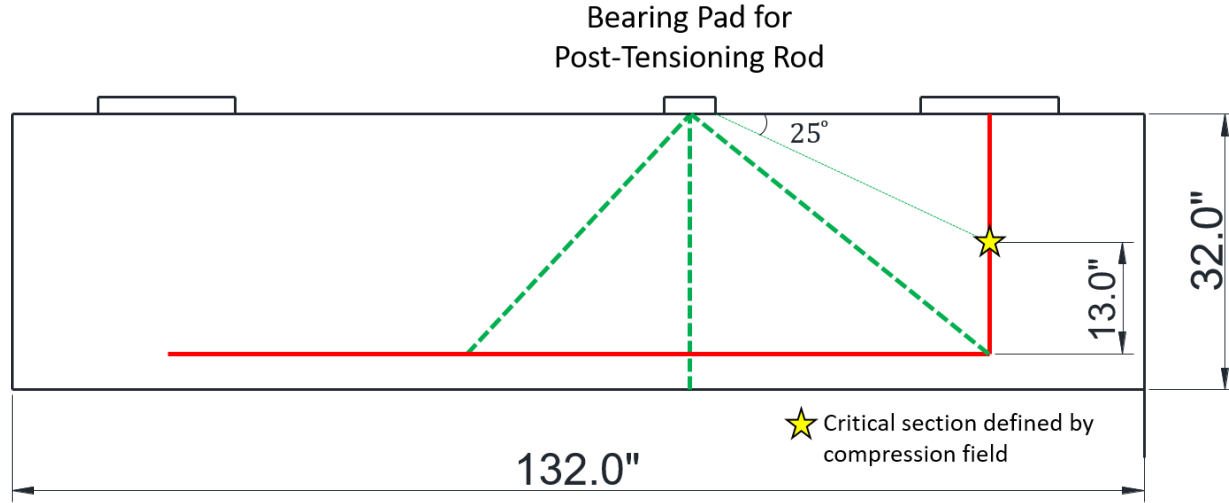


Figure 3-26 Available length estimation based on the design recommendation of Project 0-6953

The available length shall be longer than the minimum development length to satisfy the anchorage requirement. The research team used a unified approach [Eq. (3-2)] to determine the minimum required development length, which will be incorporated into the forthcoming AASHTO LRFD 10th edition. The validity of the equation was verified by Zaborac and Bayrak (2022) through 1006 tests from published literature.

$$l_d = 0.17d_b \left(\frac{\lambda_{er}f_y - \frac{F_h}{A_b}}{1.97\lambda_{f_c}'^{0.25}} \right)^2 (\lambda_{rl} \times \lambda_{cf} \times \lambda_{rc}) \quad (3-2)$$

where:

- l_d = tension development length [in.]
- d_b = nominal diameter of reinforcing bar [in.]
- λ_{er} = excess reinforcement factor
- f_y = specified yield strength of reinforcement [ksi]

F_h	= force developed by hooks or heads, [kip] (= $0.5A_{ht}vf'_c$)
A_{ht}	= net area of the head that bears on concrete
v	= concrete efficiency factor for a CTT node specified in Table 5.8.2.5.3a-1 of AASHTO LRFD 2020
f'_c	= compressive strength of concrete [ksi]
A_b	= nominal area of reinforcing bar [in. ²]
λ	= concrete density modification factor (=1.0)
λ_{rl}	= reinforcement location factor (=1.0; based on the drilled shaft reinforcing bar details)
λ_{cf}	= coating factor (=1.0; based on the drilled shaft reinforcing bar details)
λ_{rc}	= reinforcement confinement factor (=0.30; based on the drilled shaft reinforcing bar details)

The minimum development lengths of all tests conducted in this chapter were compared with the available development lengths based on the measured material properties. As presented in Table 3-4, the available length was slightly shorter than the computed development lengths; however, all drilled shaft reinforcing bars successfully yielded during the tests. This result can support the conservatism of the design recommendations of Project 0-6953, which proposed the compressive stress field between the drilled shaft and column ties to define the critical section for drilled shaft reinforcement. Furthermore, the experimental results of this project also proved that the alleviated skin reinforcement ratio (0.15%) did not affect the anchorage response of the drilled shaft reinforcement. Therefore, the design recommendation regarding the skin reinforcement ratio for drilled shaft footings subjected to uniaxial compression-only ($\geq 0.18\%$) proposed by Project 0-6953 does not affect performing the anchorage check of the drilled shaft reinforcement in drilled shaft footings subjected to large eccentric loading scenarios.

Table 3-4 Anchorage Checks performed with the recommendation of Project 0-6953

	Test ID			
	I-32-0.30-ST	I-32-0.30-HD	II-32-0.15-ST	II-32-0.15-HD
Anchorage Types	Straight	Hooked	Straight	Headed
Concrete Strength [ksi]	4.86	4.96	4.00	4.00
Drilled Shaft Bar Yield Stress [ksi]	67.0			
Available length (l_a) [in.]	13.0			
Minimum development length (l_d) [in.]	20.1	15.4	22.1	17.8
l_a/l_d	0.65	0.84	0.59	0.73

3.5. Summary

The research team planned and conducted four large-scale structural testing on drilled shaft footings to investigate the anchorage behavior of the drilled shaft reinforcement anchored at nodes under tri-axial tension in the 3D STM. Each test was designed with different anchorage types (straight and headed) and skin reinforcement ratios, and the anchorage response of the drilled shaft reinforcement was inspected through linear potentiometers and strain gauges during the tests. The primary findings and observations attained from analyzing the test data are summarized as follows:

1. All drilled shaft reinforcing bars yielded during the tests, and the loads at yielding of all drilled shaft reinforcing bars were comparable in all tests regardless of the anchorage types and skin reinforcement ratios.
2. The bar stress profiles and bond stress profiles developed from the measured strains exhibited almost identical tendencies in all tests. The strain gauges installed the closest to the top surface of the specimen (i.e., footing-drilled shaft interface) experienced a higher strain level than those near the anchorage region. Thus, the bearing action of the head could not be activated, and the tensile force in the drilled shaft reinforcement was solely resisted by bond resistance owing to the surface of the bar.
3. Furthermore, negligible bar slips occurred in all tests at the tip of the drilled shaft reinforcement. The results from the stress profiles and bar slips indicate that the anchorage response of the drilled shaft reinforcement was not influenced by the tested variables: anchorage types and skin reinforcement ratios.

4. Anchorage checks for the drilled shaft reinforcement of each test were performed based on the design recommendation of Project 0-6953. The widespread compressive stress field bounded by the minimum strut angle (25 degrees) defines the available length of the drilled shaft reinforcement. By comparing the available length with the minimum development lengths computed with the unified development length equation, which will be updated to the forthcoming AASHTO LRFD 10th edition, the conservativeness of the recommendation could be confirmed. In addition, the test results of the specimens with the 0.15% skin reinforcement ratio experimentally verified the application of the design recommendation to drilled shaft footings with the alleviated skin reinforcement ratio ($\geq 0.18\%$), which was also suggested by Project 0-6953.

The results of this chapter could support the conservativeness of the design recommendation on the anchorage check for the drilled shaft reinforcement proposed by Project 0-6953. Still, the number of available tests utilized to verify the proposal was limited; therefore, it could result in overly conservative drilled shaft anchorage requirements in actual designs. Future experimental and numerical studies on large-scale drilled shaft footings under large eccentric loading designed with various design parameters are required, and the results will solidify the validity of the design recommendation.

Chapter 4. Curved-bar Nodes

4.1. Introduction

The curve-bar node is a modeling technique used in the strut-and-tie method (STM). As depicted in Figure 4-1, a curved-bar node develops at the bend region of a continuous reinforcing bar or multiple bars where two ties are equilibrated by a strut or multiple struts. Such nodes appear in the beam-column knee joint of a straddle bent or cantilever bent caps under closing moments.

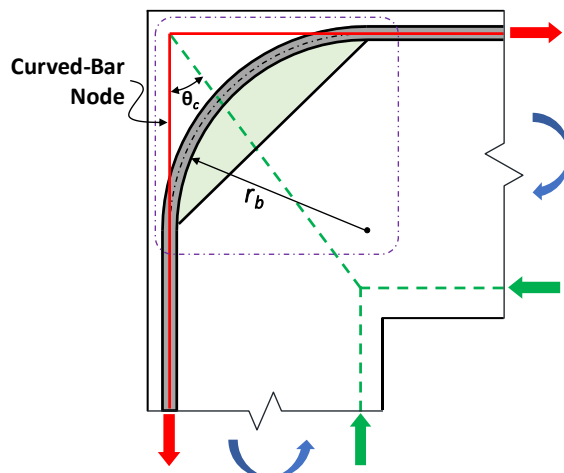


Figure 4-1 Strut-and-tie model for closing moments at a frame corner

Stress analysis by Klein (2008) indicates that stress concentrations in the bar bend region of curved-bar nodes can be critical, and the bar bend should be sufficiently large. Curved-bar nodes are also acknowledged in AASHTO LRFD Bridge Design Specifications in the commentary. However, due to lacking experimental data, the development of design recommendations in AASHTO LRFD has not yet been initiated. Example problems developed under implementation project 5-5253-01 highlighted cases in which the curved-bar nodes and stress checks at those nodes can control the design. Conversely, in those cases, structural designs based on the current state of practice may lead to over-stressing the bar bend region.

Available approaches and studies on the design of curved-bar nodes can be seen in Klein (2008), ACI 318-19 (2019), and Wang et al. (2020 and 2022). Klein (2008) proposed a method that calculates the required bend radius considering radial stresses, circumferential bond stresses, and clear side cover for the bar bend of curved-bar nodes. The purpose was to reduce the risk of overstressing concrete within the bar bend by using sufficiently large bar bends other than a bend radius of the standard bends. Also, a clear side cover with enough thickness should be used to prevent splitting the side cover. The method was experimentally investigated and verified by Wang et al. (2020 and 2022). Also, the method was incorporated in ACI 318-19 (2019). The design expressions can be seen in Section 23.10 of ACI 318-19. In general, the required bend radius should be calculated using

$$r_b \geq \frac{2A_{ts}f_y}{b_s f'_c} \quad (4-1)$$

where A_{ts} is the total area of longitudinal reinforcement; f_y is the specified yield strength of the reinforcement; b is the effective width of the strut at the curved-bar node measured transverse to the plane of the strut-and-tie model; and f'_c is the specified compressive strength of concrete.

When using Eq. (4-1), the clear side cover shall be larger than twice the bar diameter. Otherwise, further enlargement is required. In addition, if the ties force on one end of a curved-bar node is different from that on the other end, the arc length l_{cb} has to be sufficiently long to develop the circumferential bond stress, given by

$$l_{cb} \geq l_d(1 - \tan \theta_c) \quad (4-2)$$

where l_d is the required development length for straight bars; θ_c is the smaller of the two angles between the diagonal strut and the ties.

Nevertheless, the lack of experimental data limits the viability of the design expressions for curved-bar nodes. The current study aims to examine the mechanics of stress transmission at curved-bar nodes to address this knowledge gap. This chapter discusses the experimental program and test results of the investigation. Data analysis and design recommendations based on the test results are also presented. A design example is provided using the proposed design expressions.

4.2. Experimental Program

This section provides a thorough explanation of the testing techniques utilized to explore the objectives and aims of the current study. The testing framework, design of specimens, fabrication, construction of the testing frame, and the equipment utilized for data collection are discussed in detail below.

4.2.1. Specimen Design

4.2.1.1. Design Principles

Nine specimens were moderated to fulfill the objectives of this study. Each specimen was designed as a portal frame with two frame corners (or joints) under closing moments when loads are applied, as shown in Figure 4-2. Each joint had two adjacent members (a beam-column member and a leg) and load/reaction were to be applied on the legs. Regarding the load path, a permissible strut-and-tie model could be constructed, and a curved-bar node formed at the outside of each joint, making the evaluation of the curved-bar node possible when the main longitudinal reinforcement with a total area of A_{ts} was provisioned. Two primary variables were meant to be evaluated: the bend radius r_b and the diagonal strut angle θ_c . Bend radii to be evaluated included three criteria: (i) meeting the standard ASTM mandrel diameters, (ii) according to Eq. (4-1), and (iii) between

Criterion (i) and Criterion (ii). The values of θ_c were to be achieved by adjusting the effective depths of the two adjacent members, including 30 degrees, 45 degrees, and 60 degrees. In addition, the arrangement of the longitudinal reinforcement included single-layer, two-layer, and bundled bars. It should be noted that Eq. (4-2) was not taken as a criterion because an experimental study by Wang et al. (2022) showed that it is unnecessarily conservative. The research team decided to verify Eq. (4-1) first and see if it was necessary to include Eq. (4-2).

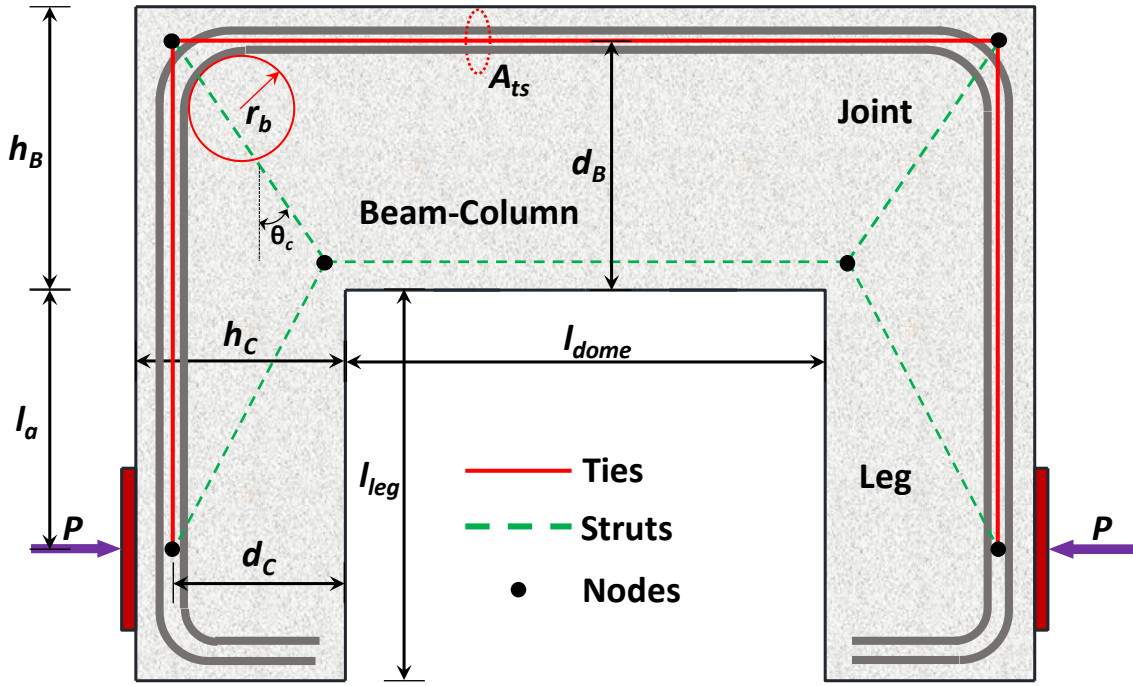


Figure 4-2 Specimen geometry and definition of parameters

These specimens were divided into four series, as summarized in Table 4-1. When the research team was planning the test matrix, material properties were assumed to be 5 ksi for concrete and 65 ksi for reinforcement. In addition, six No. 11 bars were to be used. Series A in the test matrix was meant to investigate the effect of the bend radius with a diagonal strut angle of 45 degrees. All three criteria of bend radii were included in Series A. Further, Series B and C in the test matrix consisted of different diagonal strut angles from 45 degrees. Two different bend radii were also included. Finally, the last series consisted of joints reinforced with two layers of straight bars or two layers of bundled bars. All specimens in Series D have a bend radius satisfying Criterion (ii), and the diagonal strut angle was 45 degrees.

Table 4-1 Test matrix

Series	Test No.	Angle between strut and tie, θ_c (degrees)			Test bend radius, r_b , (in.)			Remark
		30	45	60	6	8.5	11	
A	A-1							(i)
	A-2							(ii)
	A-3							(iii)
B	B-1							(i)
	B-2							(ii)
C	C-1							(i)
	C-2							(ii)
D	D-1							Two layers
	D-2							Bundled bars

4.2.1.2. Specimen Details

4.2.1.2.1. Structural configurations of specimens

All specimens had the same width, denoted as b , as 21 in. The dome length (l_{dome}) and leg length (l_{leg}) were kept the same for all specimens at 71 in. and 58 in. A load was planned to be applied a distance (l_a) of 38.5 in. below the joint while a reaction was provided on the opposite side at the same height. Two roller-supports were to be provided under the beam-column to support the self-weight. Detailed test setup design is discussed later in Section 4.2.3.

Table 4-2 shows other dimensions of each specimen. Series A and D, which were designed to have a diagonal strut angle of 45 degrees, had equal joint dimensions (h_c and h_b) 42 in. by 42 in.; the effective depths of the legs and the beam-column were 38.5 in. and 38.5 in. for Series A. For Series D, the effective depths were slightly smaller in order to maintain a similar top cover.

Table 4-2 Summary of key specimen geometry

Series	Specimen ID	b (in.)	Leg		Beam-column		Long. reinforcement		
			h_c (in.)	d_c (in.)	h_B (in.)	d_B (in.)	A_{ts} (in. ²)	r_b (in.)	Pattern
A	A-R6-45	21	42	38.5	42	38.5	9.36	6.1	6-No.11 One-layer
	A-R11-45	21	42	38.5	42	38.5	9.36	11.4	6-No.11 One-layer
	A-R9-45	21	42	38.5	42	38.5	9.36	8.7	6-No.11 One-layer
B	B-R6-30	21	25	22.5	42	38.5	9.36	6.0	6-No.11 One-layer
	B-R11-30	21	25	22.5	42	38.5	9.36	11.3	6-No.11 One-layer
C	C-R6-60	21	42	38.5	27	23.0	9.36	6.2	6-No.11 One-layer
	C-R11-60	21	42	38.5	27	23.0	9.36	11.3	6-No.11 One-layer
D	D-R11-45(T)	21	42	37.1	42	36.1	9.36	11.3	6-No.11 Two-layer
	D-R11-45(B)	21	42	37.8	42	36.8	9.36	11.3	6-No.11 Bundled

Series B and C, which were designed to have a different diagonal strut angle other than 45 degrees, had unequal joint dimensions. Specimens in Series B had joint dimensions of 25 in. by 42 in. and effective depths of 22.5 in. by 38.5 in., while those in Series C had joint dimensions of 42 in. by 27 in. and effective depths of 38.5 in. and 23 in., achieving the desired diagonal strut angles.

The longitudinal reinforcement in both adjacent members and passing through the joints consisted of six No. 11 reinforcing bars, resulting in a total area (A_{ts}) of 9.36 in. The bend radius of each specimen was measured when the reinforcement cage was built and summarized in Table 4-2.

4.2.1.2.2. Reinforcement Details

The detailed reinforcement layout of the specimens is illustrated in Figure 4-3, for example. As mentioned previously, the longitudinal reinforcement, consisting of six No. 11 bars, continuously past through the perimeter of the specimen with bar bends at the outsides of the joints. One of the joints, as the area of interest, did not have joint reinforcement to rule out undesired effects, while the other joint was heavily reinforced to prevent unwanted failure.

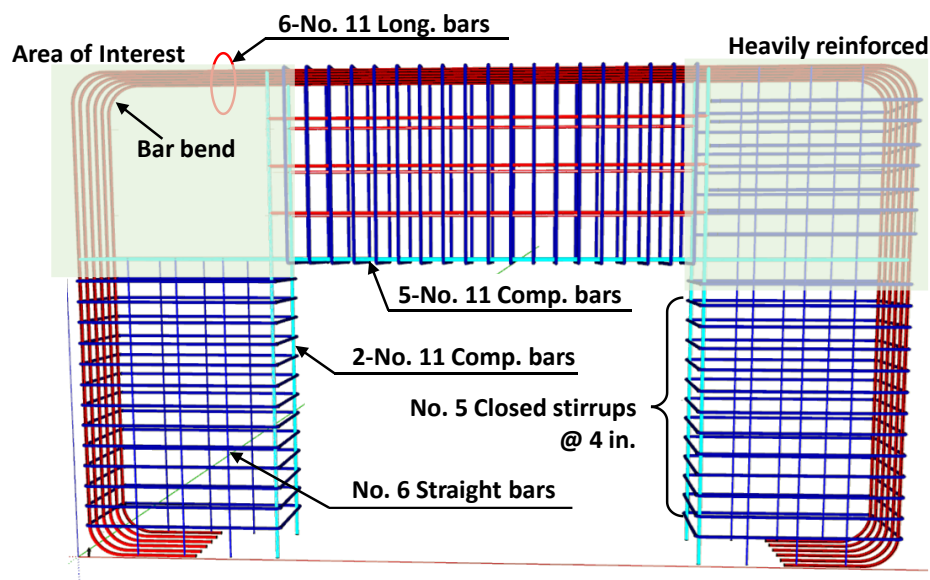


Figure 4-3 General reinforcement layout

In the beam-column member and both legs, a high amount of shear and surface reinforcement was provided to prevent premature failure. In particular, No. 5 closed stirrups spaced at 4 in. were distributed in the legs and the beam-column member. Additional No. 6 straight bars were also equally spaced appropriately to have the reinforcement in orthogonal directions. On the compression side of the beam-column member, five No. 11 bars were provided. On the compression side of the legs, two No. 11 bars were provided. All specimens were reinforced in a similar pattern as presented in Figure 4-4 through Figure 4-7 in detail.

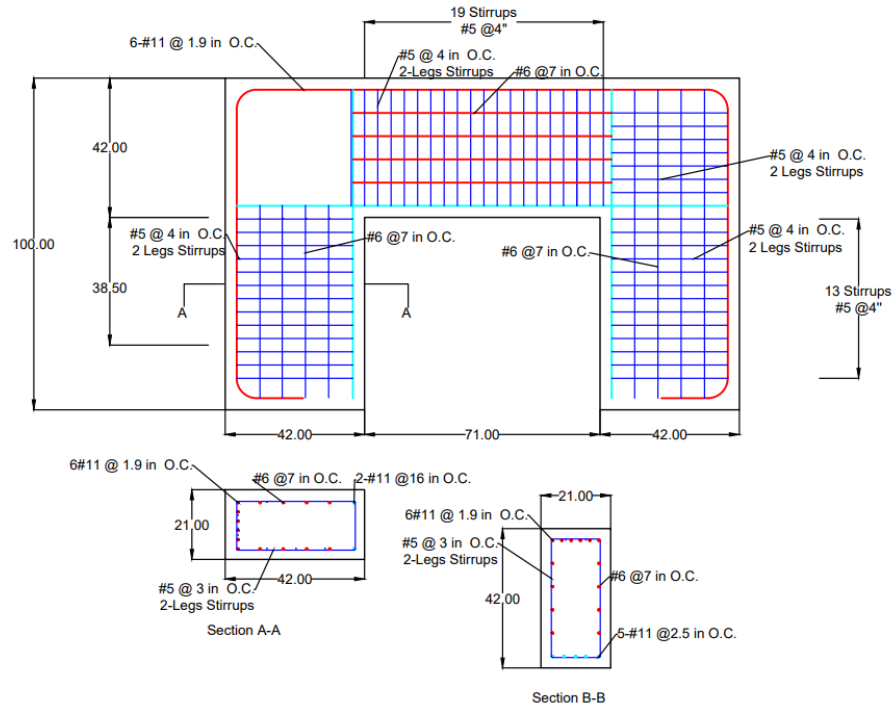


Figure 4-4 Reinforcement detail of specimens in Series A

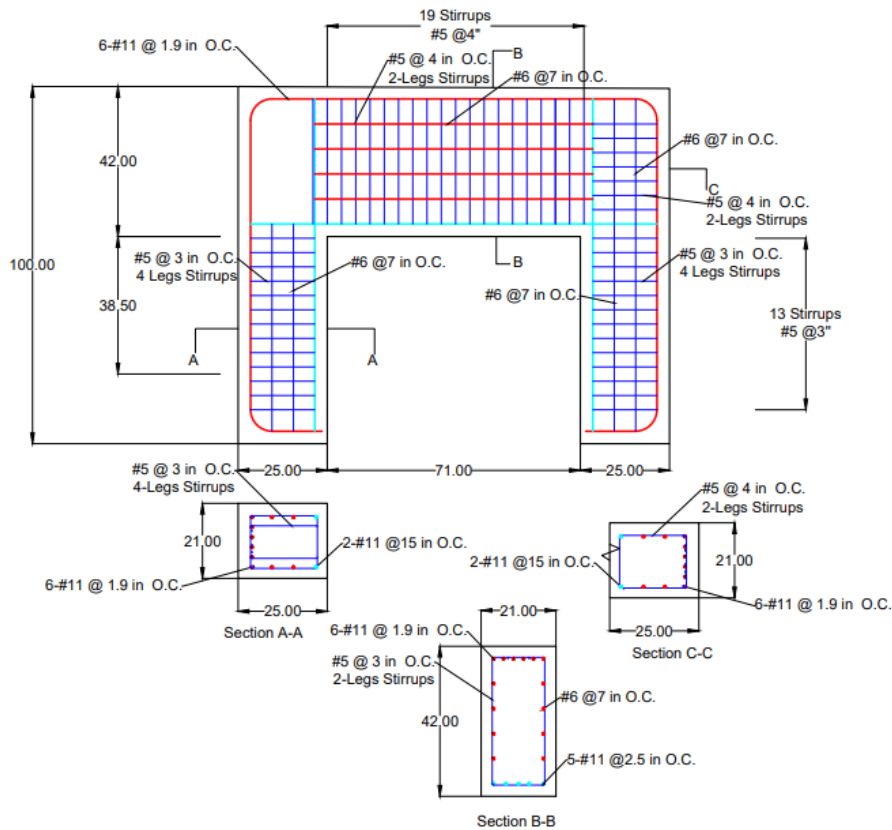


Figure 4-5 Reinforcement detail of specimens in Series B

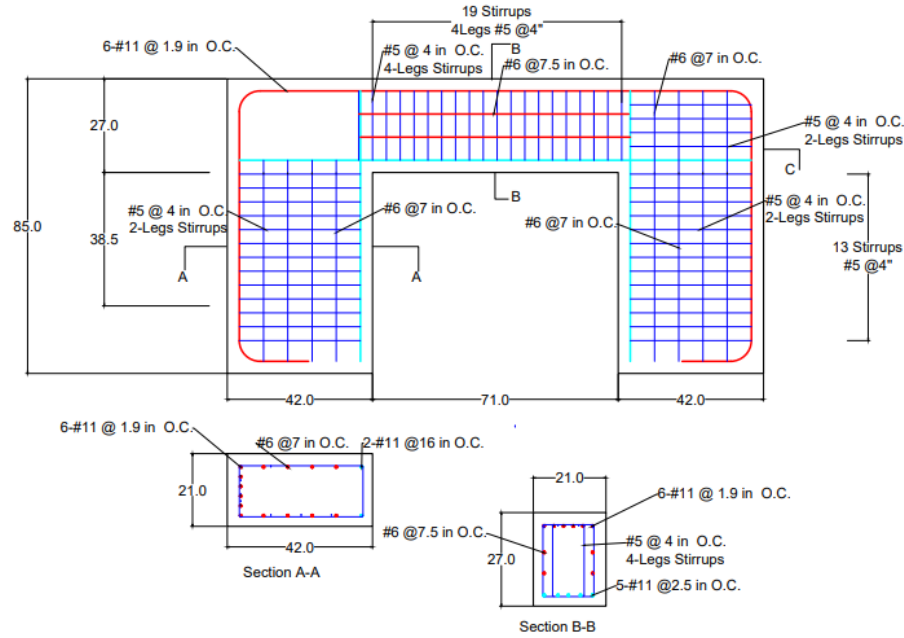


Figure 4-6 Reinforcement detail of specimens in Series C

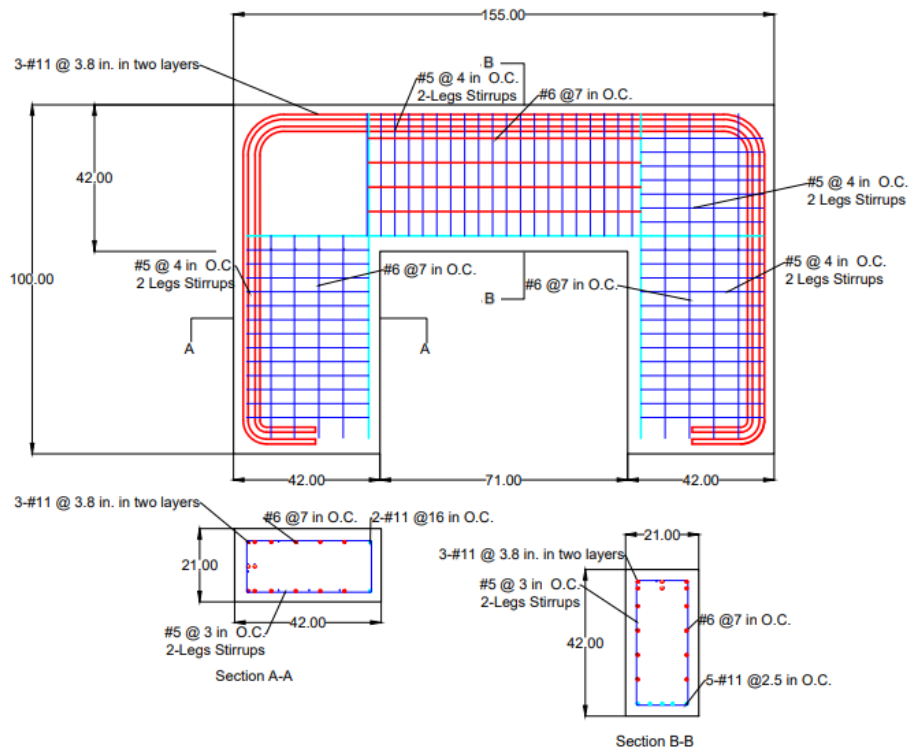


Figure 4-7 Reinforcement detail of specimens in Series D

4.2.1.3. Nomenclature

A naming system was applied for all specimens for readability, as shown in Figure 4-8. The first letter represents the series No.; the second part indicates the approximate bend radius of the specimens; the third part indicates the approximate diagonal strut angle. The letter in the parenthesis informs the arrangement of longitudinal reinforcement; T stands for two-layer, and B standards for bundled bars.

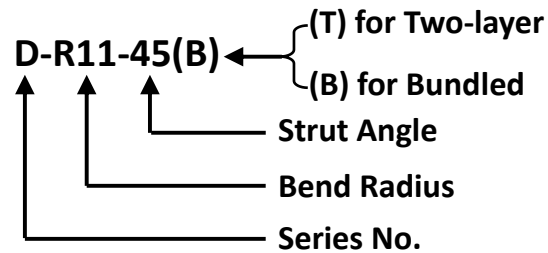


Figure 4-8 Nomenclature

4.2.2. Fabrication of Specimens

The steps of fabricating specimens are shown in Figure 4-9. Firstly, reinforcing bars were tied together to build a reinforcement cage as planned. All the steel cages were made using a similar method. Each cage was built using two channels bolted to two steel columns and various wooden spacers to ensure even spacing of the tension reinforcement throughout the specimen. Before craning the cage into the steel form, strain gauges and vibrating wire gauges were installed, which is discussed later in Section 4.2.4.



(a) Caging



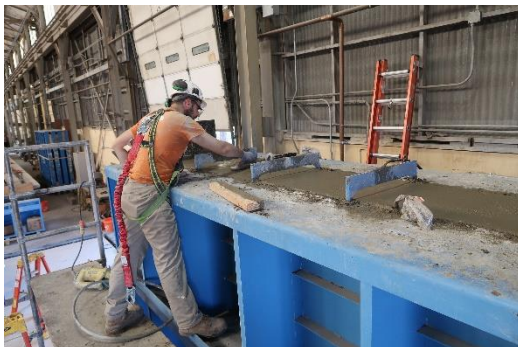
(b) Forming



(c) Slump test



(d) Casting



(e) Finishing



(f) Sampling

Figure 4-9 Fabrication of specimen

Concrete was the same for all specimens to maintain consistency. As shown in Table 4-3, the concrete mixture design had a water-cement ratio of 0.55 and a slump of 7 in. The target strength was between 4.5 ksi and 6.0 ksi. Reinforcement of ASTM A615 Grade 60 was designated.

Table 4-3 Concrete mixture proportions for all specimens

Material Type	Description	Weight
Cement	ASTM C-150 Type I/II	370 lb/cy
Fly Ash	Class F	120 lb/cy
Coarse Aggregate	3/8" River Rock	1650 lb/cy
Fine Aggregate	Concrete Sand	1503 lb/cy
Water	Water	33 gal/cy

When casting, the slump test was first conducted per ASTM C143 to confirm if the concrete was appropriate to cast. A bucket was used to contain fresh concrete and was craned above the form to pour concrete into the form. Regular vibrators and form vibrators were used to consolidate the concrete. After casting, the top surface was finished. Concrete cylinders were sampled per ASTM C31 for compressive strength testing during casting.

After longitudinal reinforcement was in place, the bend radius of each longitudinal reinforcing bar was measured, as shown in Figure 4-10. A board with 1-in. grids was placed under the bar bend, and a cord length was taken for the calculation of the bar bend. The results are summarized in Table 4-2.

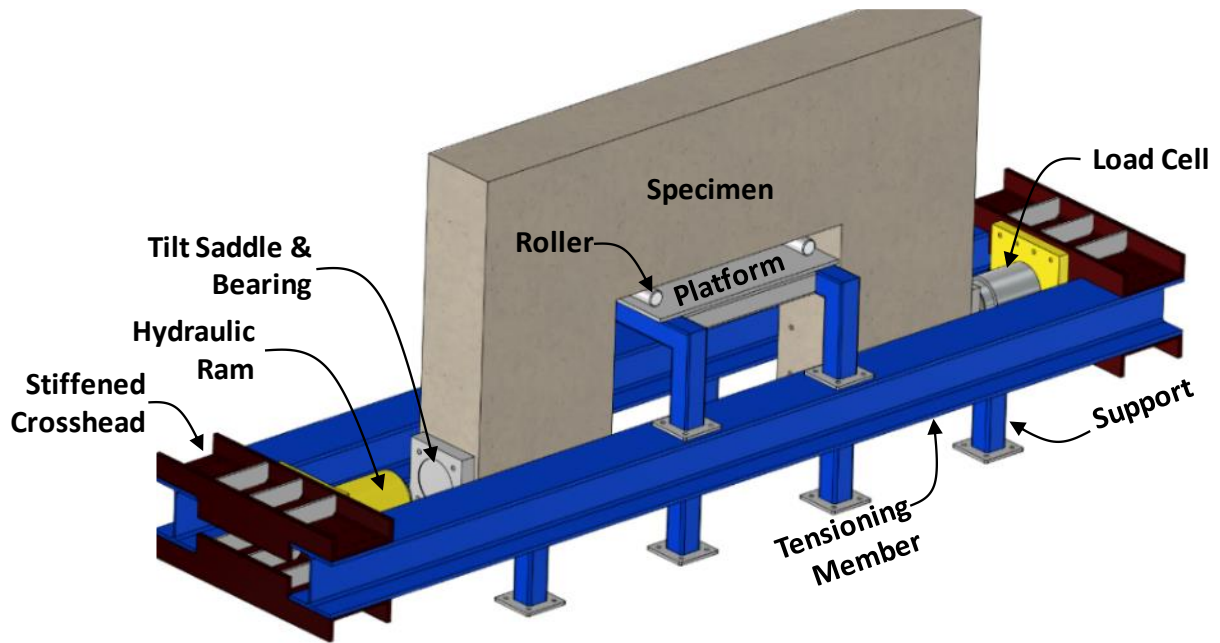


Figure 4-10 Measuring bend radius

4.2.3. Test Frame

The test frame was designed as a self-reacting system, as shown in Figure 4-11. The test setup was used to apply loads on one of the two legs and to provide a reaction on the other leg at the same height simultaneously. A hydraulic jack was mounted on one end, while a load cell with a capacity of 800 kips was mounted on the other end to measure the reaction. A tilt saddle was placed between the hydraulic jack and the leg of the specimen to take potential rotation. To avoid local crushing, a bearing plate with dimensions of 21 in. by 24 in. was placed between the tilt saddle and the specimen on each load point. Two stiffened steel crossheads are connected with longitudinal steel

I-sections as tensioning members to provide the self-containing mechanism. Underneath the specimen, two steel frames, a steel platform, and two rollers were placed to support the self-weight of the specimen and to adjust the height of the loading point.



(a) Design drawing



(b) Finished test frame

Figure 4-11 Test frame

4.2.4. Instrumentation

The instrumentation included strain gauges, vibrating wire gauges, and linear potentiometers (L-pots), as shown in Figure 4-12. The strain gauges were FLAB-5-11-5LJCT-F from Tokyo Sokki®; the vibrating wire gauges were Model 4200 from Geokon®; the L-pots had a 2-in stroke and were from Novotechnik®.



(a) Strain gauge



(b) Vibrating Wire Gauge



(c) Linear potentiometer

Figure 4-12 Sensors

The instrumentation layout is illustrated in Figure 4-13. Strain gauges were distributed along the main longitudinal reinforcement at specified positions. In general, the positions included those in alignment with the two joint faces of each joint, both ends of each bar bend, and the center of each bar bend. In addition, one strain gauge was placed between the joint face and one end of the bar bend; one strain gauge was attached in the middle at longitudinal reinforcing bars of the beam-column member; one strain gauge was put in between the load point and the joint face of each leg. It should be noted that specimens in Series B did not have a strain gauge between the joint face and the end of the bar bend on the top due to limited length.

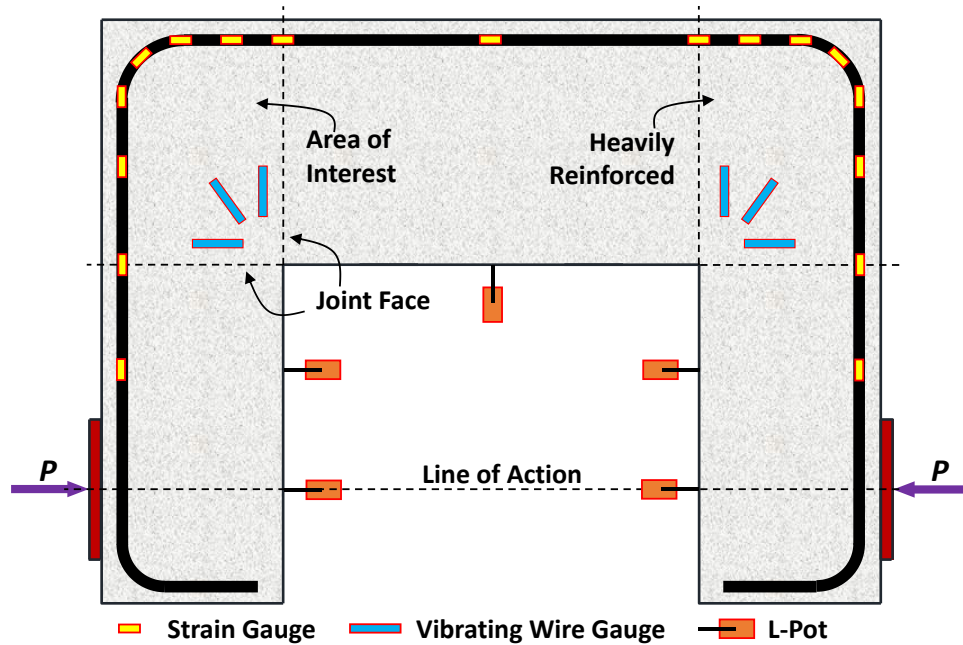


Figure 4-13 Layout of sensors

Three vibrating wire gauges were embedded in each joint, pointing in three directions: one horizontal, one vertical, and one directed along the diagonal. In addition, L-pots were placed on the inner surface of both legs at two different heights. On each leg, one L-pot was placed at the same height as the line of action of the load; while the other L-pot was placed at mid-height for additional monitoring. Also, one L-pot was placed in the middle of the beam-column.

A Digital image correlation (DIC) was employed to capture the strain map in the joint of interest. The DIC system needs speckle patterns, two specialized cameras for 3D mapping, and proper lighting, as shown in Figure 4-14. Speckle patterns were applied to the concrete surface on one side of the area of interest.

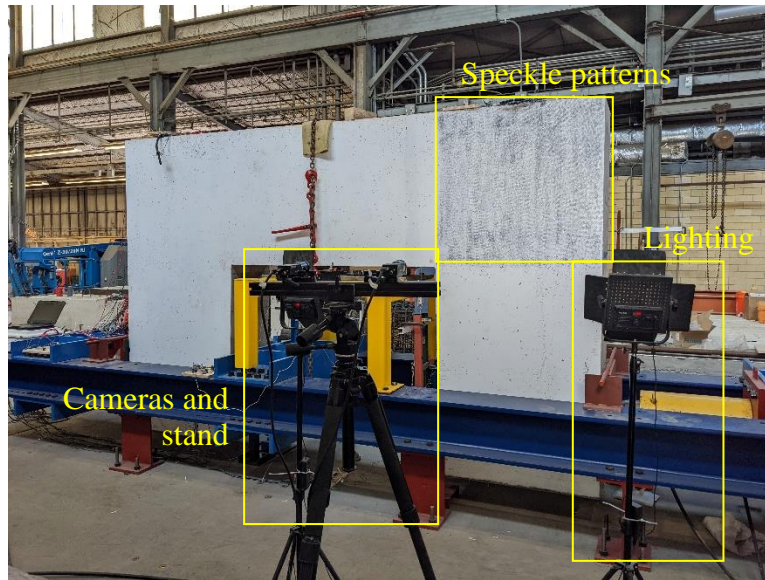


Figure 4-14 DIC system

4.2.5. Test Procedure

During each test, the loading increment was predetermined to be approximately 10 percent of the anticipated failure capacity for each step. Before the specimen was loaded, the DAQ (Data acquisition system), specifically the Agilent Keysight model, was zeroed and initiated for data collection every 4 seconds. The monitoring continued until the near-sides plates made contact, which was defined as the reaction side closest to the loading ram and the area of interest. The loading process was briefly slowed in preparation for the far side to make contact once the near side made initial contact, and the specimen was fully engaged. The loading process was paused temporarily to set up and level the L-pods appropriately before resuming. The DIC system was also initiated, capturing images at the same 4-second intervals as the DAQ system. At each loading increment, both the north and south ends of the specimen were monitored for cracks using a crack comparator card. An image of the testing region on the north face was taken at each loading increment to monitor the main diagonal crack. These procedures were repeated for each loading increment until the specimen failed.

4.3. Experimental Results and Discussion

This chapter presents the test results of specimens tested, including strength results, visual observations, and load-displacement behavior.

4.3.1. Summary of Strength Results

Table 4-4 summarizes the test results of the specimens. Measured material properties are also presented, including the compressive strength of concrete (f'_c) and yield strength of longitudinal reinforcement (f_y). The compressive strength of concrete was derived per ASTM C 39, and the

value shown in the table was the average of three cylinder test results. Similarly, the f_y -value in the table was obtained per ASTM A370. Three coupons were sent to a local laboratory for testing, and the average was taken for analysis.

Table 4-4 Summary of test results

Series	Specimen ID	f'_c (ksi)	f_y (ksi)	r_b/d	Peak Load P_{test} (kip)	Normalized Peak Shear V_{test}
A	A-R6-45	5.30	67.5	0.158	543.3	0.142
	A-R11-45	5.40	68.6	0.295	661.0	0.170
	A-R9-45	4.60	93.2	0.226	497.5	0.150
B	B-R6-30	5.79	66.9	0.155	302.3	0.122
	B-R11-30	5.60	65.6	0.293	344.0	0.143
C	C-R6-60	4.80	69.4	0.160	277.0	0.129
	C-R11-60	4.65	97.2	0.293	337.0	0.162
D	D-R11-45(T)	5.30	73.8	0.314	556.0	0.154
	D-R11-45(B)	4.80	75.8	0.306	452.4	0.136

As the compressive strength of concrete slightly varied among specimens, a procedure of normalization was applied to create the same baseline and meaningful comparison. As shown in Figure 4-15, the joint shear (V) was assumed to equal the total bar force (T). It was acknowledged that this assumption holds if concrete on the tension side does not provide tensile resistance. Nevertheless, it is reasonable to neglect concrete tensile strength after cracking. With this regard, the total bar force T , or the joint shear V , was determined by the moment equilibrium of the free body diagram, given by

$$T = V = \frac{P[l_a + (1 - j)d_B]}{jd_B} \quad (4-3)$$

where P is the applied load; j is the ratio of the sectional moment arm to the effective depth. Here, the j -value was taken as 0.9 for simplicity. It was also acknowledged that no fixed j -value could be determined as the load P increased. Nevertheless, it is practical to position the strut at $0.1h_B$ or $0.1d_B$ away from the edge for constructing permissible strut-and-tie models. Therefore, the normalization method provides a simple approximation of the joint shear, which was used as the baseline for the following sectional analysis. In addition, the ratio of the bend radius to the effective depth along the shear plane is also provided in Table 4-4.

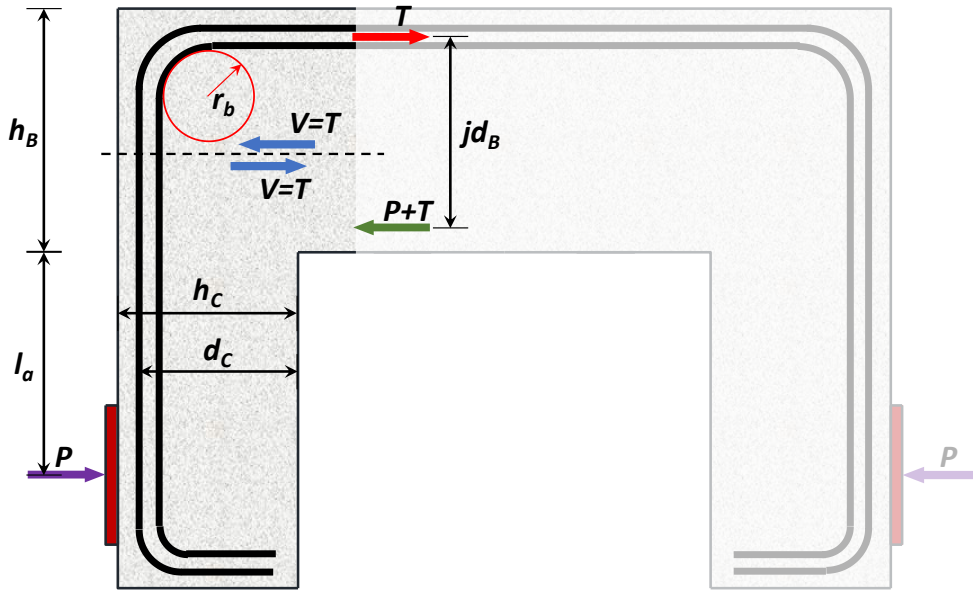


Figure 4-15 Normalization of joint shear

4.3.2. Load-Displacement Behavior and Damage Pattern

4.3.2.1. Series A – Joint with equal heights

The load-displacement curves of the three specimens in Series A are presented together in Figure 4-16. In the figure, the vertical axis is the normalized joint shear force following Eq. (4-3), and the horizontal axis is the displacement along the line of action of the applied load of the leg of interest. It should be noted that the test on Specimen A-R11-45 stopped due to equipment issues, and there was a second test for the specimen; the curve in the figure is the result of the second test.

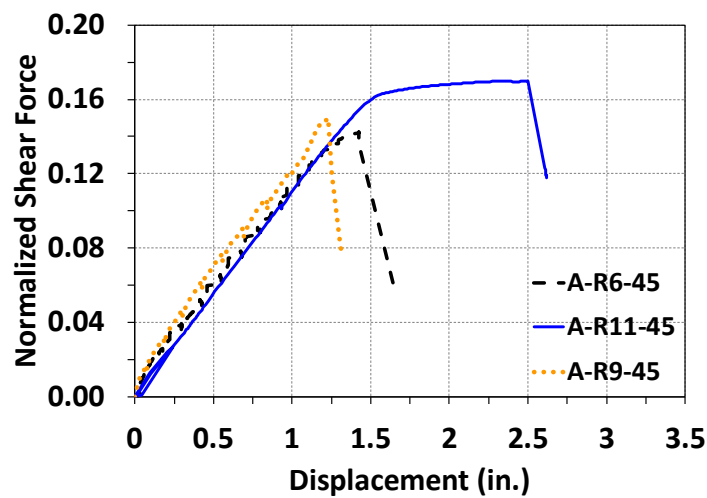


Figure 4-16 Load-displacement relationship of Series A

In general, a larger bend radius led to better behavior in terms of strength and ductility. From Figure 4-16, it can be seen that specimens with a bend radius not satisfying Eq. (4-1) (Specimens A-R6-45 and A-R9-45) had a lower normalized strength than the specimen with a bend radius of Eq. (4-1) (Specimen A-R11-45). The specimen with the largest bend radius in the series had the highest strength and post-yielding behavior. On the other hand, the other two specimens had compromised strength and a sudden drop in load-carrying capacity before the load started plateauing. In addition, a slight increase in the strength was observed when the bend radius was enlarged from 6 in. to 8.7 in.

The size of the bar bend also altered the failure mode, as seen in Figure 4-17. The specimen with a bend radius of the standard bend ended up with a failure mode of splitting in the diagonal and some detachment of top concrete. The other two specimens, having enlarged bend radii than the standard bend, failed due to the largely spalling of concrete in the side cover in the joint. Before the spalling of concrete occurred, Specimen A-R11-45 had demonstrated flexural crushing in the beam-column member. The failure modes indicate that enlarged bend radii involved more concrete in the joint to resist diagonal principal compressive stresses, while the standard bend was critical in tension. In addition, the thickness of the side cover, although not being investigated in this experimental program, can be critical, echoing studies in the literature.



(a) A-R6-45



(b) A-R11-45



(c) A-R9-45

Figure 4-17 Damage pattern after failure of Series A

The damage patterns at failure shown in Figure 4-17 also indicate that the load path of the closing knee joint specimens was in good agreement with the assumed strut-and-tie model, as seen in Figure 4-1 and Figure 4-2. The observed effects of the bar bend on the behavior reveal the appropriateness of using curved-bar nodes for such closing knee joints.

The largest crack width measured at different load levels of each specimen in Series A was plotted against the normalized test shear force to examine the growth of cracks, as presented in Figure 4-18. It can be seen in the figure that the largest crack width was growing faster along with loading when the bend radius was smaller after the onset of cracking (approximately corresponding to a normalized shear force of 0.011). Among the specimens in Series A, Specimen A-R11-45 had the smallest width all the time.

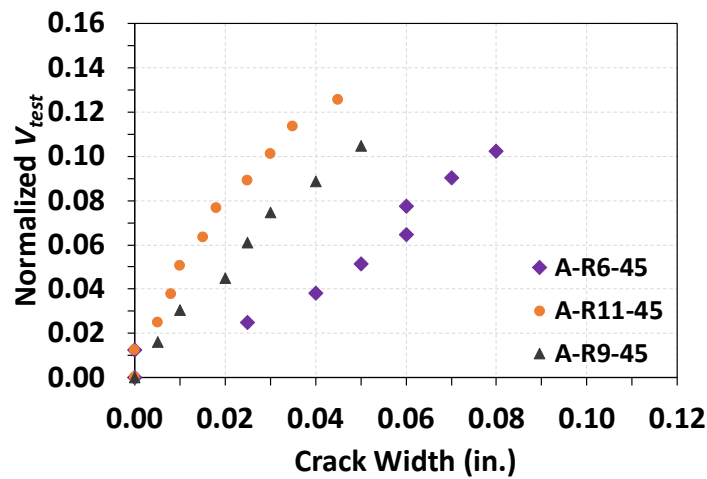
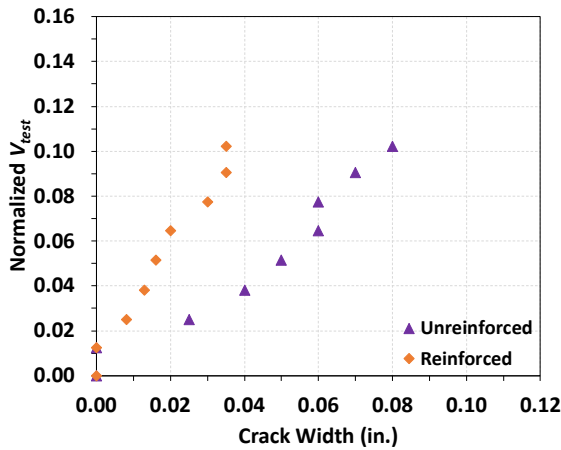
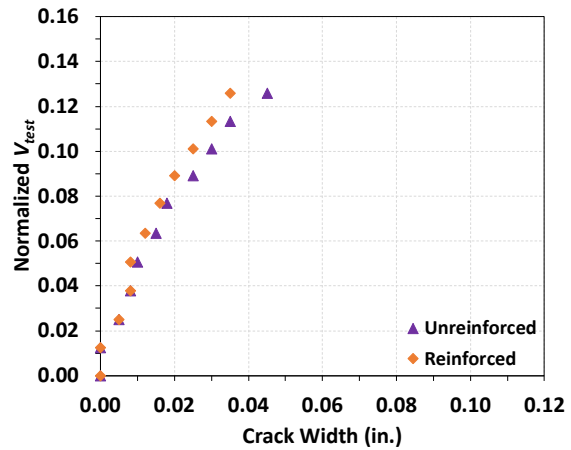


Figure 4-18 Comparison of crack width in Series A

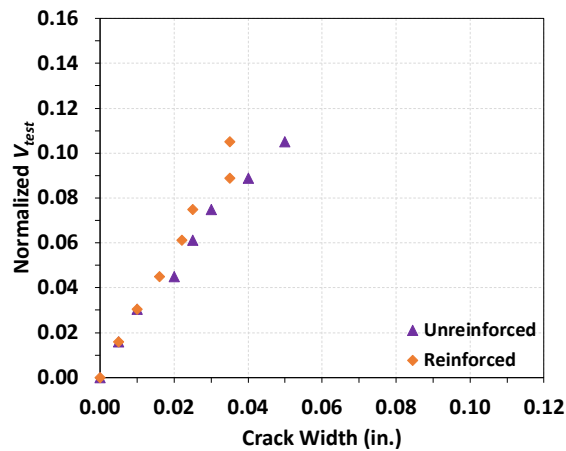
It is also interesting to compare the crack widths of each specimen's unreinforced and heavily reinforced joints, as shown in Figure 4-19. For specimens with a bend radius larger than the standard bend (Specimens A-R9-45 and A-R11-45), the crack width was growing at almost the same rate between the heavily reinforced joint and the unreinforced joint. Heavy reinforcement only slightly reduced the largest crack width if an enlarged bend radius per Eq. (4-1) was used. On the other hand, Specimen A-R6-45 greatly improved in terms of crack width. In other words, the effect of heavy reinforcement on crack width took place only when the specimen had a small bend radius. Nevertheless, even the heavily reinforced joint of Specimen A-R6-45 still had a similar crack width at each load increment compared to the unreinforced and heavily reinforced joints of the other two specimens. The observation again emphasizes the importance of using enlarged bend radii whether joint transverse reinforcement was used.



(a) A-R6-45



(b) A-R11-45



(c) A-R9-45

Figure 4-19 Effect of heavy reinforcement on crack growing of Series A

4.3.2.2. Series D – Multiple layers of reinforcement

Similarly, the load-displacement behaviors of the three specimens in Series D are presented together in Figure 4-20. It should be noted that both specimens in this series had a bend radius somewhat smaller than Criterion (ii) due to the high measured yield strength of longitudinal reinforcement. Nevertheless, Specimen D-R11-45(T), which had two layers of longitudinal reinforcing bars through the joint, also entered the load plateau. Specimen D-R11-45(B), although having an enlarged bend radius, was not able to reach the load plateau. It was plausible that the bundled reinforcing bars exerted extra stress concentration on the side cover, leading to compromised strength and early failure. Alternatively, it is also possible that Specimen D-R11-45(B) had a slightly lower compressive strength of concrete. A more detailed discussion is presented in Section 4.5.

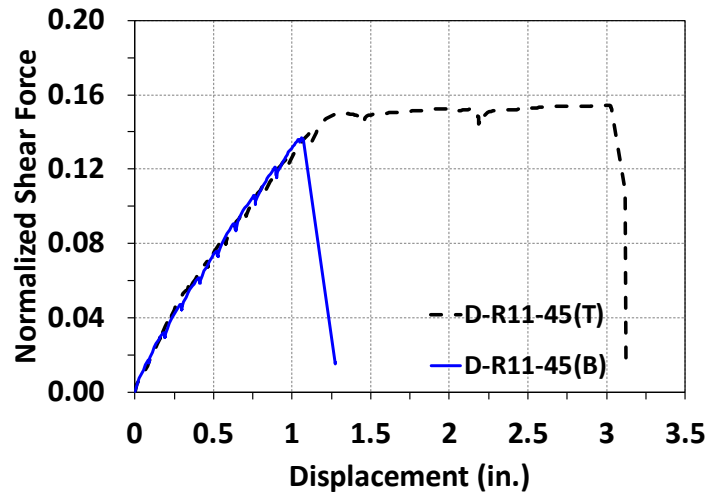


Figure 4-20 Load-displacement relationship of Series D

The failure modes of the specimens in Series D, as shown in Figure 4-21, were similar. Both specimens had large spalling of concrete on the joint side and detachment of concrete cover. The enlarged bend radius once again was proven to involve a large volume of concrete in the joint to resist the diagonal stresses, whether two-layer or bundled reinforcement. Specimen D-R11-45(T) also exhibited flexural crushing on the bottom of the beam-column member as it entered post-yielding behavior.



(a) D-R11-45(T)



(b) D-R11-45(B)

Figure 4-21 Damage pattern after failure of Series D

The largest crack width measured at different load levels of each specimen in Series D was plotted against the normalized test shear force to examine the growth of cracks, as presented in Figure 4-22. It can be seen from the figure that both specimens had almost the same crack width growing behavior along with the normalized shear force. Separated two layers of or bundled reinforcing longitudinal bars in the joint led to similar growth rates of crack width of the specimens, provided the bend radius was the same.

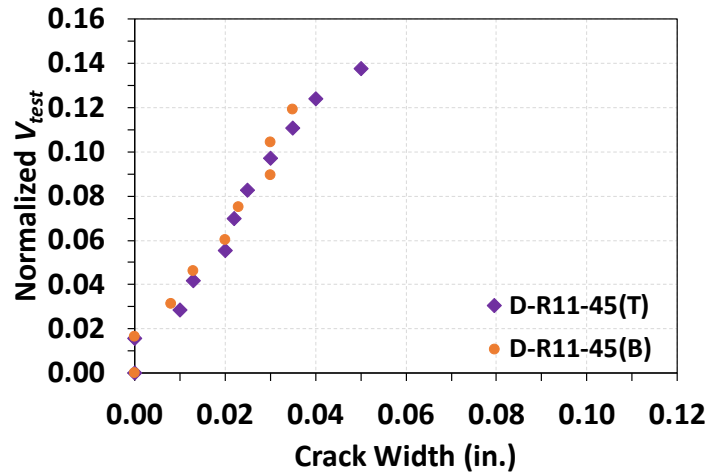
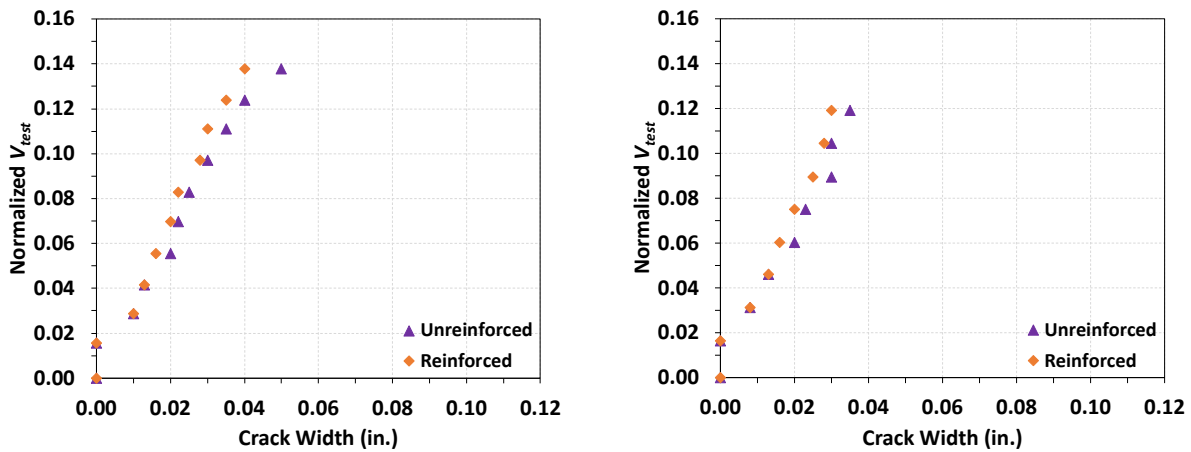


Figure 4-22 Comparison of crack width in Series D

A comparison of the largest crack width at each load step between the unreinforced joint and the heavily reinforced joint of each specimen in Series D was plotted, as shown in Figure 4-23. For both specimens, heavy reinforcement did not significantly reduce the crack width. This result echoes the observation from Series A; when enlarged bend radii satisfying Eq. (4-1) were used, joint reinforcement had a limited contribution to controlling crack widths. Using large bend radii is essential for two layers of reinforcement.



(a) D-R11-45(T)

(b) D-R11-45(B)

Figure 4-23 Effect of heavy reinforcement on crack growing of Series D

4.3.2.3. Series B – Joint with deeper beam-column

The load-displacement curves of the two specimens in Series B are presented in Figure 4-24. Similarly, the vertical axis is the normalized joint shear force following Eq. (4-3) and the horizontal axis is the displacement along the line of action of the applied load of the leg of interest. It should

be noted that the test of Specimen B-R11-30 did not reach the ultimate failure because the specimen underwent a large displacement. The test was stopped for safety reasons.

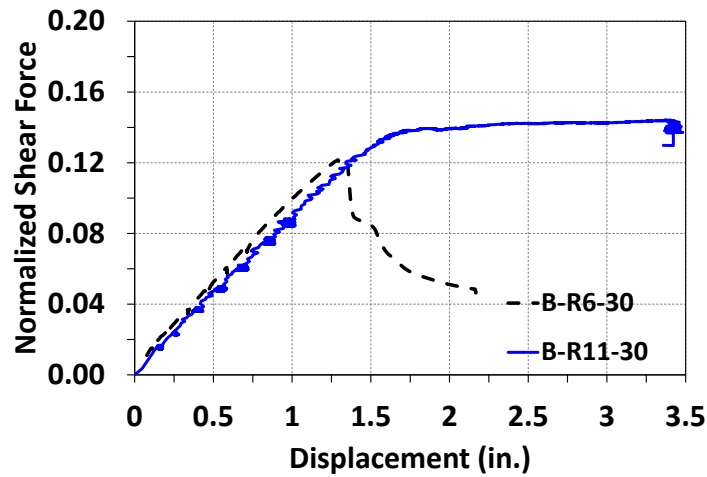
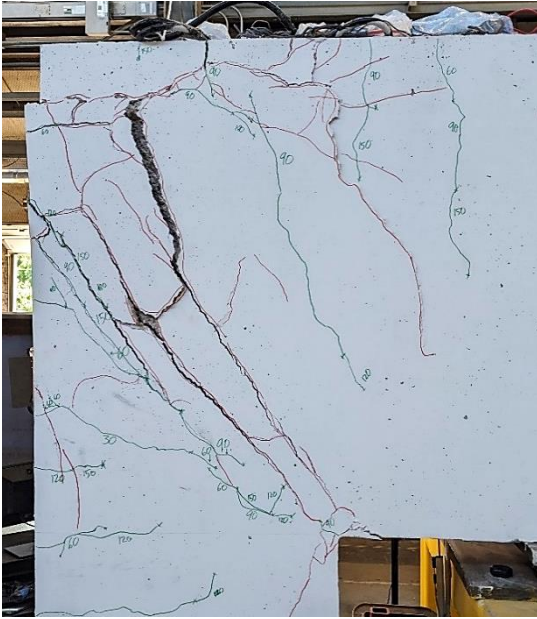


Figure 4-24 Load-displacement relationship of Series B

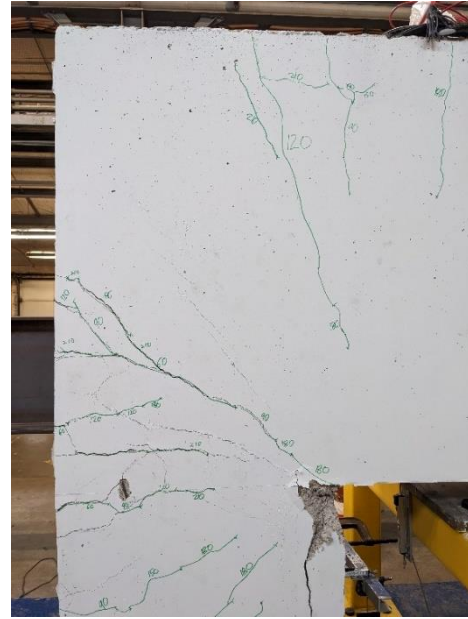
As shown in Figure 4-24, specimens in Series B also demonstrated a similar effect of the bend radius on the load-displacement behavior as exhibited by the specimens in Series A. Specimen B-R11-30, which had an enlarged bend radius following Eq. (4-1), underwent a superior ductility after the load started plateauing at a normalized shear force of approximately 0.141 until the displacement reached approximately 3.5 in., when the test was stopped for safety reasons. On the other hand, Specimen B-R6-30, which did not have an enlarged bend radius, underwent an early load drop and a lower peak normalized shear force of 0.122, 14.7 % lower than its counterpart in this series.

In addition, the load-displacement behavior of Specimen B-R11-30 implies that following Eq. ((4-1)) was already sufficient; Eq. ((4-2)), leading to a required bend radius of 23.83 in. for the specimen, appeared to be unnecessary. More discussion on the evaluation of requirements on the bend radius is presented in Section 4.5.

The size of the bar bend also altered the failure mode in a similar manner to Series A, as seen in Figure 4-25. Specimen B-R6-30, with a bend radius of the standard bend, failed due to the splitting of the diagonal strut. Specimen B-R11-30 did not reach the ultimate failure, but the leg had been largely crushed on the compression side at the re-entrant corner, indicating that the specimen was experiencing a flexural failure in the leg.



(a) B-R6-30



(b) B-R11-30

Figure 4-25 Damage pattern after end of test of Series B

The largest crack width measured at different load levels of each specimen in Series B was plotted against the normalized test shear force to examine the growth of cracks, as presented in Figure 4-26. It can be seen from the figure that the crack width growth started deviating at a normalized shear force level of approximately 0.037; Specimen B-R6-30, which had a smaller bend radius, had cracks growing faster than Specimen B-R11-30. The effect of the enlarged bend radius on reducing crack width still held for specimens with a diagonal strut angle of 30 degrees.

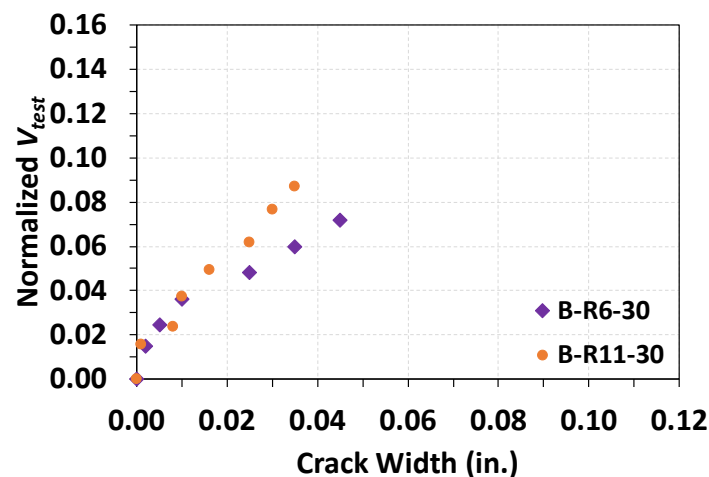


Figure 4-26 Comparison of crack width in Series B

A comparison of the largest crack width at each load step between the unreinforced joint and the heavily reinforced joint of each specimen in Series B was plotted, as shown in Figure 4-27. It can be once again interpreted that heavy joint reinforcement contributed to controlling crack width in

the joint when smaller bend radii were used, whether the diagonal strut was 45 degrees or 30 degrees. Also, the heavily reinforced joint of Specimen B-R6-R30 behaved only slightly better than the unreinforced joint of Specimen B-R11-R30 in terms of crack width growing. Using enlarged bend radii per Eq. (4-1) was once again proven essential whether joint reinforcement existed or not. Also, Eq. (4-2) appeared unnecessary for controlling crack widths.

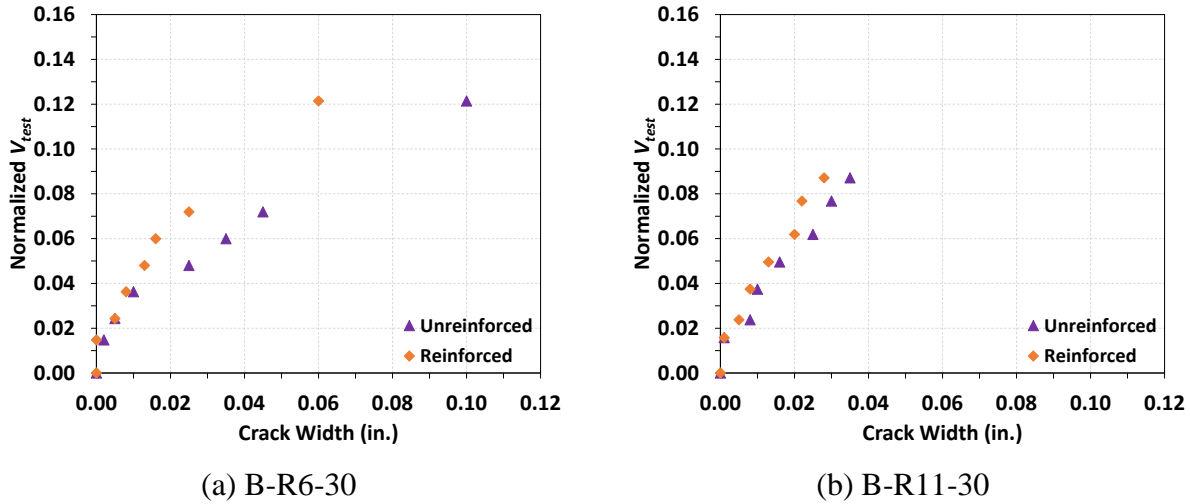


Figure 4-27 Effect of heavy reinforcement on crack growing of Series B

Test results of the specimens in Series C and other series reveal similar effects of the bend radius on the behavior of closing knee joints in terms of failure modes and strength, whether the orientation of the diagonal strut angle is 45 degrees or not. It is plausible that Eq. (4-1) and other design expressions still apply to joints with a diagonal strut angle of 30 degrees.

4.3.2.4. Series C – Joint with deeper leg

The load-displacement relationships of the two specimens in Series C were similarly plotted, as presented in Figure 4-28. It should be noted that Specimen C-R11-60 had longitudinal reinforcement with higher yield strength, so the bend radius did not satisfy Eq. (4-1). Nevertheless, it is evident that the enlarged bend radius in the joint of Specimen C-R11-60 led to higher load-carrying capacity compared to its companion Specimen C-R6-60, which had a bend radius of the standard bend. Strain readings along the longitudinal reinforcing bars on the top side of Specimen C-R11-60 were found to have exceeded 2×10^{-3} before the end of the test, the longitudinal reinforcing bars would have yielded if the bars had been Grade 60. Therefore, Specimen C-R11-60 would plausibly have exhibited post-yield load plateauing, resembling its companion specimens with an enlarged bend radius (Specimens A-R11-45 and B-R11-30). Detailed strain data is introduced in Section 4.3.3. Specimen C-R6-60, similar to Specimen A-R6-45, had compromised strength and a sudden load drop.

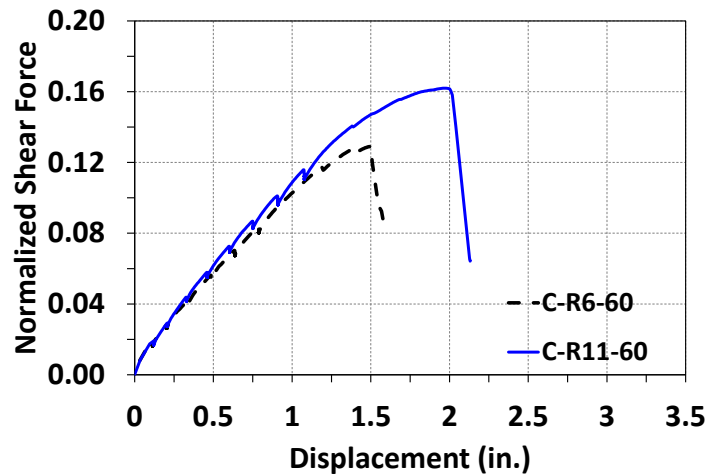
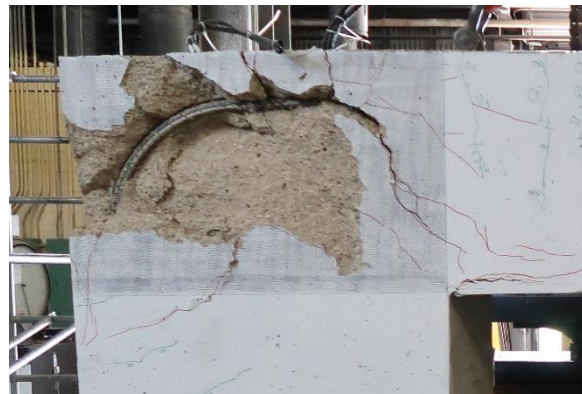


Figure 4-28 Load-displacement relationship of Series C

The failure patterns of the specimens in Series C are presented in Figure 4-29. The way the size of the bar bend affected the failure modes was similar to specimens with equally sized joints. Specifically, Specimen C-R6-60, with a bend radius of the standard bend, failed due to the splitting of the diagonal strut. In contrast, Specimen C-R11-60, which had an enlarged bend radius following Eq. (4-1), failed with extensive concrete spalling in the joint. Both specimens demonstrated some degree of concrete crushing on the compression side of the beam-column member.



(a) C-R6-60



(b) C-R11-60

Figure 4-29 Damage pattern after failure of Series C

The largest crack width measured at different load levels of each specimen in Series C was plotted against the normalized test shear force to examine the growth of cracks, as presented in Figure 4-30. It can be seen from the figure that the crack width growth started deviating at a normalized shear force level of approximately 0.058; Specimen C-R6-60, which had a smaller bend radius, had cracks growing faster than Specimen C-R11-60. The effect of the enlarged bend radius on reducing crack width still held for specimens with a diagonal strut angle of 60 degrees.

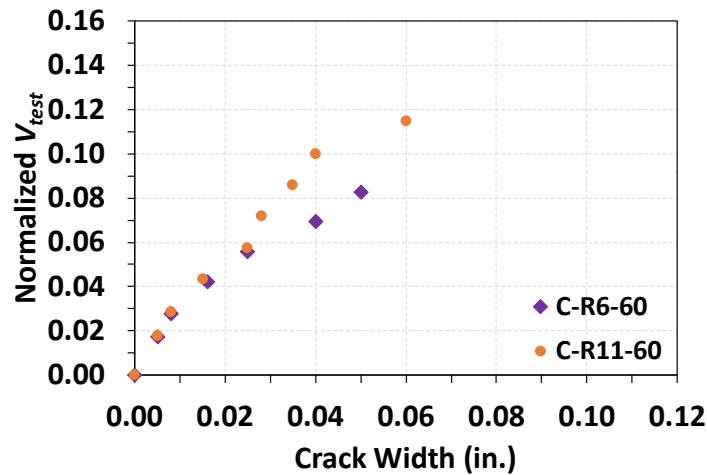


Figure 4-30 Comparison of crack width in Series C

A comparison of the largest crack width at each load step between the unreinforced joint and the heavily reinforced joint of each specimen in Series C was plotted, as shown in Figure 4-31. It can be once again interpreted that heavy joint reinforcement contributed to controlling crack width in the joint when smaller bend radii were used and when the diagonal strut was in a range between 30 degrees and 60 degrees, considering all test results introduced in previous sections. Also, the heavily reinforced joint of Specimen C-R6-R60 behaved only slightly better than the unreinforced joint of Specimen C-R11-R60 in terms of crack width growing. Using enlarged bend radii per Eq. (4-1) was once again proven essential whether joint reinforcement existed or not.

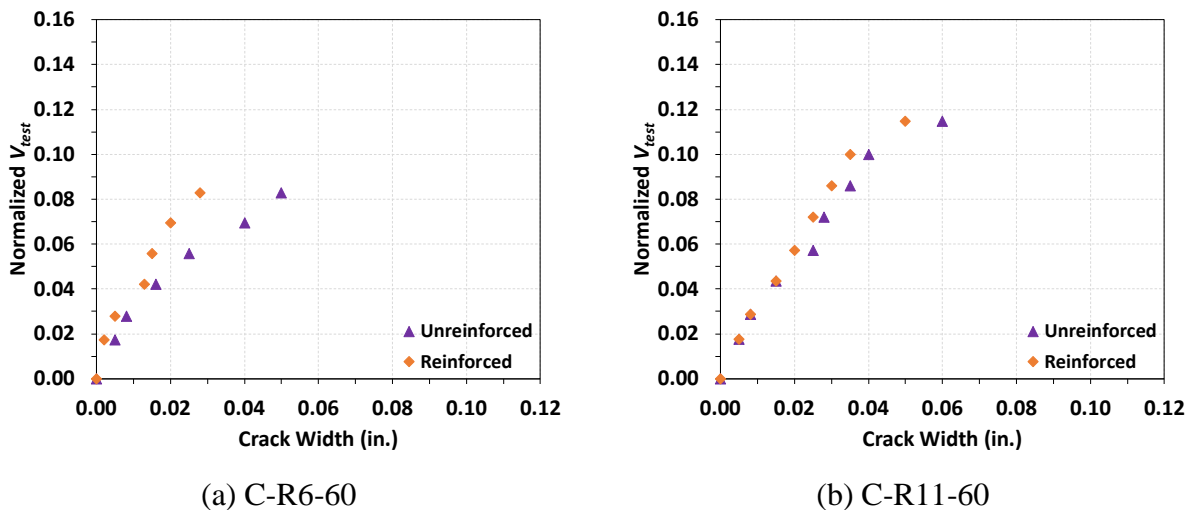


Figure 4-31 Effect of heavy reinforcement on crack growing of Series C

Test results of the specimens in Series C and other series reveal similar effects of the bend radius on the behavior of closing knee joints in terms of failure modes and strength, whether the

orientation of the diagonal strut angle is 45 degrees or not. It is plausible that Eq. (4-1) and other design expressions still apply to closing knee joints with a diagonal strut angle of 60 degrees.

4.3.3. Bar Development and Digital Image Correlation (DIC)

This section presents the compressive principal strain map captured by the DIC system and stress development in the longitudinal reinforcement. It also discusses the stress distribution in the joint of each specimen. As strut-and-tie modeling is used to examine the adequacy of RC members at limit states, it is appropriate to study the DIC strain map and bar stress near failure. Also, strut elements in the STM represent principal compressive stresses, which can be indicated by principal compressive strains captured by the DIC system. Bar stress along the longitudinal reinforcement is calculated by converting strain gauge readings into stress values by multiplying the elasticity of steel (29000 ksi). The DIC strain map and bar stresses of each specimen are superpositioned together for discussion in the following subsections.

4.3.3.1. Series A – Joint with equal heights

The superpositioned strain maps with bar stresses of specimens in Series A before failure are presented in Figure 4-32 through Figure 4-34. The magnitudes of the concrete strains and the bar stresses are presented by color brightness in the figures. Converted bar stresses between strain gauges are assumed to be linearly varied. Arrows indicate the direction of principal compressive strains, which is considered the same as principal compressive stresses. In general, it is evident that all specimens in this series had a stress concentration along the diagonal and equilibrated with the two tie forces. Also, significant stress concentration was observed at the re-entrant corner. The observations indicate that the assumed strut-and-tie model for the specimens and the approach of sizing the CCC node were appropriate. More discussion of constructing strut-and-tie models can be seen in Section 4.7.

Figure 4-32 shows the results near failure of Specimen A-R6-45, which had a bend radius of the standard bend. Stress values along the longitudinal reinforcement are marked at the corresponding positions. On the top side, the reinforcement had a yielded region between the joint face and the middle of the joint. After the middle of the joint, the bar stress decreased rapidly from the yield stress to approximately 38 ksi at the beginning of the bar bend. Similar stress variation also appeared on the leg side. The stress variation indicates that bond stresses existed, assisting in the development of bar stress. Within the region where bond stresses existed, compressive principal stresses are also developed, pointing to the re-entrant corner, as can be seen in the figure. The stress transmission induced by the interaction of tensile stresses in the bar, bond stresses along the bar, and the diagonal compressive stresses echoes studies by Ingham (1995) and Wang et al. (2020) as mentioned in Section 2.3.2.

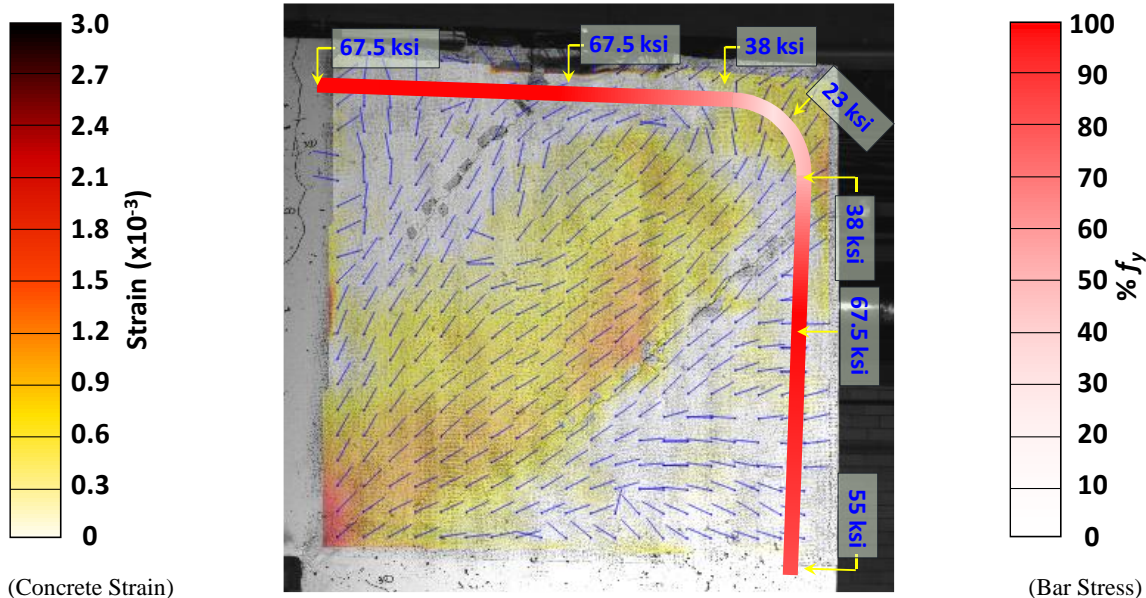


Figure 4-32 Bar stress distribution and concrete strain in the joint of Specimen A-R6-45

The stress transmission mechanism also indicates that not only did the bar bend region resist the diagonal compressive stresses, but a portion of the straight bars contributed. The sizing method for curved-bar nodes can derive a smaller bearing area than the observed compression region because the strut-and-tie model did not account for stress variation along the bars from the bar bends to the middle of the joint. Nevertheless, the method would be conservative.

It was interesting to observe that the bars on the tension side of the leg yielded at the middle of the joint but did not at the joint face, indicating the bond stresses were in the direction toward the bar bend instead of the joint face. The observation is supported by the orientation of stresses transmitted into the joint. The observation strongly indicates that the critical section of the longitudinal reinforcing bars should not be taken at the joint face, as suggested by the sectional analysis. The STM better and conservatively reflects the observation.

Similarly, the superpositioned DIC strain map and converted bar stresses of Specimen A-R11-45 is presented in Figure 4-33. It can be seen that the beginning of the bar bend on the top side nearly yielded (94% of the yield stress), while the entire straight portion of the bars in the leg yielded. Only a slight variation of tensile stresses existed within the bar bend. In this case, the diagonal principal compressive stresses extended and limited in the bar bend. Under the bar bend, the stress level was relatively low, indicating de-stress appeared on the concrete cover, causing concrete spalling. This enlarged bar bend allowed extra yield penetration and involved more concrete in the bar bend, compressing the diagonal strut and the CCC node more, providing better joint strength and ductility.

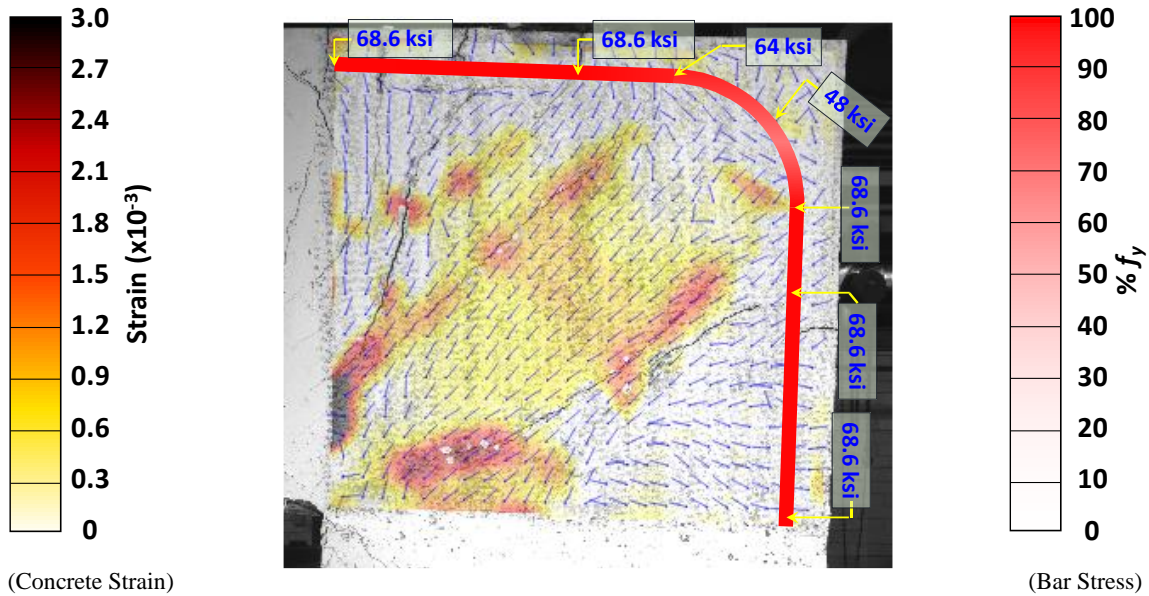


Figure 4-33 Bar stress distribution and concrete strain in the joint of Specimen A-R11-45

The results of Specimen A-R9-45 are presented in Figure 4-34. The specimen had bars with a higher yield stress of 93.2 ksi; therefore, direct comparison was not made about yield penetration. Nevertheless, shared characteristics were observed from the figure between Specimen A-R9-45 and the other two specimens in Series A. Firstly, the longitudinal reinforcing bars reached the yield stress in the middle of the joint on both the top and right sides; bar stress decreased toward each direction where bond stresses developed. More concentrated compressive principal stresses in the diagonal were also developed. Second, de-stressing happened under the bar bend, indicating the spalling of concrete.

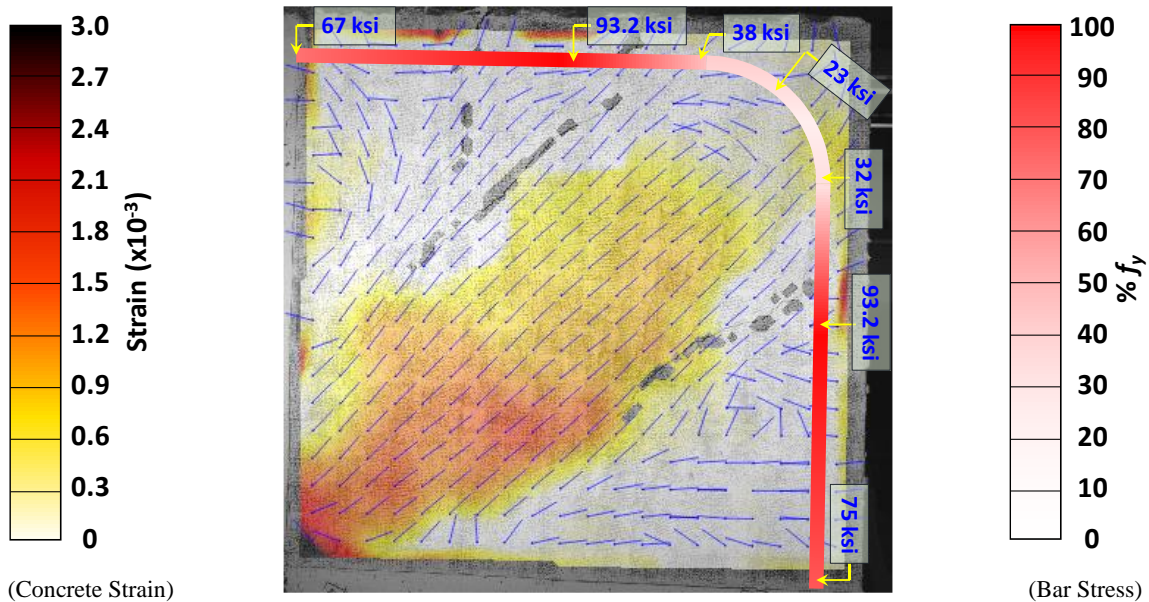


Figure 4-34 Bar stress distribution and concrete strain in the joint of Specimen A-R9-45

4.3.3.2. Series D – Multiple layers of reinforcement

The superpositioned strain maps and bar stress development of specimens in Series D before failure are presented in Figure 4-35 and Figure 4-36. The labeling and presentation are the same as the figures for Series A introduced in the previous section. It can be seen that the two specimens in this series had the highest stress concentration along the diagonal. The longitudinal reinforcement yielded almost throughout the length towards the bar bends. Also, significant stress concentration was observed at the re-entrant corner. The observations indicate that the assumed strut-and-tie model for the specimens and the approach of sizing the CCC node were appropriate.

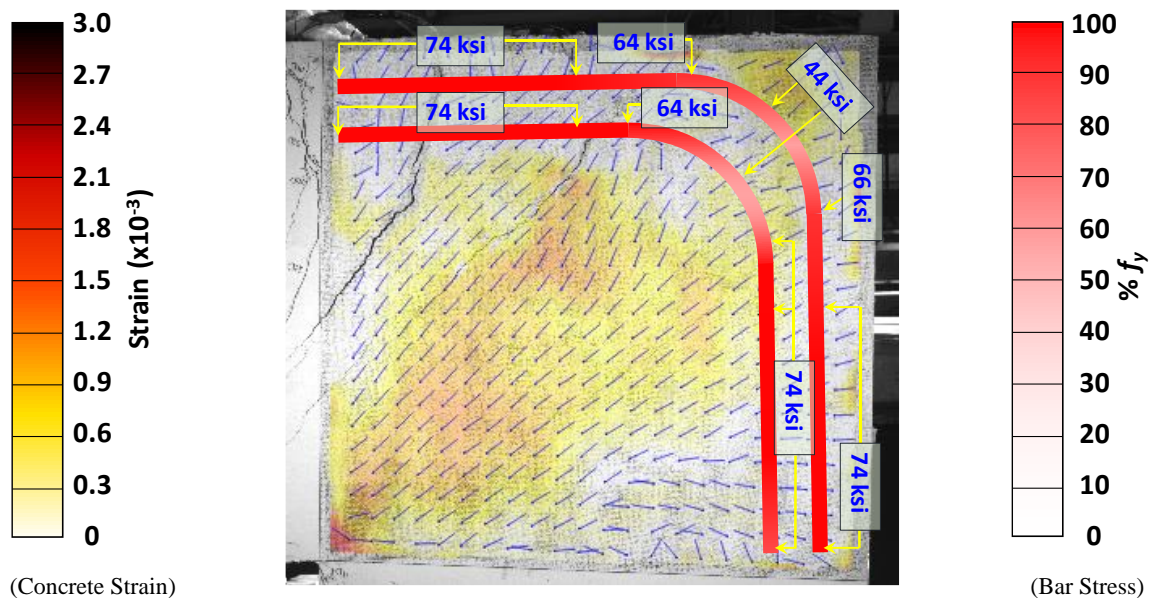


Figure 4-35 Bar stress distribution and concrete strain in the joint of Specimen D-R11-45(T)

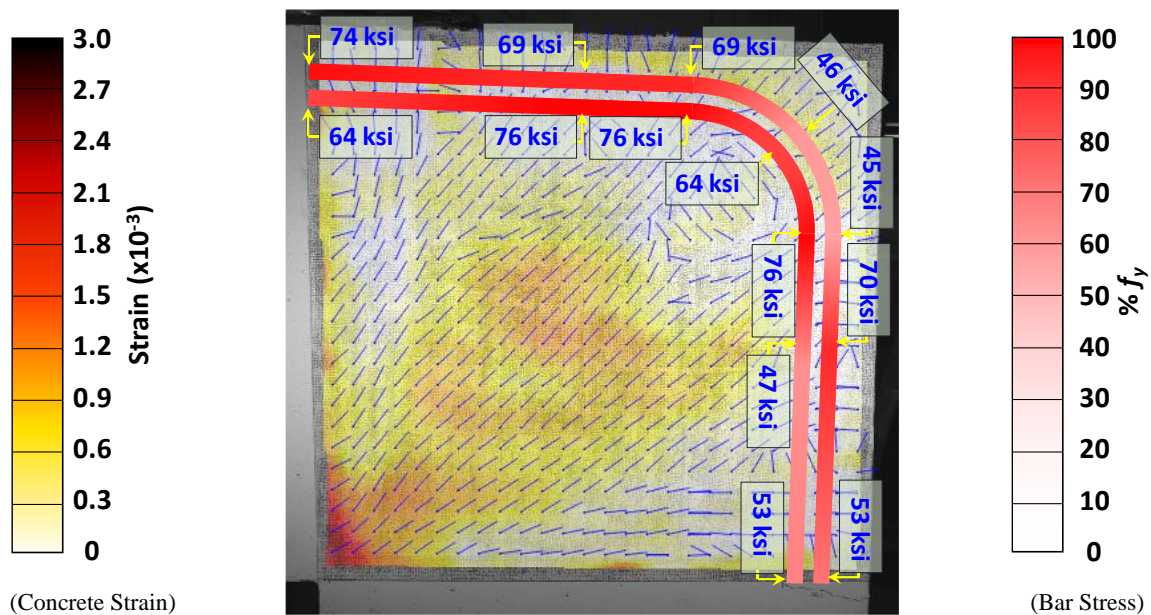


Figure 4-36 Bar stress distribution and concrete strain in the joint of Specimen D-R11-45(B)

From the bar development status before failure shown in Figure 4-35 and Figure 4-36, it can be seen that both specimens had yield penetration into the bar bend or near the bar bend of both layers on the top side. On the right side, Specimen D-R11-45(T) was able to have a slightly deeper yield penetration near the bar bend than its counterpart Specimen D-R11-45(B) on the outer layer because Specimen D-R11-45(B) had an earlier failure.

Compared to their counterpart with an enlarged bend radius in Series A (Specimen A-R11-45), both specimens in Series D had a wider zone of diagonal stress concentrations. It is plausible that two layers of bars near the side cover exerted additive splitting stress on the side cover. Further, the bundled bars tended to cause even higher splitting stress on the side cover, causing premature failure due to side cover spalling.

Consequently, the observation revealed that enlarged bend radii are still key to having better development of bar stress in the joint, and bundled bars need to be paid extra attention to avoid early splitting of the side cover.

4.3.3.3. Series B – Deeper legs

The superpositioned strain maps and bar stress development of specimens in Series B are presented in Figure 4-37 and Figure 4-38. Similarly, labeling and presentation style are the same as introduced before. It should be noted that the DIC system stopped capturing speckle images due to equipment issues at a load level of 210 kip; the strain map shown in Figure 4-37 corresponds to the load level, but the stress profile along the gauged bar corresponds to near failure. In addition, Specimen B-R11-30 did not reach the ultimate failure condition; Figure 4-38 presents the status near the end of the test.

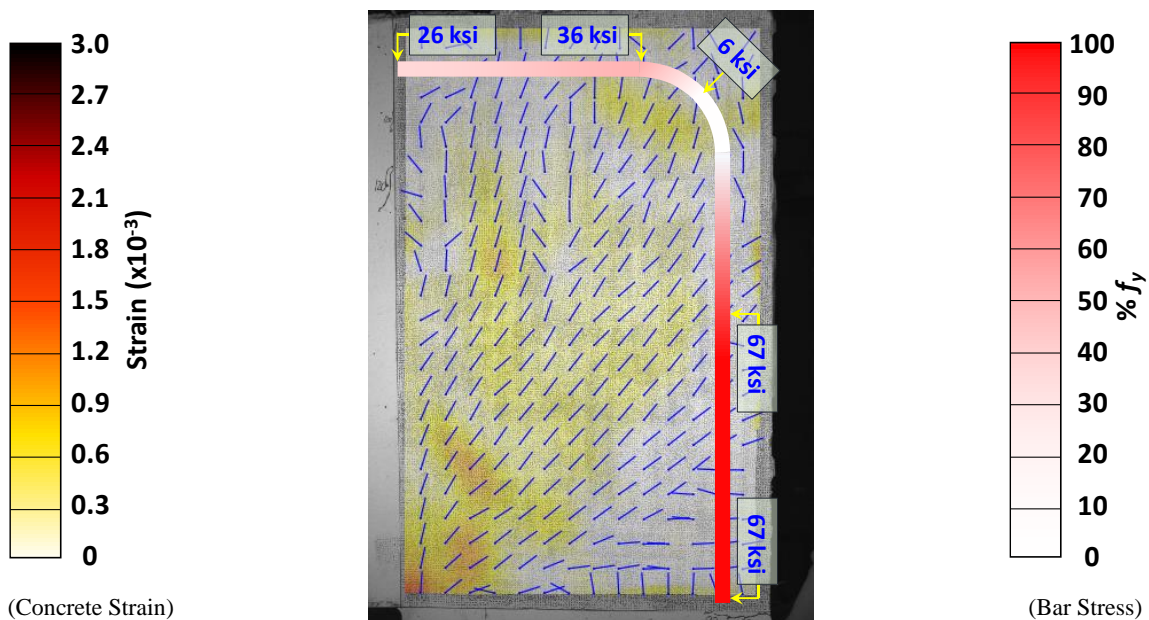


Figure 4-37 Bar stress distribution and concrete strain in the joint of Specimen B-R6-30

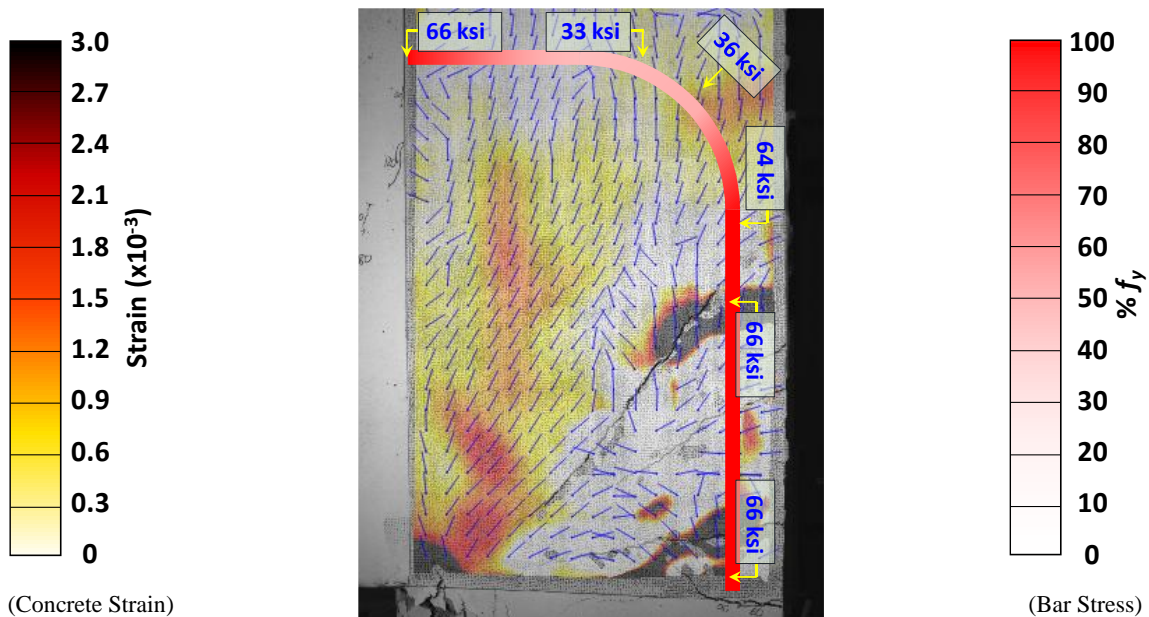


Figure 4-38 Bar stress distribution and concrete strain in the joint of Specimen B-R11-30

For Specimen B-R6-30, it can be seen from Figure 4-37 that a fan-shaped diagonal strut formed from the re-entrant corner between the bar bend and the middle of the bar on the right. This fan-shaped strut formed a larger bearing area for developing bar stresses at the joint face. The compressive stresses within the fan-shaped strut are equilibrated with the bond stresses between the bar bend and the middle of the bar. Stresses in the bar on the top side and the center of the bar bend were relatively low when the splitting of the joint concrete happened.

On the contrary, Specimen B-R11-30, as shown in Figure 4-38, had deeper yield penetration toward the bar bend, and the higher bar stresses were reached on the top side and the center of the bar bend. The diagonal strut reduced within the bar bend because bond stresses along the bars on the right side could not develop due to yield penetration.

4.3.3.4. Series C – Deeper beam-column member

The superpositioned strain maps and bar stress development of specimens in Series B are presented in Figure 4-39 and Figure 4-40. Similarly, labeling and presentation style are the same as introduced before. Similar to specimens in Series B, Specimen C-R6-60 formed a fan-shaped strut from the re-entrant corner towards not only the bar bend but between the bar bend and the middle of the straight portion. The principal compressive stresses in the fan-shaped strut were equilibrated with bond stresses between the top bars. Therefore, the bearing area provided for the diagonal strut could be larger than that within the bar bend, which is similar to other specimens with a bend radius of the standard bend.

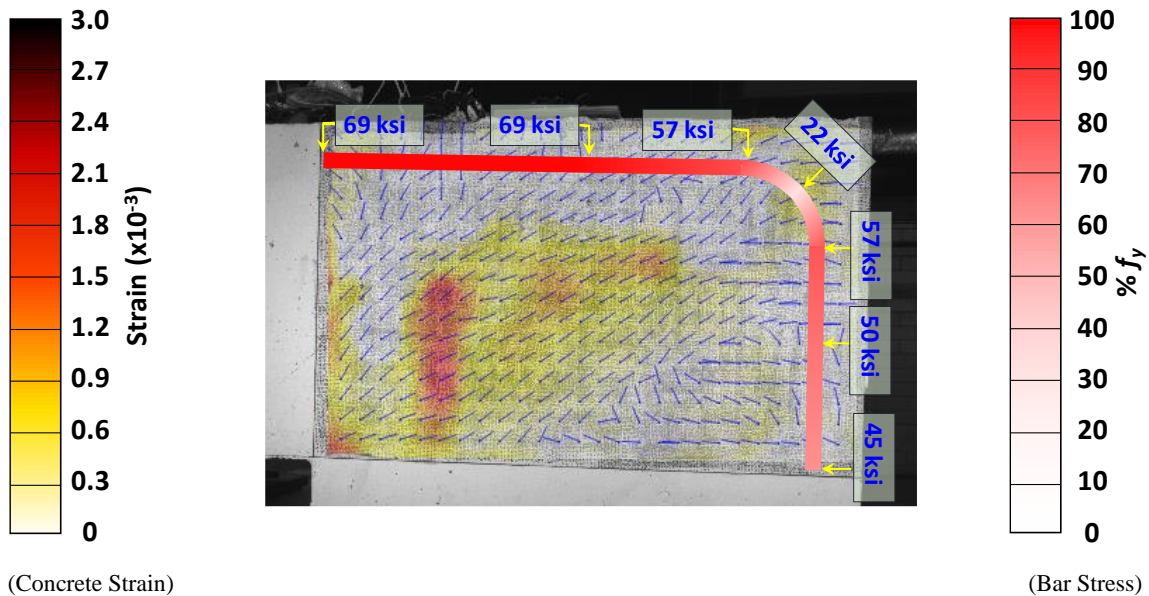


Figure 4-39 Bar stress distribution and concrete strain in the joint of Specimen C-R6-60

Specimen C-R11-60 developed higher stress along the bars on both sides and the center of the bar bend, as shown in Figure 4-40. Since the specimen had reinforcement with higher strength (97.2 ksi), bond stress still existed between the middle of the bar and the bar bend on the top side. Therefore, a fan-shaped strut formed similar to specimens with a small bend radius, as its bend radius was not sufficiently enlarged. Nevertheless, the bar stress profile in the figure showed that the bar bend was able to afford higher stress along its length.

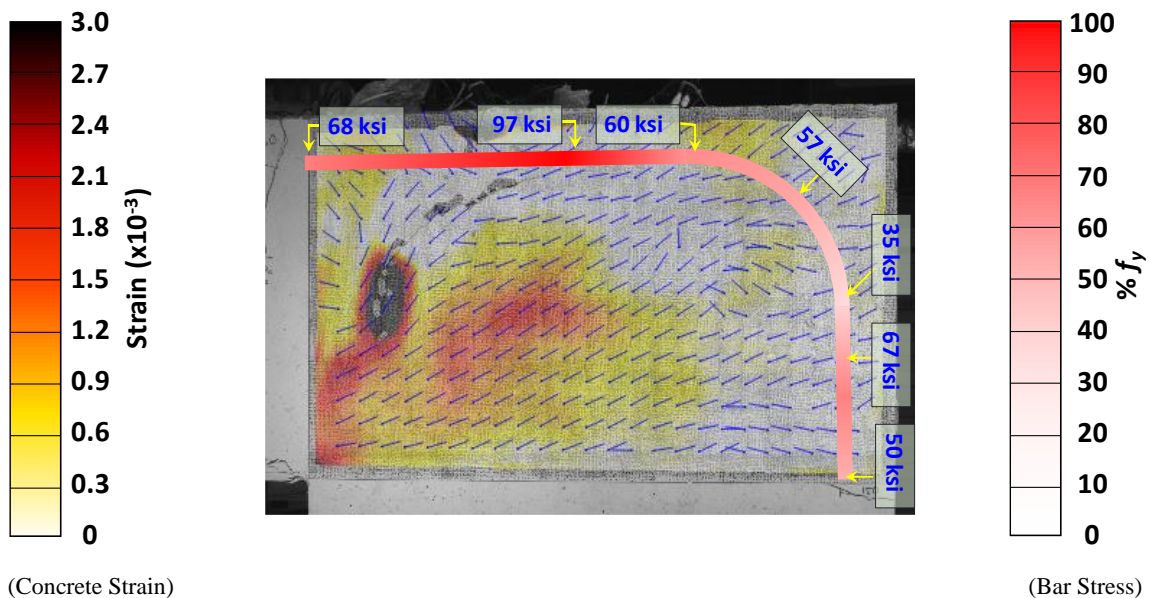


Figure 4-40 Bar stress distribution and concrete strain in the joint of Specimen C-R11-60

4.4. Evaluation of Strength and Failure Modes

4.4.1. Effect of Bend Radius and Diagonal Strut Angle

The effect of the bend radius and the diagonal strut angle on joint shear capacity was evaluated by plotting the peak normalized joint shear of specimens from Series A, Series B, and Series C together, as shown in Figure 4-41. It can be seen from the figure that enlarging the bend radius also led to an increase in strength. In particular, in Series A [Figure 4-41(a)], the normalized shear strength was increased by 5.63% when the bend radius was enlarged from the standard radius to 8.7 in. When a bend radius per Eq. (4-1) was used, the normalized V_{test} was increased from 0.142 to 0.170 (19.7%).

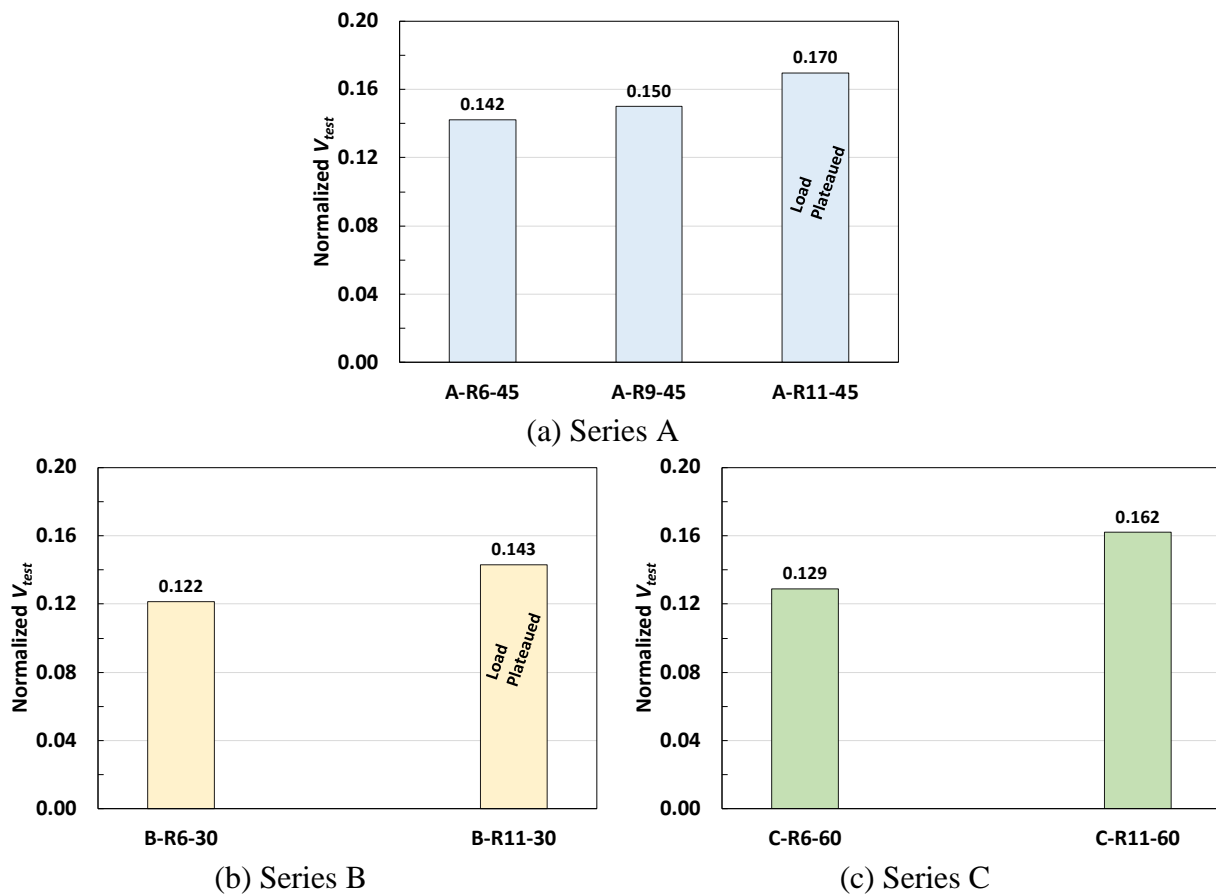


Figure 4-41 Effect of bend radius on normalized joint shear capacity

A similar trend was observed in Series B and Series C, where specimens had unequal joint dimensions. The normalized V_{test} was increased from 0.122 to 0.143 (17.2%) for Series B [Figure 4-41(b)] and from 0.129 to 0.162 (25.6%) for Series C [Figure 4-41(c)] after enlarging the bar bend from a bend radius of the standard bend to that per Eq. (4-1). It should be noted that Specimen B-R11-30 did not reach the ultimate failure; a higher normalized shear capacity would have been possible.

The bend radius at the outside of a joint critically affects the joint shear capacity. Using bend radii per Eq. (4-1) for closing knee joints is once again proven essential to maximize the joint efficiency to resist shear whether the joint dimensions are equal or not.

4.4.2. Effect of Diagonal Strut Angle

The effect of the diagonal strut angle was evaluated by comparing specimens with the same bend radius but with different diagonal strut angles (Specimen A-R6-45 vs. Specimen B-R6-30 vs. Specimen C-R6-60 and Specimen A-R11-45 vs. B-R11-30 vs. Specimen C-R11-60), as presented in Figure 4-42. When a bend radius of the standard bend was used, decreases of 9.1% and 14.1% in the normalized shear capacity were observed when altering the diagonal strut angle from 45 degrees to 60 degrees and 30 degrees, respectively. A slight difference in the normalized shear capacity existed between Specimens B-R6-30 and C-R6-60 (0.122 vs. 0.129). It can be inferred that a diagonal strut angle leads to the highest joint strength, and the capacity decreases at a similar rate if the diagonal strut angle increases or decreases.

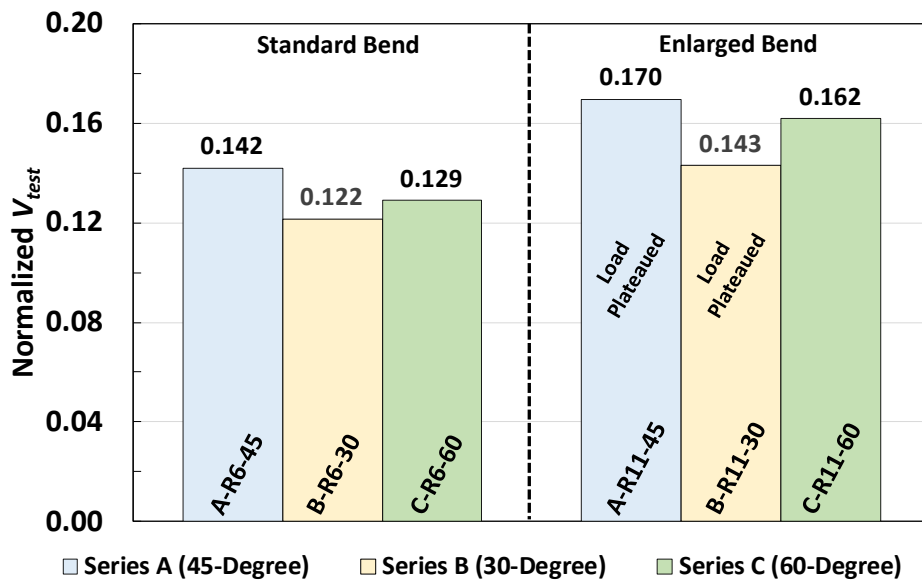


Figure 4-42 Effect of diagonal strut angle on normalized joint shear capacity

The decrease in strength due to the diagonal strut angle greater than 45 degrees diminished when enlarged bend radii per Eq. (4-1) were used. As can be seen in Figure 4-42, a decrease in strength of only 4.7% was observed when comparing Specimen A-R11-45 to Specimen C-R11-60. However, a decrease of 15.9% in strength was observed if the diagonal strut angle was decreased from 45 degrees to 30 degrees when comparing Specimen A-R11-45 to Specimen B-R11-30. Nevertheless, the result is not decisive because Specimen B-R11-30 did not reach the ultimate failure condition. It is revealed that the bend radius at the outside of a joint has significant effects on the normalized shear capacity and the diagonal strut angle.

4.4.3. Effect of Arrangement of Reinforcement

The effect of the arrangement of reinforcement passing through the outside of closing knee joints was evaluated by plotting the normalized V_{test} of specimens with the largest bend radius from Series A and Series D together, as shown in Figure 4-43. Among the three specimens, the specimen with a single layer of reinforcement had the highest normalized V_{test} (0.170), the specimen with a double layer of reinforcement was in second place (0.154), and the specimen with bundled bars had the lowest normalized V_{test} (0.136). As both Specimens A-R11-45 and D-R11-45(T) entered load plateauing and the difference in the normalized V_{test} was approximately 10%, two layers of reinforcement did not necessarily compromise the behavior.

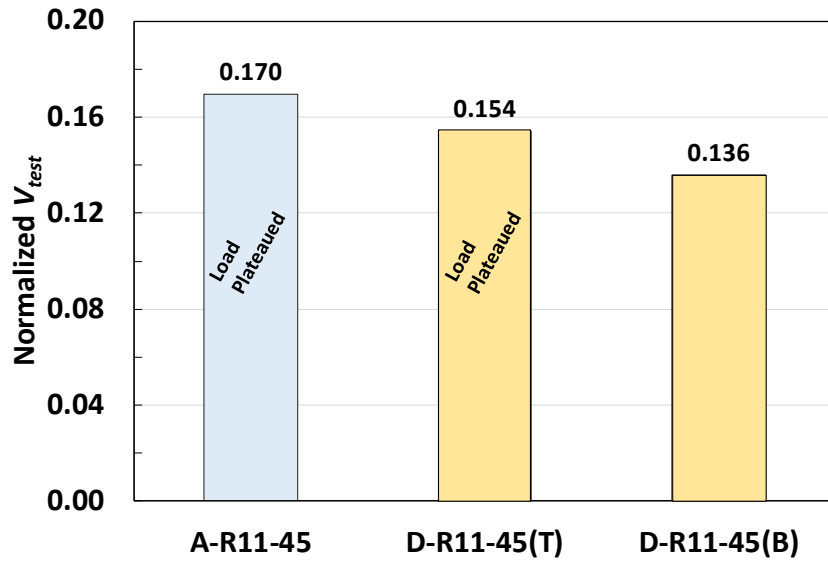


Figure 4-43 Effect of arrangement of reinforcement on joint shear capacity

However, the specimen with bundled bars [Specimen D-R11-45(B)] had a normalized V_{test} of 0.136, which is 20.0% lower than its counterpart in Series A and 11.7% lower than its counterpart in the same series. It is more evident that bundled bars in closing knee joints induce adverse effects on the strength, although an enlarged bend radius is used.

4.4.4. General Discussion on Strength and Failure Modes

The effect of the bend radius on the joint capacity and failure modes can be clearly seen in Figure 4-44. In the figure, the normalized V_{test} is plotted against a dimensionless bend radius parameter, defined as the ratio of the bend radius to the largest effective depth of the joint (r_b/d). Excluding Series D, the rate of increase in the normalized shear capacity along with the bend radius parameter for Series C was slightly higher than that for Series A, and that for Series B was the lowest. Nevertheless, as indicated previously, B-R11-30 would have had a higher load-carrying capacity, making the rate of increase in strength higher and similar to the other two series. Therefore, the effect of the bend radius on the strength can be considered the same for different diagonal strut

angles from 30 degrees to 60 degrees. Further, a diagonal strut angle of 45 degrees leads to generally higher joint shear strength.

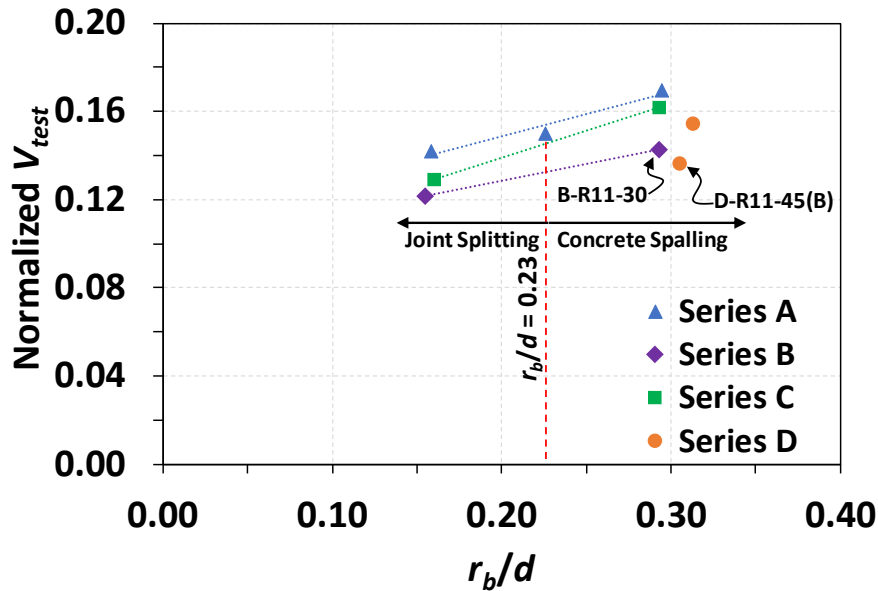


Figure 4-44 General evaluation of bend radius

For specimens in Series D, although having high values for the bend radius parameter, they did not reach the same level of the normalized shear capacity as their counterparts in Series A and C. Indeed, bundled reinforcement led to the lowest normalized shear capacity among specimens with similar values of the bend radius parameter.

In addition, based on the failure mode, specimens were categorized into two groups: failure due to joint splitting and due to concrete spalling. It can be seen from Figure 4-44 that when r_b/d was greater than 0.23, specimens tended to fail because of extensive concrete spalling. Otherwise, specimens failed in joint splitting. It should be noted that Specimen did not exhibit concrete spalling because the test was stopped earlier.

The bend radius and the diagonal strut angle should be accounted for when determining joint shear capacities. Also, the arrangement of the longitudinal reinforcement is important. However, current methods based on the sectional joint shear capacity in both AASTHO LRFD and ACI 318-19 do not consider the bend radius, which may lead to unconservative estimates of the shear strength of RC frame corners under closing moments. For instance, according to AASHTO LRFD, the nominal shear resistance V_n in the joint of a frame or bent is given by $0.380bd\lambda\sqrt{f'_c}$. Therefore, test specimens in this experimental program should have nominal shear resistances of over 650 kips, meaning that the longitudinal reinforcement could all yield. However, some of the specimens could not yield the longitudinal reinforcing bars to fully develop a load plateau.

4.5. Evaluation of Design Expression for Curved-bar Nodes

It is shown in the experimental results that the bend radius (otherwise the curved-bar node when using the STM) of longitudinal reinforcement in a closing knee joint plays an important role in affecting the behavior of closing knee joints. In this section, it is presented how the bend radius correlates to the capacity and the failure mode of closing knee joints.

4.5.1. Bend Radius Considering Radial Stresses

The experimental program revealed that the bend radius of the longitudinal reinforcement at the outside of a closing knee joint would determine if a failure happens in the joint before load plateauing does. When a larger bend radius is used, closing knee joints tend to yield tension reinforcement and exhibit significant flexural post-yield behavior in the beam-column member. On the contrary, if a small bend radius is used, closing knee joints tend to fail in the joint earlier than load plateauing and have lower overall capacity. In other words, premature failure should be expected for the assembly.

Based on the concept mentioned above, the level of premature failure was evaluated in this analysis by calculating the ratio of the test load (P_{test}) to the load that caused the ultimate sectional moment capacity in the beam-column member of the specimen (P_{calc}). As loading was applied 38.5 in. from the joint face, an axial load with an eccentricity of 59.5 in. needed to be considered when determining P_{calc} for specimens in Series A, C, and D. In contrast, specimens in Series B had shallower legs that controlled the overall flexural capacity. The flexural capacity of specimens in Series B was there determined at the leg-joint face without axial load. In this analysis, the sectional analysis software Response 2000 was used to assist in the determination of P_{calc} .

Another important purpose of the analysis was to correlate the size of the bar bend of the curved-bar node to the level of premature failure. As introduced in Section 2.3, bend radii should be sized per Eq. (2-1), which is shown here again for the reader's convenience:

$$r_b \geq \frac{2A_{ts}f_y}{b_s f'_c} \quad (4-4)$$

Therefore, the appropriateness of Eq. (2-1) could be evaluated by introducing the ratio of the actual bend radius (r_b) to the minimum required bend radius (r_{bb}), where r_{bb} is given by

$$r_{bb} = \frac{2A_{ts}f_y}{b_s f'_c} \quad (4-5)$$

The analytical results for specimens in Series A and D are summarized in Table 4-5. It should be noted that data from the first run of testing Specimen A-R11-45 was used. It should be noted that modification to the required bend radius since the thin cover effect was not considered here, as the factor turned out very close to 1.0 for the test specimens. It was also conservative not to consider the modification for analysis.

Table 4-5 Summary of analytical results for curved-bar nodes per Eq. (2-1)

Specimen ID	f'_c (ksi)	f_y (ksi)	A_{ts} (in. ²)	r_b (in.)	r_{bb} (in.)	P_{test} (kip)	P_{calc} (kip)	r_b/r_{bb}	P_{test}/P_{calc}	Remark
A-R6-45	5.3	67.5	9.36	6.1	11.35	543.3	571.7	0.54	0.95	
A-R11-45	5.4	68.6	9.36	11.4	11.32	625.5	575.3	1.00	1.09	Ductile
A-R9-45	4.6	93.2	9.36	8.7	18.06	497.5	715.4	0.48	0.70	
B-R6-30	5.8	66.9	9.36	6.0	10.30	302.3	324.1	0.58	0.93	
B-R11-30	5.6	65.6	9.36	11.3	10.45	344.0	318.0	1.08	1.08	Ductile
C-R6-60	4.8	69.3	9.36	6.2	12.88	277.0	315.0	0.48	0.88	
C-R11-60	4.7	69.4	9.36	11.3	18.64	337.0	407.6	0.61	0.83	
D-R11-45(T)	5.3	73.83	9.36	11.3	12.42	556.0	571.2	0.91	0.97	Ductile
D-R11-45(B)	4.8	75.77	9.36	11.3	14.07	452.4	591.8	0.80	0.76	

Figure 4-45 shows a plot that correlates the strength ratio (P_{test}/P_{calc}) to the bend radius ratio (r_b/r_{bb}). The shape and the color differentiate data points from each series. A dotted line in the figure represents the trend of the correlation. A horizontal dashed line in the figure separates specimens reaching the P_{calc} from those not reaching the P_{calc} . In addition, a vertical dashed line separates specimens exhibiting ductility from those failing in the joint before load plateauing.

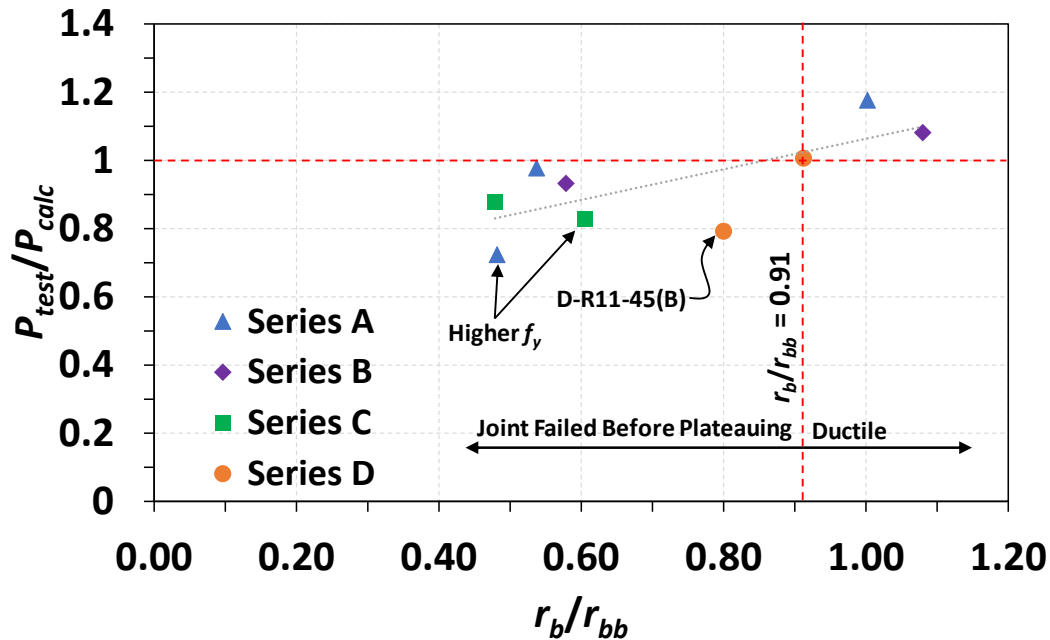


Figure 4-45 Correlation between strength ratio and bend radius ratio per Eq. (2-1)

It can be observed from Figure 4-45 that there is a seemingly linear positive correlation between the bend radius ratio and the strength ratio for all series. When the bend radius ratio exceeds 0.91, the strength ratio can be higher than 1.0, and a ductile behavior can be expected. Indeed, the trend

line indicates that a bend radius ratio of 0.858 may be sufficient. The result supports that the design expression per Eq. (4-4) is appropriate and conservative to avoid compromised strength and brittle failure.

The data point of the specimen with bundled bars [Specimen D-R11-45(B)] significantly falls below the trend line, as seen in the figure. It is indicated that an even larger bend radius ratio would be needed to obtain a similar performance to closing knee joints with a single layer of reinforcement or double layer of reinforcement, given the same material and sectional properties. On the trend line, a bend radius ratio of 0.8 corresponds to a strength ratio of 0.974. However, Specimen D-R11-45(B), which had a bend radius ratio of 0.8, delivers a strength ratio of 0.76. It is possible that a modification factor of $0.97/0.76=1.28$ is needed to enlarge the required bend radius ratio per Eq. (4-4) for bundled bars.

In addition, the two specimens with higher f_y (Specimens A-R9-45 and C-R11-R60) slightly fall below the trend line. Cautiousness may be needed when applying Eq. (4-4) for frame corners with Grade 80 reinforcement or higher.

4.5.2. Bend Radius Considering Circumferential Bond Stresses

Similar to the evaluation of the appropriateness of Eq. (2-1) introduced above, Eq. (2-3), which accounts for circumferential bond stresses along the bar bend, was evaluated using test results of specimens in Series B and C, which were expected to develop bar stresses within the bar bend regions. In the evaluation, the required bend radius was calculated per Eq. (2-3), and the bend radius ratio was derived for each of the specimens. Calculated strengths and strength ratios were also used. It should be noted that modification to the required bend radius since the thin cover effect was not considered here as the factor turned out very close to 1.0 for the test specimens. It was also conservative not to consider the modification for analysis. The analytical results are summarized in Table 4-6.

Table 4-6 Summary of analytical results for curved-bar nodes per Eq. (2-3)

Specimen ID	f'_c (ksi)	f_y (ksi)	A_{ts} (in. ²)	r_b (in.)	r_{bb} (in.)	P_{test} (kip)	P_{calc} (kip)	r_b/r_{bb}	P_{test}/P_{calc}	Remark
B-R6-30	5.8	66.9	9.36	5.8	23.89	302.3	324.1	0.25	0.93	
B-R11-30	5.6	65.6	9.36	5.6	23.83	344.0	318.0	0.47	1.08	Ductile
C-R6-60	4.8	69.3	9.36	4.8	26.43	277.0	315.0	0.23	0.88	
C-R11-60	4.7	69.4	9.36	4.7	63.99	337.0	407.6	0.18	0.83	

Figure 4-46 shows a plot that correlates the strength ratio (P_{test}/P_{calc}) to the bend radius ratio (r_b/r_{bb}) per Eq. (2-3). The shape and the color differentiate data points from each series. A dotted line in the figure represents the trend of the correlation. A horizontal dashed line in the figure separates specimens reaching the P_{calc} from those not reaching the P_{calc} . In addition, a vertical dashed line separates specimens exhibiting ductility from those failing in the joint before load plateauing.

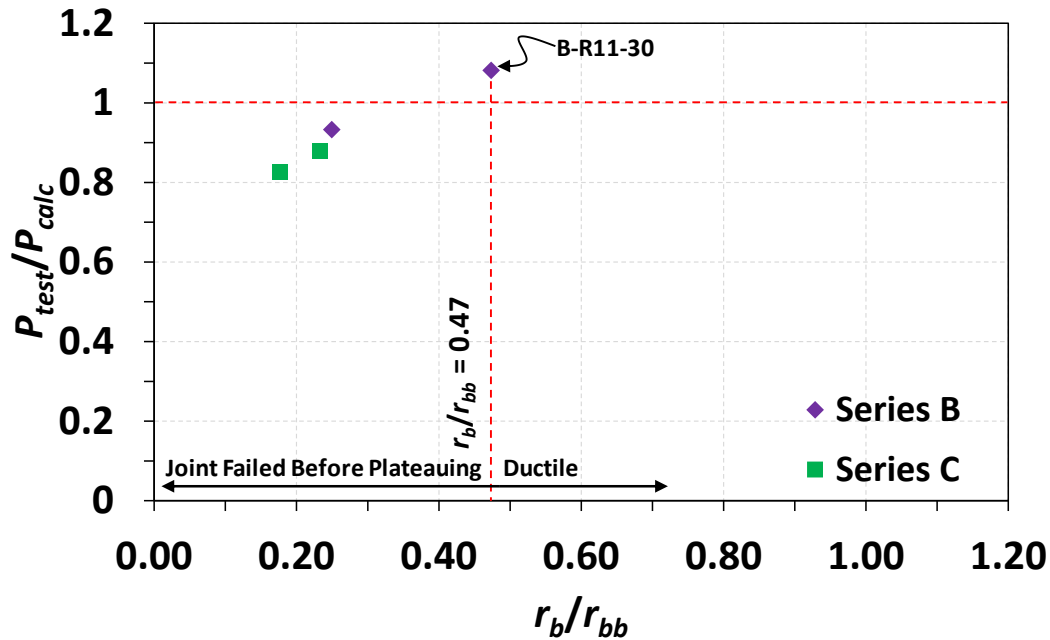


Figure 4-46 Correlation between strength ratio and bend radius ratio per Eq. (2-3)

Datapoints in Figure 4-46 reveal that a bend radius ratio of 0.47, or lower, per Eq. (2-3) is needed to develop uncompromised behavior for closing knee joints, indicating that Eq. (2-3) appears to be overly conservative and unnecessary. Eq. (2-1) is more appropriate than Eq. (2-3).

4.6. Assessment of Serviceability

The serviceability of the closing joint specimens was evaluated using measured maximum crack width at each load increment plotted against the ratio of the load to the calculated capacity in terms of percentage, as presented in Figure 4-47. The calculated capacity used in this assessment was based on the sectional analysis of the beam-column member or the leg-joint face by the software Response 2000 with measured material properties, as the same as the evaluation of curved-bar node design expressions. The concept behind using the calculated flexural capacity without consideration of the joint shear capacity was to give designers an idea about the disadvantages of using small bend radii without knowing compromised joint shear capacity.

For the assessment of serviceability in Figure 4-47, the service level load was assumed to be 33% times the calculated flexural capacity, resembling Project 0-5253. It was considered that the ratio of the resistance factor (ϕ) to the load factor (η) can be used to estimate the ratio of the service load to the nominal capacity. For closing knee joints, the diagonal strut, considered a compression element is the STM, has a ϕ -factor of 0.7, and the η -factor was assumed to be 1.4. In addition, it was assumed that the nominal capacity is approximately 2/3 of the experimental load. Consequently, the ratio of the service level to the experimental load is $(2/3)(0.7/1.4)=33\%$. Moreover, it was observed that the calculated flexural capacity of the beam-column member can

be an acceptable representation of “the full potential” of the experimental load for each specimen’s closing knee joint. The service load is represented by a horizontal line in the figure. In addition, the acceptable crack width limit was taken as 0.017 in. according to AASHTO LRFD 2020, which is represented by a vertical line in the figure. The vertical line and the horizontal line form a region labeled as unsatisfactory serviceability. Falling into the region indicates that the crack widths were larger than 0.017 in. before reaching service load level. Therefore, the service load level and the crack width limit defined a region, informing unsatisfactory serviceability.

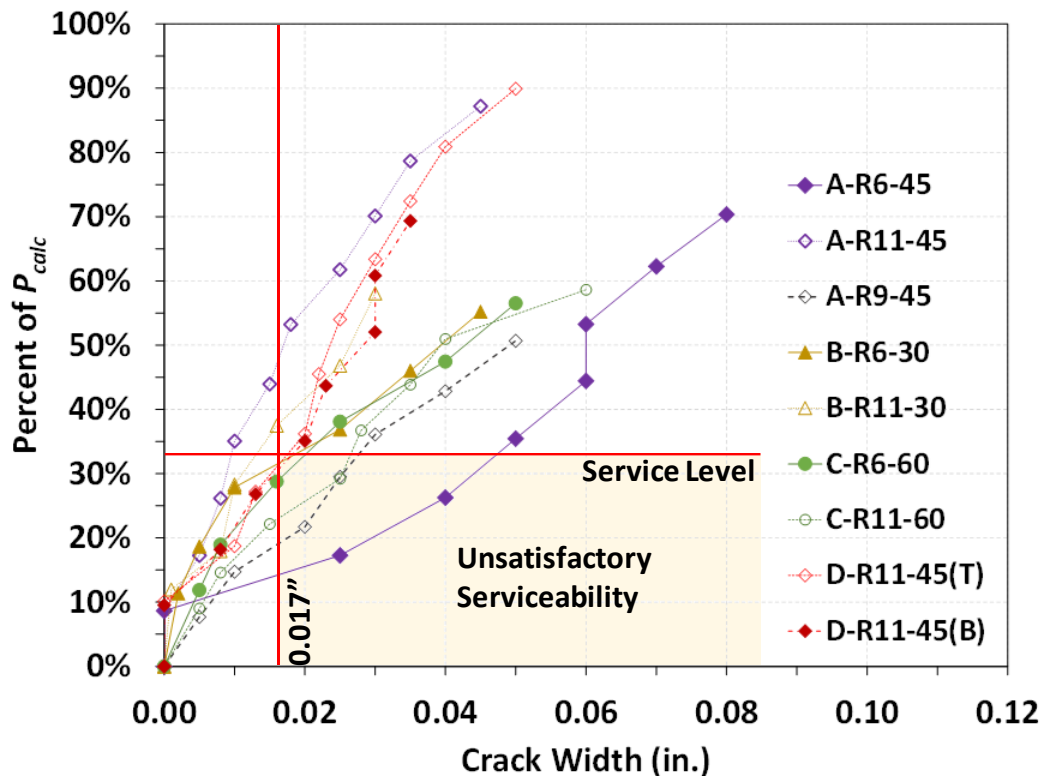


Figure 4-47 Assessment of serviceability of test specimens

It can be seen from Figure 4-47 that seven specimens in total have a portion of the load-crack width curve falling into the shaded region. All the seven specimens had a bend radius smaller than required by Eq. (2-1). It is evident that using enlarged bend radii per Eq. (2-1) also ensures closing knee joints to achieve desired serviceability even without joint reinforcement.

Among the seven specimens with unsatisfactory serviceability, the two specimens from Series D with bend radius ratios of 0.91 and 0.8 did not exhibit severe “softening” after passing the service load level. The crack width curves still followed a similar growing trend as those specimens bend radii per Eq. (2-1). On the other hand, the other five specimens, which had a bend radius ratio of less than 0.61, “softened” even before reaching the service load level. The observation once again emphasizes the importance of using larger bend radii.

4.7. Structural Capacity using the STM

This section presents detailed procedures for using the STM on the test specimens in the experimental program. The content includes the selection of strut-and-tie models based on specimen configurations and force transmission, the method of sizing nodal zones, the determination of ultimate capacity, and the evaluation of various sets of efficiency factors. The method presented in this section is intended to determine their permissible strengths under the STM's framework. The logic is different from the design, in which the amount of main longitudinal reinforcement is to be proportioned. Design recommendations of using the STM on frame corner are presented in Section 4.9.

4.7.1. Dimensions of Specimen of Interest

Portal frame specimens in the experimental program were generally modeled using the STM, as shown in Figure 4-49. To not lose generality, the structural configuration of the specimen of interest and dimensions of the strut-and-tie model are presented with variables. To facilitate readability, the terminology is defined as shown in in Figure 4-48. Specifically, the specimen consists of two identical legs and a beam-column member. Each of the legs is connected to the beam-column member with a joint. The load and the reaction are applied to the leg members.

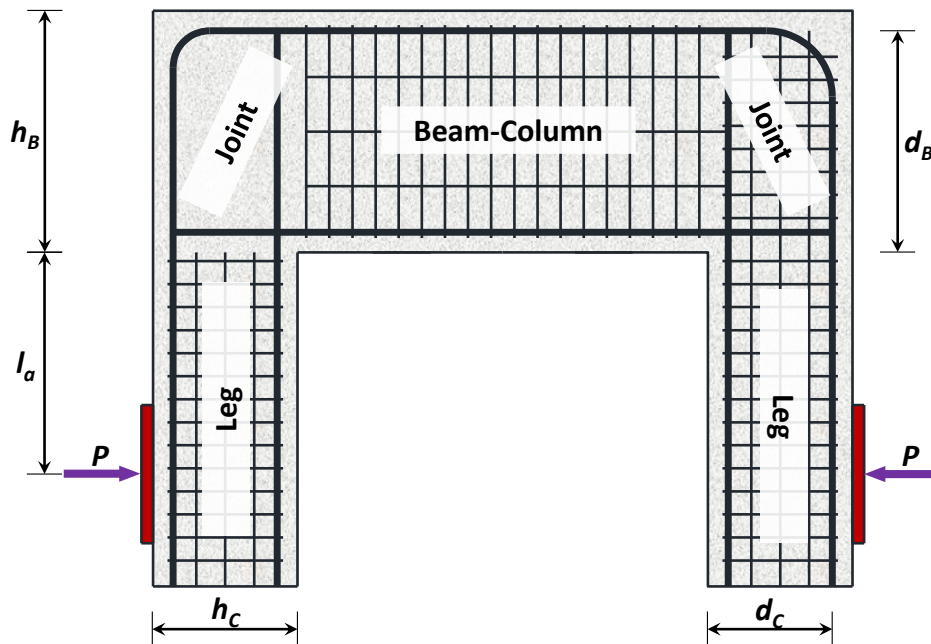


Figure 4-48 Configuration and terminology of portal specimens

Each leg has a height of h_c , and the beam-column member has a height of h_B . Rather than the total heights, the effective depths of the members deliver more information for analysis. Here, the effective depth is taken as the distance between the outmost concrete fiber of the member to the centroid of the longitudinal reinforcing bars. Accordingly, each leg has an effective depth of d_c

and the beam-column member, d_B . The load and the reaction, having the same magnitude P , are applied at the same level which is l_a away from the joint face. It should be noted that not all marked dimensions were used in the later analysis using the STM.

4.7.2. Selection of Strut-and-tie Models

With a defined specimen of interest, a permissible strut-and-tie model can be constructed according to the structural configuration. Firstly, ties can be placed by determining the tension sides by observation. In this case, a tie is placed in alignment with the centroid of tension longitudinal reinforcement of each member. As seen in Figure 4-49, in the left leg, a tie (Tie AB) is placed starting from the load point (Node A) to the intersection with the beam-column member's effective depth (Node B). On the top of the beam-column member, another tie starts from Point B to the symmetric point (Node B'), and the same arrangement is in the other leg. To maintain the equilibrium of Points B, a diagonal strut (Strut BC) is placed, connecting Node B to a point near the re-entrant corner (Node C). Symmetrically, Strut (B'C') is placed in the other joint. At Node C, two more struts are framed for equilibrium; one strut goes to the load point, and the other goes to Node C'. Hence, a basic permissible strut-and-tie model is constructed. The strut-and-tie model appropriately reflects the stress flow under the load condition, as confirmed by the DIC strain map in Section 4.3.3 and the FEA introduced later in Section 4.8.2.

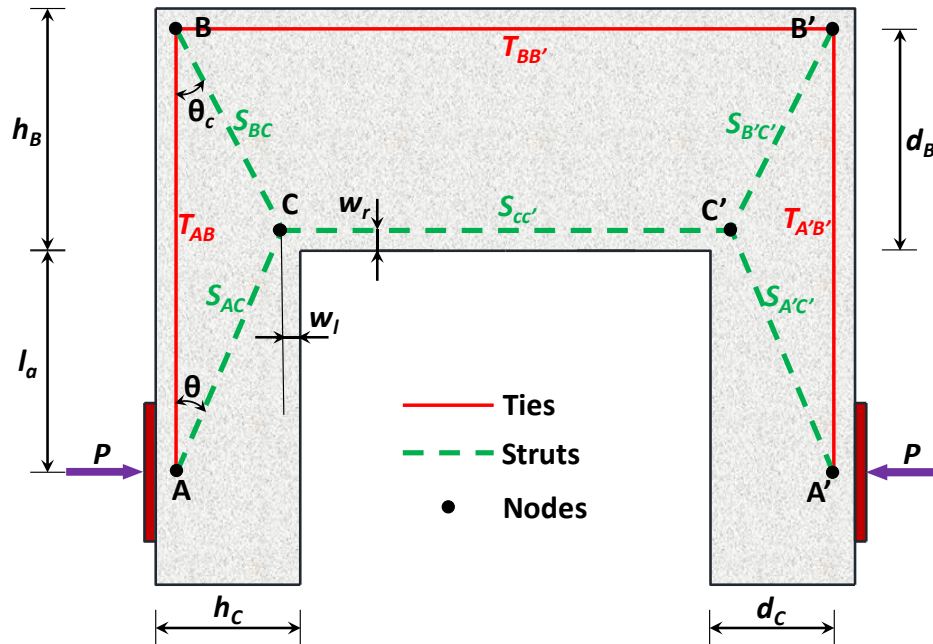


Figure 4-49 General strut-and-tie model for portal frames

In the strut-and-tie model, the exact positions of Nodes C and C' remain undetermined and assumed here to be at w_r and w_l away from the re-entrant corner, as shown in Figure 4-49. Typically, the height of the strut at the compression side of a deep member can be determined using the equivalent stress block or simply one-tenth the member height. However, the beam-

column member, in this case, is subjected to both axial and flexural loads, making the determination of the strut height, otherwise the value of w_r , iterative when using the equivalent stress block. In addition, simply using $0.1h_B$ may not guarantee an optimized result because it may underestimate the permissible force in Strut CC', causing Tie BB' to not reach its yield strength. On the other hand, the value of w_l cannot be determined using the equivalent stress block because the leg is not a flexural member. Therefore, an optimization approach with some simplification is used to determine the positions of Nodes C and C' in the later analysis. It should be noted the approach is not necessarily required in design, which is introduced in Section 4.7.5.

4.7.3. Determination of Forces

Completing the truss arrangement as a statically determinant structure, it is possible to determine the force of each member through statics. The result is summarized in Table 4-7.

Table 4-7 Member forces of the strut-and-tie model

Struts				
S_{AC}	S_{BC}	$S_{CC'}$	$S_{B'C'}$	$S_{A'C'}$
$P \csc \theta$	$P \cot \theta \sec \theta_c$	$P(1 + \cot \theta \tan \theta_c)$	$P \cot \theta \sec \theta_c$	$P \csc \theta$
Ties				
T_{AB}	$T_{BB'}$		$T_{A'B'}$	
$P \cot \theta$	$P \cot \theta \tan \theta_c$		$P \cot \theta$	

In the table, the angles θ and θ_c are correlated with the position of Node C, given by

$$\theta = \tan^{-1} \frac{d_c - w_l}{d_b - w_r} \quad (4-6)$$

$$\theta_c = \tan^{-1} \frac{d_c - w_l}{l_a + w_r} \quad (4-7)$$

4.7.4. Sizing Nodal Zones

Sizing the CCC node near the re-entrant corner is essential to determine the analytical capacity of the specimens. This section presents a general approach to sizing the CCC node, and a simplified method is also included.

4.7.4.1. General Non-hydrostatic CCC Node

The general method requires starting with an assumed position of the CCC node near the re-entrant corner, or Node C. That is, the variables w_l and w_r determine the dimensions of the CCC node. Per the STM principles, the boundary of struts is limited by the edges of the member. Also, the

boundary is perpendicular to the orientation of the strut centerline and has a width twice the distance from the edge to the centerline. With the two principles, the shape of the CCC node and of the three struts near the node can be determined, as shown in Figure 4-50. For Strut $S_{CC'}$, the bottom of the beam-column member is its lower boundary; a line that is offset twice the value of w_r is its top boundary. For Strut S_{AC} , a line with an angle θ from the concrete edge starting from the re-entrant corner becomes its lower boundary; another line that is offset a value twice the distance w_c in the figure. For Strut S_{BC} , the intersection of the extension of the vertical concrete edge and the top boundary of S_{AC} becomes the end point of its top boundary, which has an angle of θ_c from the vertical; the lower boundary is then defined by offsetting the top boundary with twice the distance w_s . Finally, the intersection of the lower boundary of Strut S_{BC} and the top boundary of Strut S_{AC} defines the last vertex of the CCC node.

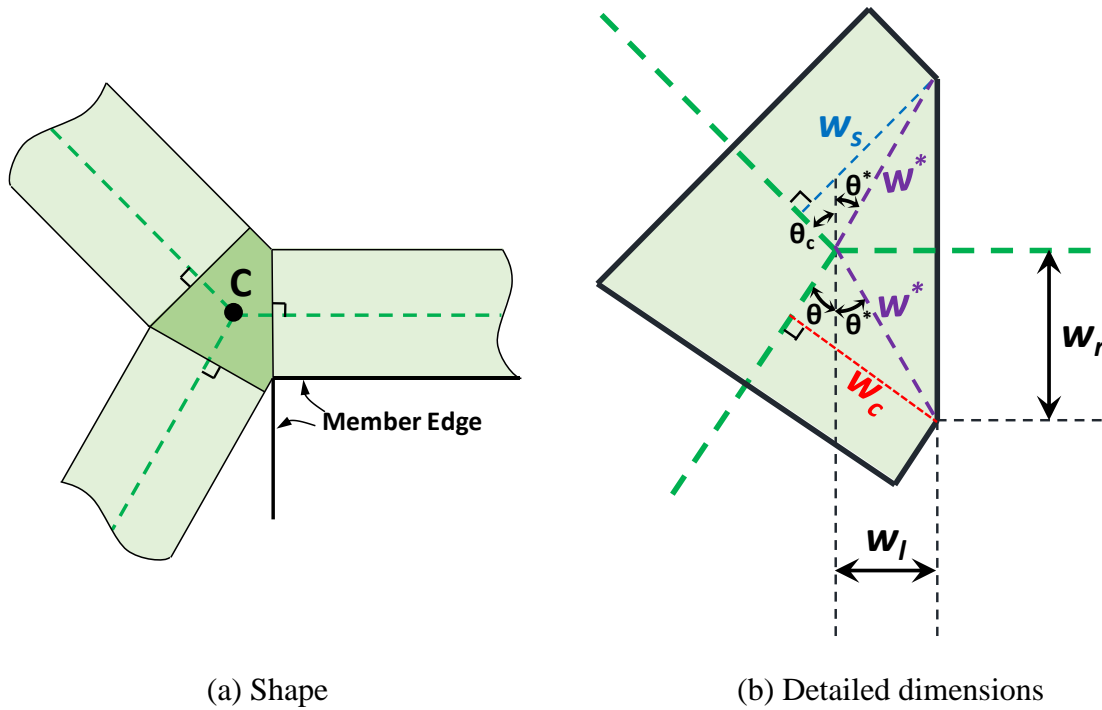


Figure 4-50 Sizing Node C near the re-entrant corner

With the defined shape of the CCC node, the widths of the three strut-to-node interfaces can be determined by geometry. As shown in Figure 4-50(b), two intermediate variables, w^* and θ^* , should be first determined by

$$w^* = \sqrt{w_l^2 + w_r^2} \quad (4-8)$$

$$\theta^* = \tan^{-1} \frac{w_l}{w_r} \quad (4-9)$$

where w^* is the distance between the CCC node and the re-entrant corner and θ^* is the angle between the line and the vertical. The two intermediate variables then can be used to determine the values of w_c and w_s , by trigonometric relationships, given by

$$w_c = w^* \sin(\theta^* + \theta) \quad (4-10)$$

$$w_s = w^* \sin(\theta^* + \theta_c) \quad (4-11)$$

Therefore, the widths of the three strut-to-node interfaces are $2w_r$, $2w_c$, and $2w_s$ for Struts S_{CC} , S_{AC} , and S_{BC} , respectively.

4.7.4.2. Simplified Non-hydrostatic CCC Node

The general method requires that the values of both w_r and w_l be specified first, and then the other dimensions of the CCC node can be derived. In this case, there are two degrees of freedom, which may lead to tedious iteration procedures in order to search for permissible nodal sizes. A simplified approach is presented here to reduce the degree of freedom for designers' convenience. Intuitively, the simplest way of assigning Strut S_{BC} is to align it with a line that connects the intersection of the two ties to the re-entrant corner. That is, Node C can only be on the line, and therefore the value of w_l relates to w_r by

$$w_l = w_r \frac{d_c}{d_b} \quad (4-12)$$

In this way, the values of θ_c and θ are the same. With the simplification, only w_r should be first specified to accomplish the rest derivation and analysis. It can be more intuitive for designers as well.

4.7.5. Determination of Analytical Ultimate Capacity

It is understood that the ultimate analytical capacity of a permissible strut-and-tie model is governed by critical elements. In the developed strut-and-tie model shown in Figure 4-49, the critical elements can be the CCC node near the re-entrant corner (Node C), the CTT curved-bar node (Node B), Tie $T_{BB'}$ and Tie T_{AB} . The load point (Node A) is not considered, given that the load-bearing area is sufficient.

As the size of Node C is undetermined and can be optimized by adjusting the variables w_l and w_r to accommodate the force demands (Tjhin and Kuchma 2002, Williams et al. 2012, and Wang 2020), the critical elements that govern the ultimate capacity include Node B and the two ties framing into Node B. In other words, the magnitude of the force in Strut S_{BC} is controlled by the critical elements.

As discussed in Sections 2.3 and 4.5, the capacity of curved bar nodes relates to the concrete within the bar bend with a bearing area of $\sqrt{2}r_b b$. Therefore, the capacity of curved-bar nodes $F_{n,cb}$ can be expressed as

$$F_{n,cb} = v_{cb} f'_c \sqrt{2} r_b b \quad (4-13)$$

where v_{cb} is the efficiency factor of curved-bar nodes. It should be noted that Equation (4-13) was developed based on the value of θ_c being 45 degrees and the neglect of circumferential bond stresses. Nevertheless, Wang (2020) implies that the equation can also be applied to determine proper bend radii even though the angle of the diagonal strut differs from 45 degrees. Also, the strength of curved-bar nodes calculated using Equation (4-13) needs to be modified by a factor of $c_c/2d_b$, where c_c is the thickness of the clear side cover, and d_b is the diameter of the reinforcing bars if the actual c_c is less than $2d_b$.

In addition, Tie $T_{BB'}$ and Tie T_{AB} should also be considered when determining the maximum potential force in Strut S_{BC} . The permissible force in a tie (F_{tie}) can be calculated by multiplying the area of the area of reinforcement for the tie by the yield strength of the reinforcement given by

$$F_{tie} = A_{ts} f_y \quad (4-14)$$

Equation (4-14) provides the upper limit to the two components of the force in Strut S_{BC} along the direction of the two ties. Hence, the maximum force that is allowed in Strut S_{BC} is given by

$$F_{max,BC} = \min \left\{ F_{n,cb}, \frac{F_{tie,BB'}}{\sin \theta_c}, \frac{F_{tie,AB}}{\cos \theta_c} \right\} \quad (4-15)$$

With determined $F_{max,BC}$, the ultimate load P_{max} can be back-calculated by equating the force S_{BC} to the value of $F_{max,BC}$. Solve for P_{max} and it is obtained that

$$P_{max} = \frac{F_{max,BC}}{\cot \theta \sec \theta_c} \quad (4-16)$$

As P_{max} is a function of θ and θ_c and therefore is a function of w_r and w_l , the value of P_{max} can be determined by substituting the values of w_r and w_l . In addition, P_{max} can be optimized by finding the derivative with regard to variables of w_r and w_l . However, the values of w_r and w_l should be able to make the CCC node sufficiently large to resist forces of S_{BC} , $S_{CC'}$, and S_{AC} . Therefore, the selection of w_r and w_l is subjected to the following equations:

$$2w_r b_s v_{CCC} f'_c \geq S_{cc'} = P_{max} (1 + \cot \theta \tan \theta_c) \quad (4-17)$$

$$2w_c b_s v_{CCC} f'_c \geq S_{AC} = P_{max} \csc \theta \quad (4-18)$$

$$2w_s b_s v_{CCC} f'_c \geq S_{BC} = P_{max} \cot \theta \sec \theta_c \quad (4-19)$$

where v_{CCC} is the efficiency factor of CCC nodes. It should be noted that when using Equation (4-17), the contribution of compression longitudinal reinforcement may be considered if the width in compression ($2w_r$) covers compression longitudinal reinforcement, which can be expressed as

$$2w_cb_sv_{CCC}f'_c + A'_sf_y \geq S_{AC} = P_{max} \csc \theta \quad (4-20)$$

The entire process is iterative, and computer coding or software can assist with determining the optimized w_r and w_l and the corresponding P_{max} . If the simplified non-hydrostatic CCC node is to be used, the procedures are summarized in Figure 4-51:

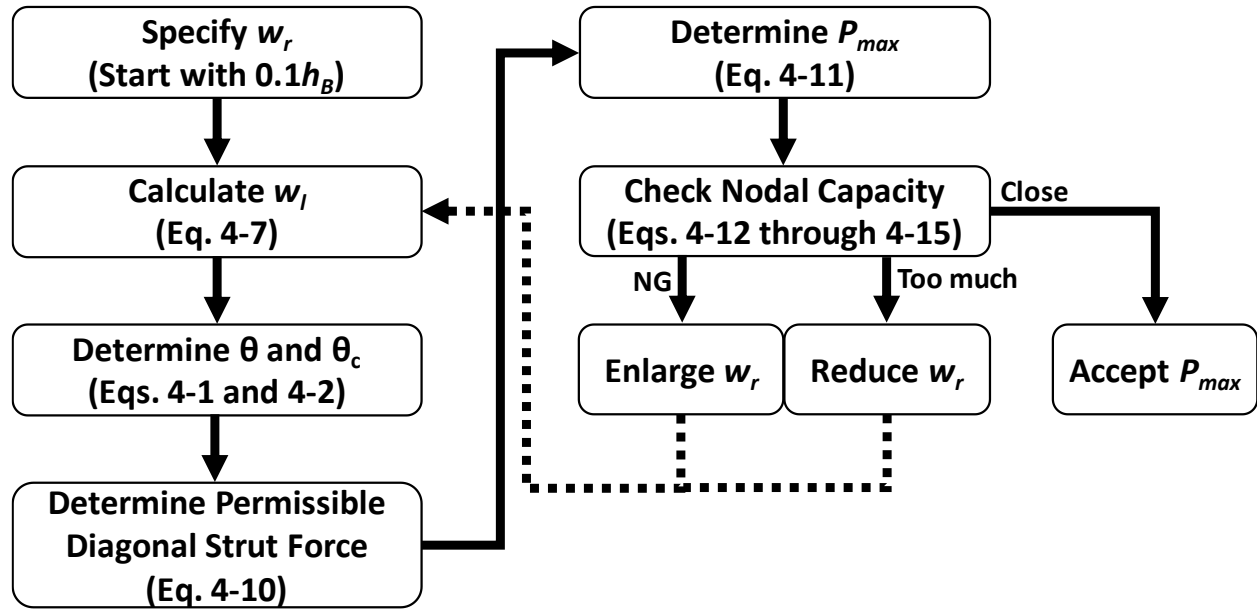


Figure 4-51 Procedures of determining of ultimate analytical capacity

4.7.6. Selection of Efficiency Factors

The efficiency factors of curved-bar nodes and CCC nodes appear in the process of determining the ultimate capacity P_{max} . In this analysis, two sets of efficiency factors are used to evaluate conservatism according to AASHTO LRFD and ACI 318-19. It should be noted that AASHTO LRFD does not include the efficiency factor of curved-bar nodes; the factor was specified as 0.5 because Eq. (4-7) was proved to be appropriate, as explained in Section 4.5. Regarding the set of efficiency factors per ACI 318-19, a coefficient of 0.85 was included because ACI 318-19 separates 0.85 from the efficiency factors in the equations. Used efficiency factors are summarized in Table 4-8. It should be noted that values in the table are based on the condition that sufficient crack control reinforcement is provided, although no reinforcement was provided in the joint of the specimens. Nevertheless, the strength of the unreinforced diagonal strut was not as low as the minimum efficiency factor needed for the analysis, as discussed in Section 4.5.

Table 4-8 Efficiency factors used for the STM analysis

		AASHTO LRFD	ACI 318-19
v_{cb}		0.5	0.6×0.85
v_{CCC}	Back face	0.85	0.75×0.85
	Interface	$0.45 \leq 0.85 - \frac{f'_c}{20} \leq 0.65$	

4.7.7. Results and Discussion

This section presents the analytical results of using the STM on the test specimens based on two assumptions for sizing the CCC node and the efficiency factors introduced above.

4.7.7.1. General Sizing Method for CCC Node

The analytical results based on the general sizing method are summarized in Table 4-9. P_{test} in the table is the peak load-carrying capacity; P_{STM} is the calculated strength using the STM. The test failure mode and predicted failure mode are also noted in the table. Test failure mode “C” means that splitting or spalling of concrete in the joint happened before load plateauing, which is attributed to insufficiently sized curved-bar node. Test failure mode “F” means that load plateauing and great ductility were observed before the ultimate failure condition, defined as flexural failure. For predicted failure modes, if the yielding of the main tie governed P_{STM} [Eq. (4-14) governed], it is denoted as “F”; otherwise Eq. (4-13) governed P_{STM} and it is denoted as “C” in the table. The strength ratio, defined as P_{test}/P_{STM} , was also presented in the table.

Table 4-9 Summary of analytical results using the general sizing method

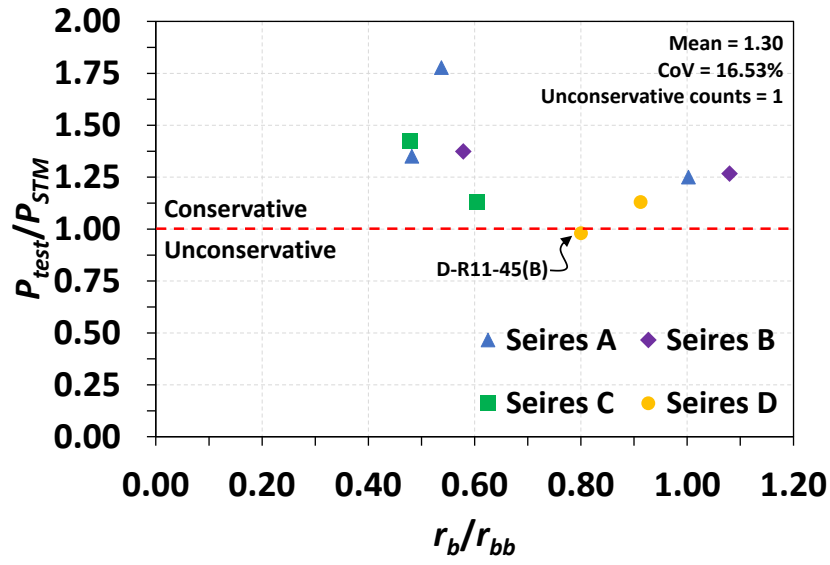
Specimen ID	P_{test} (kip)	Test Failure Mode*	AASHTO			ACI		
			P_{STM} (kip)	P_{test}/P_{STM}	Failure mode*	P_{STM} (kip)	P_{test}/P_{STM}	Failure mode*
A-R6-45	543	C	306	1.78	C	308	1.77	C
A-R11-45	626	F	500	1.25	F	511	1.22	F
A-R9-45	498	C	368	1.35	C	369	1.35	C
B-R6-30	302	C	220	1.37	C	225	1.34	C
B-R11-30	344	F	272	1.27	F	280	1.23	F
C-R6-60	277	C	194	1.42	C	196	1.42	C
C-R11-60	337	C	298	1.13	C	301	1.12	C
D-R11-45(T)	556	F	492	1.13	C	497	1.12	C
D-R11-45(B)	452	C	462	0.98	C	464	0.97	C

* C stands for failure at the curved-bar node;

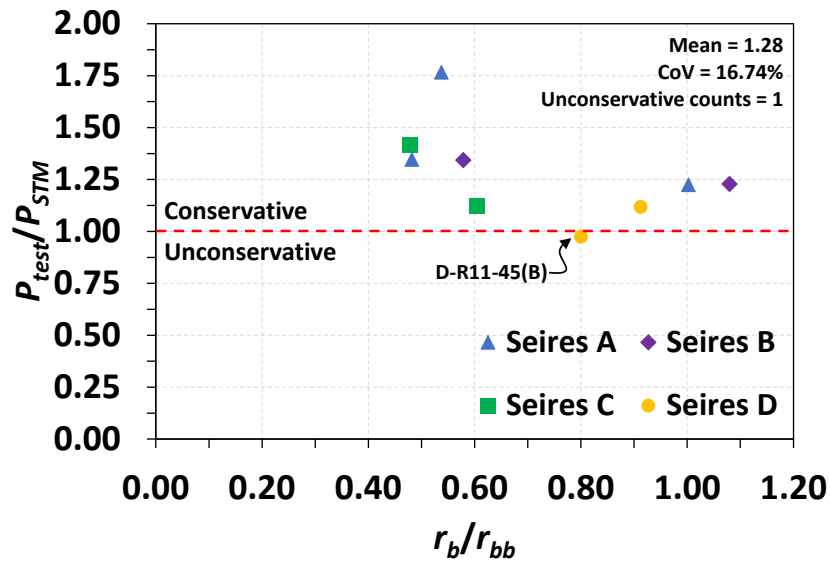
F stands for flexural failure happening first

It can be seen from Table 4-9 that the predictions of failure modes were in agreement with the test failure modes for all cases but Specimen D-R11-45(T), which had two layers of reinforcement. The observation reveals that the nodal coefficient for curved-bar nodes (0.5) accurately is appropriate for various conditions, including various diagonal strut angles and multiple layers of reinforcement. Regarding the exception, Specimen D-R11-45(T), it had a bend radius slightly smaller than that required by Eq. (4-1) and was predicted to fail at the curved-bar node. However, the curved-bar node exhibited higher strength, making it ductile and failing in flexure. This means that the nodal coefficient and the sizing method are conservative when determining failure modes.

The accuracy and conservatism of the STM with the general sizing method were further evaluated by plotting the strength ratio against the bend radius ratio of the specimens, as shown in Figure 4-52. It was considered conservative if the strength ratio was higher than 1.0. In Figure 4-52(a), the data points are based on AASTHO LRFD. The overall strength ratios have a mean of 1.3, with only one unconservative count. The result is once again considered accurate and conservative. The unconservative case is Specimen D-R11-45(B), which had bundled reinforcement. As explained before, bundled reinforcement possibly tends to exert more concentrated stress on the concrete cover, so the usable strength of the curved-bar node may need to be reduced. Nevertheless, the strength ratio for Specimen D-R11-45(B) is 0.98, which is very close to 1.0. Because the STM itself is inherently conservative, the unconservatism of predicting the strength of Specimen D-R11-45(B) is balanced.



(a) AASHTO LRFD-based efficiency factor



(b) ACI-based efficiency factor

Figure 4-52 Evaluation of the STM with general sizing method regarding bend radius ratio

The coefficient of variation is 16.53%, and scattered data points happen when the bend radius ratio is smaller than 0.6. Also, overly conservative cases concentrate in this region. It can be attributed to the fact that the bearing area under a curved-bar node can be larger than the square root of two times the bend radius, making a higher strength than Eq. (4-13). This idea is supported by the DIC strain map and bar stress development along the main tie introduced in Section 4.3.3. A Part of the straight portion of the bars contributes to developing the bars. According to the data, it may still be conservative to increase the bearing area by a factor of 1.2 to 1.3 when a bend radius of the standard bend is used.

Similar results were derived when ACI-based coefficients were applied, as shown in Figure 4-52(b). Predictions using ACI-based coefficients are slightly more accurate than using AASHTO LRFD-based coefficients. Overall, the mean of the strength ratio is 1.28, and only one unconservative count appears. The only unconservative case is also Specimen D-R11-45(B). The coefficient of variation is 16.74%, essentially the same as using AASHTO LRFD-based coefficients. Scattered data points also fall in the region where the bend radius ratio is lower than 0.6. It may also be conservative to increase the bearing area by a factor of 1.2 to 1.3 when a bend radius of the standard bend is used for the same reason. The similarity can be attributed to the fact that measured concrete strengths in the experimental program led to similar nodal efficiency factors based on AASHTO LRFD or ACI 318-19. Therefore, it can be concluded that both methods have little difference when the compressive strength of concrete is between 4.6 ksi to 5.8 ksi.

4.7.7.2. Simplified Sizing Method CCC Node

The analytical results based on the simplified sizing method are summarized in Table 4-10. The parameters and symbols used in the table are the same as in Table 4-9.

Table 4-10 Summary of analytical results using the simplified sizing method

Specimen ID	P_{test} (kip)	Test Failure Mode	AASHTO			ACI		
			P_{STM} (kip)	P_{test}/P_{STM}	Failure mode	P_{STM} (kip)	P_{test}/P_{STM}	Failure mode
A-R6-45	543	C	302	1.80	C	305	1.78	C
A-R11-45	626	F	498	1.26	F	509	1.23	F
A-R9-45	498	C	356	1.40	C	358	1.39	C
B-R6-30	302	C	217	1.39	C	223	1.36	C
B-R11-30	344	F	272	1.27	F	280	1.23	F
C-R6-60	277	C	199	1.39	C	199	1.39	C
C-R11-60	337	C	309	1.09	C	312	1.08	C
D-R11-45(T)	556	F	468	1.19	C	479	1.16	C
D-R11-45(B)	452	C	438	1.03	C	443	1.02	C

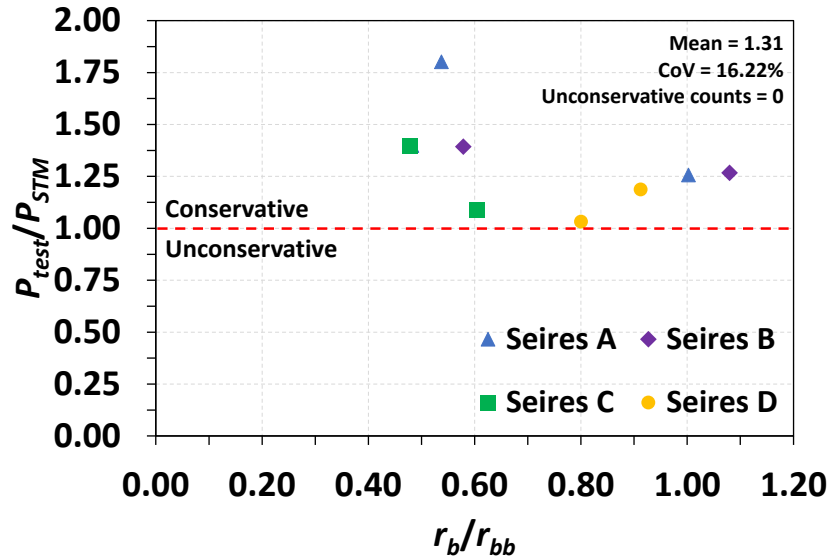
* C stands for failure at the curved-bar node;

F stands for flexural failure happening first

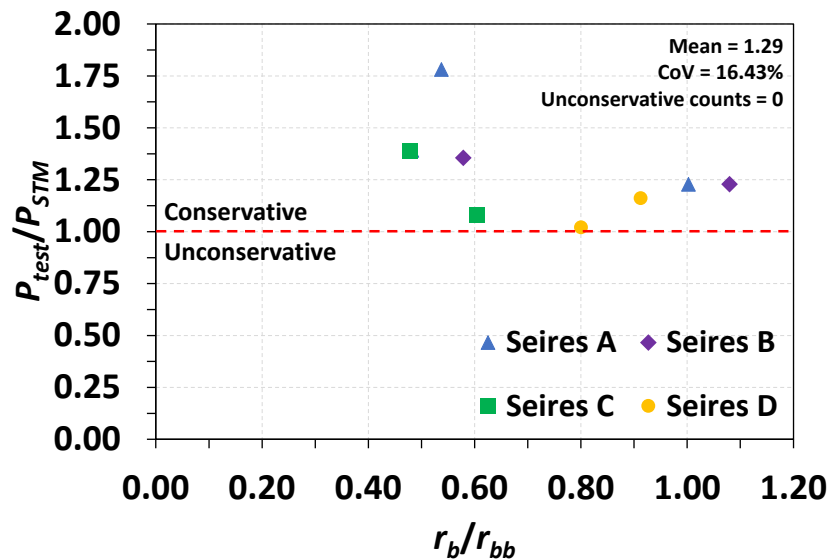
It can be seen from Table 4-10 that predicted failure modes based on the simplified sizing method are the same as that based on the general sizing method. The predicted failure mode of each test specimen was in agreement with the test failure mode except for Specimen D-R11-45(T). The exception is attributed to the same reason explained in the previous section. The nodal coefficient and the sizing method are conservative when determining failure modes.

Similarly, the accuracy and conservatism of the STM with the simplified sizing method were further evaluated by plotting the strength ratio against the bend radius ratio of the specimens, as shown in Figure 4-53. In Figure 4-53(a), the datapoints are based on AASTHO LRFD. The overall strength ratios have a mean of 1.31 with no unconservative count. The mean of the strength ratio

was little different from using the general sizing method, but all predictions are conservative. The coefficient of variation is 16.22%, and scattered datapoints and overly conservative predictions also happen when the bend radius ratio is smaller than 0.6. The reason is explained in the previous section. According to the data, it may still be conservative to increase the bearing area by a factor of 1.2 to 1.3 when a bend radius of the standard bend is used.



(a) AASHTO LRFD-based efficiency factor



(b) ACI-based efficiency factor

Figure 4-53 Evaluation of the STM with simplified sizing method regarding bend radius ratio

Similar results were derived when the simplified sizing method was used along with ACI-based nodal factors, as shown in Figure 4-53(b). Predictions using ACI-based coefficients are slightly more accurate than using AASHTO LRFD-based coefficients. Overall, the mean of the strength

ratio is 1.29, and no unconservative count appears. The coefficient of variation is 16.43%, very close to using AASHTO LRFD-based coefficients. Scattered datapoints also fall in the region where the bend radius ratio is lower than 0.6. It may also be conservative to increase the bearing area by a factor of 1.2 to 1.3 when a bend radius of the standard bend is used for the same reason. The similarity can be once again attributed to the fact that measured concrete strengths in the experimental program led to similar nodal efficiency factors based on AASHTO LRFD or ACI 318-19. Therefore, it can be concluded that both methods have little difference when the compressive strength of concrete is between 4.6 ksi to 5.8 ksi.

4.8. Finite Element Analysis

The section presents using the finite element software ATENA 3D on the analysis of the test specimens in the experimental program. A comparison of results derived from the finite element method (FEM), the STM, and the experimental program is included.

4.8.1. Model Preparation

4.8.1.1. Material Model

4.8.1.1.1. Concrete

The material type “3D Nonlinear Cementitious 2” was selected for the concrete material. Measured parameters were used for the modeling. However, parameters that were not measured in the experimental program were specified by default or as recommended values in the software. The used parameters are summarized in Table 4-11. The detailed definition of each required parameter refers to ATENA 3D theory (2018).

Table 4-11 Concrete material parameters used in the FEA

Subset	Parameters	Value	Unit
Basic	Elastic modulus, E_c	$57\sqrt{f'_c}$	ksi
	Poisson's ratio, ν	0.2	-
	Tensile strength, f'_t	$0.004\sqrt{f'_c}$	ksi
	Compressive strength, f'_c	Measured	ksi
Tensile	Specific Fracture energy, G_F	$9.84 \times 10^{-4} f'_t$	kip/in.
	Crack spacing, s_{max}	-	-
	Tension stiffening, c_{ts}	-	-
	Unloading	-	-
Compressive	Critical compression displacement, w_d	0.05	in.
	Plastic strain at compressive strength, ϵ_{cp}	f'_c/E_c	-
	Reduction of comp. strength due to cracks, $r_{c,lim}$	0.8	-
Shear	Crack Shear Stiff. Factor, S_F	20	-
	Aggregate interlock, MCF	-	-
	Aggregate Size	0.79	in.
Miscellaneous	Fail. Surface eccentricity	0.52	-
	Multiplier for the plastic flow dir. β	0.5	-
	Specific material weight, ρ	8.47×10^{-5}	kci
	Coefficient of thermal expansion, α	-	1/°F
	Fixed crack model coefficient	1.0	-

4.8.1.1.2. Reinforcement

This FE analysis used the bilinear strain hardening constitutive relationship for reinforcement. It was required to input the yield stress, strain-hardening ratio, and the ultimate stress of the reinforcement. Measured or default values were used, as summarized in Table 4-12.

Table 4-12 Reinforcement material parameters

Subset	Parameters	Values	Unit
Basic	Elastic modulus, E	29000	ksi
	Yield strength, σ_y	Measured	ksi
	Tensile strength, σ_t	Measured	ksi
	Limit strain, ϵ_{lim}	Measured	
Miscellaneous	Specific material weight, ρ	2.89×10^{-4}	kci
	Coefficient of thermal expansion, α	-	1/°F

4.8.1.1.3. Steel Plates

The elastic isotropic material model was used for the load and support plates. The model had an elastic modulus of 29000 ksi and a Poisson's ratio of 0.3 by default, as listed in Table 4-13.

Table 4-13 Elastic material parameters

Subset	Parameters	III-1.2-03-(i)	Unit
Basic	Elastic modulus, E	29000	ksi
	Poisson's ratio, ν	0.3	-
Miscellaneous	Specific material weight, ρ	2.89×10^{-4}	kci
	Coefficient of thermal expansion, α	-	$1/^{\circ}\text{F}$

4.8.1.2. Model Construction

The general view of a numerical model of concrete and support plates is presented in Figure 4-54. Resembling the test specimens, the numerical model had two legs, two joints, and a beam-column member with the same dimensions designed in the experimental program. The portal-shaped concrete member was modeled using Macroelement in the software. In addition, steel support plates and steel load plates were also modeled using Macroelement and were located at designated positions per the test setup design in the experimental program.

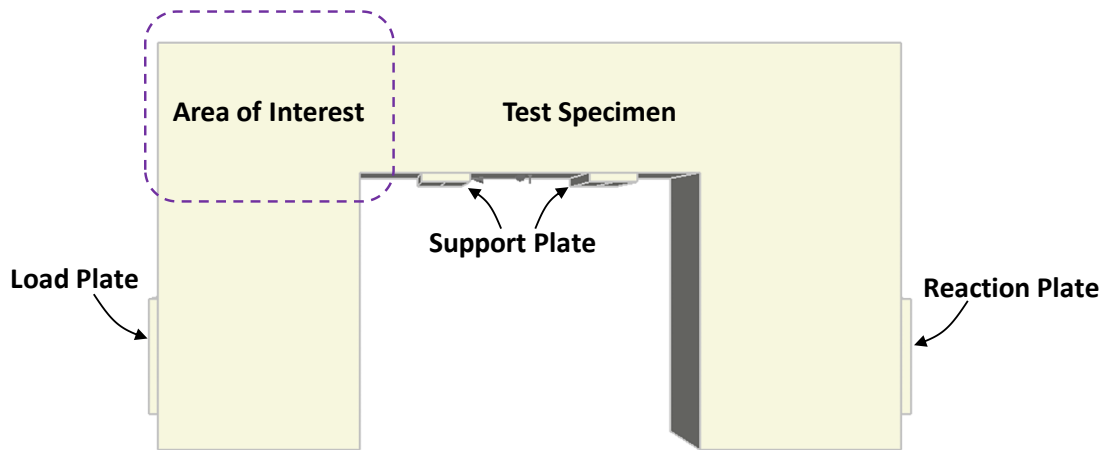


Figure 4-54 Macroelement of numerical specimens

Furthermore, inside the portal-shaped Macroelement, 1-D reinforcement elements were distributed accordingly. The layout of the 1-D reinforcement elements was the same as that of the test specimen to be modeled. It should be noted that end hooks of the longitudinal reinforcement were not included, given that the perfect bond condition was activated. The modeling result is shown in Figure 4-55.

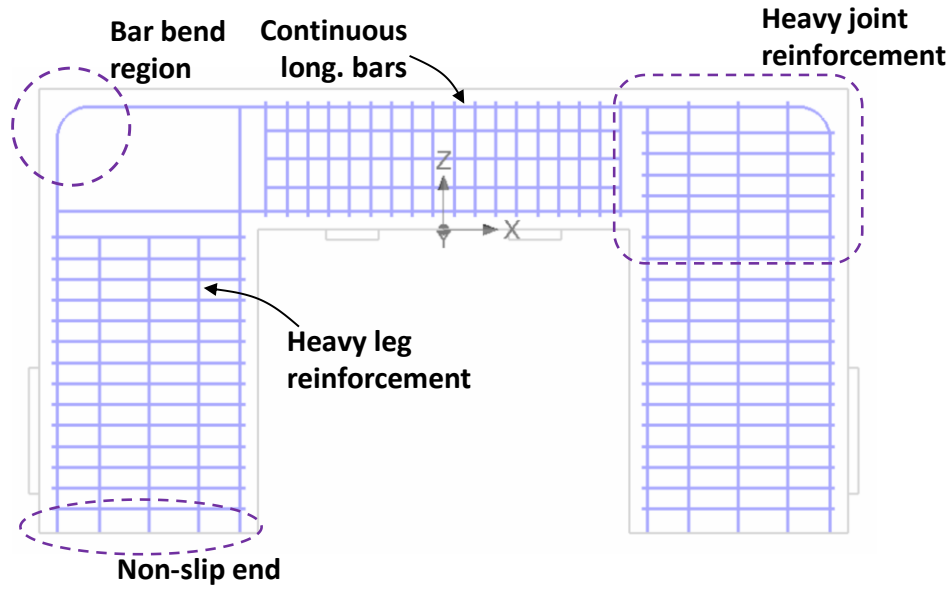


Figure 4-55 1-D reinforcement model

4.8.1.3. Boundary Conditions

Boundary conditions were assigned in alignment with the approach of applying the load, and the reaction as well as roller supports in the experimental program, as shown in Figure 4-56, for example.

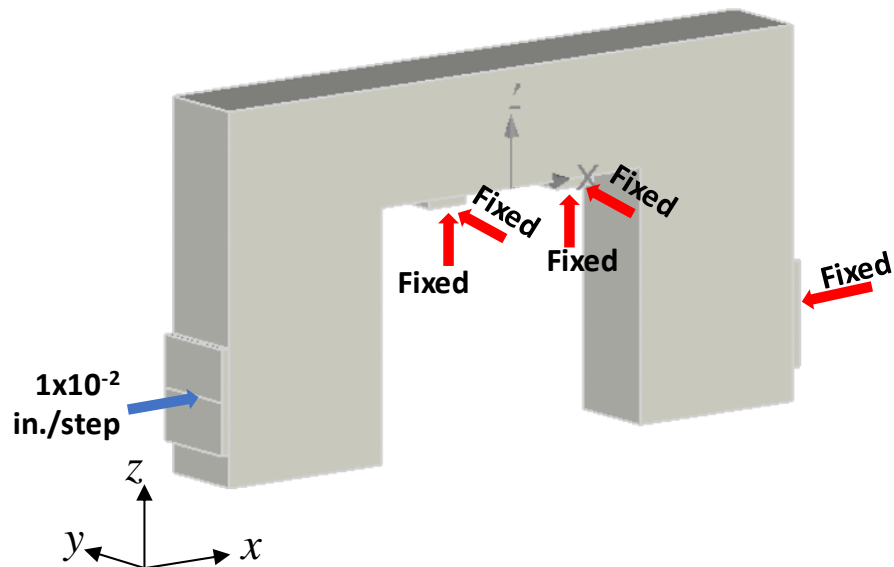


Figure 4-56 Boundary conditions for FE analysis

In particular, at the center point of the load plate model, loading was applied as prescribed displacement with a magnitude of 1×10^{-2} in. to create a displacement-controlled numerical test, which would better capture the entire load-displacement curve. Similarly, at the center point of the reaction plate model, all three orthogonal directions were not allowed to translate, reflecting the configuration of the test frame. The self-weight of the numerical portal-shaped specimen was not taken into consideration.

Underneath the model of the beam-column member, each of the two support plates had a line in the middle along the y-direction. Line support was assigned to the middle line, which was not allowed to translate along the y-direction and the z-direction.

4.8.1.4. Mesh and Contact

The Macroelement for the numerical portal specimen was meshed with eight-point linear hexahedral meshes with a general size of 4 in. For Macroelements modeling steel plates, four-point linear tetrahedral meshes with a general size of 4 in. were used. Perfect contact elements were automatically generated between the numerical deep beam and numerical steel plates. The result is shown in Figure 4-57.

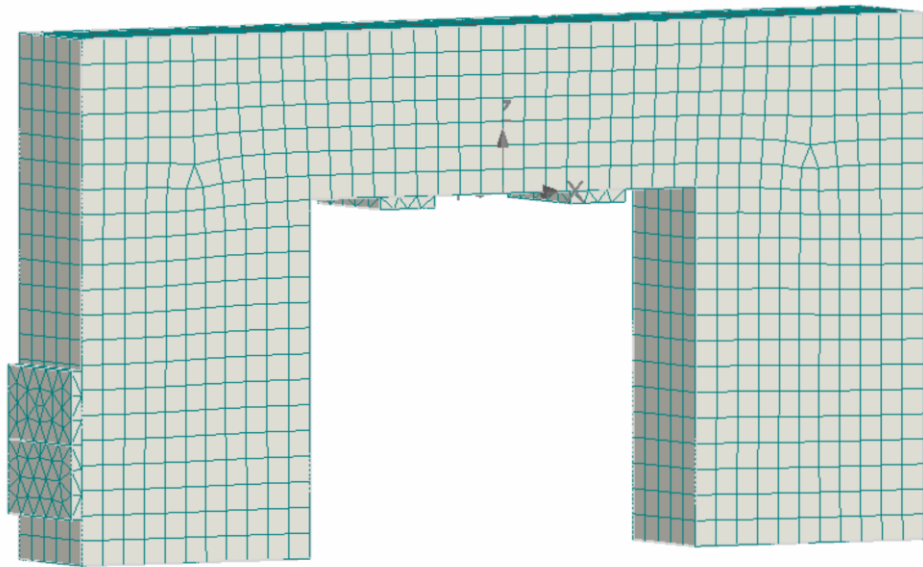


Figure 4-57 Meshing result

4.8.1.5. Solution Parameters

The standard Newton-Raphson method was used to exercise iterations for the convergence of solutions in each analysis step. Each analysis step had 40 iterations, and convergence tolerances were specified as default. Line search was activated to assist convergence.

4.8.2. Results and Discussion

4.8.2.1. Series A

Figure 4-58 shows the comparison between the FE analytical and experimental load-displacement curve of each specimen in Series A. The calculated strength using the AASHTO-based STM is also shown in the figure as a dashed line for comparison purposes. It can be seen from the figure that the FE analytical load-displacement relationship of each specimen is in good agreement with the experimental one. The stiffness matched very well, and the FEA reflected the fact that bend radius alters the load-displacement behavior. Moreover, the load plateauing was successfully captured for Specimen A-R11-45. The FE analytical peak strengths of Specimens A-R6-45 and A-R9-45 were also close to the experimental ones, with differences of -12.3% and 10.9%, respectively. The accuracy of the FEA was generally better than the STM in terms of peak strength, and the FEA was able to capture the entire load-displacement relationship.

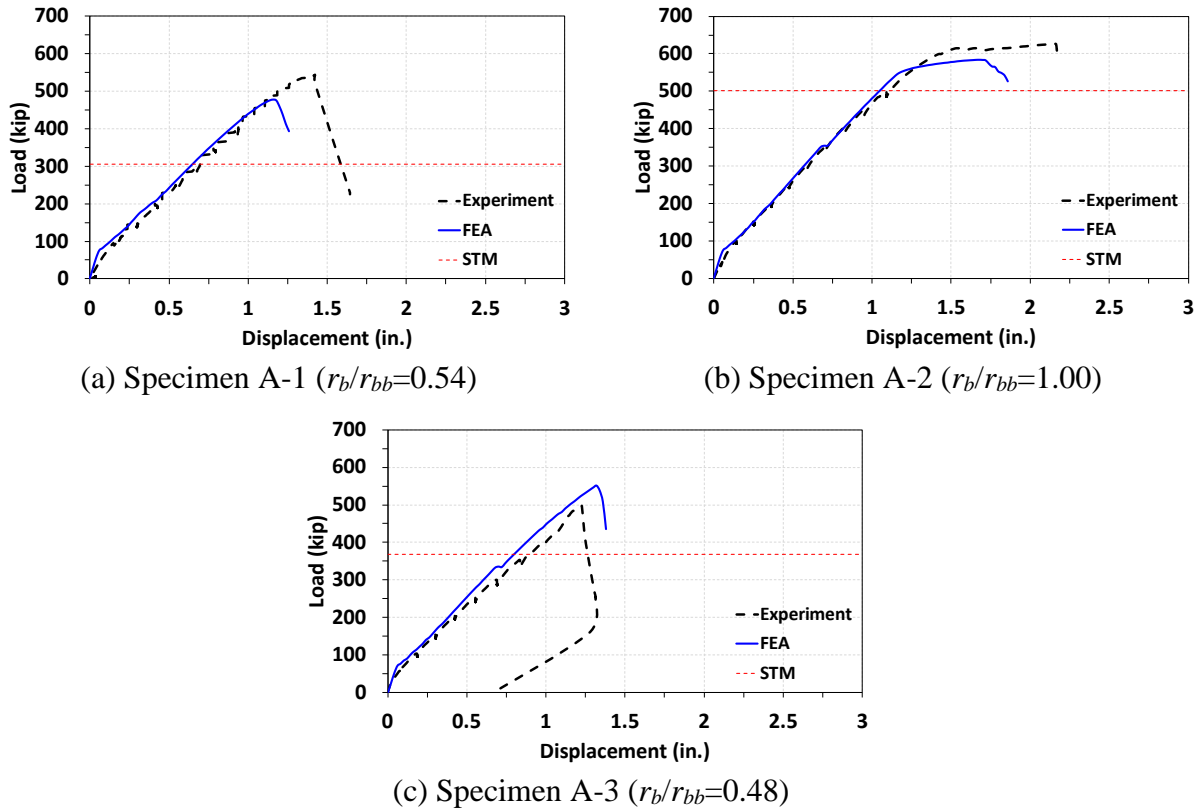


Figure 4-58 Comparison among FEM results, STM results and experimental results for Series A

In addition to load-displacement relationships, the FEA was able to output stress distribution and crack patterns. Here, the distribution of principal minimum stresses of each specimen in Series A is presented in Figure 4-59 to study the orientation of the struts, which represent the resultant of compressive principal stresses.

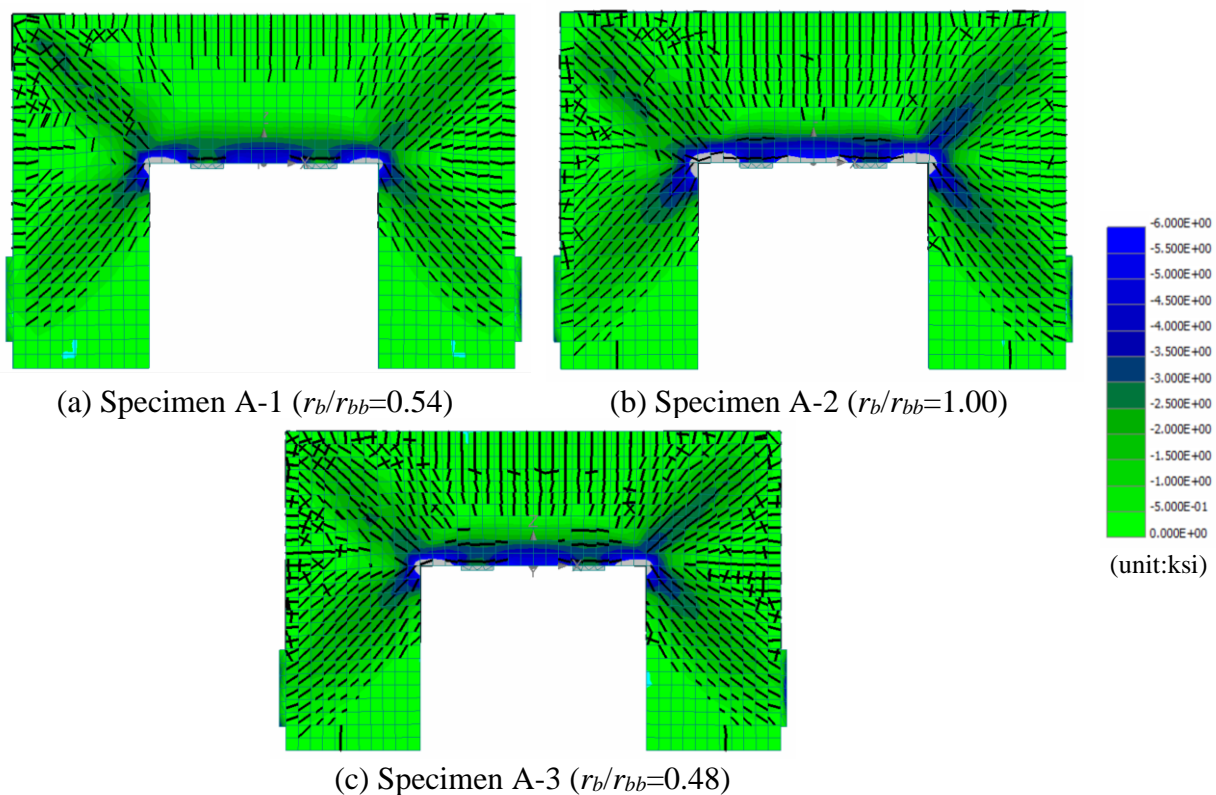


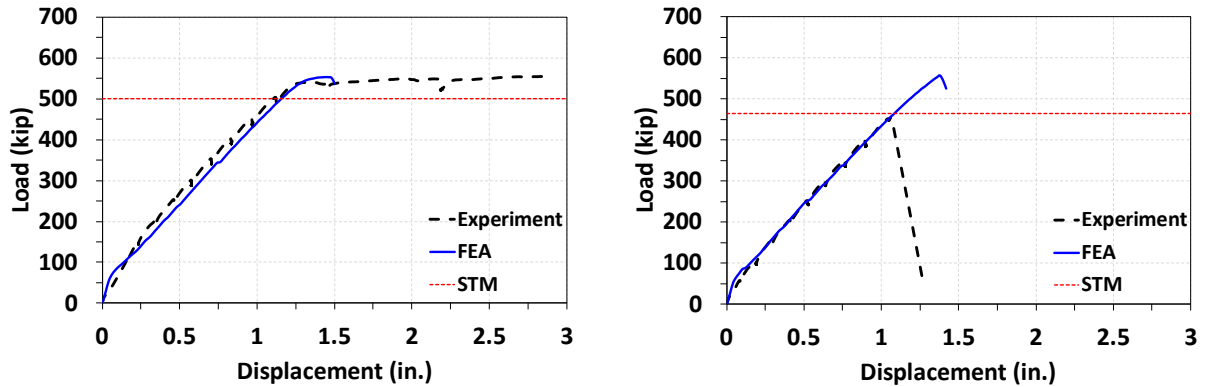
Figure 4-59 Analytical damage pattern and stress distribution of Series A near failure

It can be seen from Figure 4-59 that the FE analytical minimum principal stresses (i.e., compressive principal stresses) coincide with observed principal minimum strains by DIC in the joint (introduced in Section 6.3.7). Overall, the FE analytical crack pattern also agrees with the marked crack pattern for each specimen. The FEA also captured the phenomenon that larger bend radii better distribute cracks and compressive principal stresses in the joint, involving more concrete to resist internal loads. In addition, the assumed strut-and-tie model for such portal specimens introduced previously is appropriate, as the FE analytical load path shown in Figure 4-59 agrees.

4.8.2.2. Series D

Similarly, Figure 4-60 shows the comparison between FE analytical and experimental load displacement curve of each specimen in Series D. The calculated strength using the AASHTO-based is also shown as a dashed line in the figure for comparison purposes. In general, the FE analytical results are in a good agreement with the experimental ones. The stiffness was captured and the effect of the bend radius on the ductile behavior was reflected. For Specimen D-R11-45(T), which had two layers of reinforcement, the FEA stopped due to convergence issues a few steps after entering the load plateau. The yield strength of Specimen D-R11-45(T) was very well matched with a difference of only 3.6% compared to the experimental load-carrying capacity at the step. For Specimen D-R11-45(B), which had bundled reinforcement, the FEA was able to capture the stiffness very well; however, the peak strength was overestimated with a difference of 22.6%. In

this case, the STM had a more accurate prediction. Nevertheless, the phenomenon does not indicate that the STM is better at addressing bundled reinforcement than the FEA. Instead, both methods do not have an appropriate method of accounting for the effect of the bend radius comprising bundled reinforcement.

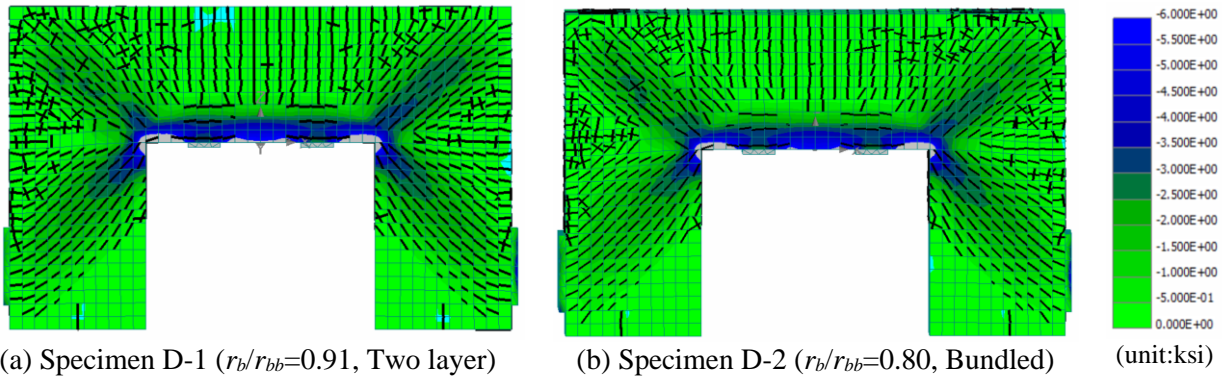


(a) Specimen D-1 ($r_b/r_{bb}=0.91$, Two layer)

(b) Specimen D-2 ($r_b/r_{bb}=0.80$, Bundled)

Figure 4-60 Comparison among FEM results, STM results and experimental results for Series D

Also, the FE analytical minimum principal stress distribution and crack patterns of specimens in Series D are presented in Figure 4-61. Again, the FE analytical results were in a good agreement with the test results, and the assumed strut-and-tie model can be a good representative of the load path in such portal structures.



(a) Specimen D-1 ($r_b/r_{bb}=0.91$, Two layer)

(b) Specimen D-2 ($r_b/r_{bb}=0.80$, Bundled)

(unit:ksi)

Figure 4-61 Analytical damage pattern and stress distribution of Series D near failure

4.8.2.3. Series B

Figure 4-62 shows the comparison between the FE analytical and experimental load-displacement curve of each specimen in Series B. The calculated strength using the AASHTO-based is also shown as a dashed line in the figure for comparison purposes. For Series B, the FE analysis captured the peak strength of each specimen and differentiated the effects of the bend radius on the behavior. For Specimen B-R6-30, the predicted peak strength was 345 kips, 14.2% higher than the test peak strength; the analytical stiffness was slightly higher than the test stiffness. A brittle

load drop occurred right at the peak load. For Specimen B-R11-30, the FE analytical peak load was 362 kips, 5.8% higher than the test peak load; the analytical stiffness was higher than the test stiffness. Some post-yield behavior was captured, but the analysis was stopped due to convergence issues. The FEA also performed well in predicting the behavior of specimens in Series B but was not as accurate as when applied to Series A and Series D.

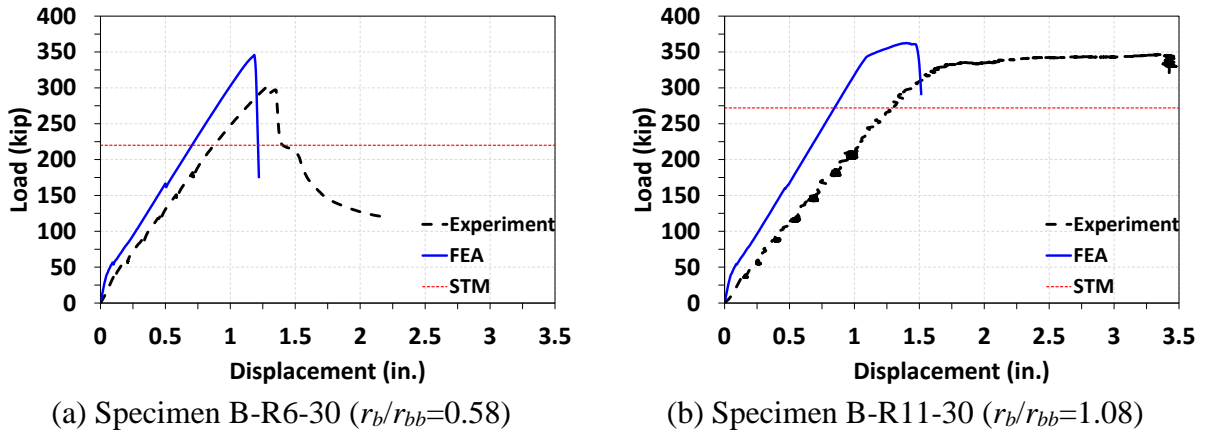


Figure 4-62 Comparison among FEM results, STM results, and experimental results for Series B

Also, the FE analytical minimum principal stress distribution and crack patterns of specimens in Series C are presented in Figure 4-63. Again, the FE analytical results were in good agreement with the test results. In particular, stress concentration in the joint flows in orientation from the re-entrant corner to the outside of the joint. The assumed strut-and-tie model can be a good representative of the load path in such portal structures.

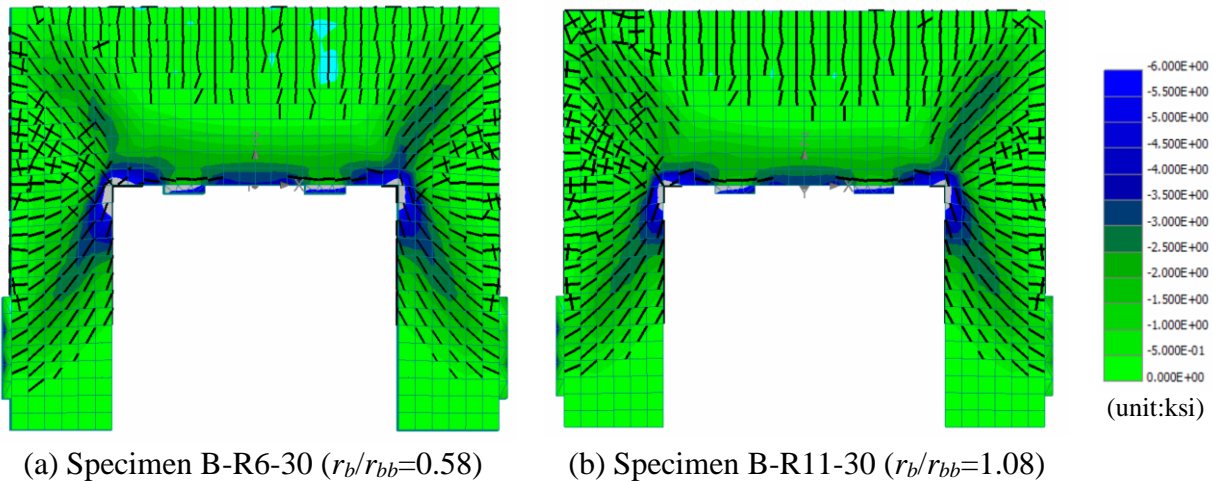


Figure 4-63 Analytical damage pattern and stress distribution of Series B near failure

4.8.2.4. Series C

Figure 4-64 compares analytical results derived from the FEA and the STM to the experimental load-displacement behavior for both specimens in Series C. In this case, the FEA also accurately

predicted the strength. There existed only a difference of 3.6% for Specimen C-R6-60 and 3.0% for Specimen C-R11-60. The stiffness, on the other hand, was calculated slightly higher than the experimental one for both specimens. In particular, the softening was not perfectly captured. Nevertheless, the FEA's predictability was generally excellent for the closing knee joints, whether having a small bend radius or an enlarged bend radius.

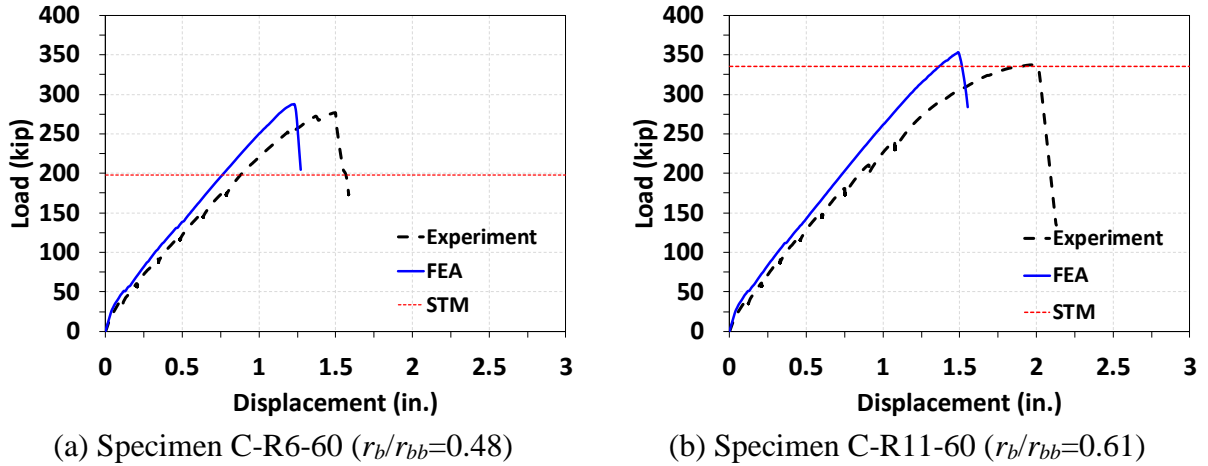


Figure 4-64 Comparison among FEM results, STM results and experimental results for Series C

Also, the FE analytical minimum principal stress distribution and crack patterns of specimens in Series C are presented in Figure 4-65. Again, the FE analytical results were in good agreement with the test results. In particular, stress concentration in the joint flows in orientation from the re-entrant corner to the outside of the joint. The assumed strut-and-tie model can be a good representative of the load path in such portal structures.

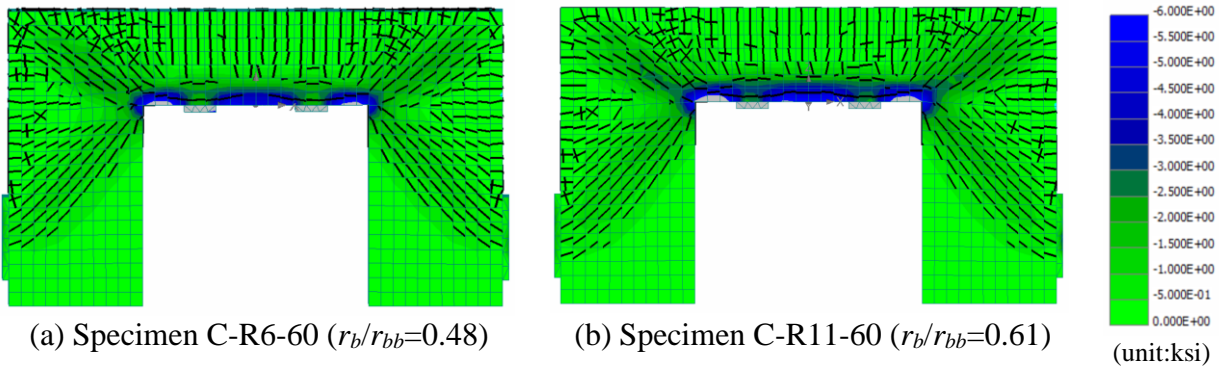


Figure 4-65 Analytical damage pattern and stress distribution of Series C near failure

4.8.2.5. Discussion and Suggestion

The 3D non-linear finite element analysis software ATENA 3D was employed to model the nine specimens in the experimental program of the current study. The software was generally able to deliver accurate predictions of structural responses for the closing knee joint specimens. Discussions and suggestions can be drawn based on the analytical results as follows:

- ATENA 3D was able to capture the effects of the bend radius on the structural responses of closing knee joints. That is, it was reflected in the FE analysis that enlarged bend radii at the outside of the corner lead to improved behavior in terms of peak strength and ductility, as demonstrated in the experimental program.
- When no detailed concrete material properties were available, using the modulus of elasticity and direct tensile strength suggested in ACI 318-19 resulted in agreeable analytical results, while the other material parameters remained default.
- A general mesh size of 4 in., approximately one-fifth of the width of the specimens, would be sufficiently fine to obtain good predictions. In addition, 8-node hexahedral meshes were applicable.
- Extra attention is needed for bundled bars. The effects of bundled bars on bond stress and on the overall joint behavior were not appropriately captured in the analysis.
- For specimens with unequal joint dimensions, the FEA tended to generate higher stiffness and slightly overestimate the peak load.

4.9. Design Recommendations

This section presents design expressions for curved-bar nodes in the STM. A design example of applying the STM with a curve-bar node on a cantilever bent cap is also provided. The design example is based on the current AASHTO LRFD and the proposed design expressions curved-bar nodes.

4.9.1. Design Expressions for Curved-bar Node

Based on the experimental and analytical results, it is suggested that curved-bar nodes appearing at the outside of closing knee joints be designed as the following guidelines:

- The bend radius (r_b) of the bar bend proportioned for a curved-bar node shall satisfy Eq. (4-21) but shall not be less than half the minimum diameter specified in Section 5.10.2.3 of AASHTO LRFD (2020).

$$r_b \geq \frac{A_{ts}f_y}{b_s v f'_c} \psi_c \quad (4-21)$$

where

- A_{ts} is the area of non-prestressed bars in the tie;
- f_y is the yield strength of the bars;
- b_s is the width of the diagonal strut framing into the curved-bar node;

- ν is the efficiency factor for curved-bar nodes, taken as 0.5
 - f'_c is the compressive strength of concrete;
 - ψ_c is the cover factor, taken as the greater of $2d_b/c_c$ and 1.0
 - d_b is the bar diameter;
 - c_c is the clear cover to the side face.
- If multiple layers of longitudinal reinforcing bars are used, the bend radius of the bar bend of every layer should be the same and satisfy Equation (4-21).
 - If bundled bars are used, the bend radius per Equation (4-21) should be further enlarged by a factor of 1.28.
 - The strut framing into the curved-bar node should be reinforced with appropriate orthogonal crack control reinforcement per Section 5.8.2.6 of AASHTO LRFD (2020).

4.9.2. Design Example using the STM with a Curved-bar Node

Cantilever bent caps are one of the most representative bridge substructures subjected to closing moments; therefore, a curved-bar node can be used at the outside of the example cantilever bent cap. This section presents a design example of a cantilever bent cap, including the use of the STM with applying the design expressions of curved-bar nodes. The example focuses on the joint region; design of the cantilever bent cap and the pier are not included.

4.9.2.1. Structural Configuration of Cantilever Bent Cap

The example structure, as shown in Figure 4-66, consists of a cantilever bent cap with cross-sectional dimensions of six feet (72 in.) in width by five feet (60 in.) in height and a square pier with six feet (72 in.) for the side length. The total length of the bent cap is 19 feet, and three girder loads are applied on the top of the bent cap. The first girder load is four feet away from the back of the column; the other two girder loads are distributed at a spacing of eight feet. The magnitudes of the girder loads are 280 kips, 280 kips, and 260 kips, as marked in the figure. The compressive strength of concrete for the example structure is 4 ksi, and the yield strength of steel reinforcement is 60 ksi.

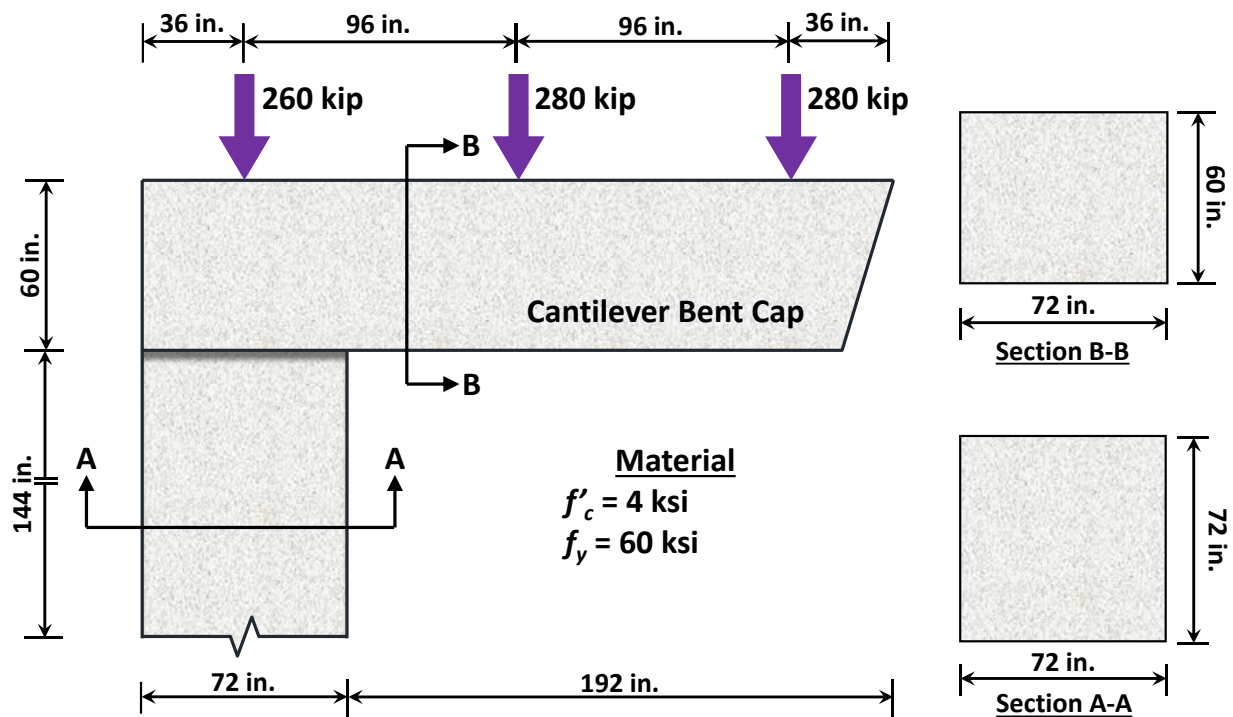


Figure 4-66 Design example of cantilever bent cap

4.9.2.2. Structural Analysis

In typical practice, before constructing a strut-and-tie model, the elastic structural analysis should be conducted to determine the stress profile over the area of the interface between D-regions and B-regions. The stress profile will assist in the placement of struts. In this example, only one interface can be located on the pier 12 feet away from the joint face.

On the interface, the resultant axial load (N) is 820 kips, and the resultant moment (M) is 6720 kip-ft (80640 kip-in.) per equilibrium. Therefore, the maximum compressive stress (f_c) and the depth of the neutral axis can be determined using the gross sectional properties given by

$$f_c = \frac{N}{A_c} + \frac{My_c}{I_g} = \frac{820 \text{ kip}}{(72 \text{ in.})(72 \text{ in.})} + \frac{(80640 \text{ kip-in.})(72 \text{ in.}/2)}{(1/12)(72 \text{ in.})(72 \text{ in.})^3} = 1.45 \text{ ksi} \quad (4-22)$$

Also, the depth of the neutral axis (y_c) can be determined by assuming f_c to be zero and solving for it. In this case, the y_c is 50.8 in. away from the edge of the compression side. The analysis result is also shown in Figure 4-67. It should be noted the approach of placing struts is not unique. Indeed, transformed cracked cross-sectional properties or the equivalent stress block may be used for refined results.

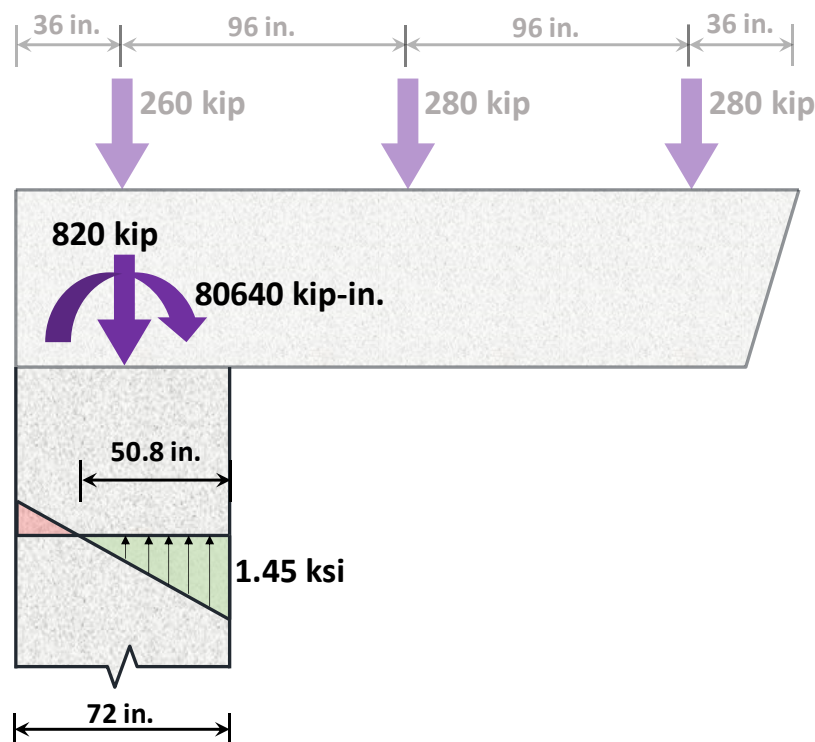


Figure 4-67 Stress distribution at B-D region interface

4.9.2.3. Development of the Strut-and-Tie Model

Based on the configuration and the stress distribution over the interface, a permissible strut-and-tie model can be constructed, as shown in Figure 4-68. The strut-and-tie model has one panel in the bent cap before entering the joint; one strut connects from the end of the panel to the node near the re-entrant corner. In the pier, two vertical struts are used to prevent the node near the re-entrant corner from receiving too many struts. In this way, two nodes are created near the joint face: one connected to the strut from the bent cap, the other connected to the outside of the frame corner. Ties are placed on the tension side of the bent cap and the pier.

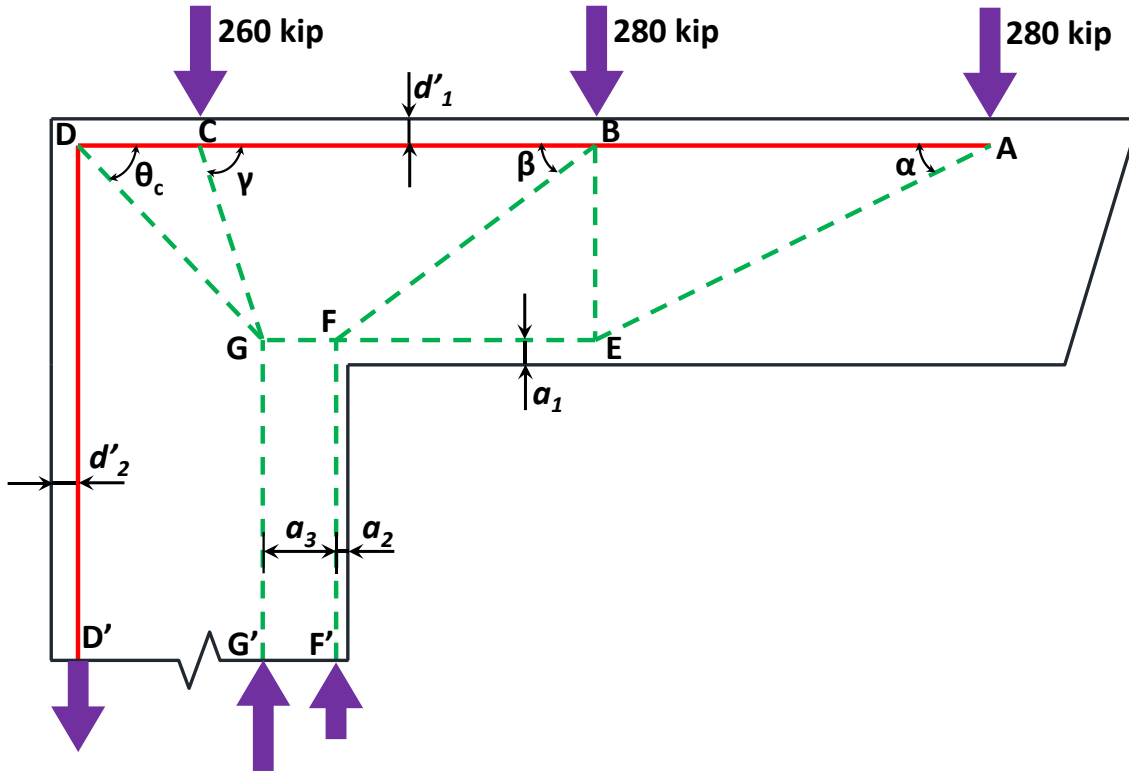


Figure 4-68 Permissible strut-and-tie model for the example structure

There are dimensions to be determined before calculating the internal force of each element, including the depths of the ties (d'_1 and d'_2) and the positions of the struts (a_1 , a_2 , and a_3). It is straightforward to align ties with the centroid of longitudinal reinforcing bars on the tension side of the bent cap and the pier. Here, both d'_1 and d'_2 are assumed to be 6.5 in. The value of a_1 can be assumed to be 0.1 times the height of the bent cap. Otherwise, the depth of the equivalent stress block can also be used. Nevertheless, either way may need iteration if nodal capacity is not satisfied. In this example, 0.1 times the height of the bent cap (6 in.) is used to begin with. The values of a_2 and a_3 are determined depending on the external loads and the position of their resultant force. The vertical strut ($S_{FF'}$) is assumed to have a force of the summation of the two girder loads outside the joint. Therefore, a_2 is placed at the centroid of the trapezoid sector of the compressive stress distribution that has a resultant of the force $S_{FF'}$. The resultant of the rest of the compressive stress, therefore, dictates the magnitude and the position (a_3) of $S_{GG'}$. Consequently, a_2 and a_3 are taken as 2.8 in. and 17.9 in., respectively. As the strut-and-tie model is constructed with all dimensions determined, member forces can then be calculated per equilibrium, as shown in Figure 4-69

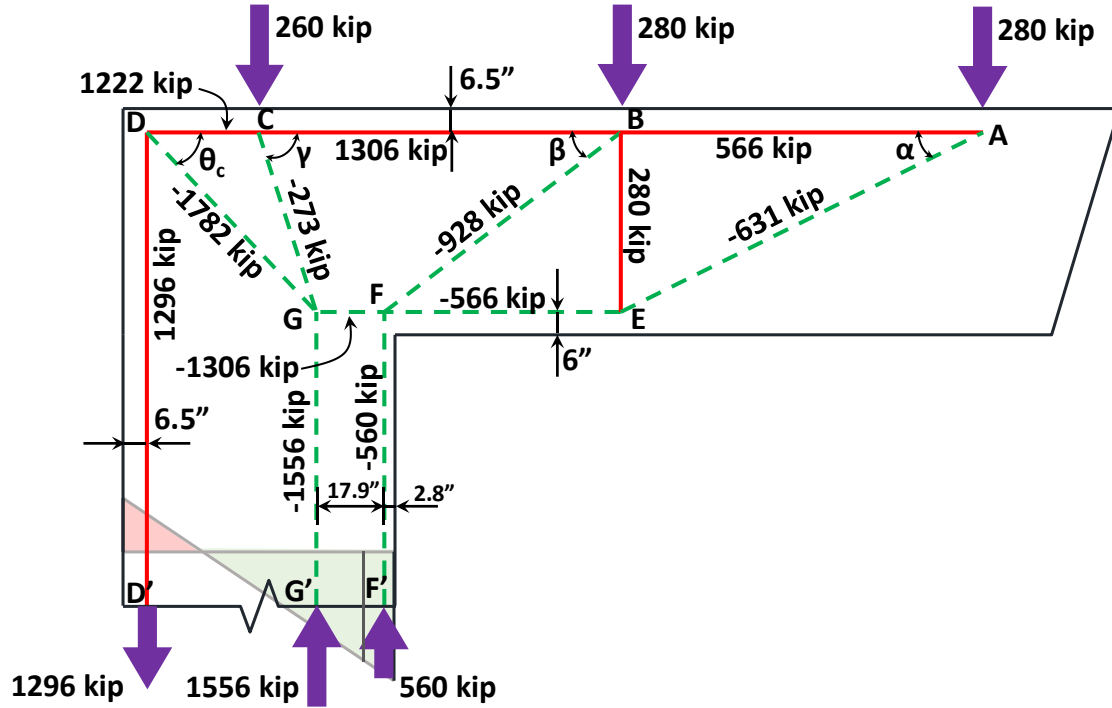


Figure 4-69 Dimensions of the strut-and-tie model and internal forces in the elements

Further, as the dimensions a_1 , a_2 , and a_3 are determined, angles between struts and the top tie can be checked. In this case, the angles α , β , and γ in Figure 4-69 are 26.3° , 37.1° , and 72.2° respectively. In addition, the diagonal strut in the joint has an angle (θ_c) of 46.7° . None of the angles are less than 25 degrees and, therefore, permissible.

4.9.2.4. Performing Nodal Capacity Check

The next step is to check nodal capacity to ensure the assumed strut-and-tie model is permissible. By observation, Node F is the critical node in the joint as it is located near the re-entrant corner. Node G is considered smear and not as critical as Node F. Therefore, only Node F is checked as following steps.

The shape of Node F is restraint by the edges and the re-entrant corner and should be sized accordingly. In particular, as Node F has four struts framing into itself, Struts S_{EF} and S_{BF} should be resolved as shown in Figure 4-70. The resultant strut (S_R) has a magnitude of 1421 kips and the angle to the horizontal (θ_s) is 23.2 degrees. With the force system determined, Node F can be shaped according to the orientations of the forces, as shown in Figure 4-71.

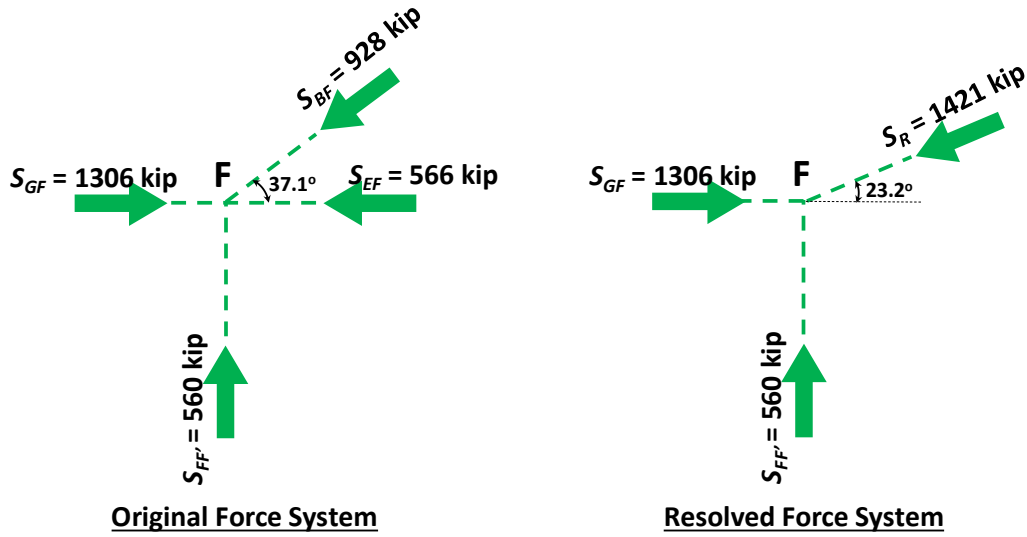


Figure 4-70 Force system at Node F

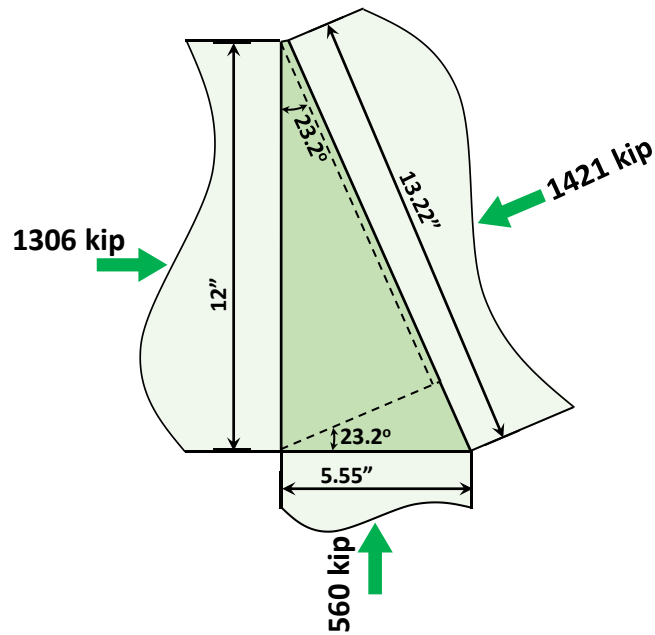


Figure 4-71 Non-hydraulic nodal shape of Node F

It can be seen from Figure 4-71, the bottom face (w_b) has a width of twice the dimension a_2 and the face on the right side (w_h) has a height of twice the dimension a_1 . The third face (w_R), which receives the resolved strut, has a width that can be determined using the widths of the previous two faces, given by

$$w_R = w_h \cos \theta_s + w_b \sin \theta_s = (12 \text{ in.}) \cos 23.2^\circ + (5.55 \text{ in.}) \sin 23.2^\circ = 13.22 \text{ in.} \quad (4-23)$$

In addition to sizing Node H, the selection of efficiency factors for all three interfaces is required before calculating the load-carrying capacity of the node. As Node F is not attached to bearing plates nor located on the compression side of a deep beam, necessary interpretation is needed to apply AASHTO LRFD-based efficiency factors. Specifically, the bottom face is shaped as a prism along the boundary and, therefore, can be considered the back face of Node F. The other two faces are both categorized as strut-to-node interfaces. Hence, the efficiency factors of all three interfaces are summarized in Table 4-14.

Table 4-14 Efficiency factors for the design example

Interface	Efficiency factor, ν
S_R	$0.85 - 4\text{ksi}/20\text{ ksi}=0.65$
$S_{FF'}$	0.85
S_{FG}	$0.85 - 4\text{ksi}/20\text{ ksi}=0.65$

Considering the resistance factor for strut ($\phi = 0.7$ per AASHTO LRFD), the capacities of the three strut-and-tie interfaces can be calculated and evaluated; the results are shown in Table 4-15

Table 4-15 Evaluation of Node F

Interface	Evaluation
S_R	$\phi F_{nR} = \phi \nu f'_c b w_R = (0.7)(0.65)(4\text{ ksi})(72\text{ in.})(13.22\text{ in.})=1732\text{ kips}$ $> S_R = 1421\text{ kips} \Rightarrow \text{OK}$
$S_{FF'}$	$\phi F_{nHH'} = \phi \nu f'_c b w_b = (0.7)(0.85)(4\text{ ksi})(72\text{ in.})(5.55\text{ in.})=951\text{ kips}$ $> S_{HH'} = 560\text{ kips} \Rightarrow \text{OK}$
S_{FG}	$\phi F_{nHI} = \phi \nu f'_c b w_b = (0.7)(0.85)(4\text{ ksi})(72\text{ in.})(12\text{ in.})=1572\text{ kips}$ $> S_{HH'} = 1306\text{ kips} \Rightarrow \text{OK}$

Therefore, all three interfaces have sufficient capacity to resist the strut forces. The strut-and-tie model is permissible; no iteration or refinement is needed.

4.9.2.5. Proportioning Ties

From the determined forces in Figure 4-69, it can be seen that Tie T_{CD} has the highest magnitude of tension (1306 kips) among all ties and controls the required amount of tension reinforcement in the joint. Here, No. 11 bars (with bar area $A_b = 1.56\text{ in.}^2$) are used, and the resistance factor (ϕ) is taken as 0.9. Therefore, the required number of longitudinal bars (N) is given by

$$N = \frac{T_{CD}}{(\phi)(A_b)(f_y)} = \frac{1306\text{ kips}}{(0.9)(1.56\text{ in.}^2)(60\text{ ksi})} = 15.5 \quad (4-24)$$

As a result, Sixteen No.11 bars arranged in two layers are used. The distance between the top edge to the center of the first row of the reinforcement is chosen to be 4.5 in., and the center-to-center distance between the two rows is 4 in. Therefore, the horizontal center-to-center spacing between the bars is equal to 8.57 in. The side cover to the center of the first reinforcing bar is selected to be 6 in. The selections will be checked later for development length and for sizing the bar bend region.

4.9.2.6. Designing Bar Bend Region

The bend radius of the bar bend has to be sized according to Equation (4-21) in Section 4.9.1, as follows:

$$r_b \geq \frac{A_{ts}f_y}{b_s v f'_c} \psi_c = \frac{[(16)(1.56 \text{ in.}^2)](60 \text{ ksi})}{(72 \text{ in.})(0.5)(4 \text{ ksi})} (1.0) = 10.4 \text{ in.} \quad (4-25)$$

where the side cover factor is taken as 1.0 because $2d_b/c_c$ is less than 1.0; therefore, the required bend radius is 10.4 in., larger than the standard bend radius of No. 11 bars. As two layers of reinforcement are to be used, the inner bend radius of both layers should comply with the result. Here, a bend radius of 12 in., corresponding to the standard bend of No. 18 bars is chosen.

4.9.2.7. Designing Crack Control Reinforcement

Crack control reinforcement shall be proportioned across the diagonal strut and other struts in the joint and other members. The minimum required crack control reinforcement ratio for the orthogonal directions is 0.3% per current AASHTO LRFD. Here, No. 7 horizontal bars are evenly distributed at a spacing of 5 in. on both sides; 4-leg No. 6 stirrups are distributed at a spacing of 8 in., resulting in horizontal and vertical reinforcement ratios:

$$\frac{A_{sx}}{b_s s_x} = \frac{(2)(0.6 \text{ in.}^2)}{(72 \text{ in.})(5 \text{ in.})} = 0.333\% > 0.3\% \Rightarrow \text{OK} \quad (4-26)$$

$$\frac{A_{sy}}{b_s s_y} = \frac{(4)(0.44 \text{ in.}^2)}{(72 \text{ in.})(8 \text{ in.})} = 0.305\% > 0.3\% \Rightarrow \text{OK} \quad (4-27)$$

4.9.2.8. Design Summary

The complete design is summarized in Figure 4-72. It should be noted that other column reinforcement is not shown in the figure. Also, an appropriate splice between the column bars and beam bars should be designed, which is not included in the example. In addition, horizontal No. 7 bars are provided in the form of hairpins to provide anchorage.

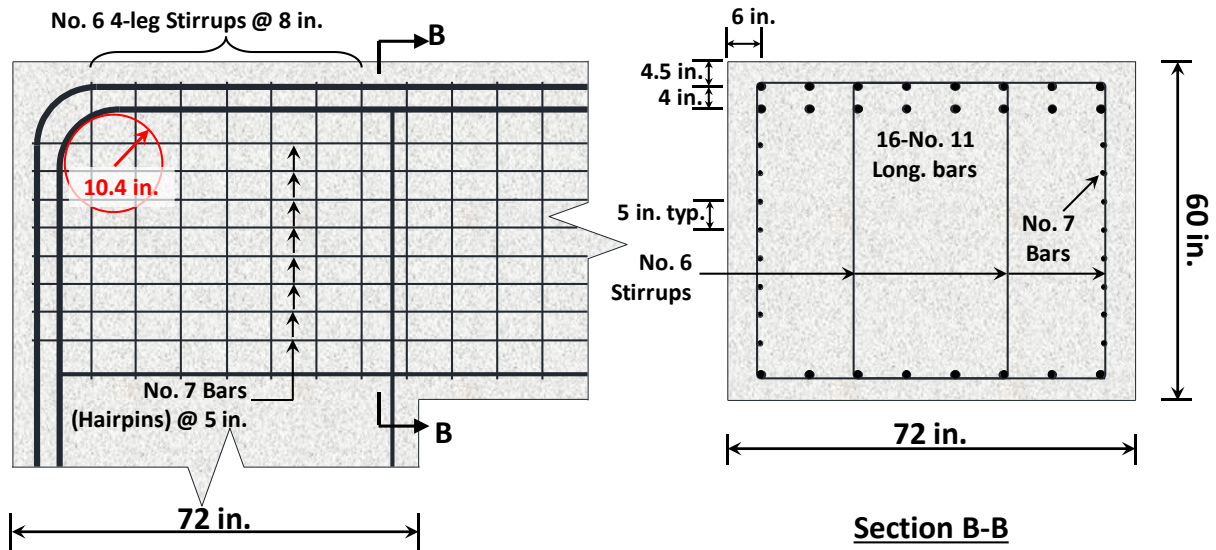


Figure 4-72 Summary of design result

4.10. Summary

Nine portal frame specimens with two joints under closing moments were designed to investigate the effect of the bend radius at the outside of the frame corner. Test variables included the size of the bar bend, the orientation of the diagonal strut, and the arrangement of longitudinal reinforcement. Conclusions based on the test results can be drawn as follows:

- The size of the bar bend at the outside of closing knee joints is essential. A bend radius of the standard bend per current codes and specifications can lead to compromised joint shear capacity. Enlarged bend radii per Eq. (2-1) are needed to develop load plateauing and ductility.
- The diagonal strut angle other than 45 degrees slightly reduces the joint capacity compared to closing knee joints with a strut angle of 45 degrees. The bend radius at the outside of the joint still plays a more important role in affecting the behavior. Enlarged bend radii per Eq. (2-1) are still important to avoid compromised strength. Using bend radii per Eq. (2-3) appears overly conservative and unnecessary.
- Using two layers of reinforcement in closing knee joints also requires enlarged bend radii per Eq. (2-1) to avoid compromised strength. However, bundled reinforcing bars plausibly exert additional stresses on the concrete side cover in closing knee joints, causing adverse effects on the strength. Bend radii that satisfy Eq. (2-1) multiplied by 1.28 may be needed for bundled bars.

- Using enlarged bend radii per Eq. (2-1) contributes to controlling crack widths in the joint. Even though no crack control reinforcement was provided, using bend radii per Eq. (2-1) demonstrated satisfactory serviceability.
- DIC strain maps and the measured development of the main reinforcement support the load path in the joint represented by the assumed strut-and-tie model. The size of the bend radius affects the volume of concrete involved in resisting the diagonal principal compressive stresses; the size of the bend radius also affects the yield penetration towards the bar bend.
- Current methods for joint shear capacity in AASHTO LRFD and ACI 318-19 do not account for the effects of the bend radius and the diagonal strut angle, which may lead to unconservative designs of closing knee joints. The STM, on the contrary, is able to account for the bend radius and the diagonal strut angle.
- A procedure for using the STM on closing knee joints, including the selection of the strut-and-tie model and sizing nodes, was developed. AASHTO-based and ACI-based nodal coefficients were applied. The STM demonstrated accurate and conservative predictions along with either AASHTO-based or ACI-based nodal coefficients.
- The STM tended to be overly conservative when the bend radius ratio was less than 0.6. When sizing the curved-bar node in a closing knee joint, it is suggested that the bearing area be multiplied by 1.2 for assessment purposes. It should be noted that the bend radius ratio shall not be less than 1.0 for design purposes.
- The nonlinear finite element analysis software ATENA 3D was able to capture the load-displacement behavior and the peak load using measured material properties. For the specimen with bundled bars and the specimens with unequal joint dimensions, the FEA tended to overestimate the peak load and stiffness.
- Design recommendations and a design example were introduced on the basis of the test results and data interpretation.

Chapter 5. Nodal Confinement

This chapter presents the experimental investigation of the effect of passive confinement provided by reinforcement on nodal capacity when applying the STM on deep beams. The chapter includes the experimental program, test results, and evaluation of strength using the sectional analysis and the STM. Design recommendations and a summary are presented at the end of the chapter.

5.1. Introduction

The strut-and-tie method (STM) is one of the most suitable approaches for the design of D-regions in reinforced concrete members. According to the lower bound theorem of plasticity, the STM generates conservative design results and thus has gained increased attention among engineering communities. Design codes have also incorporated provisions of the STM into their main bodies. After many years of development, the STM has become widely accepted.

When applying the STM, performing nodal strength checks according to the code provisions for adequate concrete strength is one of the essential steps. Experimental studies reveal that the effective concrete strength of nodal zones may be enhanced for nodal strength check if concrete within the nodal zone is surrounded by concrete. Such strength enhancement because of triaxial confinement is recognized and incorporated into major design codes.

Not only does Surrounding concrete but also reinforcement provide triaxial confinement. However, strength enhancement obtained from confining reinforcement for nodal zones has long been overlooked among code provisions of the STM. ACI 318-19 and AASHTO LRFD 2020 remain silent on the effect. On the other hand, the European code *fib* allows a 10% increase in nodal strength if proper confinement is provided. Nevertheless, *fib* does not provide detailed information about the design of confinement to nodal zones. In addition, studies on reinforcement-confined nodal zones are limited. It is still unclear if the effective strength of nodes can be enhanced by providing confining reinforcement.

The study presented in this chapter, as part of Project 0-7039, aims to experimentally investigate the effect of confining reinforcement on nodal zones. The study includes three specimens of deep beams. Each specimen is designed to have two different confinement patterns to evaluate the relationship between confining reinforcement ratio and nodal strength.

5.2. Experimental Program

5.2.1. Specimen Design

5.2.1.1. Design Principles

The structural configuration of deep beam specimen was chosen based on the experimental program of Project 0-5253 to facilitate direct comparison. The control specimen, which was without confinement in the nodal zones, was taken as Specimen II-03-CCC2021 from Project 0-5253. The specimen served the purpose of investigating the effect of triaxial confinement on nodal strength, which made it suitable to be the control specimen in the current study.

As shown in Figure 5-1, the control specimen had cross-sectional dimensions of 21 inches in width and 42 inches in height. Longitudinal reinforcement on the tension side consisted of twelve No. 11 bars to ensure sufficient flexural capacity. Similarly, the compression side had six No. 11 bars as longitudinal reinforcement. The arrangement of longitudinal reinforcement led to an effective depth (d) of 38.6 inches.

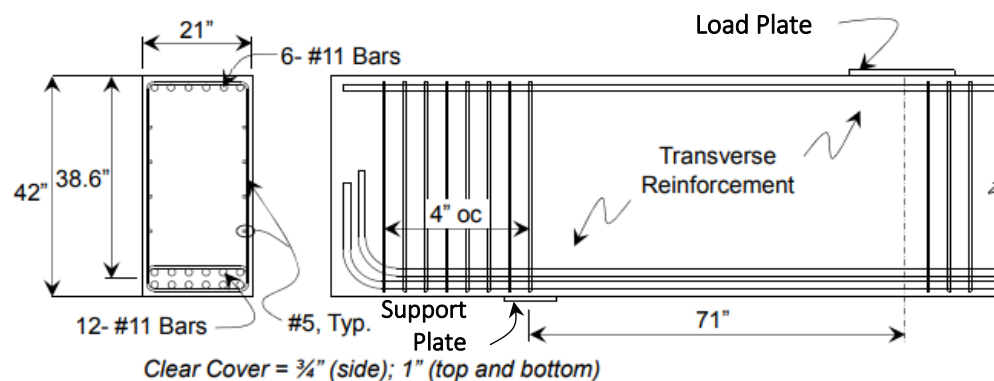


Figure 5-1 Control specimen from Project 0-5253 (figure from Report No. 0-5253-1)

The load was planned to be applied through the load plate (forming a CCC node), and reaction was provided through the support plate (forming a CCT node). Between the support plate and the load plate was the area of interest where the major diagonal strut was located, as shown in Figure 5-1. Within the area of interest, No. 5 closed stirrups at 9.5 inches and No. 5 horizontal bars at 6.6 inches were provided to maintain the minimum crack control reinforcement. Outside of the area of interest, No. 5 closed stirrups at a spacing of 4 inches were provided to eliminate undesired damages and failures. The support plate and the load plate were separated by a distance of 71 inches (namely, the shear span, $a = 71$ in.) to maintain a shear span-to-depth ratio (a/d) of 1.85. The setup made the angle of the major diagonal strut approximately 26 degrees. The exact angle varied due to slightly different material properties, which is introduced in later sections.

Confining reinforcement was imposed on selected nodal zones of the control specimen to create test specimens and investigate the potential enhancement in strength. Prior to designing the confinement, nonlinear finite element analysis was conducted on the control specimen. The preliminary finite element analysis showed that significant stress concentration occurred in a region adjacent to the load plate, as shown in Figure 5-2. In other words, the extended nodal zone of the CCC node of the major diagonal strut was subject to high stress. The CCC node was also considered to be subjected to high compressive stress. Therefore, the CCC node and its extended nodal zone were selected for confinement, as illustrated in Figure 5-3. Further, confining reinforcement was extended twice the height of the defined CCC node to maintain structural integrity. The same principle was applied to the CCT node near the support plate. It should be noted that the deep beam shown in the figures is upside down to reflect the actual loading system.

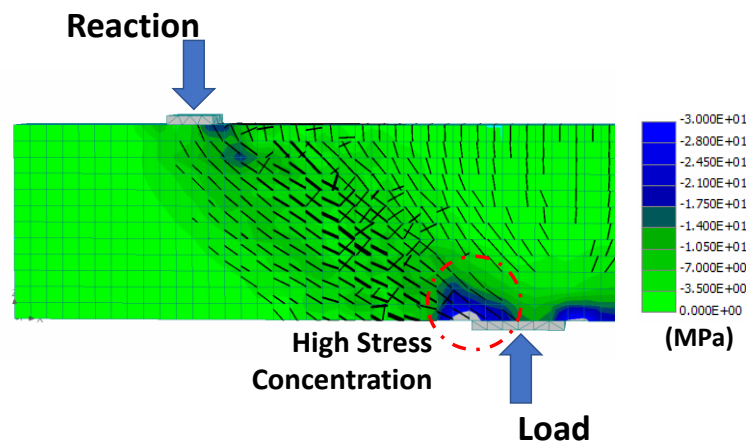


Figure 5-2 Stress concentration determined by preliminary finite element analysis results

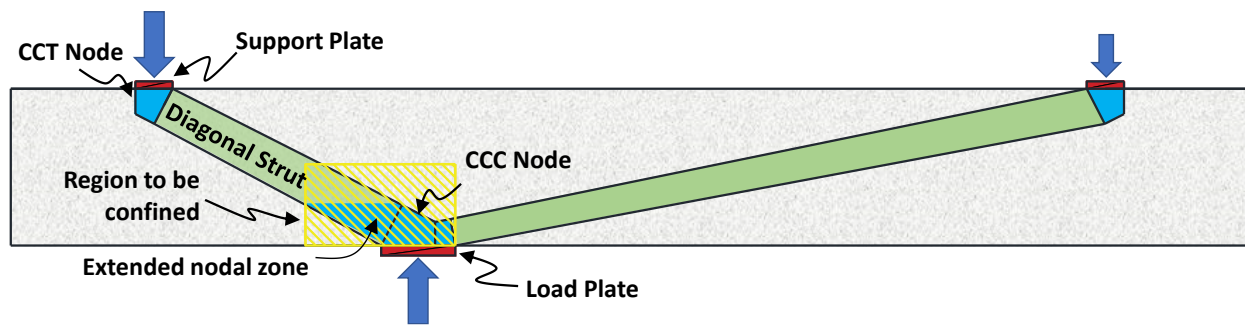


Figure 5-3 Region near CCC node to be confined

5.2.1.2. Test Matrix

Three deep beam specimens were developed, and each had two test regions, as shown in Table 5-1. The specimens were developed based on the principles introduced previously regarding the configuration and the reinforcement. That is, all the specimens had a width of 21 in. and a height

of 42 in. The main reinforcement design was the same as the control specimen from Project 0-5253 (Specimen II-03-CCC2021), and the confinement was added in the selected nodal zone. As the primary variable, the confinement pattern in each direction varied, as shown in Table 5-1 to investigate the effect of different confinement patterns.

Table 5-1 Test Matrix

Beam	Support Plate	Load Plate	Confinement at CCC Node			Confinement at CCT Node		
			Horizontal	Vertical	Through Thickness	Horizontal	Vertical	Through Thickness
I	10"x21"	20"x21"	#6@7"	#6@6"	18-#6	-	-	-
	10"x21"	20"x21"	#5@3.4"	#6@4.75"	48-#5	-	-	-
II	10"x21"	20"x21"	#6@7"	#6@6"	-	-	-	-
	10"x21"	20"x21"	#5@3.4"	#6@4.75"	-	-	-	-
III	10"x21"	20"x21"	-	-	-	-	-	-
	16"x21"	20"x21"	#6@7"	#6@6"	-	#7@4"	#6@5.5"	-

The first deep beam had only the CCC node confined, and the confinement consisted of all three orthogonal directions. The second deep beam also had only the CCC node confined, but no reinforcement through thickness was provided. As mentioned earlier, there were two tests for each deep beam specimen; the amount of confinement of the first test was less than that of the second. Lastly, the third deep beam had the first test without confinement and the second test with both nodes confined.

With the determined confinement design, it was convenient to express the patterns shown in Table 5-1 in terms of confinement ratios in the three directions. The horizontal and vertical confinement ratios, ρ_x and ρ_y , were given by

$$\rho_x = \frac{A_{sx}}{bs_x} \quad (5-1)$$

$$\rho_y = \frac{A_{sy}}{bs_y} \quad (5-2)$$

where A_{sx} is the total area of horizontal confining reinforcement within s_x ; A_{sy} is the total area of vertical confining reinforcement within s_y ; b is member width; s_x and s_y are bar spacing in the horizontal and vertical directions, respectively. Regarding rebars through the thickness, the confinement ratio ρ_z was defined by the total area of rebars through-thickness for confinement divided by the area of the region to be confined. In this case, the region to be confined had an area of 710 in-square. Therefore, the resulting confinement ratios of the tests are shown in Table 5-2

Table 5-2 Resulting Confinement Ratio

Beam	Confinement Ratio at CCC Node			Confinement Ratio at CCT Node		
	ρ_x (%)	ρ_y (%)	ρ_z (%)	ρ_x (%)	ρ_y (%)	ρ_z (%)
I	0.60	0.70	1.10	-	-	-
	1.20	0.88	2.10	-	-	-
II	0.60	0.70	-	-	-	-
	1.20	0.88	-	-	-	-
III	-	-	-	-	-	-
	0.60	0.70	-	1.43	0.76	-

5.2.1.3. Nomenclature

A nomenclature was developed to better identify the specimens, as shown in Figure 5-4. The first letter indicates the series number. The second part indicates where confinement was provided. The third part indicates the relative amount of confinement of the test region; *H* for the higher amount of confinement in the beam and *L* for the lower amount. The last part indicates if cross ties were used in the test region.

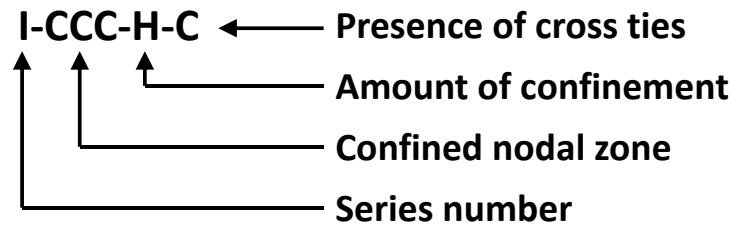
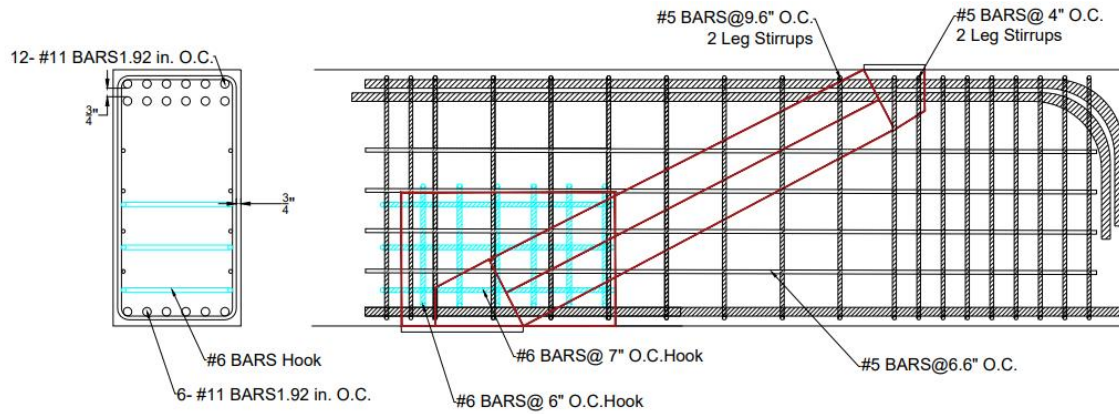


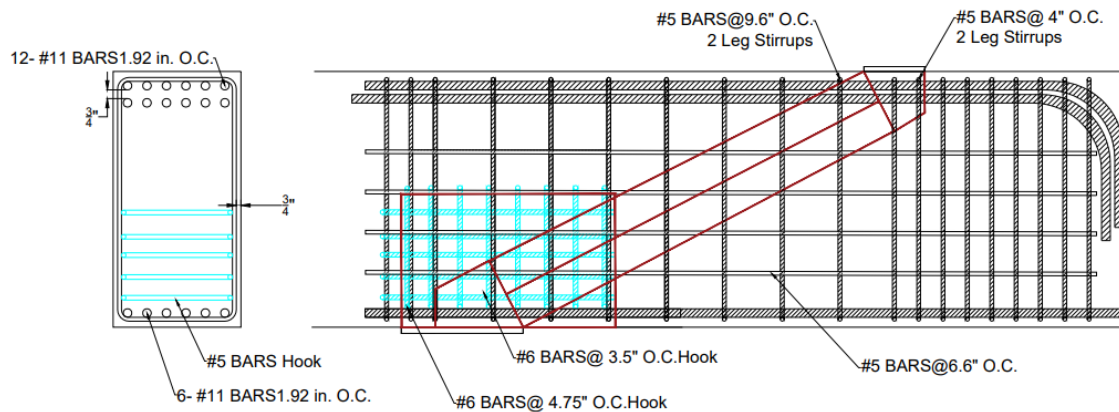
Figure 5-4 Nomenclature

5.2.1.4. Specimen Details

In the first test region of the first beam (Specimen I-CCC-L-C), three horizontal No. 6 hooked bars spaced 7 inches apart and six No. 6 vertical hooked bars spaced 6 inches apart were provided on each side of the beam. In addition, eighteen No. 6 hooked bars were provided across the thickness as crossties. For the second test region (Specimen I-CCC-H-C), a greater amount of confining reinforcement was provided to reach a higher potential strength. In particular, five No. 5 horizontal hooked bars spaced at 3.4 inches and eight No. 6 vertical hooked bars spaced at 4.75 inches were provided on each side of the beam. Also, forty-eight No. 5 hooked bars were provided as crossties. In this beam, no additional confinement was provided near the support plate. Details of the first beam are shown in Figure 5-5.



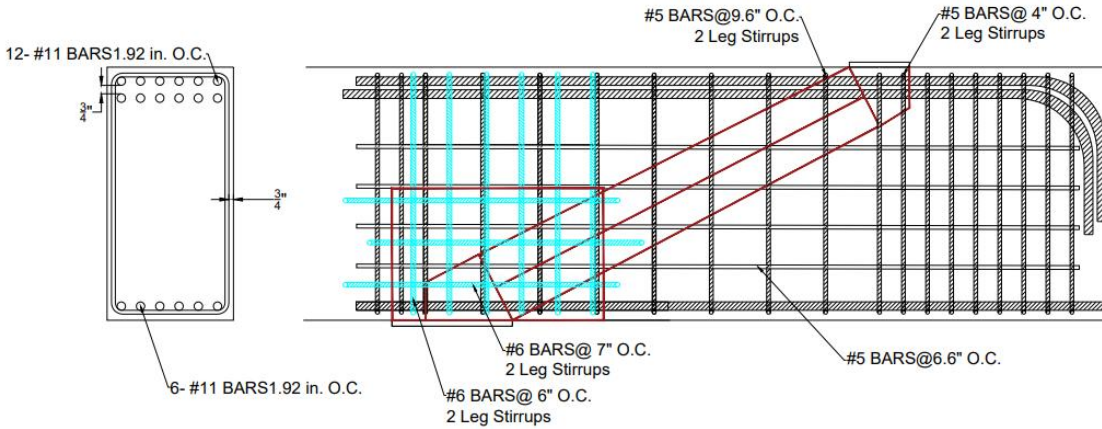
(a) Specimen I-CCC-L-C



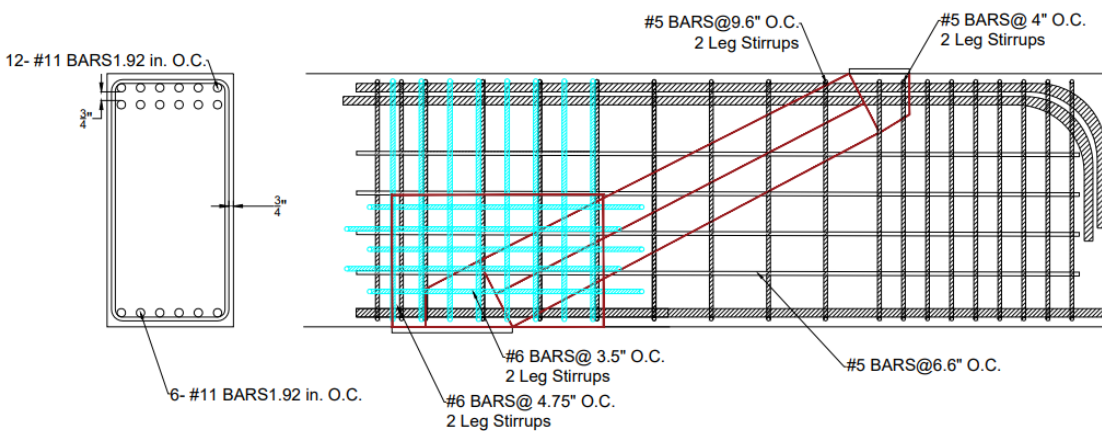
(b) Specimen I-CCC-H-C

Figure 5-5 Design of beam I

The design of the first beam caused congestion in both the test regions, provided the number of hooked bars and hooked cross ties. To improve constructability but maintain potential efficiency, the same amount of confining reinforcement in different arrangements was provided to the second beam for both Specimens II-CCC-L and II-CCC-H. As shown in Figure 5-6, vertical hooked bars were replaced with closed stirrups at the same spacing to avoid clashes. Horizontal hooked bars were replaced with longer straight bars as well. Furthermore, all cross ties were removed, as the first series test showed they were barely engaged, which is introduced in Section 5.3.4.



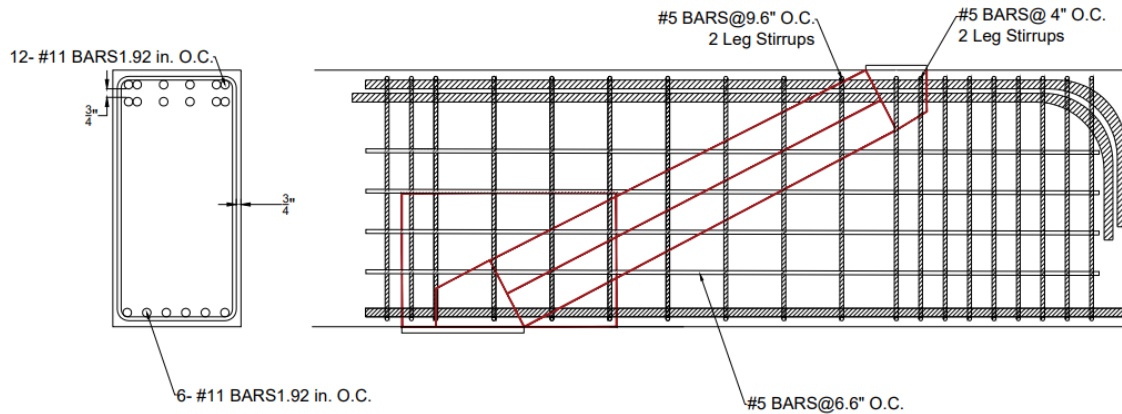
(a) Specimen II-CCC-L



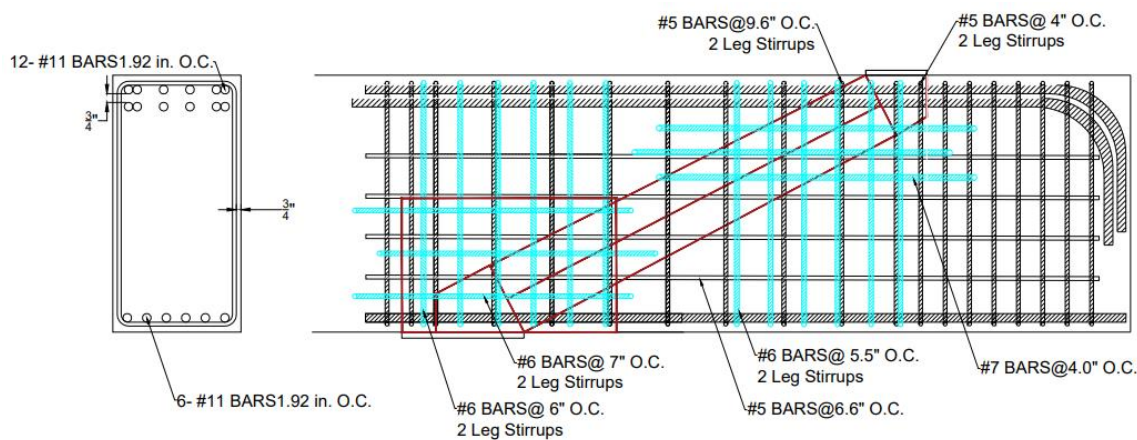
(b) Specimen II-CCC-H

Figure 5-6 Design of beam II

The third beam was designed to have one test region acting as another control group and to have the other test region with both the CCC and the CCT nodes confined. For the first test, no confining reinforcement was provided. Identified as Specimen III-Control, the test was technically a replica of Specimen II-03-CCC2021 in Project 0-5253. As Project 0-5253 showed, test shear strength can have widely scattered data; therefore, one replica was included in the third beam for direct comparison. The second test region had the CCT node confined and attached to a larger bearing plate to ensure failure at the CCC node. This was done with the expectation that the modification would better quantify the effects of the confinement at the CCC node. Details of the third beam are shown in Figure 5-7.



(a) Specimen III-Control



(b) Specimen III-CCC/CCT-L

Figure 5-7 Design of beam III

5.2.2. Fabrication of Specimens

5.2.2.1. Concrete Mixture Design

Concrete was selected to closely match the concrete mixture used in Project 0-5253 to minimize unwanted effects due to variations in concrete compressive strength. The design compressive strength of the concrete was 3600 psi to 5000 psi to match both TxDOT common practice and Project 0-5253. Detailed information for the concrete mixture design is shown in Table 5-3. When placing concrete for each deep beam specimen, standard 4-inch-by-8-inch cylinders were made according to ASTM C31 for material tests. Compression tests were conducted according to ASTM C39.

Table 5-3 Concrete mixture design

Item	Description	Quantity
Cement	ASTM C150 Type I/II	332 lb/cy
Fly Ash	Class F	110 lb/cy
Coarse Aggregate	3/4" Dolomite	1930 lb/cy
Fine Aggregate	Concrete Sand	1455 lb/cy
Water	-	30 gal
Slump	-	6 to 8 in

5.2.2.2. Steel Reinforcement

All specimens in this experimental program used Grade 60 rebar, complying with ASTM A615 requirements. Each size of the reinforcement used in each specimen was sampled for tensile testing according to ASTM A370. Three coupons were tested for each bar size.

5.2.2.3. Construction

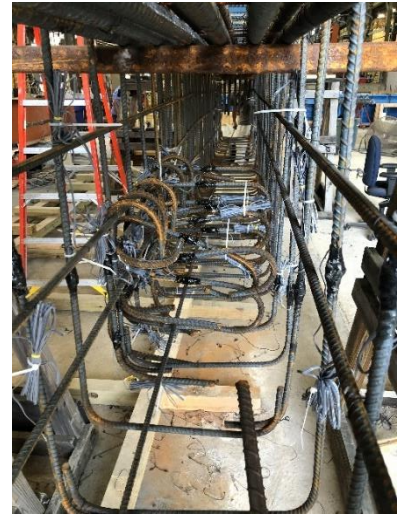
For each specimen, the main rebar cage was first fabricated. Four wooden chairs and two square steel pipes were used to support longitudinal reinforcement on the tension side. Several wooden spacers were used to position the longitudinal reinforcing bars correctly. Closed stirrups were then distributed over the length, and web horizontal crack control reinforcement was positioned according to the plan. After the first part of the reinforcement was built, confining reinforcement was placed into the cage, as was longitudinal reinforcement on the compression side. The procedure is shown in Figure 5-8.



(a) Top longitudinal rebar



(b) Stirrups and web reinforcement



(c) Confining reinforcement



(d) Confined region

Figure 5-8 Fabrication of rebar cage

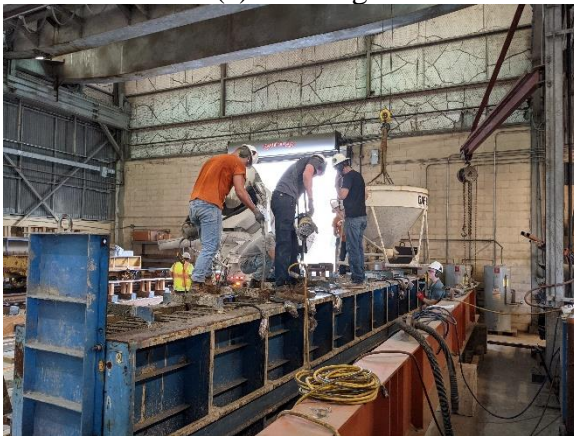
After being built, the entire rebar cage was craned into the steel formwork to be prepared for a cast. The steel formwork had wood support plates to lift the bottom of the formwork to the desired height. In addition to portable vibrators, external pneumatic vibrators on the side forms were activated during the cast for consolidation. The top surface was finished with wooden screeds after the form was filled with concrete. In the meantime, concrete cylinders were made for material testing. The procedure is shown in Figure 5-9.



(a) Forming



(b) Casting



(c) Vibrating



(d) Finishing



(e) Concrete cylinder samples

Figure 5-9 Cast of deep beam specimen

As shown in Figure 5-10, building a heavily reinforced confining zone was one of the greatest difficulties of this process. With a high amount of confinement and many hooked bars and crossties installed in the first deep beam specimen, congestion and conflicts with the main rebar cage were unavoidable. Although the specimens were carefully vibrated using portable vibrators and form vibrators for concrete consolidation, honeycombing still occurred in the test region of I-CCC-H-C. The honeycomb was repaired with Sika Top 123 Plus with a modulus of elasticity of 2940 psi

and a 28-day compressive strength of 6 ksi. The modulus of elasticity was selected to cope with the deformation of concrete during the test.

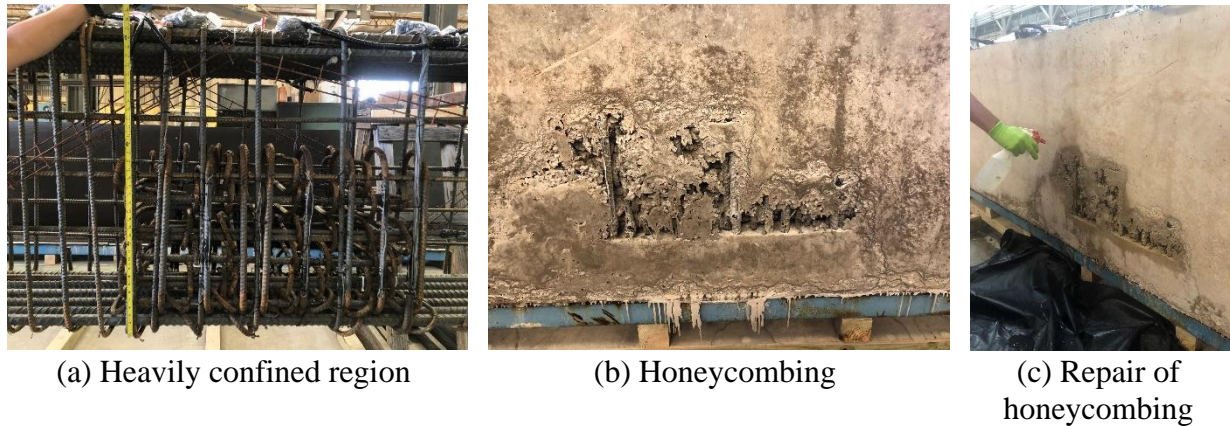


Figure 5-10 Cause of honeycombing and repair

As mentioned previously, the congestion was improved by replacing vertical hooked bars with closed stirrups and by replacing horizontal hooked bars with straight bars. In addition, crossties were removed, as shown in Figure 5-11. As a result, in spite of having a high amount of confinement, conflicts and congestion were almost eliminated for Specimen II-CCC-H.

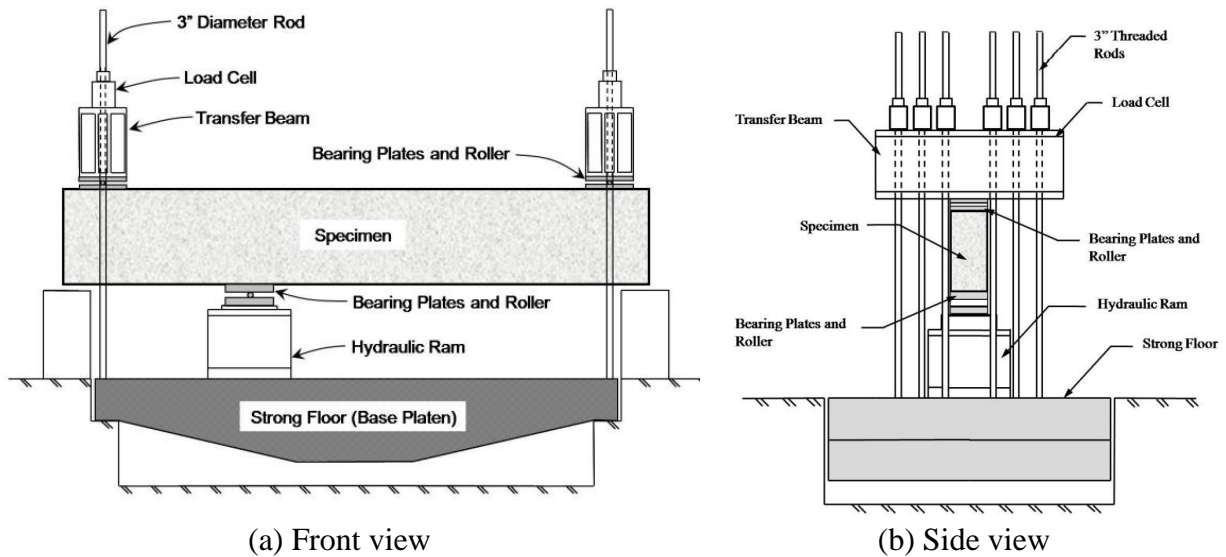


Figure 5-11 Improved design of confinement

5.2.3. Test Setup and Instrumentation

For consistency, the loading frame and instrumentation layout were the same as those originally used in Project 0-5253, as shown in Figure 5-12. Six 3-inch threaded rods were used on each end of the specimen to provide a reaction. Through each of the threaded rods, a load cell with a capacity of 500 kips was anchored with a steel plate and an anchoring nut to measure the magnitude of reactions. A transfer beam was sandwiched between the load cells and the support plate on each

side to distribute the load evenly. Under the support plate, a roller was placed to allow rotation of the end. The load was applied using a 2000-kip hydraulic ram through steel plates and a roller underneath the specimen.



(c) Test frame photo

Figure 5-12 Testing setup (from TxDOT 0-5253-R1)

Four linear potentiometers were used to monitor displacements at different positions: the center of each support, mid-span, and the center of the load plate, as shown in Figure 5-13. Strain gauges were also used to monitor strain in the confining reinforcement during each of the tests. A National Instruments (NI) data acquisition (DAQ) was used to record readings from each sensor.

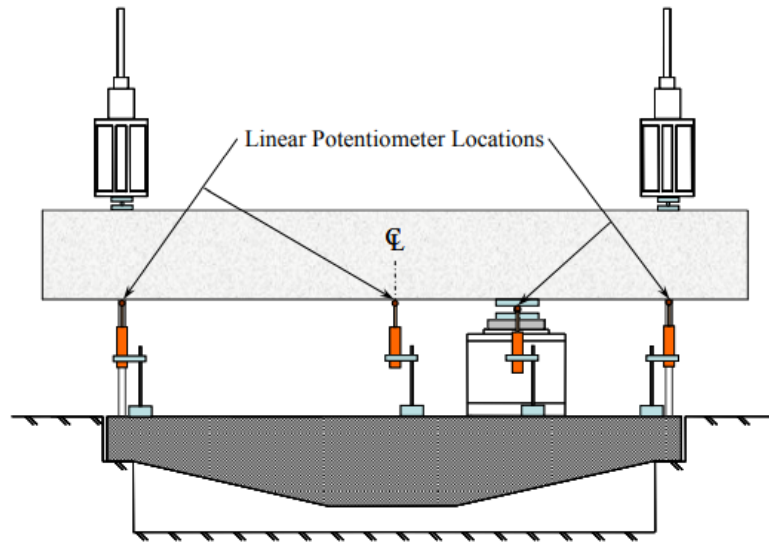


Figure 5-13 Locations of linear potentiometers (from Project No. 0-5253-1)

Strain gauges were distributed at multiple places to monitor the engagement of crack control reinforcement and confining rebars. In general, for crack control reinforcement, strain gauges were installed along the centerline of the idealized diagonal strut, as shown in Figure 5-14. Both horizontal and vertical reinforcement were strain-gauged at positions that intersected the centerline.

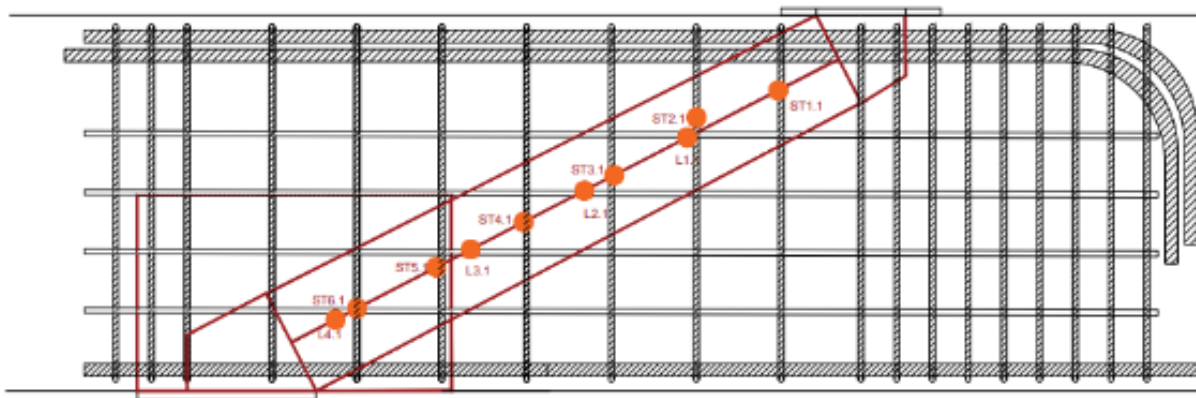


Figure 5-14 Strain gauge layout on crack control reinforcement

Furthermore, rebars that consisted of confinement at the CCC node were also strain-gauged at selected positions. For Series I, in general, each of the first five vertical confining rebars was instrumented with two strain gauges over its height; each horizontal confining rebar was instrumented with three gauges over its length; each of the crossties was strain-gauged at the middle. For Series II and Specimen III-CCC/CCT-L, the strain gauge layout was simplified as strain gauges above the load plate had low strain readings. The updated layout included three strain gauges distributed over the height of each of the three vertical confining rebars. The updated layout

also included two strain gauges distributed over the length of the horizontal confining reinforcement outside the region above the load plate. Examples of the strain gauge layouts on confinement are illustrated in Figure 5-15.

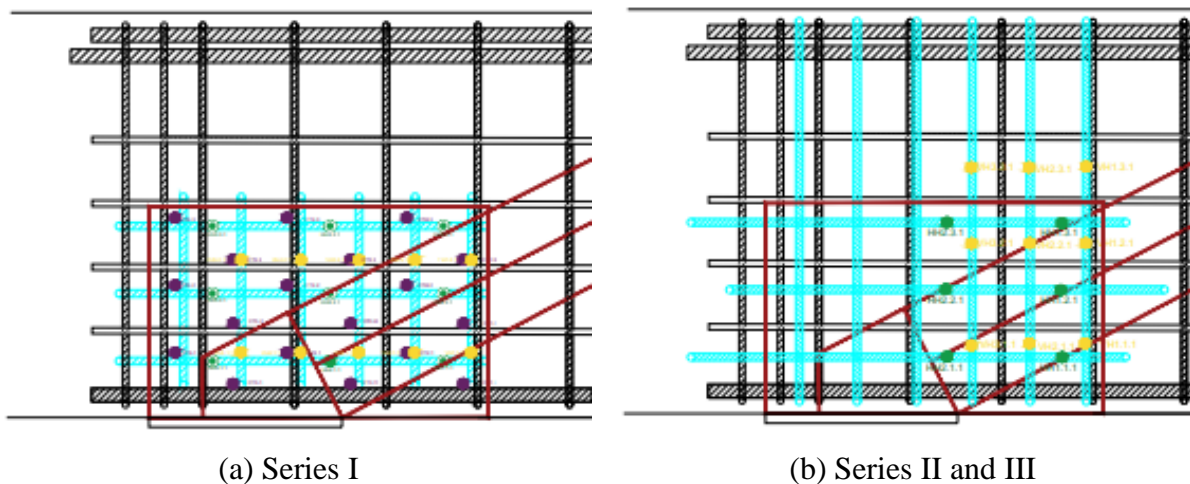


Figure 5-15 Example strain gauge layout on confining reinforcement

In addition to traditional sensors, a digital image correlation (DIC) system was used to capture the strain field within the nodal and extended nodal zones. Therefore, DIC speckle patterns were applied over 35 in. by 20 in. above the load plate to enclose the region of confinement. A photo of the complete test setup is shown in Figure 5-16.

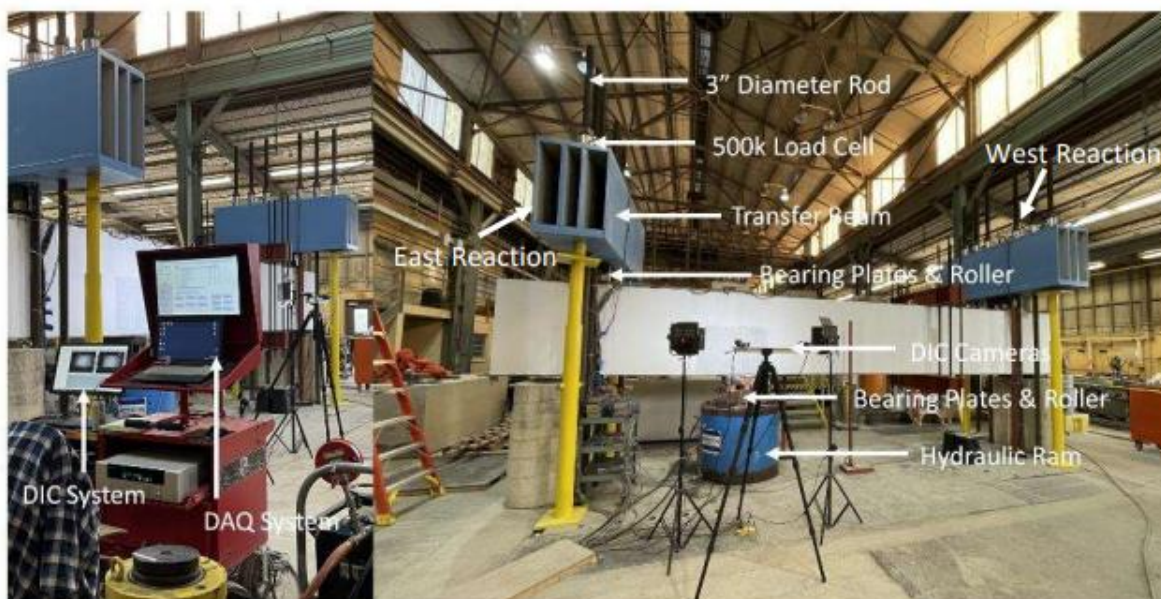


Figure 5-16 Test setup

Before each test, the hydraulic loading ram was placed in position, and the loading plate setup was centered on top of the hydraulic ram. The specimen was placed between the tie-down rods, rested

on the concrete support, and centered. A manual jack was used to level out the beam. A metal shim was placed under the beam to keep it leveled. Steel reaction plates were placed into positions with hydro stone to ensure full contact between the beam and pin joint steel plate due to surface roughness and leveling of the steel pin joint setup. The reaction beams then fed through the tie-down rods, were leveled, and rested on the yellow supporting column. Then, the twelve 500-kip load cells were fed through the rods, and nuts were tied. Before the test, the specimen was preloaded with approximately 10% of the anticipated capacity to be in contact with the reaction beam. Then, nuts were hand-tied to about 1 kip to 5 kips based on load cell reading to ensure even loading across all six tie-down rods in order to prevent torsional movement and overloading a particular rod during testing. Linear potentiometers were then installed under the specimen.

5.2.4. Test Procedure

The load rate was 1 kip per second, and at every 10% increment of estimated beam capacity, loading was paused to observe and mark cracks on the beam, as shown in Figure 5-17. This loading and marking process was repeated until a diagonal shear crack was almost fully formed based on visual observation, or 80% of the expected failure load was reached. Afterward, the hydraulic ram would load the deep beam to failure, defined as a load drop to approximately 80% of the peak load after the peak load was reached.



Figure 5-17 Concrete crack marking and measuring

Before testing the second testing region of the same beam, post-tension clamps were added to the failed regions to restore sufficient shear strength, as shown in Figure 5-18. The post-tension force in each set of clamps was loaded to 1.1 times the predicted reaction force in the nearby support.

After the clamps were installed, the hydraulic ram was relocated to the second test region for testing. The exact same testing procedure was applied for the second test.



Figure 5-18 Post-tension clamping as external protection

5.3. Test Results

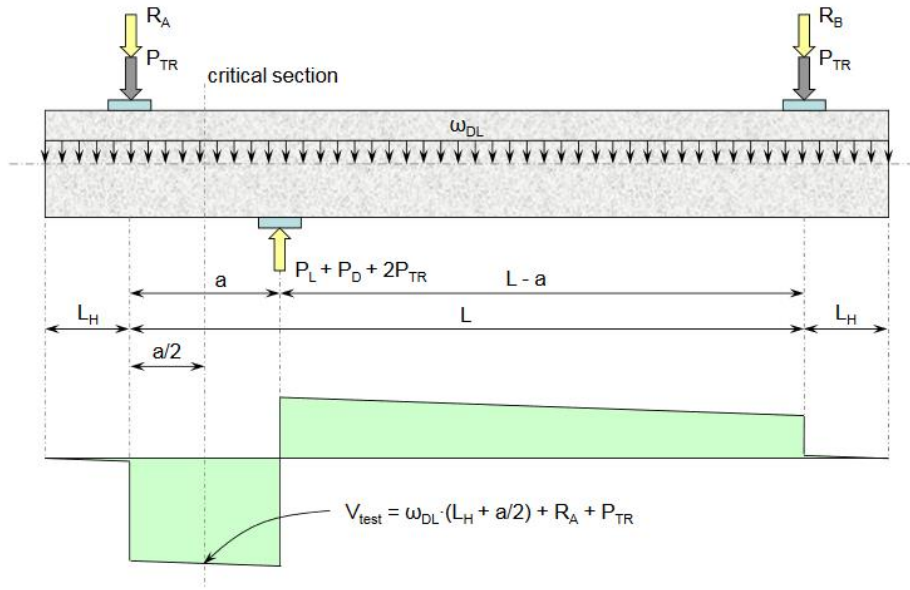
5.3.1. Summary of Strength Results

Table 5-4 summarizes the results of the tests performed for this task. The test results of selected control specimens from Project 0-5253 are also provided for comparison. In the table, R_{test} represents the total reaction acting on the support plate ($R_A + P_{TR}$); P_{test} represents the total applied load on the load plate ($P_L + P_D + 2P_{TR}$); and V_{test} is the total shear force applied in the middle of the shear span, as illustrated in Figure 5-19. The values of R_{test} , P_{test} , and V_{test} were determined considering the self-weight of the specimen (ω_{DL}) and the weight of the spreader beam (P_{TR}) on the support plate. The compressive strength of concrete (f'_c) was derived from the cylinder tests, and the yield strengths of longitudinal reinforcement (f_{yl}), confinement (f_{yc}), and web reinforcement were derived from steel coupon test.

Table 5-4 Summary of Strength Results

Series	Specimen ID	b (in.)	d (in.)	f'_c (ksi)	$f_{y,\#11}$ (ksi)	$f_{y,\#5}$ (ksi)	$f_{y,\#6}$ (ksi)	$f_{y,\#7}$ (ksi)	R_{test} (kip)	P_{test} (kip)	V_{test} (kip)
I	I-CCC-L-C	21	38.6	4.03	66.0	67.0	66.7	-	539	795	552
	I-CCC-H-C	21	38.6	3.86	66.0	67.0	66.7	-	493	692	507
II	II-CCC-L	21	38.6	3.68	66.5	63.9	65.9	-	480	719	494
	II-CCC-H	21	38.6	3.84	66.5	63.9	65.9	-	503	704	516
III	III-Control	21	38.6	3.21	67.1	68.9	-	-	440	617	454
	III-CCC/CCT-L	21	38.6	3.35	67.1	68.9	66.1	76.3	553	819	567
Project 0-5253	II-03-CCC2021	21	38.6	3.29	64.0	65.0	-	-	486	722	500
	III-1.85-03*	21	38.6	4.99	69.0	64.0	63.0*	-	398	597	412
	III-1.85-03b*	21	38.6	3.30	69.0	62.0	67.0*	-	457	681	471

* The two specimens did not include #6 bars. Yield strength denoted in the cell corresponding to the yield strength of the horizontal web reinforcement reported in Project 0-5253.



where, $P_L = R_A + R_B$ $L = 255.25''$
 $P_D = \omega_{DL}(2L_H + L)$ $L_H = 38.375''$
 $P_{TR} = 7.8 \text{ kip}$
 $\omega_{DL} = 0.92 \text{ kip/ft}$

Figure 5-19 Force diagram of a typical specimen test (adopted from Project 0-5253)

5.3.2. Failure Patterns

5.3.2.1. Series I: Confinement with Cross Ties

Figure 5-20 shows the cracking patterns of Specimens I-CCC-L-C and I-CCC-H-C on both the front and back sides after failure. Both test regions showed signs of crushing concrete or severe cracks proximal to the load plate. In other words, the extended nodal zone of the CCC node exhausted its strength. On the other hand, the region near the support plate (i.e., the CCT node) seemingly experienced less severe damage. No evident sign of crushing of concrete in the nodal zone or in the extended nodal zone of the CCT node. That is, concrete did not necessarily crush on the strut-to-node interface.

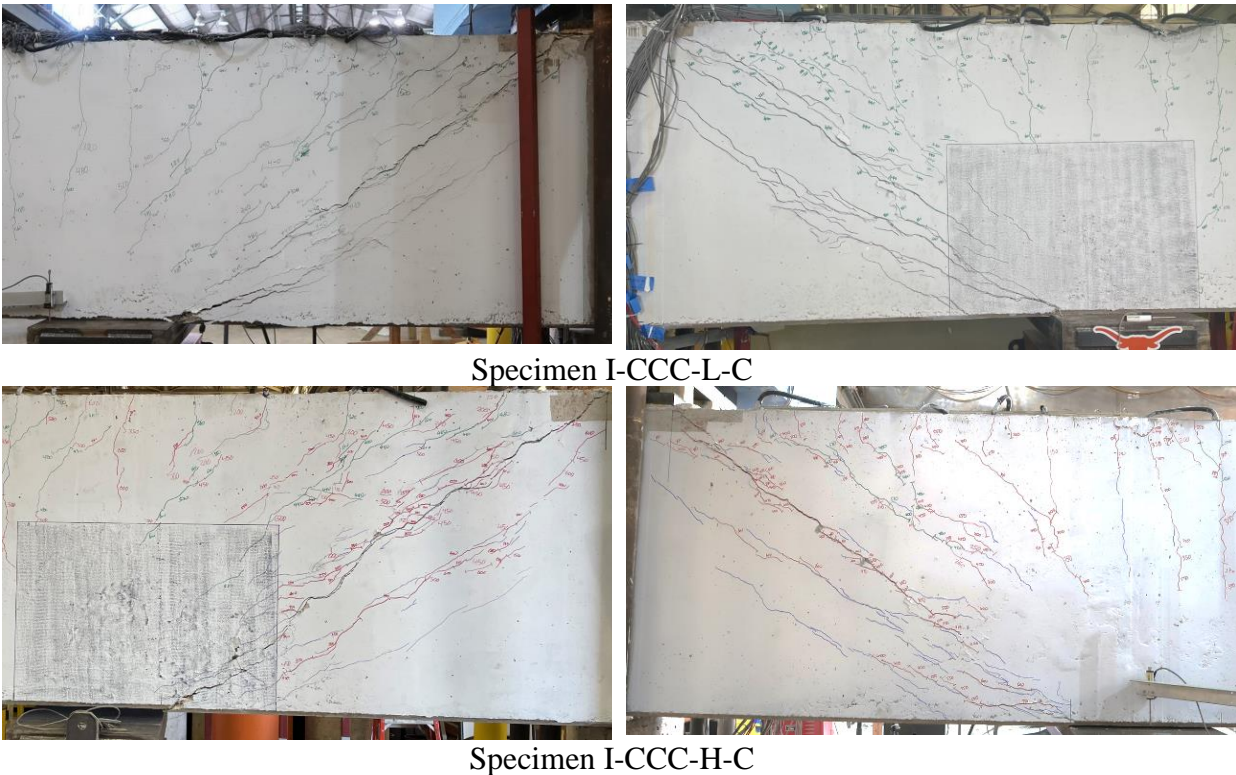
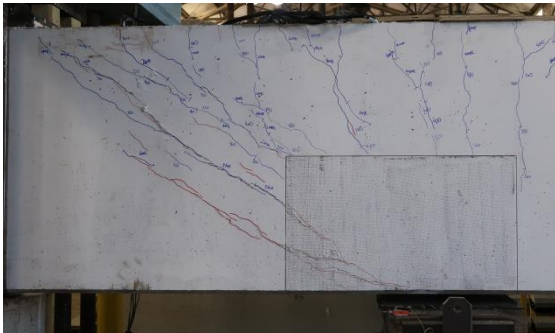


Figure 5-20 Crack pattern at failure of Series I specimens

5.3.2.2. Series II: Confinement without Cross Ties

As shown in Figure 5-21, similar failing damage patterns were observed in the test of Specimen II-CCC-L. The extended nodal zone of the CCC node experienced some crushing of concrete, but the area near the support plate (the CCT node) did not exhibit significant crushing or severe damage. However, in addition to some signs of crushing at the load plate, Specimen II-CCC-H had more severe cracking near the support plate. The crushing of concrete around the CCC node was an important controlling factor of the peak load and the failure mechanism for both specimens.



Specimen II-CCC-L



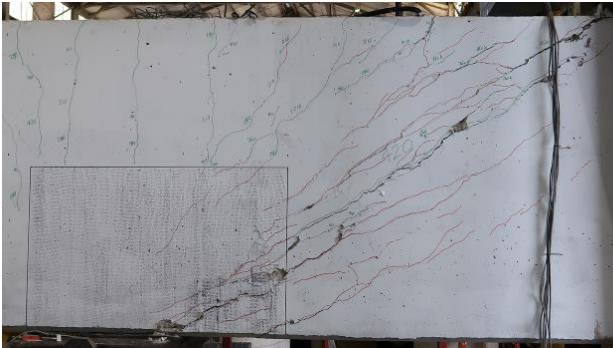
Specimen II-CCC-H



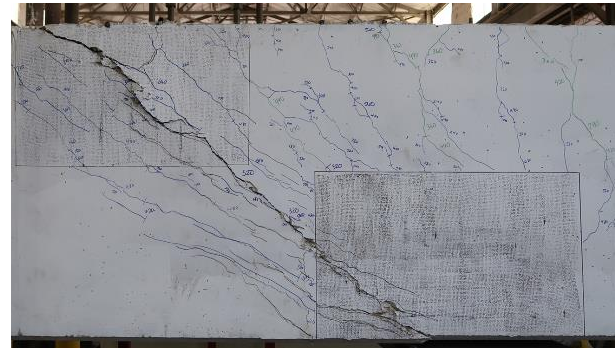
Figure 5-21 Crack pattern at the failure of Series II specimens

5.3.2.3. Series III: Multiple Purpose

As shown in Figure 5-22, both Specimens III-Control and III-CCC/CCT-L had crushed concrete near the strut-to-node interface of the CCC node. There was also some crushing and spalling of concrete in the middle of the diagonal strut. Moreover, both specimens showed severe cracking near the edge of the support plate, indicating the CCT node had plausibly maxed out its capacity at failure. It was likely that both the CCC node and the CCT node were controlling the peak load.



Specimen III-Control



Specimen III-CCC/CCT-L

Figure 5-22 Crack pattern at the failure of Series II specimens

5.3.3. Visual Observations

5.3.3.1. Overall Crack Propagation

The crack pattern of each test at failure showed similarities, with the shear crack developing between the edges of the load plate and the support plate, delineating the idealized strut defined in Project 0-5253. The cracking consisted of a primary crack connecting the inner edge of the load plate to the edge of the support plate and surrounding cracks, which were identified as secondary and tertiary cracks. The primary crack had the largest crack width compared to the surrounding cracks. The general crack pattern is shown in Figure 5-23.

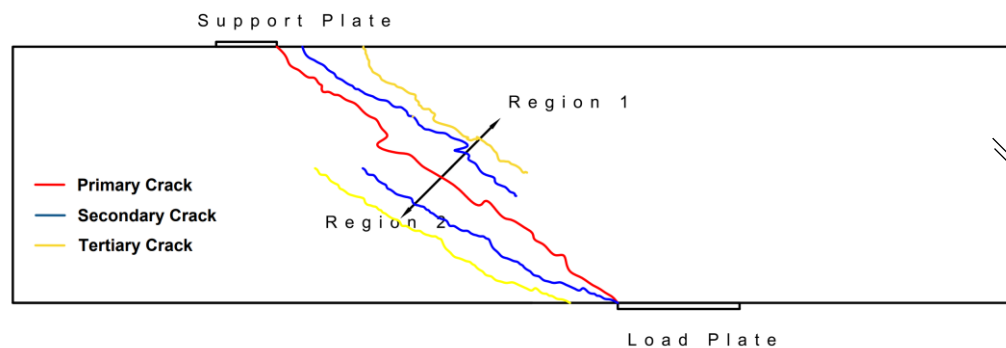


Figure 5-23 Crack pattern at failure

Regarding the order of crack formation, in the first five tests, cracks developed similarly, with the primary crack initiating in the early stage, typically in the middle of the strut. It then propagated from the initial crack toward the support and load plates. The secondary shear cracks proximal to Region 1 slowly formed from the propagation of the flexural crack. The secondary shear cracks did not fully develop into the nodes during the test. The sixth specimen, on the other hand, had cracks more evenly distributed in a larger area. More cracks continuously propagated between the load plate and the support plate.

5.3.3.2. Growth of Crack Width

The maximum observed crack width of each test was plotted at each load increment versus the load, as shown in Figure 5-24. The load shown in the figure is the V_{test} normalized by the square root of the compressive strength of the concrete times the effective shear area. Instead of f'_c , the square root of f'_c was selected because crack width was considered a parameter related to the tensile strength of concrete. The maximum crack width at each load increment was found at the mid-span or slightly close to the support plate. In the figure, square marks are used for Series I; triangular marks represent Series II; circles stand for Series III. Also, darker colors are used for the first test of a specimen, while brighter colors are used for the second test for readability.

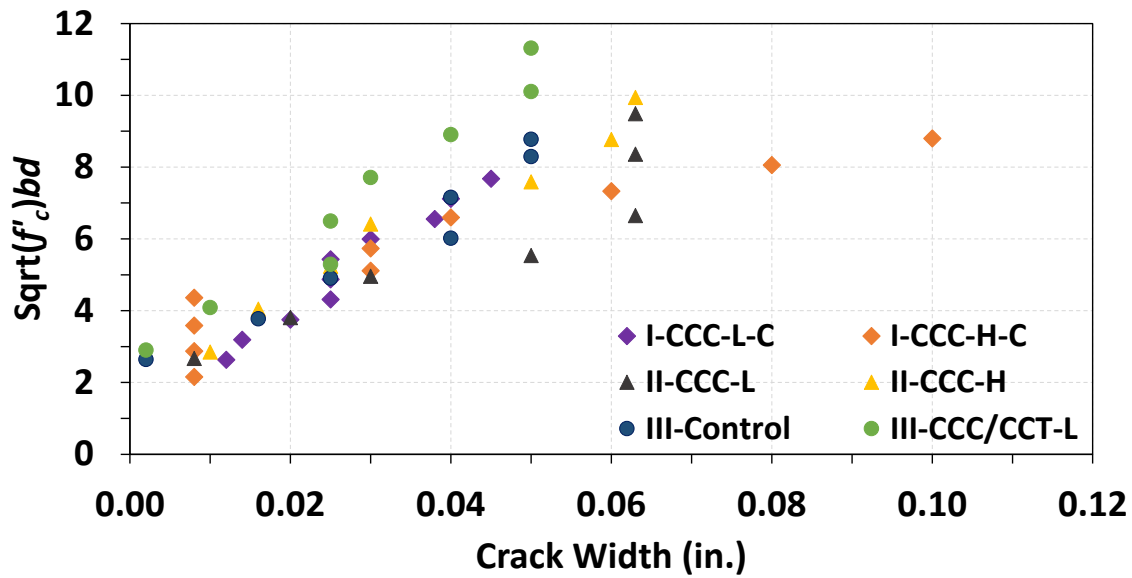


Figure 5-24 Growth of crack width versus normalized load

It can be seen from Figure 5-24 that the growth of the crack width of all specimens, except for Specimens I-CCC-H-C and II-CCC-L, follows a seemingly linear trend with regard to the normalized load. The slope does not obviously differ among specimens in Series I and II compared to Specimen III-Control, which had zero confinement. The observation indicates that confining only the CCC node, no matter how much confinement was provided, did not help control the maximum crack width or stiffen the shear region.

For Specimen III-CCC/CCT-L, which had both nodes confined, experienced an overall steeper slope of the growth of the crack width despite a jump at a load level of $5.29\sqrt{f'_c}bd$. It can be inferred that confining both nodes potentially led to higher shear stiffness and better crack control than other specimens. It can also be inferred that the transverse separation across the diagonal strut was lower than all the other specimens.

Specimens I-CCC-H-C and II-CCC-L demonstrated anomalies when the normalized load reached a level approximately of $5.5\sqrt{f'_c}bd$. Specimen I-CCC-H-C, which had a higher confinement ratio and crossties, exhibited a reduced slope until stopping crack marking. However, its companion specimens, Specimens I-CCC-L-C and II-CCC-H, did not undergo a similar softening. It is plausible that the honeycombing affected the overall shear stiffness. In addition, Specimen II-CCC-L had a jump when reaching a load of approximately $5.53\sqrt{f'_c}bd$, leading to the widest maximum crack width among all specimens at the load level. Nevertheless, the last two load increments did not further widen the maximum crack width of Specimen II-CCC-L, ending up with a similar maximum crack width to the other specimens.

In sum, whether softening or anomalies existed or not, when compared to Specimen III-Control, confining only the CCC node (specimens in Series I and II) behaved similarly or inferior in terms of crack control or the transverse separation across the diagonal strut. Confining the CCC and the CCT nodes simultaneously (Specimen III-CCC/CCT-L) contributed to shear stiffness, having better crack control and lower transverse separation of the diagonal strut.

5.3.4. Strains and Damage Patterns

In this section, the engagement of confining rebars near the CCC node and crack control reinforcement within the shear span are presented and discussed in terms of strain gauge readings. Damage patterns are superpositioned on the presented strain profile to assist the discussion.

5.3.4.1. Within Shear Span

5.3.4.1.1. Strain Data and Crack Patterns

Figure 5-25, Figure 5-26, and Figure 5-27 present inferred stress levels from the measured strains of selected positions on crack control reinforcement at a load level of approximately 95% of the peak load. The stress level in the figures is reflected in terms of the percentage of the yield stress by color darkness. That is, darker color means closer to the yield strength. In the figures, crack patterns and the idealized diagonal strut are superpositioned for comparison. Orange cracks indicate major cracks that were considered related to the ultimate failure.

It can be seen from the figures that compared to Specimen III-Control, specimens with only CCC nodal confined demonstrated a similar pattern. The primary crack related to the ultimate failure connects the diagonal of the idealized diagonal strut, while surrounding secondary cracks generally delineate the boundary of the idealized diagonal strut. A few shear cracks fall under the idealized diagonal strut. The crack pattern reveals that the ideal diagonal strut well enveloped the principle compressive stress for specimens with the CCC node confined or without confinement. However, for Specimen III-CCC/CCT-L, cracks spread larger than the region of the idealized diagonal strut and were distributed more evenly. It is evident that a larger volume of concrete was involved in contributing to resisting shear stresses.

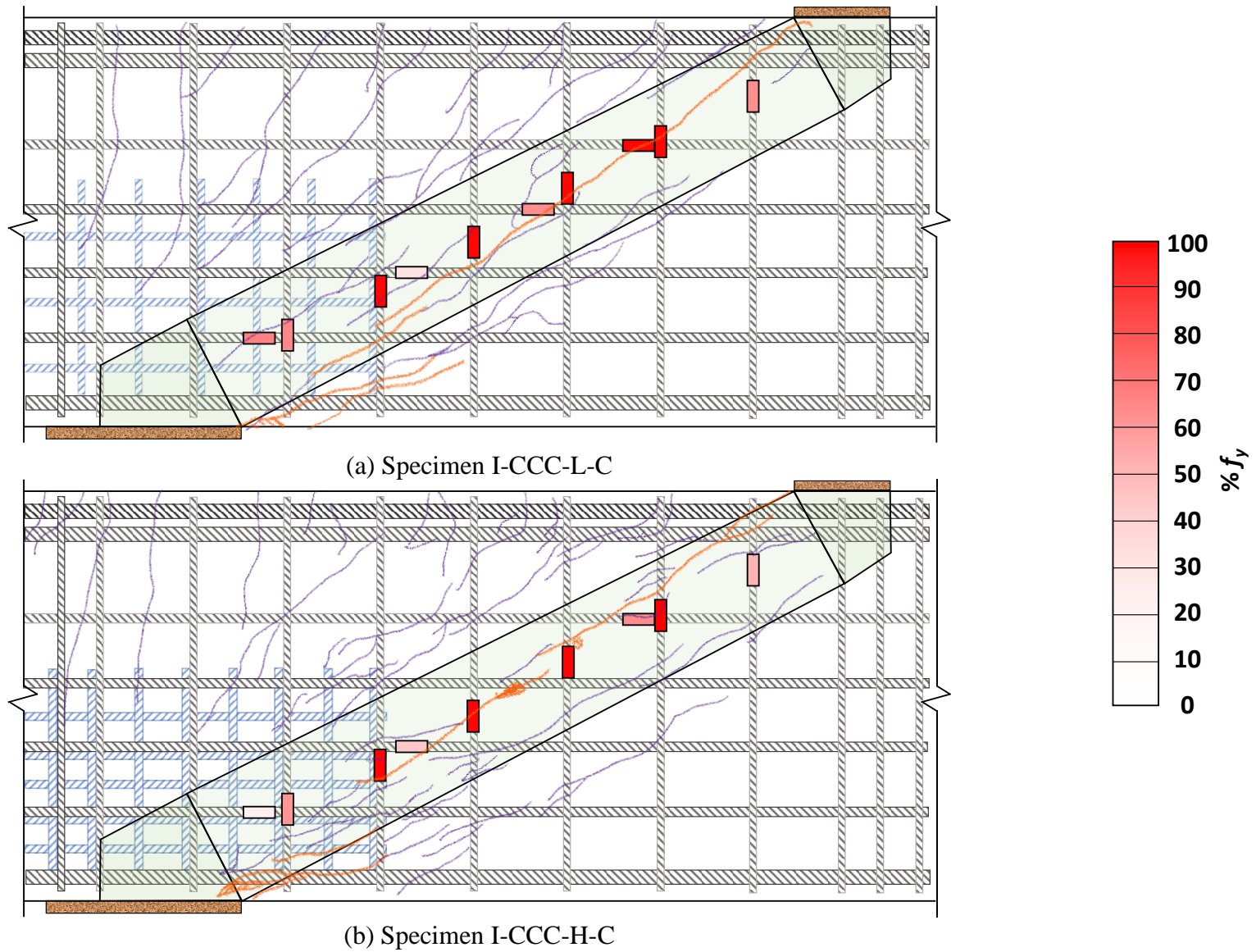


Figure 5-25 Strain readings and damage patterns of Series I

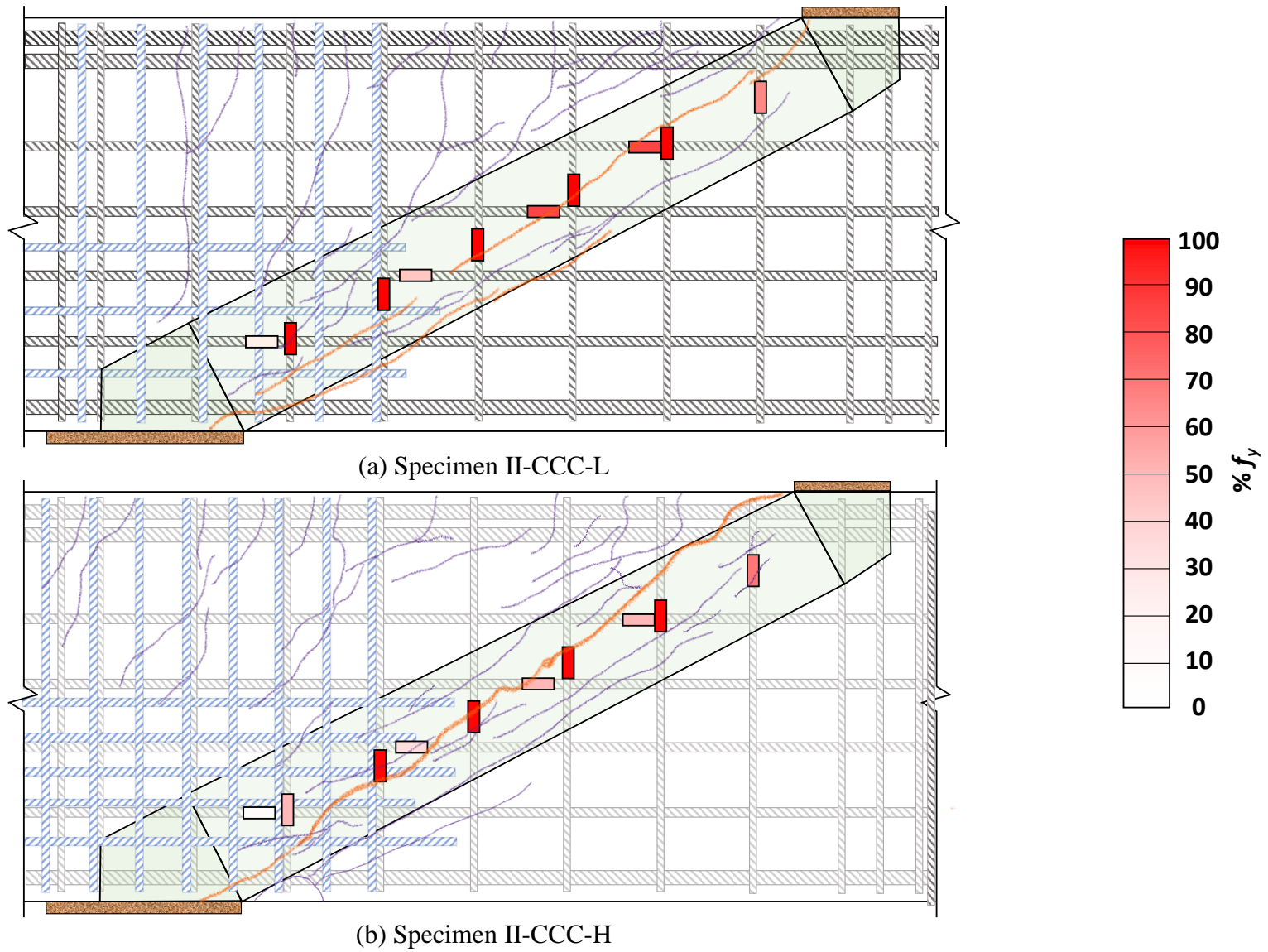
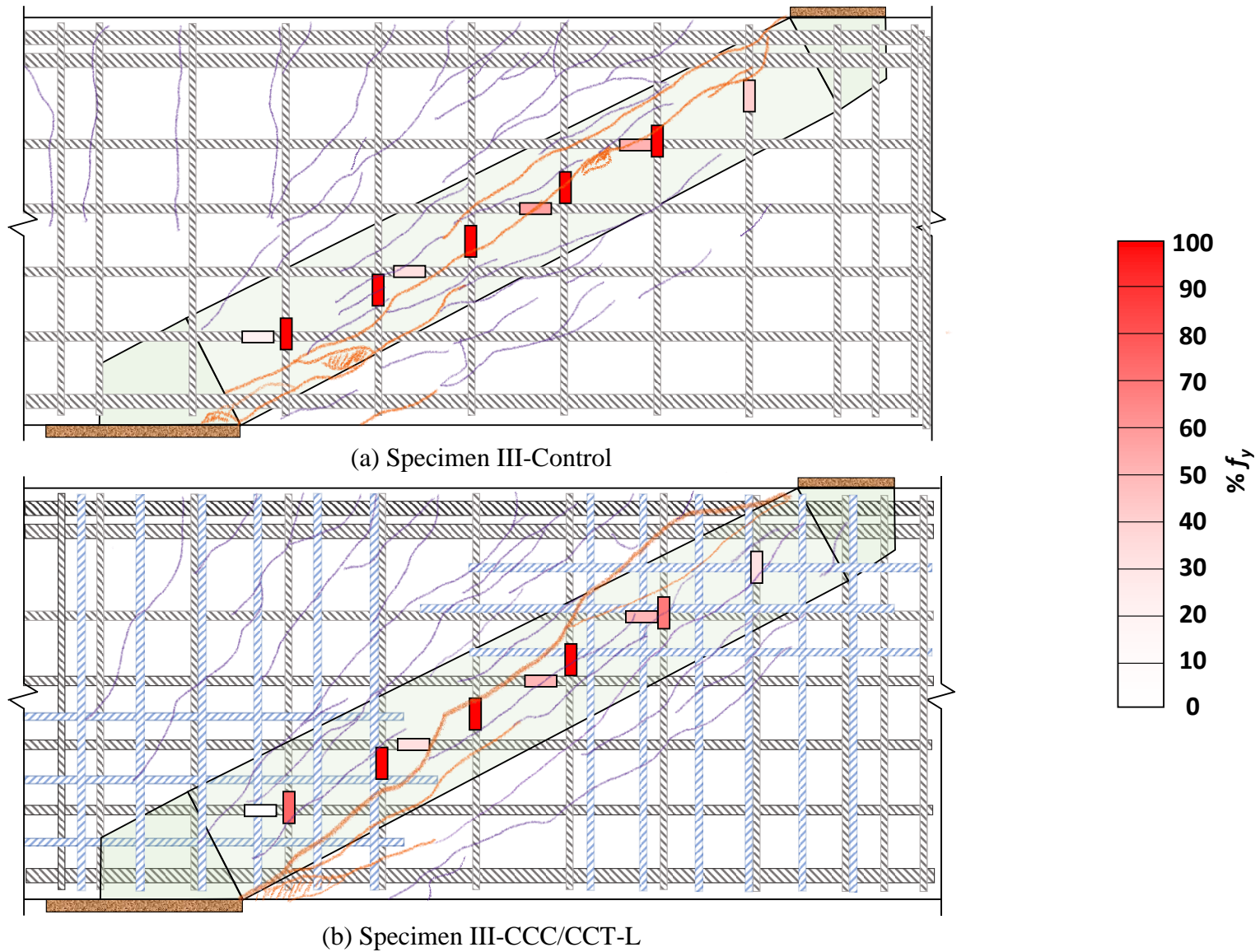


Figure 5-26 Strain readings and damage patterns of Series II



Taking a closer look at the crack distribution points out another shared behavior among specimens with the CCC node confined only and the control specimen; almost no cracks appeared close to the CCT node. Near the CCT node, only the splitting diagonal crack related to the failure appeared without a conspicuous sign of crushing concrete. Contrary to that, more distributed cracks appeared closer to the CCC node. In addition, a high amount of confinement in the extended nodal zone seemed to assist the distribution. That is, near the CCC extended nodal zone, a higher confinement ratio (Specimens I-CCC-H-C and II-CCC-H) was prone to having narrower cracks spreading in a wider area, while a lower confinement ratio (Specimens I-CCC-L-C, II-CCC-L) tended to have a couple of wide cracks, so did the control specimen without confinement. Different from all other specimens, Specimen III-CCC/CCT-L behaved uniquely. As the specimen had both nodes confined and the confinement almost extended through the entire diagonal strut, more cracks were able to distribute evenly within the shear span and connected both nodes.

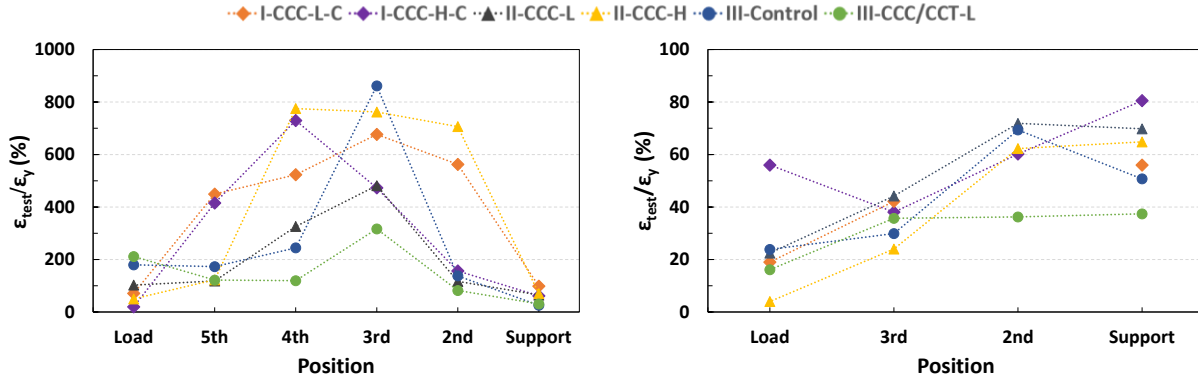
Several general trends can also be observed from the inferred stress levels along the diagonal strut. It should be noted that the third strain on the horizontal reinforcement was lost. None of the horizontal crack control reinforcement along the diagonal strut had yielded for all tested specimens at a load of 95% of the peak load. Also, the horizontal stresses appeared to have an increasing trend from the CCC node to the CCT node except for Specimen I-CCC-L-C. Specimen I-CCC-L-C was found to have the highest stress on the first horizontal web reinforcement, which is plausibly due to a crack crossing the gauged position, causing a stress concentration.

On the other hand, stresses in the middle four vertical web rebars exceeded the yield strength, while stresses in the bars near the CCC node and the CCT node were lower than the yield strength. There are two exceptions; Specimen III-Control had the bar near the CCC node yielded, and Specimen III-CCC/CCT had the second bar near the CCT node not yielded. Vertical reinforcement as confinement appeared to have taken part in controlling stress and strain levels within the nodal zones.

5.3.4.1.2. Strain Profile along Shear Span

As the discussion on stresses presented above does not reveal more information about the strain profile within the area of interest, strain readings of each specimen along the diagonal strut were plotted with regard to positions, as shown in Figure 5-28. The figure includes strain data obtained from both vertical and horizontal web reinforcement at $V_{test} = 400$ kips. A load of 400 kips was selected as one of the baselines for comparison because all specimens were able to reach this level. The horizontal axis indicates the distance from the CCC node. It can be seen from Figure 5-28(a) that all specimens, except for Specimen III-CCC/CCT, experienced not only yielding but also a significantly high level of strains ranging from 380% to 780% of the yield strain between the mid-span and the CCT node. The third strain gauge also indicates a high strain level for most specimens. Specimen III-CCC/CCT, on the other hand, was able to have all vertical web reinforcement remain unyielded at the load level. On the first vertical rebar near the CCC node, specimens with confinement experienced a lower strain level than Specimen III-Control did. It also appears that a

high confinement ratio further lowered the strain level. On the first bar near the CCT node, Specimen III-CCC/CCT-L still underwent the lowest strain, while other specimens had the bar remain unyielded.

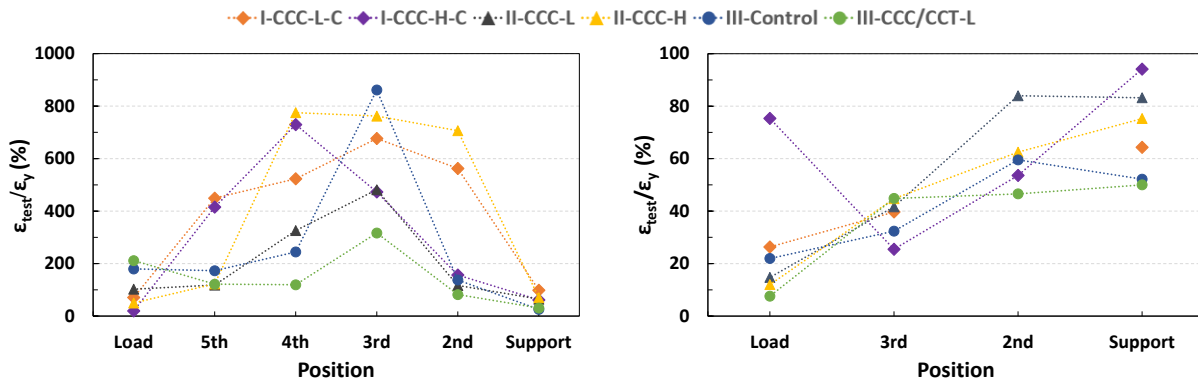


(a) Vertical web reinforcement

(b) Horizontal web reinforcement

Figure 5-28 Strain profile along shear span at 400 kip

Regarding the horizontal strain profiles, as shown in Figure 5-28(b), all strain readings remain at a low level, and the specimen with both nodes confined still had the lowest strain readings at the two locations near the CCT node. As the horizontal strain readings around the mid-span were much lower compared to the vertical strain readings, the transverse strain of the diagonal strut was mainly contributed to by vertical strain. Specimen III-CCC/CCT, which had both nodes confined, exhibited a lower level of transverse strain through the diagonal strut. However, other test specimens (Series I and Series II), although maintaining low transverse strains in the confined region, demonstrated no significant difference around the mid-span of the diagonal strut. With this regard, singly confined struts still had high transverse strain through the diagonal, which might have caused a higher degree of reduction to the effective compressive strength of concrete.



(a) Vertical web reinforcement

(b) Horizontal web reinforcement

Figure 5-29 Strain profile along shear span at 95% of peak load

As V_{test} reached 95% of the peak, vertical strain readings at all positions, especially the middle four strain readings, along the diagonal strut generally increased for all specimens. On the other hand,

the horizontal strain profiles still remained lower than the yield strain. However, Specimen III-CCC/CCT-L still had much lower transverse strain along the diagonal strut than the control and all other specimens. The observation echoes that the crack width propagation of Specimen III-CCC/CCT-L kept the smallest, as shown in Figure 5-24. The observation also indicates that doubly confined diagonal struts appear to have higher capacity, providing more reserve strength before the crushing of concrete at the CCC node.

5.3.4.2. Strains Within Confined Region

Figure 5-30, Figure 5-31, and Figure 5-32 present stresses inferred from measured strains distributed along selected confining rebars at a load level of approximately 95% of the peak load. The stress level in the figures is presented in terms of the percentage of the yield stress by color darkness. That is, darker color means closer to the yield strength. As strain readings were localized and so were inferred stresses, it was assumed that a linear variation existed between two neighbor strain readings for the purpose of creating the visuals. Discontinuity of stresses in the figures means that the strain gauge failed to response. In addition to inferred stresses, all the figures are superpositioned with depicted cracks. The idealized diagonal strut, the CCC nodal zone, and the extended nodal zone are also included in the figures.

Figure 5-30 shows the engagement of the confining reinforcement of specimens in Series I. Both specimens demonstrated shared characteristics regarding the strain profile. Firstly, little to no strains were observed in crossties. Secondly, vertical confining reinforcement right above the load plate, otherwise the CCC nodal zone, was barely engaged, while the engagement of vertical confining reinforcement increased as closer to the outmost extended nodal zone. Thirdly, horizontal confining reinforcement had noticeable strain at positions outside the diagonal strut where flexural cracks intersected and within the CCC node. Nevertheless, horizontal confining reinforcement stayed at stress levels not higher than 60% of the yield strength. It is evident that most confining rebars did not respond to the shear force transmitted through the diagonal strut. Only vertical confining reinforcement distributed within the extended nodal zone effectively contributed. The observation supports the insight that confining the extended nodal zone would be the most effective.

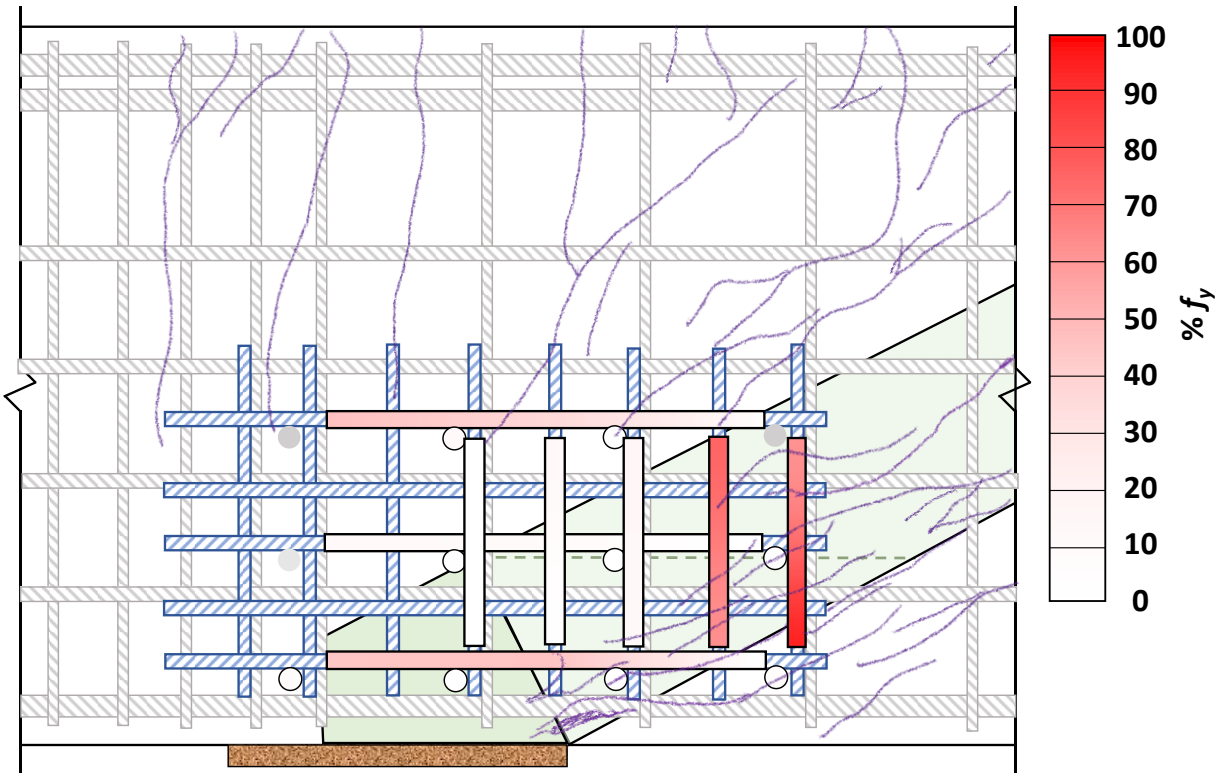
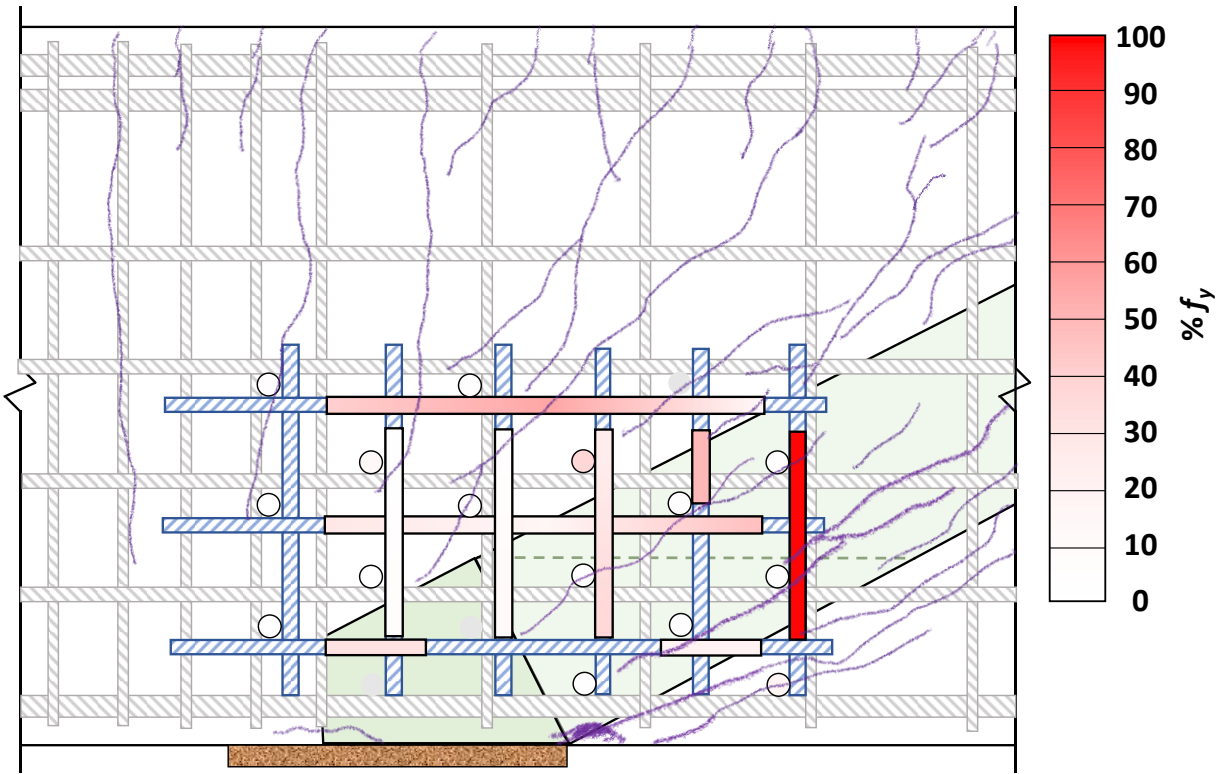
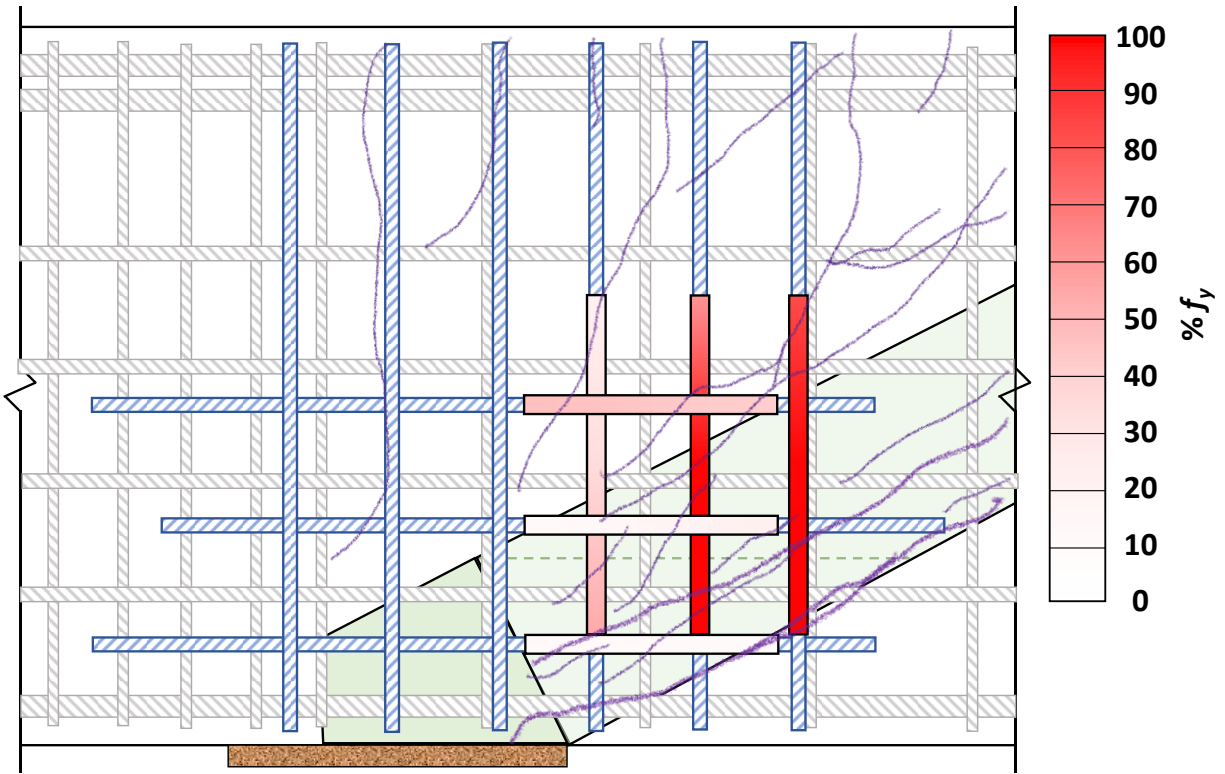


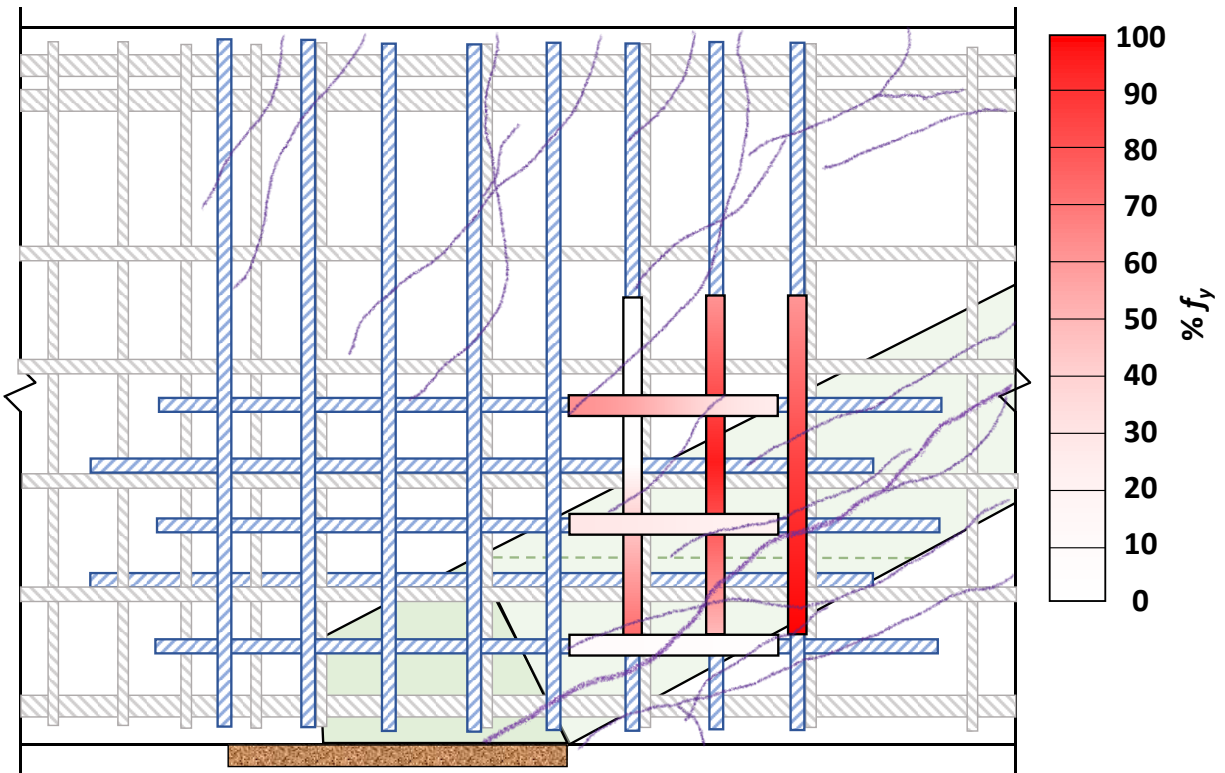
Figure 5-30 Engagement of confining reinforcement in Series I specimens

Vertical confining reinforcement within the extended nodal zone was engaged differently in magnitude between the two specimens in Series I. For Specimen I-CCC-L, which had a lower confinement ratio, the outmost vertical confining rebar almost yielded (95% of the yielded strength) at the top and yielded with a plastic strain of almost four times the yield strain at the bottom. Other vertical confining rebars demonstrated less than 51% of yield strength. On the other hand, Specimen I-CCC-H, which had a higher confinement ratio, had no confining rebars yielded. The highest measured strain was 94% of the yield strain at the bottom of the first vertical confining rebar. It appears that a higher confining ratio effectively reduced the deformation of the confined region. Nevertheless, as the confined regions had shown the initiation of concrete crushing and severe cracks proximal to the load plate, it is possible that the amount of confinement would have been higher than the balanced reinforcement ratio. Further adding confinement would have a diminishing efficacy on improving strength because the crushing of concrete had become the governing failure mechanism.

As most strain gauges did not detect significant strain readings, the positions of strain gauges were adjusted for specimens in Series II, as introduced in Section 5.2.3. Measurements of strains of Series II and Specimen III-CCC/CCT-L are displayed in Figure 5-31 and Figure 5-32, respectively. It can be seen from the figures that the three specimens in Series II and Series III demonstrated similar characteristics in terms of strain profiles, as discussed for Series I in the previous paragraph. The outmost two vertical confining rebars within the extended nodal zone also engaged the most; horizontal confining rebars reacted to flexural stresses more than shear stresses from the diagonal strut. Furthermore, Specimen II-CCC-L and Specimen III-CCC/CCT-L had multiple positions of confining rebars yielded, while Specimen II-CCC-H had only one place, which was the bottom of the outmost vertical confining rebar. These similarities support an insight that replacing congested hooked bars with stirrups and straight bars as confinement would not affect the engagement of the reinforcing bars but largely improve the constructability. In addition, confining both nodes had no noticeable difference compared to specimens singly confined strut given the same confinement ratio (Specimens I-CCC-L-C and II-CCC-L) in terms of localized strain profile.



(a) Specimen II-CCC-L



(b) Specimen II-CCC-H

Figure 5-31 Engagement of confining reinforcement in Series II specimens

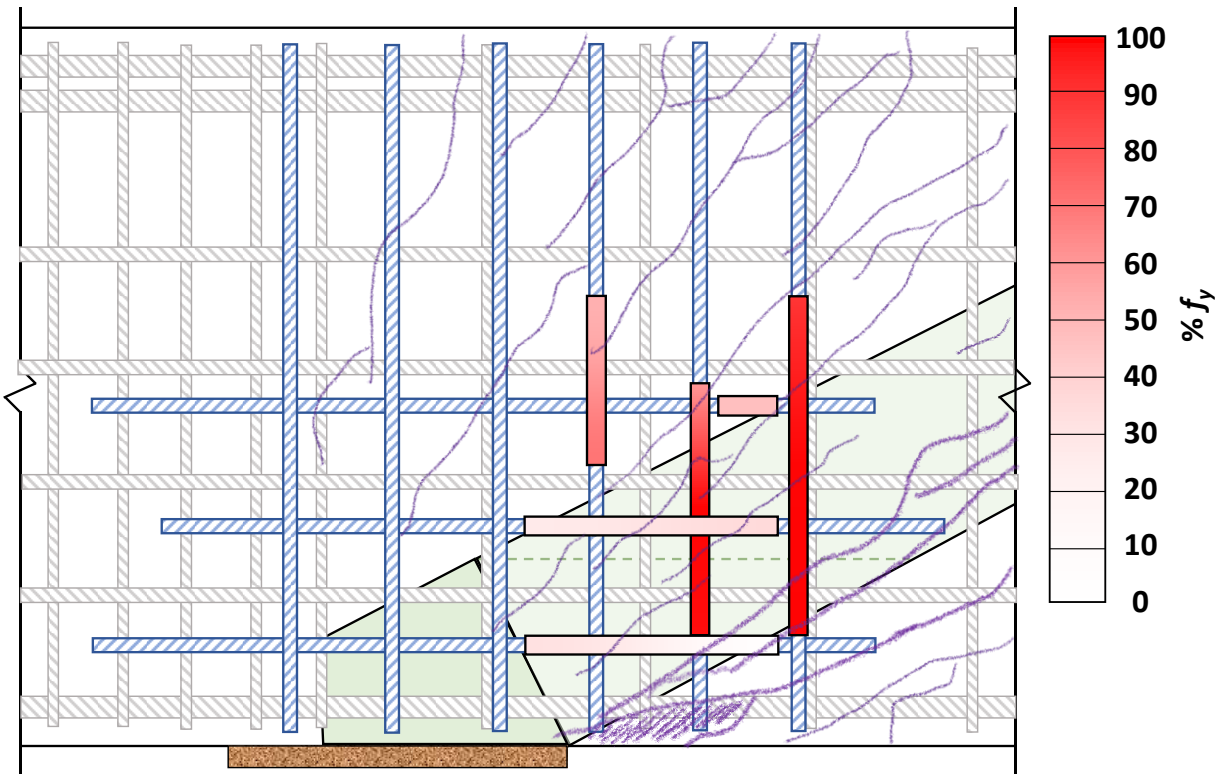
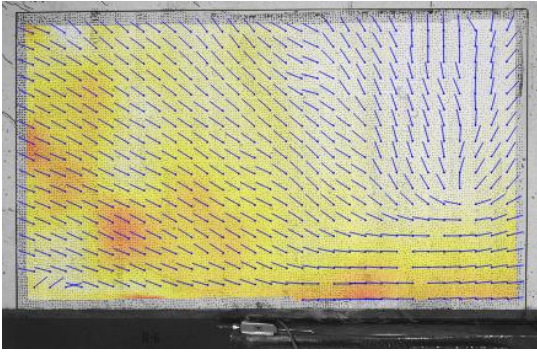


Figure 5-32 Engagement of confining reinforcement in Specimen III-CCC/CCT-L

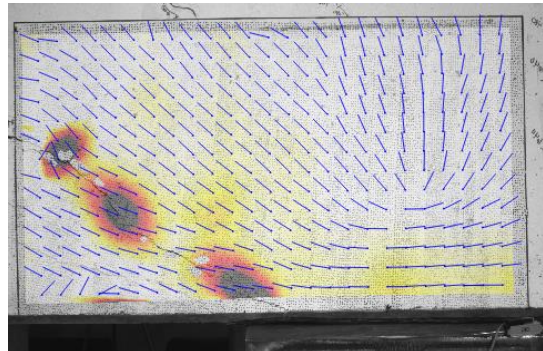
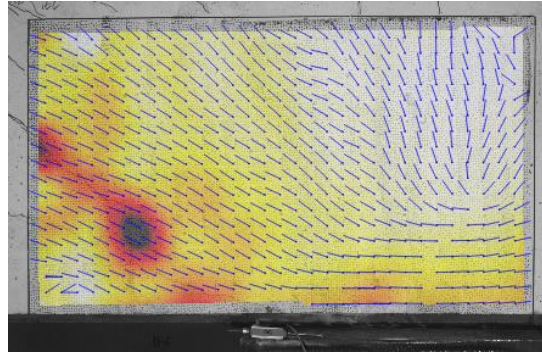
In sum, the strain profiles discussed above provide insights into the efficacy of confinement in the CCC node. Vertical confining reinforcement within the extended nodal zone performed more effectively than within the CCC nodal zone and horizontal confining reinforcement, while crossties were barely engaged. Moreover, using stirrups and straight bars as vertical and horizontal reinforcement did not alter the effects but largely improved congestion. Last but not least, a higher confinement ratio ($\rho_x = 1.2\%$ and $\rho_y = 0.88\%$) might be able to reduce the deformation in the confined region, but further adding confinement would expect a diminishing efficacy.

5.3.5. Digital Image Correlation Results

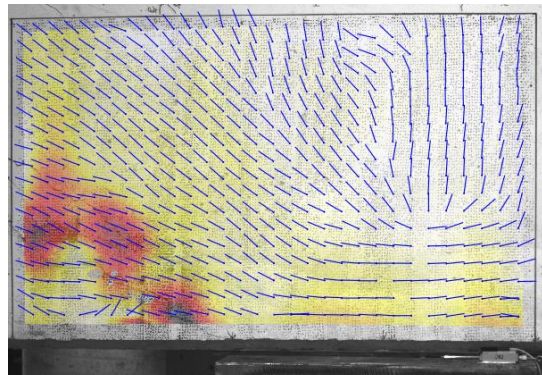
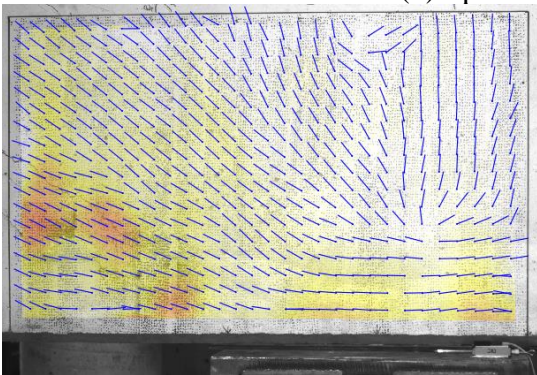
Minimum principal strain maps at the peak load and before severe crushing of concrete captured by the DIC system over the CCC nodal zone and the extended nodal zone of specimens in Series II and III are presented in Figure 5-33. The unit shown in the figure for the principal strain map is 10^{-6} in./in. The principal direction is indicated in the figure by blue arrows. It should be unfortunately noted that the DIC data of the specimens in Series I was not successfully captured due to calibration issues. In addition, DIC images of Specimen II-CCC-H were disturbed at a load of approximately 479 kips, and only the strain map before concrete crushing is presented.



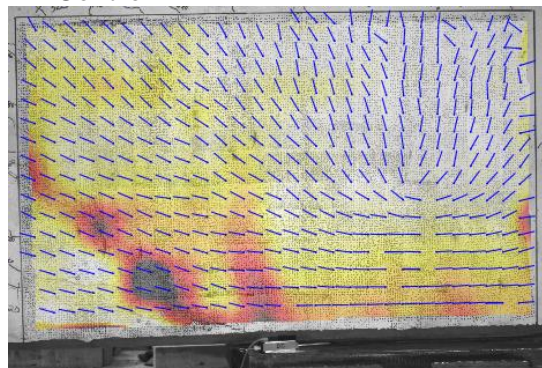
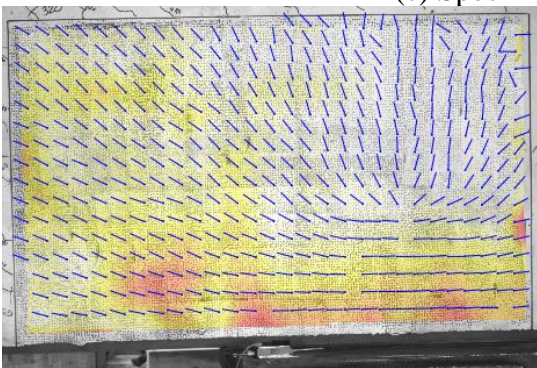
(a) Specimen II-CCC-L



(b) Specimen II-CCC-H



(c) Specimen III-Control



(d) Specimen III-CCC/CCT-L

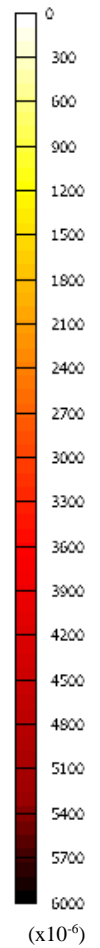


Figure 5-33 Strain map at peak load and before crushing

As observed from Figure 5-33, whether having the CCC node confined or not, concrete around the area near the edge of the load plate exhibited high strain concentrating at few localized hot spots at the peak load. The magnitude of the localized strains fell between 0.24% to 0.34%. This strain level exceeded reached the concrete strain corresponding to the peak stress. In other words, concrete crushing had initiated at those hot spots when the peak load was reached. Afterward, strains at these hot spots kept growing while the load-carrying capacity was dropping, and severe crushing of concrete happened at those high-strain spots. The observation reveals that concrete crushing near the edge of the load plate was an important governing mechanism of failure, which verifies the preliminary FEA result shown in Figure 5-2.

A categorization was established to further facilitate the interpretation of the DIC data according to the principal compressive strain state. As the principal compressive strain states could be an indicator of the principal compressive stress state, the monitored region was categorized into four zones: I) a compressive-stress-concentration zone, II) a low-compressive-stress zone, III) a compressive-stress-free zone, and IV) a nodal zone, as shown in Figure 5-34 for example.

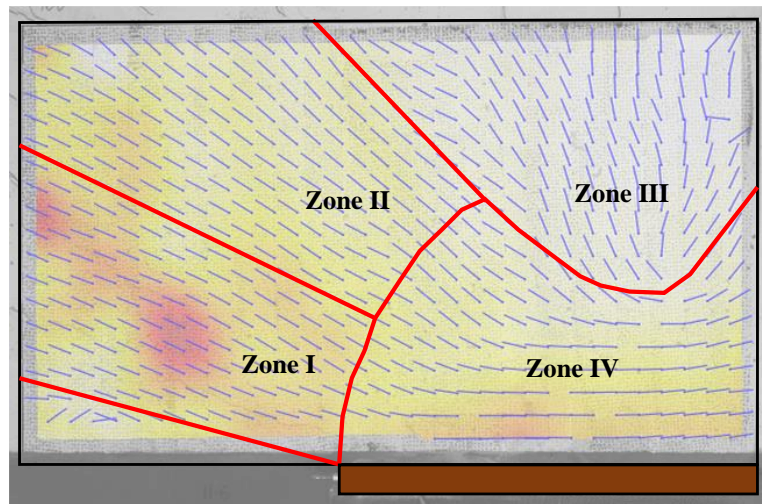


Figure 5-34 Example categorization of strain map within monitored region

Among the four zones, Zone IV, or the nodal zone, is first determined for later delineation. Within Zone IV, both principal strains are compressive, so are both principal stresses. Zone IV has boundaries that receive compressive stress perpendicularly from Zones I and II, which are introduced later. Therefore, a curved boundary starting from the edge of the load plate was defined on the left side. The curved boundary on the left indicates that the diagonal strut had varied angles, instead of a constant orientation, when entering the nodal zone. The curved boundary stops when reaching the top boundary, which separates Zone IV from the compressive stress-free zone (Zone III). Lastly, the bearing area provided by the load plate becomes the bottom boundary, receiving bearing stresses perpendicular to the bearing area.

It can be seen from Figure 5-34 that in Zone IV, the principal compressive strains horizontally flow above the load plate. These strains indicate the existence of the flexural compressive stress block. The directions of the principal compressive strains are gradually turning with varying angles, so are the directions of principal compressive stresses when exiting the nodal zone.

Zone III, by definition, is free of compressive stresses. Due to the noise of the DIC system, low compressive strain would be significantly affected, and it was difficult to define the compressive stress-free zone perfectly. Here, the boundary of Zone III approximately corresponds to the contour line representing a strain of 0.03%. It is observed that the left boundary of Zone III is approximately 45 degrees independent of whether confinement exists or not. This boundary also becomes the upper boundary of Zone II.

Zone II generally has principal compressive strains ranging from 0.03% to 0.10%. This zone is enclosed by the 45-degree upper boundary mentioned above and a lower boundary with an angle of 26 degrees. The lower boundary is approximately in alignment with the theoretical diagonal strut angle, as later introduced in Section 5.4.2.1. The principal compressive strain keeps changing direction from 26 to 45 degrees while reducing its magnitude.

In Zone I, where localized hot spots appear, the magnitude of the principal compressive strain varies from 0.1% to 0.34%. The direction of principal strains within this zone also changes, but not as significantly as in Zone II. The angle fell between 20 and 26 degrees, forming the lower and upper boundaries, respectively. Hot spots are located approximately in the middle of Zone I and have a principal strain angle of around 23 degrees. The region below the lower boundary has principal compressive strains lower than 0.1% and are not categorized.

The categorization gives an approach to evaluating the arrangement of the diagonal strut. Firstly, the strain states within Zone I and Zone II reveal that the diagonal strut consisted of numerous infinitesimal struts. These struts perpendicularly entered Zone IV. In Zone II, these struts generally had lower stresses than in Zone I did, and their direction rotated from 26 to 45 degrees while the stress level diminished. In Zone I, the change in the direction of the principal compressive strain was lower. It indicates that a single diagonal strut and fan-shaped struts better model the principal compressive stresses in the shear span, echoing the study by Thomas et al. (2006). In addition, the results are independent of the existence of confining reinforcement. All investigated specimens exhibited similar stress flow as described.

Under the STM provisions, the sizing method for the CCC nodal zone can be evaluated by superpositioning the theoretical diagonal strut and the CCC nodal zone with the DIC results, as shown in Figure 5-35. This superposition visualizes whether the amount of confinement affected the sizing method. In the figure, the CCC nodal zone, the extended nodal zone, and the diagonal strut are all based on the sizing method per AASHTO LRFD (2020), which is introduced in Section 5.4.2.1. The results are summarized in Table 5-5.

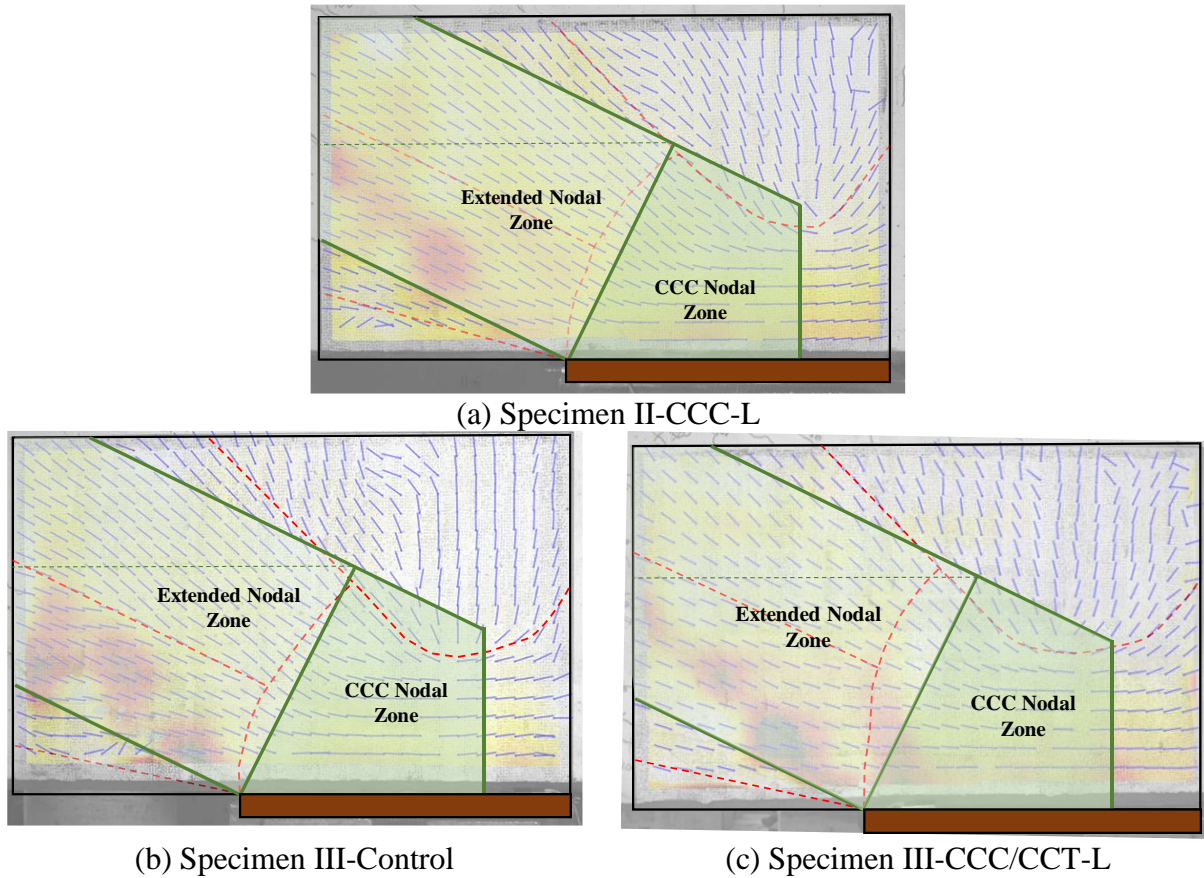


Figure 5-35 Comparison between STM nodal zone and DIC strain map

According to the visualization shown in Figure 5-35, the CCC nodal zone of each specimen is in good agreement with Zone I, whether confined or not. The difference in the height of the back face is not larger than 1.5 in., and the difference in the width of the strut-to-node interface is insignificant. The division of the bearing area based on the reaction provided by each support plate is also in alignment with the stress distribution. Nevertheless, the DIC-identified strut-to-node interface is a curved face, perpendicularly receiving numerous infinitesimal struts with varying orientations and stress magnitudes. The STM strut-to-node interface cannot model such phenomenon precisely. In addition, a single diagonal strut in accordance with the STM provisions, which has only one direction and evenly distributed stresses, cannot perfectly model the DIC-identified infinitesimal struts. It can also be seen from the figure that hot spots are concentrated in the lower portion of the extended nodal zone near the strut-to-node interface instead of the entire strut-to-node interface.

The DIC results provide an insight that measures should be taken to address not only reinforced concrete plasticity but also the discrepancies in stress distribution when developing modeling techniques of the STM. It is achieved by applying nodal efficiency factors in design codes and past studies. Following the concept, reasonable nodal efficiency factors can be correlated with the hot spots identified by the DIC results. In particular, DIC virtual extensometers were distributed to

measure the average principal strains in longitudinal and transverse directions (ϵ_2 and ϵ_1 , respectively) over the crushed spot, as shown in Figure 5-36. Also, the average magnitude of compressive stresses over the STM strut-to-node (denoted as f_b summarized in Table 5-6) was calculated.

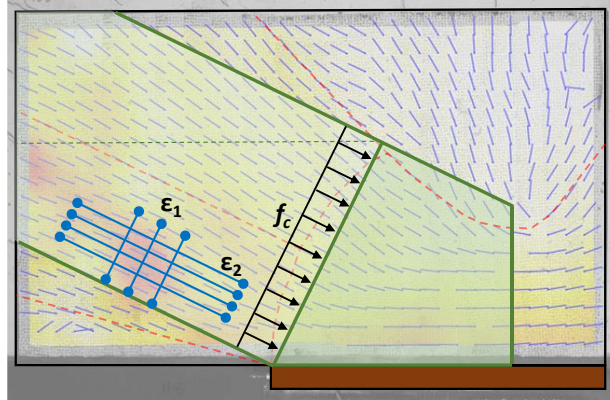


Figure 5-36 DIC virtual extensometer and average compressive stress on nodal face

With determined the value of f_b for each specimen, the efficiency factors $\nu (=f_b/f'_c)$ was calculated and plotted with respect to ϵ_2 and ϵ_1 , as shown in Figure 5-37. It should be noted that the data of Specimen II-CCC-H was disturbed at a load of approximately 479 kips, corresponding to a ν -value of 0.64. In addition, Specimen III-Control underwent unloading at a load of approximately 560 kips, corresponding to a ν -value of 0.83, and hence the curve shown in the figure is the result of re-loading. The strain data of the two disturbed specimens at the peak may not be reliable. Nevertheless, the peak efficiency factor was not affected.

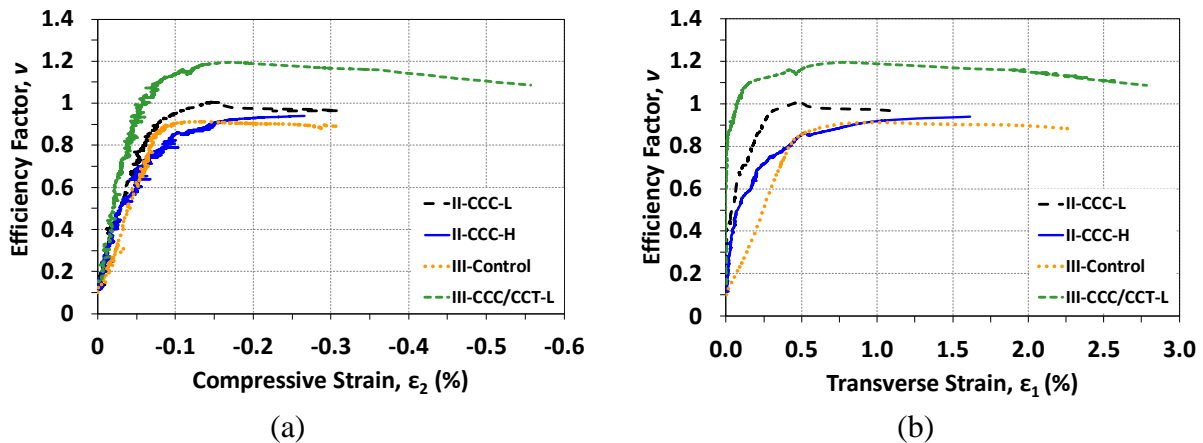


Figure 5-37 Efficiency factor versus compressive/transverse strain readings

The plots in Figure 5-37 successfully correlate the average strains at the monitored hot spot to the strut-to-nodal efficiency factor for each specimen. It is shown that Specimen III-CCC/CCT-L exhibited the highest efficiency factor, 1.19. Specimens II-CCC-L and II-CCC-H reached efficiency factors of 0.99 and 0.95, respectively, and Specimen III-Control reached 0.92. In

addition, Specimen III-CCC/CCT-L had the highest stiffness and the lowest average transverse strain. Specimen II-CCC-L was in the second place before reaching the peak compared to Specimen III-Control. The results agree with the observed crack patterns and strain profile on confining reinforcement, as introduced previously.

Critical compressive and transverse strains of Specimen II-CCC-L were compared to Specimen III-CCC/CCT-L. The former specimen reached compressive and transverse strains of -0.145% and 0.475%, respectively; the latter specimen reached compressive and transverse strains of -0.166% and 0.766%, respectively. The critical compressive strains of both specimens were similar but somewhat less than the typical range of critical compressive strain of concrete (-0.2% to -0.3%). Nevertheless, the results are reasonable because the average strain was taken. Regarding the critical transverse strains, Specimen III-CCC/CCT-L reached 1.61 times higher than Specimen II-CCC-L. According to the MCFT, the monitored hot spot of Specimen III-CCC/CCT-L should have had a lower compressive strength than that of Specimen II-CCC-L. However, the efficiency factor for the strut-to-nodal interface of Specimen III-CCC/CCT-L was higher. It is disclosed that the doubly confined strut had a better performance of redistributing compressive stress by involving a larger volume of concrete in resisting loads. This finding also consistently supports the insights derived from crack patterns and rebar strain readings.

In sum, DIC results disclose that the STM cannot perfectly model the stress state. Instead, the STM is a simplified method to approximate the stress state when the structure is at the limit state. If using the current AASTHO LRFD provisions, varying compressive principal stress angles and curved strut-to-node interfaces cannot be reflected. Also, stress concentrations are not necessarily on the strut-to-node interface nor with constant magnitude. Measures such as using nodal efficiency factors are taken to address the inconsistencies. The determination of nodal efficiency factors is based on correlating the average stress magnitude over the STM theoretical strut-to-node interface area to the critical regions in the extended nodal zone, where a high level of concrete crushing is expected. The results indicate that doubly confined struts are expected to have a higher nodal efficiency factor than singly confined struts and non-confined struts. More discussions are presented in Section 5.4.2.

5.4. Analysis of Test Results

5.4.1. Evaluation of Strength with Sectional Shear Strength

To facilitate direct comparison, V_{test} of each test specimen introduced in the previous chapter was normalized with regard to the concrete compressive strength times the effective shear area. Specimens with a confined CCC node were compared to the control specimens (III-1.85-CCC2021 and III-Control), as plotted in Figure 5-38. It can be seen from the figure that the normalized test shear strengths of the two control specimens reached similar results (0.19 and 0.17), indicating that both the control specimens can be appropriate benchmarks.

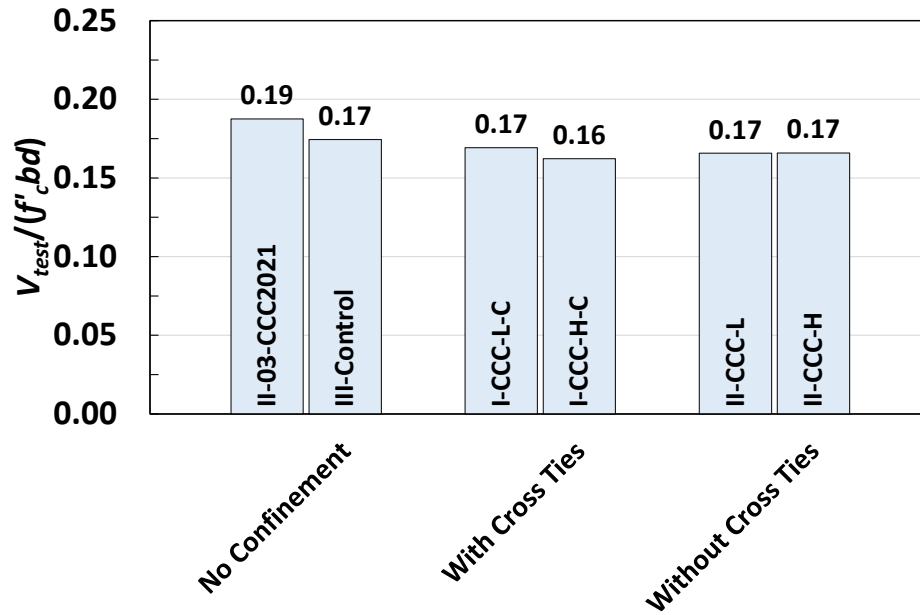


Figure 5-38 Comparison of sectional shear strength of specimens with confined CCC node

The specimens with crossties for the confinement of the CCC node (Specimens I-CCC-L-C and I-CCC-H-C) ended up with almost the same normalized shear strength (0.17 and 0.16, respectively). In addition, both specimens had normalized shear strengths that were similar to or lower than the control specimens. This result reveals that providing confinement, whether high amount or low amount, to the CCC node did not increase the normalized shear strength in the shear span.

It was first posited that the lack of strength enhancement was due to the honeycomb and reinforcement congestion that occurred during construction. The number of hooked bars and hooked cross ties did cause serious difficulties. However, the test results of specimens without crossties and with improved rebar arrangement (Specimens II-CCC-L and II-CCC-H) indicate that neither did the improved designs also increase shear strength. Both specimens had a normalized shear strength of 0.17, equal to or below the control specimens' normalized strengths. The expected effect of increasing the strength of the CCC node did not seem to materialize.

It was also considered the possibility that the unconfined CCT node was weaker than the confined CCC node, placing a cap on the shear strength. If this were the case, the strength of the CCC node would have increased if the CCT node had not failed first. However, all four specimens in Series I and Series II had some degree of crushing in the CCC node when reaching V_{test} as revealed by the visual observation and the DIC strain maps, yet damage in the CCT node was not as significant. Crushing of concrete near the CCC node was an important mode of failure, and this observation echoes the statement in Project 0-5253 that the stress condition of the CCT node did not govern the behavior.

Specimen III-CCC/CCT-L was developed after testing the second beam and had both nodes confined with a larger bearing plate attached to the CCT node. In this test, the failure mode was also primarily the crushing of concrete near the CCC node. Damage near the CCT node was still not as significant. The governing failure mode was not conspicuously different from specimens in Series I and II. The normalized shear strength of Specimen III-CCC/CCT-L was 0.21, at least 23.5% higher than any other specimens in the experimental program. Confining both nodes seemed to successfully increase the normalized shear strength.

In addition, the increase in strength due to confinement of both the CCC node and CCT node is more evident in comparison to a different group of control specimens from Project 0-5253, as shown in Figure 5-39. These control specimens also had a larger support plate (16 inches by 20 inches) for the CCT node and did not confine the CCT or CCC nodes, making a direct comparison with Specimen III-CCC/CCT-L possible. The comparison reveals that Specimen III-CCC/CCT-L had a higher normalized strength than the companions (Specimen III-1.85-03 and Specimen III-1.85-03b). However, the companion specimens had significantly different normalized shear strengths from one another, despite having almost the same structural configuration. The researchers on Project 0-5253 acknowledged that the test normalized shear strength can be widely scattered. Specifically, comparing the normalized shear strength of Specimen III-CCC/CCT-L to the control specimens observed strength increases of 16.7% and 110%. The range is too large to be convincing. Therefore, using normalized shear strength in the shear span is not optimal, which highlights the fact that sectional shear analysis is not ideal for analyzing deep beams.

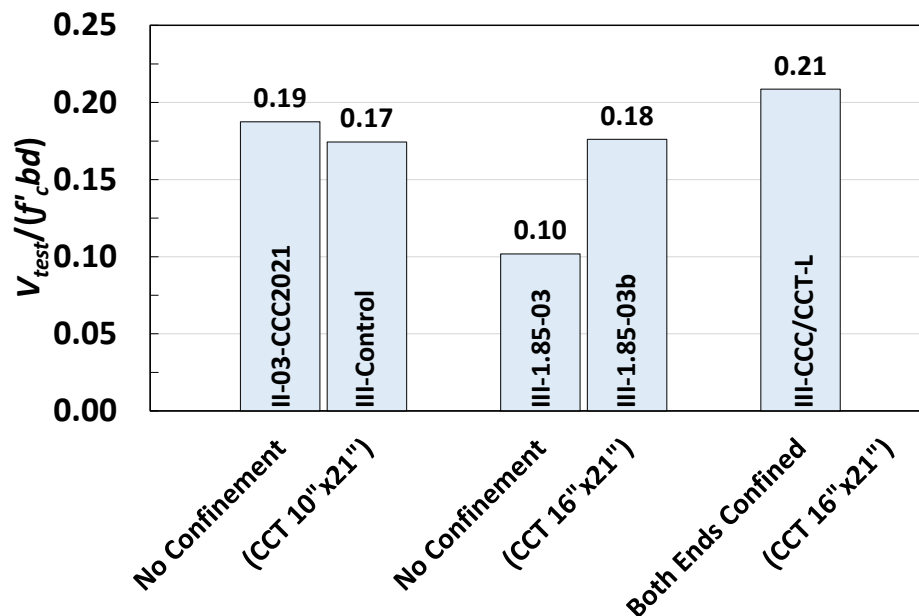


Figure 5-39 Comparison of sectional shear strength of specimens with confinement of both or neither nodes

Figure 5-39 also supports the fact that the CCT node did not effectively control the behavior in terms of peak shear. The second and first groups of control specimens (Specimens III-1.85-03 and III-1.85-03b versus Specimens II-03-CCC2021 and III-Control) only differed in the size of their support plate. The second group had a support plate of 16 inches by 20 inches, compared to the first group's 10-inch-by-20-inch plate. The test results, as shown in Figure 5-39, disclose that the normalized shear strength of the second group was similar to or much less than that of the first group. It seems that the enlarged support plate was detrimental to the shear strength. However, none of the four specimens had significant damage in the CCT node. It can hardly confirm that a larger support plate attached to the CCT node was governing.

5.4.2. Evaluation of AASHTO LRFD's STM Provisions

5.4.2.1. Formulation of sizing nodes and results

Since the sectional shear analysis could not confirm whether providing confinement contributes to the shear strength of deep beams, the STM, which specializes in the analysis of D-regions, was applied to analyze each specimen to determine efficiency factors for both CCC and CCT nodes. In the configuration of the test region shown in Figure 5-40, a single diagonal strut connects the subdivided CCC node above the load plate to the CCT node beneath the support plate with an angle denoted as θ . The diagonal strut angle can be determined geometrically using the equation given by

$$\theta = \tan^{-1} \frac{d - h_a/2}{a'} \quad (5-3)$$

where h_a is the height of the exterior strut on the compression side and a' is the adjusted shear span.

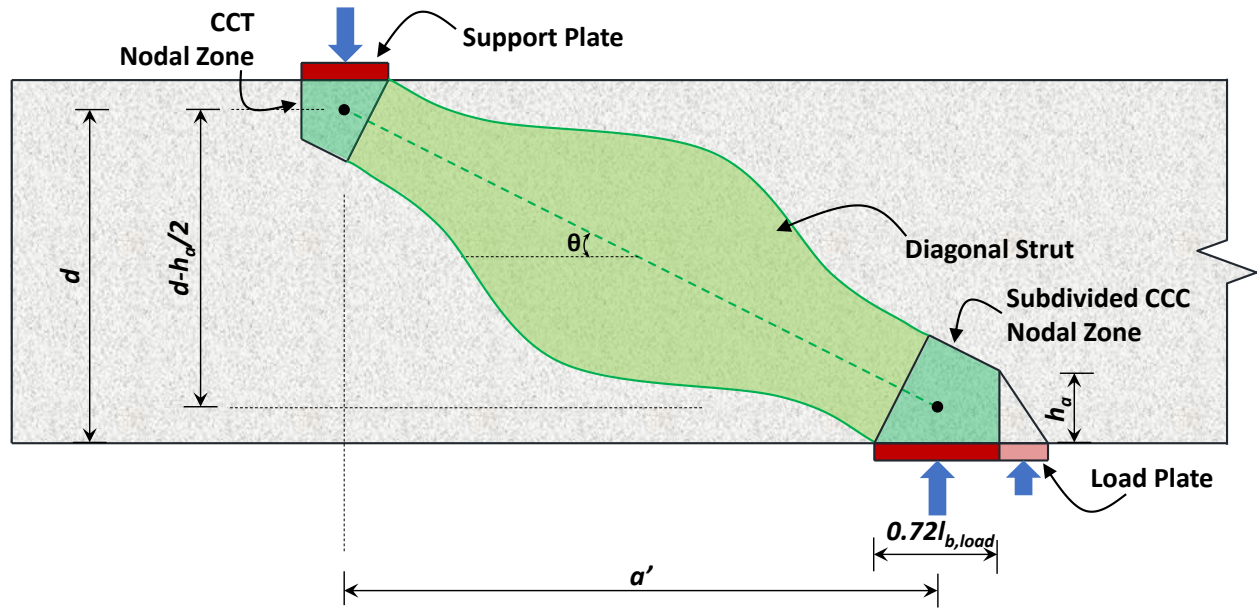


Figure 5-40 Geometry of test region and diagonal strut

Although various methods are provided in the literature, in this study, the value of h_a was assumed to be the equivalent stress block (chosen for consistency with Project 0-5253). As the CCC node was subdivided, the exact position of the end of the diagonal strut was not right above the center of the load plate. Rather, it was positioned above the center of the left portion, which had a length of 0.72 times the plate width ($0.72l_b$) according to the load distribution to the load plate. Therefore, the adjusted shear span a' can be expressed as

$$a' = a - 0.14l_{b,load} \quad (5-4)$$

Once the diagonal strut angle is determined, the CCC node and the CCT node can be sized accordingly. Non-hydrostatic nodes were used for both the CCC node and the CCT node in this study. Regarding the CCC node, the shape was defined as shown in Figure 5-41(a). The width of the strut-to-node interface of the CCC node ($w_{s,CCC}$) is therefore given by

$$w_{s,CCC} = 0.72l_{b,load} \sin \theta + h_a \cos \theta \quad (5-5)$$

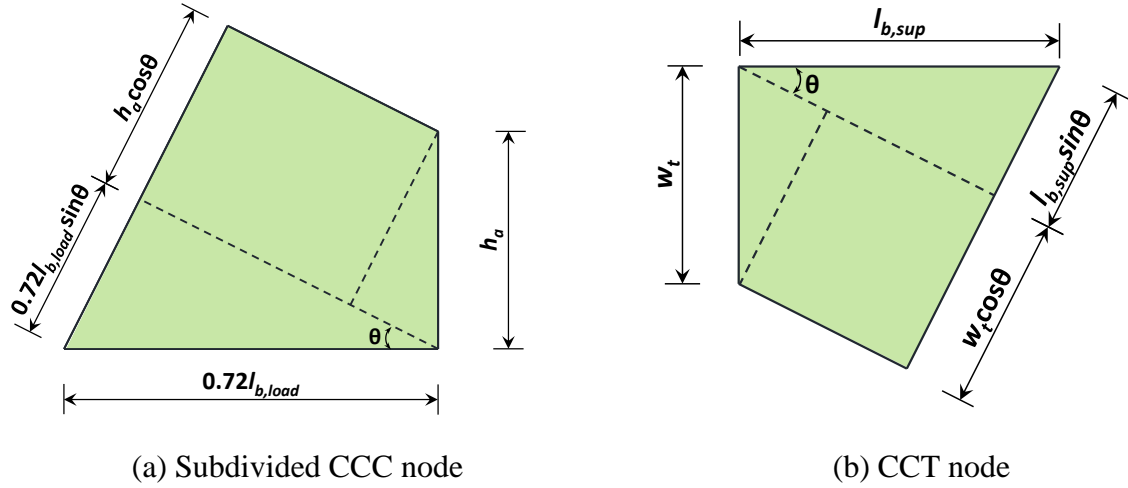


Figure 5-41 Size of CCC node and CCT node

Similarly, the width of the strut-to-node interface of the CCT node, as shown in Figure 5-41(b), is given by

$$w_{s,CCT} = l_{b,sup} \sin \theta + w_t \cos \theta \quad (5-6)$$

where the height of the back face w_t is taken to be twice the distance from the concrete edge to the centroid of the longitudinal reinforcing bars on the tension side. The sizing result of each specimen is shown in Table 5-5. The sizing results of the specimens in Series II and III have been reasonably verified by the DIC data as introduced in Section 5.3.5. This sizing method is reasonable and practical for applying the STM on deep beams.

Table 5-5 Sizing results of CCC node and CCT node

Series	Specimen I.D.	θ (degree)	CCC Node			CCT Node		
			$l_{b,load}$ (in.)	h_a (in.)	$w_{s,CCC}$ (in.)	$l_{b,sup}$ (in.)	w_t (in.)	$w_{s,CCT}$ (in.)
I	I-CCC-L-C	26.35	20	9.25	14.68	10	6.8	10.53
	I-CCC-H-C	26.25	20	9.55	14.93	10	6.8	10.52
II	II-CCC-L	26.10	20	9.99	15.31	10	6.8	10.51
	II-CCC-H	26.20	20	9.68	15.05	10	6.8	10.52
III	III-Control	25.62	20	11.40	16.51	10	6.8	10.46
	III-CCC/CCT-L	25.78	20	10.94	16.11	16	6.8	13.08
Project 0-5253	II-03-CCC2021	25.88	20	10.65	15.86	10	6.8	10.48
	III-1.85-03	26.67	20	8.30	13.88	16	6.8	13.26
	III-1.85-03b	25.60	20	11.45	16.55	16	6.8	13.05

5.4.2.2. Evaluation of Nodal Efficiency Factor

5.4.2.2.1. Efficiency Factor of CCC Node

The effect of confinement on the CCC node was evaluated using the test nodal efficiency factor, ν , which is determined by calculating the ratio of applied normal stresses over the nodal face to the compressive strength of the concrete. It should be noted that only the strut-to-node interface was evaluated and is presented here because no noticeable crushing was observed on the back face or on the bearing face. In other words, the efficiency factor was controlled by the strut-to-node interface. It should also be noted that the efficiency factor is an indicator of the average peak stress over the strut-to-node area at which the extended nodal zone has concrete largely crushed. The strut-to-node interface does not necessarily exhibit crushing of concrete.

For the CCC node shown in Figure 5-41(a), a force $0.72P_{test}$ was applied on the load plate per STM principles, and therefore the strut force acting on the strut-to-node interface was $0.72P_{test}/\sin\theta$ per equilibrium. The normal stress and the corresponding nodal efficiency factor of the strut-to-node interface were then determined simultaneously. The analytical results of the ν -value of the specimens' CCC node are summarized in Table 5-6.

Table 5-6 Efficiency factor of CCC node

Series	Specimen I.D.	P_{test} (kip)	f'_c (ksi)	f_b (ksi)	ν ($=f_b/f'_c$)
I	I-CCC-L-C	795	4.03	4.18	1.04
	I-CCC-H-C	692	3.86	3.59	0.93
II	II-CCC-L	718	3.68	3.66	0.99
	II-CCC-H	703	3.84	3.63	0.95
III	III-Control	617	3.21	2.96	0.92
	III-CCC/CCT-L	818	3.35	4.00	1.19
Project 0-5253	II-03-CCC2021	722	3.29	3.58	1.09
	III-1.85-03	597	4.99	3.29	0.66
	III-1.85-03b	681	3.30	3.26	0.99

The ν -value was plotted with regard to the compressive strength of concrete, as presented in Figure 5-42. In the figure, the AASHTO LRFD specified ν -value is indicated with a solid line. It can be seen from the figure that the efficiency factors of all test specimens are above the current AASHTO LRFD provisions, whether the CCC node was confined or not, indicating the AASHTO LRFD specified ν -value is already conservative. For specimens with a singly confined strut, the CCC nodal efficiency factor ranged from 0.93 to 1.04. In fact, higher confinement did not necessarily lead to higher ν -values. This range of the CCC nodal efficiency factor was similar to their companion specimens, falling between 0.92 and 1.09. As the concrete compressive strength was less than 4.0 ksi or slightly greater than 4.0 ksi, the f'_c -value was not considered to affect the CCC

nodal efficiency factor. In other words, singly confined struts with an f'_c -value less than 4.0 ksi did not gain strength increase compared to struts without additional confinement at the CCC node.

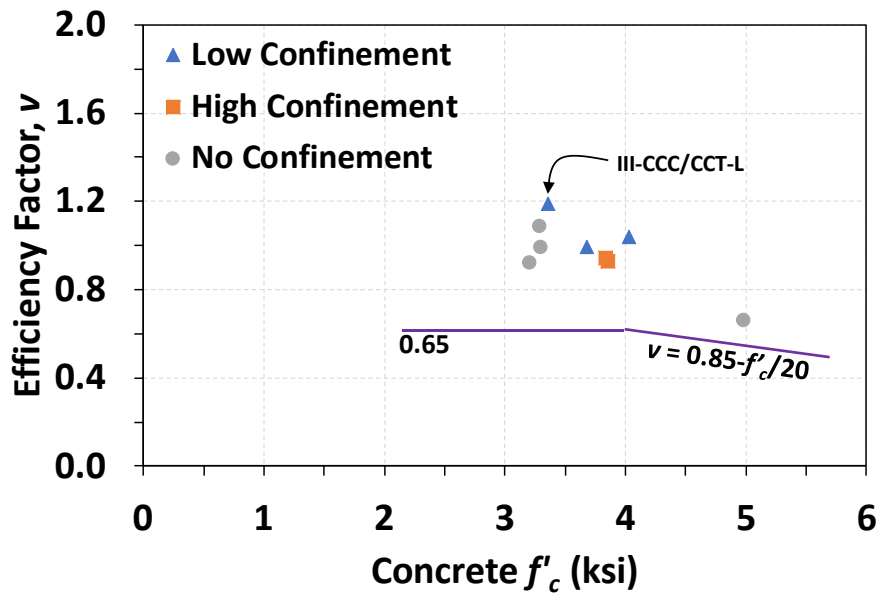


Figure 5-42 Efficiency factor of the CCC strut-to-node interface

If struts are doubly confined, however, the confinement did seem to provide an increase in strength. Specimen III-CCC/CCT/L, which had a lower amount of confinement at the CCC node but had both nodes confined, had a CCC nodal efficiency factor of 1.19. The value was 9.2% to 29.3% higher than its counterparts with no confinement from this project and Project 0-5253.

An evaluation database established in Project 0-5253, as shown in Figure 5-43, provides more comparisons. In the figure, the data points of the current study were plotted together to observe the effect of confinement in a larger picture. The results also support the insight that doubly confined struts performed better than non-confined and singly confined struts. It is observed that given the f'_c -value less than 4.0 ksi, the CCC nodal efficiency factor mostly fell between 0.66 and 0.97, with only one exception of 1.19. Specimen III-CCC/CCT-L also had an efficiency factor of 1.19, higher than all other data points from the database. However, other data points from this study had less noticeable improvement in the efficiency factor. An increase of 9.2% or higher in the CCC nodal efficiency factor of doubly confined struts can be conservatively expected, given the most commonly used concrete compressive strengths in Texas.

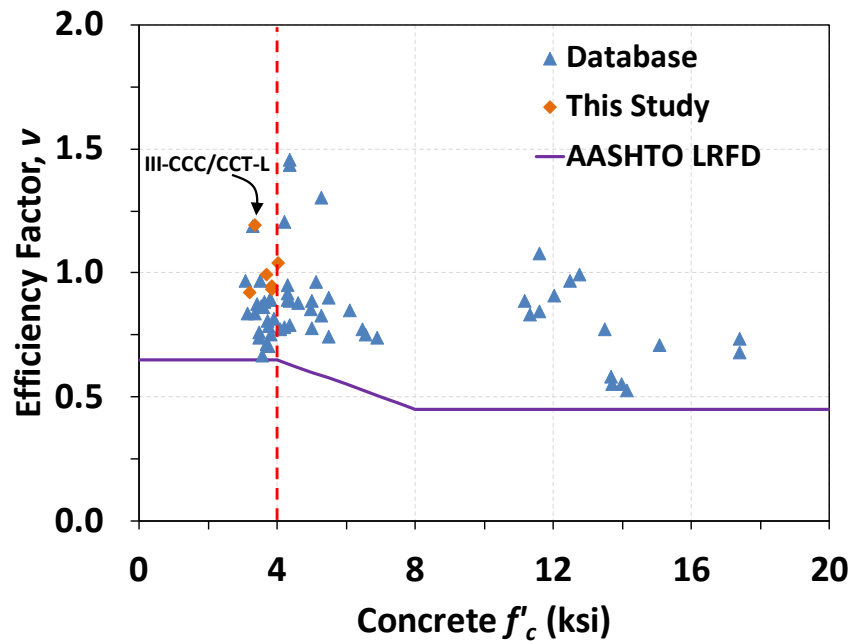


Figure 5-43 CCC nodal efficiency factor from evaluation database from Project 0-5253

5.4.2.2.2. Efficiency Factor of CCT Node

A similar approach was applied to evaluate the efficiency factor of the CCT node, as summarized in Table 5-7. Also, the analytical results were similarly plotted with regard to the concrete strength, as shown in Figure 5-44. It should again be noted that only the strut-to-node interface of the CCT node was analyzed because the back face and the bearing face did not experience noticeable damage. In addition, test results of counterpart specimens from Project 0-5253 (indicated as solid circles in the figure) also did not report severe damage in the CCT node. In fact, Project 0-5253 states that the CCT node did not govern the behavior. That is, the CCT node of all test specimens in this experimental program and control specimens from Project 0-5253 might have reached a higher nodal strength. It can be inferred that a slightly higher efficiency factor would have been reached. Nevertheless, the figure still provides insights into the lower bound of ν -values for CCT nodes. As the support plate was taking a load level of R_{test} , the strut-to-node interface was taking $R_{test} \sin\theta$, and the stress along the interface can be determined.

Table 5-7 Efficiency factor of CCT node

Series	Specimen I.D.	R_{test} (kip)	f'_c (ksi)	f_b (ksi)	ν ($=f_b/f'_c$)
I	I-CCC-L-C	539	4.03	5.49	1.36
	I-CCC-H-C	493	3.86	5.05	1.31
II	II-CCC-L	480	3.68	4.95	1.34
	II-CCC-H	503	3.84	5.16	1.34
III	III-Control	440	3.21	4.63	1.44
	III-CCC/CCT-L	553	3.35	4.63	1.38
Project 0-5253	II-03-CCC2021	486	3.29	5.06	1.54
	III-1.85-03	398	4.99	3.19	0.64
	III-1.85-03b	457	3.30	3.86	1.17

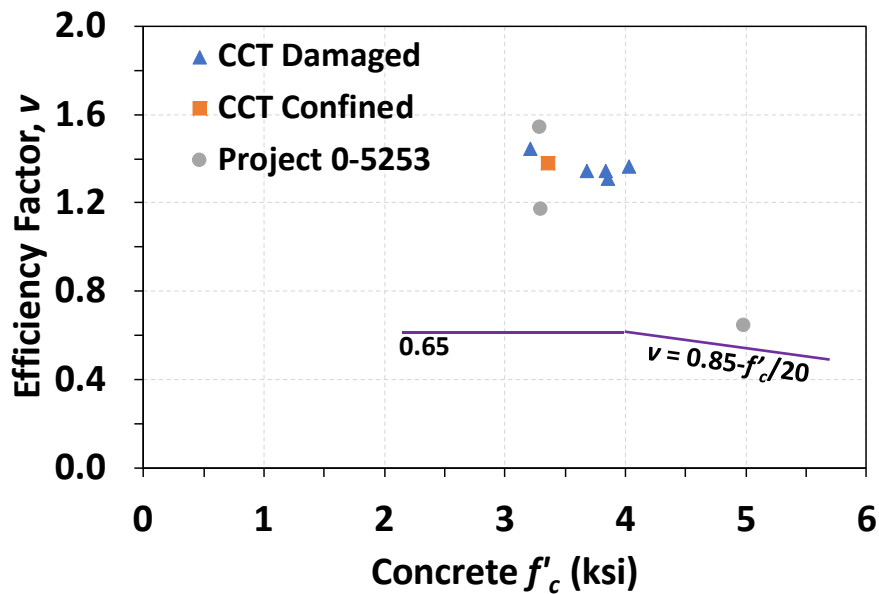


Figure 5-44 Efficiency factor of the CCT strut-to-node interface

It can be seen from Figure 5-44 that the confined CCT node did not have an evident increase in strength. The ν -value of the confined CCT node, 1.37, was indeed within the range that data was scattered (1.17 to 1.54) for concrete with compressive strength less than 4.0 ksi. The data points were also plotted together with the database analysis in Project 0-5253, as shown in Figure 5-45. It is revealed that ν -values of CCT nodes fell within the range of 0.65 to 1.79 given compressive strength of concrete less than 4.0 ksi. Data points from the study may have been better than most tests in the database, but they still fell within the range where data points were scattered. Also, the results of confined CCT node were not outstanding.

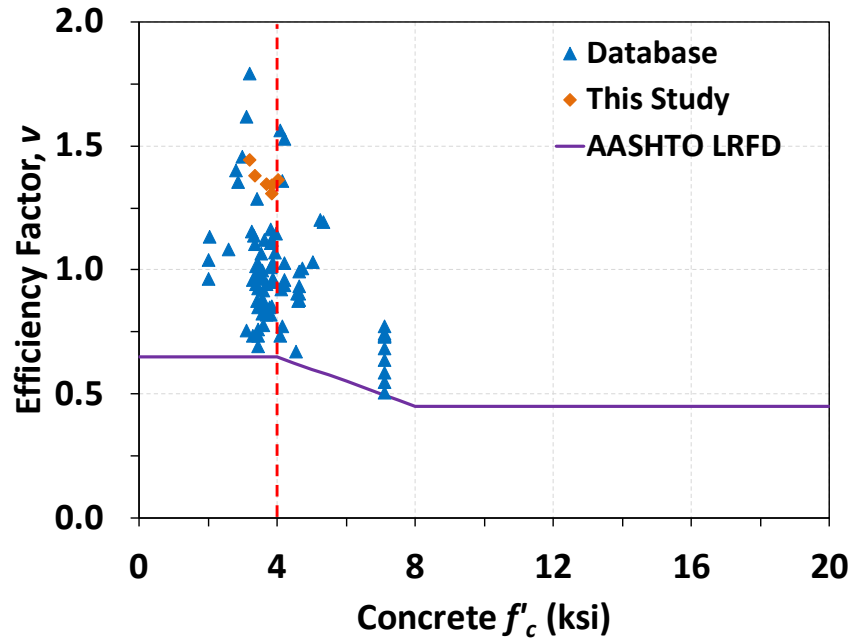


Figure 5-45 CCT nodal factor from evaluation database from Project 0-5253

5.5. Design Recommendations

Based on the test results, design recommendations concerning the confinement of nodal zones within deep beams on the basis of current AASHTO LRFD's STM provisions are proposed as follows:

1. Design methods based on sectional analysis (i.e., evaluating normalized sectional shear stresses) are not recommended for deep beams. Instead, the STM better reflects the stress state at the limit state, delivering conservative designs.
2. The current sizing method per AASHTO LRFD Commentary C5.8.2.1 is appropriate. That is, using an equivalent rectangular stress block to determine the width of the back face of CCC nodes in deep beams. In addition, the subdividing method, in accordance with Commentary C5.8.2.2, for the bearing face of CCC nodes in deep beams is also appropriate.
3. Given the compressive strength of concrete less than 4.0 ksi, if a strut connecting a CCC node and a CCT node has both end nodes effectively confined by addition reinforcement, a 10% increase in strength may be considered when checking the nodal strength of the CCC node. For design purposes, the limiting compressive stress, f_{cu} , at the nodal face may be taken as

$$f_{cu} = 1.1mvf'_c \quad (5-7)$$

where parameters have the same definition per AASHTO LRFD 5.8.2.5.3

4. Confining reinforcement is considered effective if the provided amount in both horizontal and vertical directions, plus the existing crack control reinforcement, is higher than 1.0%. Horizontal confining reinforcement shall be equally spaced over a distance twice the height of the back face from the bearing edge. These horizontal confining rebars shall be properly developed; the critical section may be taken along the centerline of the strut. Vertical confining reinforcement shall be provided as stirrups, equally spaced over a distance covering the entire CCC nodal zone and the extended nodal zone.
5. The performance of crossties remains unclear, and more research is needed.

5.6. Summary

In order to investigate the effect of nodal zone confinement provided by reinforcing bars on the nodal strength, three deep beams, with and without additional confining reinforcement, were designed and constructed, and each was put through two tests. The test specimens, which were developed on the basis of test results from Project 0-5253, had a similar structural configuration and shear span. Two confinement patterns were tested and compared to the control specimens. Based on the test results, the researchers drew several observations and conclusions, as follows:

1. The extended nodal zone of the CCC node above the load plate was predicted to have the highest stress concentration by the preliminary nonlinear finite element analysis. The region to be confined was accordingly selected to include the nodal zone and the extended nodal zone of the CCC node. The height over which horizontal confining reinforcement was extended was twice the height of the back face of the CCC node. The same principle was also applied to the CCT node.
2. All test specimens showed signs of damage and crushing in the concrete of the CCC node in the area adjacent to the support plate. In other words, the extended nodal zone of the CCC node was subjected to severe stress concentration, as predicted by the finite element analysis software. Strain data on confining rebars and the DIC strain maps verified this phenomenon. It is appropriate to distribute confining reinforcement in the entire CCC nodal zone and the extended nodal zone. The CCT node, however, appeared to suffer damage in some cases while having no failing mechanism in others.
3. Doubly confined struts have better behavior than singly confined struts and non-confined struts in terms of crack propagation, crack width, transverse strain along the strut and normalized shear strength.
4. Test results of normalized sectional shear strength reveal that specimens with confinement only in the CCC node did not exhibit increased strength. On the other hand, the strength of

the specimen with confinement in both the CCC node and the CCT node increased by 16.7% to 110%. However, the widely scattered data indicates that normalized sectional shear strength may not be an appropriate evaluation tool for the effects of confinement on strength.

5. Test efficiency factors of both the CCC node and the CCT node were evaluated on the bases of STM principles and code provisions. The analysis results reveal that confinement, regardless of amount, does not appear to increase the CCC nodal strength if only the CCC node is confined. On the other hand, if struts have both the CCC node and the CCT node confined, a 9% or higher increase in the CCC nodal strength can be expected. However, confining the CCT node led to no obvious increase in strength. More research is needed on confined CCT nodes to better understand the efficiency factor.
6. Design recommendations are proposed on the basis of the test results. The STM is preferable for designing deep beams, and effective confining reinforcement of 1.0% in both directions can augment the CCC nodal strength by 10% for doubly confined struts.

This study has limitations, including the shear-to-depth ratio and interaction between crosstie confinement and concrete confinement. Firstly, all specimens had a shear-to-depth ratio of 1.85. It is unclear if a strength increase due to confinement can be expected for deeper beams. Second, crossties did not exhibit engagement plausibly because the load plate was entirely in contact over the member width. It is speculated that crossties may assist with concrete confinement to enhance the m-factor. Moreover, it is plausible that nodal efficiency factors of the CCC and CCT nodes of a strut are related to the amount of crack control reinforcement crossing the strut. In other words, in addition to confining the nodal zones of a strut, generally increasing the amount of crack control reinforcement to higher than 0.3% possibly results in higher strength. It will require further experimental studies to verify the speculations.

Chapter 6. Spacing of Web Reinforcement

This chapter presents the experimental program intended to investigate the effects of the spacing of web crack control reinforcement on the behavior of deep beams. Test results and design recommendations are included as well.

6.1. Introduction

The current design provisions within AASHTO LRFD Bridge Design Specifications regarding the strut-and-tie method (STM) require that spacing of crack control reinforcement in both the vertical and horizontal directions be the lesser of $d/4$ or 12 in. However, it has been reported that the constructability and detailing can be quite difficult due to tightly distributed reinforcement. Although certain design provisions are considered over-designed due to a lack of sufficient experimental data and understanding, AASHTO LRFD still contains a knowledge gap regarding crack control spacing and its limitations. This study aims to especially explore the current limitations of crack control reinforcement within deep beam members and whether the current specifications can be relaxed.

Strut elements in the STM represent two force members that carry compressive stresses. Depending on the load path, the geometry of a strut varies, resulting in configurations such as prismatic, fan, and bottle-shape struts. When transferring from one end to the other, the compressive stresses disperse as they flow through the member and funnel into the support, forming a bottle-shaped strut. As the load attempts to maintain equilibrium, the transverse tensile stresses appear along the strut potentially decreasing its overall capacity. An issue arises due to the strut failing prematurely due to a wide-open shear crack. To ensure the serviceability and avoidance of premature reinforced concrete structures, minimum crack control reinforcement is typically provided as specified in AASHTO LRFD specifications. The current AASHTO LRFD provisions specify a minimum of 0.3% crack control reinforcement in both horizontal and vertical directions when the STM provisions are used (AASHTO LRFD 2020). This minimum crack control reinforcement can eliminate the complexity of checking strut capacity as well as minimize the crack width by carrying the tensile stresses developed due to the bottle-shape strut. As a result, the struts can effectively transfer loads within reinforced concrete structures. However, there is a need to bridge the gap and develop an understanding on the limitation of the spacing of crack control reinforcement regarding capacities and serviceability.

As stated previously, AASHTO LRFD (2020) specifications limit the maximum spacing to the smaller of $d/4$ and 12.0 in. If supported by data representative of bridge structures, the “ $d/4$ limit” can be relaxed and substantial savings in bridge design and construction can be materialized. Hence, the main purpose of the current study is to investigate the feasibility of relaxing the maximum spacing requirement of crack control reinforcement. This is accomplished through a

large-scale experimental program of three specimens (or six tests) and a finite element analysis for a parametric study.

Expanding the research work that was completed by Ferguson Structural Engineering Laboratory in Project 0-5253 in the year 2008, this study aims to ultimately prove whether the crack control limitations may be relaxed for disturbed regions being designed with AASHTO LRFD. Project 0-5253 is the basis of what is present in AASHTO LRDF Bridge Specifications 2020, and the primary goal is to continue the expansion of understanding and knowledge.

6.2. Experimental Program

This section describes in detail the testing methodologies used to investigate the study's objectives and goals. The experimental program investigates different shear-span-to-depth ratios (a/d ratios) and deep beam geometries while increasing the spacing limit from $d/4$ to $d/2$ or 12 in. to 24 in. Details regarding the testing matrix, specimen design, specimen fabrication, testing frame construction, and instrumentation used for data collection are discussed below.

6.2.1. Specimen Design

6.2.1.1. Test Matrix

In order to fulfill the objective of this experimental program, the report of Project 0-5253 was reviewed. Project 0-5253 completed thirty-seven deep beam specimens categorized into five series (Series I-IV and M) based on individual project tasks. Among the test series, Series III and IV were related to this study. In particular, Series III in Project 0-5253 addressed the design of minimum web reinforcement in both the longitudinal and transverse directions. The specimens in this series compared the results among five varied combinations of web densities: 1) 0.3% each way, 2) 0.25% vertical and 0.15% horizontal, 3) 0.2% each way, 4) 0.1% each way, and 5) 0% each way. Series IV, on the other hand, primarily addressed the depth effect of the beam on strength and serviceability, consisting of specimens with two types of web reinforcement ratio: 1) 0.3% each way and 2) 0.2% each way. Project 0-5253 concluded that a web reinforcement ratio of 0.3% in each orthogonal direction should be distributed across a strut. The recommendation was incorporated in the current AASHTO LRFD (2020).

The experimental program in the current study, as an extension of Project 0-5253, used the mentioned Series III and IV specimens as a baseline for comparison to develop the test matrix. In particular, the web reinforcement density was chosen as 0.3% in each orthogonal direction to comply with the current AASHTO LRFD (2020), while the spacings of the web reinforcement were chosen to be different from the baseline specimens for the current study. The companion specimens from Project 0-5253 are summarized and shaded in Table 6-1. The definition of each parameter is shown in Figure 6-1.

Table 6-1 Specimen testing details

Beam No.	Specimen ID.	b_w (in.)	h (in.)	d (in.)	ρ_v (%)	Vertical web reinforcement	ρ_h (%)	Horizontal web reinforcement	Support plate (in.)	Load plate (in.)	a/d	Spacing Criteria*
	III-1.2-03-(i)	21	42	38.6	0.30	2 Legs No. 5 at 9.5 in.	0.29	No. 5 at 10.1 in.	16 x 21	20 x 21	1.20	(i)
B1	III-1.2-03a-v(ii)	21	42	38.6	0.31	4 Legs No. 5 at 19 in.	0.29	No. 5 at 10.1 in.	16 x 21	20 x 21	1.20	(ii)
	III-1.85-03-(i)	21	42	38.6	0.29	2 Legs No. 5 at 10.0 in.	0.29	No. 5 at 10.1 in.	16 x 21	20 x 21	1.85	(i)
B1	III-1.85-03b-v(ii)	21	42	38.6	0.29	4 Legs No. 5 at 20.0 in.	0.29	No. 5 at 10.1 in.	16 x 21	20 x 21	1.85	(ii)
	III-1.2-03-(i)	21	42	38.6	0.30	2 Legs No. 5 at 9.5 in.	0.29	No. 5 at 10.1 in.	16 x 21	20 x 21	1.20	(i)
B2	III-1.2-03a-h(ii)	21	42	38.6	0.31	2 Legs No. 5 at 9.5 in.	0.29	No. 7 at 19 in.	16 x 21	20 x 21	1.20	(ii)
	III-1.85-03-(i)	21	42	38.6	0.29	2 Legs No. 5 at 10.0 in.	0.29	No. 5 at 10.1 in.	16 x 21	20 x 21	1.85	(i)
B2	III-1.85-03a-h(ii)	21	42	38.6	0.31	2 Legs No. 5 at 9.5 in.	0.29	No. 7 at 19 in.	16 x 21	20 x 21	1.85	(ii)
	IV-2123-1.85-03-(i)	21	23	19.5	0.30	2 Legs No. 4 at 6.25 in.	0.30	No. 4 at 6.25 in.	16 x 21	16.5 x 21	1.85	(i)
B3	IV-2123-1.85-03a-v(ii)	21	23	19.5	0.30	2 Legs No. 5 at 9.8 in.	0.30	No. 4 at 6.25 in.	16 x 21	16.5 x 21	1.85	(ii)
B3	IV-2123-1.85-03b-v(ii)	21	23	19.5	0.30	4 Legs No. 4 at 12.5 in.	0.30	No. 4 at 6.25 in.	16 x 21	16.5 x 21	1.85	(ii)

(i) Crack control reinforcement meets the AASHTO LRFD Spacing requirements: min ($d/4$ or 12 in.), TX Project 0-5253

(ii) Crack control reinforcement relaxes the AASHTO LRFD Spacing requirements: min ($d/2$ or 24 in.), TX Project 0-7039

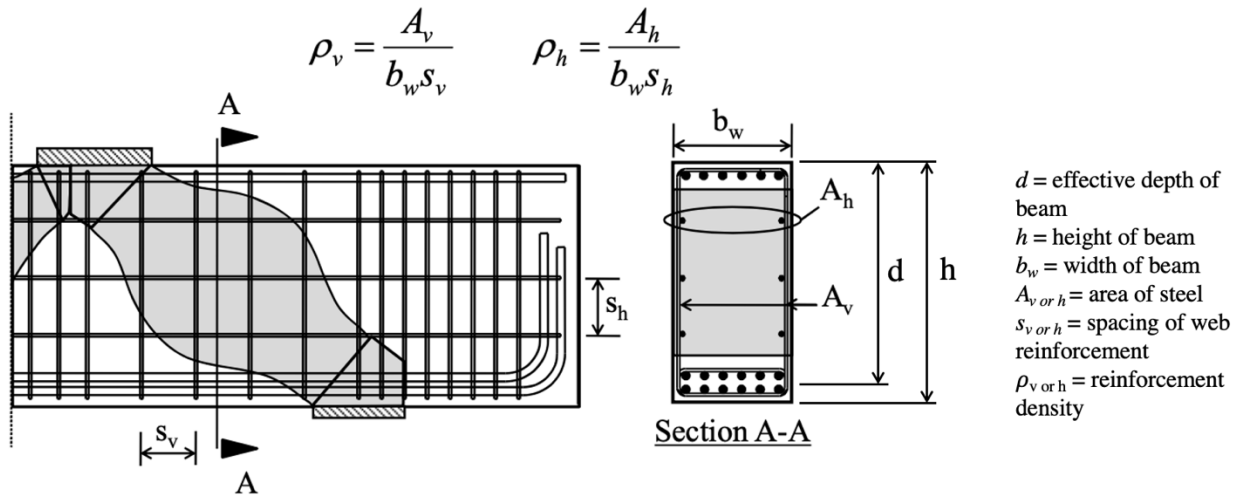


Figure 6-1 Definition of vertical and horizontal web reinforcement (Tuchscherer et al. 2008)

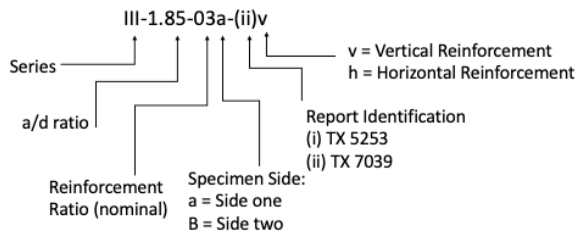
One or two tests were developed to be directly compared to the baseline specimens from Project 0-5253. The overall geometry, the boundary conditions, the aspect ratio, and the web reinforcement density in each direction of each specimen remained the same as the companion specimen. However, specimens in the current project had a larger spacing of both the vertical and horizontal web reinforcement to confirm or deny the task objective of relaxing the spacing requirement from $d/4$ or 12in. to $d/2$ or 24 in. Only one of the two types of web reinforcement (vertical or horizontal) was relaxed, while the arrangement of the other remained the same to rule out undesired effects.

A total of three deep beams (denoted as B1, B2, and B3 in Table 6-1) were fabricated with varied a/d ratios (1.2 and 1.85) and depths (23 in. and 42 in.). The selection was made to observe this attempt across a greater range of specimen types. Each of the three specimens had two separate tests to optimize the data collection.

For Beams B1 and B3 where vertical spacing s_v was increased to accommodate $d/2$ instead of $d/4$ or 24 in. instead of 12 in., the vertical reinforcing bar area A_v would also need to be increased in order to maintain the vertical rebar density of 0.3%. Here, this was achieved by increasing the number of stirrup legs within the area of interest; the stirrups had four legs in this study instead of the two in Project 0-5253. Similarly, for Beam B2, where the horizontal spacing s_h was increased to accommodate $d/2$ instead of $d/4$ or 24 in. instead of 12 in., the horizontal reinforcing bar area A_h was needed to be increased in order to maintain the horizontal rebar density of 0.3%. This was accomplished by increasing the rebar size of the web reinforcement.

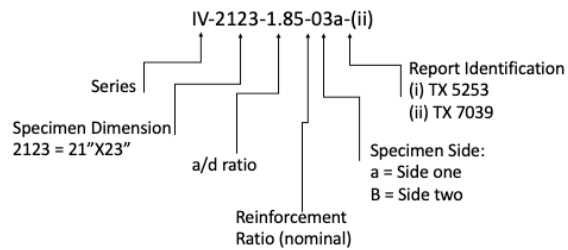
The identification process for these specimen numbers is explained in Figure 6-2(a) for Series III-based deep beams (Beams B1 and B2) and Figure 6-2(b) for Series IV-based deep beams (Beam B3). This numbering system is almost identical to that used in Project 0-5253 for recognizability.

Specimen I.D. for Specimen 1 and 2- B1, B2



(a) Series III

Specimen I.D. for Specimen 3- B3



(b) Series IV

Figure 6-2 Description of nomenclature for specimen I.D.

6.2.1.2. Specimen Detail

The detailing of all three specimens was similar to those of Project 0-5253. Figure 6-3 and Figure 6-4 were modified and adopted from Project 0-5253. Figure 6-3 references the beam geometry and reinforcement for B1 and B2, which had a height of 42 in., while Figure 6-4 references B3, which had a height of 23 in. All aspects of this detailing remained the same except for the vertical or horizontal web reinforcement spacing per specimen in the area of interest. The load and support plate dimensions were identical to those from Project 0-5253 and were chosen to allow for full bearing of the specimen to eliminate confinement effects and to ensure shear would be the primary mode of failure. A tight stirrup spacing of 4 in. elsewhere and excess tension reinforcement were provided to ensure the main failure mode would be shear in the area of interest. The clear side cover, top cover, and bottom were selected chosen to remain consistent with Project 0-5253: $\frac{3}{4}$ in. for side cover and 1 in. for top and bottom cover. These specimens were fabricated using steel formwork and side form vibrators, later discussed in Section 6.2.2, while remaining in in-door conditions where durability was not an area of concern. There were no consolidation issues with any of the specimens, and no honeycomb was seen. Thus, the clear covers were appropriate for these specimens.

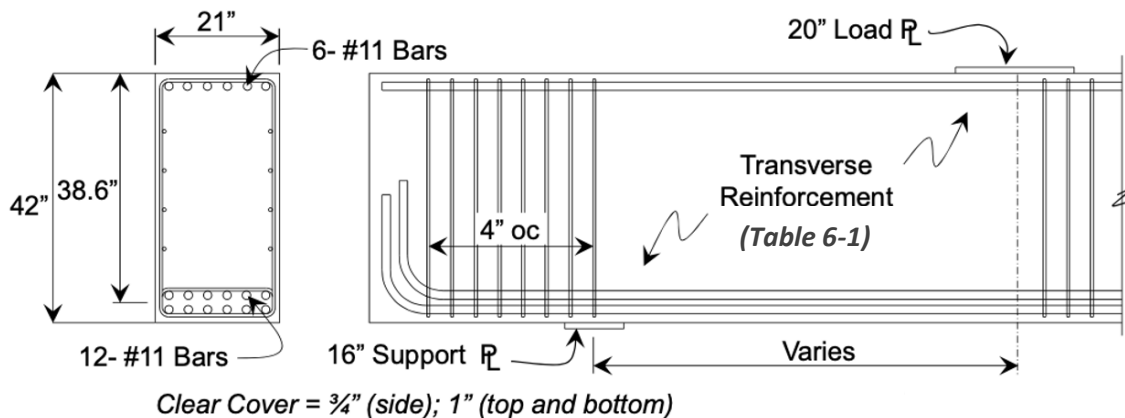


Figure 6-3 Beams B1 and B2 details

Unlike Beams B1 and B2, where two varying a/d ratios were planned, Beam B3 looked at only one a/d ratio of 1.85. The design was because, in Project 0-5253, the specimens in Series IV that had a height of 23 in. did not include a configuration having an a/d ratio of 1.2 and a web reinforcement density of 0.3% for direct comparison.

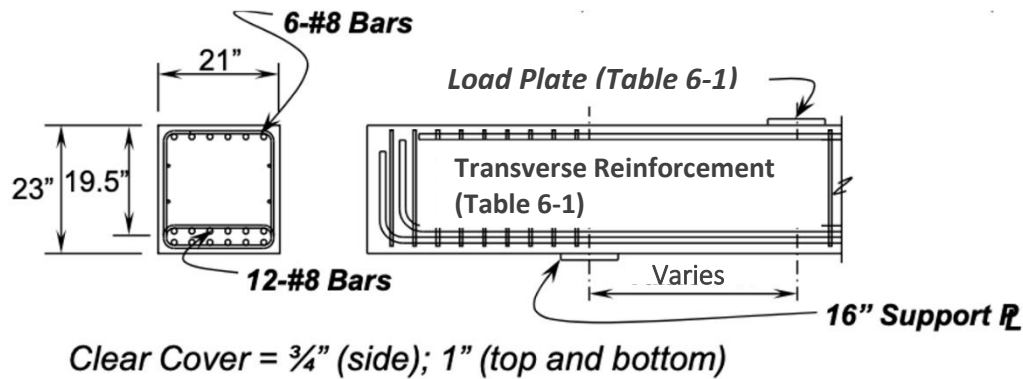


Figure 6-4 Beam B3 details

AutoCAD drawings are presented in Figure 6-5 for Beam B1, Figure 6-6 for Beam B2, and Figure 6-7 for Beam B3's reinforcement cage designs. It is important to note that the area of interest lied between the support plate and the load plate. Each of the specimens was 332 in. in length to ensure the two tests do not impact one another for how far apart their D-regions are. The first 38.375 in. from the edge of the specimen was to provide development length for longitudinal reinforcement and to fit with the test frame. It should be noted that in the fabrication of Beam B1 there was an error in this excess space. Instead of 38.375 in. being measured from the edge of the specimen to the center of the support plate, it was fabricated to be 33 in. However, the span of the D-region, the d variable within the a/d ratio, remained unchanged and was correct. The cage within the D-region was accurate, and the desired relaxed spacing was also accurate. The missing 5.375 in. was accounted for in the dead weight calculations for the ultimate capacity, which is discussed in later sections. This fabrication error was considered minor and did not impact the testing results since the total deadweight difference between the correct spacing of 38.375 in. and 33 in. is 0.219 kips otherwise 219 lbs.

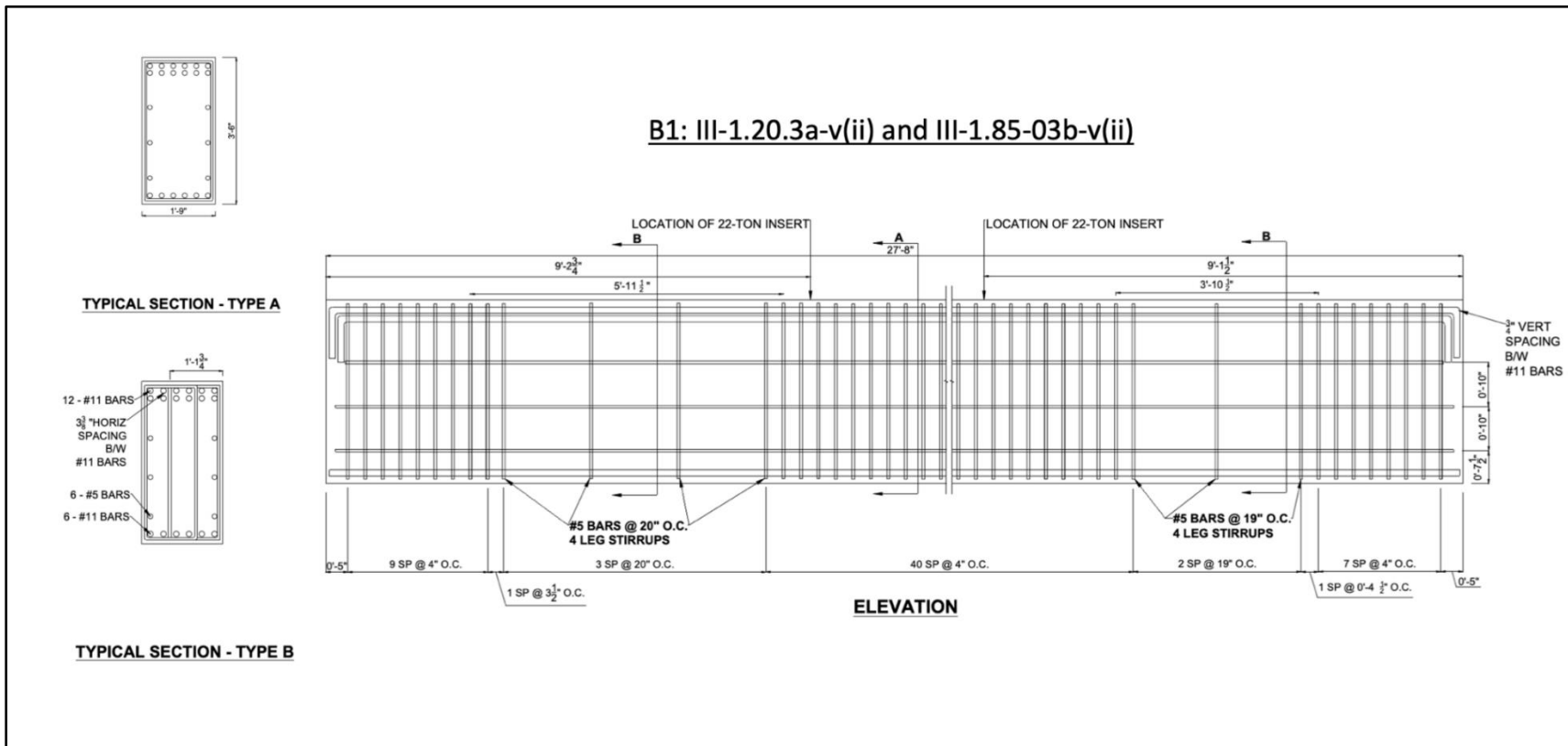


Figure 6-5 Reinforcement cage design of Beam B1

B2: III-1.20.3a-h(ii) and III-1.85-03b-h(ii)

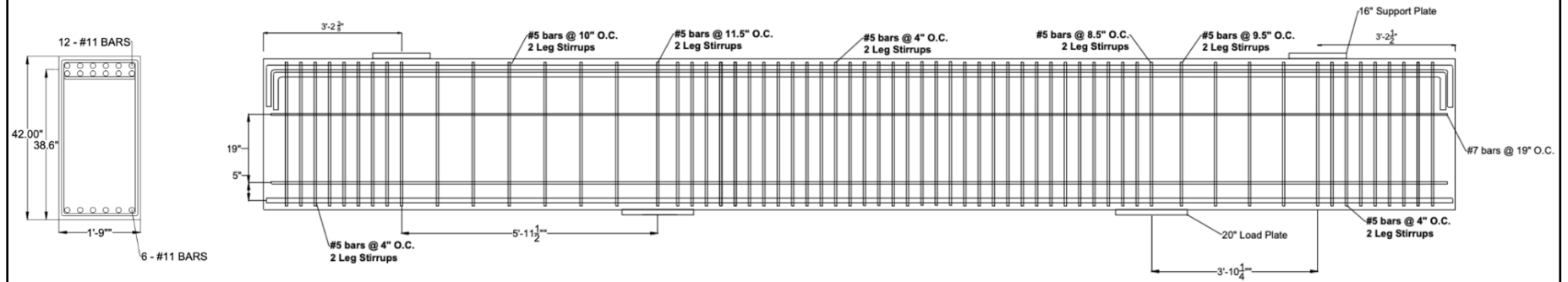


Figure 6-6 Reinforcement cage design of Beam B2

B3: IV-2123-1.85-3a-v(ii) and IV-2123-1.85-03b-v(ii)

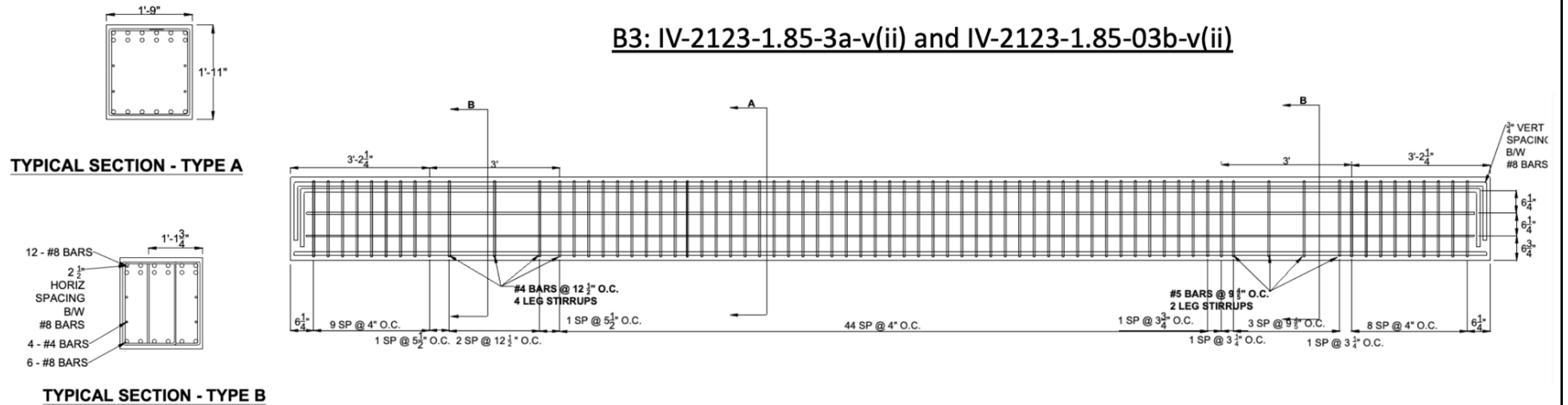


Figure 6-7 Reinforcement cage design of Beam B3

6.2.2. Specimen Fabrication and Strain Gauging

All three specimens were fabricated using a similar methodology. Four wooden chairs and two square pipes were used to suspend the cage, as seen in Figure 6-8, which shows the cage fabrication for Beam B1. Various wooden spacers were made to help space the tension reinforcement even accurately throughout the entire beam. The cage was built tension side up since the testing frame was constructed to accommodate this specimen orientation.



Figure 6-8 Fabrication setup for cage assembly

The only instrumentation that the cages received was the application of strain gauges. The strain gauges that were used for this experimental study and that were sought to be appropriate for this experiment's objective were Tokyo Measuring Instruments' product FLAB-5-11-5LJCT-F. The application of the gauges consisted of CN adhesive material, M-Coat A from Micro Measurements, SB and Scotch VM tape made of butyl rubber for waterproofing, electrical tape, and Epoweld 8173 Coating Material, otherwise known as epoxy for impact resistance during concrete casting. The strain gauges were placed in a similar and consistent pattern among all tests. Adopted from Project 0-5253, Figure 6-9 reflects the generic strain gauge placement for all specimens. The strain gauges were placed along the assumed centerline of the strut. This entailed that both horizontal and vertical reinforcement in this region were gauged. All legs of the stirrup, both internal and external, were gauged in three locations along the strut. If the structural tests consisted of 4-legged stirrups, all four legs were gauged; this strain gauge plan was mimicked on both sides of the specimen. The redundancy was to accommodate any risk of strain gauge damage through concrete casts. Longitudinal gauges were placed to measure the rebar strain along the shear span on the outermost tensile reinforcement. This allowed the maximum stress to be monitored until the beam reached failure during testing. Beam B1 consisted of a total of 48 strain gauges, where 22 gauges were applied to Test 1 [Specimen III-1.20-03a-v(ii)], and 26 gauges were applied to Test 2 [(Specimen III-1.85-03b-v(ii)]. Beam B2 consisted of a total of 44 strain gauges, where 20 gauges were applied to Test 1, [Specimen III-1.20-03a-h(ii)], and 24 gauges were applied to Test 2, [Specimen III-1.85-03b-h(ii)]. Beam B3 consisted of a total of 46 strain gauges, where 20 gauges were applied to Test 1, [Specimen IV-2123-1.20-03a-(ii)], and 26 gauges were applied to Test 2, [Specimen IV-2123-1.85-03b-(ii)].

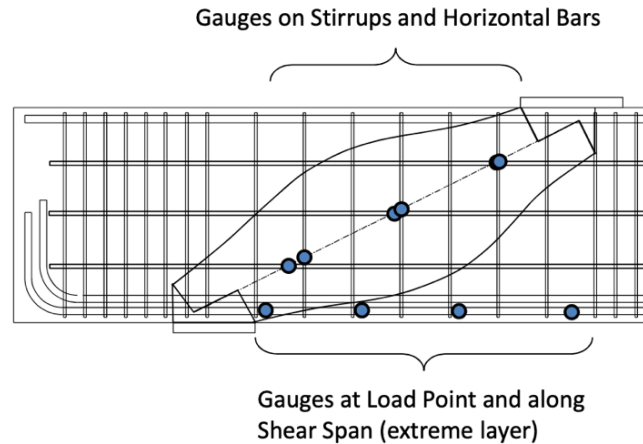


Figure 6-9 Strain gauge placement for this experimental program (Adopted from Project 0-5253)

After the steel cage was built, the strain gauge wires were routed and bagged to prevent damage and prepare for casting. Each of the four-legged stirrups was gauged, and wires routed along the strut. This can be seen in Figure 6-10 when it was completed for Beam B1. Before bagging the strain gauges, all the gauges were appropriately labeled so they could be later identified when setting up instrumentation for testing and wiring these gauges into the Data Acquisition System (DAQ).



Figure 6-10 Gauges along the strut with wiring and packaging for B1

The steel cage was lifted and placed inside the steel formwork with $\frac{3}{4}$ -in. spacers placed on all four sides of the specimen and 1-in. chairs placed on the soffit (see Figure 6-11). It is important to note that the relaxation of crack control reinforcement made fabrication easier. 4-legged stirrups did not add complexities to the rebar cage, and the applicable specimens were still easily constructed. This observation is vital to note since it contributes to the objective of the experimental program. Not only does relaxing the crack control requirement simplify rebar detailing, but it also simplifies

constructability. Once a rebar cage was completed and placed into the steel formwork, it was ready to be cast. Each cast involved two steel form vibrators and two internal vibrators, as seen in Figure 6-12. Concrete casting was done with three lifts for Beams B1 and B2 and two lifts for Beam B3 and vibrated thoroughly. After casting, the specimen was covered in a plastic sheet for curing and kept in ambient laboratory conditions.



Figure 6-11 Cage lift onto steel soffit and placement in formwork



Figure 6-12 Specimen casting and vibration techniques

The concrete mix design for all specimens was the same to allow for consistency. The main goal of choosing the concrete compressive strength was to imitate the compressive strengths reported in Project 0-5253. Since Beams B1 and B2 were a combination of two specimens from Project 0-5253, the best attempt was made to match the compressive strengths of those specimens. In Project 0-5253, Specimen III-1.20.3-(i) was reported to have an f'_c value of 4220 psi, and Specimen III-1.85.3-(i) reported an f'_c value of 4990 psi. Based on historical data from the concrete plant, 3000 psi concrete with $\frac{3}{4}$ aggregate and a slump of 7 in. was used due to the concrete plant's typical practice to overdesign concrete strength. A 7-in. slump was used to improve the workability of the concrete and ensure no honeycombing effect, especially with such small clear covers and spacing among the tension reinforcement. The read-mix plant's average reported strength for the mix selected was 4770 psi, which was desired for Beams B1, B2, and B3. Table 6-2 summarizes the concrete mix proportions proposed by the concrete plant and what was used on all the specimens.

Table 6-2 Concrete mixture proportions for all specimens

Material Type	Description	Weight
Cement	ASTM C-150 Type I/II	332 lb/cy
Fly Ash	Class F	110 lb/cy
Coarse Aggregate	3/4" Dolomite	1930 lb/cy
Fine Aggregate	Concrete Sand	1455 lb/cy
Water	Water	30 gal/cy

For each specimen on the day of casting, 25 concrete cylinder samples were taken for 7-, 14-, 21-, and 28-day compression testing following ASTM C192 procedures (see Figure 6-13(b)). Additional cylinders were made for the day of material testing, including compression tests, splitting tensile tests, and modulus of elasticity. The slump was also measured following ASTM C143 at each concrete cast, as seen in Figure 6-13(a).

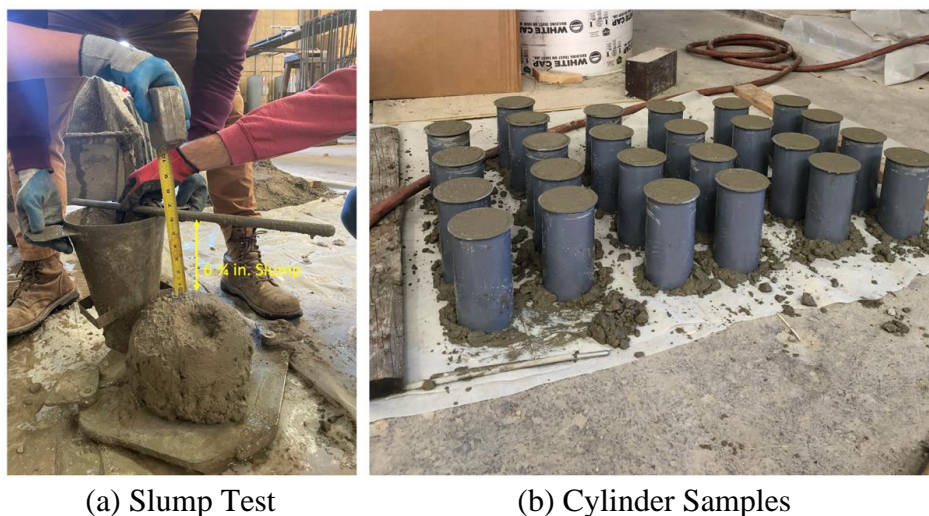


Figure 6-13 Cylinder samples and slump procedure on cast days

Table 6-3 reflects the concrete material properties that were found through the testing cylinders made through casting. The table also presents the test rebar yield strengths for each size of the reinforcement. Compressive strength, f'_c , was tested according to ASTM C39. Split tensile strength, f'_t , was tested in accordance with ASTM C496. The modulus of elasticity of the concrete, M.O.E., was calculated following the procedures in ASTM C469. Do note that Beam B2 compressive cylinder data was seen to be abnormally low during 7-day to 28-day testing. It was under the belief that abnormally high temperatures in the laboratory impacted curing. For this reason, core samples were drilled out of the Beam B2 after testing. These cores were tested according to ASTM C42, and the compressive value is presented in Table 6-3 for Beam B2. All cylinders were cured in the same manner which was to cure them near the specimen to best replicate and recreate the specimen's actual ambient conditions. Cylinders were placed under a plastic tarp near the beam's casting area. Rebar testing was also completed after casting. Complying with ASTM A370, all rebar yield information is shown in Table 6-3. When ordering rebar from the manufacturer, it was requested that all rebar for the specimen be made of the same heat.

Table 6-3 Summary of material testing results from all specimens

Specimen ID.	f'_c (psi)	f'_t (psi)	E_c (ksi)	f_y #4 (ksi)	f_y #5 (ksi)	f_y #6 (ksi)	f_y #7 (ksi)	f_y #8 (ksi)	f_y #11 (ksi)
III-1.2-03a-v(ii)	4593	455	5186	N/A	63.9	65.9	N/A	N/A	66.5
III-1.85-03b-v(ii)	4668	400	5186	N/A	63.9	65.9	N/A	N/A	66.5
III-1.2-03a-h(ii)	3391	330	6033	N/A	69.5	67.7	76.3	N/A	66.9
III-1.85-03a-h(ii)	3391	330	6033	N/A	69.5	67.7	76.3	N/A	66.9
IV-2123-1.85-03a-v(ii)	4125	478	3710	64.5	84.4	N/A	N/A	69.6	N/A
IV-2123-1.85-03b-v(ii)	4125	478	3710	64.5	84.4	N/A	N/A	69.6	N/A

6.2.3. Test Setup

6.2.3.1. Testing Frame

Once the specimens were demolded from their steel formwork, they were moved with an overhead crane using Meadow Burke anchors that were cast on the top face of the specimen. The design of the loading frame and the instrumentation reflected and imitated those originally used in Project 0-5253. Figure 6-14(a) shows the test setup used for all three specimens for structural testing. Figure 6-14(b) shows the section view of the testing setup highlighting the load transfer path. These images have been replicated from the report of Project 0-5253. Ferguson Structural Engineering Laboratory has a 96,000-pound base platen, a strong floor, installed for the purposes of these beam tests back in 2008. The test frame was designed for a reverse-beam test. A double-acting hydraulic ram would be placed on the strong floor at the desired location to achieve the correct a/d ratio, and

the beam to be tested was balanced above it. The beam would not be resting on the ram but rather on 4-ft concrete cylinders. During testing, the hydraulic ram's piston would rise until it contacted the bottom face of the specimen. It would then lift the beam until it raised off the concrete cylinder supports and came into contact with the transfer beams. One 7.8-kip transfer girder would hold six canister load cells on the west and east side of the testing frame, as seen in Figure 6-15. These load cells were pinned with a reaction nut and thus were experiencing the compression forces reacting on that side of the testing frame. A total of twelve 3-in. threaded rods were used to ensure no fatigue occurred during loading. Each of the support plates, one on the east side and one on the west side, was a pinned roller comprising 2-in. steel plates and a 2-in. diameter steel rod. The steel rod was welded to one of the plates to ensure the pinned roller behaved appropriately and allowed lateral translation. The horizontal deflection was then taken by the six threaded rods into the strong floor. The support plates were hydrostoned onto the specimen to ensure the surface was leveled and planar, eliminating eccentricity in loading.

Since the hydraulic ram was never placed in the center of the beam, it was understood that during one of the tests, the beam would come into contact with the transfer beams at varied times due to uneven loading. The transfer girders were not resting on the concrete beam specimen but resting on steel tube sleeves placed around the outer-most threaded rods. The specimens would need to be lifted approximately 2 in. before contacting the transfer beams. This would ensure that the specimen was not loaded with weight from the transfer beams until testing. These steel sleeves can be seen in Figure 6-15.

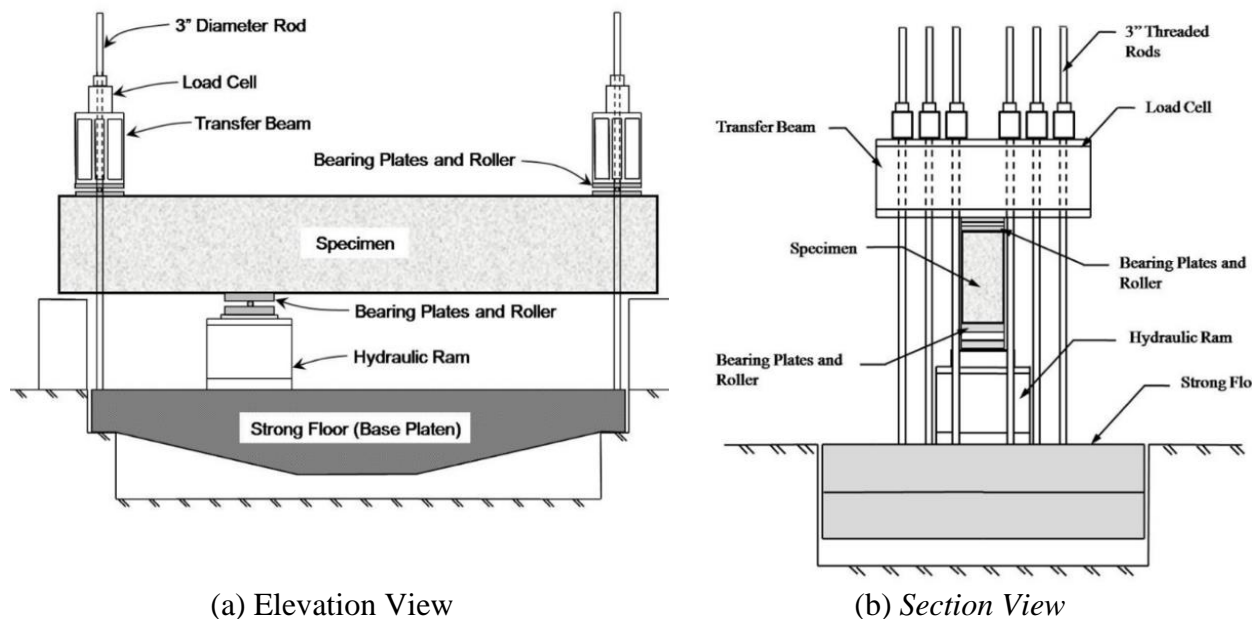


Figure 6-14 Test frame for all structural tests

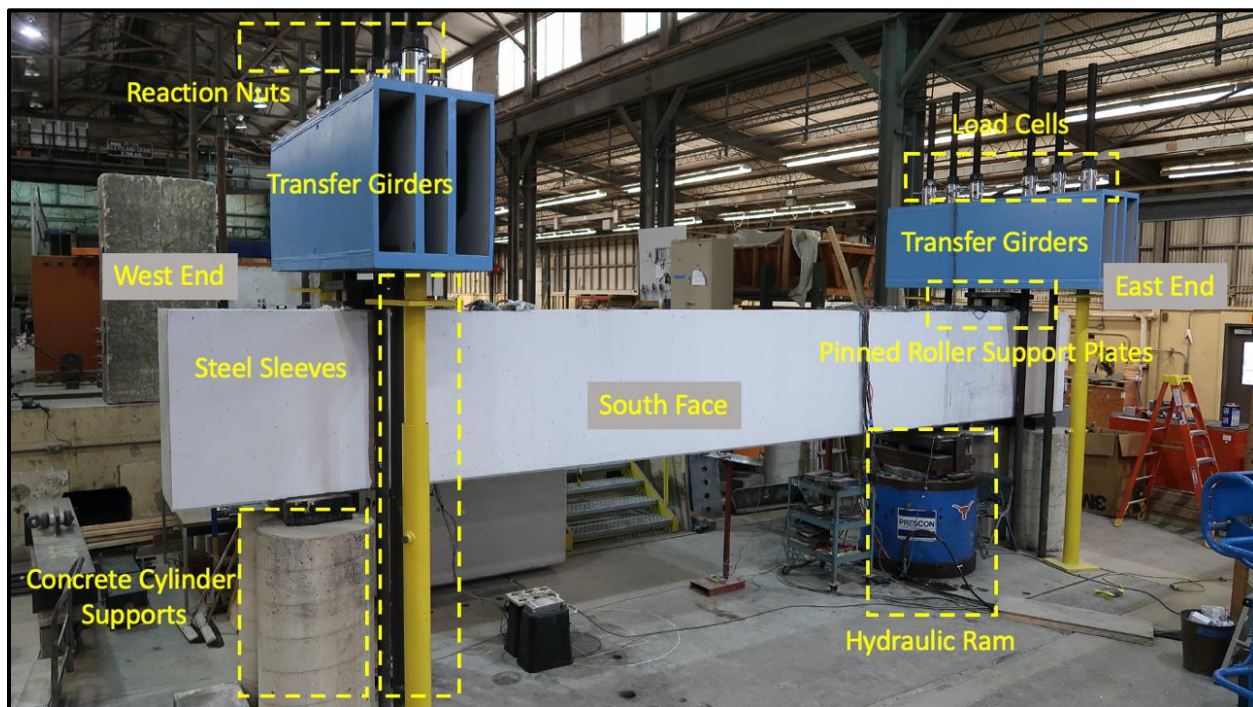


Figure 6-15 Test setup

6.2.3.2. Balancing of Load Cells and Issue with Beam B3

It is important to note that prior to each structural test, there was a procedure conducted known as “load cell balancing,” which prevented torsional effects from occurring during loading. Since all canister load cells were not identical in height and the surface of the transfer beam in which they rested was not perfectly leveled, it would result in uneven loading between the north and south ends. For instance, if the three load cells on the north end of the west transfer girder happened to be taller canisters, it would result in a larger reaction force on the north end since they engaged with the reaction nut at a greater degree. At low loads, there was no noticeable difference between the north and south ends; however, at higher loads, the difference would result in cracking differences between the north face and south face. To avoid these torsional effects, the beam was loaded to a low load, below the expected load at which the first crack was to appear, and the research team adjusted the reaction nuts accordingly to match the load read by each load cell on the DAQ. This balancing process worked well except for Beam B3. Since Beam B3 was a 23 in. specimen, the load at which the first crack occurred would be substantially lower than Beams B1 and B2. It also indicated that it would take a larger applied load until both ends, east and west, made it to full contact with the transfer girders. During the balancing of Beam B3, it was noticed that the first crack occurred at a ram-applied load of 55 kips. This is similar to what was observed in Project 0-5253. At 55 kips, only one side was in full contact with the support plate and thus was only balanced on that side. The specimen was immediately unloaded due to the concern of cracking it further. This did not impact the ultimate capacity of the specimen or serviceability. Since the

specimen was not fully balanced, there was fear of torsional effects; however, since the loads were low these effects were not great or impactful.

6.2.3.3. Instrumentation

Three main instrumentation tools used in addition to strain gauges for testing were load cells, linear potentiometers (L-pods), and a Digital Image Correlation system (DIC). 500-kip canister load cells were used to measure the reactions at both the west and east sides of the specimen during testing. Four L-pods were used on the test frame, as illustrated in Figure 6-16, which was adopted from Project 0-5253. Two L-pods were placed directly under the beam support plates, one at the load plate and the last at the specimen's center. These L-pods were not placed and tared until the beam was completely engaged with the support plates. The main intention of the L-pods was to support two main points:

- L-pods placed under the reaction plates should experience no deflection changes to ensure the testing frame is operating appropriately
- L-pods at the center of the specimen and the ram offer live information during testing to plot load vs. deflection and indicate when the specimen is failing

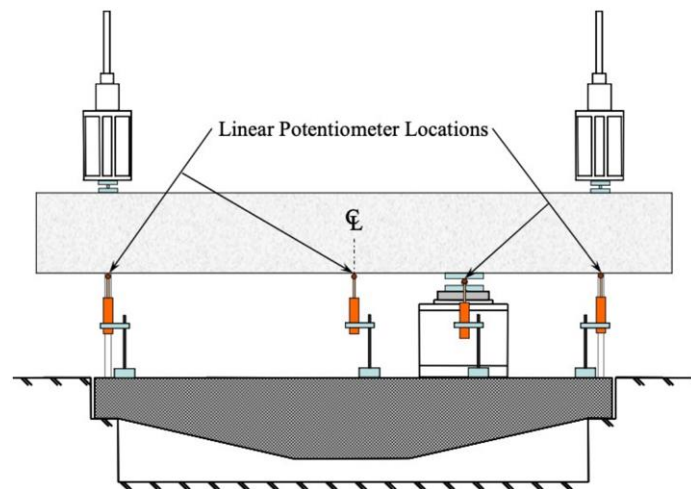


Figure 6-16 Linear potentiometer locations among the test setup (Adopted from Project 0-5253)

The DIC system was employed to capture the surface strain map during loading. The south side of the testing specimen was chosen to apply DIC speckle patterns on the concrete surface. These dots allowed the DIC system to track displacements of the speckle patterns through testing. The entire area of interest was covered with these painted dots, as seen in Figure 6-17. The DIC cameras were calibrated using calibration boards prior to testing to account for laboratory lighting and conditions.



Figure 6-17 Speckling for DIC applied to area of interest

6.2.4. Testing Procedure

Each test had an established loading increment that was 10 percent of the expected capacity at failure. The DAQ, Agilent Keysight model, scanning every 3-second interval, was tared and began collecting data before the loading of the specimen began. Once the specimen was loaded, it was monitored until the near-side s plate came into contact. The near side is defined as the reaction side of the beam that is closest to the loading ram and, thus the area of interest. Once that side was initially in contact, the loading was slightly slowed in anticipation of the far side coming into contact. Once the far side was in contact, the specimen was fully engaged. The loading was temporarily halted as the L-pods were set up and leveled in their appropriate positions. The DIC system was started capturing images at the same 3-second intervals as the DAQ system did. At each load increment, the specimen was monitored for cracks on both the north and south ends using a crack comparator card. An image of the testing region on the north face was taken at each loading increment to monitor the main diagonal crack. These steps were repeated for each loading increment until failure.

Each deep beam was tested twice. In preparation for the second test, a post-tensioned clamp was added along the diagonal crack on the previous test to repair the region. This would allow the failure from Test 1 not to affect the results of Test 2. The clamp was post-tensioned to approximately 1.15 times the expected shear anticipated in that region for Test 2. This clamp can be seen in Figure 6-18. Once the clamp was secured, the hydraulic ram was moved to the necessary location for Test 2, and the procedures were repeated.



Figure 6-18 Post-tensioned clamp added to specimen after Test 1 in preparations for Test 2

6.3. Test Results and Discussion

The experimental results of large-scale structural testing are presented in this section. This section is divided into holistic elements below that address this research task and project goals. These subsections are as follows:

- Ultimate strength results of each of the six structural tests and how they performed in comparison to their companion specimens from Project 0-5253 (Section 6.3.2)
- Crack widths based on serviceability loading for all six structural tests and how they compare to their companion specimens from Project 0-5253 (Section 6.3.4)
- Crack control reinforcement engagement along the path of the strut (Section 6.3.5)

6.3.1. Summary of Strength Results and Material Testing Data

The experimental results of all six structural tests are presented in Table 6-4. Information regarding the specimen geometry described and presented in Section 6.2 is again repeated and shown. The companion specimens from Project 0-5253 are also included to denote values that were pulled and depicted in graphs introduced in later sections. These companion specimens are shaded in Table 6-4 for the reader's convenience. The variables listed within Table 6-4 are described as follows.

b_w	=	beam width, in.
d	=	effective depth, in.
f'_c	=	compressive strength of concrete in accordance with ASTM C39, psi.

f_{yl}	=	yield strength of the longitudinal reinforcement in accordance with ASTM A370, ksi.
f_{yv}	=	yield strength of the vertical web reinforcement in accordance with ASTM A370, ksi.
f_{yh}	=	yield strength of the horizontal web reinforcement in accordance with ASTM A370, ksi.
a/d	=	shear span-to-depth ratio, whether 1.20 or 1.85 in this testing sequence
V_{test}	=	maximum shear carried in test region, including the estimated self-weight of the specimen and transfer girders, kip

Table 6-4 Summary of Experimental Results

Beam No.	Specimen ID.	b_w (in.)	h (in.)	d (in.)	f'_c (psi)	f_{yl} (ksi)	f_{yv} (ksi)	f_{yh} (ksi)	a/d	V_{test} (kip)	$\frac{V_{test}}{f'_c b_w d}$	Spacing Criteria
	III-1.2-03-(i)	21	42	38.6	4220	66	68	68	1.20	829	0.24	(i)
B1	III-1.2-03a-v(ii)	21	42	38.6	4593	67	64	64	1.20	752	0.20	(ii)
	III-1.85-03-(i)	21	42	38.6	4990	69	64	63	1.84	412	0.10	(i)
B1	III-1.85-03b-v(ii)	21	42	38.6	4668	67	64	64	1.84	612	0.16	(ii)
	III-1.2-03-(i)	21	42	38.6	4220	66	68	68	1.20	829	0.24	(i)
B2	III-1.2-03a-h(ii)	21	42	38.6	3391	67	70	76	1.20	634	0.23	(ii)
	III-1.85-03-(i)	21	42	38.6	4990	69	64	63	1.84	412	0.10	(i)
B2	III-1.85-03a-h(ii)	21	42	38.6	3391	67	70	76	1.84	457	0.17	(ii)
	IV-2123-1.85-03-(i)	21	23	19.5	4160	66	66	66	1.85	329	0.19	(i)
B3	IV-2123-1.85-03a-v(ii)	21	23	19.5	4125	70	64	65	1.85	315(f)	0.19	(ii)
B3	IV-2123-1.85-03b-v(ii)	21	23	19.5	4125	70	65	65	1.85	346(f)	0.20	(ii)

(i) Crack control reinforcement meets the AASHTO LRFD Spacing requirements: min ($d/4$ or 12 in.), Project 0-5253

(ii) Crack control reinforcement relaxes the AASHTO LRFD Spacing requirements: min ($d/2$ or 24 in.), this experimental study

(f) The test was halted due to the crushing of concrete near the load plate and the tensile reinforcement yielding along the tie

As noted in Table 6-4, the specimens with a depth of 23 in. [Specimens IV-2123-1.85-03a-v(ii) and IV-2123-1.85-03b-v(ii)] in this experimental setup failed in flexure. Specifically, both tests for Beam B3 had longitudinal reinforcement on the tension side yielding and observed concrete crushing and spalling near the load plate. The roller at the load plate began to rotate to such a degree the tests were stopped and declared to have failed in flexure. The diagonal shear crack had not fully reached the load plate, where the CCC node was modeled in the later STM analysis. Further discussion of this failure can be found in Section 6.3.3.3. The results of these flexural failures were still considered valid for the later evaluation of the strength of the diagonal strut since the STM does not consider flexural and shear failure modes separately. All other structural tests failed through the direct-strut transfer mechanism. This was observed when the diagonal shear crack was fully developed to the load and support plates, and concrete crushing was observed near the strut-to-nodal interfaces.

The evaluation of the strength of the specimens was completed using the same methodology as Project 0-5253 to allow for direct comparison to the companion specimens. Specifically, shear force across the critical section of the area of interest, V_{test} , was calculated in consideration of the applied load and dead loads. The critical section was the middle of the diagonal strut, otherwise the halfway point between the support plate and load plate. Because the load cells took only the raw reaction force from the applied load, additional dead loads were considered for calculations. The dead loads included the self-weight and the weights of the transfer girders. These weights were added to the V_{test} calculation to accurately calculate the appropriate shear. Figure 6-19 shows the typical configuration and calculation of V_{test} for all three beams (six structural tests). In the figure, P_L is the total load reading from the load cell instrumentation within the frame, which is the addition of R_A and R_B , which are the reaction loads. P_{TR} is representative of the dead weight of the transfer beams that were used in the testing frame. These blue transfer beams were the same that were used in Project 0-5253 and thus also equal to 7.8-kips. P_D is the self-weight of the specimen, and its calculation can be seen in Figure 6-19. This figure is adopted and slightly modified from Project 0-5253.

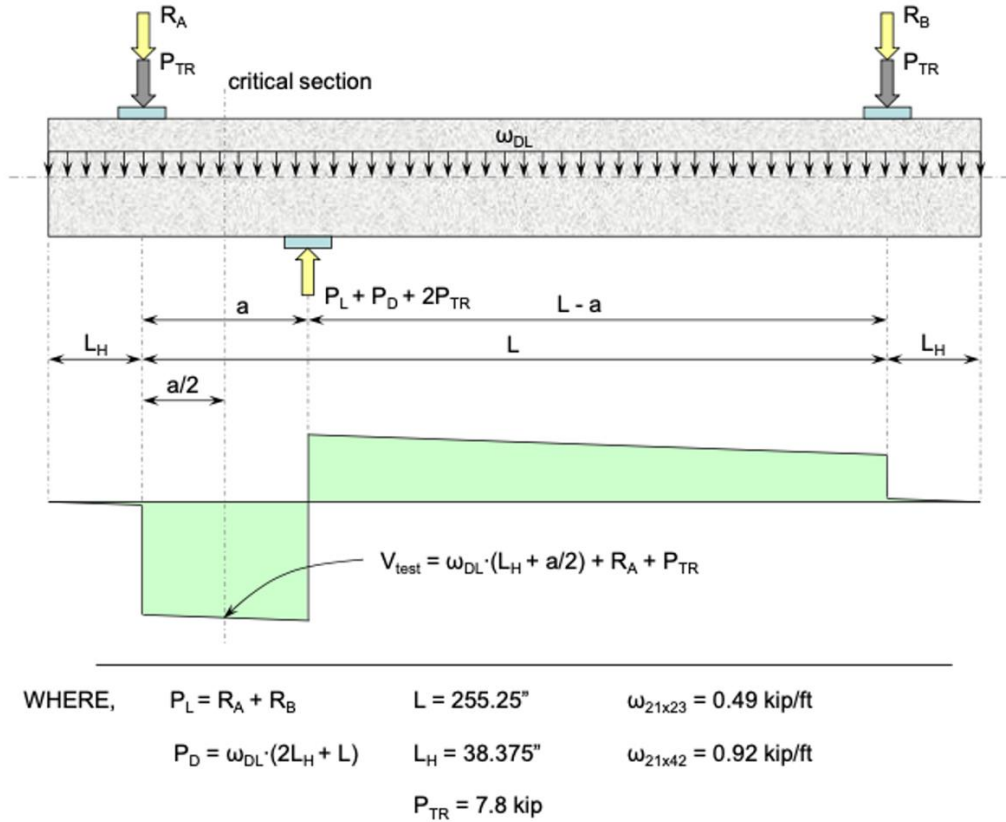


Figure 6-19 Force and shear diagram for all structural beam tests (adopted from Project 0-5253)

The test shear capacity, V_{test} , was normalized to facilitate direct comparison. The normalization was to divide the V_{test} by the specimen's cross-sectional properties times the concrete compressive strength, as used in Project 0-5253. Using f'_c instead of the square root of f'_c was deemed legitimate because the crushing of concrete was observed near the strut-to-node interfaces of Beams B1 and B2. Beam B3 had tie failure along with concrete crushing both at the loading plate at failure at the CCT node, which made the normalization with f'_c still valid.

6.3.2. Ultimate Strength Results and Comparison to STM Estimations

The STM per current AASHTO LRFD design provisions was applied to calculate the ultimate capacity of the specimen. The sizing approach used for the CCC and the CCT nodes was the same as described in Section 5.4.2. With the sized nodal zones, the capacities of the following elements were then calculated to determine the control failing mechanism. A sample calculation can be found in Appendix A.

- CCC Node Strut Interface
- CCC Node Back Face
- CCC Node Bearing Face
- CCT Node Strut Interface
- CCT Bearing Face
- Tie Force

Once these capacities were calculated, the lowest capacity was identified and assumed to be the permissible forces of the strut-and-tie model. It is a typical practice not to check the CCT back face since the distribution of bond stresses behind the node is not concentrated at its assumed location, and the stress level does not cause the crushing of concrete. All other elements listed above were then back calculated in terms of P_L , corresponding to the applied load at the load plate. The lowest value of P_L found would be the expected failure load of the specimen and a clear indication of which element will experience failure first and what should be physically observed. Once P_L was estimated through this methodology, V_{STM_Calc} was determined in a similar matter to determining V_{test} for the structural tests. The only difference is the R_A value for a structural test was known by the load cells' readings, while the STM results were back-calculated from P_L using statics and test frame geometry. Once V_{STM_Calc} was calculated, it was normalized using the same expression, $f'_c b_w d$. A summary of these normalized shear capacities can be seen in Figure 6-20.

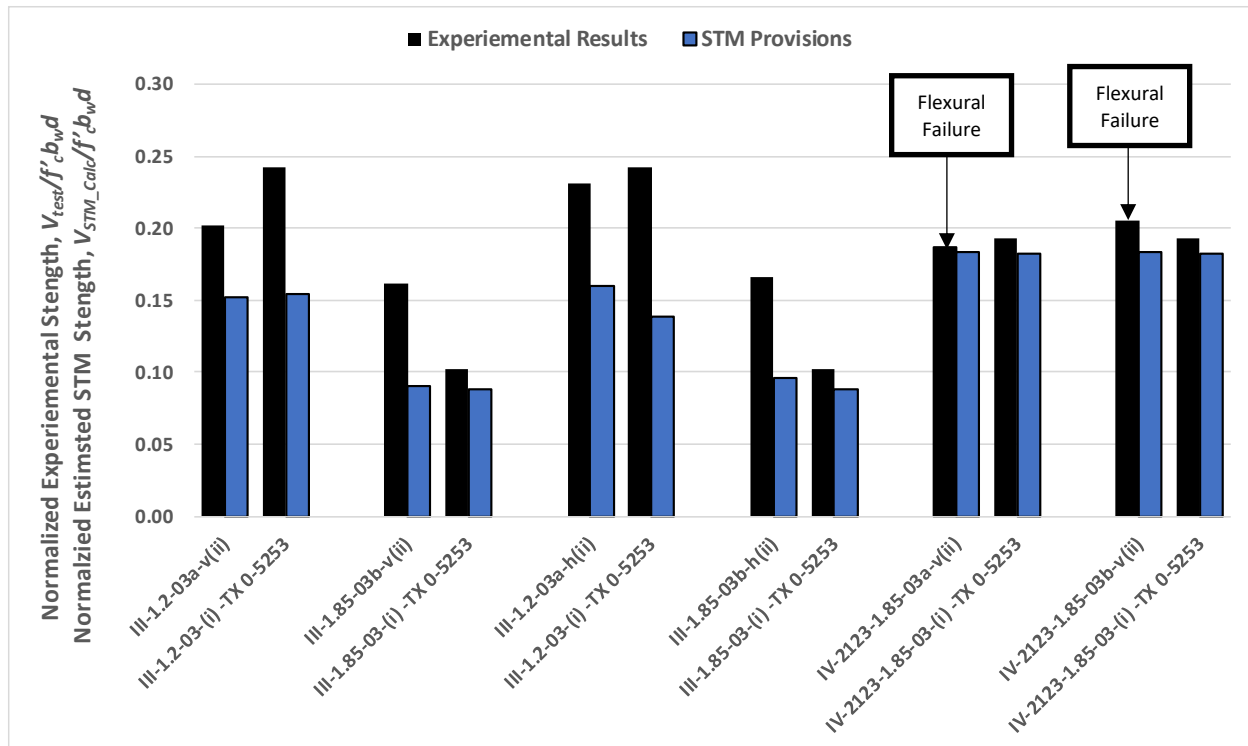


Figure 6-20 Summary of normalized ultimate capacities of structural tests with their normalized STM estimation and their Project 0-5253 counterpart

As observed in Figure 6-20, every structural test conducted in this experimental program exceeded the STM capacity prediction. The strut-and-tie model still proved to be a conservative estimation of specimen capacity even when the crack control spacing was relaxed from $d/4$ to $d/2$. Whether

the crack control spacing changed for the vertical bars, as seen in Beams B1 and B3, or the horizontal spacing was relaxed, as seen in Beam B2, capacity still far surpassed what was assumed. No alterations are needed to occur for elemental capacities within STM according to the current AASHTO LRFD provisions.

6.3.3. Comparison to Project 0-5253 Companion Specimens

A valuable indicator in identifying whether the test results of the experimental program made logical sense was the comparison to Project 0-5253. All basis for calculating shear capacities and normalization was based on this previous research program; thus, comparisons of the specimens were appropriate. Project 0-5253 reported V_{test} , f'_c , and specimen geometries for capacity normalization. These values are listed in Table 6-4 and later pulled for visualization purposes in Figure 6-20. Specific comparison and crack pattern observation between this experimental study and Project 0-5253's counterparts can be found in later sections. To observe correlations between all structural tests, Figure 6-21 was produced. A ratio of V_{test} to V_{STM_Calc} was calculated for every structural test and plotted against f'_c . A benchmark was plotted to show that all specimens tested, and their companion specimens surpassed the calculated capacities. The results suggest that the conservatism within the strut-and-tie modeling analysis is still present and satisfactory whether crack control spacing is relaxed with the compressive strength of concrete ranging from 3391 psi to 4668 psi. It can be seen in Figure 6-21 for the 21" by 23" specimens that calculated capacities were accurate representations of structural capacities. The 21" X 23" specimens highlighted are from both Beam B3 within the experimental program and Project 0-5253. The analytical results indicate that the STM generated better predictions for deep beams failing in flexure.

The analysis suggests that the crack control spacing changes between the two specimens had no impact on the conservatism of the STM on the three structural tests conducted. The coverage of f'_c included commonly used concrete compressive strength in the field. AASHTO LRFD STM design provisions overall deliver conservative predictions seemingly independent of the compressive strength of concrete when deep beams fail in shear; the method delivers accurate predictions for deep failing in flexure, whether the spacing requirements are relaxed or not. In sum, the STM holds to be an accurate modeling method for deep beams.

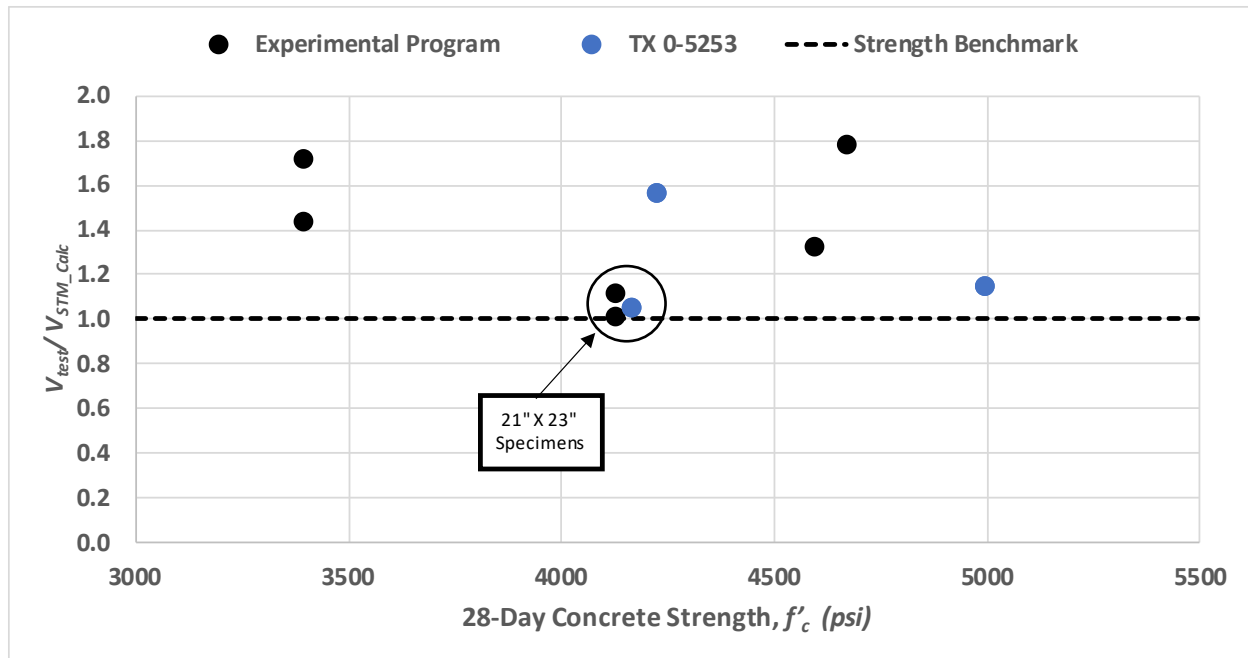


Figure 6-21 Normalized shear capacity ratio to compressive concrete strength for B1, B2, B3, and Project 0-5253 companion specimens

Figure 6-22 further suggests that the current STM design provisions do an appropriate job of conservatively estimating capacity. The ratio of V_{test} to V_{STM_Calc} ratio was plotted against s/d , which is the ratio of the spacing of crack control reinforcement to the effective depth. The same strength benchmark from Figure 6-21 was plotted again in Figure 6-22. Two additional benchmarks are shown to reflect the spacing limits. The blue dashed benchmark plotted vertically at s/d of 0.25 reflects the current spacing limit in AASHTO LRFD. The black dashed benchmark plotted vertically at s/d of 0.50 reflects the suggested spacing relaxation and the actual crack control spacing of this experimental study's specimens. It is seen that all Project 0-5253 specimens correlate around the current AASHTO spacing limit benchmark, while all tests from Beams B1, B2, and B3 correlate around the relaxed spacing limit benchmark. Although the s/d ratio was increased, the predictive ability of the STM on this program's specimens was not inferior. It should be noted that the experimental vertical and horizontal spacing relaxation is also differentiated in the figure.

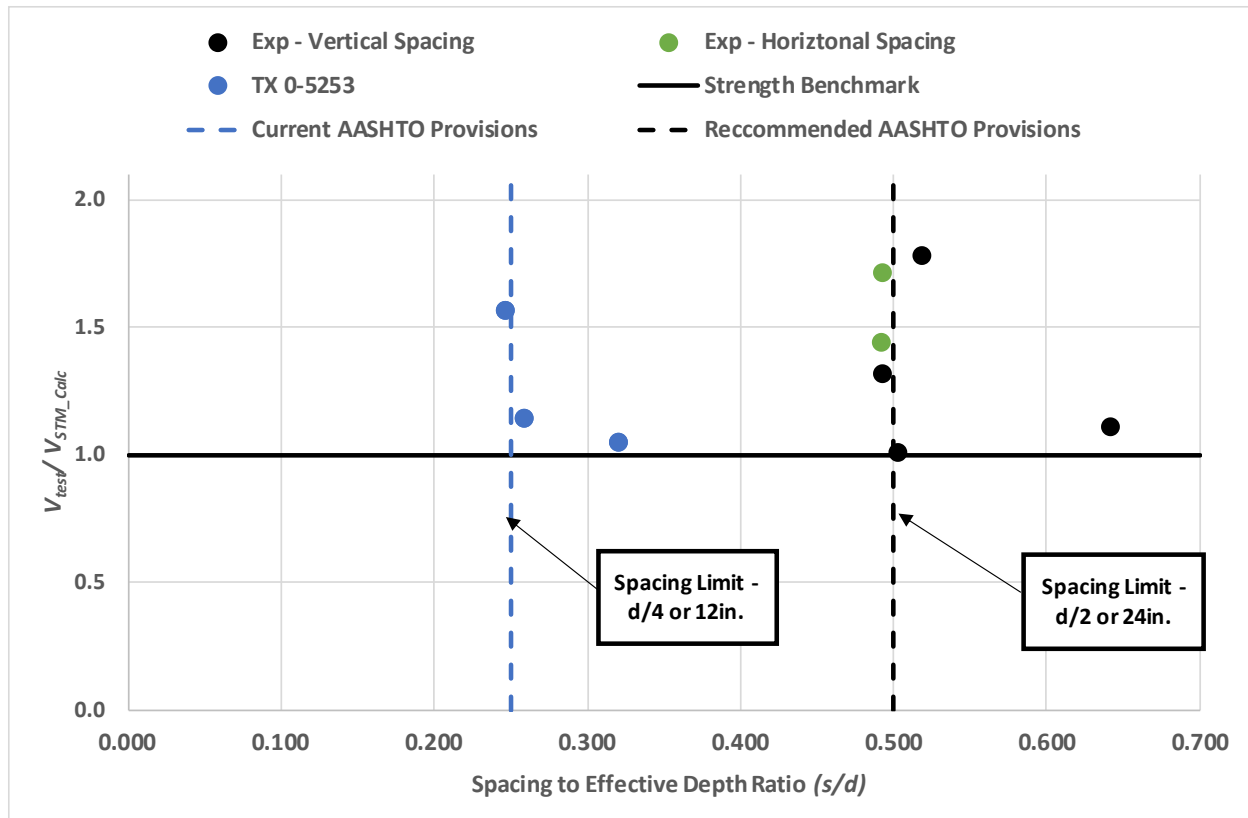


Figure 6-22 Normalized shear capacity ratio to spacing and effective depth ratio for B1, B2, B3, and Project 0-5253 companion specimens

6.3.3.1. Beam B1 – Ultimate Capacity Discussion, Crack Pattern Observations, and Failure Mode Analysis

Beam B1 was comprised of two various web reinforcement spacings and a/d ratios. Test 1 of Beam B1 [Specimen III-1.2-03a-v(ii)] had an a/d ratio of 1.20. This test's companion specimen from Project 0-5253 is denoted as Specimen III-1.2-03-(i). Figure 6-23 isolates Specimen III-1.2-03a-v(ii) with its companion and depicts the normalized peak shear capacities and estimated capacities per AASHTO LRFD's STM provisions for both tests. The STM capacity estimate was not the same between Specimens III-1.2-03a-v(ii) and III-1.2-03-(i), although the specimen geometries were identical due to the difference in concrete compressive strengths, resulting in a different CCC strut-to-node interface capacity. Figure 6-23 also shows the specimen cracking patterns observed at failure for both structural tests. The image corresponding to Specimen III-1.2-03-(i) was pulled directly from the published report of Project 0-5253. White lines were used on these images to highlight and emphasis the cracking on the concrete surface. Note that the images are rotated 180 degrees showing that the CCC node is on top of the image while the CCT node is at the bottom of the image. The testing frame was oriented to be a reverse bending test with tension reinforcement on the top for simpler cage manufacturing. However, the tension reinforcement in the field is typically on the bottom of deep beams due to common loading patterns. To avoid confusion, the images were rotated to reflect in-field conditions.

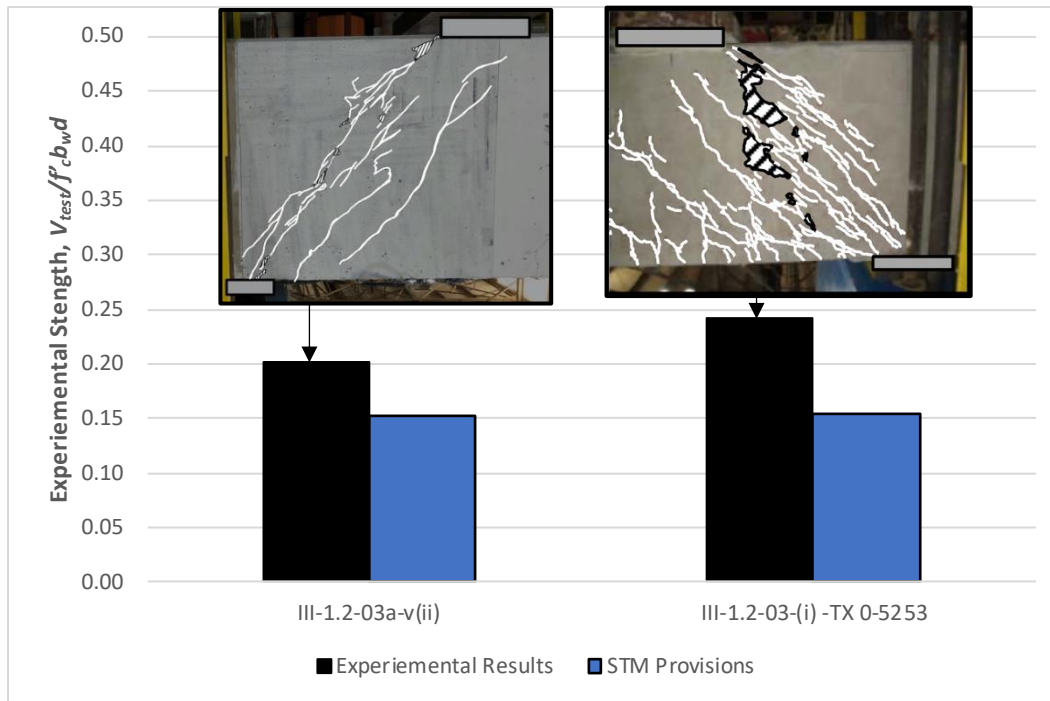


Figure 6-23 III-1.2-03a-v(ii)'s and its Project 0-5253's normalized ultimate capacities with STM estimations

Although the ultimate shear capacities were normalized to accommodate the difference in the compressive strength of concrete, there was still a decrease in capacity observed between Specimens III-1.2-03a-v(ii) and III-1.2-03-(i). Approximately a 17% reduction in strength was seen when the vertical crack spacing was relaxed. To reemphasize, this reduction does not infer any issue with the current STM provision when estimating capacity; however, it does suggest a slight reduction in the strength of the diagonal strut due to cracking pattern variation. Specimen III-1.2-03-(i) shows a significantly larger number of discontinuous cracks along the path of the interior diagonal strut. This was to be expected since the orthogonal grid of crack control reinforcement is distributed along the strut. Cracks tended not to be continuous when a stirrup was along its path since the tensile stresses would transfer through the reinforcement instead of widening cracks. However, for Specimen III-1.2-03a-v(ii), two primary diagonal cracks formed and delineated the shape of a bottleneck, and there was not much discontinuity. It is plausibly due to the vertical crack control reinforcement being more widely spaced; therefore, fewer diagonal cracks would continue to grow and widen rather than having more discontinuous cracks. A larger primary crack along the strut was considered detrimental, resulting in a reduction in strength for less aggregate interlock. Analysis of how these cracks impacted the serviceability is introduced in Section 6.3.4.2. The failure mode of Specimen III-1.2-03a-v(ii) was just as predicted from STM back calculations, which showed the CCC back face and CCC nodal strut interface to be the first elements of failure in the assumed strut-and-tie model. This was physically observed as the strut crushing, which was seen both in Specimens III-1.2-03a-v(ii) and III-1.2-03-(i). The concrete spalling because of crushing is depicted in Figure 6-23 and observed to be more prevalent near the CCC node.

Test 2 of Beam B1 had an a/d ratio of 1.85. This test's companion specimen from Project 0-5253 is denoted as Specimen III-1.85-03-(i). Similarly, Figure 6-24 isolates Specimen III-1.85-03b-v(ii) with its companion and depicts both structural tests normalized ultimate shear capacities and estimated capacities per the STM provisions in AASHTO LRFD. The organization of Figure 6-24 is made in a similar manner to Figure 6-23.

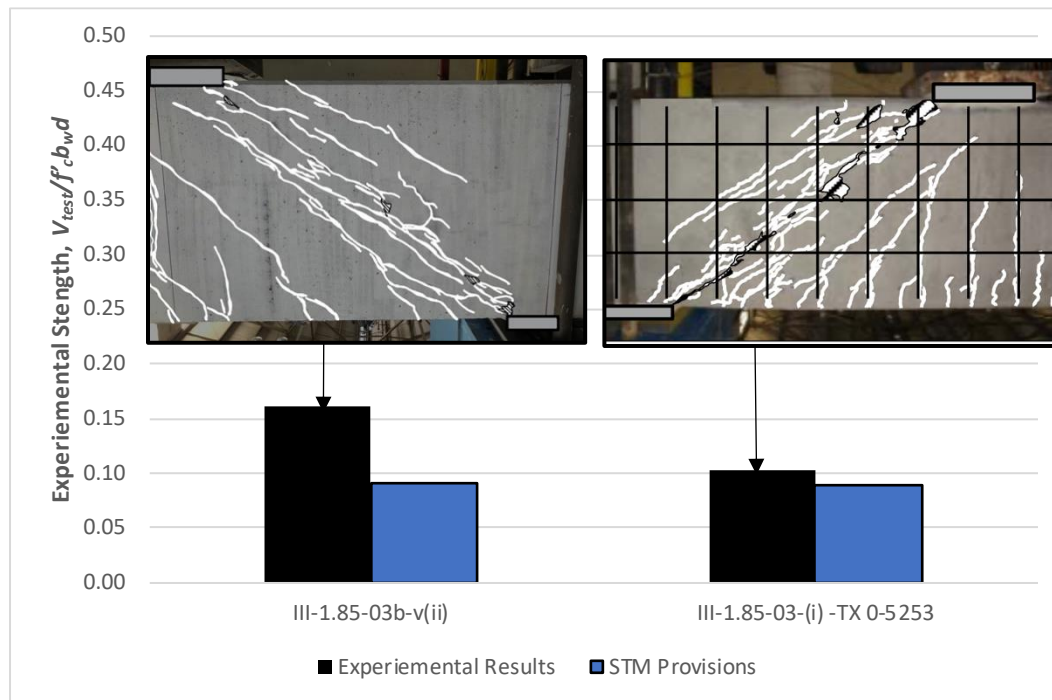


Figure 6-24 Beam 1 Test 2's and its Project 0-5253's normalized ultimate capacities with STM estimations

Unlike Specimen III-1.2-03a-v(ii) and its companion, Specimen III-1.85-03b-v(ii) proved to have a higher ultimate capacity compared to its companion specimen from Project 0-5253 when normalization was applied. This is not to be assumed that Specimen III-1.85-03-(i) of Project 0-5253 was inferior to Specimen III-1.85-03b-v(ii) but rather reflects the significant scatter that typically exists for shear results in deep beam structural tests and evaluations. Project 0-5253 reported seeing an unusually low normalized capacity in shear with this specimen, plausibly because high concrete compressive strength has low efficiency factors. For reference, Project 0-5253 also tested a similar specimen, identified as Specimen III-1.85-03b, which had the same specimen geometries, the same load and support plate dimensions, and the same reinforcement densities in the horizontal and vertical direction. This specimen is noted as Specimen III-1.85-03b-(i) for consistency throughout the rest of this experimental study and report. The only difference between the two specimens was the crack control reinforcement size and spacing, but it still satisfied the minimum required orthogonal densities (0.3%). The test of Specimen III-1.85-03b reported a weaker concrete compressive strength of 3,330 psi compared to the companion specimen chosen for this experimental study which was 4,990 psi. Despite f'_c being lower, Specimen III-1.85-03b-(i) had a higher ultimate shear capacity of 471 kips compared to Specimen III-1.85-03-(i)'s 412 kips, as seen in Table 6-4. Project 0-5253 reports that this discrepancy in

capacities is unexplained since all testing procedures, concrete mix designs, casting, and fabrications processes, and such remained the same. If Specimen III-1.85-03b-(i) was chosen to be the companion specimen for III-1.85-03b-v(ii), normalized V_{test} results would be observed in Figure 6-25. In this case, there was a loss in capacity of approximately 8% when the spacing limit was relaxed. It can be argued that due to the possible scattering in capacities if the normalized capacity of Specimen III-1.85-03b-v(ii) is close to the counterpart of Project 0-5253. Nevertheless, the STM calculated capacity was still conservative; relaxing the spacing limits is permissible.

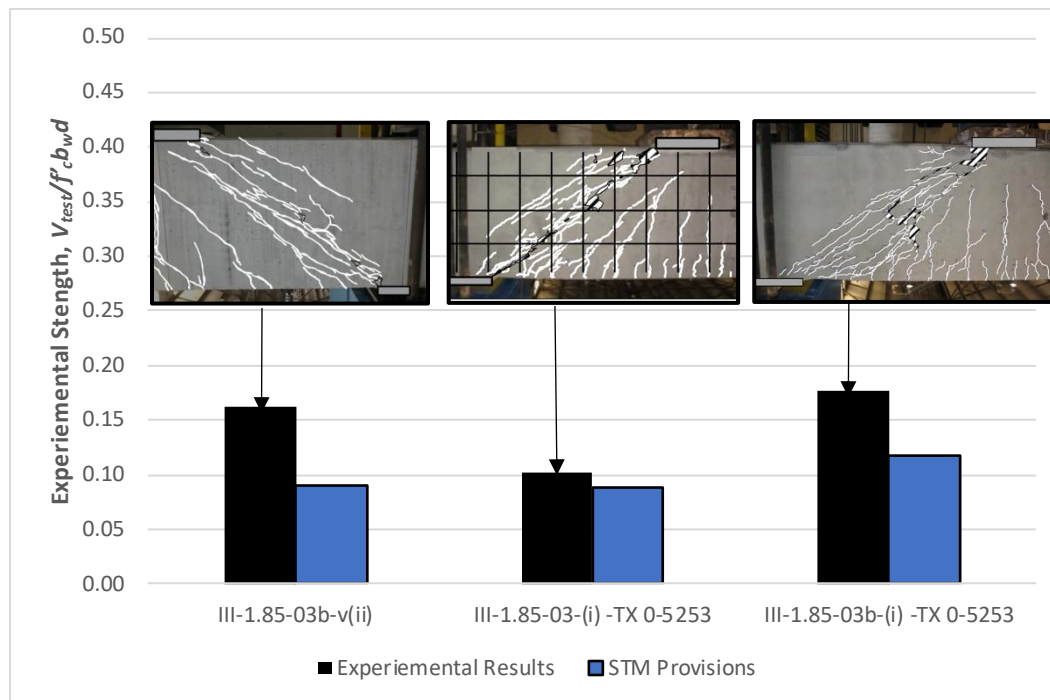


Figure 6-25: Normalized Capacities of Beam 1 Test 2 and additional Project 0-5253 specimens

For the purposes of this discussion, Specimen III-1.85-03-(i) is used for the comparison of cracking patterns and failure modes. Similar to the discussion for Specimen III-1.2-03a-v(ii) earlier in this section, Specimen III-1.85-03b-v(ii) exhibited less discontinuity and distribution in cracking. Similarly, larger vertical web reinforcement spacing leads to largely spaced and wider cracks with fewer numbers. Even though the cracking pattern was different, the failure modes remained the same and agreed with what the strut-and-tie model predicted for the area of concern. The failure mode for both Specimens III-1.85-03b-v(ii) and III-1.85-03-(i) was the crushing of the strut confirmed with concrete spalling at the CCC node.

6.3.3.2. Beam B2 – Ultimate Capacity Discussion, Crack Pattern Observations, and Failure Mode Analysis

The design of Beam B2 was similar to Beam B1, comprising two test regions with different spacings and configurations to offer a holistic conclusion. However, Beam B2 altered the

horizontal crack control reinforcement spacing, while Beam B1 altered the vertical crack control reinforcement spacing.

Test 1 of Beam B2 had an a/d ratio of 1.20. This test's companion specimen from Project 0-5253 is denoted as III-1.2-03-(i), the same companion specimen as III-1.2-03a-v(ii). Figure 6-26 isolates Specimen III-1.2-03a-h(ii) with its companion and depicts their normalized ultimate shear capacities and estimated capacities per STM provisions of AASHTO LRFD. A description of the development of this figure type of ultimate capacity analysis for all structural tests in this program can be read in Section 6.3.3.1.

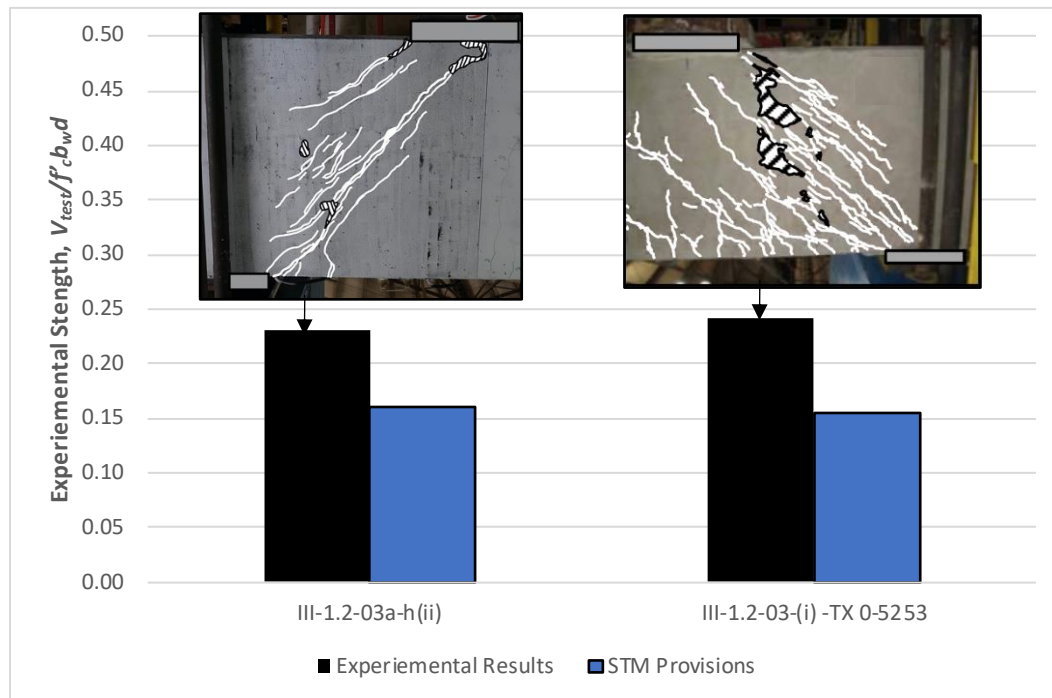


Figure 6-26 Beam 2 Test 1's and its Project 0-5253's normalized ultimate capacities with STM estimations

Similar to Specimen III-1.2-03a-v(ii), Specimen III-1.2-03a-h(ii) performed slightly lower in ultimate capacities compared to the companion specimen. A possible explanation for the decrease in capacity is that distributing horizontal reinforcing bars at a larger spacing also resulted in fewer but wider cracks, which is later discussed in Section 6.3.4.2. Nevertheless, the difference in strength is observed to be approximately 5% for Specimen III-1.2-03a-h(ii), which is much lower than the 17% decrease in capacity from Specimen III-1.2-03a-v(ii), indicating that relaxing the spacing requirement of horizontal web reinforcement had less impact on the strength.

It is understood that to increase the resistance of the diagonal strut, both vertical and horizontal crack control plays a vital role. However, based on the inclination of the strut, vertical or horizontal crack control reinforcement can be more effective in limiting cracks than the other (Tan et al. 1997). Shallower strut angles would engage more vertical reinforcement, while steeper strut angles engage more horizontal reinforcement. This is because cracks form parallel to the compressive

strut since the tensile stresses are perpendicular to compressive stresses. This suggests that it would be optimal for the crack control reinforcement to be along or parallel to the tensile stresses to carry those stresses and prevent cracking. The reinforcement that is closest to 90 degrees to the strut would be the most effective. This means horizontal bars are closer to forming 90 degrees with the strut than vertical bars are when the angle of the strut is large, suggesting steep geometry. In the case of Specimens III-1.2-03a-v(ii) and III-1.2-03a-h(ii) with an a/d ratio of 1.20, the angle of the strut, θ , is approximately 37 degrees. This is still considered a shallower strut angle since it is larger than 1.13. This means the vertical crack control plays a slightly more significant role in crack prevention than horizontal bars (Tan et al. 1997). Therefore, it is expected that Specimen III-1.2-03a-h(ii) performed a better capacity compared to Specimen III-1.2-03a-v(ii) because only the spacing of the horizontal web was relaxed. It should be noted that Specimen III-1.2-03a-v(ii) still had the same reinforcement density in the vertical and horizontal directions as Specimen III-1.85-03a-h(ii), however, the vertical reinforcement was made up of four-leg stirrups. It is also seen in Figure 6-26 that Specimen III-1.2-03a-h(ii) had a similar discontinuous cracking pattern as the companion specimen. This is unlike what was seen in Figure 6-23 and discussed in Section 6.3.3.1, implying that changing horizontal web reinforcement spacing had less effect on the behavior. Despite the discrepancies in ultimate shear capacities between Specimens III-1.2-03a-v(ii) and III-1.2-03a-h(ii), which the STM cannot capture, it still holds that altering either the horizontal or vertical to a more relaxed spacing limitation of $d/2$ will not impact the conservatism of the STM.

The failure mode of the strut crushing was once again observed and confirmed the predictions made by the strut-and-tie model. Figure 6-26 shows concrete crushing and spalling primarily near the CCC node, which agrees with the STM calculations stating the CCC nodal interface and the CCC back face are the top two elements with the lowest capacities.

Test 2 of Beam B2 had an a/d ratio of 1.85, denoted as Specimen III-1.85-03a-h(ii). The test result shows that the specimen still behaved appropriately, given the horizontal reinforcement spacing being changed. As discussed in Section 6.3.3.1, the companion specimen, Specimen III-1.85-03-(i), performed unknowingly low yet still surpassed the STM capacity prediction; thus, it is still a valid test that can be used for comparison. As seen in Figure 6-27, Specimen III-1.85-03a-h(ii) performed substantially higher in ultimate capacity than Specimen III-1.85-03-(i). The cracking patterns were similar between the specimens in that there were similar discontinuous cracks. Because the two specimens had the same vertical crack control reinforcement spacing and different horizontal web reinforcement spacings, changing the horizontal web reinforcement spacing once again did not impact the crack propagation for shallow diagonal struts. The failure mode observed was still the same as predicted by the STM. The CCC back face, and CCC nodal interfaces reached their designed capacities first, resulting in the crushing of concrete, as visible by concrete spalling along the strut.

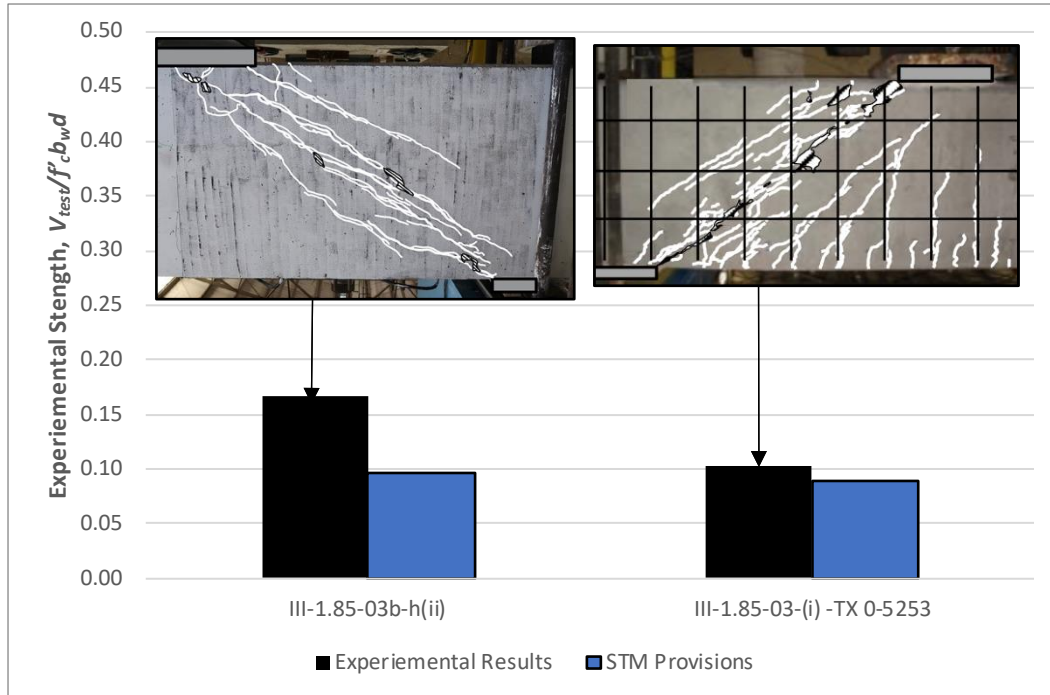


Figure 6-27 Beam 2 Test 2's and its Project 0-5253's normalized ultimate capacities with STM estimations

However, just as discussed in Section 6.3.3.1, Specimen III-1.85-03b, otherwise denoted III-1.85-03b-(i) for this program study, from Project 0-5253 shows III-1.85-03a-h(ii) to perform worse with a 6% decrease in the ultimate capacity. Nevertheless, the decrease in strength is considered insignificant, and horizontal crack control reinforcement spacing limits can be relaxed and have little to no effect on the strut capacity. The conservatism of the STM on specimens with relaxed horizontal web reinforcement still holds well.

Investigating the difference between the decrease in strength of Specimens III-1.85-03b-v(ii) and III-1.85-03a-h(ii) compared to Specimen III-1.85-03b-(i) reveals a similar conclusion to the discussion seen about the difference in capacities between Specimens III-1.2-03a-v(ii) and III-1.2-03a-h(ii) seen earlier in this section. With an a/d ratio of 1.85, the angle of the strut, θ , is approximately 26 degrees. This is considered a shallower strut angle since it falls very close to the 25-degree minimum stated in AASHTO LRFD. This means the vertical crack control plays a slightly more significant role in crack prevention than horizontal bars and why Specimen III-1.85-03a-h(ii) performed slightly better than Specimen III-1.85-03b-v(ii) with a smaller percent decrease in capacity compared to Specimen III-1.85-03b-(i) as seen in Figure 6-28 below.

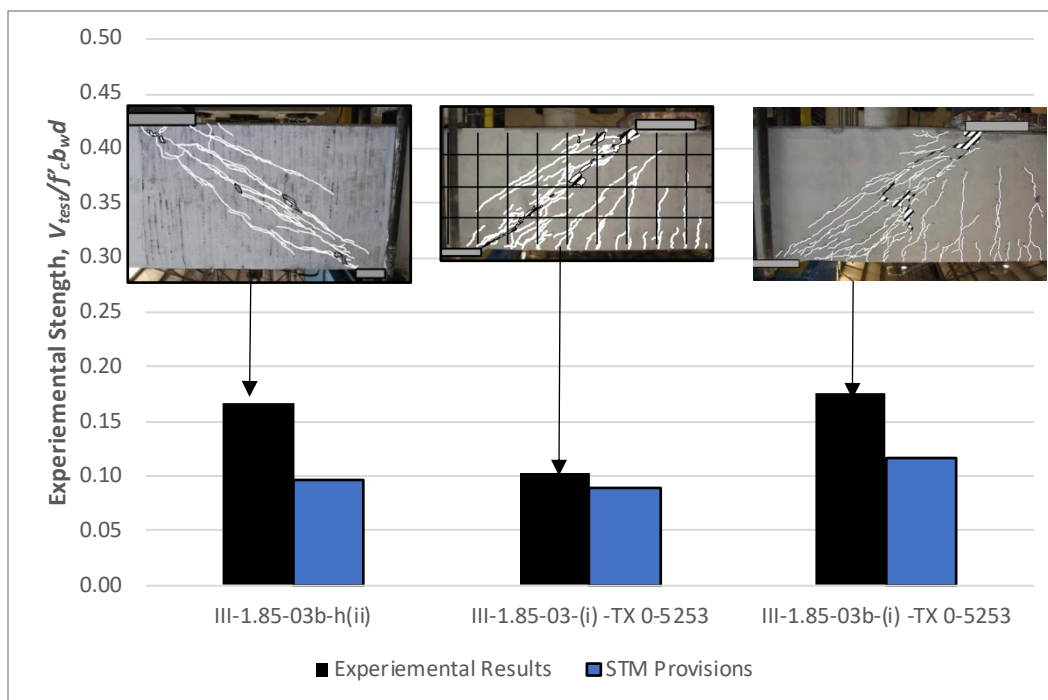


Figure 6-28 Normalized capacities of Beam 2 Test 2 and additional TX Project 0-5253 specimens

6.3.3.3. Beam B3 – Ultimate Capacity Discussion, Crack Pattern Observations, and Failure Mode Analysis

Beam B3 was the only large-scale specimen of the three to be 23 in. in depth. Both tests conducted on Beam B3 had an a/d ratio of 1.85. It was reported in Project 0-5253 that the 23 in. deep specimens with a/d ratios of 1.20 experienced flexural failures due to the relationship between the nodal region and shear span length. Since the shear span length is much lower with a smaller a/d ratio, the shear capacity was increased, resulting in the flexural failure observed in those specimens. The companion specimen selected for this experimental program avoided these specimens not because the flexural failure makes them invalid data points; however, engineering judgment chose the 23 in. companion specimen with an a/d ratio of 1.85 to allow for comparison with Beam B1 and Beam B2 results. Unfortunately, both Specimens IV-2123-1.85-03a-v(ii) and IV-2123-1.85-03b-v(ii), which had varied vertical crack control reinforcement arrangements, failed in flexure, unlike their counterpart in Project 0-5253. Both tests in Beam B3 experienced flexural failures since the outermost tensile reinforcement bar yielded. Concrete was aggressively spalling along the back face of the CCC node, along with a significant rotation of the load plate roller. Figure 6-29 and Figure 6-30 show a wider view of the structural tests with highlighted cracks. The broader view in the figure emphasizes the spalling of concrete outside the area of interest. It is also emphasized how the diagonal crack never fully forms and reaches the CCC node, and wide flexural cracks form, allowing the longitudinal reinforcement to have large plastic deformation, resulting in a plateau on the load-deflection curve.

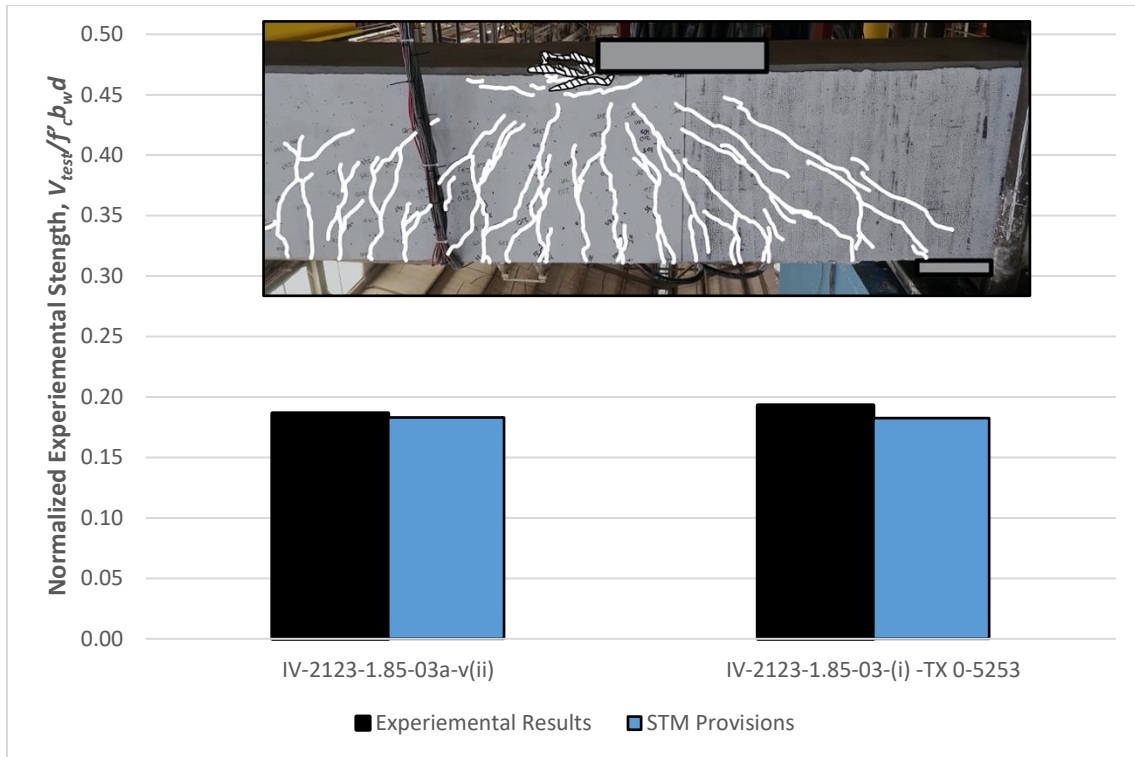


Figure 6-29 Beam 3 Test 1's and its Project 0-5253's normalized ultimate capacities with STM estimations

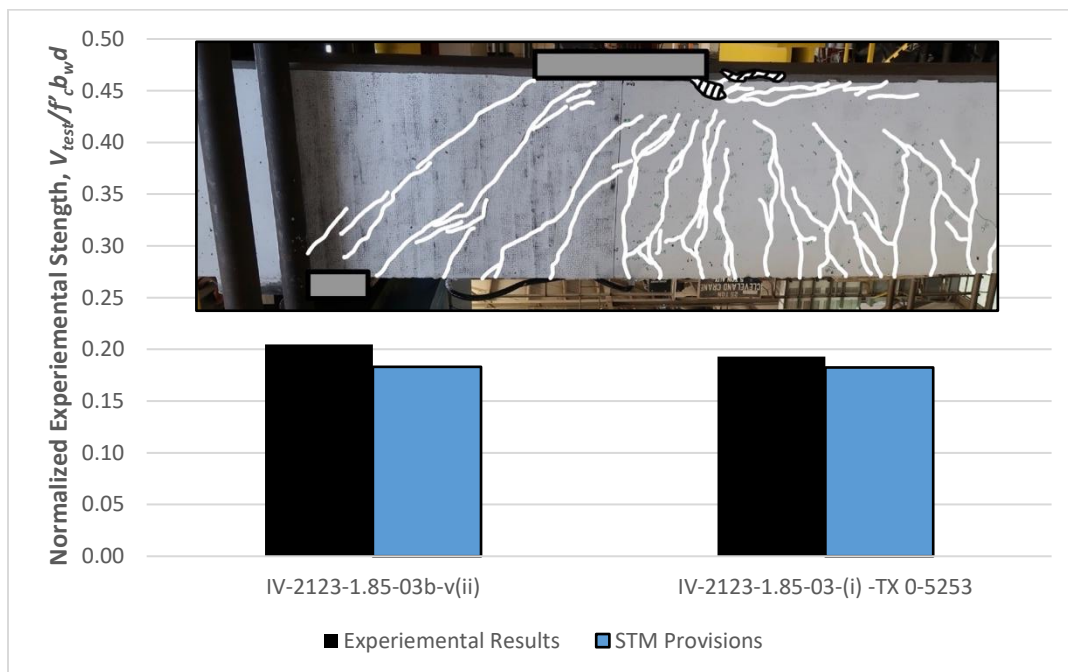


Figure 6-30 Beam 3 Test 2's and its Project 0-5253's normalized ultimate capacities with STM estimations

When following the AASHTO LRFD provisions to calculate the capacities of individual elements using the STM, it was found that the elements that would fail first would be the CCC node back

face for IV-2123-1.85-03a-v(ii) and CCC node strut interface for IV-2123-1.85-03b-v(ii). It was plausible that Specimen IV-2123-1.85-03-(i) in Project 0-5253 would also have the same failure modes since specimen geometry because tension reinforcement never changed between the two specimens. Using the current STM provisions of AASHTO LRFD to predict the STM capacity of IV-2123-1.85-03-(i) from Project 0-5253 delivers crushing of the CCC back face and yielding of the tie using measured material properties summarized in Table 6-3. Project 0-5253 observed failure along the strut at the CCC node instead of flexural failure for this specimen, possibly because of a large scatter in deep beams' shear capacities.

Both Figure 6-29 and Figure 6-30 show that the test result of this experimental program still surpassed calculated capacities and showed higher shear capacity compared to the companion Specimen IV-2123-1.85-0.3-(i). Although both Test 1 and Test 2 failed in flexure, it can be inferred that the shear strength capacity of the specimen was higher than the amount of shear needed to result in the flexural failure. In other words, these specimens are not inferior in any way to Specimen IV-2123-1.85-0.3-(i), and it can be concluded that the crack control reinforcement spacing can be relaxed though specimen depth has changed.

The shear capacity, V_{test} , was calculated for Specimens IV-2123-1.85-03a-v(ii) and IV-2123-1.85-03b-v(ii) by taking the applied load at flexural failure, corresponding to the load when the load-deflection began to plateau, and summing the load cells at the reaction during the plateau to find R_A . Following Figure 6-19, V_{test} was calculated like all other specimens and normalized accordingly. V_{STM_Calc} was determined exactly in the same manner as described in Section 6.3.2. That is, V_{STM_Calc} was estimated by solving for the capacities of the strut-and-tie model elements and then back calculating from each of the elements (i.e., CCC node interface) using equilibrium to solve for the applied load P_L . The lowest P_L was selected to calculate V_{STM_Calc} using the same formula as V_{test} described in Section 6.3.1. For Beam B1, Beam B2, and their companion specimens, the lowest P_L was found to be at the CCC nodal interface or the CCC back face. For Beam B3, the lowest P_L was found to be the same, where the CCC node strut interface governs both Specimens IV-2123-1.85-03a-v(ii) and IV-2123-1.85-03b-v(ii). For Beam B3, when AASHTO LRFD BDS Section 5.8.2.5 is followed, and when calculating the CCC back face capacity, the compression reinforcement is accounted for. This means V_{STM_Calc} was a lower bound of capacity and a conservative calculation. The tie capacity would have been the third strut-and-tie element to fail. As seen in Figure 6-29 and Figure 6-30 above, both Test 1 and Test 2 of B3 surpassed the lower bound V_{STM_Calc} . This allowed the program of study to conclude once again that the relaxation of crack control spacing does not impact experiential behavior or capacity. Thus, no alterations need to be made to the current AASHTO LRFD provision for STM capacity calculations.

The experimental shear capacities and calculated shear capacity are accurately close to one another. Specimen IV-2123-1.85-03a-v(ii) consisted of 2-leg stirrups, while Specimen IV-2123-1.85-03b-v(ii) consisted of 4-leg stirrups. The capacity difference between Test 1 and Test 2 is approximately 9% when theoretically, they are designed assuming the same shear capacity. The

capacity difference between Test 1 with the 2-leg stirrups and its V_{STM_Calc} value was 2%. The capacity difference between Test 2 with the 4-leg stirrups and its V_{STM_Calc} value was 12%. The capacity difference between the selected companion specimen with the strut crushing failure mode and its V_{STM_Calc} value was 5%. In summary, the current design provisions in AASHTO LRFD will provide an accurate design capacity for shallower deep beams failing in flexure.

6.3.4. Serviceability Results and Analysis

One of the main goals of this experimental study was to confirm that if the spacing limits were relaxed, this would also have little to no impact on the serviceability of reinforced concrete deep beams. This section explores the current design provisions and the individual specimen tests response compared to their Project 0-5253 counterpart.

As described in Section 6.2.4, the testing procedure for all structural tests included measuring crack widths at each loading increment. During the established loading break, the research team measured the crack widths of the diagonal strut crack both on the north specimen face and the south specimen face using a crack comparator card. It was observed that the maximum crack width was typically at the mid-height of the specimen, which was also noted in Project 0-5253. Plots within Section 6.3.4 are comprised of data points that were physically measured, and the larger crack widths on whether the north or south face of the specimen was graphed. Project 0-5253 took the two independent measurements and averaged the two. Since the experimental program directly impacts serviceability, a more conservative approach was taken to only plot the highest crack width at each load increment.

6.3.4.1. Design Provisions Cracking Limits

There are a handful of design provisions that handle and evaluate serviceability data using varied benchmarks. During the time Project 0-5253 was being conducted, two main design provisions were used since AASHTO LRFD did not have any tolerable crack width discussion. ACI 224R-01 and the concrete design recommendations developed by the *fédération internationale du béton* (*fib*; i.e., international concrete federation) were used to development crack width benchmarks at service loads. Table 6-5 is directly pulled from Project 0-5253 and summarizes the crack width maximums at service loads per exposure conditions. The research team chose to pursue the 0.016 in. as the benchmark for the current analysis.

Table 6-5 Tolerable widths of flexural cracks per design provisions at the time of Project 0-5253

Exposure Condition	ACI 224R-01	<i>fib</i> (1999)
Dry air, protective membrane, indoors	0.016 in.	0.016 in.
Humidity, moist air, soil, cyclic wet and dry	0.012 in.	0.012 in.

The design provisions to date have slightly changed or remained the same. ACI 224R-01 was reapproved by ACI Committee 224R in 2008, suggesting the values in Table 6-5 have remained

in same in terms of crack tolerances. *fib* Model Code, published in 2010, transitioned into a stricter crack width tolerance compared to the limitations in 1999. *fib* Model code 2010 states that for an exposure class of X0, dry air indoors, the tolerable crack width is 0.3 mm or approximately 0.012 in. AASHTO LRFD BDS 9th edition from 2020 also briefly mentions a tolerable crack width of 0.017 in. in the commentary of Section 5.6.7. All these values are summarized in Table 6-6.

Table 6-6 Tolerable widths of flexural cracks

Exposure Condition	ACI 224R-01	<i>fib</i> (2010)	AASHTO LRFD BDS 9th Ed. 2020
Dry air, protective membrane, indoors	0.016 in.	0.012 in.	0.017 in.

Recognizing the various design provision width limits, 0.016 in. was still used in this experimental study as a benchmark. Though AASHTO LRFD has a more lenient crack width limit of 0.017 in., and this study is focused on AASHTO provisions, 0.016 in. will still be used as both an element of conservancy and allow for direct comparison with Project 0-5253.

In parallel with tolerable crack widths and their applicable benchmarks for acceptable serviceability, loading condition benchmarks also need to be established. Similar to Project 0-5253, three major assumptions before developing an estimation methodology for service loads:

- AASHTO LRFD Strength I governs design which is the load case 1.25DC + 1.75LL. Strength I is referenced to the basic load combination with vehicular loading excluding wind loading. Do note, in Project 0-5253, the load case for Strength I was denoted as 1.25DL + 1.75LL (AASHTO LRFD 2008). Despite varied nomenclature, they inherently represent the same loading combination.
- The service load is made up of 75% dead load, AAHSTO load type DC, and 25% live load, AASHTO load type LL.
- The nominal capacity of the specimen should be approximately 2/3 of the experimental capacity.

According to LRFD methodology, there are strength reduction factors (ϕ) and load factors (η) that are applied when relating nominal loads and service loads. For strut-and-tie modeling within AAHSTO, the ϕ -value should be equivalent to 0.70 for compression elements. Since the crack widths being analyzed for serviceability are along the diagonal compression strut, it can be assumed that $\phi = 0.70$. With the first two assumptions made above and with $\phi = 0.70$, the load factor, η , will be approximately 1.4. Modified from Project 0-5253, Figure 6-31 summarizes the abovementioned assumptions. The assumption that the experimental capacity is 1.5 times larger than the nominal capacity was justified due to the deep beam database analysis that Project 0-5253 completed, where they found this correlation. The path to declaring 0.33 as the service load

benchmark was derived from a handful of assumptions. It is important to recognize that 0.33, or 33% of ultimate capacity, is the only benchmark representation that attempts to represent most deep beams, and some error is inherently derived from it. In other words, 0.33 is a relaxed benchmark that will appear in figures throughout the serviceability discussion.

$$\begin{aligned} \phi \text{ Nominal Capacity} &\approx \eta \text{ Service Load} \\ \frac{\phi}{\eta} &\approx \frac{\text{Service Load}}{\text{Nominal Capacity}} \end{aligned}$$

Assumptions:

- 1). Load Case: 1.25 DC + 1.75LL
- 2) DC = 75 % of Service Load
LL = 25% of Service Load
- 3). Nominal = 2/3 Experimental

} $\eta = 1.4$

$$\frac{2}{3} \frac{0.70}{1.4} = 0.33 \approx \frac{\text{Service Loads}}{\text{Experimental Capacity}}$$

ϕ = strength reduction factor, 0.70
 η = load factor
DC = dead loads, components and attachments
LL = live load

Figure 6-31 Estimate of service load as a function of experimental capacity

Figure 6-32 shows a holistic diagonal crack width distribution of all six structural tests within this experimental program. The two established benchmarks are seen as dashed lines within the figure. A positive correlation is observed between crack width along the x-axis and the percent of an ultimate load along the y-axis. As loads continuously get applied, the main diagonal crack along the strut continues to widen as tensile stresses continue to pull the crack open.

It is immediately observed that all structural specimens satisfy or are very close to reaching the assumed serviceability benchmarks. Since no specimens show data points to be within quadrant III, identified in Figure 6-32, it can be inferred that the relaxation of crack control reinforcement will not have a negative impact on serviceability. It can be seen Specimens III-1.85-03b-v(ii), III-1.85-03b-h(ii), and III-1.85-03a-h(ii), are along the 0.016 in. tolerance benchmark. Do recall current AASHTO LRFD 2020 provisions suggest 0.017 in. to be an appropriate benchmark. It is interpreted that these specimens pass the serviceability requirement.

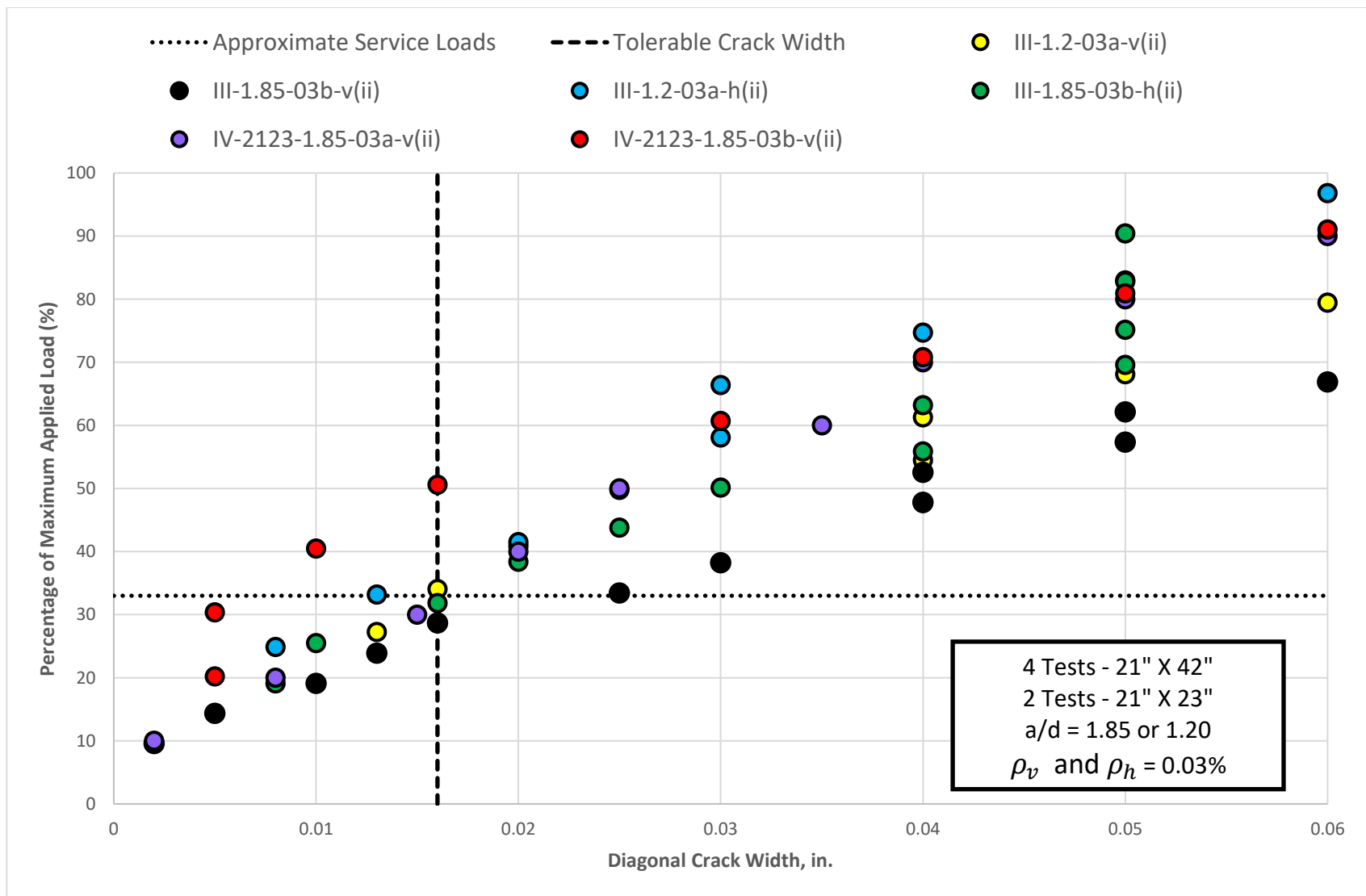


Figure 6-32 Crack width data for all 6 structural tests

Figure 6-32 reflects that all specimens satisfy or are close to the allowable tolerances set forth in this research program. There is no trend between varied a/d ratios and whether one had an overall smaller average crack width than the other. Nevertheless, a trend is visible between the relaxed vertical web rebars and the relaxed horizontal web rebars. Specimens III-1.85-03b-v(ii) and III-1.20-03a-v(ii) from Beam B2 generally showed a wider crack width, while Specimens III-1.85-03b-h(ii) and III-1.20-03a-h(ii) showed a narrower crack width. Relaxing the vertical web rebar spacing more significantly affects serviceability than relaxing the horizontal web rebar spacing. This trend can be more easily seen in Figure 6-33. Figure 6-33 also provides the crack widths of the companion specimens from Project 0-5253.

No trend can be visually seen between the B3 tests, IV-2123-1.85-03a-v(i) and IV-2123-1.85-03b-v(i), where the a/d ratio remained the same, but there were different stirrup configurations used. IV-2123-1.85-03a-v(ii) had 2-legged stirrups, while IV-2123-1.85-03b-v(ii) had 4-legged stirrups, and they both performed equally the same. If the reinforcement density was satisfied (0.3%), stirrup leg quantity did not correlate with serviceability, and this observation was also seen in Project 0-5253. However, there is a visible trend regarding the load stages at which the diagonal crack was no longer growing. Most of the specimens no longer saw the primary diagonal crack width grow at around 50-90% of the ultimate load but rather saw an increase in parallel secondary diagonal cracks.

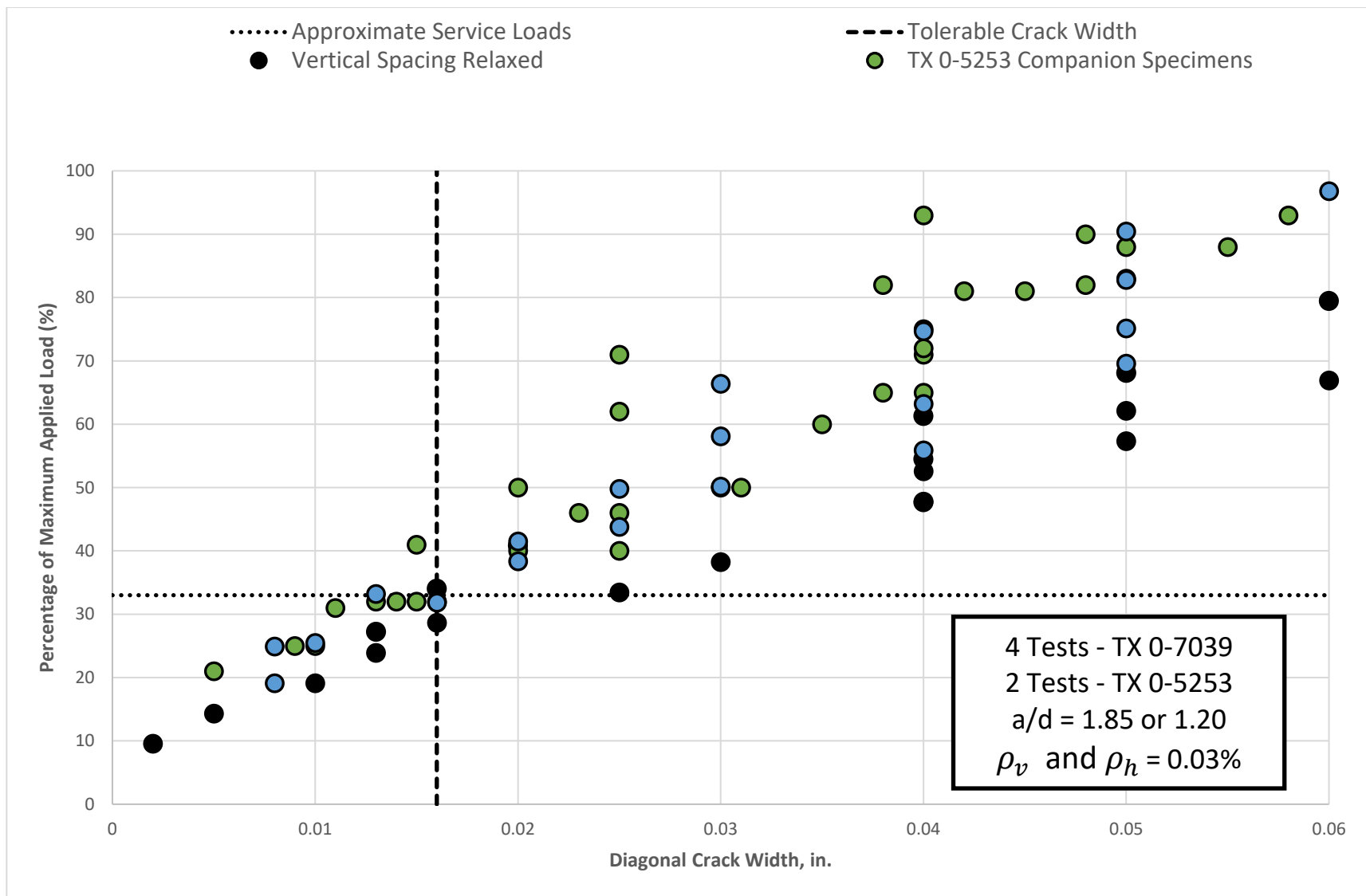


Figure 6-33 Crack width data for B1 and B2 along with their TX Project 0-5253 companion specimen

6.3.4.2. Beam B1 - Observed Cracking Widths

Using the same plotting methodology as Section 6.3.4.1 delivers Figure 6-34 and Figure 6-35. In the figures, the observed behavior of Specimens III-1.2-03a-v(ii) and III-1.85-03b-v(ii) were plotted along with data pulled from Project 0-5253's report.

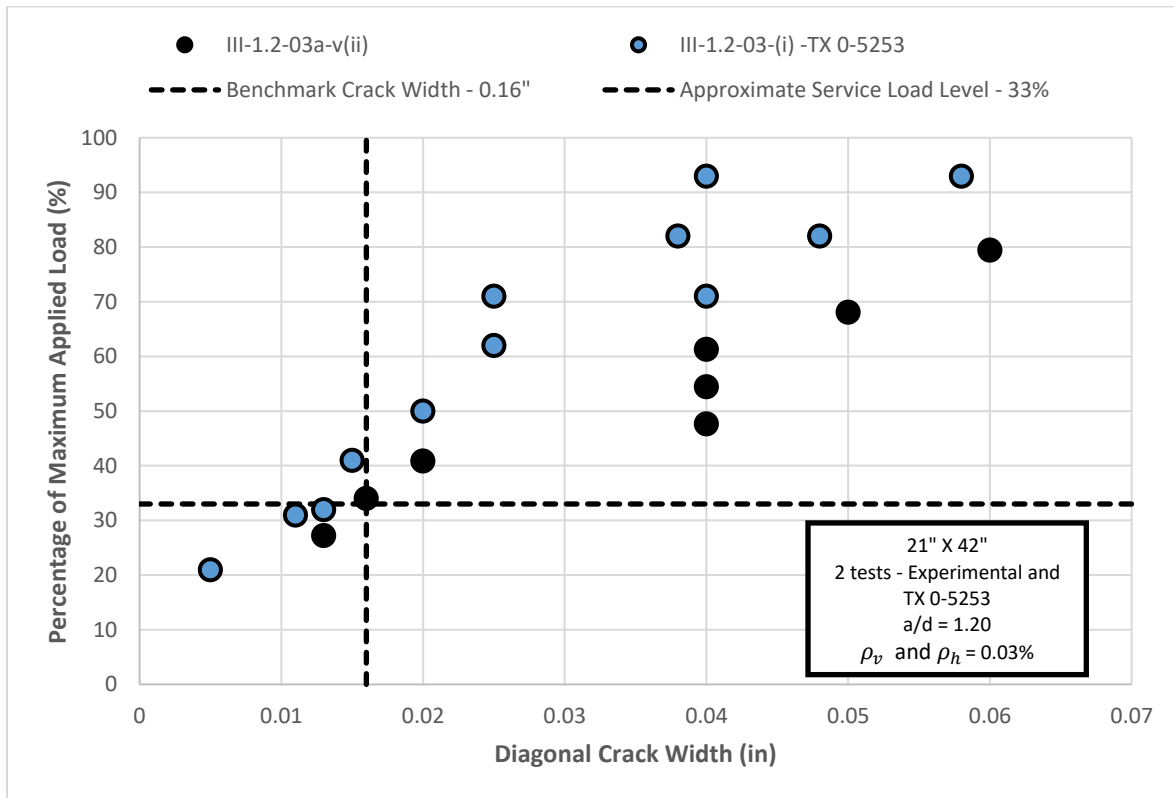


Figure 6-34 Diagonal crack widths for III-1.2-03a-v(ii), 21" X 42" a/d = 1.20

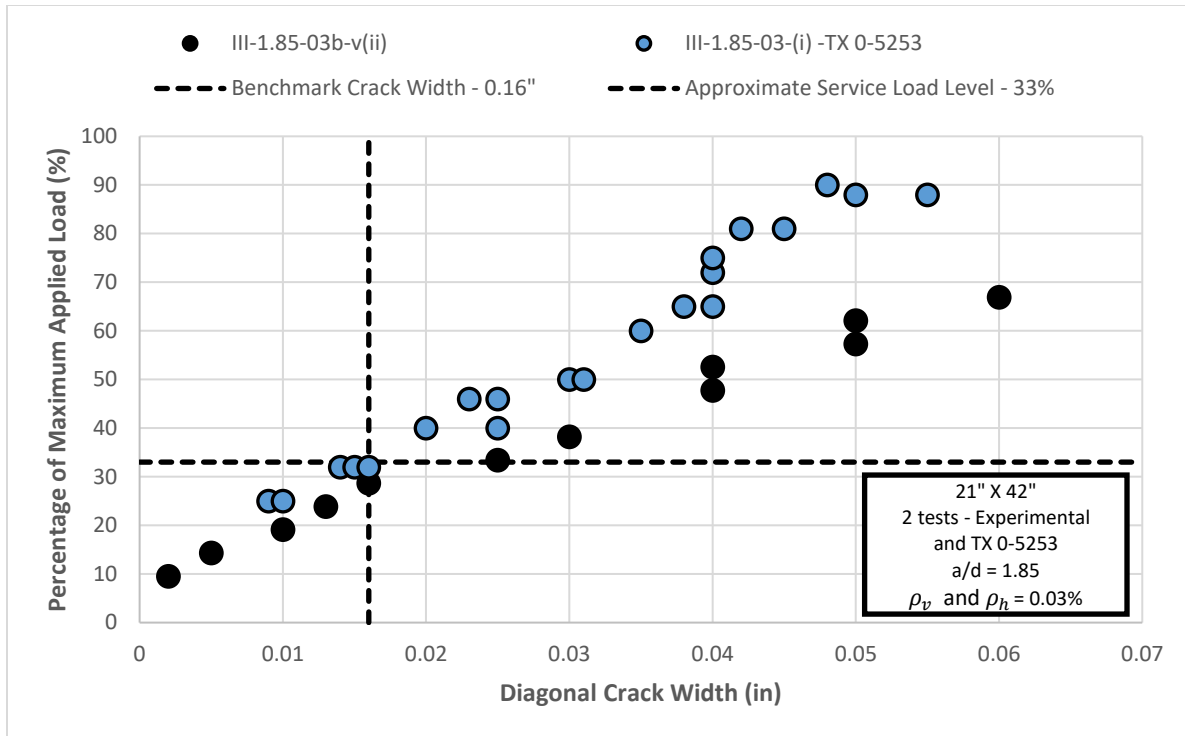


Figure 6-35 Diagonal crack widths for III-1.85-03b-v(ii), 21" X 42" a/d = 1.85

It is seen that both tests in Beam B1 underperformed in terms of serviceability compared to their counterpart in Project 0-5253. This is not to say that Specimens III-1.2-03a-v(ii) and III-1.85-03b-v(ii) did not have acceptable severability results since they did abide by the tolerance benchmarks. However, this is to be expected based on the crack control spacing. When the spacing is relaxed, there are visibly fewer discontinuously distributed cracks but wider widths, as discussed in Section 6.3.3. A primary diagonal continuous crack forms and continuously became wider as the load increased. This supports the trends seen in Figure 6-34 and Figure 6-35, where Specimens III-1.2-03a-v(ii) and III-1.85-03b-v(ii) experienced the same crack width as Project 0-5253 but at lower load levels. The companion specimens had tighter web reinforcement making it more difficult to widen the primary crack due to the reinforcement carrying the tensile stresses. It may still be concluded that the relaxation of vertical crack control reinforcement still satisfies serviceability tolerances for deep beams.

Do note that crack widths were not collected at higher loads on Specimen III-1.85-03b-v(ii) due to safety concerns. As discussed in Section 6.3.3, this test had two cycles of loading due to the uncertainty of failure. The crack width data plotted in the figures was collected from the first loading round. During the second cycle of loading, the specimen was not approached and loaded to failure. Since Project 0-5253 showed the companion specimen, Specimen III-1.85-03-(ii), to fail at a lower-than-expected limit, the author determined it to be unsafe to approach the specimen after it had surpassed the capacity reported in Project 0-5253.

6.3.4.3. Beam B2 - Observed Cracking Widths

Figure 6-36 and Figure 6-37 plot the observed behavior of Beam B2 [Specimens III-1.2-03a-h(ii) and III-1.85-03a-h(ii)] along with data pulled from Project 0-5253's report. Unlike Beam B1, Beam B2 tests did seem to perform more similarly to their Project 0-5253 companion specimens. This observation is encouraging to see since Beam B2 increased the horizontal crack control reinforcement spacing. Although the horizontal web reinforcement spacing was relaxed and altered, it did not impact the crack width behavior. This concludes that relaxing the horizontal crack control reinforcement spacing does not impact the serviceability of deep beams with shallower strut angles, as discussed earlier.

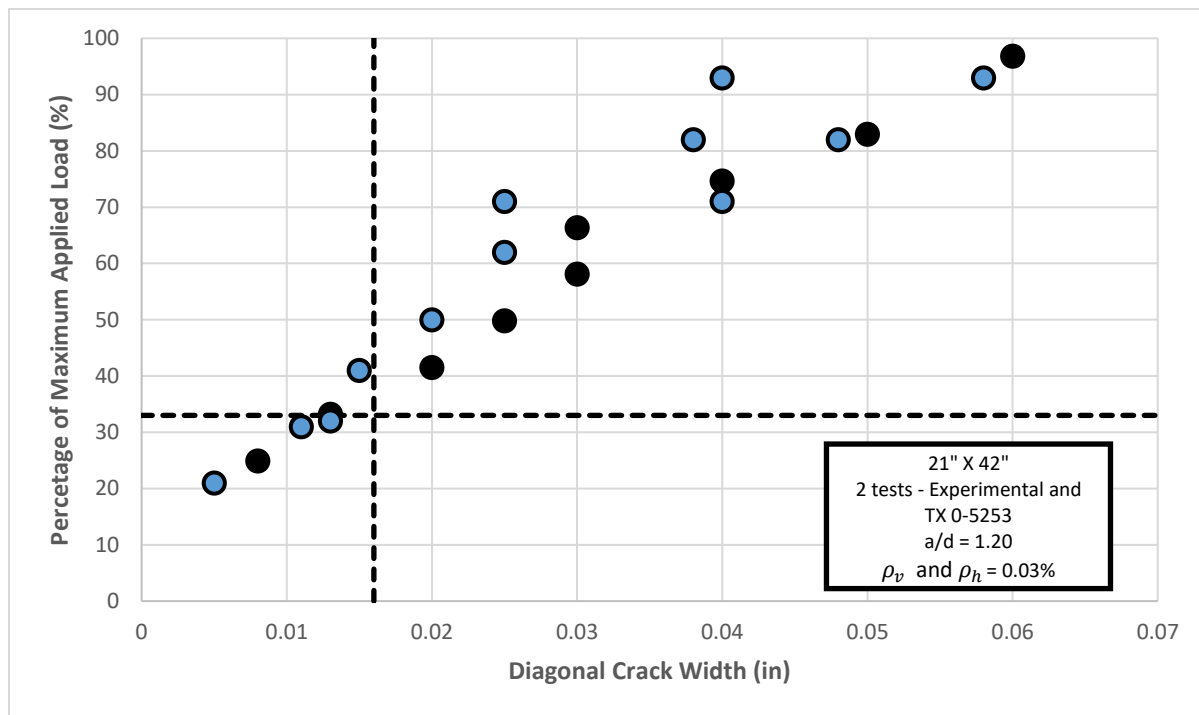


Figure 6-36 Diagonal crack widths for III-1.2-03a-h(ii), 21" X 42" a/d = 1.20

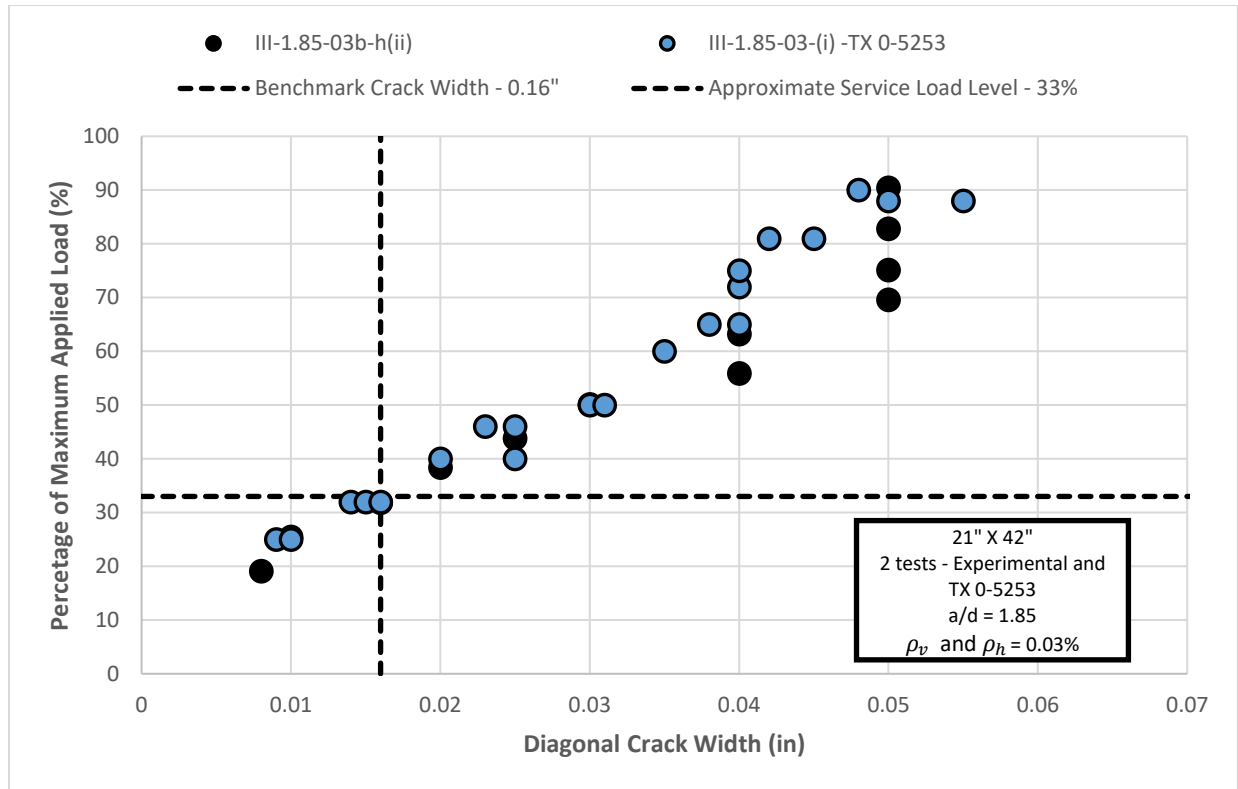


Figure 6-37 Diagonal crack widths for III-1.85-03a-h(ii), 21" X 42" a/d = 1.85

6.3.4.4. Beam B3 - Observed Cracking Widths

Figure 6-38 and Figure 6-39 plot the observed behavior of Beam B3 [Specimens IV-2123-1.85-03a-v(ii) and IV-2123-1.85-03b-v(ii)] along with data pulled from Project- 5253's report. The same trend seen in Beam B1 tests was also observed in Beam B3 tests. Specimens IV-2123-1.85-03a-v(ii) and IV-2123-1.85-03b-v(ii) underperformed in crack widths compared to their counterpart in Project 0-5253 because of larger crack widths at higher loads once service loads have exceeded. This does not suggest that Specimens IV-2123-1.85-03a-v(ii) and IV-2123-1.85-03b-v(ii) do not satisfy serviceability. As mentioned in Section 6.3.4.2 for Beam B1, the lack of vertical reinforcement crossings along the diagonal strut means the cracking widths will be much more aggressive at lower loads. However, this does not impact service loads but is more impactful at ultimate loading conditions. This further supports the conclusion made in Section 6.3.4.2.

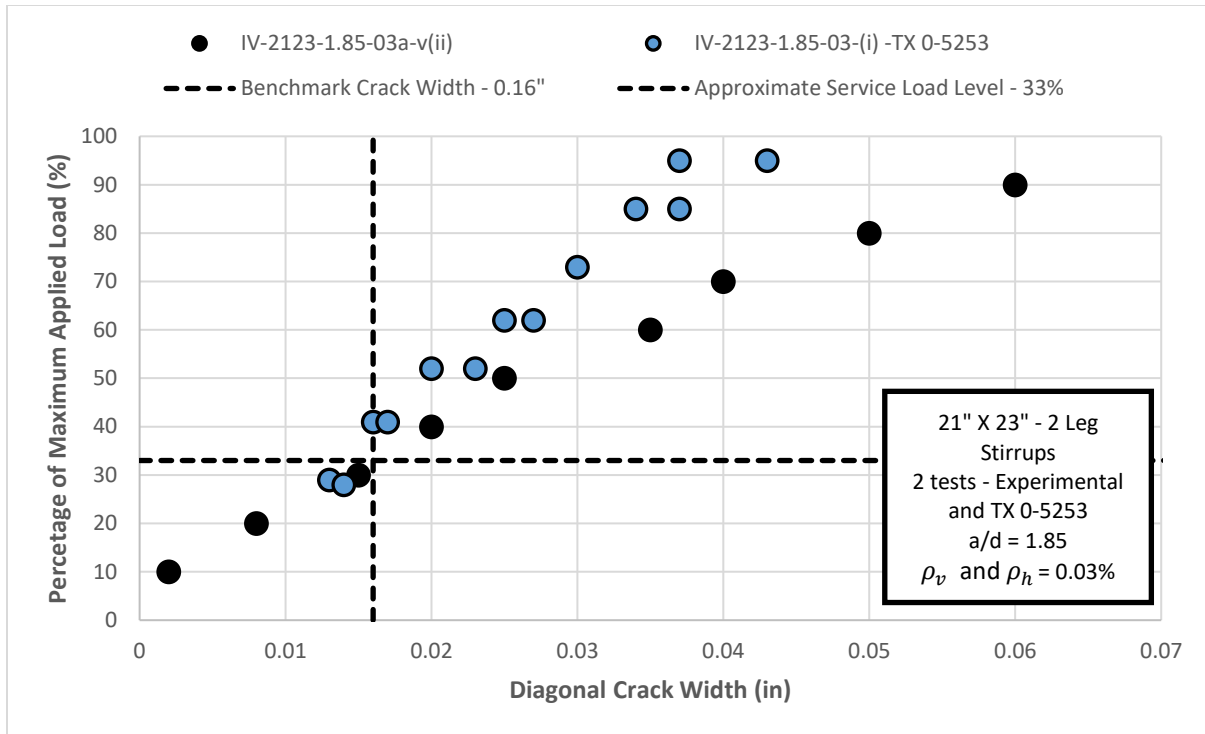


Figure 6-38 Diagonal crack widths for IV-2123-1.85-03a-v(ii), 21" X 23" a/d = 1.85

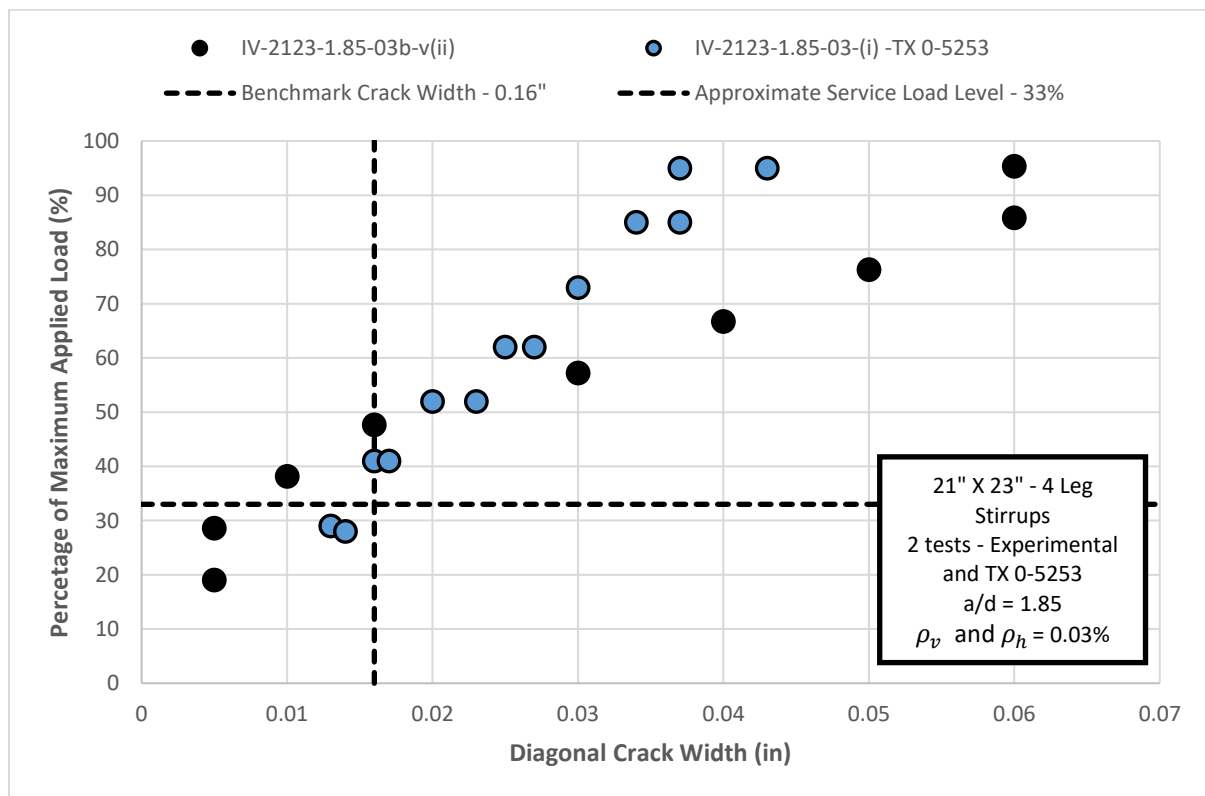


Figure 6-39 Diagonal crack widths for IV-2123-1.85-03b-v(ii), 21" X 23" a/d = 1.85

6.3.5. Crack Control Reinforcement Engagement

As mentioned in Section 5.2.2, strain gauges were placed along the diagonal strut to collect information on rebar strain during testing. This section analyzes the strain readings observed on each structural test conducted in this program.

Strain data was collected throughout the loading period of the tests. However, the figures in this section present only two strains captured through this time frame. The two strains in the figures represent the strain experienced at that condition under service loads, 33% of the ultimate load, and at 95% ultimate load. The reasoning behind selecting 95% of ultimate capacity to present strain values rather than the strain at ultimate is to ensure accurate strains are plotted. At ultimate loads, the likelihood that the strain gauge remained undamaged or surpassed its allowable elongation increases. To avoid this uncertainty, 95% of the ultimate load capacity was selected.

Not all strain gauges installed remained undamaged. A handful of strain gauges have been damaged at some point between installation and testing. One possible major cause of these damaged strain gauges is concrete casting. Some figures below will not have a strain value for a gauge due to the loss of that gauge.

6.3.5.1. Beam B1– Crack Control Reinforcement Strains and Analytical Discussion

Figure 6-40 indicates the strains along the strut at both service loads and 95% ultimate capacity. Figure 6-40 also clearly depicts where these strains were present by connecting the lot to an AutoCAD sect of the area of interest. All figures for all six structural tests are presented in this way for the reader's convenience and understanding. Do note that all plots have various scales for strain and should not be used to compare to one another. The main intention of these figures is to ensure the crack control reinforcement was nowhere near yielding at service loads, common trends in strut geometry and rebar engagement, and that both vertical and horizontal reinforcement is playing appropriate roles.

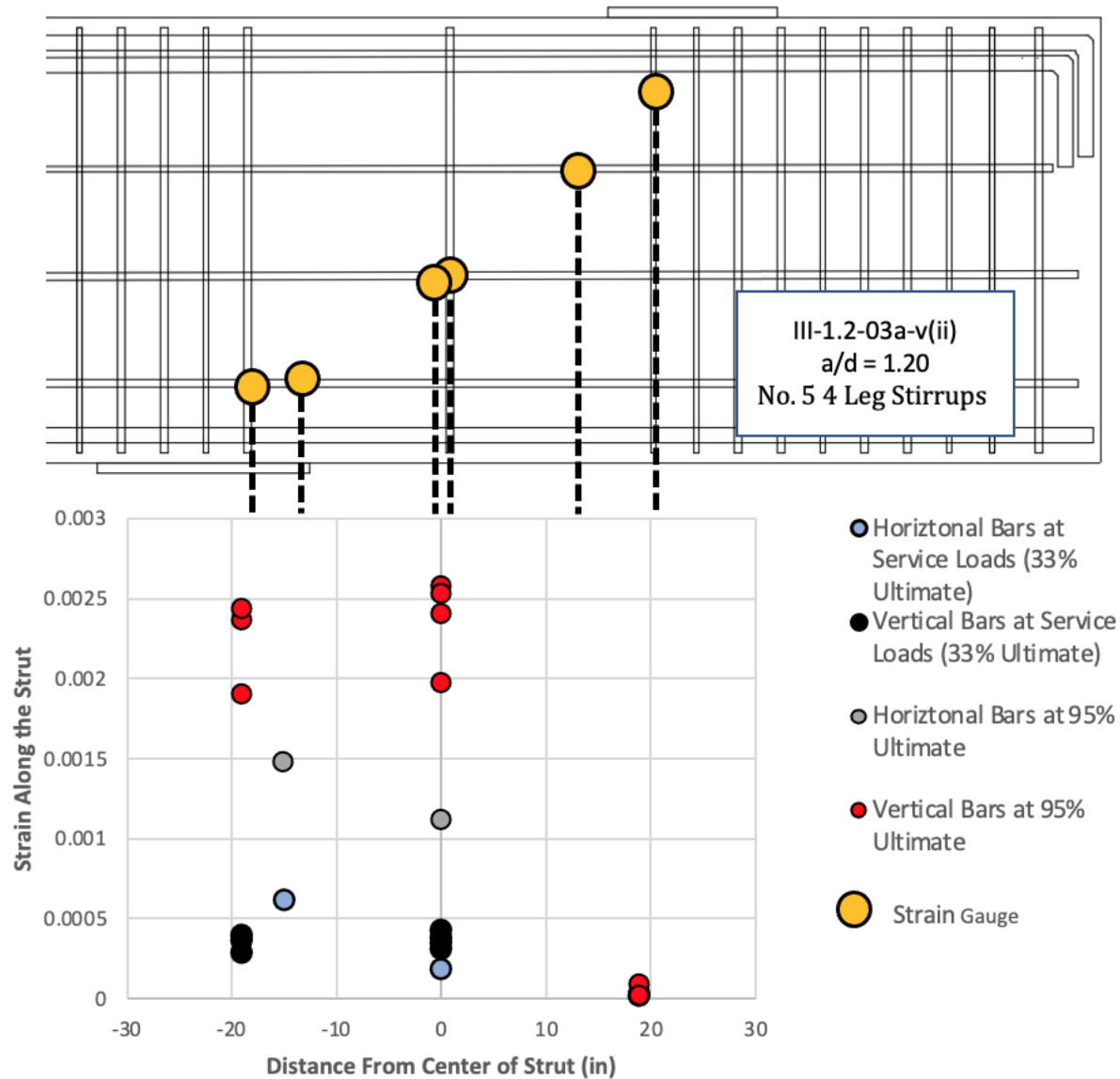


Figure 6-40 Strain engagement along the strut for III-1.2-03a-v(ii), a/d = 1.20

Figure 6-40 shows the strains from Specimen III-1.2-03a-v(ii). At service loads, it is a good indication that the strains experienced along the strut are nowhere near yielding. At ultimate loads, it is observed that the mid-section of the strut experiences significantly larger strains. This is to be expected since the primary diagonal crack is always observed to begin at the mid-section of the strut. The largest crack width is this primary crack, and as it continues to grow at higher loads, it is expected that crack control reinforcement near this crack is going to experience high strains due to the higher tensile stresses. Figure 6-40 supports the strut phenomena and physical crack observations. Vertical and horizontal crack control reinforcement is appropriately engaged based on its relative location near the mid-section of the strut. However, vertical web reinforcement is more engaged compared to horizontal crack control reinforcement. This supports previous

arguments that vertical crack control reinforcement plays a more crucial role due to the strut angle. This pattern is seen throughout all specimens.

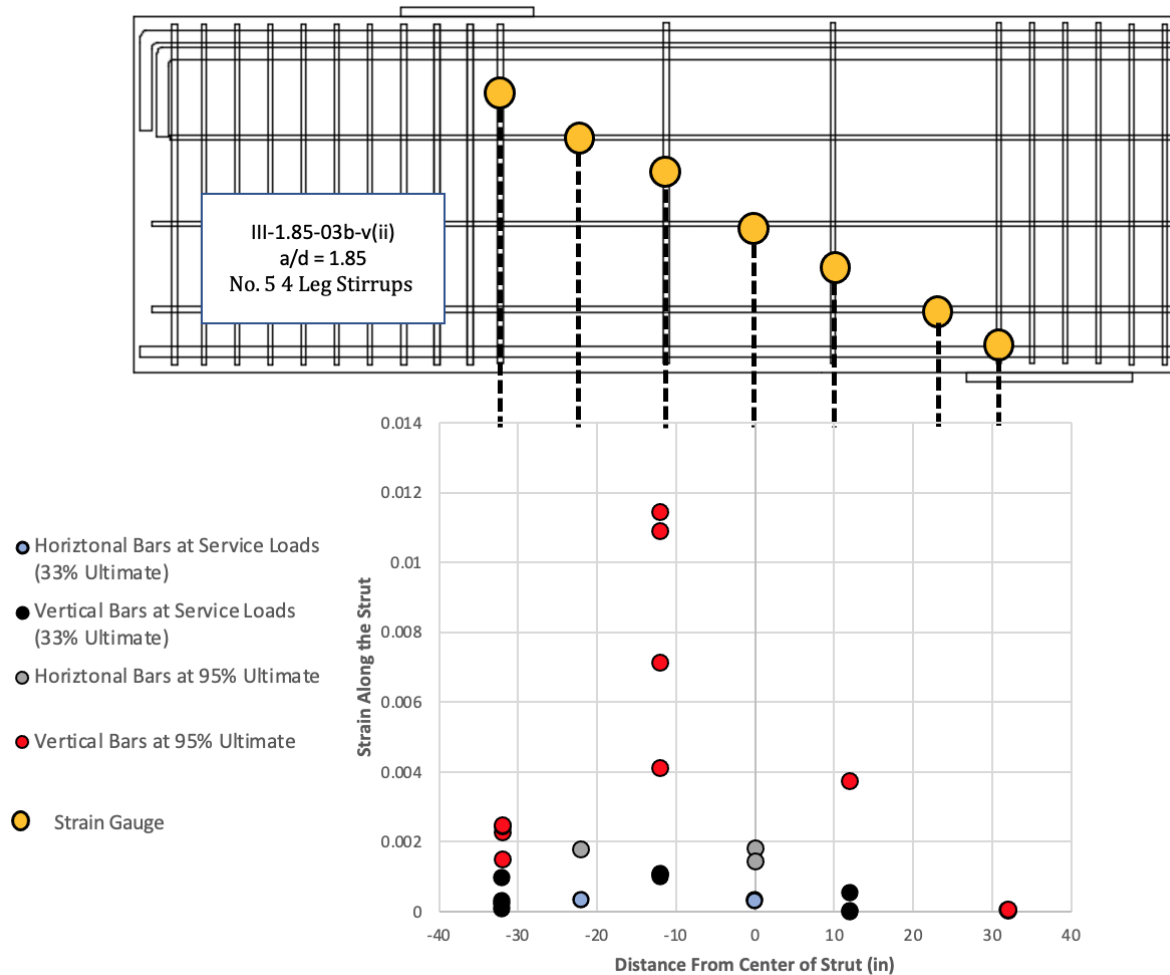


Figure 6-41 Strain engagement along the strut for III-1.85-03b-v(ii), a/d = 1.85

Figure 6-41 shows the strain values for Specimen III-1.85-03b-v(ii) and reflects similar conclusions that were also made in Figure 6-40. The strains at service loads were below yielding, while the strains at 95% capacity were much higher. The strain gauges near the mid-section were beyond yielding. Figure 6-41 also supports that all four legs of the stirrups are fully engaged. The mid-section is once again the most engaged and crucial location along the strut due to the primary crack growth. It is also observed that the vertical crack control bars are more engaged than the horizontal ones.

6.3.5.2. Beam B2– Crack Control Reinforcement Strains and Analytical Discussion

Figure 6-42 shows the strains from Specimen III-1.2-03a-h(ii), and Figure 6-43 shows the strains from Specimen III-1.85-03a-h(ii). Similar conclusions can be drawn from these figures as were drawn from B1's tests. The mid-section of the strut experiences the highest strains, and this is correlated with the physical crack observations and patterns. Even though the horizontal spacing is relaxed for this specimen test, the vertical crack control bars are still more engaged than the horizontal bars due to the angle of the strut.

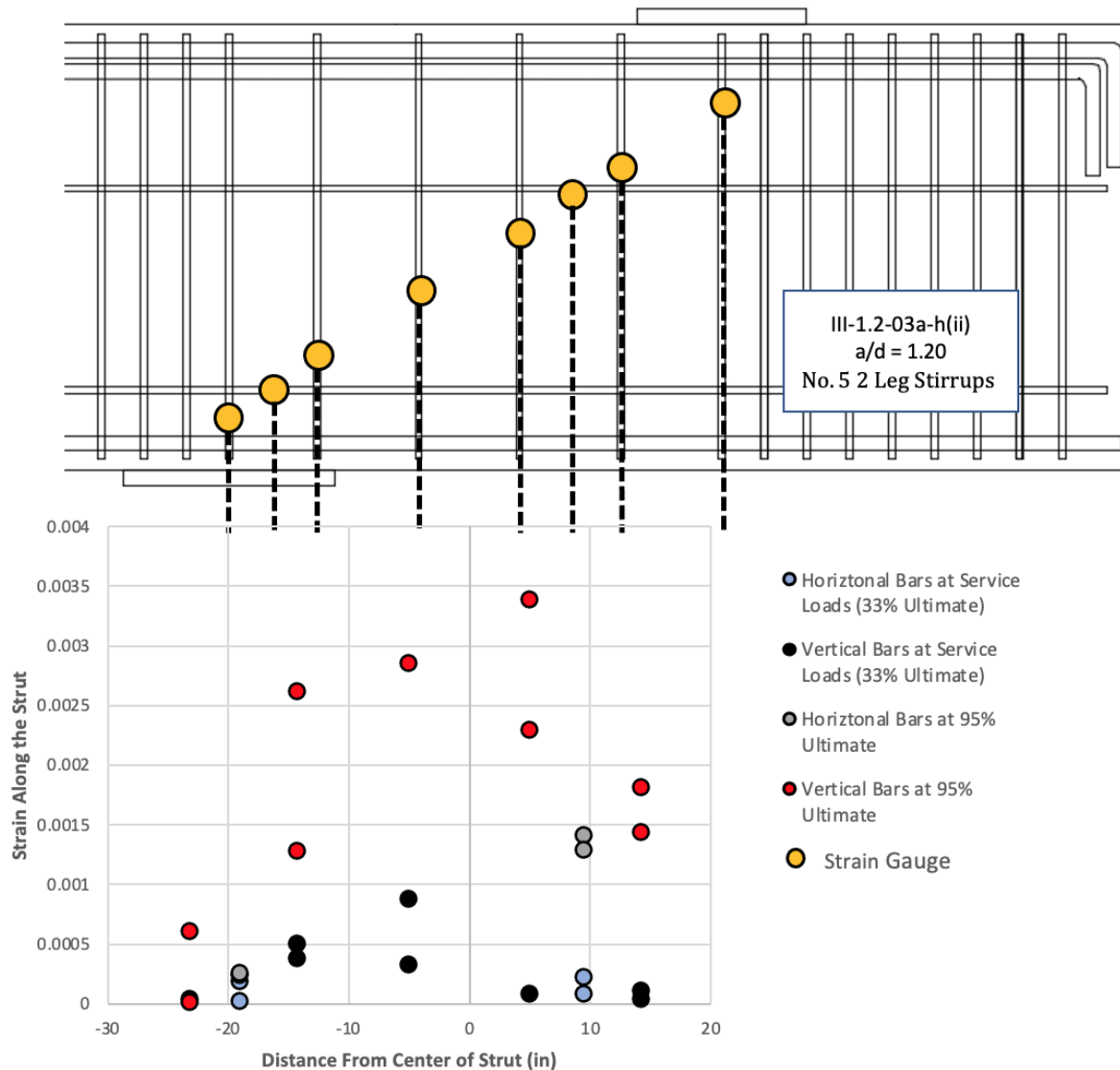


Figure 6-42 Strain engagement along the strut for III-1.2-03a-h(ii), $a/d = 1.20$

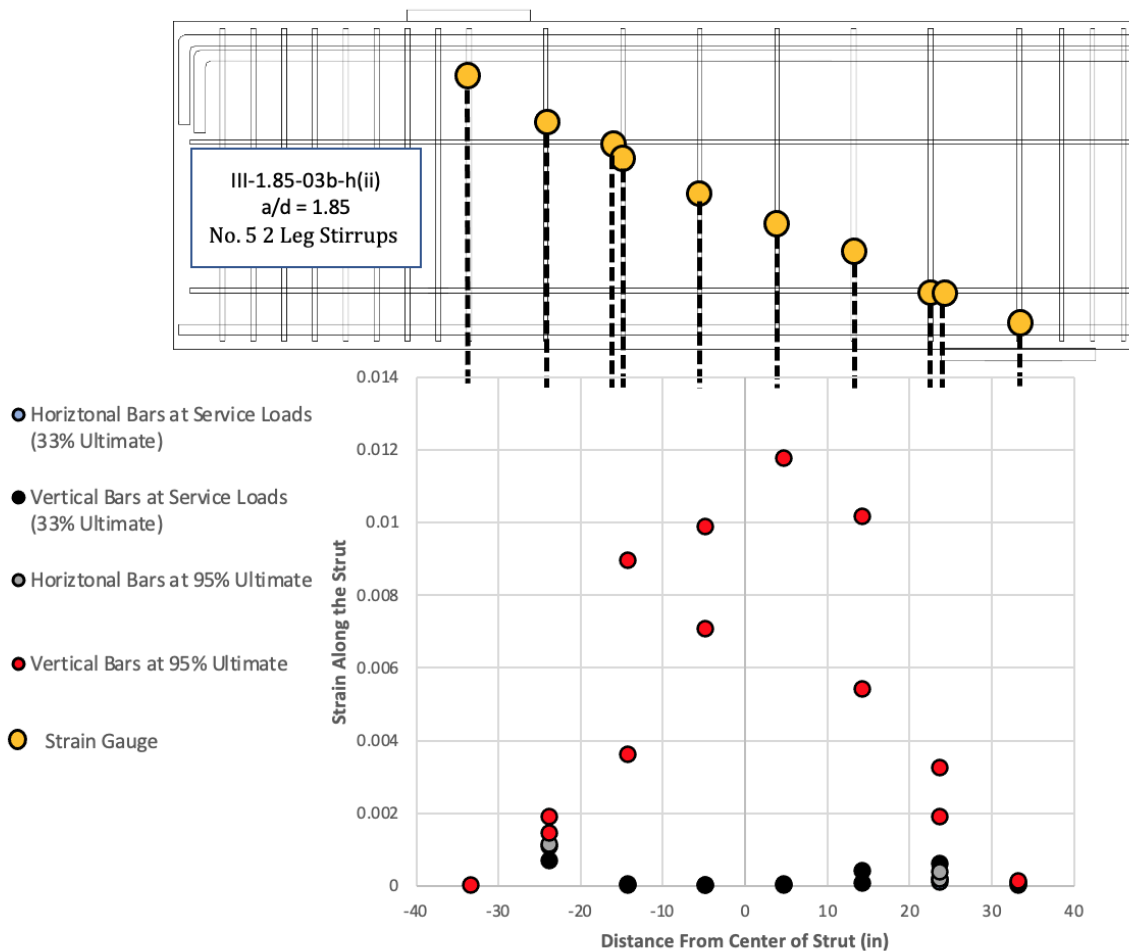


Figure 6-43 Strain engagement along the strut for III-1.85-03a-h(ii), $a/d = 1.85$

There is a correlation between a/d ratio and strains seen at the mid-section at 95% ultimate capacity. For Specimens III-1.2-03a-v(ii) and III-1.2-03a-h(ii) where $a/d = 1.20$, the strains at the mid-section were surpassed yielding but only by approximately 1-3 microstrains. For Specimens III-1.85-03b-v(ii) and III-1.85-03a-h(ii), where $a/d = 1.85$, the strains at the mid-section were far passed the yield strain by approximately 8-10 microstrains. The difference between the two a/d ratios makes relative sense since the smaller a/d ratio has a lower transverse strain in the mid-section and thus is stiffer than $a/d = 1.85$.

6.3.5.3. Beam B3– Crack Control Reinforcement Strains and Analytical Discussion

Figure 6-44 shows the strains from IV-2123-1.85-03a-v(ii), and Figure 6-45 shows the strains from IV-2123-1.85-03b-v(ii). It is observed that strain gauges placed on both vertical and horizontal reinforcement at the same location from the center of the strut report very similar strains. This suggests that both types of crack control reinforcements, vertical and horizontal, are engaged as they should be, and there are no abnormalities. Beam B3 observes the same trend as Beam B1 and

Beam B2, where the mid-section strut strains are the highest, reaffirming the crack patterns and vertical bars being more engaged than horizontal.

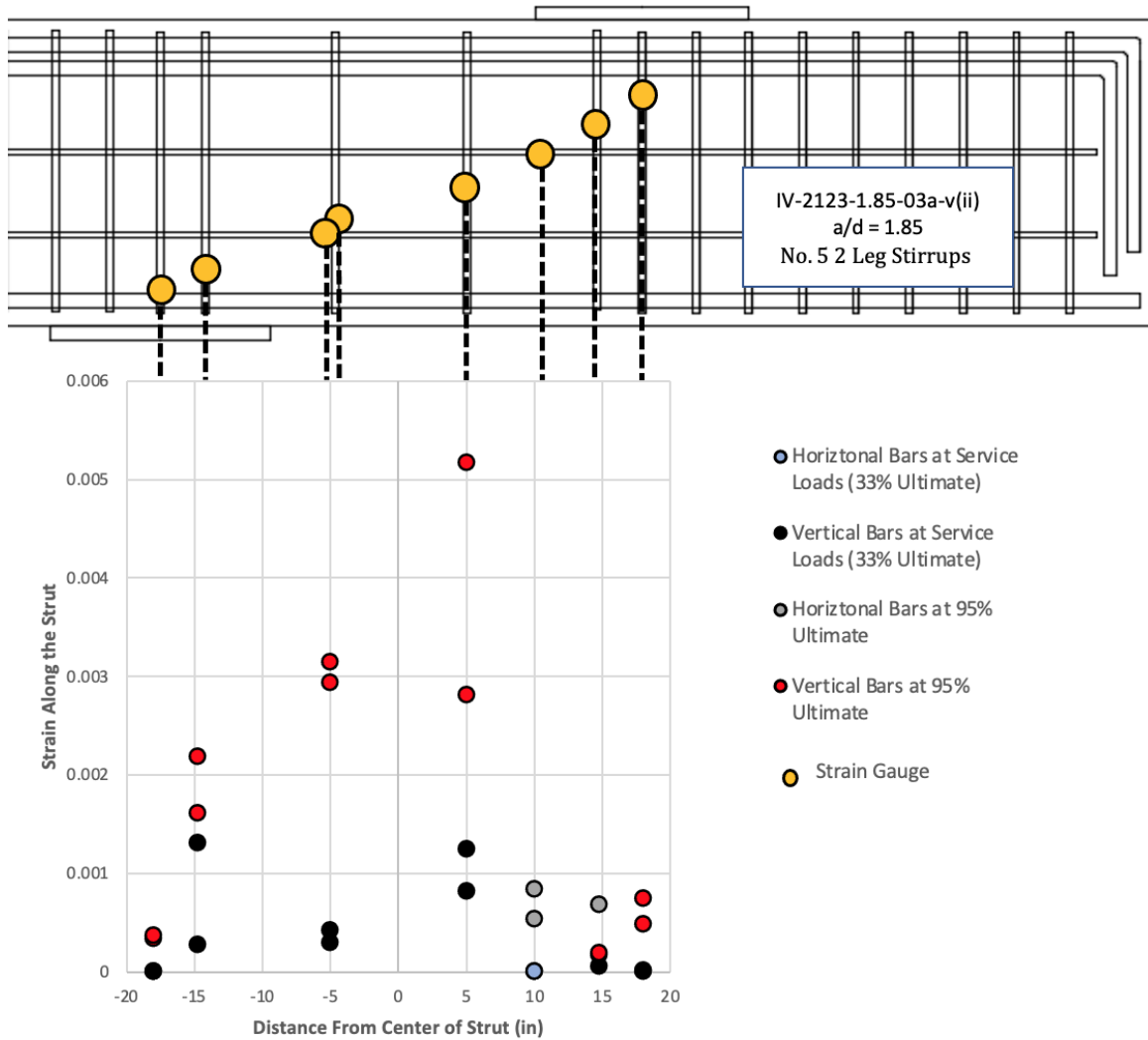


Figure 6-44 Strain engagement along the strut for IV-2123-1.85-03a-v(ii), a/d = 1.85

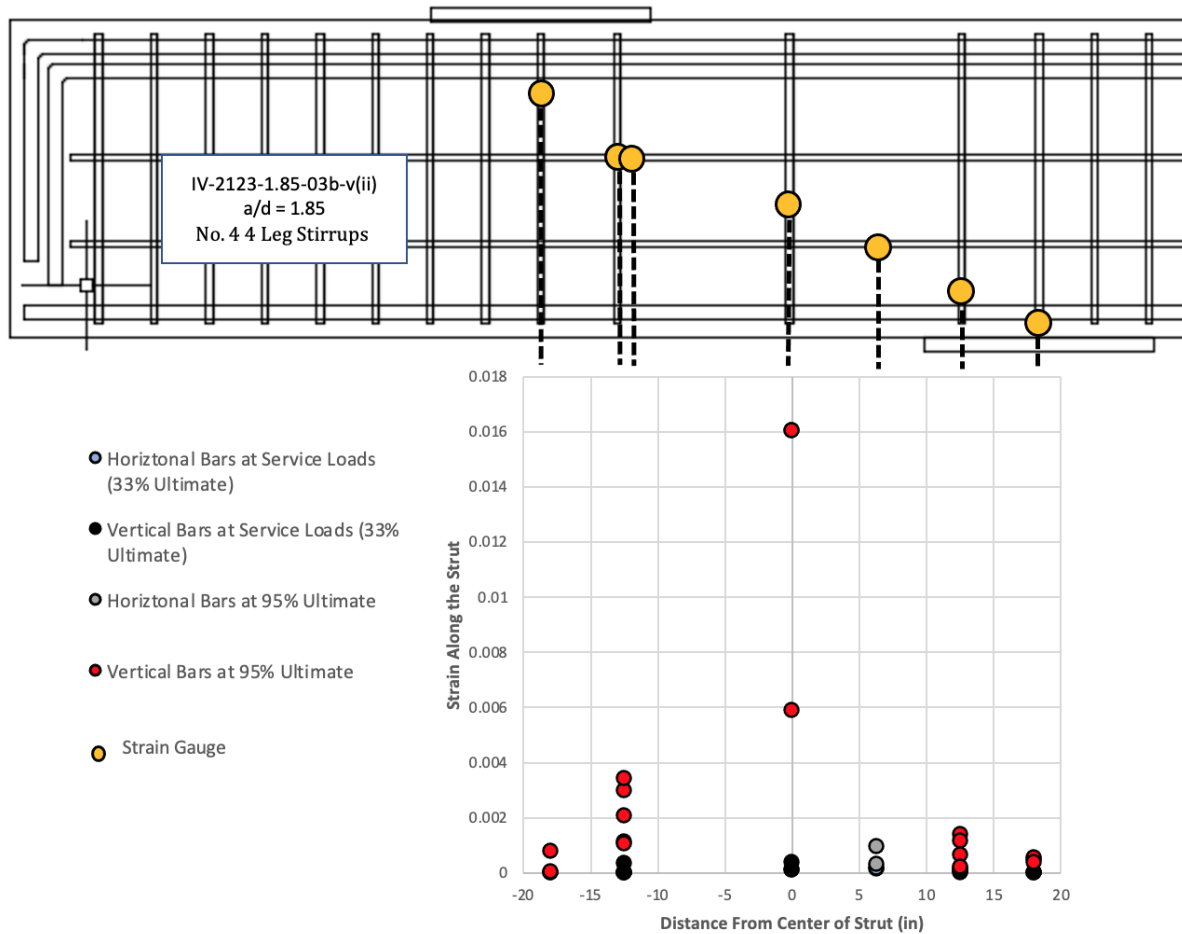


Figure 6-45 Strain engagement along the strut for IV-2123-1.85-03b-v(ii), $a/d = 1.85$

6.3.6. Longitudinal Strains

Longitudinal strain gauges placed along the outermost tension bar were also monitored. This was intended to monitor the engagement of the tie and verify if the stress along the tie agrees with the assumed strut-and-tie model within the D-region. Strain readings obtained from the longitudinal reinforcement of each specimen were presented similarly to those of crack control reinforcement in the previous section. Strain readings at a load of approximately 95% of the peak load and at the service level were extracted and presented here.

6.3.6.1. Beam B1's longitudinal strain results

Strain distribution along the longitudinal reinforcement of Specimen III-1.2-03a-v(ii) is presented in Figure 6-46. Strain gauges were distributed at three selected positions along the longitudinal reinforcing bars, as marked in the figure. Strain readings at the positions were extracted at two load levels: service level and 95% of the peak load and were plotted in the chart. It can be seen in the figure that at a load of 95% of the peak load, all three strain readings were close to or surpassed the yield strain, indicating that the entire segment of the tie within the D-region can be considered

to have yielded by the load level. The observation confirms that using a one-panel strut-and-tie model for deep beams with an a/d ratio of 1.2 but a relaxed vertical web reinforcement spacing is still appropriate. Also it is also confirmed that the tie needs to be developed near the CCT node.

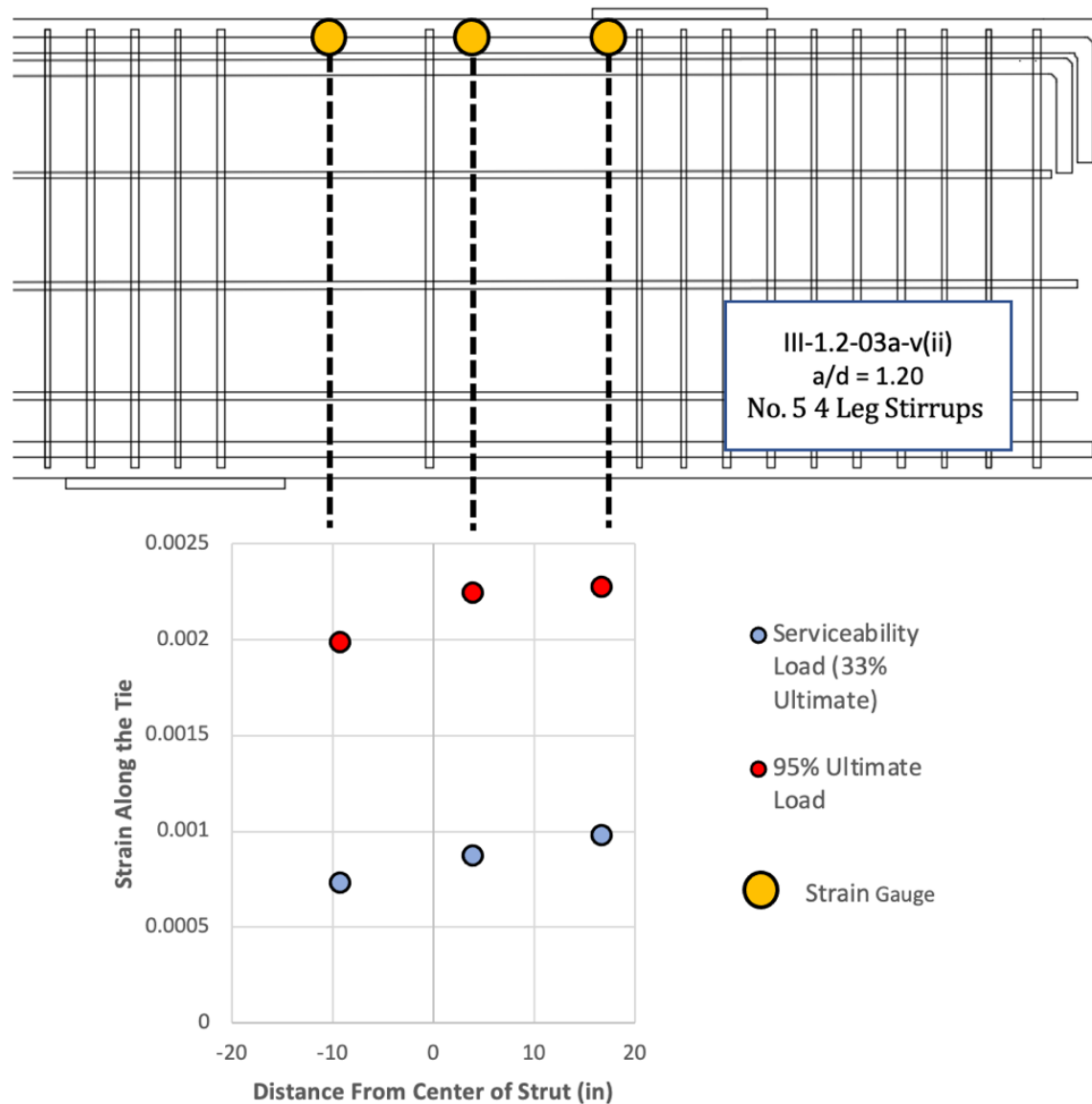


Figure 6-46 Engagement of longitudinal reinforcement of Specimen III-1.2-03a-v(ii)

Similarly, a plot of the strain reading distribution of Specimen III-1.85-03b-v(ii) was created, as shown in Figure 6-47. It can also be observed that all three strain gauges at a load level of 95% of the peak load responded readings higher than the yield strain. It is confirmed that the entire tie yielded, and therefore using a one-panel strut-and-tie model for deep beams with an a/d ratio of 1.85 but with a relaxed spacing of vertical web reinforcement is still appropriate. The tie also needs to be developed near the CCT node.

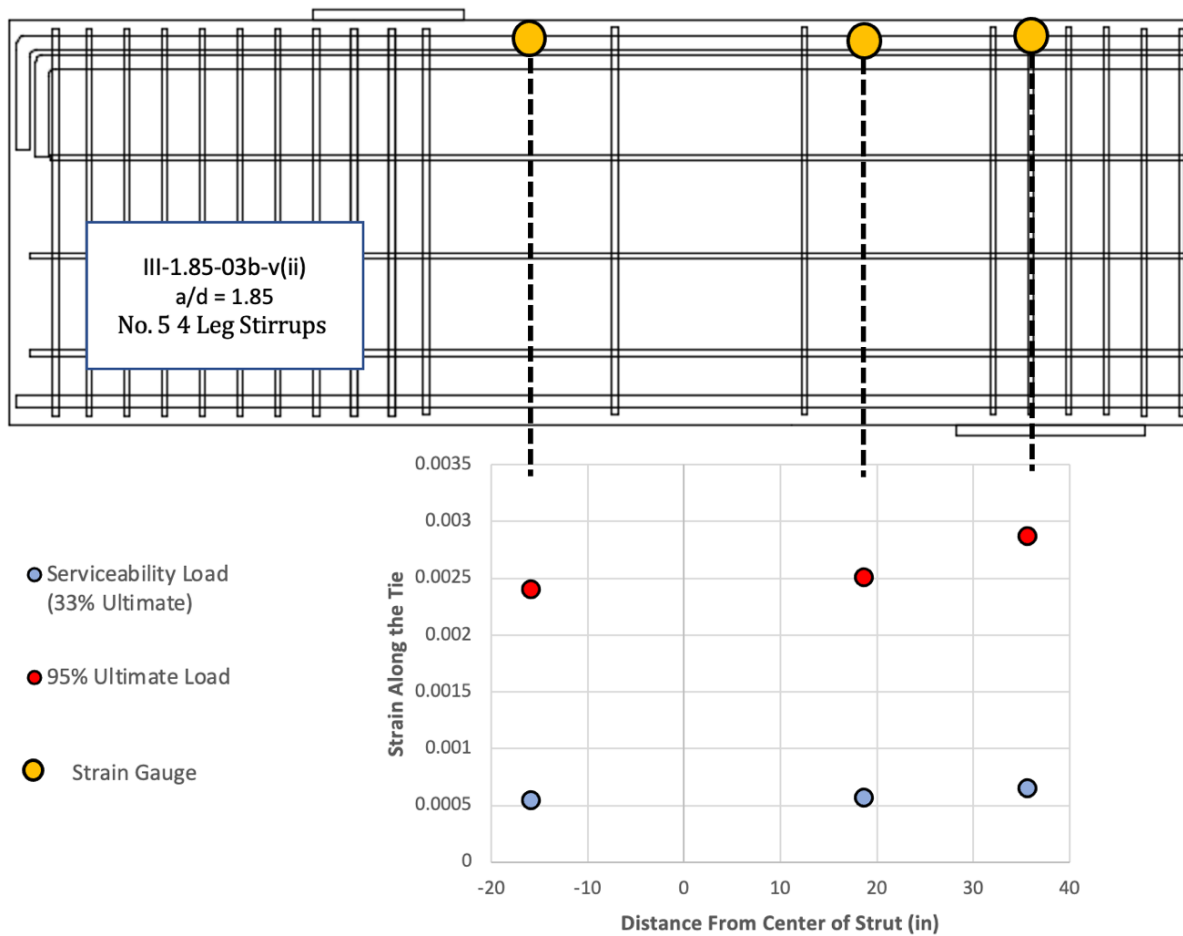


Figure 6-47 Engagement of longitudinal reinforcement of Specimen III-1.85-03b-v(ii)

6.3.6.2. Beam B2's longitudinal strain results

Strain distribution along the longitudinal reinforcement of Specimen III-1.2-03a-h(ii) is presented in the same approach in Figure 6-48. At 95% of the peak load, the strain profile of Specimen III-1.2-03a-h(ii) was slightly different from Specimen III-1.2-03a-v(ii). Three strain readings within the shear span nearly yielded one; the other at the CCT node remained low. Nevertheless, the inferred stress along the tie can still be considered constant; hence, a one-panel strut-and-tie model is appropriate. Fully developing the longitudinal reinforcement near the CCT node is conservatively required.

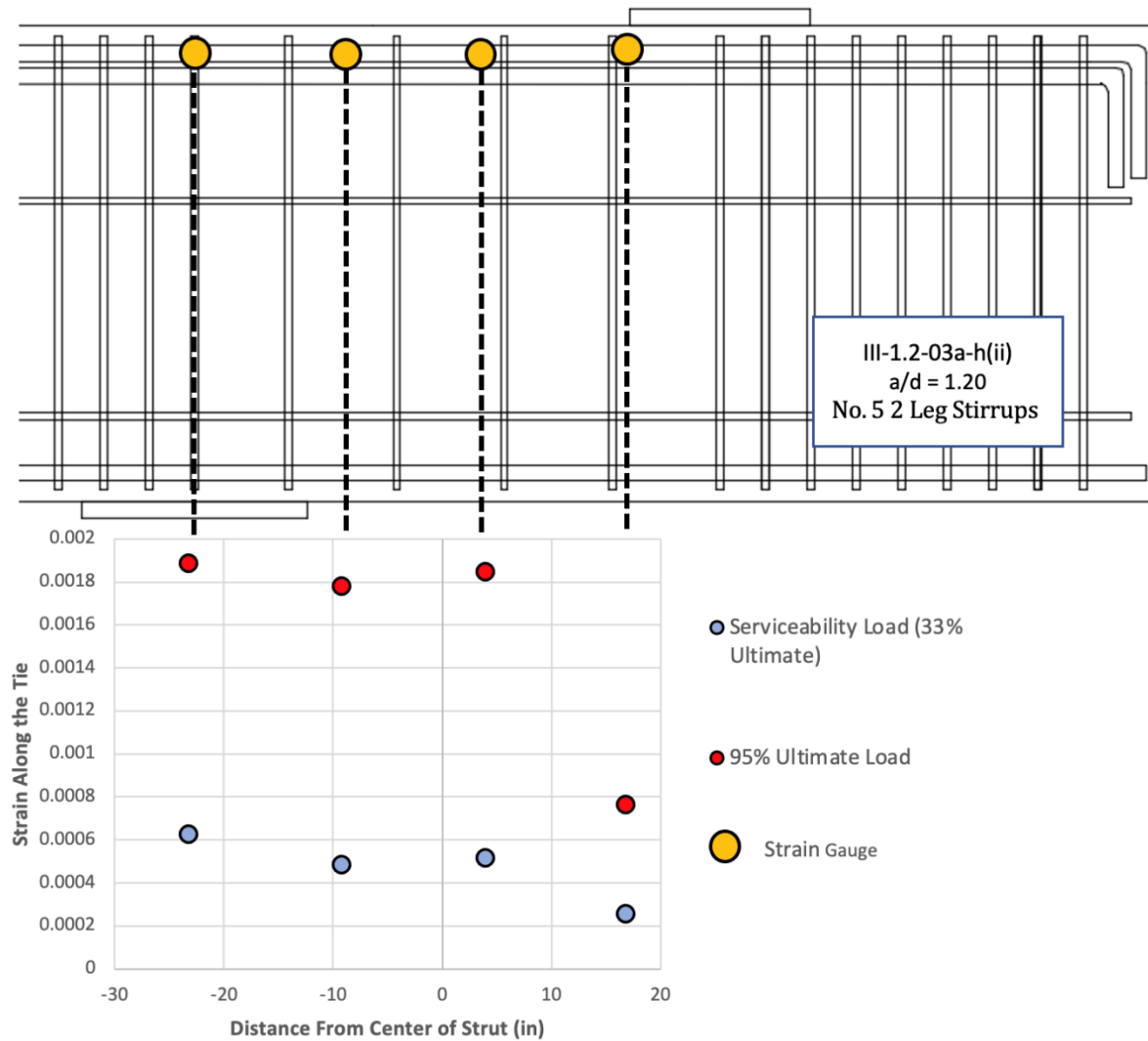


Figure 6-48 Engagement of longitudinal reinforcement of Specimen III-1.2-03a-h(ii)

Similarly, strain distribution along the longitudinal reinforcement of Specimen III-1.85-03a-h(ii) was plotted as shown in Figure 6-49. It can be seen in the figure that all three strain readings along the longitudinal reinforcement surpassed the yield strain. Therefore, a one-panel strut-and-tie model is appropriate to use for deep beams with an a/d ratio of 1.85 but with relaxed spacing of horizontal web reinforcement. The tie also needs to be fully developed near the CCT node.

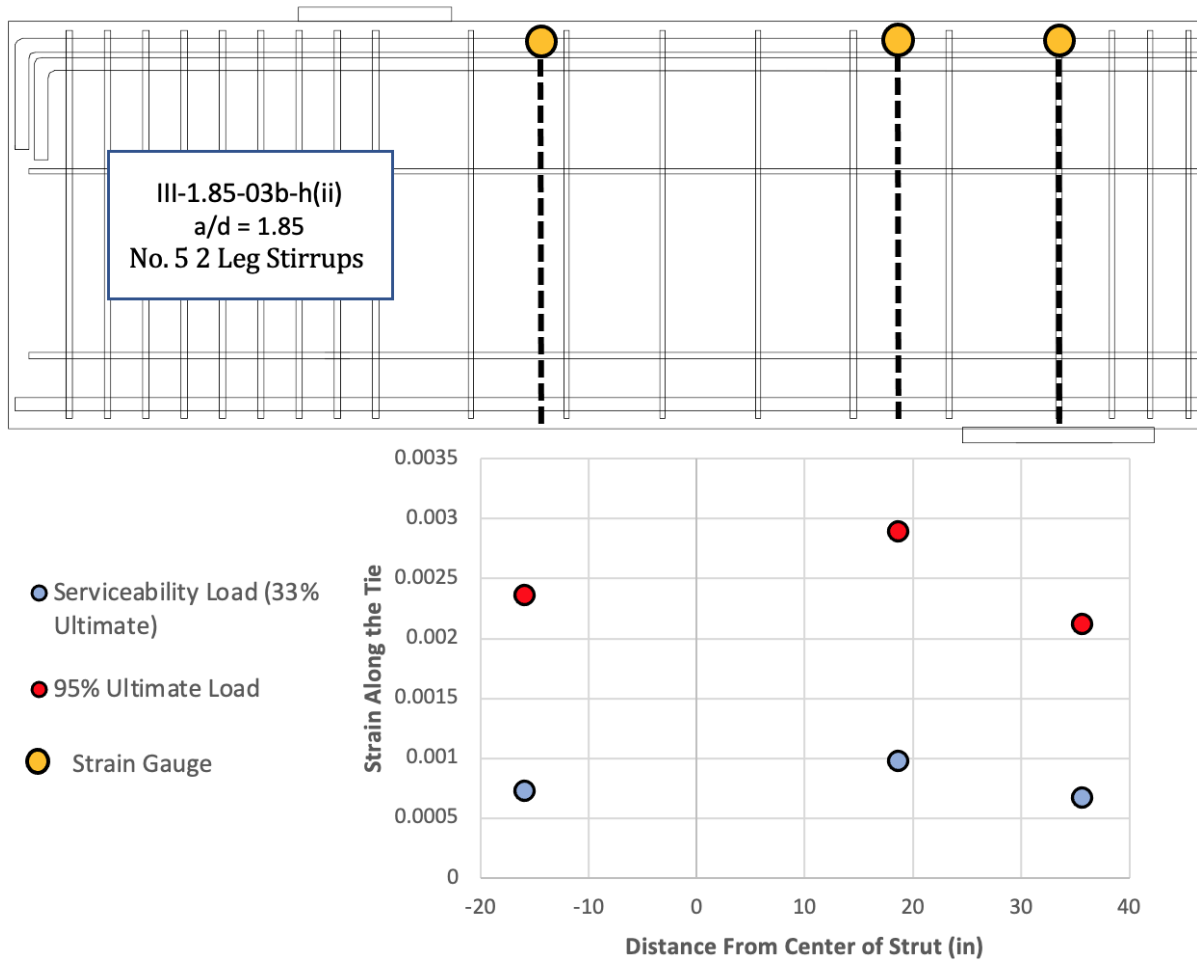


Figure 6-49 Engagement of longitudinal reinforcement of Specimen III-1.85-03a-h(ii)

6.3.6.3. Beam B3's longitudinal strain results

Strain distribution along the longitudinal reinforcement of Specimen III-1.2-03a-h(ii) is presented in the same approach in Figure 6-50. It can be seen in the figure that all three strain readings at 95% of the peak load surpassed the yield strain; hence the tie had entirely yielded in the section. Therefore, using a one-panel strut-and-tie model is appropriate for deep beams with a height as small as 23 inches with relaxed vertical web reinforcement spacing. Also, the tie has to be developed near the CCT node.

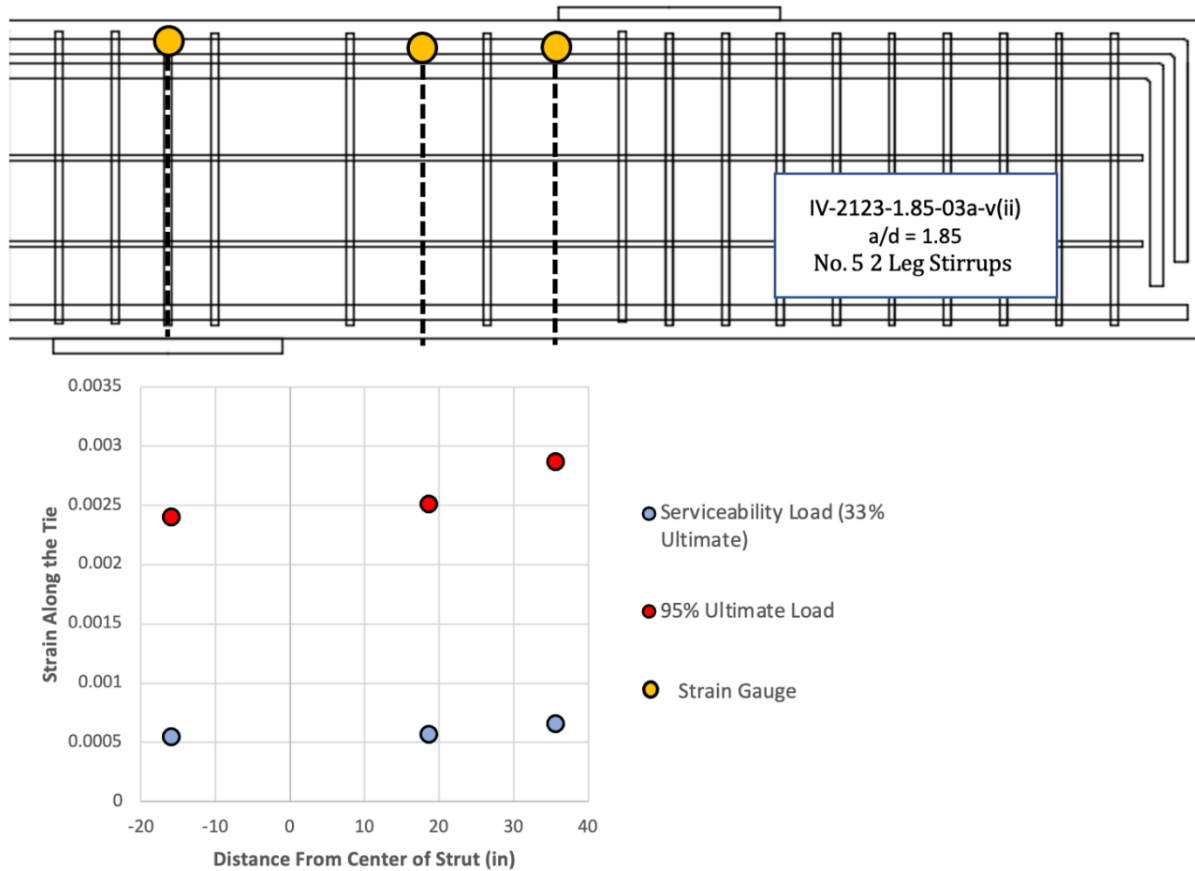


Figure 6-50 Engagement of longitudinal reinforcement of Specimen IV-2123-1.85-03a-v(ii)

Similarly, strain distribution along the longitudinal reinforcement of Specimen IV-2123-1.85-03b-v(ii) is presented in Figure 6-51. The specimen's strain status was also similar to the other specimens in the experimental program with one exception. The strain reading near the support plate responded a very high strain, which plausibly can be attributed to cracks crossing the position. Other than this, all other strain readings responded values surpassing the yield strain. Using a one-panel strut-and-tie model is appropriate for deep beams with a height as small as 23 inches with relaxed vertical web reinforcement spacing. Also, the tie has to be developed near the CCT node.

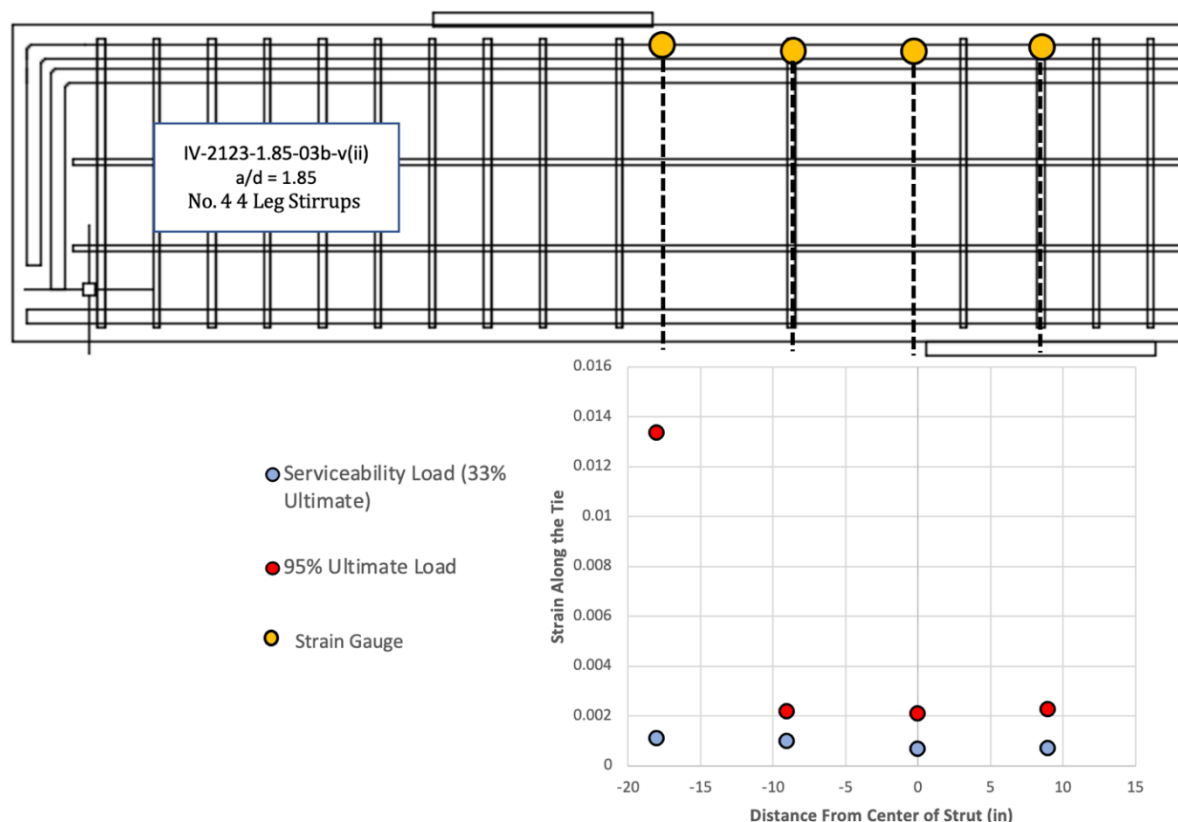


Figure 6-51 Engagement of longitudinal reinforcement of Specimen IV-2123-1.85-03b-v(ii)

6.3.7. Digital Image Correlation Measurements

As introduced in Section 6.2.3, a DIC system was employed to capture the strain map of the area of interest (i.e., the shear span) during each of the tests. One major advantage of using the DIC was to examine the appropriateness of selected permissible strut-and-tie models. As strut-and-tie modeling is intended to provide an estimate for ultimate strength (Birrcher et al., 2009), it was legitimate to study DIC strain maps of the test specimens. In addition, strut elements in the STM represent idealized principal stresses, and principle compressive strains can be assumed in the same orientation as corresponding principal stresses (Vecchio and Collins, 1986). In this regard, the DIC strain map in terms of principal compressive strains of each specimen was output as presented in Figure 6-52. In the figure, small arrows indicate the orientation of the principal strains, and the brightness of the color marks the magnitude.

It can be inferred from Figure 6-52 that principal compressive stresses were concentrated along a line that connected the support plate and the load plate for Beams B1 and B2, whether the shear span-to-depth ratio was 1.2 or 1.85 and whether the web reinforcement was relaxed along the horizontal direction or the vertical direction. It is still appropriate to use a one-panel strut-and-tie model for the shear span. However, it can be seen from the figure that there were two separated.

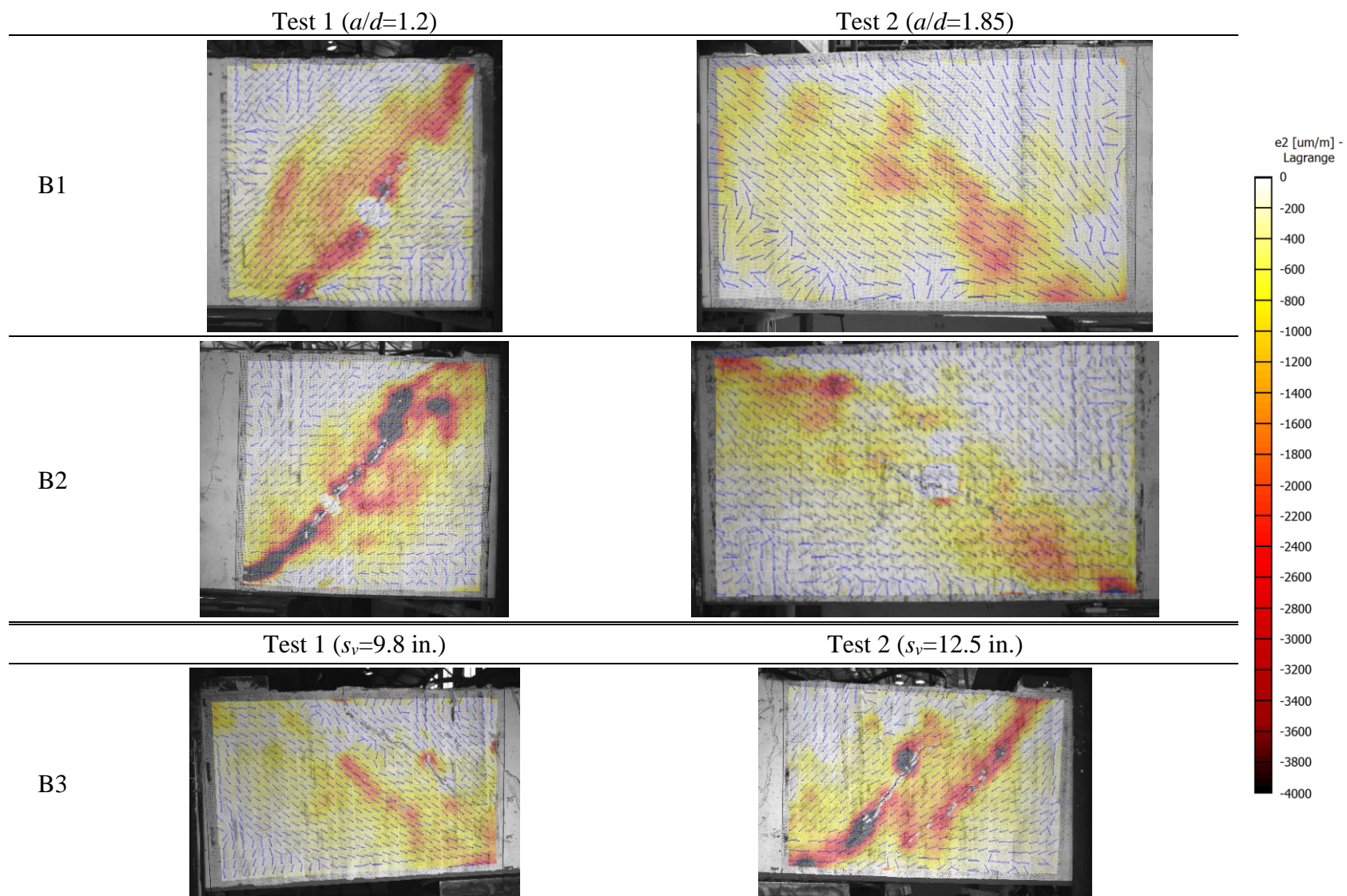


Figure 6-52 DIC compressive principal strain map at the end of test

Principal compression fields formed within the shear span, although the a/d ratio was 1.85, less than the supposedly transitioning a/d ratio (2.5) from the one-panel model to the two-panel model. The effect of the two-panel mechanism might still have moderately existed. The contribution of the two-panel mechanism and affecting factors remained not clearly known; nonetheless, using a one-panel strut-and-tie model would lead to conservative results. Also, the STM better represents the stress distribution than the average sectional shear stress along the section at the mid-span.

6.4. Finite Element and Parametric Study

The finite element (FE) analysis aims to provide numerical test results as a supplement to support conclusions drawn from the experimental program. The non-linear finite element analysis software ATENA 3D was used in this FE analysis. Three steps were taken to complete the FE analysis: 1) model preparation, 2) model validation, and 3) parametric analysis. In the first step, FE models were built based on benchmark specimens selected from the experimental program of Project 0-5253. Second, the constructed models were validated by comparing the outcomes of the FE analysis to those of the experimental results. Finally, numerical specimens with more combinations of the spacing of crack control reinforcement were modeled to provide numerical test results. The FE analytical strength of the numerical specimens was compared to STM strength to investigate the feasibility of relaxing the requirements for web reinforcement spacings.

6.4.1. FE Model Preparation

6.4.1.1. Benchmarks

Benchmark specimens were selected from Project 0-5253, including Specimens III-1.2-03-(i) and III-1.85-03-(i), to be inconsistent with the experimental program in the current study. The two benchmark specimens were tested to fail in shear within the area of interest, making them good selections to fulfill the purpose of the finite element analysis. The structural configurations of the benchmark specimens are introduced in Section 6.2.1.2.

6.4.1.2. Material Model

6.4.1.2.1. Concrete

As the two benchmark specimens had different concrete properties, two groups of concrete material properties were used in the FE analysis. The material type “3D Nonlinear Cementitious 2” was selected for both groups of concrete material. As the experimental program of Project 0-5253 did not provide all required material parameters, recommended values were used for the FE modeling. Detailed definitions of required parameters refer to ATENA 3D theory (2018). The used parameters in the software are listed in Table 6-7.

Table 6-7 Concrete material “3D Nonlinear Cementitious” parameters

Subset	Parameters	III-1.2-03-(i)	III-1.85-03-(i)	Unit
Basic	Elastic modulus, E_c	3700	4026	ksi
	Poisson's ratio, ν	0.2	0.2	-
	Tensile strength, f'_t	0.26	0.28	ksi
	Compressive strength, f'_c	4.22	4.99	ksi
Tensile	Specific Fracture energy, G_F	2.56×10^{-4}	2.78×10^{-4}	kip/in.
	Crack spacing, s_{max}	-	-	-
	Tension stiffening, c_{ts}	-	-	-
	Unloading	-	-	-
Compressive	Critical compression displacement, w_d	0.05	0.05	in.
	Plastic strain at compressive strength, ϵ_{cp}	-1.14×10^{-3}	-1.23×10^{-3}	-
	Reduction of comp. strength due to cracks, $r_{c,lim}$	0.8	0.8	-
Shear	Crack Shear Stiff. Factor, S_F	20	20	-
	Aggregate interlock, MCF	-	-	-
	Aggregate Size	0.79	0.79	in.
Miscellaneous	Fail. Surface eccentricity	0.52	0.52	-
	Multiplier for the plastic flow dir. β	0.5	0.5	-
	Specific material weight, ρ	8.47×10^{-5}	8.47×10^{-5}	kci
	Coefficient of thermal expansion, α	-	-	1/°F
	Fixed crack model coefficient	1.0	1.0	-

6.4.1.2.2. Reinforcement

The bilinear stress-strain constitutive relationship was used for reinforcement. It was required to input the yield stress, strain-hardening ratio, and the ultimate stress of the reinforcement. The longitudinal reinforcement and the web crack control reinforcement had different properties and should be input separately. In addition, each specimen had its own set of reinforcement properties. Four sets of properties were input for modeling the reinforcement. Parameters are summarized in Table 6-8

Table 6-8 Reinforcement material parameters

Subset	Parameters	III-1.2-03-(i)		III-1.85-03-(i)		Unit
		Long.	Web	Long.	Web	
Basic	Elastic modulus, E	29000		29000		ksi
	Yield strength, σ_y	68	65	68	65	ksi
	Tensile strength, σ_t	79	76	79	76	ksi
	Limit strain, ε_{lim}	0.1	0.1	0.1	0.1	
Miscellaneous	Specific material weight, ρ	2.89×10^{-4}		2.89×10^{-4}		kci
	Coefficient of thermal expansion, α	-		-		1/°F

6.4.1.2.3. Steel Plates

The elastic isotropic material model was used for the load and support plates. The model had an elastic modulus of 29000 ksi and a Poisson's ratio of 0.3. Other used parameters are listed in Table 6-9

Table 6-9 Elastic material parameters

Subset	Parameters	III-1.2-03-(i)	III-1.85-03-(i)	Unit
Basic	Elastic modulus, E	29000		ksi
	Poisson's ratio, ν	0.3		-
Miscellaneous	Specific material weight, ρ	2.89×10^{-4}		kci
	Coefficient of thermal expansion, α	-		1/°F

6.4.1.3. Model Configuration

The overall model configuration is shown in Figure 6-53. Resembling Specimens III-1.2-03-(i) and III-1.85-03-(i), the numerical specimen consisted of three primary parts: 1) a deep beam, 2) load and support plates, and 3) reinforcement. The entire deep beam was modeled using a rectangular Macroelement volume with dimensions of 21 in. in width by 42 in. in height by 332 in. in length. At each position where a support plate and a spreader beam were installed, another Macroelement was used to model the support plate. The dimensions of the Macroelement were 2 in. by 16 in. by 21 in., which was the same as the support plate used in the experimental program.

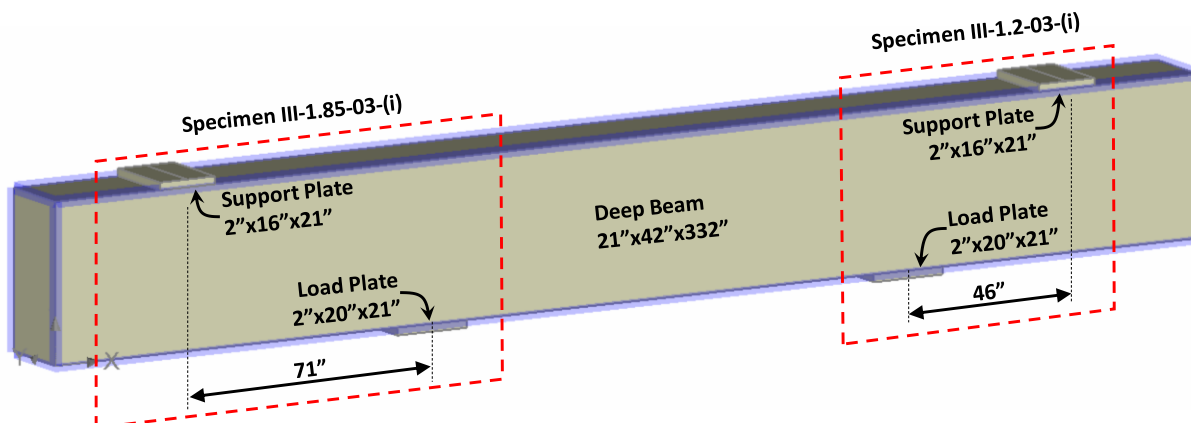


Figure 6-53 Macroelements of deep beam and steel plates

Each side of the numerical specimen was intended to conduct one numerical test. On the lefthand side of the numerical specimen, Specimen III-1.85-03-(i) was modeled, and therefore, a Macroelement resembling the load plate with dimensions of 2 in. by 20 in. by 21 in. was positioned 71 in. horizontally away from the Macroelement representing the support plate. Similarly, another Macroelement was used to model the other load plate for Specimen III-1.2-03-(i), being positioned 46 in. horizontally away from the Macroelement that represented the near support plate.

Inside the Macroelement representing the deep beam, 1-D reinforcement elements were laid out for modeling reinforcing bars. All coordinates of the 1-D reinforcement elements were placed according to the layout of reinforcement reported in the experimental program of Project 0-5253. The cross-sectional area of the reinforcement was specified per the experimental program. The bends of closed stirrups were not modeled; instead, each closed stirrup was modeled as consisting of four straight continuous 1-D reinforcement elements. In addition, the hook and the hook extension on each end of longitudinal reinforcing bars were not needed, given perfect bond was used. The modeling result is shown in Figure 6-54.

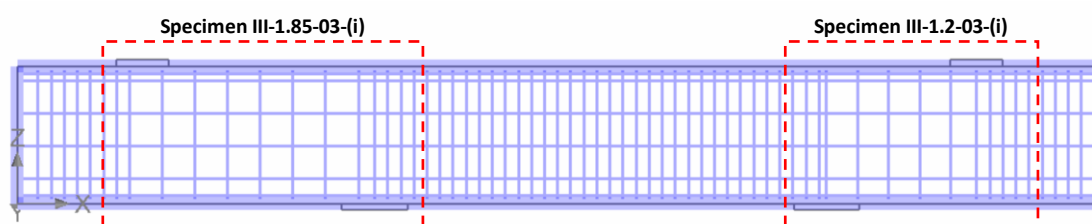


Figure 6-54 Layout of 1-D Reinforcement elements

6.4.1.4. Boundary Conditions

Boundary conditions were assigned according to how the load was applied and how reactions were provided. In the experimental program, rollers were placed underneath the load plate and above the support plates. One of the rollers above the support plates was fixed as a pinned connection.

Per the arrangement, a line support with y-direction (into the paper) and z-direction (up-and-down) unmovable were assigned to the center of each Macroelement representing the support plates or the load plate. For the pinned roller, the x-direction (left-and-right) was also fixed.

Loading was applied by assigning prescribed deformation to the line support underneath the Macroelement representing the load plate. The assigned prescribed deformation was 5×10^{-3} in. upward, meaning that a displacement of 5×10^{-3} in. upward would be applied in each analysis step. To ensure that the displacement was applied evenly, the displacement was distributed at the center and the two ends on the centerline of the Macroelement. The self-weight of the numerical deep beam was taken into consideration.

6.4.1.5. Mesh and Contact

The Macroelement for the numerical deep beam was meshed with eight-point linear hexahedral meshes with a size of 4 in. For Macroelements modeling steel plates, four-point linear tetrahedral meshes with a general size of 4 in. were used. Perfect contact elements were automatically generated between the numerical deep beam and numerical steel plates. The result is shown in Figure 6-55.

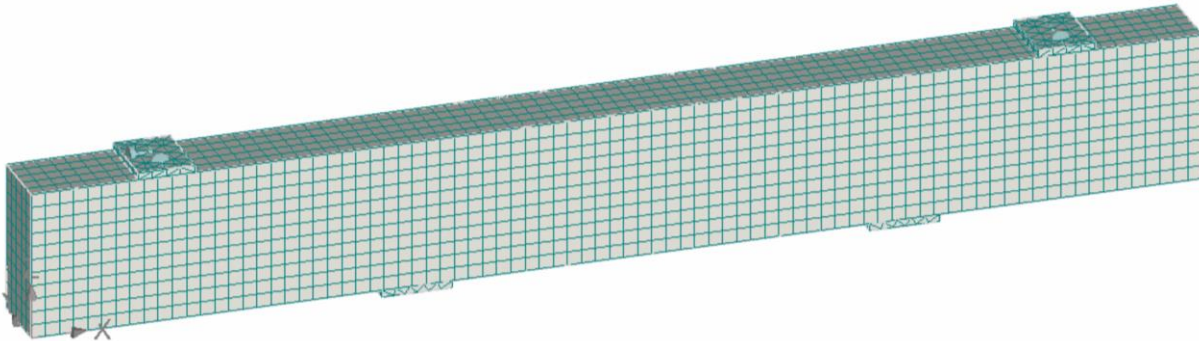


Figure 6-55 Meshing result

6.4.1.6. Solution Parameters

The standard Newton-Raphson method was used to exercise iterations for the convergence of solution in each analysis step. Each analysis step had 40 iterations, and convergence tolerances were specified as default. Line search was activated to assist convergence.

6.4.2. FE Model Validation

Figure 6-56 shows plots of the comparison between the experimental and FE analytical results in terms of load-displacement relationships. It can be seen from the figure that the FE analytical results are in good agreement with the experimental results. Regarding the structural stiffness, the FE analysis accurately captured the behavior. For Specimen III-1.2-03-(i), the analytical stiffness was almost the same as the experimental stiffness. For Specimen III-1.85-03-(i), on the other hand,

the analytical stiffness was slightly higher than the experimental stiffness. Regarding the peak load-carrying capacity, the analytical result of Specimen III-1.2-03-(i) reached a value of 842 kip, which was 14.3 percent lower than the experimental results. For Specimen III-1.85-03-(i), the analytical peak load was 581 kips, 8.4 percent higher than the experimental result. Provided that many assumed material parameters were used, the predictive ability of the FE models was considered agreeable.

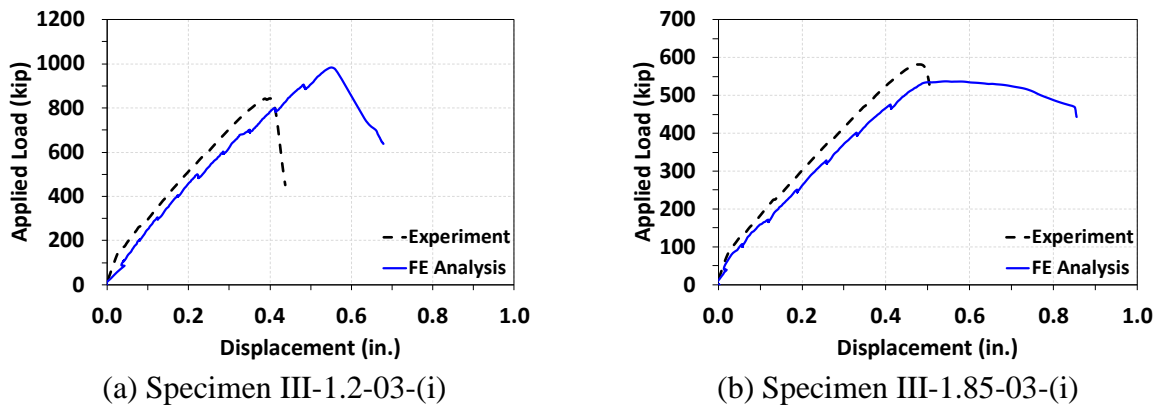


Figure 6-56 Comparison of load-displacement relationship between experiment and FEA

The experimental cracking patterns at the peak load of Specimens III-1.2-03-(i) and III-1.85-03-(i) are presented together with the FE analytical ones in Figure 6-57. The finite element models once again were verified to have the ability to capture the cracking patterns of both benchmark specimens. It can be observed that the directions and distributions of shear cracks and flexural cracks were captured by the FE analysis.

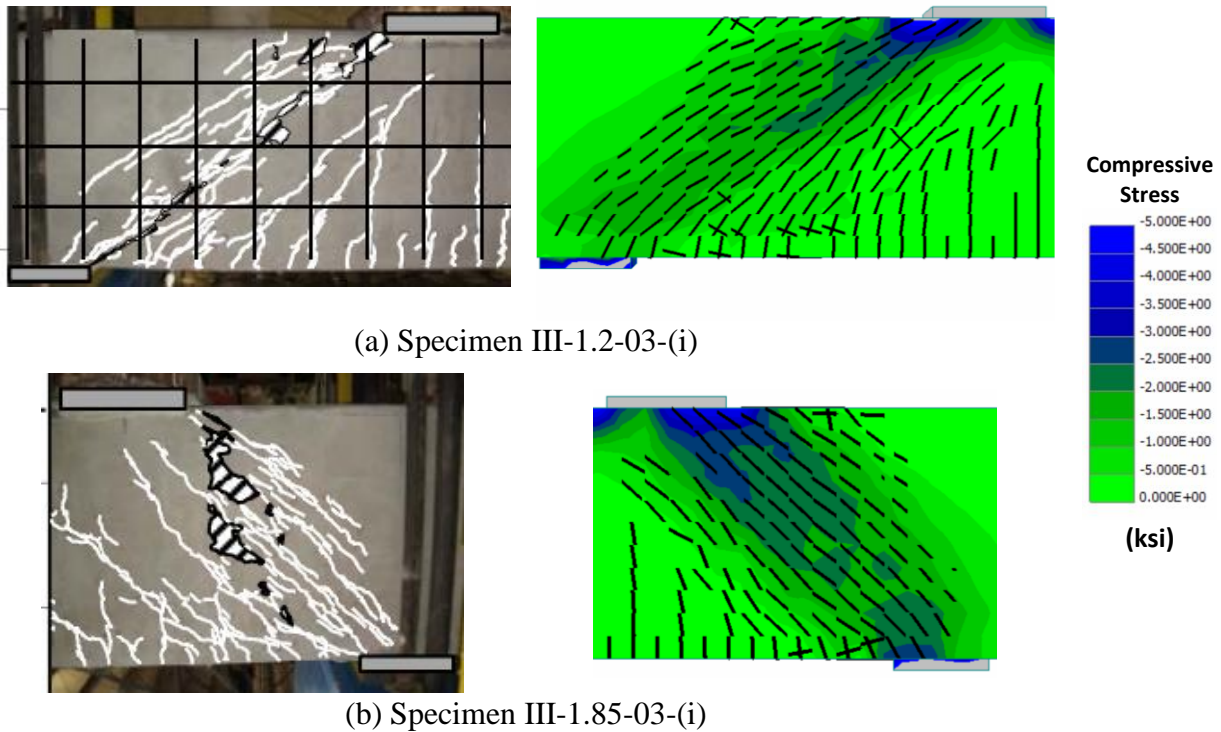


Figure 6-57 Comparison between experimental and FE analytical crack patterns

The validation results show that the modeling technique, including material models, the structural configuration, the meshing approach, and the solution parameters, was acceptable for the FE parametric analysis, which is introduced in the later section.

6.4.3. FE Parametric Analysis

The FE parametric analysis aims to provide supplementary numerical data to support the experimental finding that the STM is still applicable when the spacing requirement is relaxed. In the experimental program of the current study, the specimens had either vertical web reinforcement spacing or horizontal web reinforcement spacing doubled compared to their companion specimens in Project 0-5253. Although successfully providing insights that the STM performed well whether the spacing was doubled, the number of experimentally investigated cases is somewhat limited.

The FE parametric analysis introduced in this section investigates more combinations of vertical web reinforcement and horizontal web reinforcement spacings while the web reinforcement ratio, 0.3%, is maintained. In addition, two different deep beam heights and two different shear span ratios, which were selected according to test specimens in Project 0-5253, are included.

6.4.3.1. Numerical Specimens

6.4.3.1.1. Analysis Matrix

In this “numerical” test program, two different cross-sections and two different a/d ratios were selected on the basis of specimens developed in Project 0-5253, as summarized in Table 6-10. The cross-sections included 21 in. by 42 and 21 in. by 75 in. The height of 75 in. was selected because it delivered an opportunity to delve into both the spacing limits of $d/2$ and 24 in. Also, the a/d ratios included 1.85 and 1.2. Therefore, four distinct combinations were created, and each of these combinations had its particular companion specimen from Project 0-5253 or the experimental program in the current study. For each combination, several cases of different web reinforcement spacings were included to provide numerical data. Sixteen cases in total were planned, as shown in Table 6-10.

Table 6-10 Summary of number of numerical specimens

Cross-section	Crack control reinforcement ratio	Shear span ratio a/d	
		1.85	1.2
21 in. \times 42 in.	0.3%	3 cases	3 cases
21 in. \times 75 in.	0.3%	4 cases	6 cases

Table 6-11 and Table 6-12 show selected web reinforcement spacings for the deep beam cross-section of 21 in. by 42 in. with a/d ratios of 1.85 and 1.2. The companion specimen of this cross-section had vertical web reinforcement of No. 5 stirrups spaced at 9.5 in. and horizontal web reinforcement of two No. 5 bars spaced at 10 in. To create more cases, either or both the vertical and horizontal spacings were doubled by using larger bars or more legs. Three combinations for each a/d ratio were created, as noted in shaded cells in Table 6-11 and Table 6-12. In the tables, each numerical case has an ID introduced in Section 6.4.3.1.2.

Table 6-11 Web reinforcement spacings for deep beams of 21 in. by 42 in. with $a/d=1.85$

Series I 21 in. \times 42 in. $a/d = 1.85$		Vertical spacing, s_v	
		19 in. (4-leg #5 stirrups)	19 in. (2-leg #7 stirrups)
Horizontal spacing, s_h	10 in. (#5 bars)	1.85-H10-V19(4-leg)	
	20 in. (#7 bars)	1.85-H20-V19(4-leg)	
			1.85-H20-V19(2-leg)

Table 6-12 Web reinforcement spacings for deep beams of 21 in. by 42 in. with $a/d=1.2$

Series II 21 in. \times 42 in. $a/d = 1.2$		Vertical spacing, s_v	
		19 in. (4-leg #5 stirrups)	19 in. (2-leg #7 stirrups)
Horizontal spacing, s_h	10 in. (#5 bars)	1.2-H10-V19(4-leg)	
	20 in. (#7 bars)	1.2-H20-V19(4-leg)	
			1.2-H20-V19(2-leg)

Similarly, various vertical and horizontal web reinforcement spacings were selected between 9.5 in. and 38 in. for numerical specimens with a cross-section of 21 in. by 75 in. and a/d ratios of 1.85 and 1.2. The selections included a spacing that complied with the current AASHTO LRFD spacing requirement and spacings that were relaxed to $d/2$ and 24 in. In addition, there was one selection between the current requirement and the target relaxation. Ten cases in total were included for the cross-sections, as shown in Table 6-13 and Table 6-14.

Table 6-13 Web reinforcement spacings for deep beams of 21 in. by 75 in. with $a/d=1.85$

Series III 21 in. \times 75 in. $a/d = 1.85$		Vertical spacing, s_v			
		9.5 in. (2-leg #5 stirrups)	19 in. (2-leg #7 stirrups)	24 in. (2-leg #8 stirrups)	38 in. (4-leg #7 stirrups)
Horizontal spacing, s_h	10 in. (#5 bars)	1.85-H10-V9.5(2-leg)			
	20 in. (#7 bars)				
	24 in. (#8 bars)		1.85-H20-V19(2-leg)		
	38 in. (4-#7 bars)				
				1.85-H24-V24(2-leg)	1.85-H38-V38(4-leg)

Table 6-14 Web reinforcement spacings for deep beams of 21 in. by 75 in. with $a/d=1.2$

Series IV 21 in. \times 75 in. $a/d = 1.2$		Vertical spacing, s_v			
		9.5 in. (2-leg #5 stirrups)	19 in. (2-leg #7 stirrups)	24 in. (2-leg #8 stirrups)	38 in. (4-leg #7 stirrups)
Horizontal spacing, s_h	10 in. (#5 bars)	1.2-H10-V9.5(2-leg)			
	20 in. (#7 bars)				
	24 in. (#8 bars)		1.2-H20-V19(2-leg)	1.2-H20-V24(2-leg)	
	38 in. (4-#7 bars)		1.2-H24-V19(2-leg)	1.2-H24-V24(2-leg)	
					1.2-H24-V38(4-leg)
					1.2-H38-V38(4-leg)

6.4.3.1.2. Nomenclature

A nomenclature was coined to identify specimens, as shown in Figure 6-58. The first part represents the cross-sectional dimension of the specimen; the second part is the a/d ratio; the third part is the horizontal web reinforcement spacing; the fourth part is the vertical web reinforcement spacing and the number of legs of stirrups.

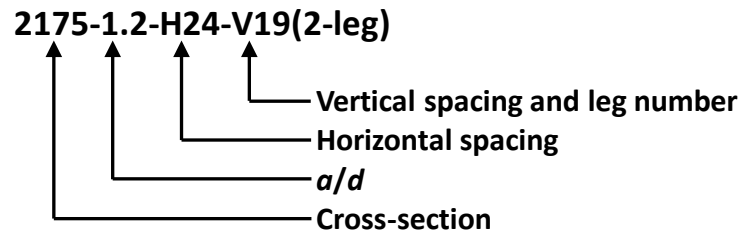
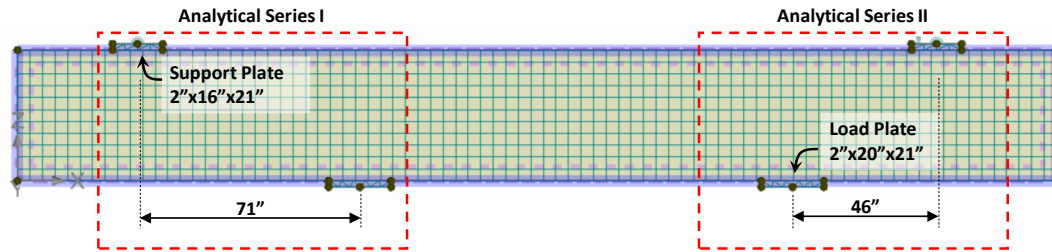


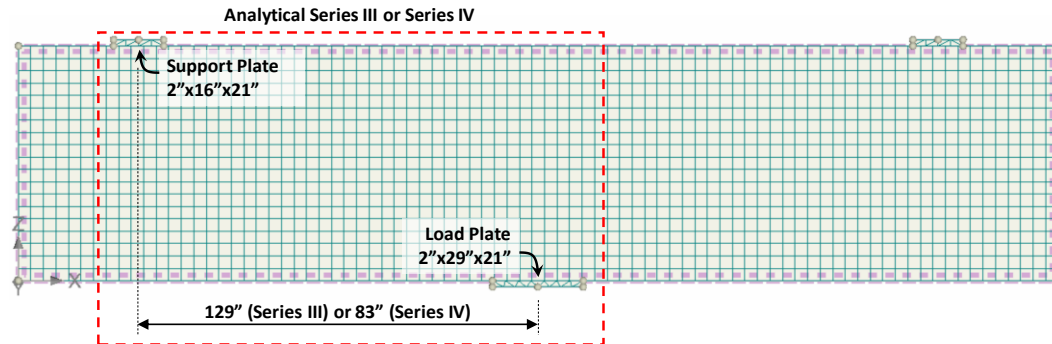
Figure 6-58 Nomenclature of numerical test specimens

6.4.3.1.3. Model Preparation

The general configurations of the numerical deep beams listed in Table 6-11 through Table 6-14 are shown in Figure 6-59. Figure 6-59(a) presents numerical specimens with cross-sectional dimensions of 21 in. by 42 in. Identical to their counterpart specimens in Project 0-5253 (Specimens III-1.85-03-(i) and III-1.2-03(i)), the numerical specimens had a total length of 332 in. and had Macroelements representing support and load plates positioned accordingly. Similarly, Figure 6-59(b) presents numerical specimens with cross-sectional dimensions of 21 in. by 75 in. and with a length of 332 in. based on their counterpart specimens in Series IV of Project 0-5253. Also, Macroelements simulating load and support plates were placed to create the corresponding a/d ratio. The mesh size of all numerical specimens was 4 in., as used for the model validation. Also, the Macroelement for the deep beam was meshed using eight-point hexahedral elements, while simulated steel plates were meshed using four-point tetrahedral elements.



(a) Numerical specimen in Series I and II



(b) Numerical specimen in Series III and IV

Figure 6-59 General configuration of numerical specimens

The reinforcement pattern again was the same as used in Project 0-5253 and the current study, as shown in Figure 6-60. Specifically, longitudinal reinforcement on the tension and compression sides was identical to the counterparts. Outside of the area of interest, otherwise, the shear span, tightly distributed 1-D elements for stirrups were assigned accordingly. In the area of interest, the distribution of 1-D elements for web reinforcement was based on Table 6-11 through Table 6-14.

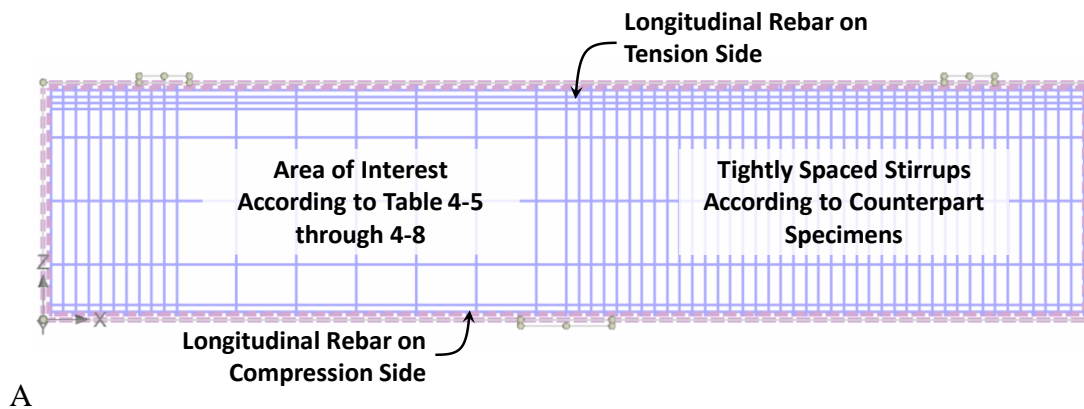


Figure 6-60 Example arrangement of 1-D elements for reinforcement

The concrete material model was again “3D Nonlinear Cementitious 2” and the parameters used for numerical deep beams of 21 in. by 42 in. and 21 in. by 75 in. are shown in Table 6-15 and

Table 6-16, respectively. Specified concrete strengths were from the current study or the counterpart specimens in Project 0-5253, and other parameters were automatically generated.

A prescribed displacement of 0.002 in. for a more refined result was applied to the centerline of the Macroelement simulating the load plate, while the Macroelements representing the support plates were not allowed to move out-of-plan nor vertically. One of the support plates was not permitted to translate horizontally.

Table 6-15 Concrete material parameters for numerical deep beam of 21 in. by 42 in.

Subset	Parameters	$a/d = 1.2$	$a/d = 1.85$	Unit
Basic	Elastic modulus, E_c	3862	3894	ksi
	Poisson's ratio, ν	0.2	0.2	-
	Tensile strength, f'_t	0.3	0.27	ksi
	Compressive strength, f'_c	4.59	4.67	ksi
Tensile	Specific Fracture energy, G_F	2.95×10^{-4}	2.62×10^{-4}	kip/in.
	Crack spacing, s_{max}	-	-	-
	Tension stiffening, c_{ts}	-	-	-
	Unloading	-	-	-
Compressive	Critical compression displacement, w_d	0.02	0.02	in.
	Plastic strain at compressive strength, ϵ_{cp}	-1.19×10^{-3}	-1.20×10^{-3}	-
	Reduction of comp. strength due to cracks, $r_{c,lim}$	0.8	0.8	-
Shear	Crack Shear Stiff. Factor, S_F	20	20	-
	Aggregate interlock, MCF	-	-	-
	Aggregate Size	0.79	0.79	in.
Miscellaneous	Fail. Surface eccentricity	0.52	0.52	-
	Multiplier for the plastic flow dir. β	0.5	0.5	-
	Specific material weight, ρ	8.47×10^{-5}	8.47×10^{-5}	kci
	Coefficient of thermal expansion, α	-	-	1/°F
	Fixed crack model coefficient	1.0	1.0	-

Table 6-16 Concrete material parameters for numerical deep beam of 21 in. by 75 in.

Subset	Parameters	$a/d = 1.2 \text{ \& } 1.85$	Unit
Basic	Elastic modulus, E_c	4002	ksi
	Poisson's ratio, ν	0.2	-
	Tensile strength, f'_t	0.28	ksi
	Compressive strength, f'_c	4.93	ksi
Tensile	Specific Fracture energy, G_F	2.76×10^{-4}	kip/in.
	Crack spacing, s_{max}	-	-
	Tension stiffening, c_{ts}	-	-
	Unloading	-	-
Compressive	Critical compression displacement, w_d	0.02	in.
	Plastic strain at compressive strength, ϵ_{cp}	-1.23×10^{-3}	-
	Reduction of comp. strength due to cracks, $r_{c,lim}$	0.8	-
Shear	Crack Shear Stiff. Factor, S_F	20	-
	Aggregate interlock, MCF	-	-
	Aggregate Size	0.79	in.
Miscellaneous	Fail. Surface eccentricity	0.52	-
	Multiplier for the plastic flow dir. β	0.5	-
	Specific material weight, ρ	8.47×10^{-5}	kci
	Coefficient of thermal expansion, α	-	1/°F
	Fixed crack model coefficient	1.0	-

6.4.3.2. Analytical Results and Discussion

6.4.3.2.1. Summary of analytical results

Analytical results of the total applied load at the load plate, denoted as P_{FEM} , are summarized in Table 6-17. The parameter of concrete compressive strength f'_c of each numerical specimen is also provided for later discussion. In addition, the STM was also applied to each of the numerical specimens to evaluate the conservatism. The first numerical specimen in each series (shaded in the table) is the control group which had a web reinforcement spacing per current AASHTO LRFD spacing provisions. For Series I and Series II, the control specimens (with IDs Project 0-5253-III-1.85-03(i) and Project 0-5253-III-1.2-03(i)) are from the benchmark specimens for the model validation.

Table 6-17 Summary of analytical results

Series	Analysis ID	f'_c (ksi)	P_{FEM} (kip)	P_{STM} (kip)	P_{FEM}/P_{STM}
Series I	Project 0-5253-III-1.85-03(i)	4.99	581	-	-
	2142-1.85-H10-V19(4-leg)	4.67	559	457	1.22
	2142-1.85-H20-V19(4-leg)	4.67	542	457	1.19
	2142-1.85-H20-V19(2-leg)	4.67	544	457	1.19
Series II	Project 0-5253-III-1.2-03(i)	4.22	842	-	-
	2142-1.2-H10-V19(4-leg)	4.59	839	670	1.25
	2142-1.2-H20-V19(4-leg)	4.59	842	670	1.26
	2142-1.2-H20-V19(2-leg)	4.59	810	670	1.21
Series III	2175-1.85-H10-V9.5(2-leg)	4.93	1494	1041	1.43
	2175-1.85-H20-V19(2-leg)	4.93	1501	1041	1.44
	2175-1.85-H24-V24(2-leg)	4.93	1445	1041	1.39
	2175-1.85-H38-V38(4-leg)	4.93	1407	1041	1.35
Series IV	2175-1.2-H10-V9.5(2-leg)	4.93	1614	1034	1.56
	2175-1.2-H20-V19(2-leg)	4.93	1540	1034	1.49
	2175-1.2-H20-V24(2-leg)	4.93	1510	1034	1.46
	2175-1.2-H24-V19(2-leg)	4.93	1441	1034	1.39
	2175-1.2-H24-V24(2-leg)	4.93	1418	1034	1.37
	2175-1.2-H24-V38(4-leg)	4.93	1356	1034	1.31
	2175-1.2-H38-V38(4-leg)	4.93	1299	1034	1.26

6.4.3.2.2. Evaluation of analytical strength

The effects of web reinforcement spacings on the analytical strengths were evaluated by calculating the strength ratio of each specimen to its control specimen in the series. It should be noted that the control groups of Series I and Series II had a different f'_c from the rest numerical specimens, so the strength ratio was modified proportionally in consideration of f'_c . Therefore, the strength ratio η was, in general, given by

$$\eta = \left(\frac{P_{FEM}}{f'_c} \right) / \left(\frac{P_{FEM}}{f'_c} \right)_{\text{control}} \quad (6-1)$$

With the established evaluation criterion per Equation (6-1), the η -value was calculated for each of the specimens listed in Table 6-17. The analytical results for numerical specimens of 21 in. by 42 in. are presented in Figure 6-61. In the figure, a solid red line encloses the specimen complying with the current AASHTO LRFD's spacing requirements ($d/2$). In addition, a dashed red line encompasses specimens complying with the target relaxed spacing requirement ($d/4$). Different brightness of shading is used to make categorizations in the figure too. It can be seen from Figure

6-61(a) that there is no significant difference in strength ratio between the evaluated specimens and the control specimen for Series I. Relaxing either only the vertical spacing or both the vertical and horizontal spacings did not cause a noticeable reduction in strength for specimens of 21 in. by 42 in. with an $a/d = 1.85$. However, some reduction in strength appeared when the a/d ratio was 1.2, as seen in Figure 6-61(b). When relaxing the spacings in horizontal and vertical directions to $d/2$, the strength ratio can be as low as 0.88, as observed from Specimen 2142-1.2-H20-V19(2-leg). Specimens with an a/d ratio of 1.2 were affected more in terms of strength when the spacings were relaxed. The observation agrees with the experimental results in the current study, as introduced in Section 6.3.2.

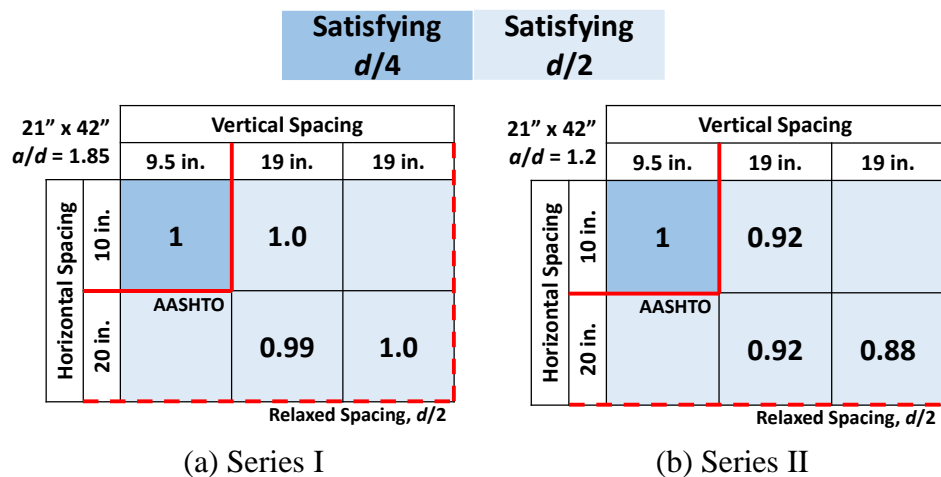
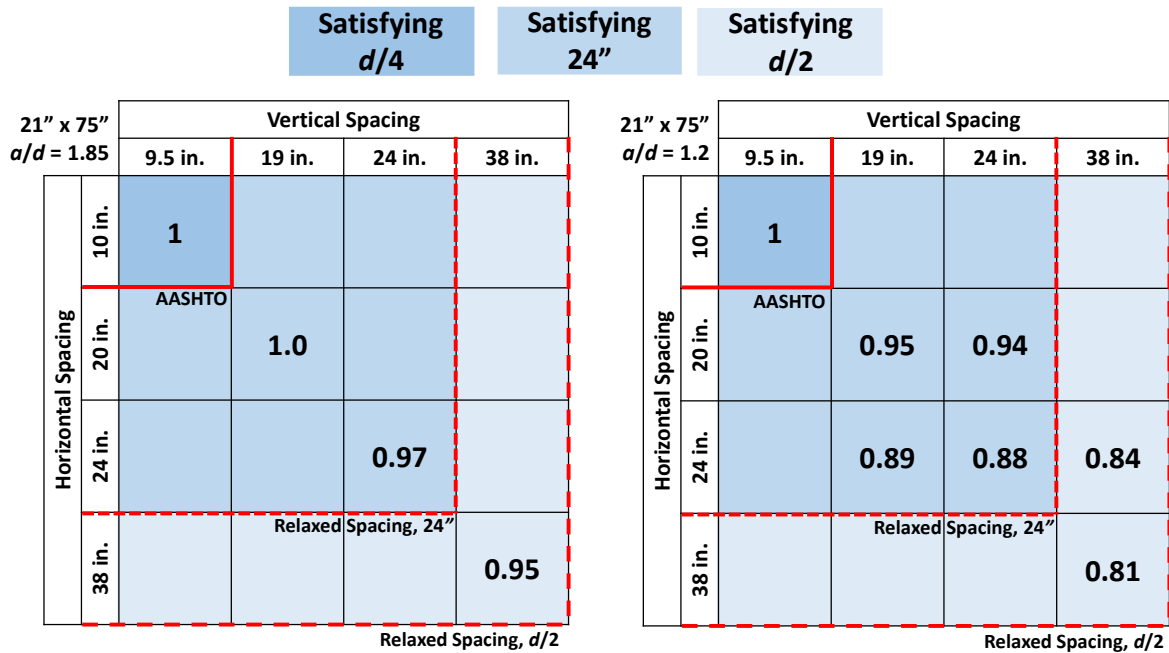


Figure 6-61 Strength ratio compared to control specimen for 21 in. by 42 in.

The same approach of evaluating the strength ratio was also conducted for numerical specimens in Series III and Series IV, and the results are shown in Figure 6-62. Similarly, solid red lines, dashed lines, and brightness of shading are used to categorize the numerical specimens satisfying different spacing criteria. In this case, one more criterion of complying with 24 in. is included because the limitation of 24 in. was smaller than $d/2$ and therefore controlled. A similar trend is observed from the figure that relaxing spacing requirements led to a reduction in strength. Indeed, the larger the spacings were relaxed, the more the reduction in strength was observed for both cross-sections. Specimens with an a/d ratio of 1.2 had more reduction in strength than specimens with an a/d ratio of 1.85. If considering all analyzed cases, the lowest strength ratio was 0.81 for Series IV and 0.95 for Series III. If considering a relaxed spacing criterion of 24 in. only, the lowest strength ratio was 0.88 and 0.97 for Series IV and Series III, respectively.



(a) Series III

(b) Series IV

Figure 6-62 Strength ratio comparing to control specimen for 21 in. by 75 in.

In addition, relaxing vertical spacing seemingly caused a smaller reduction in strength than relaxing horizontal spacing did. Numerical Specimen 2175-1.2-H20-V19(2-leg) had a strength ratio of 0.95, and the strength ratio reduced to 0.94 when the vertical spacing was relaxed to 24 in. However, the strength ratio reduced to 0.85 when the horizontal spacing was relaxed to 24 in. This phenomenon was not observed in Series I and Series II nor in the experimental program of this research project. Horizontal spacing requirements are plausibly more crucial for deep beams with a very deep effective depth.

6.4.3.2.3. Comparison between FEM and STM results

Although relaxing spacing requirements resulted in some strength reduction, the STM still generated conservative predictions compared to FEM for all numerical specimens. All analytical results generated by the STM and the FEM were plotted together, as shown in Figure 6-63. As STM does not consider web reinforcement spacing, all numerical specimens in a particular series had the same STM analytical strength, represented by a red line in the figure. It can be seen from the figure that all the FEM predictions in a series are higher than the STM predictions by a factor ranging from 1.19 to 1.56. In addition, the STM tended to be more conservative for the cross-section 21 in. by 75 in.

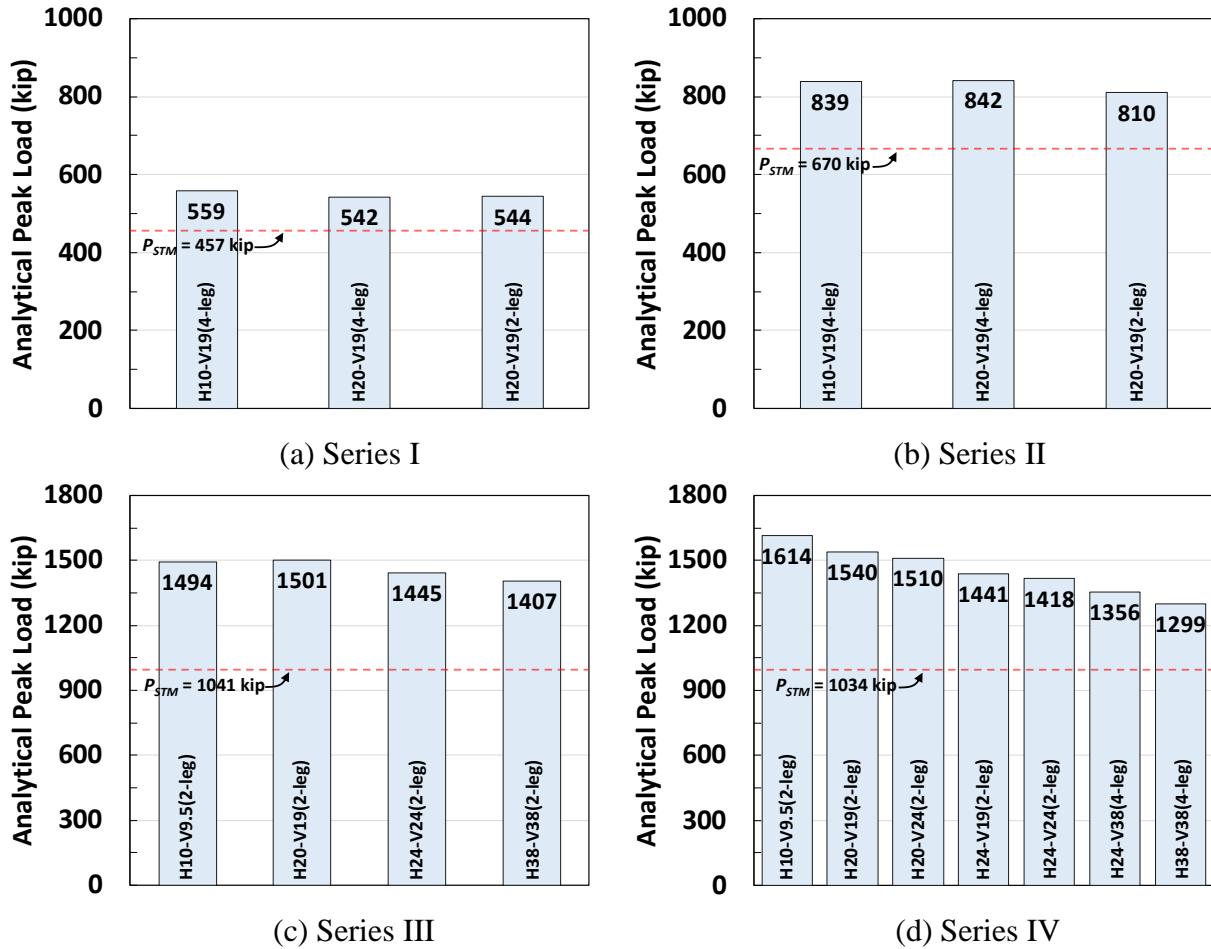


Figure 6-63 Strength compared to STM results

The analytical results boost the confidence in using the STM on deep beams with relaxed requirements for web reinforcement spacing. The STM always delivered conservative predictions when spacing requirements were relaxed to $d/2$ or 24 in or even further. Moreover, even though the limit of 24 in. was not enforced, the STM still gave conservative results.

Plotting the ratio of predictions by the FEM to predictions by the STM regarding a normalized spacing parameter, s_{hs_v}/d^2 shows a big picture, as shown in Figure 6-64. The parameter was coined for comparison of STM results and FEM results on the same basis. In the figure, a horizontal line separates conservative results from unconservative results. No unconservative results were derived for STM over a spectrum of the parameter between 0.02 to 0.3. This range covers cases satisfying current provisions ($s_{hs_v}/d^2 \leq 0.0625$), and the relaxed spacing requirement ($s_{hs_v}/d^2 \leq 0.25$). However, predictions by STM gradually have diminished conservatism while the parameter s_{hs_v}/d^2 increases. Nevertheless, this phenomenon is not as evident given the effective depth being 38.6 in. (Series I and II). It is implied that the STM can be refined if web reinforcement spacing is considered. The FEM provided insights into future research on the refinement of STM in terms of the normalized spacing parameter. It is suggested that more experimental studies be conducted regarding the effects of web reinforcement spacings on strength efficiency factors in the STM.

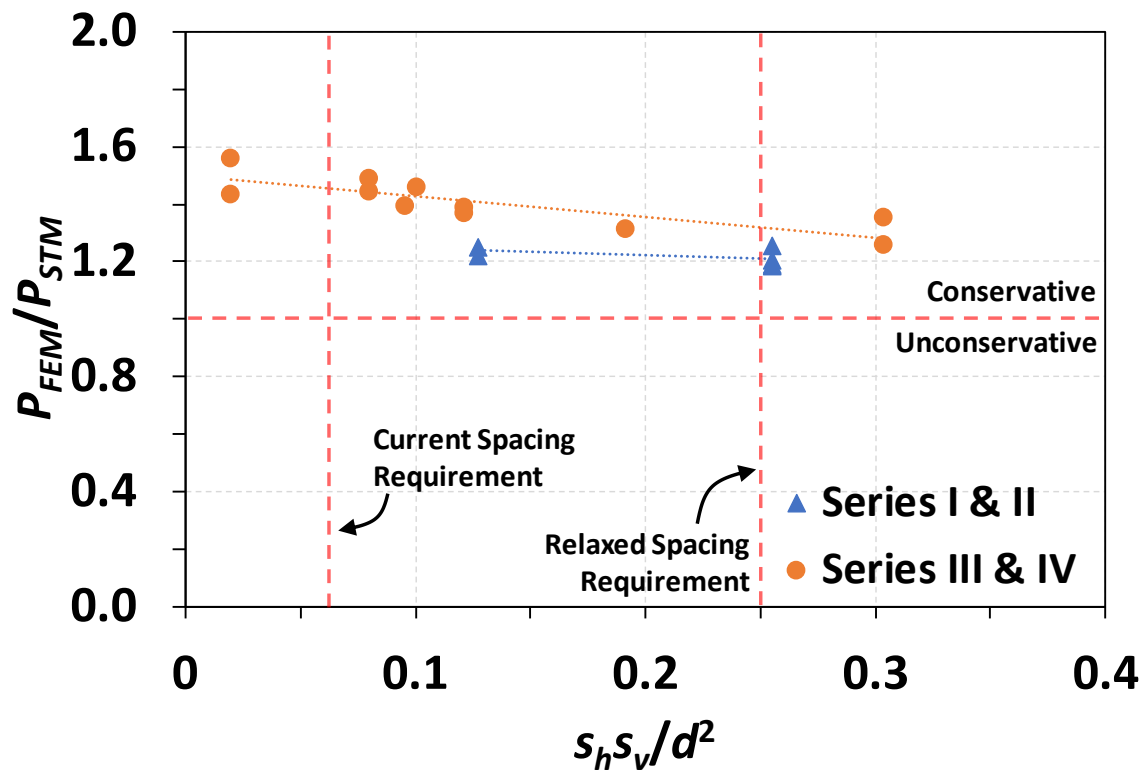


Figure 6-64 Evaluation of strength generated from FEM and STM vs. spacing requirements

6.5. Summary

This chapter highlights the project objective and achievements. Along with conclusions and observations made through structural testing, recommendations for design with the STM per AASHTO LRFD are also presented.

6.5.1. Summary of Experimental Program and FEA

Project 0-7039 Task 5 examines whether crack control reinforcement can be relaxed from the current AASHTO LRFD strut-and-tie specification of $d/4$ or 12 in. to $d/2$ or 24 in. Furthering the research conducted at Ferguson Structural Laboratory under Project 0-5253, Task 5 expands the current knowledge on strut-and-tie design considerations. A total of three large-scale reinforced concrete deep beams were designed and fabricated. Out of these three deep beams, six structural tests were completed. These deep beams had depths ranging from 23 to 42 in. with D-regions designed to fail in shear. These specimens were replicated from specimens tested in Project 0-5253 with the only variation being in the crack control spacing. After analysis of the experimental results, the following conclusions can be made:

- While relaxing the spacing requirement of vertical crack control reinforcement poses a slight reduction in normalized shear strength, relaxing the spacing requirement of horizontal crack control reinforcement poses little to no detriment.
- Current STM design provisions in AASHTO LRFD remain conservative and appropriate in estimating structural capacities even when the requirement of crack control spacing is relaxed to $d/4$ or 24 in.
- For shallower strut angles, vertical crack control reinforcement plays a more critical role in preventing premature failure of the strut than horizontal crack control reinforcement.
- Relaxing crack control spacing independently for either the vertical or horizontal directions will not impact serviceability limits under service loads recommended by AASHTO LRFD.
- After service loads, relaxing vertical crack control reinforcement will result in wider diagonal crack widths along the strut at lower loads compared to relaxing horizontal crack control spacing. Relaxed crack control spacing does alter the cracking patterns to behave in a less discontinuous manner.
- Transverse strain along the centerline of the strut is exceptionally larger at the mid-section of the strut compared to all other regions along the strut at 95% ultimate capacity of the specimen.

- At 95% capacity of the specimen, the vertical strain is larger than the horizontal strain at the mid-section of the strut suggesting the vertical crack control reinforcement plays a significant role.
- The constructed FE models successfully captured the behavior of the benchmark specimens, which validated the predictive ability of the modeling technique. Further FE parametric analysis generally echoes the experimental results that relaxing the spacing requirements results in a somewhat reduction in shear strength. Nevertheless, the STM still gives conservative predictions, supporting using the STM on deep beams based on the relaxed spacing requirements.
- The FE analysis discloses that web reinforcement spacings affect the shear strength of deep beams. However, the current STM provisions cannot appropriately reflect the phenomenon, implying that refinement will be needed according to the web reinforcement spacings.

6.5.2. Suggested modification to AASHTO LRFD design provisions and Future Studies

Based on the experimental findings, it is suggested that AASHTO LRFD consider relaxing the crack control spacing requirement of $d/4$ or 12 in. to $d/2$ or 24 in. while making no modifications to strut-and-tie design provisions for nodal or other element capacities. This would allow ease in detailing and constructability. It is also suggested that AASHTO LRFD include commentary regarding the observation of vertical crack control reinforcement being more effective with shallower strut angles, while horizontal crack control reinforcement would be more effective with narrower strut angles.

Further study is needed to observe the capacity and serviceability effects if both vertical and horizontal crack control reinforcement can be relaxed at the same time. It is assumed that this should be possible; however, without experimental data or a finite element parametric study, these conclusions cannot be made certain through this experimental program. Refinement of the STM will also be needed according to the web reinforcement spacings.

Chapter 7. Conclusions

In conclusion, the strut-and-tie method (STM) is a simple, rational, and conservative method for designing D-regions in reinforced concrete members. Its development dates back over a century and has been continuously refined. The STM has evolved into a reliable method that is widely used in practice. The recent research efforts by the Texas Department of Transportation (TxDOT) have further improved the accuracy and conservativeness of the STM, resulting in its adoption in the AASHTO LRFD Bridge Design Specifications. However, there are still areas that require further research and guidance to optimize the use of the STM in common design scenarios. These include the behavior of nodes with three orthogonal directions of tension ties (tri-axial tension) in drilled shaft footings, the use of curved-bar nodes in closing knee joints, the consideration of passive confinement reinforcement in nodal zones, and the maximum spacing of crack control reinforcement. Addressing these knowledge gaps would enhance the applicability of the STM and provide more efficient and cost-effective design solutions for reinforced concrete members.

Bridging those knowledge gaps for the STM required a thorough review of past studies and design codes relevant to its application. The research team presented an extensive literature review. Based on the review, several primary findings and research needs were identified. For instance, while the anchorage of drilled shaft reinforcement in a drilled shaft footing is important, there is a lack of experimental data on the use of hooked reinforcing bars or mechanical terminators to assist with the development of the bar stress when the bars are anchored with tri-axial tensions. Similarly, curved-bar nodes have been acknowledged in AASHTO LRFD and have been incorporated in ACI 318-19; however, lacking sufficient experimental data, especially for large reinforcing bars, hinders the applicability. Further, the effect of confining reinforcement in nodal zones needs more attention, as there are currently no specific design guidelines or recommendations for this practice. Last but not least, the spacing of crack control reinforcement across struts is a critical consideration, but the " $d/4$ limit" in the STM provisions is not well-based on experimental data and requires further research. Overall, the review highlighted the need for additional experimental data to inform design codes and practices related to these key areas.

Chapter 3 details the four large-scale structural tests conducted by the research team to investigate the anchorage behavior of drilled shaft reinforcement under tri-axial tension in the 3D STM. The tests were designed with different anchorage types and skin reinforcement ratios, and the response of the drilled shaft reinforcement was measured through linear potentiometers and strain gauges. The results showed that all drilled shaft reinforcing bars yielded during the tests, and the loads at yielding were comparable in all tests regardless of the tested variables. The stress profiles and bar slips indicated that the anchorage response of the drilled shaft reinforcement was not influenced by the anchorage types and skin reinforcement ratios. The design recommendation of Project 0-6953 regarding anchorage checks for the drilled shaft reinforcement is still valid and found to be conservative. However, the limited number of tests conducted suggests the need for future experimental and numerical studies to verify the proposal and avoid overly conservative drilled

shaft anchorage requirements in actual designs. Overall, the results of Chapter 3 provide valuable insights into the behavior of drilled shaft reinforcement under tri-axial tension and the validity of the design recommendation.

In Chapter 4, nine portal frame specimens with two closing knee joints were tested to investigate the effect of the bend radius at the outside of the frame corner. The size of the bar bend was found to be critical, as a standard bend radius per current codes and specifications could lead to compromised joint shear capacity. Enlarged bend radii per the given equation are needed to develop load plateauing and ductility. The angle of the diagonal strut angle other than 45 degrees slightly reduces the joint capacity, but the bend radius still plays a more critical role in affecting the behavior. Two layers of reinforcement in closing knee joints also require enlarged bend radii to avoid compromised strength. Using bend radii per the given equation contributes to controlling crack widths in the joint, even without crack control reinforcement. Being able to account for the bend radius as a curved-bar node and the diagonal strut angle, the STM accurately and conservatively predicts the peak load and the failure mode of closing knee joint, unlike current sectional methods for joint shear capacity in AASHTO LRFD and ACI 318-19, which likely lead to unconservative predictions. The nonlinear finite element analysis software ATENA 3D captures the load-displacement behavior and peak load using measured material properties. Design recommendations and a design example were introduced based on the test results and data interpretation.

In Chapter 5, the effect of nodal zone confinement on nodal strength was investigated by designing and testing three deep beams (six tests), with and without additional confining reinforcement. The test specimens had a similar structural configuration and shear span, and two confinement patterns were tested and compared to the control specimen. The researchers drew several observations and conclusions, including that confining the CCC and CCT nodal zones increases nodal strength, doubly confined struts have better behavior than singly confined or non-confined struts, and effective confining reinforcement of 1.0% in both directions can augment the CCC nodal strength by 10% for doubly confined struts. Limitations were identified, including the shear-to-depth ratio and the interaction between crosstie confinement and concrete confinement. Further experimental studies are needed to verify some of the speculations.

Chapter 6 presents the experimental program and finite element analysis conducted to examine whether crack control reinforcement can be relaxed from the current AASHTO LRFD strut-and-tie specification of $d/4$ or 12 in. to $d/2$ or 24 in. The chapter presents conclusions and observations made through structural testing and suggests modifications to AASHTO LRFD design provisions. It was found that relaxing the spacing limits potentially leads to a slight reduction in the shear capacity. Nevertheless, the STM can still make conservative predictions despite the relaxation. It is recommended that AASHTO LRFD consider relaxing the crack control spacing requirement of $d/4$ or 12 in. to $d/2$ or 24 in. while making no modifications to strut-and-tie design provisions for nodal or other element capacities. It is also recommended further study to observe the capacity and

serviceability effects if both vertical and horizontal crack control reinforcement can be relaxed at the same time and refinement of the STM according to web reinforcement spacings.

Moving forward, additional research will be needed to build on the findings of this study and further refine design provisions for the STM. This could include additional experimental testing, parametric studies using finite element analysis, and field inspections of real-world RC deep members. By refining our understanding of RC deep members and improving design provisions accordingly, we can ensure that these important structural elements can be safely and effectively used in a wide range of applications.

References

- AASHTO LRFD Bridge Design Specifications, Ninth Edition, American Association of State Highway and Transportation Officials, Washington, DC, 2020.
- ACI 318-02, Building Code Requirements for Structural Concrete (ACI 318-02) and Commentary (318R-02), American Concrete Institute, Farmington Hills, MI, 2002, 443 pp
- ACI Committee 224, “Control of Cracking in Concrete Structures” (ACI 224R-01), *ACI Manual of Concrete Practice*, American Concrete Institute, Farmington Hills, MI, 2002.
- ACI Committee 318-19, Building Code Requirements for Reinforced Concrete (ACI 318-19) and Commentary (318-19), American Concrete Institute, Farmington Hills, MI, 2019, 473 pp
- Adebar P, and Zhou L, Design of Deep Pile Caps by Strut-and-tie Models, *ACI Structural Journal*, 93.4, 1996, pp. 437-448.
- Adebar P, Discussion of an Evaluation of Pile Cap Design Methods in Accordance with the Canadian Design Standards, *Canadian Journal of Civil Engineering* 31.6, 2004, pp. 1123-1126.
- Adebar, P., and Zhou, Z., “Bearing Strength of Compressive Struts Confined by Plain Concrete,” *ACI Structural Journal*, V. 90, No. 5, 1993, pp. 534-541
- Adebar, P., and Zhou, Z., “Design of Deep Pile Caps by Strut-and-Tie Models,” *ACI Structural Journal*, V. 93, No. 4, 1996, pp. 437-448.
- Adebar, P., Kuchma, D., and Collins, M., “Strut-and-Tie Models for the Design of Pile Caps: An Experimental Study,” *ACI Structural Journal*, V. 87, No. 1, 1990, pp. 81-92.
- Anderson N. S, and Ramirez J. A, “Detailing of Stirrup Reinforcement,” *ACI Structural Journal*, Vol. 86, No. 5, Sept-Oct 1989, pp. 507-515
- Angelakos D, Bantz E. C, and Collins M.P, Effect of Concrete Strength and Minimum Stirrups on Shear Strength of Large Members, *ACI Structural Journal*, Vol. 98, No. 3, May-June 2001, pp. 290-300.
- Araujo J M, Design of Rigid Pile Caps Through an Iterative Strut-and-Tie Model, *Journal of Advanced Concrete Technology*, Vol 14, No.14, Japan Concrete Institution, 2016, pp. 397-407
- AS 3600, Concrete Structures, Standards Association of Australia, 1994.
- Asin M, The Behavior of Reinforced Concrete Continuous Deep Beams, Delft University Press, Delft, Netherlands, 2000.
- ASTM A 615/A 615M - 08, *Standard Specification for Deformed and Plain Carbon-Steel Bars for Concrete Reinforcement*, American Society for Testing and Materials, West Conshohocken, PA, March 2008.
- ASTM A370-21, Standard Test Methods and Definitions for Mechanical Testing of Steel Products, ASTM International, West Conshohocken, PA, 2021, www.astm.org

- ASTM A615 / A615M-18e1, Standard Specification for Deformed and Plain Carbon-Steel Bars for Concrete Reinforcement, ASTM International, West Conshohocken, PA, 2018, www.astm.org
- ASTM C 143/C 143M - 08, *Standard Test Method for the Slump of Hydraulic-Cement Concrete*, American Society for Testing and Materials, West Conshohocken, PA, March 2008.
- ASTM C 192/C 192M - 19, *Standard Practice for Making and Curing Concrete Test Specimens in the Laboratory*, American Society for Testing and Materials, West Conshohocken, PA, December 2018.
- ASTM C 39/C 39M - 05, *Standard Test Method for Compressive Strength of Cylindrical Concrete Specimens*, American Society for Testing and Materials, West Conshohocken, PA, November 2005.
- ASTM C 42/C 42M - 20, *Obtaining and Testing Drilled Cores and Sawed Beams of Concrete*, American Society for Testing and Materials, West Conshohocken, PA, April 2020.
- ASTM C 469/C 469M - 22, *Standard Test Method for Static Modulus of Elasticity and Poisson's Ratio of Concrete in Compression*, American Society for Testing and Materials, West Conshohocken, PA, 2022.
- ASTM C 496/C 496M - 17, *Standard Test Method for Splitting Strength of Cylindrical Concrete Specimens*, American Society for Testing and Materials, West Conshohocken, PA, October 2017.
- ASTM C150 / C150M-19a, Standard Specification for Portland Cement, ASTM International, West Conshohocken, PA, 2019, www.astm.org
- ASTM C31 / C31M-19, Standard Practice for Making and Curing Concrete Test Specimens in the Field, ASTM International, West Conshohocken, PA, 2019, www.astm.org
- ASTM C39 / C39M-18, Standard Test Method for Compressive Strength of Cylindrical Concrete Specimens, ASTM International, West Conshohocken, PA, 2018, www.astm.org
- Batchelor D V B, and Campbell T I., Effectiveness Factor for Shear in Concrete Beams, *Journal of Structural Engineering*, V. 112, No. 6, 1986, pp. 1464-1477
- Bazant Z P, and Xiang Y, Size Effect in Compression Failure: Splitting Crack Bond Propagation, *Journal of Structural Engineering*, ASCE, 2 (162), 1997, pp. 162-172
- Bazant Z.P, and Planas J, *Fracture and Size Effect in Concrete and Other Quasi Brittle Materials*, CRC Press, New York, NY, USA, 1998.
- Bircher D. B, Tuchscherer R G, Huizinga M R, and Bayrak O, "Minimum Web Reinforcement in Deep Beams", *ACI Structural Journal*, Vol. 110, No. 2, Mar-Apr 2013, pp. 297-306.
- Bircher D, Tuchscherer R, Huizinga M, Bayrak O, Wood S, and Jirsa J, *Strength and Serviceability Design of reinforced concrete deep beams*, Center of Transportation Research, the University of Texas at Austin, Austin, TX, 2009, 379 pp.
- Bircher, David, Robin Tuchscherer, Matt Huizinga, Oguzhan Bayrak, Sharon Wood, and James Jirsa, *Strength and Serviceability Design of Reinforced Concrete Deep Beams*, Rep. No. 0-5253-1, Center for Transportation Research, The University of Texas at Austin, 2009

- Blanton J. J, and Rodriquez M, Behavior of Connections and Floors Diaphragms in Seismic-Resisting Precast Concrete Buildings, *PCI Journal*, Vol. 50, No. 2, Mar-Apr 2005, pp. 56-75.
- Blevot S, and Fremy R, Smelled sur Pieux, *Annales de l'institut Technique de Batiment et de travaux publics*, Vol. 20, No. 230, 1967, pp. 223-295
- Botros A, Klein G, Lucier G, Rizkalla S, and Zia P, Dapped Ends of Prestressed Concrete Thin-Stemmed Members: Part 1, Experimental Testing and Behavior, *PCI Journal*, Vol. 62, No. 2, 2017, pp. 61-82.
- CAC: Concrete Design Handbook, 3rd Edition, Ottawa, Cement Association of Canada, 2005
- Canadian Standard Association, Design of Concrete Structures, CSA-A23.3-04, Mississauga, ON, Canada, 2004.
- Canadian Standards Association, *Canadian Highway Bridge Design Code CSA-S6-06*, Canadian Standards Association, Mississauga, Ontario, Canada, 2006.
- CEB-FIP, CEB-FIP Model Code 1990, Thomas Telford Services, Ltd., London, UK, 1993.
- CEN EN 1992-1-1, Eurocode 2: Design of Concrete Structures. Part 1-1: General Rules and Rules for Buildings, European Committee for Standardization, Brussels, Belgium, 2004.
- Červenka, V., Jendele, L., and Červenka, J. "ATENA Program Documentation Part 1: Theory," Prague, Czech Republic, Červenka Consulting s.r.o., 2018, 319 pp.
- Chen G, Plastic Analysis of Shear in Beams, Deep Beams, and Corbals, Rep. No. R237, Dept. Of Structural Engineering, Technical University of Denmark, Copenhagen, 1988.
- Clarke, J., "Behavior and Design of Pile Caps with Four Piles," *Technical Report* No. 42.489, Cement and Concrete Association, Wexham Springs, 1973, 19 pp.
- Collins M P, and Michell D, Rational Approach to Shear Design, The 1984 Canadian Code Provisions, *ACI Structural Journal*, V. 83, No. 6, 1986, pp. 925-933.
- Collins M.P, and Kuchma D.K., How Safe Our Large, Lightly Reinforced Beams, Slabs, and Footings? *ACI Structural Journal*, Vol. 96, No. 4, July-Aug 1999, pp. 482-490.
- CRSI Handbook, Concrete Reinforcing Steel Institute, Chicago, 1992
- CSA A233-14 Specifications, Canadian Standard Association, Canada, 2014, 295 pp
- Design Code for Concrete Structures, GB50010-2010, China Construction Industry Press, Beijing, China, 2010.
- Deutsch G P, and Walker D N O, Pile Caps, Civil Engineering Research Project, University of Melbourne, 1963, pp 75.
- Febres C. G, Montesano G. P, and Wight J. K, "Strength of Struts in Deep Concrete Members Designed Using Strut-and-Tie Method," *ACI Structural Journal*, Vol. 103, No. 4, July-August 2006, pp. 577-586
- fib, fib Model Code for Concrete Structures 2010, International Federation of Concrete Wilhelm Ernst & Sohn, Germany, 2013

- Fong I, Chen J, and Hang L, Shear Behavior of High Strength Concrete Deep Beams, Proc. 5th East Asian-Pacific Conf. on Structural Engineering and Construction, Gold Coast, Qld, 1995, pp. 1747-1752.
- Foster S J, and Gilbert R I, The Design of Non-Flexural Members with Normal and high Strength Concrete, *ACI Structural Journal*, V. 93, No. 1, 1996, pp. 3-10
- Foster S J, and Malik A R, Evaluation of Efficiency Factor Models used in Strut-and-Tie Modeling of Non-Flexural Members, *Journal of Structural Engineering*, May 2002, pp. 569-77.
- Foster S J, Structural Behavior of Reinforced Concrete Deep Beams, Doctorate Thesis, University of New South Wales, 1992.
- Frank, J., Vecchio., Michael, P., Collins. The modified compression-field theory for reinforced concrete elements subjected to shear. *ACI Journal*, Vol. 83, No. 2, pp. 219-231. doi: 10.14359/10416
- Frantz G. C, and Breen J. E, "Cracking on the Side Faces of Large Reinforced Concrete Beams," *ACI Structural Journal*, 1980, pp. 307-313
- Furuuchi H, Takahashi Y, Ueda T, and Kakuta Y, Effective Width for Shear Failure of RC Deep Slabs, *Transactions of the Japan Concrete Institute*, V. 20, 1998, pp. 209-216.
- Geever I, and Devdas M, Strength of Reinforced Concrete Pier Caps – Experimental validation of Strut-and-Tie Method, , *ACI Structural Journal*, Vol 116, No.1, Jan. 2019, pp. 261-273
- Hawkins N M, "Bearing Strength of Concrete Banded through Rigid Plates, Magazine of Concrete Research, London, Vol. 20, No. 32, 1968, pp. 31-40.
- Ingham, J., "Seismic Performance of Bridge Knee Joints," PhD dissertation, University of California, San Diego, La Jolla, CA, 1995,
- Ismail K S, Guadagnin M, and Pilakoutos K, Shear Behavior of Reinforced Concrete Deep Beams, *ASCE Structural Journal*, Vol 114, No.1, 2017, pp. 87-99
- Ismail K S, Guadagnin M, and Pilakoutos K, Strut-and-Tie Modeling of Reinforced Concrete Deep Beams, *Journal of Structural Engineering*, ASCE, 2017, pp. 1-13
- Joint ACI-ASCE Committee 326, Shear and diagonal tension, *ACI Journal*, Proc.Vol. 59, No. 1-3, 1962, pp. 1-30, 227-344 and 352-396.
- Klein G, Botros A, Andrew B, and Holloway K, Dapped Ends of Prestressed Concrete Thin-Stemmed Members: Part 2, Design, *PCI Journal*, Mar-Apr 2017, pp. 83-99.
- Klein G. J, Curved-Bar Nodes, A Detailing Tool for Strut-and-Tie Models, *Concrete International Journal*, Sept. 2008, pp. 42-47.
- Luo, Y. H.; Durrani, A. J.; Bai, S.; and Yuan, J., "Study of Reinforcing Detail of Tension Bars in Frame Corner Connections," *ACI Structural Journal*, V. 91, No. 4, July-Aug. 1994, pp. 486-496.
- MacGregor J C, Reinforced Concrete – Mechanics and Design, 3th Edition, Practice Halls, Englewood Cliffs, N J, 1997.

- Mander, J. B., et al., Theoretical Stress-Strain Model for Confined Concrete, *Journal of Structural Engineering*, Vol. 114, No. 8, 1988, pp. 1804–1826, [https://doi.org/10.1061/\(asce\)0733-9445\(1988\)114:8\(1804\)](https://doi.org/10.1061/(asce)0733-9445(1988)114:8(1804)).
- Marti P, Basic Tools of Reinforced Concrete Beams Design, *ACI Structural Journal*, V. 82, No. 1, 1985, pp. 46-56.
- Martinez G. A, Beiler K. S, Ghiami A. R, Polo G. A, Shinn R. L, Hrynyk D. T, and Bayrak O, Testing and Analysis of Two Deep Beams Designed Using Strut-and-Tie Method, *ACI Structural Journal*, Vol. 114, No. 6, Nov-Dec 2017, pp. 1531-1542.
- Matlock A H, Curved-Bar Nodes, Strut-and-Tie Models for dapped-End Beams, *Concrete International Journal*, Vol. 24, No. 6, 2012, pp. 35-40.
- Matlock A. M, and Theryo T. S, Strength of Prestressed Concrete Members with Dapped ends, *PCI Journal*, Vol. 31, No. 5, Sept-Oct 1986, pp. 58-75.
- Moody K.G, Wiest I. M, Elstner R. C, and Hognestad E, Shear Strength of Reinforced Concrete Beams, Part 1-Test of Simple Beams, *ACI Journal, Proc.* Vol. 51, No. 4, 1954, pp. 317-333.
- Morsch, E., "Der Eisenbetonbau, seine Theorie and Anwendung" (Reinforced Concrete, Theory and Application), Verlag Konrad Wittwer, Stuttgart, 1912.
- Nielsen M P, Braettrup M W, Jensen B C, and Bach F, Concrete Plasticity, Beam Shear in Joints-Punching Shear, Special Publication, Danish Society for Structural Science and Engineering, Technical University of Denmark, Lyngby, 129.
- Nielsen M. P, Limit Analysis and concrete Plasticity, CRS Press, LLC, 1999, 936 pp.
- Nilsson I. H. F, and Losberg A, Reinforced Concrete Corners and Joints Subjected to Bending Moment, *Journal of the Structural Division, ASCE*, Vol. 102, No. ST6, June 1976, pp. 1229-1255.
- Ostlund L, The Influence of Bending Radius and Concrete Cover for Deformed Bars on the Risk of Splitting Failure in Reinforced Concrete Structures, The Royal Institute of Technology, Stockholm, Sweden, 1983, 92 pp.
- Park J, Kushma D, and Souza R, Strength Predictions of Pile Caps by a Strut-and-tie Model Approach, *Canadian Journal of Civil Engineering* 35.12, 2008, pp. 1399-1413.
- Paulay T, and Priestley M, Seismic Design of Reinforced Concrete and Masonry Buildings, New York, John Wiley and Sons, 1992, 768 pp.
- PCI Industry Handbook Committee, 2010, *PCI Design Handbook, Precast and Prestressed Concrete*, MNL-120, Seventh Edition, Chicago, IL, PCI
- Ritter, W., "Die Bauweise Hennebique"(The Hennebique System), *Schweizerische Bauzeitung*, Bd. XXXIII, No. 7, January 1899.
- Ricketts D R, and MacGregor J C, Ultimate Behavior of Continuous Deep Reinforced Concrete Beams, *Structural Engineering Rep*, No. 126, Dept. Of Civil Eng. University of Alberta, Edmonton, Canada, 1995.
- Schlaich J, Scafer K, and Jennewein M, "Towards a Consistent Design of Structural Concrete," *PCI Journal Special Report*, Vol. 32, No. 3, 1987, pp. 75-150.

- Schlaich J, Scafer K, and Jennewein M, Tests on Reinforced Concrete Deep Beams, ACI Journal, 83.4, 1986, pp. 614-623.
- Smith K N, and Vantsiohi A S, Shear Strength of Deep Beams, ACI Structural Journal, V. 79, No. 22, 1982, pp. 201 – 213
- Souza R, Kushma D, Park J, and Bittencourt T, Adaptable Strut-and-tie Models for Design and Verification of Four Pile Caps, ACI Structural Journal, 106.2, 2009, pp. 142-150.
- Standard Specification for Design and Construction of Concrete Structures, JSCE, 1986
- Stroband, J., and Kolpa, J. J., “The Behaviour of Reinforced Concrete Column-to-Beam Joints. Part 1: Corner Joints Subjected to Negative Moments,” Report 5-83-9, Stevin Laboratory, Delft University of Technology, Delft, the Netherlands, 1983, 105 pp.
- Subedi N K, Reinforced Concrete Two Span Continuous Deep Beams, Proc. Inst. of Civil Engineering and Building, 1998, pp. 12-25
- Subedi N K, Wordy A E, and Kubota N, Reinforced Concrete Deep Beams – some Test Results, Mag. Concrete Research, Vol. 38, No. 137, 1996, pp. 206-219
- Swann R. A, Flexural Strength of Corners of Reinforced Concrete Portal Frames, Technical Report TRA/434, Cement and Concrete Association, London, November 1969, 14 pp.
- Tan K. H, Kong F. K, Teng S, and Wing L. W, Effect of Web Reinforcement on High Strength Concrete Deep Beams, ACI Structural Journal, Vol. 94, No. 5, Sept-Oct 1997, pp. 572-581
- The European Standard EN 1992-1-1, 2004, Design of Concrete Structures, British Standard Institutions, Brussels, Belgium, 2004.
- Thompson M K, Jirsa J O, and Breen J E, CCT Nodes Anchored by Headed Bars-Part 2: Capacity of Nodes, ACI Structural Journal, Vol. 102, No. 6, Nov-Dec. 2005, pp. 65 – 73
- Thompson M K, Young M L, Jirsa J O, Breen J E, and Klinger R E, Anchored by Headed Reinforcement in CCT Nodes, Center for Transportation Research Report 1855-2, Australia, 2002, 160 pp
- Thompson, M. K., Ziehl, M. J., Jirsa, J. O., & Breen, J. E., CCT nodes anchored by headed bars-part 1: Behavior of nodes. ACI Structural Journal, Vol. 102, No.6 , 2005, pp. 808-815
- Tjhin, Tjen N., and Daniel A. Kuchma. “Example 1b: Alternative design for the nonslender beam (deep beam).” SP-208 Examples for the Design of Structural Concrete with Strut-and-Tie Models. Ed. Karl-Heinz Reineck. Farmington Hills, Michigan: American Concrete Institute, 2002, 250 pp
- Tuchscherer R G, Birrcher C. S, Williams C S, Deschener D. J, and Bayrak O, Evaluation of Existing Strut-And-Tie Methods and recommended Improvements, ACI Structural Journal, Vol. 111, No. 6, Nov-Dec 2014, pp. 1451-1460
- Tuchscherer R, Birches D, Huizinga M, and Bayrak O., Distribution of Stirrups Across Web of Deep Beams, ACI Structural Journal, Vol. 108, No. 1, Jan-Feb 2011, pp. 108-115
- Tuchscherer R, Birrcher D, Huizinga M, and Bayrak O, “Strength and Serviceability Design of Reinforced Concrete Deep Beams,” Report No. 0-5253-1, Center for Transportation Research, University of Texas, Austin, Texas, December 2008

- Tuchscherer R, Birrcher D, Huizinga M, and Bayrak O., “Distribution of Stirrups Across Web of Deep Beams,” *ACI Structural Journal*, Vol. 108, No. 1, Jan-Feb 2011, pp. 108-115
- Tuchscherer R, Birrcher D, Williams C, Deschenes D. J, and Bayrak O, “Evaluation of Existing Strut-And-Tie Methods and recommended Improvements,” *ACI Structural Journal*, Vol. 111, No. 6, Nov-Dec 2014, pp. 1451-1460
- Tuchscherer, R, Birrcher, D., Huizinga, M., and Bayrak, O, Confinement of Deep Beam Nodal Regions, *ACI Structural Journal*, V. 107, No. 6, Nov-Dec 2010, pp. 534-541
- Vecchio F J, and Collins M P, Compression Response of Cracked Reinforced concrete, *Journal of Structural Engineering*, V. 119, No. 2, 1993, pp. 3590-3610.
- Walraven J, and Lehwalter N, Size Effects in Short Beams Loaded in Shear, *ACI Structural Journal*, Vol. 91, No. 5, 1994, 585-594
- Wang, H.-C., “Behavior and Design of Concrete Frame Corners: Strut-and-Tie Method Approach,” PhD Dissertation, Purdue University, West Lafayette, IN, Dec. 2020, 336 pp.
- Wang, H.-C.; Williams, C.S.; and Klein, G.J., “Effect of Bend Radius of Reinforcing Bars on Knee Joints under Closing Moments,” *ACI Structural Journal*, V. 117, No. 5, Sept. 2020, pp. 315-326.
- Wang, H.-C.; Williams, C.S.; and Klein, G.J., “Effect of Reinforcement Layers, Side Cover, and Bond Stress on Curved-Bar Nodes” *ACI Structural Journal*, V. 119, No. 3, May 2022, pp. 277-290
- Warwick W B, and Foster S J, Investigation into the Efficiency Factor used in Non-Flexural Reinforced Concrete Design, UNICIV Rep, No. R-320, School of Civil Eng., University of New South Wales, Kensington, Sydney, Australia, 1993.
- Widianto, and Bayrak O, Example 11: Deep Pile Caps with Tension Piles, Sp-273 further Examples for the Design of Structural Concrete with Strut-and-tie Models, Ed. Karl-Heinz Reineck and Lawrence C. Novak. Farmington Hills, Michigan, ACI, 2011, 288 pp.
- Williams C, Deschenes D, and Bayrak O, Strut-and-Tie Model Design Examples for Bridges of reinforced concrete deep beams, Center of Transportation Research, the University of Texas at Austin, Austin, TX, 2012, 258 pp.
- Windisch A, Souza R, Kushma D, Park J, and Bittencourt T, Discussion of Adaptable Strut-and-tie Models for Design and Verification of Four Pile Caps, *ACI Structural Journal*, 107.1, 2010, pp. 119-120.
- Yang K. H, and Achour A. F, Strut-and tie Model Based on Crack Band Theory for Deep Beams, *J. Struct. Eng*, Vol. 12, 2010, pp. 1-33.
- Yi Y, Kim H, Boehm R, Webb Z, Choi J, Wang H.-C., Murcia-Delso J, Hrynyk T, and Bayrak O, “3D Strut-and-Tie Modeling for Design of Drilled Shaft Footings,” Report No. 0-6953-R1, Center for Transportation Research, University of Texas, Austin, Texas, December 2008.
- Yoon Y.S., Cook W.D, and Mitchell D., Minimum Shear Reinforcement in Normal, Medium, and High-Strength Concrete Beams, *ACI Structural Journal*, Vol. 93, S54, Sept. – Oct. 1996, pp. 576-584.

- Yung Y. M, and Ramirez J. A, Strength of Struts and nodes in strut-and-tie model, Journal of Structural Engineer, ASCE, Vol. 122, No. 1, 1996, pp. 20-29
- Zaborac J, Choi J, Bayrak O. Assessment of deep beams with inadequate web reinforcement using strut-and-tie models. Engineering Structures. 2020 Sept. 1;218:110832.
- Zaborac J and Bayrak O. Unified approach for reinforcement development length using the partly cracked elastic stage for bond strength. Engineering Structures. 2022 May 2022 10.1002/suco.202200117
- Zhang J.H, Li S.S, Xie W, and Gue Y.D, “Experimental Study on Shear Capacity of High Strength Reinforcement Concrete Deep Beams with Small-Depth Ratio,” *Materials* 2020, Vol. 13, No. 1218, pp. 1-19.

Appendix A. Intermediate Results of Strut-and-Tie Models of Test Portal Specimens

A-1 General Sizing Method

AASHTO parameters

Specimen ID	P_{STM} (kip)	BC (kip)	AC (kip)	CC' (kip)	BB' (kip)	BA (kip)	Failure Mode
A-R6-45	306	490	466	647	341	352	Curved-bar failure
A-R11-45	500	865	814	1080	579	642	Flexural Failure
A-R9-45	368	606	578	779	411	446	Curved-bar failure
B-R6-30	220	526	515	466	246	465	Curved-bar failure
B-R11-30	272	707	671	623	351	614	Flexural Failure
C-R6-60	194	451	440	411	217	395	Curved-bar failure
C-R11-60	298	796	782	630	332	723	Curved-bar failure
D-R11-45(T)	492	907	833	1101	609	672	Curved-bar failure
D-R11-45(B)	462	822	765	1012	551	610	Curved-bar failure

Specimen ID	θ_c (°)	θ (°)	θ^* (°)	$2w_r$ (in.)	$2w_l$ (in.)	$2w_c$ (in.)	$2w_s$ (in.)
A-R6-45	44.1	41.0	56.7	4.2	6.4	7.6	7.5
A-R11-45	42.1	37.9	65.9	5.6	12.6	13.4	13.1
A-R9-45	42.7	39.6	67.0	4.2	9.9	10.3	10.1
B-R6-30	27.9	25.4	57.1	4.2	6.5	7.7	7.7
B-R11-30	29.8	23.9	33.7	9.9	6.6	10.0	10.6
C-R6-60	28.8	26.2	55.2	4.2	6.1	7.3	7.3
C-R11-60	24.7	22.4	71.5	4.2	12.6	13.2	13.2
D-R11-45(T)	42.2	36.2	68.0	5.6	13.8	14.4	13.9
D-R11-45(B)	42.1	37.1	70.1	4.9	13.6	13.8	13.4

ACI parameters

Specimen ID	P_{STM} (kip)	BC (kip)	AC (kip)	CC' (kip)	BB' (kip)	BA (kip)	Failure Mode
A-R6-45	308	490	465	651	343	349	Curved-bar failure
A-R11-45	511	876	820	1107	596	642	Flexural Failure
A-R9-45	369	606	578	781	412	445	Curved-bar failure
B-R6-30	225	526	514	476	251	462	Curved-bar failure
B-R11-30	280	707	675	630	350	614	Flexural Failure
C-R6-60	196	451	440	414	218	394	Curved-bar failure
C-R11-60	301	796	782	636	336	722	Curved-bar failure
D-R11-45(T)	497	907	829	1116	619	663	Curved-bar failure
D-R11-45(B)	464	822	763	1019	555	606	Curved-bar failure

Specimen ID	θ_c (°)	θ (°)	θ^* (°)	$2w_r$ (in.)	$2w_l$ (in.)	$2w_c$ (in.)	$2w_s$ (in.)
A-R6-45	44.5	41.3	52.8	4.2	5.5	6.9	6.9
A-R11-45	42.9	38.5	61.7	5.9	11.0	12.3	12.1
A-R9-45	42.8	39.7	66.2	4.2	9.5	10.0	9.8
B-R6-30	28.5	26.0	52.3	4.2	5.4	6.7	6.8
B-R11-30	29.7	24.5	35.1	8.5	6.0	9.0	9.4
C-R6-60	29.0	26.4	53.5	4.2	5.7	7.0	7.0
C-R11-60	24.9	22.6	70.9	4.2	12.1	12.8	12.8
D-R11-45(T)	43.0	36.9	64.8	5.7	12.2	13.2	12.8
D-R11-45(B)	42.5	37.5	68.6	5.0	12.8	13.2	12.8

A-2 Simplified Sizing Method

AASHTO parameters

Specimen ID	P_{STM} (kip)	BC (kip)	AC (kip)	CC' (kip)	BB' (kip)	BA (kip)	Failure Mode
A-R6-45	302	490	459	648	346	346	Curved-bar failure
A-R11-45	498	908	812	1140	642	642	Flexural Failure
A-R9-45	356	606	557	784	429	429	Curved-bar failure
B-R6-25	217	526	504	483	265	454	Curved-bar failure
B-R11-25	272	711	671	630	359	614	Flexural Failure
C-R6-60	199	451	305	586	387	231	Curved-bar failure
C-R11-60	309	796	512	992	683	408	Curved-bar failure
D-R11-45(T)	468	907	787	1119	650	633	Curved-bar failure
D-R11-45(B)	438	822	721	1027	589	573	Curved-bar failure

Specimen ID	θ_c (°)	θ (°)	θ^* (°)	$2w_r$ (in.)	$2w_l$ (in.)	$2w_c$ (in.)	$2w_s$ (in.)
A-R6-45	45.0	41.0	45.0	5.3	5.3	7.5	7.5
A-R11-45	45.0	37.8	45.0	9.8	9.8	13.7	13.8
A-R9-45	45.0	39.7	45.0	7.2	7.2	10.1	10.1
B-R6-25	30.3	25.6	30.3	7.7	4.5	7.4	7.8
B-R11-25	30.3	23.9	30.3	10.7	6.2	10.0	10.8
C-R6-60	59.1	40.7	59.1	4.3	7.1	8.2	7.3
C-R11-60	59.1	37.1	59.1	7.7	12.9	14.9	13.2
D-R11-45(T)	45.8	36.5	45.8	9.7	10.0	13.8	13.9
D-R11-45(B)	45.8	37.4	45.8	9.3	9.6	13.3	13.4

ACI parameters

Specimen ID	P_{STM} (kip)	BC (kip)	AC (kip)	CC' (kip)	BB' (kip)	BA (kip)	Failure Mode
A-R6-45	305	490	461	651	346	346	Curved-bar failure
A-R11-45	509	908	820	1151	642	642	Flexural Failure
A-R9-45	358	606	558	786	429	429	Curved-bar failure
B-R6-25	223	526	506	488	265	454	Curved-bar failure
B-R11-25	280	711	675	639	359	614	Flexural Failure
C-R6-60	199	451	305	586	387	231	Curved-bar failure
C-R11-60	312	796	514	995	683	408	Curved-bar failure
D-R11-45(T)	479	907	793	1129	650	633	Curved-bar failure
D-R11-45(B)	443	822	724	1032	589	573	Curved-bar failure

Specimen ID	θ_c (°)	θ (°)	θ^* (°)	$2w_r$ (in.)	$2w_l$ (in.)	$2w_c$ (in.)	$2w_s$ (in.)
A-R6-45	45.0	41.4	45.0	4.9	4.9	6.9	6.9
A-R11-45	45.0	38.4	45.0	8.9	8.9	12.5	12.6
A-R9-45	45.0	39.8	45.0	7.0	7.0	9.8	9.8
B-R6-25	30.3	26.1	30.3	6.8	4.0	6.5	6.8
B-R11-25	30.3	24.5	30.3	9.5	5.6	9.0	9.6
C-R6-60	59.1	40.7	59.1	4.2	7.0	8.1	7.2
C-R11-60	59.1	37.4	59.1	7.4	12.5	14.4	12.8
D-R11-45(T)	45.8	37.1	45.8	8.9	9.2	12.7	12.8
D-R11-45(B)	45.8	37.7	45.8	8.9	9.2	12.7	12.8

Appendix B. Analysis Example using the STM

Appendix B contains a sample calculation of how all estimated capacities were found through STM per AASHTO LRFD 2020 provisions. It also highlights how V_{test} , shear capacity, was calculated per specimen. The sample calculation follows Specimen III-1.85-03b-v(ii), otherwise denoted at III-1.85-03b-(ii)v throughout this thesis.

B-1. Geometries of Strut-and-Tie Model

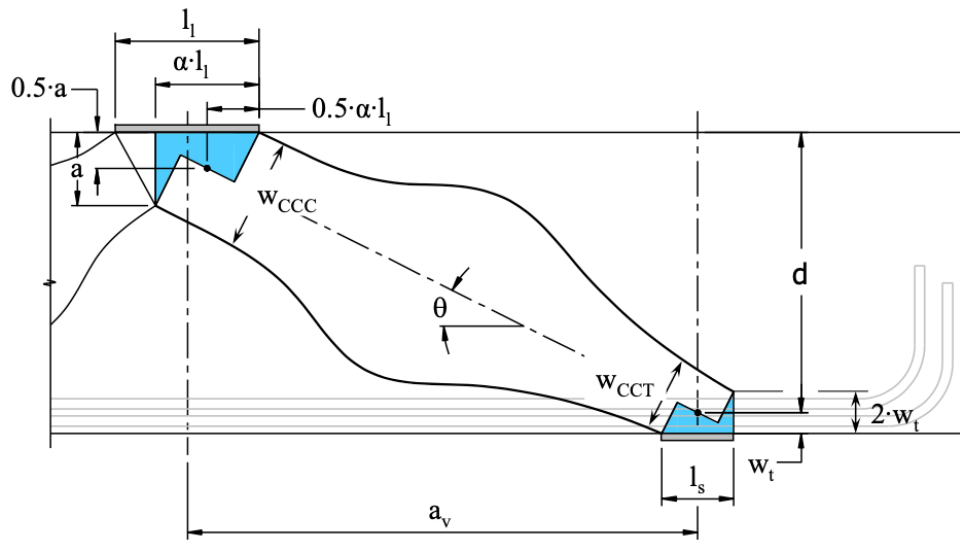


Figure B-7-1 Truss model and variables (Tuchscherer et al. 2008)

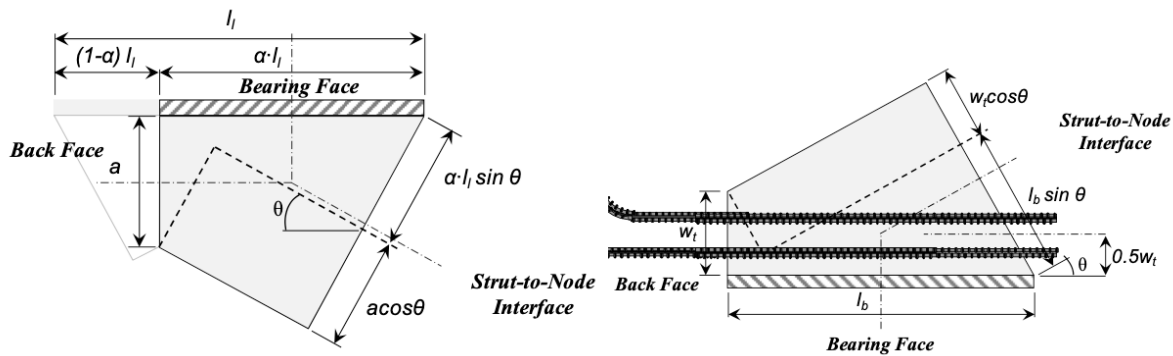


Figure B-7-2 CCC and CCT nodes and variables (Tuchscherer et al. 2008)

The variables are as such and calculated for III-1.85-03b-v(ii) below.

α = portion of the load that is actually taken to the support

$$\alpha = \mathbf{0.72 \text{ for B1 Test 1}}$$

a = length of back face for CCC node in a rectangular beam, in

$$a = \left(\frac{A_s f_s - A'_s f'_s}{0.85 f'_c b_w} \right) = \left(\frac{(18.73 \text{ in}^2 \cdot 66500 \text{ psi}) - (9.37 \text{ in}^2 \cdot 66500 \text{ psi})}{0.85 \cdot 4668 \text{ psi} \cdot 21 \text{ in}} \right) \\ = \mathbf{7.48 \text{ in for B1 Test 2}}$$

A_s = area of reinforcement on the tension side of the beam, in.²

A'_s = area of reinforcement on the compression side of the beam, in.²

f_s = yield stress of reinforcement on tension side of beam, psi

f'_s = yield stress of reinforcement on compression side of beam, psi

f'_c = compressive strength of concrete, psi

θ = angle of the strut relative to the horizontal axis, degrees

$$\theta = \tan^{-1} \left(\frac{d - a/2}{a_v} \right) = \tan^{-1} \left(\frac{38.6 \text{ in.} - 7.48 \text{ in.}/2}{71.41 \text{ in.}} \right) = \mathbf{26.02^\circ \text{ for B1 Test 2}}$$

d = effective depth of the rectangular section, in.

a_v = shear span of the D-region, in.

When calculating the strut angle, θ , a_v is used as an approximation. However, for full accuracy a_v should be replaced with $a_v - l_l - (0.5 \cdot \alpha \cdot l_l)$. This is not done here to replicate the process of Project 0-5253 and the approximations they made.

w_t = length of backface of CCT node in a rectangular beam, in.

$$w_t = 2 \cdot (h - d) = 2 \cdot (42 \text{ in} - 38.6 \text{ in}) = \mathbf{6.8 \text{ in for B1 Test 2}}$$

h = height of specimen, in.

W_{CCC} = width of strut at the CCC node, in.

$$W_{CCC} = (\alpha \cdot l_t \sin \theta) + (a \cdot \cos \theta) = (0.72 \cdot 21 \text{ in} \cdot \sin(26.02^\circ)) + (7.48 \text{ in} \cdot \cos(26.02^\circ))$$

$$= \mathbf{12.43 \text{ in for B1 Test 2}}$$

l_t = the length of the loading plate, in.

W_{CCT} = width of strut at the CCT node, in.

$$W_{CCT} = (l_s \cdot \sin \theta) + (w_t \cdot \cos \theta) = (16 \text{ in} \cdot \sin(26.02^\circ)) + (6.8 \text{ in} \cdot \cos(26.02^\circ))$$

$$= \mathbf{13.82 \text{ in for B1 Test 2}}$$

l_s = the length of the support plate, in.

B-2. Estimated Capacities per AASHTO LRFD 2020

Calculated the nodal capacities at the necessary faces per AASHTO LRFD provisions. CCT back face is not calculated since it will not control. The tie capacity is also calculated. Once the capacity is calculated, the applied and is then back calculated. The lowest applied load will determine with STM element governs failure and which capacity will be used to calculate V_{STM_Calc} that is used to compare to V_{test} from experimental data.

Tie Capacity - AASHTO LRFD Eq. 5.8.2.4.1-1

$$P_{tie} = f_y \cdot A_{st} = 66.5 \text{ ksi} \cdot 12 \cdot 1.48 \text{ in}^2 = 1181.04 \text{ kips}$$

Tie Back Calculation – Applied Load at CCC Node at Expected Capacity

$$P = \frac{P_{tie} \cdot \tan(\theta)}{\alpha} = 1 \frac{1181.04 \text{ kips} \cdot \tan(26.02^\circ)}{0.72} = \mathbf{800.53 \text{ kips}}$$

CCC Node/Strut Interface Capacity - AASHTO LRFD Eq. 5.8.2.5-1 and 5.8.2.5.3

$$P_{CCC,Strut} = m \cdot v \cdot f'_c \cdot A_{cn} = m \cdot \left(0.85 - \frac{f'_c}{20 \text{ ksi}}\right) \cdot f'_c \cdot W_{CCC} \cdot b_w = 1 \cdot \left(0.85 - \frac{4.668 \text{ ksi}}{20 \text{ ksi}}\right) \cdot$$

$$4668 \text{ psi} \cdot 12.43 \text{ in} \cdot 21 \text{ in} = 751.32 \text{ kips}$$

CCC Node/Strut Interface Capacity – Applied Load at CCC Node at Expected Capacity

$$P = \frac{(P_{CCC,Strut} \cdot \sin(\theta))}{\alpha} = \frac{(751.32 \text{ kips} \cdot \sin(26.02))}{0.72} = \mathbf{457.64 \text{ kips}}$$

CCC Node/Back Face Capacity - AAHSTO LRFD Eq. 5.8.2.5-1 and 5.8.2.5.3

$$P_{CCC,Back} = m \cdot v \cdot f'_c \cdot A_{cn} + f_y \cdot A_s = m \cdot (0.85) \cdot f'_c \cdot a \cdot b_w + f_y \cdot A_s = 1 \cdot (0.85) \cdot 4668 \text{ psi} \cdot 7.48 \text{ in} \cdot 21 \text{ in} + 9.36 \text{ in}^2 \cdot 66.5 \text{ ksi} = 1246 \text{ kips}$$

CCC Node/Back Face Capacity – Applied Load at CCC Node at Expected Capacity

$$P = \frac{(P_{CCC,Back} \cdot \tan(\theta))}{\alpha} = \frac{(623.02 \text{ kips} \cdot \tan(26.02))}{0.72} = \mathbf{845 \text{ kips}}$$

AASHTO LRFD BDS Section 5.8.2.5 suggests non-prestressed reinforcement can be considered to have augmentation to the capacity calculation for the back face of CCC nodes.

CCC Node/Bearing Face Capacity - AAHSTO LRFD Eq. 5.8.2.5-1 and 5.8.2.5.3

$$P_{CCC,Bearing} = m \cdot v \cdot f'_c \cdot A_{cn} = m \cdot (0.85) \cdot f'_c \cdot l_l \cdot b_w = 1 \cdot (0.85) \cdot 4668 \text{ psi} \cdot 20 \text{ in} \cdot 21 \text{ in} = 1333.18 \text{ kips}$$

CCC Node/Bearing Face Capacity – Applied Load at CCC Node at Expected Capacity

$$P = \frac{(P_{CCC,Bearing})}{\alpha} = \frac{(1333.18 \text{ kips})}{0.72} = \mathbf{1877.72 \text{ kips}}$$

CCT Node/Strut Interface Capacity - AAHSTO LRFD Eq. 5.8.2.5-1 and 5.8.2.5.3

$$P_{CCT,Strut} = m \cdot v \cdot f'_c \cdot A_{cn} = m \cdot \left(0.85 - \frac{f'_c}{20 \text{ ksi}}\right) \cdot f'_c \cdot W_{CCT} \cdot b_w = 1 \cdot \left(0.85 - \frac{4.668 \text{ ksi}}{20 \text{ ksi}}\right) \cdot 4668 \text{ psi} \cdot 13.82 \text{ in} \cdot 21 \text{ in} = 835.79 \text{ kips}$$

CCT Node/Strut Interface Capacity – Applied Load at CCC Node at Expected Capacity

$$P = \frac{(P_{CCT,Strut} \cdot \sin(\theta))}{\alpha} = \frac{(835.29 \text{ kips} \cdot \sin(26.02))}{0.72} = \mathbf{508.78 \text{ kips}}$$

CCT Node/Bearing Face Capacity - AAHSTO LRFD Eq. 5.8.2.5-1 and 5.8.2.5.3

$$P_{CCT.Bearing} = m \cdot v \cdot f'_c \cdot A_{cn} = m \cdot (0.85) \cdot f'_c \cdot l_s \cdot b_w = 1 \cdot (0.85) \cdot 4668 \text{ psi} \cdot 16 \text{ in.} \cdot 21 \text{ in} = 1097.91 \text{ kips}$$

CCT Node/Bearing Face Capacity – Applied Load at CCC Node at Expected Capacity

$$P = \frac{(P_{CCT.Bearing})}{\alpha} = \frac{(1097.91 \text{ kips})}{0.72} = \mathbf{1524.38 \text{ kips}}$$

Based on the calculation above the Node/Strut Interface Capacity is the failure mode that will govern.

B-3. V_{test} and V_{STM_Calc} Sample Calculation

The calculation of V_{test} was based on experimental results. The calculation of V_{STM_Calc} is a similar equation, however, statics is used to back calculate the reaction load at the support plate.

V_{test} Calculation for III-1.85-03b-v(ii)

$$V_{test} = \omega_{DL} \cdot \left(L_H + \frac{a_v}{2} \right) + R_A + P_{TR} = 0.96 \frac{\text{kip}}{\text{ft}} \cdot \frac{\left(33 \text{ in.} + \frac{71.41 \text{ in.}}{2} \right) \left(\frac{1}{12} \right) \text{ ft}}{\text{in.}} + 599 \text{ kips} + 7.8 \text{ kips} = \mathbf{612.07 \text{ kips}}$$

V_{STM_Calc} Calculation for III-1.85-03b-v(ii)

$$V_{STM_Calc} = \omega_{DL} \cdot \left(L_H + \frac{a_v}{2} \right) + \alpha P_{CCC,Back} + P_{TR} = 0.96 \frac{\text{kip}}{\text{ft}} \cdot \frac{\left(33 \text{ in.} + \frac{71.41 \text{ in.}}{2} \right) \left(\frac{1}{12} \right) \text{ ft}}{\text{in.}} + (457.64 \text{ kips} \cdot 0.72) + 7.8 \text{ kips} = \mathbf{342.68 \text{ kips}}$$

Appendix C. Proposed Changes to AASHTO LRFD (2008)

Bridge Design Specification

5.8.2.2—Structural Modeling

The structure, and a component or region thereof, may be modeled as an assembly of steel ties and concrete struts interconnected at nodes to form a truss capable of carrying all the applied loads to the supports. As illustrated in Figure 5.8.2.2-1, nodes may be characterized as:

- CCC: nodes where only struts intersect
- CCT: nodes where a tie intersects the node in only one direction
- CTT: nodes where ties intersect in two different directions
- Curved-bar: nodes formed by the bend region of a continuous reinforcing bar (or bars) where two ties extending from the bend region are intersected by a strut or the resultant of two or more struts. The bar bend should be specified to be 90-degree.

The angle between the axes of a strut and tie should be limited to angles greater than 25 degrees.

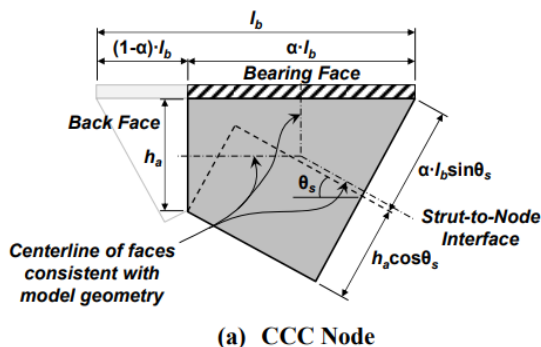


Figure 5.8.2.2-1—Nodal Geometries

C5.8.2.2

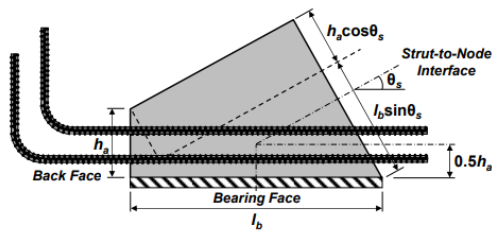
Cracked reinforced concrete carries load principally by compressive stresses in the concrete and tensile stresses in the reinforcement. The principal compressive stress trajectories in the concrete can be approximated by straight struts. Ties are used to model the primary reinforcement.

The following general guidelines for model development should be considered:

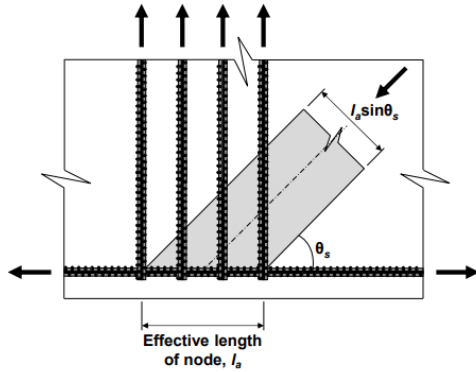
- At the interface of a B-Region and a D-Region, ensure the internal forces and moment within the B-Region are applied correctly to the D-Region.
- A tie must be located at the centroid of the reinforcement that carries the tensile force.
- Minimize the number of vertical ties between a load and a support using the least number of truss panels possible while still satisfying the 25-degree minimum, as shown in Figure C5.8.2.2-3.
- The strut-and-tie model must be in external and internal equilibrium.
- Ensure proper reinforcement detailing.

The angular limits are provided in order to mitigate wide crack openings and excessive strain in the reinforcement. When the angular limit cannot be satisfied, the truss configuration should be altered as appropriate. Where a strut passes through a cold joint in the member, the joint should be investigated to determine that it has sufficient shear-friction capacity. If a D-Region is built in stages, forces imposed by each stage of construction on previously completed portions of the structure must be carried through appropriate strut-and-tie models.

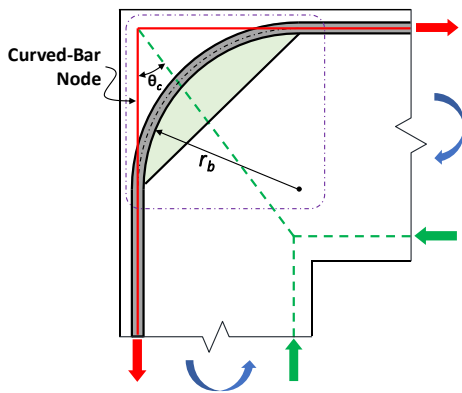
The concept of curved-bar nodes is discussed in the literature (Klein 2008, Wang et al. 2020, Wang et al. 2022, and Wang et al. 2022). Curved-bar nodes resulting from bending larger bars such as No. 11 are



(b) CCT Node



(c) CTT Node



(d) Curved-bar Node

- h_a = length of the back face of an STM node (in.)
 l_a = effective length of a CTT node (in.)
 l_b = length of the bearing face (in.)
 α = fraction defining the bearing face length of a portion of a nodal region
 θ_s = angle between strut and longitudinal axis of the member (degrees)
 r_b = bend radius at the inside of the bar (or bars) of a curved-bar node. (in.)
 θ_c = the smaller of the two angles between the axis of the strut (or the resultant of two or more struts) and the ties extending from a curved-bar node

discussed and experimentally investigated (Williams et al., 2012 and Wang et al. 2023). Bend regions with a bend other than 90-degree, or ties anchored by a 180-degree bend are considered in ACI 318-19. However, these two types are not included in the specification as it is not as well vetted by experimental data.

Figure 5.8.2.2-1 (continued)—Nodal Geometries

5.8.2.5—Proportioning of Node Regions

5.8.2.5.3—Limiting Compressive Stress at the Node Face

5.8.2.5.3a—General

Unless confinement reinforcement is provided and its effect is supported by analysis or experimentation, the limiting compressive stress at the node face, f_{cu} , shall be taken as:

$$f_{cu} = mvf'_c \quad (5.8.2.5.3a-1)$$

where:

m = confinement modification factor, taken as $\sqrt{A_2/A_1}$ but not more than 2.0 as defined in Article 5.6.5,

where:

A_1 = area under the bearing device (in.²)

A_2 = notional area specified in Article 5.6.5 (in.²)

v = concrete efficiency factor:

- 0.45 for structures that do not contain crack control reinforcement as specified in Article 5.8.2.6
- as shown in Table 5.8.2.5.3a-1 for structures with crack control reinforcement as specified in Article 5.8.2.6

f'_c = compressive strength of concrete for use in design (ksi) In addition to satisfying strength criteria, the node regions shall be designed to comply with the stress and anchorage limits specified in Articles 5.8.2.4.1 and 5.8.2.4.2

If appropriate confinement reinforcement is provided and if the specified compressive strength of concrete is not higher than 4.0 ksi, the limiting compressive stress at the node face determined per Eq. 5.8.2.5.3a-1 may be increased by 10%. Confinement reinforcement is considered appropriate if

- both nodes of the strut in consideration are provided with a reinforcement ratio of 1.0% in the vertical and the horizontal directions, and

C5.8.2.5.3a

Concrete efficiency factors have been selected based on simplicity in application, compatibility with other sections of the specifications, compatibility with tests of D-Regions, and compatibility with other provisions. Eq. 5.8.2.5.3a-1 is valid for design concrete compressive strengths up to 15.0 ksi and therefore stress-block factors, k_c and α_1 , for high-strength concrete need not be applied to this equation. The efficiency factors specified herein were derived for nonhydrostatic nodes and are shown graphically in Figure C5.8.2.5.3a-1.

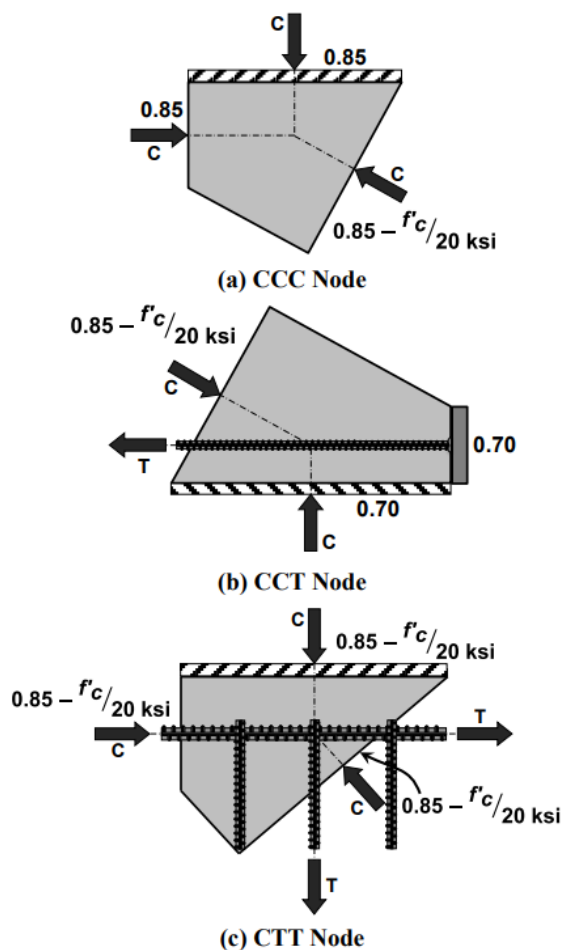


Figure C5.8.2.5.3a-1—Depiction of Efficiency Factors

- Vertical confinement reinforcement, which may be in a form of stirrups, is distributed across the extended nodal zone; horizontal confinement reinforcement is distributed at least over a height twice the height of the back face.
- Confinement reinforcement should be fully developed. The critical section may be taken along the centerline of the strut.

5.8.2.5.3c

Curved-bar nodes shall be designed and detailed in accordance with the following requirements:

- The bend radius of the bar bend shall satisfy Eq. 5.8.2.5.3c-1 but shall not be less than half the minimum diameter specified in Article 5.10.2.3.

$$r_b \geq \frac{A_{ts}f_y}{b_s v f'_c} \psi_c \quad (5.8.2.5.3c-1)$$

where:

A_{ts} = the area of non-prestressed bars in the tie;

f_y = the yield strength of the bars;

b_s = the width of the diagonal strut (or resultant struts) framing into the curved-bar node;

v = the efficiency factor for curved-bar node, taken as 0.5

f'_c = the compressive strength of concrete;

ψ_c = cover factor, taken as the greater of $2d_b/c_c$ and 1.0

where:

○ d_b is the bar diameter;

○ c_c is clear cover to the side face.

- If multiple layers of longitudinal reinforcing bars are used, the bend radius of the bar bend of every layer should be the same and satisfy Eq. 5.8.2.5.3c-1.

An experimental investigation (Wang et al. 2023) reveals that providing appropriate confinement reinforcement to both end nodes of a strut results in a reduction in crack width and an increase in the overall strength of the strut by 10%.

The increase in the strength of struts due to confinement for compressive strength of concrete higher than 4.0 ksi lacks support by test data. In addition, the effect of confinement reinforcement through the thickness for nodal zones is not yet supported by experiments.

C5.8.2.5.3c

The purpose of Eq. 5.8.2.5.3c-1 is to avoid overstressing concrete within the bar bend region of a curved-bar node (Klein 2008, Wang et al. 2020). The equation applies to curved-bar nodes proportioned with multiple layers of reinforcement and with different tie forces (Wang et al. 2022 and Wang et al. 2023). Studies (Wang et al. 2022 and Wang et al. 2023) have shown that the equation addressing circumferential bond stresses provided in the literature (Klein 2008) along the bar bend can be overly conservative.

The cover factor ψ_c is intended to prevent the splitting of side concrete near the bar bend. A study (Wang et al. 2023) also has shown that bundled bars plausibly exert stress concentration near the side cover. For both cases, a further enlarged bend radius is required.

- If bundled bars are used, the bend radius per Eq. 5.8.2.5.3c-1 should be further enlarged by a factor of 1.28.
- Struts framing into the curved-bar node should be reinforced with appropriate orthogonal crack control reinforcement in accordance with Article 5.8.2.6.

5.8.2.6—Crack Control Reinforcement

Structures and components or regions thereof, except for slabs and footings, which have been designed using the efficiency factor of Table 5.8.2.5.3a-1, shall contain orthogonal grids of bonded reinforcement. The spacing of the bars in these grids shall not exceed the smaller of $d/4$ and $d/2$ and 24.0 in. The reinforcement in the vertical direction shall satisfy the following:

$$\frac{A_v}{b_w s_v} \geq 0.003 \quad (5.8.2.6-1)$$

and the reinforcement in the horizontal direction shall satisfy the following:

$$\frac{A_h}{b_w s_h} \geq 0.003 \quad (5.8.2.6-1)$$

where:

- A_v = total area of vertical crack control reinforcement within spacing s_v (in.²)
 b_w = width of member's web (in.)
 s_v, s_h = spacing of vertical and horizontal crack control reinforcement, respectively (in.)
 A_h = total area of horizontal crack control reinforcement within spacing s_h (in.²)

Where provided, crack control reinforcement shall be distributed evenly near the side faces of the strut. Where necessary, interior layers of crack control reinforcement may be used.

C5.8.2.6

This reinforcement is intended to control the width of cracks and to ensure a minimum ductility for the member so that, if required, significant redistribution of internal stresses is possible. This behavior is consistent with the plasticity basis of STM as discussed in Article C5.5.1.2.3.

The total horizontal reinforcement can be calculated as 0.003 times the effective area of the strut denoted by the shaded portion of the cross section in Figure C5.8.2.6-1. Crack-control reinforcement is intended to provide restraint for the spread of compression present in a bottle-shaped strut. It does not serve as the primary tie shown in Figure C5.8.2.6-1. For thinner members, this crack control reinforcement will consist of two grids of reinforcement, one near each face. For thicker members, multiple grids of reinforcement through the thickness may be required in order to achieve a practical layout. Further discussion on the distribution of shear reinforcement through the thickness of thin and thick members can be found in Article C5.8.2.5.2.

An investigation of the effect of various amounts of crack control reinforcement indicated that beyond a reinforcement ratio corresponding to 0.003 times the effective area of the strut there continued to be a reduction of crack widths, but the efficacy of the increasing steel reached a point of diminishing returns. Specimens tested by Birrcher et al. (2009) and Larson et al. (2013) showed that the width of the first diagonal crack forming in a deep beam was unacceptably large (i.e. greater than 0.016 in.) if crack control

reinforcement provided in that specimen was less than 0.003 times the effective area of the strut.

A study (Wang et al. 2023) has shown that requirements for the spacings of crack control reinforcement in both the horizontal and vertical directions may be relaxed to the smaller of $d/2$ and 24.0 in. without compromising the conservatism of the STM.

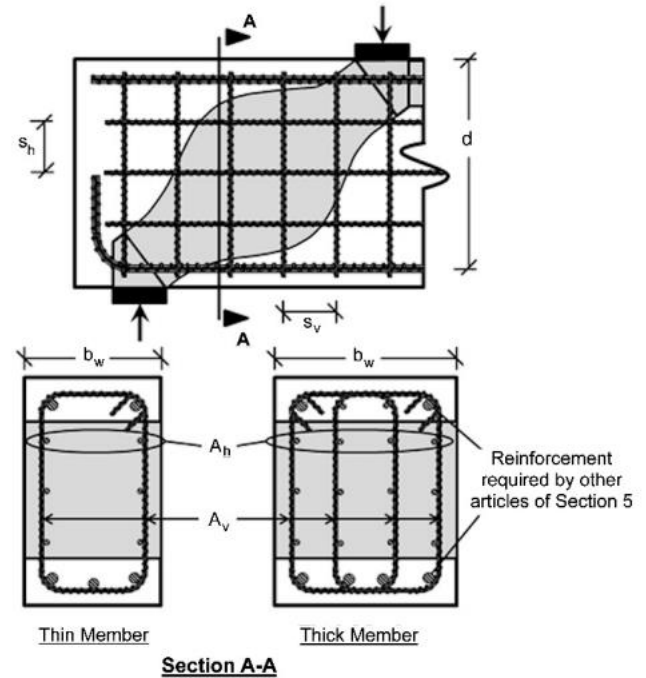


Figure C5.8.2.6-1—Distribution of Crack Control Reinforcement in Struts